CONTAMINANT FREEZE-OUT IN HEAT EXCHANGERS

VOLUME II - BASIC INVESTIGATION OF CONTAMINANT FREEZE-OUT

TECHNICAL REPORT NO. ASD-TDR-63-508, VOLUME II

JULY 1963

RAM-JET DIVISION
AIR FORCE AERO-PROPULSION LABORATORY
AERONAUTICAL SYSTEMS DIVISION
AIR FORCE SYSTEMS COMMAND
WRIGHT-PATTERSON AIR FORCE BASE, OHIO

PROJECT NO. 3084, TASK NO. 308404

PREPARED UNDER CONTRACT NO. AF 33(657)-8695
BY ARTHUR D. LITTLE, INC., CAMBRIDGE, MASSACHUSETTS

BY THE FOLLOWING AUTHORS:

R. B. HINCKLEY
J. C. BURKE
F. E. RUCCIA
R. P. BERTHIAUME
R. C. REID
E. M. DRAKE
I. W. DINGWELL
M. E. WEBER

NOTICES

When Government drawings, specifications, or other data are used for any purpose other than in connection with a definitely related Government procurement operation, the United States Government thereby incurs no responsibility nor any obligation whatsoever; and the fact that the Government may have formulated, furnished, or in any way supplied the said drawings, specifications, or other data, is not to be regarded by implication or otherwise as in any manner licensing the holder or any other person or corporation, or conveying any rights or permission to manufacture, use, or sell any patented invention that may in any way be related thereto.

Qualified requesters may obtain copies of this report from the Armed Services Technical Information Agency, (ASTIA), Arlington Hall Station, Arlington 12, Virginia.

This report has been released to the Office of Technical Services, U.S. Department of Commerce, Washington 25, D.C., for sale to the general public.

Copies of this report should not be returned to the Aeronautical Systems Division unless return is required by security considerations, contractual obligations, or notice on a specific document.

FOREWORD

This report was prepared by Arthur D. Little, Inc., Cambridge, Massachusetts, under Air Force Contract No. AF 33(657)-8695, under Task No. 308404 of Project No. 3084, "Propulsion Fluid and Heat Transfer Sub-systems". The work was administered under the direction of the Ram-Jet Division, Air Force Aero-Propulsion Laboratory, Aeronautical Systems Division; Mr. D. H. Mudd was project engineer for the Ram-Jet Division.

The work covered in this report began in April 1962 and was concluded in June 1963. Mr. R. B. Hinckley was the program director at Arthur D. Little, Inc., responsible for this activity.

The chief areas of interest of the other authors were: J. C. Burke, report preparation, data correlation and "hand calculation" solutions; F. E. Ruccia, design, construction and operation of the experimental facility; R. P. Berthiaume, design and fabrication of the test heat exchanger; R. C. Reid, analyses of deposition mechanisms and frost properties; E. M. Drake, mass transfer analysis; I. W. Dingwell, variable heat transfer computer program; and M. E. Weber, constant heat transfer computer program.

In addition to the authors mentioned on the title page, several other individuals performed significant contributions to this program. Acknowledgement should be made to James Franklin, Raymond McMillen and David Coombs for their efforts in construction and operation of the test facility; to Walter Liebfried and John Burke for the construction and instrumentation of the test heat exchangers; to Henry Survilas and Charles Hansen for the photographic aspects of the test program; and to Robert Gallagher for his assistance in programming the variable heat transfer computer solutions.

This report is the final report and it concludes the work on Contract No. AF 33(657)-8695.

ABSTRACT

We have conducted an analytical and experimental study to investigate the principal mechanisms of water and carbon dioxide freeze-out and to develop a method for predicting the effects of contaminant freeze-out on heat exchanger performance. This program has included an analytical study of the various mechanisms by which contaminant freeze-out may occur. A test facility was constructed having the capability of simulating a wide range of air stream pressures, temperatures, mass flow, and concentration conditions. A glass-walled test heat transfer section allowed visual and photographic observations of the frost formation as well as measurements of its effects on heat transfer and pressure drop. Based on the analytical and experimental results, the importance of the various mechanisms of contaminant freeze-out has been evaluated and a method generated for predicting the effect of contaminant freeze-out on heat exchanger performance.

TABLE OF CONTENTS

LIST OF FIGURES

LIST OF SYMBOLS

A	-	flow area
A_N	-	area density
A_S	-	total heat exchanger surface area
C_p	-	specific heat
D	-	tube diameter
f''	-	friction factor
h	-	carrier stream film coefficient
K	-	Boltzmann's constant
k	-	thermal conductivity
L	-	heat exchanger total length
m	-	cosine of contact angle
N_N	-	number density
ΔP	-	pressure drop
R_c	-	radius of critical nuclei
S	-	saturation ratio
T	-	stream temperature
T_w	-	wall temperature
t	-	frost thickness
$\bar{t}$	-	mean frost thickness
u	-	carrier stream overall heat transfer coefficient
W	-	carrier stream flow
W_c	-	contaminant flow
x	-	radius ratio
X	-	heat exchanger frosted length
σ	-	surface tension
v	-	volume/molecule
δ	-	tube half-clearance
ρ	-	density
θ	-	time
μ	-	viscosity

SUBSCRIPTS

o	-	denotes zero-time condition
F	-	denotes frost property

LIST OF APPENDIXES

A. INTRODUCTION

Air consists of an invariable mixture of oxygen, nitrogen and other well-known constituents with variable concentrations of water vapor, carbon dioxide and other gases that may be considered contaminants. Whenever air is cooled to cryogenic temperatures, the freeze-out of water and carbon dioxide as frost will degrade heat exchanger performance unless some means is provided for their removal. The overall problem of contaminant freeze-out involves both the accumulation of frost and ice within the heat exchanger and the passage of these contaminants through the heat exchanger as solid particles in the exit stream. Deposits within the heat exchanger will tend to reduce the air stream free flow area and insulate the air stream from the cold surfaces. Contaminants passing through the heat exchanger as solid particles may cause plugging in downstream components.

In many cryogenic processes, such as the commercial production of oxygen, methods to circumvent the contaminant freeze-out problem have been employed sucessfully. Some plants rely largely on chemical methods for removing at least the carbon dioxide while some use additional chemicals for water removal. Other processes employ metal-packed accumulators or regenerators in which both carbon dioxide and water vapor are frozen out, subsequently to be re-evaporated by direct contact with dry exit gases. A later development to cope with the freeze-out problem employs reversing heat exchangers, in which the incoming air stream and the waste exit gases are at all times in thermal contact with each other. At periodic intervals, the air and waste exit gas swap channels and the waste gas removes the frost accumulation by evaporation.

Each of these systems, however, has certain inherent limitations, not the least of which is the size and weight of equipment. The reversing heat exchanger, for example, must have air and waste gas channels that are equal in heat transfer and flow areas to accomodate the low pressure waste gas during its passage through either channel.

The possible use of light weight, high performance heat exchangers for cryogenic processes involving air and its contaminants presently is under consideration. In such exchangers, tube spacing and overall size of equipment must be held to a practical minimum to achieve light weight. Degradation in performance due to flow area blockage by freeze-out, therefore, is especially severe.

Furthermore, weight and volume limitations may rule out most of the commercial techniques of contaminant removal. It is likely that new design approaches to the contaminant problem, closely molded to heat exchanger system requirements, will be necessary for high performance light weight heat exchangers. The development of these techniques will probably require accurate knowledge of the mechanisms of contaminant freeze-out and its effects on heat exchanger performance.

The objectives of the program discussed in this report have been to define the mechanisms of contaminant freeze-out and to develop methods for predicating the effect of contaminant freeze-out on heat exchanger performance.

**Manuscript released by author on July 30, 1963
for publication as an ASD Technical Documentary Report.**

B. SUMMARY

An analytical and experimental program to investigate the principle mechanisms of water and carbon dioxide freeze-out and to develop analytical methods for predicting the effects of contaminant deposition on heat exchanger performance, has been conducted.

A test facility was constructed incorporating a glass-walled test heat exchanger section to permit visual and photographic observation of frost formation together with measurments of the effect of the frost on heat transfer and pressure drop. Several parameters that might affect the deposition rate of contaminants, such as carrier stream pressure, flow rate, water and carbon dioxide content, coolant temperature and gas to wall temperature difference, were varied during these studies to permit evaluation of their contribution to the problem. Tube diameters and tube spacings in the test section were varied to investigate the effects of heat exchanger geometry. Nucleation of the contaminants in the inlet air stream was promoted to observe the effect of impingement of particles in the heat exchanger.

The majority of the tests were operated at constant carrier stream flow (i. e. increasing pressure drop); however, for comparison, a few tests were also conducted at constant pressure drop (i.e. decreasing flow).

In parallel with the experimental effort, analytical studies of the mechanisms of mass transfer and nucleation were conducted and the relative importance of these mechanisms compared. Analytical techniques were developed for estimating the density and thermal conductivity of water and carbon dioxide frost as deposited in heat exchangers. The basic effects of the area blockage and surface insulation caused by frost deposition on heat transfer and fluid flow relationships were defined. Calculation methods, involving both simplified "hand calculations" approximations and more rigorous digital computor solutions, were developed for predicting the effects of contaminant deposition on heat exchanger performance.

Based on the analytical and experimental results, the importance of the various mechanisms of freeze-out has been evaluated and a method generated to permit reasonable prediction of the effect of freeze-out on heat exchanger performance.

C. PREVIOUS STUDIES

Surprisingly few papers have been published in the area of heat transfer under frosting conditions and in all of these the only contaminant investigated was water. Kamei et al (12)* froze water out in a vertical pipe cooled with brine and measured the frost properties and decrease in the rate of heat transfer. Temperatures of the air in the range of 500-510°R and, in the brine coolant, near 437°R with air velocities near 20-40 ft/sec were studied. All the water froze out on the wall by combined eddy and diffusive mass transfer mechanism and the rates were in agreement with the usual mass transfer equations. Heat transfer rates were decreased as expected as an insulating frost layer built up. Almost dry air was used and with the small temperature differences between the air and wall, no gas phase nucleation or fogging was noted. A similar experiment was reported by Beatty et al (1) and Chan(3) although slightly higher coolant and air temperatures were employed. Prins (14) carried out some rough experiments wherein water frost was built up by blowing humid air across a bank of coolant tubes in which ammonia was vaporized. The quantitative

* Numbers in parenthesis refer to references on page 30.

data on rates of deposition and heat transfer reported are at best approximate but agreed with predicated estimates using mass and heat transfer equations suitable for crossflow exchangers. Three low temperature (circa 160°R) studies (10, 13, 16) were reported on liquid oxygen containers. Most of the frost formed by nucleation in the bulk vapor phase and some subsequently settled on the cold walls by a natural convection mechanism.

Probably the best work to date was reported by Chung and Algran (4). Humid air was blown over a cold tube at various angles and the rates of heat and mass transfer measured. Air temperatures near 530°R were employed and the test surface held at close to 460°R. The experiment appeared to be very well instrumented and the data again confirmed the usual mass and heat transfer rate equations. In addition to the experimental work, an analysis of the effect of frost in the rates of mass and heat transfer was presesented. Finally, Hall and Tsao (9) conducted a series of heat transfer experiments in the liquid nitrogen temperature range but with water-free(and carbon dioxide free) gas. Various pressures, gas temperatures, and flow velocities were studied and the typical Nusselt-Reynolds-Prandtl number relation verified.

In all but the very low temperature studies reviewed, the experiments exercised care to minimize any gas phase nucleation, i.e., the humidities and temperature differences were maintained low enough to prevent any appreciable gas phase supersaturation. The general conclusion reached is that under these conditions, the usual mass and heat transfer rate relations are valid--if the correct surface temperatures were used in these relations.

Useful background information on the mechanism of nucleation and on the properties of porous material such as frosts has appeared in the literature. The basic theory of nucleation has been discussed by many authors. The work by Courtney (5) constitutes a good review and extension of previous work. Theoretical studies on the relationship between density and thermal conductents for porous materials are presented by Woodside (20) and Gorring et al (8).

D. ANALYTICAL SURVEY OF THE MECHANISMS OF CONTAMINANT FREEZE-OUT

The separation of a condensible component from a gas stream being cooled by contact with cold walls may occur either by nucleation in the bulk stream or by mass transfer to the cold walls. The process of mass transfer results in direct condensation or freeze-out of the condensible vapor on the tube walls. If the bulk stream becomes saturated, nucleation is possible. Nucleation results in the formation of particles in the bulk stream which may subsequently be attached to the tube walls by impingement. In general terms, situations in which a "humid" stream is cooled rapidly with little surface contact tend to favor bulk stream nucleation; on the other hand, if a low relative humidity stream is cooled more slowly with an abundance of surface contact,mass transfer is the predominant mechanism. In the paragraphs below, the processes of mass transfer and nucleation will be discussed, and their relative importance evaluated.

1. Mass Transfer

When air containing water vapor or carbon dioxide is cooled as it flows through a heat exchanger, mass transfer to the walls will occur as soon as the wall temperature drops below the saturation temperature corresponding to the partial pressure of the impurity in the bulk stream. The driving force for mass transfer of a contaminant to the walls is the difference between the bulk gas concentration and the saturation concentration at the wall (or frost) - gas interface. The saturation concentration at the wall decreases exponentially with decreasing temperatures in accordance with the vapor pressure curve. For a process involving only mass transfer (i.e., no nucleation) the concentration in the bulk stream decreases in accordance with prior mass transfer. Typically, the frost distribution profile resulting from mass transfer in a heat exchanger has an airfoil shape. Proceeding downstream from the point of initial frosting (i.e., the point at which the wall temperature reaches saturation) the frost thickness increases to a maximum and then tapers off. The initial increase in frost thickness is due to the rapid decrease in wall saturation humidity at (near) constant bulk stream humidity; the subsequent decrease in frost thickness results from the more gradual decrease in bulk stream humidity.

The process of mass transfer is quite amenable to analysis. Mass transfer coefficients can be obtained as functions of stream conditions and surface geometry by various semi-empirical correlations similar to, and having approximately the same accuracy as, heat transfer correlations. Step-wise calculation of the mass transfer rates along a heat exchanger can be employed to determine both the frost distribution profile and the bulk stream contaminant concentration. Details of these calculation techniques are presented in Appendix No. 1. Such mass transfer calculation procedures are practical for hand calculations if a limited number of situations are to be explored. However, in general, machine computation tends to be more efficient if a wide range of variables is to be studied.

2. Nucleation

Should the bulk gas phase exceed saturation ratios of unity, there is the distinct possibility of bulk phase nucleation. If there are sufficient foreign nuclei in the gas (such as dust, salt fragments, etc.) then heterogeneous nucleation is probable and saturation ratios of only slightly greater than unity are attained. However, if the gas phase is relatively free of such foreign bodies, then nucleation will be more homogeneous in nature and values of saturation ratio greater than 5 or 10 for water, or 2 to 3 for carbon dioxide may be attained before any appreciable nucleation is achieved.

a. Homogeneous Nucleation

The mechanism of homogeneous nucleation has been discussed thoroughly in the literature (2, 5, 7, 15, 19) but it is still difficult to obtain a reliable value of the rate in any given situation. Generally, the theory indicates that the rate of formation of nuclei per cm^3-sec is given as:

$$\text{rate} = K_1 \exp - \frac{16}{3} \pi \frac{\sigma^3 v^2}{(KT)^3 (\ln S)^2} \qquad (1)$$

where K_1 is a constant in the range of 10^{21} to 10^{25}, σ is the surface tension of the nuclei, ergs/cm^2, v is the volume/molecule in the nuclei, cm^3/molecule, K is Boltzmann's constant, 1.38 x 10^{-16} ergs/molecule - ^oK, T the absolute temperature, ^oK, and S the saturation ratio. The rate of formation of nuclei is very sensitive to temperature and saturation level. It is generally assumed that an "appreciable" rate of nuclei formation occurs when 10^5 nuclei/cm^2-sec are formed. For water air mixtures such rates occur near S = 5 at 473^o R, S = 10 at 420^o R and S = 20 at 384^o R. Thus a cold gas with little water may be expected to sustain larger supersaturations before nucleating.

The actual nucleation process removes very little contaminant as each nuclei may contain less than 100 molecules. However, as the nuclei grow, they may rapidly deplete the gas stream and lower the saturation value to near unity. Courtney (5) has analyzed this growth process and calculated the rate of depletion for many typical cases assuming isothermal systems. The difficult problem to analyze, however, results from the competing mechanisms of growth and further nucleation for any gas stream which is being cooled. If cooling is rapid, then nucleation predominates and one finds enormous numbers of small particles. For slow cooling, the growth process limits further nucleation and large particles can be formed. At the present time, there is no adequate way to handle this general case analytically. The subject of homogeneous nucleation is treated in greater detail in Appendix No. 2.

b. Heterogeneous Nucleation

Heterogeneous nucleation has been analyzed by Fletcher (6) and the rate of formation of such nuclei is given by Equation (1) multiplied by the grouping:

$$A_N N_N \exp - \left[f(m,x) \right] \qquad (2)$$

where A_N and N_N are the areas and number density of the foreign nuclei and f(m,x) a function of m, the cos of the contact angle of contaminant deposited on the foreign nuclei, and x, the ratio of the radius of the foreign particle to the radius of a critical sized homogeneously formed nuclei R_c. R_c is given approximately as ($2\sigma v/kT\ln S$) where the terms have the same meaning as in Equation (1); typical values are very small, i.e., for water-air systems at 420^o R, if S = 10, $R_c \backsim 6$Å and if S = 1.1, $R_c \backsim 150$Å. Thus, for any reasonably sized foreign particles, x is very large and it may be shown that

$$f(m,x) = \frac{(2 + m)\ (1 - m^2)^2}{2} \qquad (3)$$

$$x \longrightarrow \infty$$

The most effective particle is one which has a contact angle approaching unity, i.e , m approaches unity, and f(m,x) approaches zero. This type of particle is completely wetted by the condensible component.

Although the theory of heterogeneous nucleation is well defined, it is not practicable to use the theory directly since values of m are not known. In fact, there is no general agreement as to what are "effective" nuclei to induce nucleation. Often materials which may be expected to be wettable are not effective nucleating agents (11, 15, 17, 18). About all one can conclude at the present time is that if effective nucleating particles are present, nucleation rates are rapid even for very low values of supersaturation and the resulting particles may grow to reasonable size. For a more detailed discussion of heterogeneous nucleation the reader is referred to Appendix No. 3.

c. Particle Impingement

Dynamic considerations determine whether particles formed in the bulk stream will impinge against a heat exchanger tube or be carried through in the gas stream. In general, large particles, having a relatively high ratio of inertia force to drag force will tend to impinge on the tubes. Small particles having relatively less inertia to drag will tend to be carried along by the air stream. The tendency of given size particles to impinge against a tube wall depends, of course, on flow velocity and heat exchanger geometry. However, "bracketing" calculations, based on nominal heat exchanger conditions, have indicated that particles less than 1 micron will not impinge on the tube walls to any significant extent. Particles greater than 100 microns, on the other hand, will be readily thrown out against the tube walls.

Under conditions such that particles form in the gas stream, the nucleation of additional small particles competes with the growth of particles previously formed. In general, high supersaturation ratios, or a large number of small foreign particles, favor the formation of a large number of small frost particles. Relatively low supersaturation ratios or a small number of large foreign particles favor the formation of a small number of relatively large particles. Calculations of growth rates (included in Appendix No. 2) indicate particle diameters will fall in the range of 1 to 100 microns for typical saturation ratios and residence times to be expected in heat exchangers. Hence, without detailed study of specific situations, which would be of somewhat marginal value in view of the basic limitations of nucleation theory, it is impossible to conclude whether nucleated particles will impinge or carry-through.

d. Liquid Nitrogen Injection

The injection of liquid nitrogen into a humid carrier stream provides a means of inducing homogeneous nucleation. Since the rates of cooling can be made extremely fast, this technique might be capable of producing particles small enough to pass through a heat exchanger without substantial impingement.

The results of an analytical investigation of liquid nitrogen injection, presented in Appendix No. 4, have indicated that the liquid nitrogen drop is the single most important variable governing particle size, as long as the liquid nitrogen

spray rate has adequate capacity to chill the carrier stream to high saturation ratios.

For liquid nitrogen drops originally with a diameter of $\sim$10 microns or less, the process may be characterized by the formation of enormous numbers of small nuclei and little subsequent growth; final ice particles are in the sub-micron range.

For liquid nitrogen drops originally with a diameter of $\sim$1000 microns or larger, the process is characterized by the formation of a few nuclei and rapid growth to particles with diameters of 40-80 microns.

For sprays in the intermediate size region, little can be said quantitatively as the process is too complex for easy analysis; a best estimate is that ice particles with diameters of 1 to 10 microns are formed.

The results of the analytical studies would indicate that with a high liquid nitrogen spray rate, and extremely small liquid nitrogen drop size, it might be possible to produce nucleated particles small enough to pass through a heat exchanger with little hold-up.

3. Relative Importance of Nucleation and Mass Transfer

The analytical difficulties in analyzing nucleation processes make it impossible to quantitatively define the effects of nucleation and mass transfer under all conditions. However, in many specific cases it is possible to determine which mechanism is predominant. For instance, when liquid nitrogen is injected into the inlet of a heat exchanger, at rates and drop sizes sufficient to result in saturation ratios much greater than unity, we can generally assume that most of the contaminant freeze-out will occur by nucleation. In the absence of liquid nitrogen injection, we can use mass transfer analysis as a tool to determine whether or not the bulk stream saturation can become high enough to make nucleation a possibility.

The temperature difference between the bulk stream and the cold tube walls is one important factor influencing the balance between mass transfer and nucleation. As previously noted, the driving force for mass transfer is the difference between the bulk gas concentration and the saturation concentration at the wall. The saturation concentration at the wall decreases exponentially with decreasing temperature and thus reaches a value near zero for very cold walls. Thus the rate of mass transfer is a weak function of wall temperature when the latter is considerably below the dew point. However, the temperature driving force causing bulk gas cooling and tending to increase bulk gas saturation is almost proportional to the gas-to-wall temperature difference over a wide temperature range. This qualitative reasoning leads one to the conclusion that if the wall temperature is maintained at or slightly below the dew point temperature of the gas (low gas-wall Δ T), most of the contaminant removal occurs by mass transfer to the walls. On the other hand, if the wall temperature is much below the dew

point (high gas-wall Δ T), then contaminant removal by mass transfer processes although increased somewhat, may be unimportant relative to the bulk phase nucleation caused by the rapid chilling of the gas.

The forementioned ideas may be illustrated by a typical example. Suppose a water-air gas mixture at 150 psia and 620° R were cooled by flowing down a tube 0.12-inch diameter at 100 ft/sec. The coolant tube temperature varies in such a way that the difference between gas and wall is held constant over the length of the exchanger. The inlet water concentration is 4320 ppm corresponding to a dew point of 560° R under this pressure. The gas phase saturation ratio is plotted as a function of bulk gas temperature in Figure 1. For a (T - Tw) = 2° R, the water begins to condense out at a gas stream temperature of 562° R and there is sufficient mass transfer that the gas phase never reaches a saturation level greater than unity even as cooling proceeds. A similar case holds even for (T - Tw) = 20° R. When (T - Tw) = 60° R, the water removal begins at a point where the gas phase is near 620° R and continues throughout the exchanger. However, for this large value of (T - Tw) there is a rapid cooling of the gas so that even though the water concentration is continually decreasing, the temperature is decreasing rapidly enough to cause a continual increase in the saturation ratio. When the gas temperature reaches about 490° R, the bulk gas phase becomes saturated and bulk phase nucleation is possible. The extension of the 60° curve beyond S = 1 has been made assuming no nucleation. In this case, over 90% of the water was removed before the bulk gas became saturated. Finally, the curve identified as (T - Tw) = ∞ indicates the limiting case of no mass transfer and, of course, the bulk gas becomes saturated at the dew point temperature of 560° R.

The initial relative humidity of the air stream entering a heat exchanger also has an important effect on the balance between nucleation and mass transfer. In Figure 1, at a gas-wall ΔT of 60° R, the bulk stream saturation ratio was progressively increasing. However, since the initial saturation ratio was quite low, over 90% of the contaminant had been removed by the time the bulk stream had reached saturation. It would appear reasonable that if the initial saturation ratio had been nearer to unity, the bulk stream would have reached saturation before such a large portion of the contaminant had been removed by mass transfer.

In Appendix No. 1, the relative importance of nucleation and mass transfer has been examined for water vapor over a range of gas-wall ΔT for two bracketing inlet saturation conditions:

(1) Saturated bulk gas-inlet wall temperature below dew point.

(2) Inlet wall temperature at (or above) dew point - inlet bulk gas unsaturated.

In this study, it was assumed that nucleation would occur as soon as the saturation ratio reached unity - and would continue at a rate sufficient to prevent the saturation ratio from exceeding unity. This assumption is reasonable if sufficient foreign particles are present to force heterogeneous nucleation. However, it will tend to overestimate nucleation in relatively particle free air. Typical results for an inlet water concentration of 4320 ppm are tabulated below:

Gas-Wall ΔT (^{o}R)	Per Cent Nulceation	
	Saturated Inlet Gas	Inlet Wall at Dew Point
0	0	0
40	0	0
60	25	3
100	42	7
200	75	14

These results indicate that for gas-wall ΔT below about 40^{o} R, water freeze-out is entirely by mass transfer regardless of inlet saturation. In the region 40^{o} R to 100^{o} R, mass transfer is generally the predominant mechanism, although for the case of saturated inlet gas and ideal nucleation conditions (i.e., sufficient foreign particles that heterogeneous nucleation limits the saturation ratio to unity) nucleation may become appreciable. At a gas-wall ΔT of 200^{o} R, nucleation may be predominant for a saturated inlet gas; however, for low inlet humidities mass transfer is still predominant.

The above discussion has been primarily concerned with water vapor. The basic trends are similar for carbon dioxide. However, in the case of carbon dioxide, it is extremely unlikely that the inlet gas would be saturated. It is felt that since the air will enter the heat exchanger well above the dew point of carbon dioxide the condition of the inlet wall temperature being at (or above) the dew point of carbon dioxide is quite realistic. Calculations performed on this basis indicate that no nucleation is possible below a gas-wall ΔT of about 15^{o} R; moreover, even at gas-wall ΔT as high as 200^{o} R, approximately 75% of the carbon dioxide is removed by mass transfer before nucleation can occur.

In summary, the analytical results indicate that mass transfer is the predominant mode of contaminant deposition for water vapor at moderate gas-wall ΔT and unsaturated inlet stream conditions. However, in the presence of high gas-wall ΔT and saturated inlet conditions, nucleation may also be important. It appears that the freeze-out of carbon dioxide will occur primarily by mass transfer under all conditions of practical interest. The injection of liquid nitrogen into the air stream in quantities sufficient to produce large saturation ratios can, of course, be used to promote nucleation under virtually all conditions.

4. Surface Effects

A study of surface adhesion was conducted to determine whether surface effects would be important to the deposition of water and carbon dioxide. This study involved a survey of the literature and a rather qualitative series of "breadboard tests" to evaluate surface coatings. Details on this work are presented in Appendix No. 5.

The results show that some difference in adherence apparently exists for metals of different thermal conductivity. For example, the shear strength of ice is about twice the shear strength between ice and clean metal. This "half" ratio strength between the ice and sub-strate is inversely proportional to the thermal conductivity of the sub-strate material. At least this trend was indicated in tests with ice layers on copper, iron, brass, aluminum, wood, glass, and plastics. We would not expect much difference in frost deposition in copper or aluminum exchangers; smooth stainless steel tubes might be slightly better.

Many coating materials have been used to decrease the formation of ice on cold surfaces. Among the materials tried are oils, fats, rubber, wax, alcohols, glycerine, sulfonated alcohols, fatty acid salts, phthalic anydride, polymers, nitrocellulose, varnishes and many others. None were perfect. Many, if not most, decreased the strength of the ice-solid bond. The better surfaces were hydropholic in nature and (with liquid water) showed low interfacial tensions. The effectiveness of the coating varied with the mode of deposition. With heavy water sprays none were particularly effective; with light sprays, the ice formation rate was noticeably decreased in the initial phases. In all cases, once an ice layer was formed, the effect of the coating was drastically reduced.

In previous natural convection frosting tests at Arthur D. Little, Inc., in which the deposition occurred by nucleation in the bulk gas the effects of coating the surface with silicone oil were pronounced. Essentially no frost formed during the test. We have a difficult time attributing this effect to the hydrophobic nature of the surface. More likely, it made the surface very smooth and mechanically hindered attachment of frost. At points where there were microscopic "bumps", clufts of frost grew rapidly; in between, no noticeable frost adhered. In contrast to these results, our "breadboard" forced convection tests indicated only a very slight reduction in frost formation on a tube coated with silicone oil.

Our general conclusion from this study was that surface coatings will be not particularly effective in preventing frost deposition by mass transfer. However, certain coatings might tend to retard frost build-up by nucleation. Surface coatings might also have some application in facilitating the removal of frost by mechanical or other means.

E. FROST PROPERTIES

The density and thermal conductivity of water and carbon dioxide frosts must be known to evaluate the severity of area blockage and thermal insulation effects resulting from contaminant deposition. These frosts as formed in heat exchangers are porous materials whose densities and thermal conductivities differ from those of the pure solids. For materials of this sort, many analytical and experimental correlations are presented in the literature for relating thermal conductivity to density. Data on frost density is much less plentiful.

A survey of experimental data and analytical methods pertinent to the determination of the density and thermal conductivity of water and carbon dioxide frosts is presented in Appendix No. 6. The major results are summarized below.

Based on an evaluation of the various analytical models for relating frost thermal conductivity to density, it was concluded that for reasonably low density frosts (i.e., $\rho_F < 0.5\ \rho_{solid}$) typical for water frost, Woodside's model (20) yields the best agreement with experimental data. For high density frosts, typical of carbon dioxide, Riemann's (8) truncated sphere model seems appropriate. Using these models, generalized plots have been prepared for determining water and carbon dioxide frost thermal conductivities from given frost density values. These plots are presented in Figures 2 and 3.

Some information appears in the literature on water frost density. This data indicates that at temperatures well below 32° R (say 0° F), when the distillation effect is small, water frost density is primarily dependent on flow velocity. A correlation plot of water frost density vs. flow velocity has been prepared based on a limited amount of literature data and including some data obtained in the present experimental program. This correlation, is presented in Figure 4. This plot indicates that at an air velocity of 60 ft/sec, the density of water frost will be about .25 gm/cc.

No data on carbon dioxide frost density could be found in the literature. However, as will be discussed below, it was possible to obtain a limited amount of frost density data in the experimental program. This data indicated a carbon dioxide frost density of about 1 gm/cc at a nominal heat exchanger velocity of 60 ft/sec.

F. EXPERIMENTAL PROGRAM

An experimental program was conducted to investigate the freeze-out of water and carbon dioxide from an air stream over a wide range of conditions. Freeze-out was accomplished with each of three counterflow heat exchangers consisting of both in-line and staggered tube configurations. The air stream was simulated with nitrogen gas (or helium, in a few specific cases) that acted as the carrier when contaminated with known amounts of water vapor and carbon dioxide. The flow of this carrier stream was normal to the outside of the tube elements; the coolant flow was inside of the tubes. The heat exchangers were mounted in a glass shell which permitted the tube elements to be viewed and photographed under all test conditions.

1. Test Facility

The test facility was designed for heat exchanger carrier gas inlet pressures in the range of 30 to 300 psia, carrier mass velocities in the range 10 to 100 lbs/sec ft. sq., and coolant inlet temperatures down to 50° R. The test facility carrier and coolant streams were supplied from high pressure cylinder manifolds. Contaminant concentration was controlled by the addition of carbon dioxide and water to the carrier stream upstream of the heat exchanger. Coolant inlet temperature control was obtained in an auxiliary cryogenic heat exchanger. Provisions were also included for a liquid nitrogen stream to be injected into the carrier upstream of the heat exchanger to induce nucleation of the contaminants.

A schematic of the test facility is shown in Figure 5.

a. Equipment Arrangement

All equipment required for control and instrumentation of the facility was mounted in a test skid. The skid, shown in Figure 6, is thirteen feet long, four and a half feet high, and three feet wide. The top of the skid served as a platform for the test heat exchanger and photographic equipment. Two 20-cylinder high pressure nitrogen manifolds, which served as the source of the carrier and coolant flows, and a 500-gallon liquid nitrogen tank, which supplied refrigeration for the coolant were, for reasons of size, located apart from the skid. Additional details on the test equipment arrangement are shown in the photographs of Appendix No. 7.

b. Stream Control

Three basic flow streams are required for the test facility. These streams are the carrier, coolant, and spray streams. All three are supplied by high pressure manifolds.

In the majority of the tests in which the coolant inlet temperature was 140° R or above, nitrogen was used for all three streams. However, when the coolant inlet temperature was near liquid hydrogen temperature,helium gas was used as a coolant. In a few of these liquid hydrogen temperature tests, helium was also used for the carrier stream. Nitrogen was the only fluid used for the spray stream. When using nitrogen, the carrier and coolant systems had a rate capacity of approximately .15 lb/sec for a thirty-minute period and the spray stream about .03 lb/sec.

Flow control and measurement of each stream was accomplished by choked orifices preceded by pressure regulators. Secondary flow measurement of each stream was obtained from the known volume and pressure decay of the manifolded cylinders.

The temperature control of the coolant down to 160° R was achieved by passing this stream through coils submerged in an auxiliary liquid nitrogen bath located on the test skid. For coolant inlet temperatures well above the condensing point of nitrogen (330° R or above), low pressure nitrogen (100-200 psig) was used as coolant. The low pressure nitrogen coolant had the advantage of (nearly) constant specific heat, resulting in very regular (almost linear) temperature profiles in the test heat exchanger. For coolant inlet temperatures near 140° R supercritical nitrogen (typically at 600-700 psig) was used as coolant. The use of supercritical nitrogen eliminated the possibility of condensation of the coolant stream. In the supercritical coolant tests, the large variations in coolant specific heat with temperature resulted in very non-linear temperature profiles in the test heat exchanger. The liquid nitrogen spray stream at about 1000 psig was also cooled in a separate coil of the auxiliary heat exchanger. Liquid hydrogen temperatures were achieved through use of helium gas that was passed through coils immersed in liquid hydrogen.

c. Contaminant Addition and Measurement

Water was added to the air stream from a positive displacement metering pump. It was heated at the injection point in the air stream to improve its rate of evaporation. A 50 cc. burette was used as the reservoir at the pump inlet to allow for measurement of the water addition to the carrier during the performance of the test. Specific humidities up to 1 per cent have been achieved with this system.

Carbon dioxide was added to the air stream from a high pressure cylinder initially filled with one atmosphere of carbon dioxide and pressurized to 2200 psi with nitrogen. This "mixing bottle" was connected in parallel with the air stream manifold and both were blown down together during a test giving a controlled concentration of .05 per cent by weight of carbon dioxide in nitrogen.

The water and carbon dioxide content of the heat exchanger inlet and exit streams were measured on continuous reading instruments connected to multipoint recorders. A Beckman infrared analyzer was used for the carbon dioxide concentration measurements and a Consolidated Electrodynamics Corporation humidity meter was used for measurement of the water concentration.

The gas sample streams were heated to about 910° R at the sampling points to vaporize the solid and liquid phases of the contaminants to eliminate erroneous readings resulting from contaminant accumulation in the sample lines. The sample probes at the heat exchanger inlet and exit could be rotated to face upstream or downstream in order to differentiate between vapor and solid contaminants.

2. Test Heat Exchangers

The test heat exchanger assembly consisted of an inner glass tube (either 1-inch or 2-inch) which contained the heat transfer section, surrounded by a 6-inch I.D. glass tube which insulated and prevented frosting of the inner glass. The annular space between the glass tubes was purged with dry nitrogen or helium gas. The general arrangement of these glass sections is shown in Figures 7 and 8. In the event of failure of the outer glass and to protect operating personnel, the 6-inch glass section was surrounded with a metal hood that is vented at the top through a screen and has a viewing section in the vicinity of test heat exchanger formed by a pane of bulletproof glass 1-inch thick and 9-feet wide. This viewing section can be seen in Figure 6.

In the heat transfer section, the air stream flows within the annulus formed by the inner glass tube and an instrumented core. The coolant flows within tubes located in this annular space. The general direction of the air and coolant are opposite resulting in temperature profiles typical of counterflow heat exchangers. Three heat transfer sections covering two general types of heat transfer configurations have been used in our studies. Their principal characteristics are given in Table 1. Drawings are included in Appendix No. 7.

a. Spiral Heat Transfer Sections

In the spiral heat transfer sections, the coolant flows in copper tubes that are wound in a spiral that is fitted in the annular carrier gas space. The carrier stream flows nearly perpendicular to these tubes, simulating an in-line tube array. Two such heat exchangers were fabricated. One of these consisted of three 3/16-inch O.D. tubes parallel wound with an outside diameter of approximately 1-inch. This configuration has been used at air stream pressures of 300 psia and coolant pressures of 1000 psi and is shown in Figures 7 and 8B.

The second heat exchanger consisted of a single 3/8-inch O.D. spiral wound tube with an outside diameter of approximately 2-inches. This unit was operated at air stream pressures of 90 psia (maximum pressure limited by 2-inch glass tube pressure rating) and 1000 psi coolant pressures. This heat exchanger is shown in Figure 9B.

b. Axial Heat Transfer Section

In this configuration, the 3/16-inch O.D. coolant tubes are parallel with the center line of the inner glass tube. The air flow is baffled so as to flow perpendicular to the tubes, which were arranged in a staggered pattern. Air stream pressures up to 90 psia and coolant streams of 1000 psi have been used with this unit. The passages and baffle arrangement are shown in Figure 9A.

c. Heat Exchanger Instrumentation

Each heat exchanger was instrumented so that the pressure and temperature of the air stream was measured at five axial locations. The coolant pressures and temperatures were measured at the inlet and outlet of the heat exchanger. Thermocouples connected to multipoint recorders were used for all temperature measurements. Coolant pressures were measured on Borden tube gauges as were the carrier stream pressures in the test heat exchanger. Three of the carrier stream pressures were also measured with transducers that were read out on multipoint recorders.

3. Test Program

The test program was conducted to determine the effects of 12 principal variables. These are listed in Table 2 with the range over which each was investigated. This test program was divided into five test series.

a. Flow Test Series

The flow test series was performed with the 1-inch spiral heat exchanger to investigate the effects of carrier stream pressure, flow velocity, water and carbon dioxide content, gas to wall differential temperature, coolant inlet temperature and liquid nitrogen spray. Fourteen tests were performed in this test series.

b. Liquid Hydrogen Test Series

The liquid hydrogen test series was performed with the 1-inch spiral heat exchanger to extend the range of coolant inlet temperatures from 140° R to 50° R. Six tests were performed in this test series.

c. Configuration Test Series

In the configuration test series the effect of tube size was investigated with the 2-inch spiral heat transfer section. The 2-inch axial heat transfer section, having staggered tubes, was used to determine the effect of staggered tubes as compared with in-line tubes. This test series consisted of six tests.

d. Verification Test Series

The verification test series was performed, with the 1-inch spiral heat transfer section, to extend and verify the results of the preceeding testing. In this test series, the range of water concentration was increased to 1.0 per cent; additional data was developed on water and carbon dioxide frost density; an extended length "low-water content" test was conducted for better definition of the carbon dioxide pressure drop increase; and an additional liquid nitrogen spray test was conducted. Nine tests were performed in this test series.

e. Extended Test Series

In the extended test series, tests were performed with the 1-inch spiral heat transfer section, to investigate the effect of constant pressure drop operation (all prior tests had been performed at constant carrier stream flow) and to study the effects of varying inlet conditions on frost deposition. Five tests were performed in this test series.

The important test parameters for each of the tests performed are summarized in Table 3. The detailed reduced data for the test program is included in Volume III to this final report. Discussion and analysis of the test results is presented in the following section.

G. ANALYSIS OF TEST DATA

The primary test data consisted of photographs of the deposition in the test heat exchanger, contaminant concentration readings at the inlet and exit of the test heat exchanger, and measurements of pressures and temperatures along the heat exchanger. As mentioned above, the detailed reduced data is included in Volume III to this final report. From the photographs we were able to study the distribution and physical characteristics of the deposit formation. The contaminant concentration readings defined the quantity of water and carbon dioxide entering and leaving the test heat exchanger. The measurements of pressure and temperature indicated the effects of contaminant deposition on heat transfer and pressure drop.

1. Physical Characteristics of Deposit Formation

For low gas-wall temperature difference (100° R or less) the water and carbon dioxide frost accumulated as a relatively dense coating, fairly uniformly distributed around the heat exchanger tubes. The frost seemed to adhere quite securely to the tubes and no deposit migration due to shear was evident. A close-up photograph of this type of deposit formation is shown in Figure 10.

Typically, the water and carbon dioxide frosts are deposited in two distinct locations dependent on their respective saturation temperatures. As shown in Figure 11, the start of frosting correlated quite well with the points at which the tube wall temperature reached the saturation temperature corresponding to the inlet contaminant concentration. It was found that, in general, the bulk of the deposition was complete by the location at which the carrier stream temperature had dropped to saturation at 10% of the inlet contaminant concentration.

Measurements of frost thickness, obtained from close-up photographs indicated that the frost thickness increased to a maximum after the start of frosting and then decreased again. This "air foil" profile is in accordance with the frost distribution resulting from mass transfer. As will be shown later, agreement between experimental frost thicknesses and frost thickness predicted by mass transfer theory was quite good. From the measurements of frost thickness and the known quantity of inlet contaminant it was possible to estimate the frost density. The density of water frost was found to be approximately .25 gm/cc; the carbon dioxide density, approximately 1 gm/cc. A discussion of the experimental measurement of frost thickness and density is included in Appendix No. 9.

The discussion above applies to the majority of the tests in which mass transfer was the predominant mode of contaminant deposition. However, in those tests in which nucleation was predominant, the nature of the deposit formation was substantially different.

In tests in which liquid nitrogen was injected into the inlet carrier stream, nucleation was induced in the bulk gas stream. In this situation, the frost formed as particles in the bulk stream and was subsequently entrapped in the heat exchanger by impingement. This deposit formation appeared to be less dense and less adherent than that resulting from mass transfer. Migration of the frost due to gas shear was evident. A close-up photograph of this type of deposit formation is shown in Figure 12.

It appeared that particle size, as controlled by liquid nitrogen spray rate, was the predominant factor influencing frost distribution in the spray tests. Low liquid nitrogen spray rates induced low saturation ratios favoring the formation of a small number of relatively large particles. These large particles were readily separated by impingement causing the frost to be concentrated near the inlet of the heat exchanger. High liquid nitrogen spray rates induced high saturation ratios favoring the formation of a large number

of relatively small particles. These small particles were less susceptible to impingement separation and as a consequence the frost was distributed over a larger percentage of the heat exchanger area.

In tests at high gas-wall temperature difference (approximately 200° R) the mechanisms of both mass transfer and nucleation were important. The resulting deposit formation was a combination of the effects of mass transfer to the wall and nucleation in the bulk stream with subsequent attachment by impingement. A close-up photograph of this type of deposit formation is shown in Figure 13.

2. Contaminant Concentration in Heat Exchanger Exit Gas

Measurements of the contaminant composition in the exit gas have indicated that the major portion of the inlet contaminant accumulates as frost in the test heat exchanger. Generally, the exit contaminant composition was found to be near saturation at the exit temperature, for carbon dioxide and also for water at relatively high exit temperatures. However, for water at low exit temperatures, it was usually impossible to measure the actual exit concentration since the test instrumentation could not go below about 10 ppm.

From mass transfer theory, it would be expected that at low gas-wall temperature differences, the exit gas would contain only contaminant in the vapor phase at a concentration equal to or less than saturation. The experimental data tend to be in agreement with this reasoning.

In the presence of bulk stream nucleation, caused either by a high gas-wall temperature difference or by liquid nitrogen spray, some particle carry-through might be anticipated. However, test results have indicated that even when such nucleation was induced very little contaminant was present in the exit gas even at high liquid nitrogen spray ratios. Evidently, under our test conditions, the heat exchanger core is quite efficient as an impingement separator for removing solid particles. This result has been demonstrated for both in-line and staggered tube heat exchanger configurations. However, these experimental results may in part be limited by the liquid nitrogen spray nozzle design. It is possible that the drops produced by the nozzle (about 40 microns) were too large to produce extremely small frost particles, even when high spray rates were used.

3. Flow Characteristics

Most of the tests were conducted at constant air flow. Therefore, the increase in pressure drop across the test heat exchanger was a measure of the degradation of heat exchanger flow area due to deposit formation. However, in two tests in the extended test series the pressure drop across the heat exchanger was maintained constant. In this case, deposit formation resulted in reduced air flow.

Pressure taps spaced at intervals along the test heat exchanger indicated the distribution of pressure drop as well as the overall heat exchanger pressure drop. In all cases, the regions of high pressure drop coincided with the regions in

which the frost thickness was a maximum. It was also found that in most tests the pressure drop due to water frost was much greater than the pressure drop due to carbon dioxide frost - even when the mass addition of carbon dioxide was equal to or somewhat greater than the mass diffusion addition of water. This seeming inconsistency is due to the lower density (or greater specific volume) of the water frost compared to the carbon dioxide frost. In a limited number of tests in which the water content was reduced to a minimum, it was possible, however, to develop high pressure drops due to carbon dioxide frost. Detailed analysis and correlation of the experimental pressure drop and flow data is presented in Appendix No. 10. The major results are summarized in the paragraphs below.

Typical plots of heat exchanger pressure drop as a function of the contaminant deposition time are shown in Figure 14. The tests represented on this plot were similar in all respects except for the concentration of water. In this particular group of tests, no carbon dioxide was present; therefore, the pressure drop increase was solely due to accumulation of water frost. The result shows that the rate of pressure drop increase is strongly dependent on inlet air water content. Inspection of Figure 14 indicates that, at any given level of pressure drop appreciably above the clean heat exchanger pressure drop, the product of the per cent water and water addition time for the various tests is approximately equal. Therefore, the data might be expected to fall into a single curve if plotted against water addition mass. The water addition mass has, in fact, been found to be a good correlating parameter for a large portion of the test data. However, as discussed below, it is advantageous to utilize a somewhat more general correlation scheme which also accounts for variations in heat exchanger area and frost density.

In correlating the pressure drop data, it was found convenient to plot the ratio of frosted heat exchanger pressure drop to clean heat exchanger pressure drop as a function of the mean area blockage. The mean area blockage parameter serves to generalize the effects of deposition time, contaminant flow rate, heat exchanger surface area, tube clearance, and frost density. The mean area blockage is the area blockage which would exist if the frost were distributed uniformly over the total heat exchanger area. This parameter is calculated by the equation.

$$\bar{t}/\delta_o = \frac{\int_o^\theta W c d\theta}{\rho_F A_s} \qquad (4)$$

where:

$\bar{t}$ = mean frost thickness

δ_o = tube half clearance

$\int_o^\theta W c d\theta$ = total contaminant mass addition

θ = contaminant addition time

ρ_F = frost density

A_s = total heat exchanger surface area

A correlation plot of pressure drop ratio vs. mean area blockage is presented in Figure 15. This plot includes data for a wide range of constant flow tests including variations in pressure, flow velocity, coolant inlet temperature and contaminant concentration. These tests do not include liquid nitrogen spray or high gas-wall Δ T and in all cases frost deposition was predominantly by mass transfer. Also, in all cases, the carbon dioxide pressure drop effect was insignificant so the mean area blockage was computed solely from the water addition mass.

It was found from Figure 15 that tests having approximately equal frosted length fraction (X/L) fell along a single plot. For instance, all the data of Figure 14 fell close to a single curve. Reducing "frosted length" served to increase pressure drop at a constant value of mean area blockage, since the true area blockage in the frosted length was increased. In computing the frosted length fraction (X/L), it was assumed that the start of frosting corresponded to the point at which the wall temperature reached the inlet contaminant saturation temperature. The end of the frosted length was defined as the location at which the carrier gas temperature had dropped to saturation at 10% of the inlet contaminant concentration.

The data presented in Figure 15 was obtained in constant flow tests on the 1-inch spiral heat transfer section, when water was the only contaminant of interest. As shown in Appendix No. 10, however, data from low gas-wall ΔT tests on the 2-inch spiral and 2-inch axial heat transfer sections also fit this correlation plot. Likewise, data from the constant pressure drop tests correlates reasonably well when the square of the flow ratio $(W_o/W)^2$ for the constant pressure drop tests is taken to be analogous to the pressure drop ratio $(\Delta P/\Delta P_o)$ for the constant flow tests. Similar data obtained in tests in which carbon dioxide was the major contaminant also is in reasonable agreement with the correlation plot of Figure 15.

In three tests in the extended test series, inlet conditions were varied in the course of the tests. In other respects these tests were similar to the low gas-wall Δ T mass transfer deposition tests conducted at constant inlet conditions and correlated in Figure 15. The results indicated that when the frosted length was increased during the course of a test, by decreasing inlet air temperature or increasing coolant flow, the rate of pressure rise was less than that of a comparable test at constant inlet conditions. When the inlet air temperature was increased during the test, the frosted length tended to remain constant - although the frosted zone shifted downstream. In this case, the pressure drop increase was similar to that of a comparable test at constant inlet conditions.

A correlation plot similar to Figure 15 is presented for liquid nitrogen spray tests in Figure 16. In this case, a frosted length fraction computed from temperature profiles has little significance as a correlating factor since the contaminant deposition involves nucleation rather than mass transfer. However, liquid nitrogen spray ratio appears to serve a similar function. This plot indicates that at a given value of mean area blockage the pressure drop ratio is reduced by increasing liquid nitrogen spray rate. This result is in accordance with the photographic and visual evidence indicating that higher spray rates resulted in more uniform frost distribution throughout the heat exchanger and consequently greater frosted lengths. However, increasing the spray ratio beyond 33% did not result in further decrease in pressure drop. It may be that beyond the 33% point, the frost particle size has reached a minimum, controlled by liquid nitrogen drop size, and further increases in spray rate have little effect on frost particle size. The data plotted is for the 1-inch spiral configuration; however, data from liquid nitrogen spray tests on the other heat transfer sections also fit the correlation plot.

The effect of high gas-wall ΔT on pressure drop has also been studied. The results, as shown in Appendix No. 10, are not clear-cut. For the case of the 1-inch configuration, the pressure drop increase at high gas-wall ΔT is somewhat less than at low gas-wall ΔT. With the two-inch spiral configuration, the opposite effect is observed. Actually at high gas-wall ΔT, two effects occur. First, the mass transfer frosted length is generally quite short, tending to increase pressure drop. Secondly, however, only a portion of the freeze-out is due to mass transfer and the nucleating frost might be distributed over a greater length than the mass transfer frost. Evidently, the balance between these effects may vary from test to test if all other operating conditions are not precisely the same.

In summary, the correlation scheme illustrated in Figure 15, appears to correlate, with reasonable accuracy, all of the low gas-wall ΔT (i.e., mass transfer) test data obtained under a variety of operating conditions and with different heat transfer geometries. We would expect this correlation method to be quite general - and to be valid for constant pressure drop as well as constant flow tests if the pressure drop ratio $(\Delta P/\Delta P_o)$ is replaced by the more general flow parameter $\left[\Delta P/\Delta P_o/(W_o/W)^2\right]$. The liquid nitrogen spray test data, in Figure 16, also seems to correlate reasonably well. However, in this instance, we feel that the correlation may not be completely general since it does not account for liquid nitrogen drop size. The data for the high gas-wall ΔT tests does not lend itself to any simple correlation scheme because of the combined effects of mass transfer and nucleation.

4. Heat Transfer

Our test results at constant flow have indicated very little change in overall heat flow due to deposit formation. In a large measure, this is due to the fact that in an efficient (i.e., low heat transfer ΔT) heat exchanger, an appreciable reduction in heat transfer coefficient will result in a small change

in overall heat flow. By way of further explanation, it may be noted that in a counterflow heat exchanger, the maximum heat flow, corresponding to infinite heat transfer coefficients, is a function of the inlet temperatures and flow rates of the hot and cold fluids. The actual heat flow increases with increasing heat transfer coefficient and approaches this maximum as an asymtote. However, in the asymtotic region of a plot of heat flow versus heat transfer coefficient, the heat flow is a relatively weak function of heat transfer coefficient.

Calculation of heat transfer coefficients from the test data were inherently rather inaccurate, since the error in the fluid temperature measurements was an appreciable portion of the heat transfer Δ T. A typical plot of overall heat exchanger heat transfer coefficient ratio (frosted over clean) vs. mean area blockage is presented in Figure 17. As described in Appendix No. 10, the overall heat exchanger heat exchanger coefficient is computed by dividing the total heat flux by the product of the total heat transfer area and the mean carrier-coolant temperature difference. Although the data has appreciable scatter, this plot indicates that the changes in overall heat transfer coefficient are much less, for comparable area blockage, than the changes in pressure drop.

In the constant pressure tests, the reduction in heat flow was substantially greater than that in the constant flow tests. However, in this case, the reduction in heat flow was primarily related to the decrease in carrier stream flow (and available sensible heat). The effects due to degradation in heat transfer coefficients appeared to be relatively small and were difficult to assess quantitatively because of the shifting temperature profiles.

H. ANALYTICAL METHODS FOR PREDICTING THE EFFECTS OF CONTAMINANT FREEZE-OUT ON HEAT EXCHANGER PERFORMANCE

In the course of developing analytical methods for predicting the effects of contaminant freeze-out on heat exchanger performance, several complementary approaches were pursued. Analysis of the effect of a given frost layer on the performance of a single tube row served to identify the principal relationships governing performance degradation. Combination of the single tube row analysis with data on frost properties and frost distribution provided the basis for calculation of overall heat exchanger performance. In accomplishing the calculation of overall heat exchanger performance both a simplified "hand calculation" method and more rigorous computer solutions were found to have merit. Detailed discussion of the various aspects of this development are included in Appendixes 11, 12 and 13. The major results are summarized below.

1. Single Tube Row Analysis

As a first step in considering the effects of contaminant deposition on heat exchanger performance, it is useful to investigate the effect of a frost layer of given thickness and thermal conductivity on the flow and heat transfer capacity of a single tube row. The geometric model for this analysis, consisting of adjacent tubes separated by clearance 2 δ_o and coated with a frost thickness t is shown in Figure 18.

The pressure drop across the tube row is directly proportional to flow per unit area and inversely proportional to fluid density. Therefore, making use of the geometric relationships of Figure 18 and neglecting variations in friction factor, the pressure drop ratio may be written as:

$$\frac{\Delta P/\Delta P_o}{(W/W_o)^2} = \left[\frac{1}{1 - t/\delta_o}\right]^2 \rho_o/\rho \qquad (5)$$

where:

ΔP ~ pressure drop

W ~ flow rate

t ~ frost thickness

δ ~ tube half clearance

ρ ~ fluid density

subscript $_o$ represents clean conditions.

Similar, although slightly more complex, relationships can be developed to relate variations in the carrier stream overall heat transfer coefficient, (U), which includes both gas film resistance and frost resistance, to area blockage (t/δ_o) and a "frost Nusselt number" ($h_o \delta_o/kF$) based on the initial carrier side film coefficient, h_o, the tube half clearance, δ_o, and the frost thermal conductivity kF.

For close packed tubes (pitch/diameter ≤ 1.4) the ratio of overall carrier stream heat transfer coefficients may be written as:

$$\frac{U_o}{U} = (1 - t/\delta_o)^{.6} (W_o/W)^{.6} + (h_o \delta_o/kF)(t/\delta_o) \qquad (6)$$

The derivation of these equations is presented in Appendix No. 11. The results are plotted in Figures 19 and 20. These plots show that, for constant flow density, the pressure drop parameter is a single valued function of area blockage, increasing as area blockage increases. This relationship is independent of whether the system is constant flow or constant pressure drop.

The heat transfer parameter is dependent on the "frost Nusselt number", area blockage and the system operating line. For constant pressure drop the overall heat transfer coefficient must always decrease - the rate of decrease being

dependent on the frost Nusselt number. High values of frost Nusselt number (i.e., low frost thermal conductivity) result in a rapid decrease in heat transfer. For constant flow, the overall heat transfer coefficient may actually increase if the frost thermal conductivity is high, since the increased film coefficient associated with reduced flow area outweighs the insulating effect of the frost. For the tests conducted in this program the frost Nusselt number was of the order of 5.0. Therefore, frost formation would be expected to reduce the overall carrier gas coefficient.

The single tube analysis has illustrated, in a qualitative manner, the effects of frost thickness and thermal conductivity on the performance of a heat exchanger tube row. In applying these results it is obviously necessary to know frost thermal conductivity. Since the contaminant addition will be known on a mass basis, frost density is required to determine frost thickness. In considering the overall heat exchanger in which frost thickness varies with length, it also is necessary to know the distribution of frost thickness so that the flow and heat transfer effects can be integrated along the length of the heat exchanger. Therefore, an analytical approach requires methods of determining both frost distribution and frost properties. Procedures for estimating frost density and thermal conductivity were outlined previously in Section E above. A mass transfer model for frost distribution is discussed below.

2. Mass Transfer Model for Frost Distribution

Analytical and experimental results indicate that mass transfer is generally the most important mechanism governing the distribution of frost in heat exchangers. Analysis indicates that mass transfer is definitely the predominant mode of contaminant freeze-out for moderate gas-wall ΔT. However, as gas-wall ΔT increases, nucleation may become more of a factor, particularly if the inlet air is near saturation. Our experimental program has confirmed that mass transfer is the predominant mode of freeze-out for moderate gas-wall ΔT over a wide range of conditions. The tests have also indicated that even with large gas-wall ΔT's in the order of 200° R the distribution of contaminants and the pressure drop is not really grossly different than would result from mass transfer.

Mass transfer is amenable to fairly straightforward analysis. An important feature of the mass transfer analysis is that it is relatively simple to develop the history of bulk stream saturation ratio as the mass transfer calculations are performed. This information indicates whether or not nucleation is a possibility under the particular conditions studied. On the other hand, the process of nucleation, including nucleation rates, particle growth, and particle impingement is almost impossible to describe analytically. Therefore, we have concluded that the mass transfer mechanism is the most practical mechanism to serve as a basis for an analytical model of frost distribution.

As discussed previously, mass transfer rates can be computed from the product of the concentration driving force between the stream and wall and the mass transfer coefficient. Mass transfer coefficients may be determined from semi-empirical correlations. A step-wise calculation procedure applied to a heat exchanger can be used to determine both the distribution of frost along the wall and the bulk stream saturation ratio. Details on this calculation procedure are included in Appendix No. 1. Such step-wise calculations can be performed manually; however, digital computer solutions may be more practical if many calculations are to be performed.

3. Discussion of Calculation Procedures

Both computer solutions and hand calculation methods have been considered for predicting deposit accumulation and the resultant effects on heat exchanger performance. Both approaches require prior knowledge of water and carbon dioxide density and thermal conductivity. The computer solution is capable of developing accurate frost profiles from mass transfer theory and integrating the pressure drop and heat transfer effects along the heat exchanger as part of a unified calculation proceudre with a minimum of simplifying assumptions. In order to avoid extended tedious calculations, it is generally necessary to employ some rather arbitrary assumptions regarding frost distribution and flow density in the hand calculations techniques.

It has been concluded that both methods have value. Hand calculation techniques are useful as a simple, flexible means of approximating the effects of contaminant deposition on heat exchanger performance. The hand calculation method may be used both as a basis for data correlation techniques and as a rough independent check on the credibility of either experimental data or computer solution. On the other hand, computer solutions are generally required for maximum calculation accuracy, especially in those cases in which heat exchanger inlet conditions are varying. Estimates of calculation accuracy for the various analytical methods are presented in section 6 below.

4. Hand Calculation Method

A simplified hand calculation analysis based on the assumption of uniform frost thickness within an effective frosted zone has been valuable in analyzing and correlating test data. The effective frosted length is calculated from the heat exchanger temperature profiles. The start of frosting is taken to be the point at which the tube wall temperature reaches saturation at the inlet concentration; the end of frosting is taken to be the point at which the stream temperature reaches saturation at 10% of the inlet concentration. The assumption of uniform frost thickness in a frosted zone allows the area blockage in that zone to be calculated readily. Knowing the area blockage, the degradation in flow capacity and heat transfer in the frosted zone can be determined from Figures 19 and 20. The overall changes in flow capacity and heat transfer for the heat exchanger can, in turn, be obtained by combining the performance of the clean and frosted sections. The details of the calculation procedure are discussed in Appendix No. 11. A comparison of the results with experimental data is presented in section 6 below.

5. Digital Computer Solutions

Digital computer solutions permit a much more detailed calculation of the actual conditions in the heat exchanger than would be practical for hand calculations.

Temperatures and pressures vary both with time and position in the heat exchanger. To allow for such variations, material, momentum, and energy balances were written in differential form along with the appropriate heat transfer rate expressions and solved as a function of length for the clean exchanger. This zero-time solution established temperature and pressure profiles for the carrier gas, and the temperature profile for the coolant. The wall temperature gradient and heat flux were then calculated.

With the zero-time values established, one then assumes that the entering carrier gas is instantaneously contaminated with some pre-set water and carbon dioxide concentration. By following a control volume of this gas down the heat exchanger, the rates of mass transfer to the wall were estimated and the humidity profiles determined.

With these data, one chooses an appropriately small time increment and determines frost depositions along the heat exchanger. At the end of this time increment, the frost mass deposited in any differential length was converted to a thickness using the frost density-velocity correlation described earlier. The differential momentum balance equations were then solved to yield a new pressure profile and the energy balance and heat transfer equations solved to yield new temperatures. In the latter, account must now be taken of the thermal resistance of the frost layer employing the calculated thickness and estimated frost conductivity. As before, then, new mass transfer fluxes were estimated, and the next time step chosen.

This step-wise iteration technique is continued until the end of the test or until some predetermined pressure drop is attained. The tediousness of the calculations necessitated the use of a high-speed IBM 7090 computer.

From such a method, it is possible to print-out at any time the pressure and temperature gradients in the coolant and carrier stream, the wall and frost carrier gas interface temperature gradients, the humidity gradients, and the frost distribution profile. Variable inlet conditions may be handled by this technique.

a. Constant Heat Transfer Computer Program

In developing a machine program to solve the various differential expressions governing the frosting process in the heat exchangers, it was found that neglecting variations in heat transfer was a great simplification. Experimental evidence had indicated that variations in heat transfer in our test program were generally quite small. Therefore, it was decided to first develop a simplified constant

heat transfer model to test the utility of a computer solution for frosting heat exchangers. This model assumes that heat transfer rates are constant with time and position within the heat exchanger and are equal to the clean heat exchanger heat transfer rates. As formulated, the program was applicable only to constant flow, constant inlet temperature operation.

The frost distribution profiles and pressure drop data generated by the constant heat transfer model were found to be in reasonable agreement with test data. A typical comparison of these results with experimental data is presented in section 6 below. A detailed discussion of this constant heat transfer model is presented in Appendix No. 12. It may also be noted that Appendix No. 12 includes the derivation of the basic equations used for both the constant heat transfer model and the more general variable heat transfer computer program.

b. Variable Heat Transfer Computer Program

Based on the promising results of the constant heat transfer program, it was decided to implement a more complex computer program which would be capable of determining heat transfer effects as well as pressure drop.

This variable heat transfer program was also designed to handle varying inlet conditions and to contend with either constant flow or constant pressure drop operation. The computer output includes a record of stream saturation for both carbon dioxide and water to serve as an indication of the possibility of nucleation.

The variable heat transfer computer solution is described in Appendix No. 13. A comparison of computer results and experimental data is presented in the following section.

6. Comparison of Analytical Results and Experimental Data

Figures 21 and 22 present a comparison of frost profiles and pressure drop computed by three analytical techniques with experimental data. The three analytical methods are:

a. The hand calculation method.

b. The constant heat transfer computer program.

c. The variable heat transfer computer program.

In this comparison, which was applied to the data of test V-5, the water frost density was taken as 15.5 lb/ft^3; the water frost thermal conductivity, .15 BTU/hr ft^2 ^oR. The frost density value was obtained from the correlation plot of Figure 4. The frost thermal conductivity value, however, is about twice the value predicted by Figure 2. This adjustment in frost thermal conductivity was based on preliminary computer runs (see Appendix No. 12) which indicated that the water frost thermal conductivity should be increased for better agreement with experimental frost profiles and heat transfer results.

The results of Figure 21 indicate that the variable heat transfer computer program results in a more representative distribution of frost than does the constant heat transfer program. The difference is most apparent at the upstream end of the frost layer. Here the constant heat transfer program predicts a very steep increase in frost, much steeper, in fact, than is the case experimentally. The variable heat transfer program, however, which includes a more realistic evaluation of the changes in surface temperature due to the thermal resistance of the frost, results in an increase which is very similar to the experimental data. The variable heat transfer program also predicts the peak frost thicknesses more accurately than the constant heat transfer program. Figure 21 also presents the uniform frost thickness profile used for the hand calculation method. Here it is assumed that all the frost is distributed uniformly in a hypothetical frosted length. The beginning of this frosted length is taken to be the point at which the wall reaches saturation. The end of the effective frosted length is taken to be the point at which the air stream saturation humidity drops to 10% of the initial humidity. It may be noted that all analytical techniques predict the start of frosting somewhat in advance of the experimental data. The significance of this is not completely clear, nor is it felt to be especially significant. It may, in fact, be due to the coolant inlet temperature input to the computer solutions being slightly lower than the true experimental value.

Figure 22 presents a comparison of the pressure drops predicted by these three techniques with the experimental data. The constant heat transfer program which results in the greater peak frost thickness also results in the more accelerated rate of pressure rise. The variable heat transfer program and the hand calculation method are in surprisingly close agreement. It is felt that, in general, these two methods would not produce such similar results considering the wide differences in calculation techniques. It should be noted that all the analytical methods tend to under-predict the pressure drop increase near the beginning of the test and then show a faster rate of pressure rise near plug-up. This phenomena has been more-or-less characteristic of the comparisons between analyses and test. Some probable reasons are discussed in the following paragraphs.

Additional application of the constant heat transfer and hand calculation method to experimental data are discussed in Appendixes No. 11 and 12. A more extensive comparison between the variable heat transfer model and the experimental data is presented below.

Figure 23 presents comparisons between the variable heat transfer computer solution and experimental pressure drop (or flow) data for tests F-3, V-5, V-7, and E-2. Tests F-3 and V-5 are constant-flow tests, in which water frost is the only contaminant. Test V-7 is a constant-flow test, in which carbon dioxide frost is the major contaminant. Test E-2 is a constant pressure drop test, having initial conditions very similar to those of Test F-3. It should be noted that the results for tests F-3, V-5 and E-2 refer to overall heat exchanger performance. The results for V-7 apply to the last quarter of the test heat exchanger.

For tests F-3, V-5 and E-2 the frost density and thermal conductivity were taken as 15.5 lb/ft^3 and .15 BTU/hr ft ^{o}R respectively; for test V-7, 65 lb/ft^3 and .13 BTU/hr ft ^{o}R.

For test F-3, the results show excellent agreement between analysis and experimental data.

In test V-5, the analytical results tends to under-predict the pressure drop at the beginning of the test and over-predict the pressure drop near plug-up. This effect seems to be characteristic of many of the comparisons between experiment and analysis, although especially pronounced in test V-5. This discrepancy might arise from a number of causes. Our experimental measurements of frost density have indicated that frost density may increase with time, whereas the computer solution assumes a constant frost density. Effects due to surface roughness and non-uniform circumferential distribution of frost on the heat exchanger tubes may also play a part. It should also be noted that friction factor data for tube banks of extremely small pitch to diameter ratio, as is the case in a frosted heat exchanger, is subject to a rather broad tolerance. In view of all these considerations, it is felt that the agreement between analysis and experiment is as good as could reasonably be expected.

The heat exchanger air flow results for test E-2, a constant pressure drop test, appear to be in reasonably good agreement. Here, too, though,we note that the analysis tends to slightly under-estimate the effects of deposit formation near the beginning of the test.

For test V-7, the agreement between analysis and experiment seems to be quite good throughout the majority of the test. However, as the heat exchanger approaches plug-up, the analytical pressure drop appears to lag behind the experimental value. The shape of the curves is very similar and it may be noted that the discrepancy shown could easily result from an error in frost density of about 10-15%.

It has been generally difficult to obtain valid comparisons between experimental and analytical heat transfer effects, since in most of our tests, the reduction in heat transfer due to deposit formation has been extremely small and almost within the range of experimental error.

Figure 24 presents comparisons of predicted and experiment coolant temperature rise for tests F-3 and E-2. The coolant temperature rise is, of course, directly proportional to the heat transfer in the test heat exchanger. The computer solution when applied to Test F-3 indicates that the coolant temperature rise should drop about four degrees during the progress of the test. The experimental data is roughly in accordance with the computer prediction, particularly if the initial two points, which may be influenced by the initial heat exchanger cool-down, are disregarded. The agreement between experiment and analysis for test E-2 appears to be quite good. In this test, we note that the overall heat transfer changes quite substantially during the course of the test. Test E-2 is a constant pressure drop test in which the air flow decreases as deposits accumulate. A major portion of the loss in heat transfer is directly related to the reduction in air flow.

In quoting estimated accuracies for the various methods of calculation, a tolerance band should be applied to the time scale as well as the normal dependent variables such as pressure drop or heat transfer. This dual tolerance stems from the method of calculation which is essentially divided into two areas: (1) the calculation of frost volume ingested, and (2) the determination of the effects of a given frost volume on heat exchanger flow and heat transfer characteristics. The calculation of frost volume ingested depends on the use of frost density values, which are subject to prediction error, as well as known inputs of time, air-flow and contaminate concentration. Errors due to frost density can be reasonably thought to be equivalent to errors in establishing the true deposition time. In going from frost volume to changes in pressure drop or heat transfer, the calculation procedures utilize many factors which are subject to some error, such as the model for frost distribution, data on frost friction factor, data on frost thermal conductivity and the assumption that the frost is uniformly distributed around the heat exchanger tubes in a circumferential direction. Errors associated with any of these factors should logically be applied against the dependent variables such as heat transfer, flow or pressure drop.

The logic of the dual tolerance approach can be most readily illustrated by a simple example. Suppose we are considering a situation where the pressure drop is rising very rapidly with time, such as frequently occurs in our test program near heat exchanger plug up. In this case a 20% increase in time might be equivalent to 100% change in pressure drop. If all aspects of the calculation procedure were correct except for a 20% error in frost density, we might expect the analytical result to be displaced from the experimental result by a factor of 20% in time. However, at a specified value of time, the discrepancy in pressure drop would be 100%. Under these conditions, it would certainly seem more reasonable to quote the error as a 20% error in time rather than 100% error in pressure drop.

The same frost density information is used in both the hand calculation and computer studies. We would expect this density information to have a tolerance of approximately $\pm$ 20%. This estimate is reasonably well substantiated for water frost where a fair amount of data is available. However, for CO_2 frost where very little data is available, the tolerance has not been well established. However, our best judgment is that a tolerance of $\pm$ 20% should be applied to the time scale for all calculation methods to account for errors in frost density.

The errors in computing pressure drop and heat transfer with the computer solution should be somewhat greater than the tolerances associated with the heat transfer and friction factor data available for the configurations under consideration. This additional tolerance results from factors such as the frost distribution and the surface roughness effects of the frost layer. In general, we would expect the over-all error to be in the neighborhood of $\pm$ 20%. For the case of the hand calculation solution, additional error is associated with the relatively crude means of establishing frost distribution. On this basis, we would anticipate the error in the dependent variable for the hand calculation solution to be on the order of $\pm$ 30%.

It must be pointed out that the above estimates of calculation accuracy are in themselves very approximate. Our comparisons with experimental data, while very encouraging and generally within the tolerances mentioned above, have not been sufficient to establish errors in a statistical fashion. We would expect the tolerances associated with the analytical solution to be somewhat a function of the circumstances to which the solution is being applied. In particular, we might expect the error to be larger when the water content is high enough to cause the water to deposit as liquid. The analytical model assumes all contaminant deposits as a porous solid. The distribution of this frost is established by mass transfer theory, and the frost density is estimated from an empirical correlation. When the water content is high enough to cause the water to deposit as liquid, the liquid flows downstream, and eventually freezes as water ice after it passes into a region below its freezing point. The net result is that both the distribution of frost and the density of the frost are influenced by transition through the liquid phase. We have not applied our analytical methods extensively to this case, although preliminary comparisons with test V-2, in which some transition through the liquid phase occurred, showed normal agreement between experiment and analysis.

We might also note that the high water content pressure drop data correlates reasonably well with data obtained at low water contents. The results of Figures 2 and 3 Appendix 9 show that the high water content pressure drop data appears to plot slightly higher than--but reasonably close to--the low water content data when the tests are compared on the basis of equal area blockage (or equal water mass addition). It is felt that differences which do slow up in the data conditions are within the range of accuracy for the experimental water content. For these reasons we feel that the analytical method is capable of handling water contents up to about 1% without drastic increases in the calculation tolerances applicable to the low water content situation.

In summary, the analytical methods appear to be in reasonable agreement with experimental data. It is felt that the constant heat transfer computer solution has essentially served its purpose as an intermediate step in the program and that it has relatively limited general value. However, both the hand calculation method and the variable heat transfer computer are useful methods for predicting the effect of contaminant freeze-out on heat exchanger performance. The hand calculation method is best suited for making quick approximations. The variable heat transfer computer program would generally be expected to provide better accuracy. It also is much more adaptable to considering varying inlet conditions and supplies much more detailed information, such as bulk stream saturation ratios, than is practical for the hand calculation approach.

I. CONCLUSIONS

1. For moderate gas-wall ΔT ($\Delta T \leq 100^{\circ}R$) contaminant freeze-out appears to be primarily due to mass transfer. For high gas-wall ΔT ($\Delta T \geq 200^{\circ}R$) nucleation may be important. Increasing the inlet stream relative humidity tends to increase the possibility of nucleation.

2. For moderate gas-wall ΔT, the deposit formation is relatively a dense adherent material - more or less uniformly distributed around tubes. Axial frost distribution appears to be in accordance with mass transfer theory.

3. In the presence of liquid nitrogen spray or a high gas-wall ΔT, freeze-out may occur in the bulk gas stream due to nucleation. The resulting deposit, which forms on heat exchanger tubes by impingement, appears lighter in density and tends to migrate. It appeared that particle size, as controlled by bulk gas stream saturation ratio, was the predominant factor influencing frost distribution.

4. In all tests, a major portion of deposit accumulated in heat exchanger. Exit contaminant concentrations were generally near saturation.

5. The measured density of the "mass transfer" frost was of the order of .25 gm/cc for water frost; 1 gm/cc for carbon dioxide. Analytical methods have been developed for estimating the frost thermal conductivity from known density values.

6. Experimental pressure drop and heat transfer results appear to be in general accordance with the computed area blockage and frost insulation.

7. Digital computer and hand calculation solutions based on mass transfer theory have been successful in predicting the effects of contaminant deposition on heat exchanger performance. In constructing plots of performance versus contaminant deposition time with these methods, we would assign a time axis tolerance of about $\pm$ 20% to both methods. The performance axis tolerance would be about $\pm$ 20% for the computer solution and about $\pm$ 30% for the hand calculation solution.

LIST OF REFERENCES

1. Beatty, K. O., E. B. Finch, and E. H. Schoneborn, Sept. 11-13, General Discussion on Heat Transfer, ASME-IRE, London, 1951.

2. Becker, R., and Doring, W., Ann. Physik 24, 719 (1935).

3. Chen, M. M., Ph.D. Thesis, Mech. Eng., M.I.T., Cambridge, Mass., 1960.

4. Chung, P. M., and A. B. Algren, Heating, Piping and Air Conditioning 30, No. 9, 171; No. 10, 115 (1958).

5. Courtney, W. G., and Clark, W. J., "Kinetics of Condensation from the Vapor Phase", Texaco Exp., Inc.; TM-1250, July 1961; TM-1340, April 1962.

6. Fletcher, N. H., J. Chem. Phys. 29, 572 (1958).

7. Frenkel, J., "Kinetic Theory of Liquids", Dover Pub., Inc., New York 1955.

8. Gorring, R. L., and Churchill, S. W., Chem. Eng. Prog. 57, 53 (1951).

9. Hall, T. A., and Tsao, P. H., Proc. Roy. Soc. (London) A191, 6, (1947).

10. Holten, D. C., B.S. Thesis, Univ. of Colorado, 1957.

11. Izmailova, G. I., P. S. Prokhorov, and B. V. Peruagin, Coll. J. (USSR) 19, 557 (1957).

12. Kamei, S., T. Mizushina, S. Kifune, and T. Koto, Chem. Eng. (Japan) 14, No. 1, 53 (1950).

13. Loper, J. L., Trans. ASHRAE 66, 104 (1960).

14. Prins, L., Kaltetechnik 8, 160, 182 (1956).

15. "The Physical Chemistry of Aerosols", Disc. Faraday Soc., No. 30, (1960), p. 20, 39, 145, 376.

16. Ruccia, F. E., and C. M. Mohr, "Atmospheric Heat-Transfer to Vertical Tanks Filled with Liquid Oxygen", Proc. of the 1958 Cryogenic Eng. Conf., Cambridge, Mass., Sept. 3-5, 1958.

17. Schaefer, V. J., Ind. Eng. Chem. 44, 1300 (1952).

18. Turnbull, D., and B. Vonnegut, Ind. Eng. Chem. 44, 1292 (1952).

19. Volmer, M., "Kinetik der Phasenbuildung", Edwards Bros. Ann Arbor, 1945.

20. Woodside, W., Can. J. Physics 36, 815 (1958).

TABLE 1

HEAT EXCHANGER DATA

Heat exchanger configuration	1" spiral (in-line)	2" spiral (in-line)	2" axial (staggered)
Heat exchanger length (in)	49	48	37
No. of parallel coolant tubes	3	1	20
Coolant tube O.D. (in)	3/16	3/8	3/16
Coolant tube wall thickness (in)	.030	.032	.032
Coolant tube material	Cu	Cu	Cu + SS (see note)
Total air side surface area (ft^2)	1.76	4.4	3.0
Air to coolant surface area ratio	1.472	1.205	1.535
Air side flow area (in^2)	.150	.310	.278
Coolant side flow area (in^2)	.0379	.0762	.234
Air to coolant flow area ratio	3.96	4.08	1.19
Average distance of the tubes from the glass wall and instrument core (in)	.031	.031	.035

NOTE:
In the 2" axial configuration, 18 tubes were copper; 2 were stainless steel.

TABLE 2

VARIABLES INVESTIGATED

		Range
1.	Pressure (psia)	15 to 300
2.	Mass velocity (lb/ft^2-sec)	10 to 100
3.	Water content (wt. per cent)	.001 to 1.0
4.	Carbon dioxide content (wt. per cent)	0 and .05
5.	Gas to wall differential temperature ($^\circ$ R)	5 - 200
6.	Ratio liquid nitrogen spray flow/carrier flow	.2 to .46
7.	Coolant tube O.D. (in)	3/16 and 3/8
8.	Tube arrangement	In-line and staggered
9.	Coolant inlet temperature ($^\circ$ R)	410 to 50
10.	Air inlet temperature ($^\circ$ R)	520 to 560
11.	Operating line	Constant flow and constant ΔP
12.	Varying inlet conditions	Varying inlet air temperature varying coolant flow

TABLE 3

TEST PARAMETER SUMMARY

Test No.	Carrier: Mass Flow ($\frac{lbs}{sec\text{-}ft^2}$)	Carrier: Inlet Pressure ($\frac{lbs}{in^2}$)	Carrier: H_2O conc. (%)	Carrier: CO_2 conc. (%)	Coolant: Inlet Temp. (^oR)	Coolant: Heat Ratio $\frac{(WC_p)_c}{(WC_p)_a}$	Spray: Mass Ratio $\frac{W_s}{W_a}$	Variables[1] Investigated
F-1	10	30	.005	0	260	1.0	-	1
F-2	30	90	.006	0	304	1.0	-	3
F-3	30	90	.026	0	304	1.0	-	3
F-4	30	90	.045	0	304	1.0	-	3
F-5	30	90	.052	0	304	1.0	-	3
F-7	30	90	.001	.05	170	1.0	-	5
F-8	30	90	.016	.05	170	1.0	-	5
F-9	30	90	.020	.05	170	.5	-	5
F-12	30	90	.018	.05	150	2.0	-	5
F-10	50	90	.018	.05	170	1.0	-	2
F-11	15	90	.030	.05	180	1.0	-	2
F-13	39(2)	90	.012	.05	170	1.0	.33	6
F-14	37(2)	90	.012	.05	170	1.0	.25	6
F-17	100	300	.017	.05	150	1.0	-	1
H-1	30(4)	90	min	.05	160	1.0	-	system check run
H-2	30(4)	90	min	.05	50	1.0	-	1, 4
H-3A	30	90	min	.05	50	1.0	-	1, 4
H-4	13	90	min	.05	50	2.3	-	1, 4
H-5	30	90	min	.05	50	1.75	-	1, 4
H-6	30	90	.025	.05	50	1.75	-	1, 4, 5
C-1	30	90	.025	.05	160	1.0	-	5, 8
C-2	39(2)	90	.025	.05	160	1.0	.2	6, 8
C-3	30	90	.025	.05	150	2.0	-	5, 8
C-4	37(2)	90	.025	.05	150	1.0	.35	6, 8
C-5	30	90	.025	.05	160	1.0	-	7, 8
C-6	30	90	.025	.05	160	2.0	-	7, 8
V-1	10	30	.025	.05	190	1.0	-	1, 3, 4
V-2	30	90	.1	-	300	1.0	-	3
V-3	30	90	.32	.05	305	1.0	-	3
V-4	10	30	1.0	.05	180	1.0	-	3
V-5	30	90	.027	-	410	1.0	-	3
V-6	30	90	neg	.05	160	1.0	-	4
V-7	30	90	neg	.044	165	1.0	-	4
V-8	15	90	.025	.047	170	1.0	-	2
V-9	35(2)	90	.029	.046	.75	1.0	.46	6
E-1	30	90	.025	.055	150	varies	-	12
E-2	30(5)	90	.029	.051	304	1.0(5)	-	11
E-3	30(5)	90	.09	.05	304	1.0(5)	-	11
E-4	30	90	.025	.05	145	1.0	-	12
E-5	30	90	.025	.05	145	1.0	-	12

NOTES:

1. Numbers refer to variable designations given in Table 2.
2. Mass flow is based on the sum of the carrier and spray streams.
3. Tests C-1 through C-4 were performed with 2-inch staggered tube heat exchanger and test C-5 and C-6 were performed with 2-inch spiral tube heat exchanger.
4. Equivalent volumetric helium flow.
5. Initial condition - air flow decreases during test.

P = 150 PSIA

Vg = 100 FT/SEC

D = 1/8 IN.

Ho = 4320 PPM

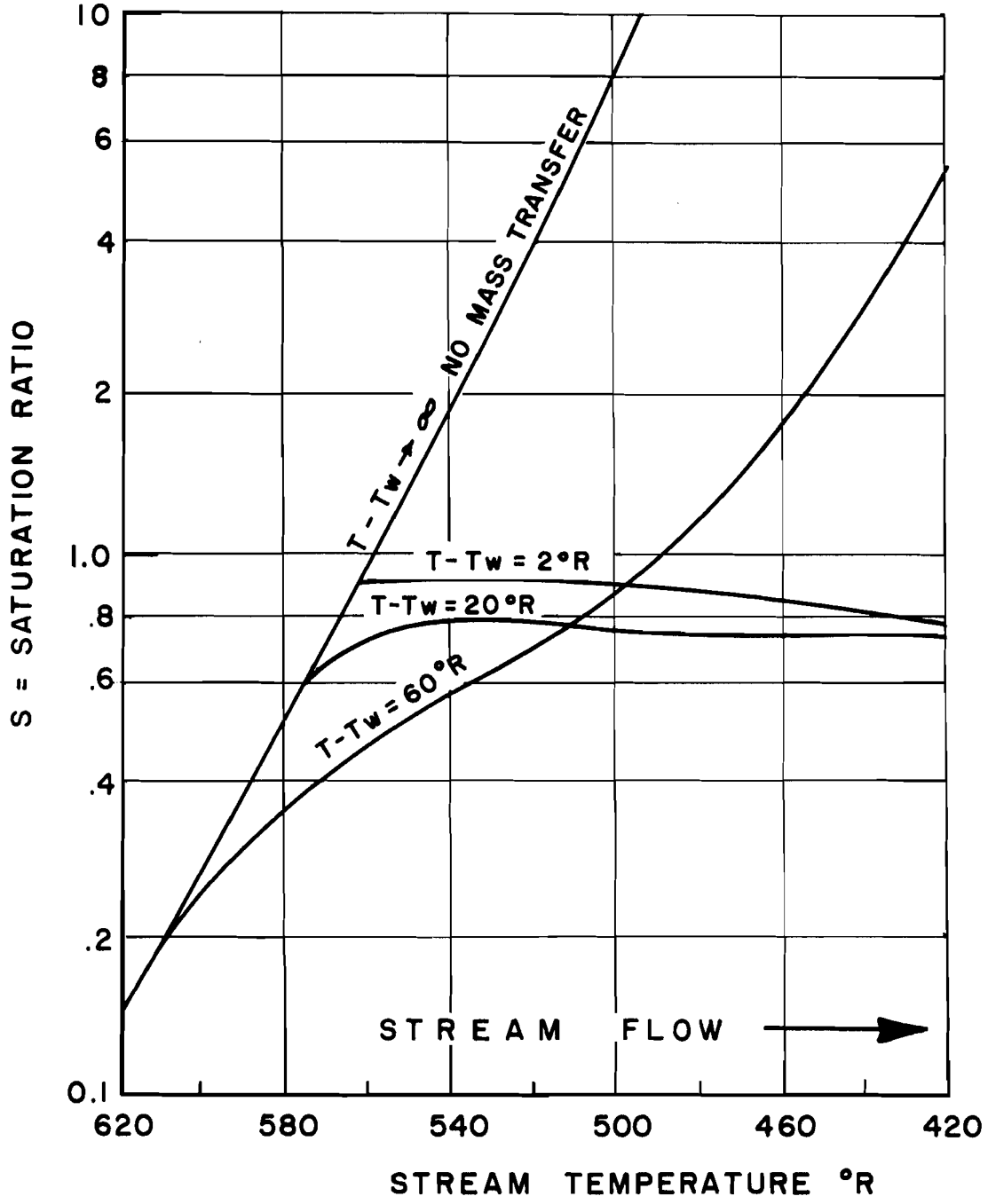

FIGURE 1 EFFECT OF WATER VAPOR REMOVAL BY MASS TRANSFER TO TUBE WALLS ON SATURATION RATIO

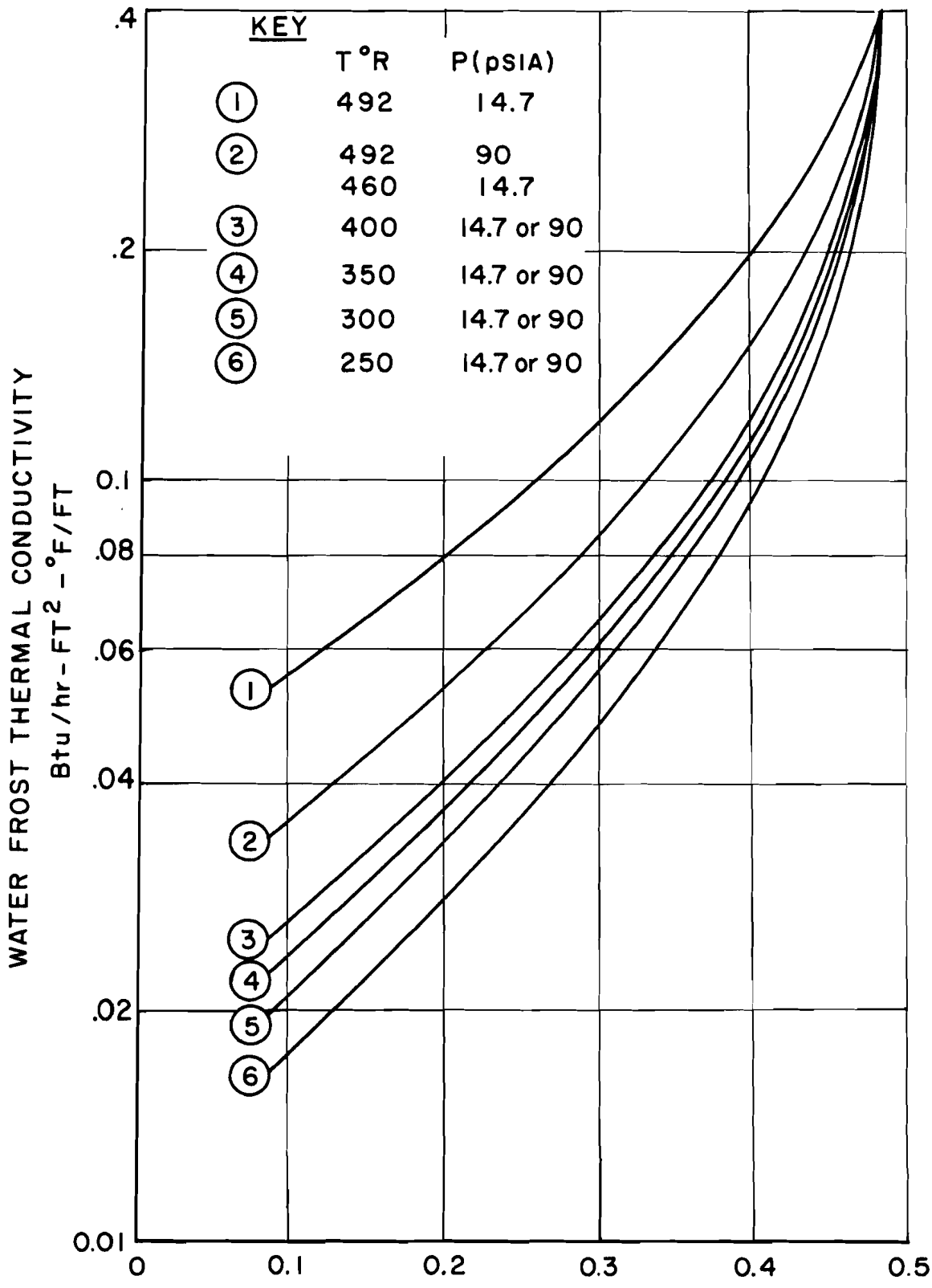

FIGURE 2 LOW-DENSITY WATER FROST THERMAL CONDUCTIVITY

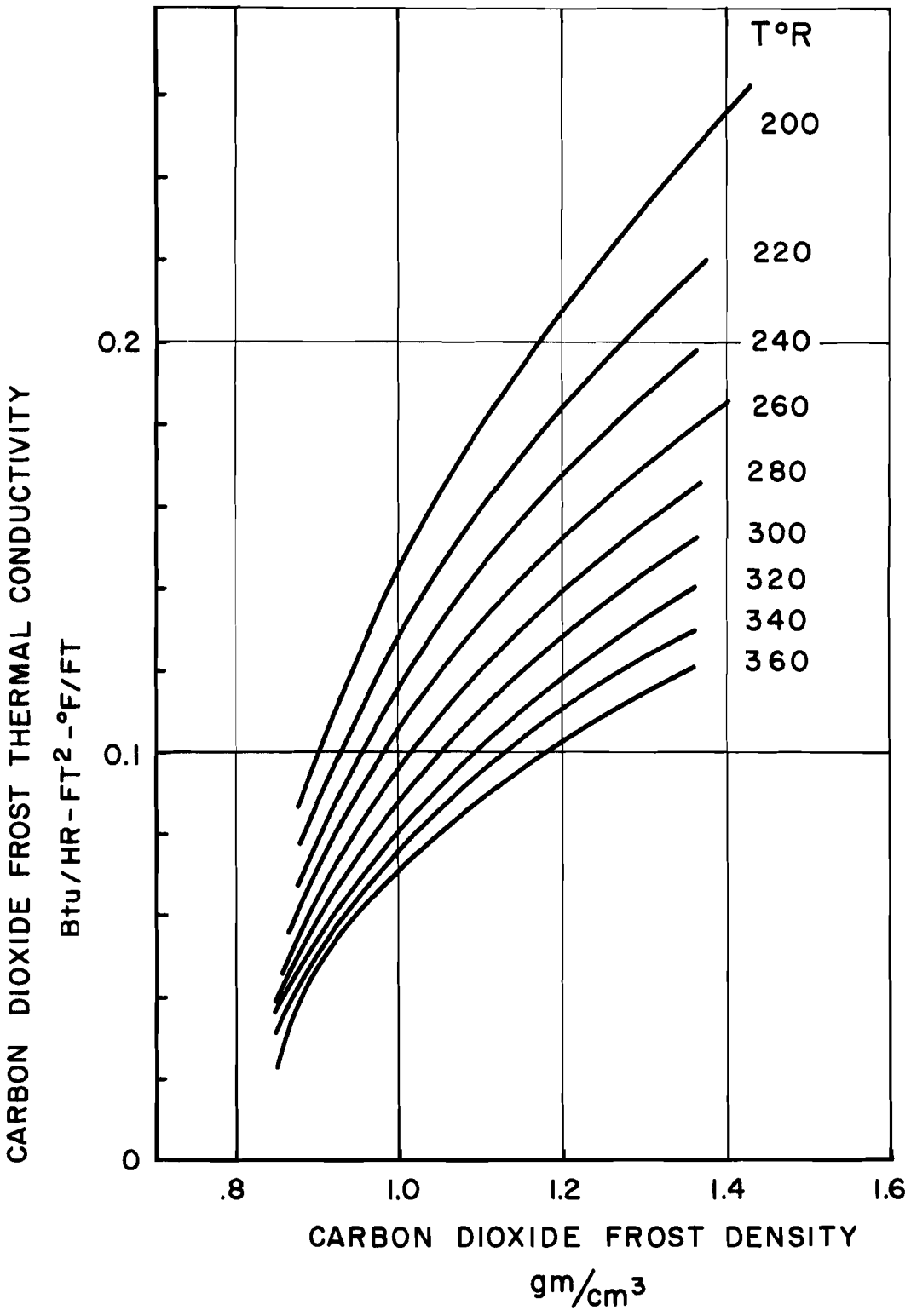

FIGURE 3 THERMAL CONDUCTIVITY OF CARBON DIOXIDE FROST

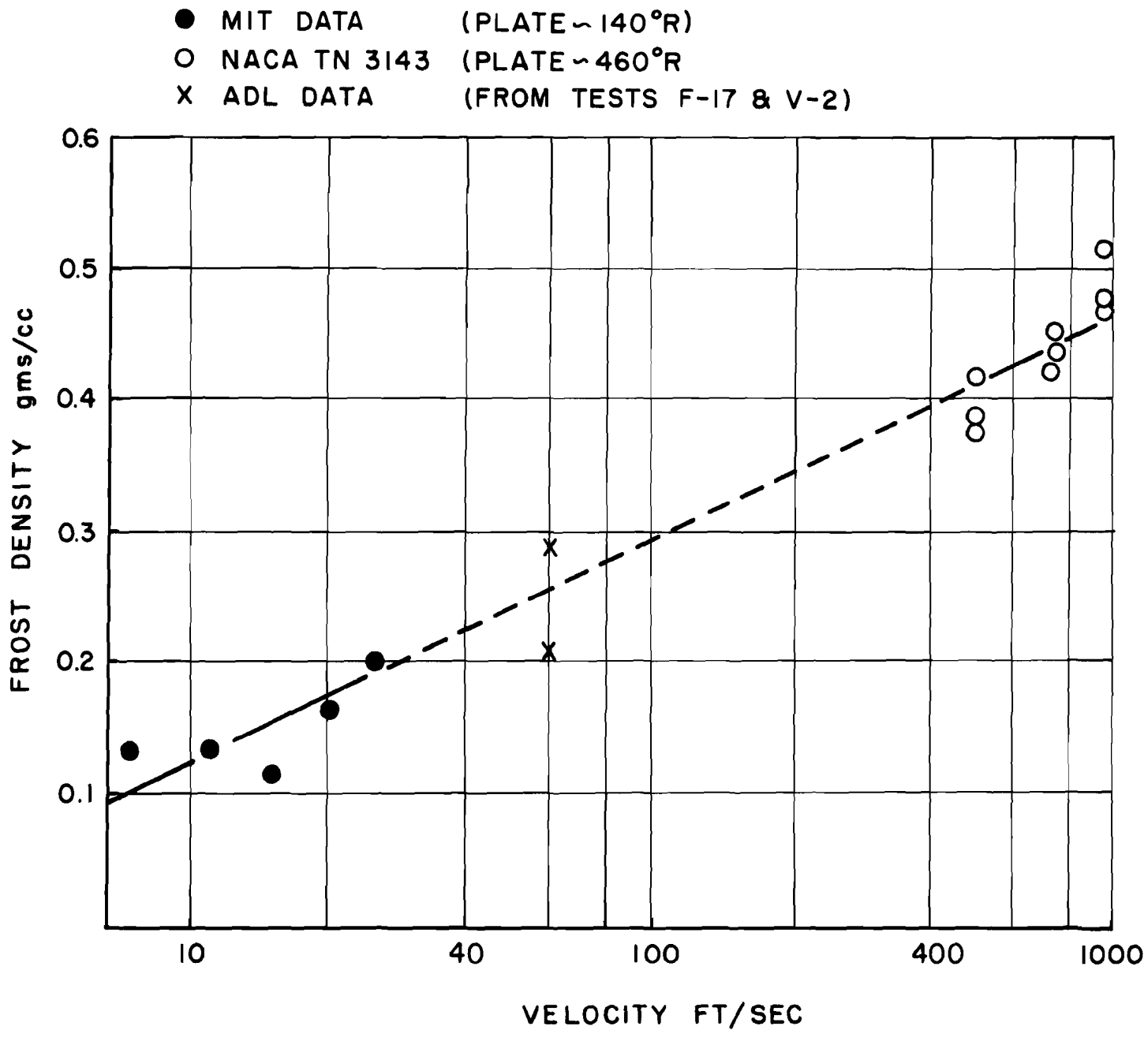

FIGURE 4 WATER FROST DENSITY

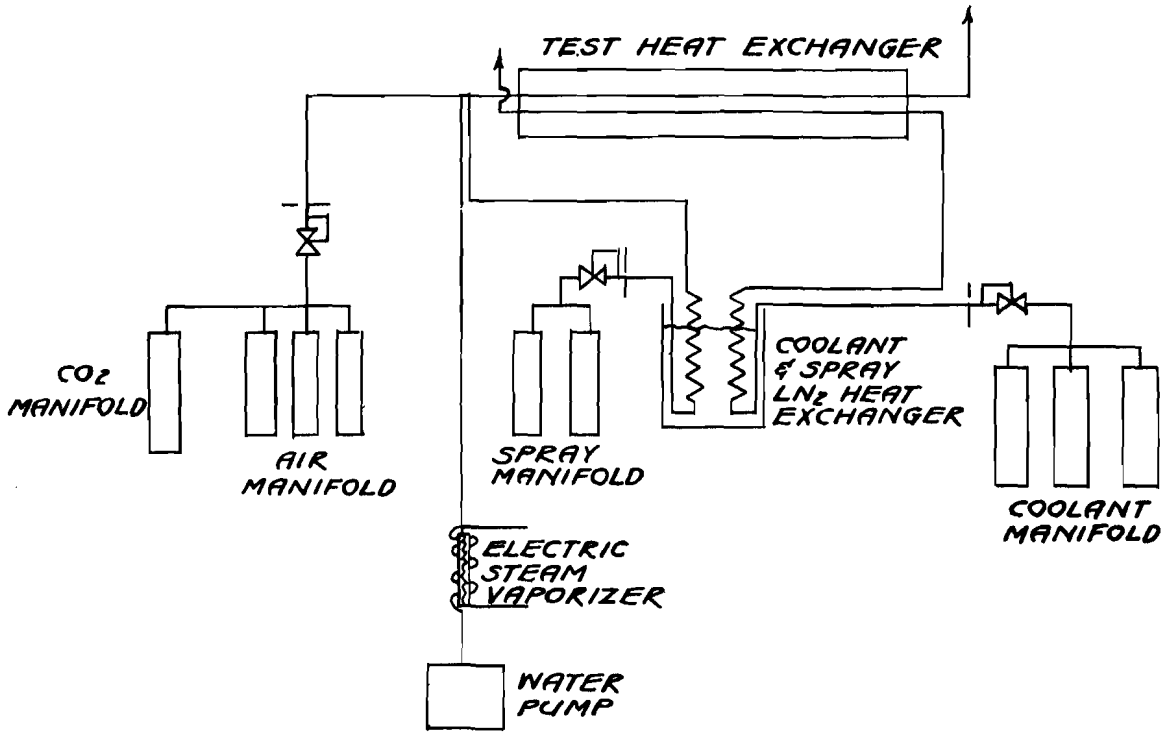

FIGURE 5 TEST FACILITY SCHEMATIC

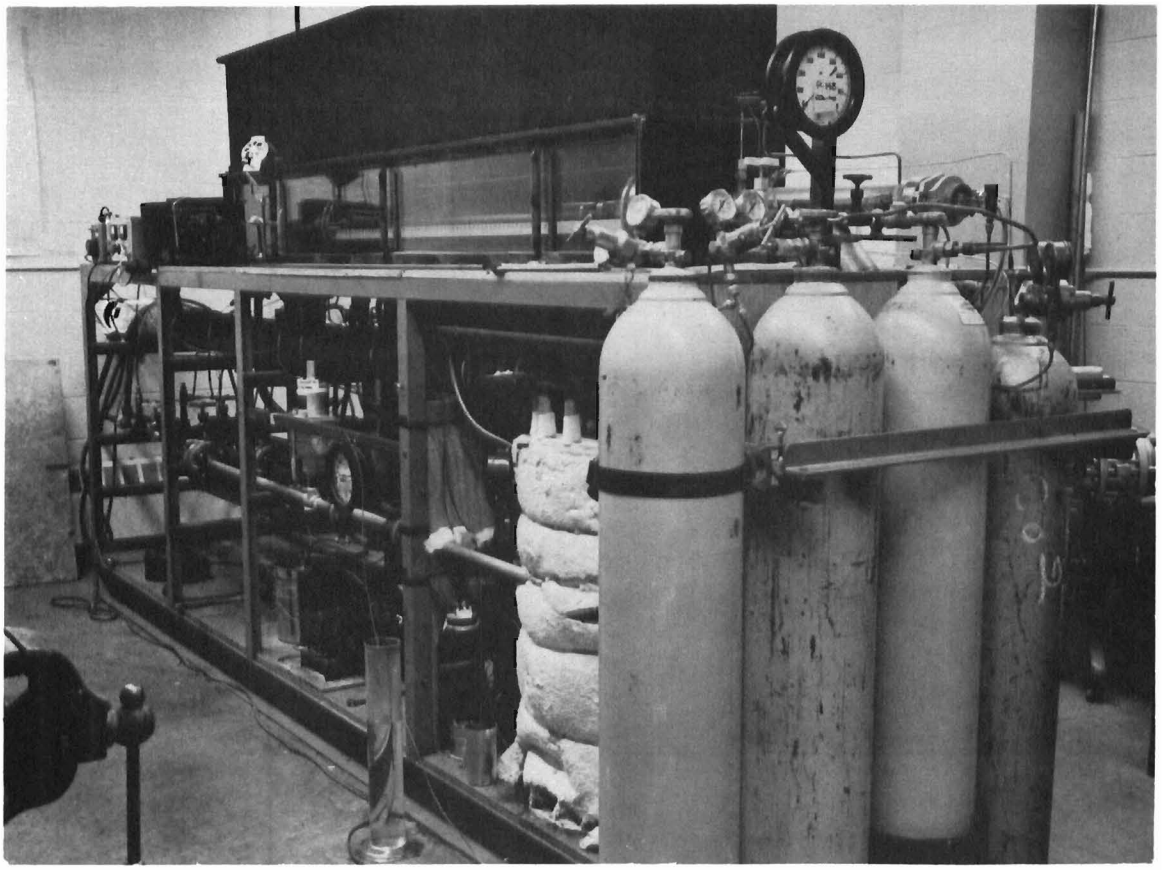

FIGURE 6 TEST-SKID VIEWING SIDE

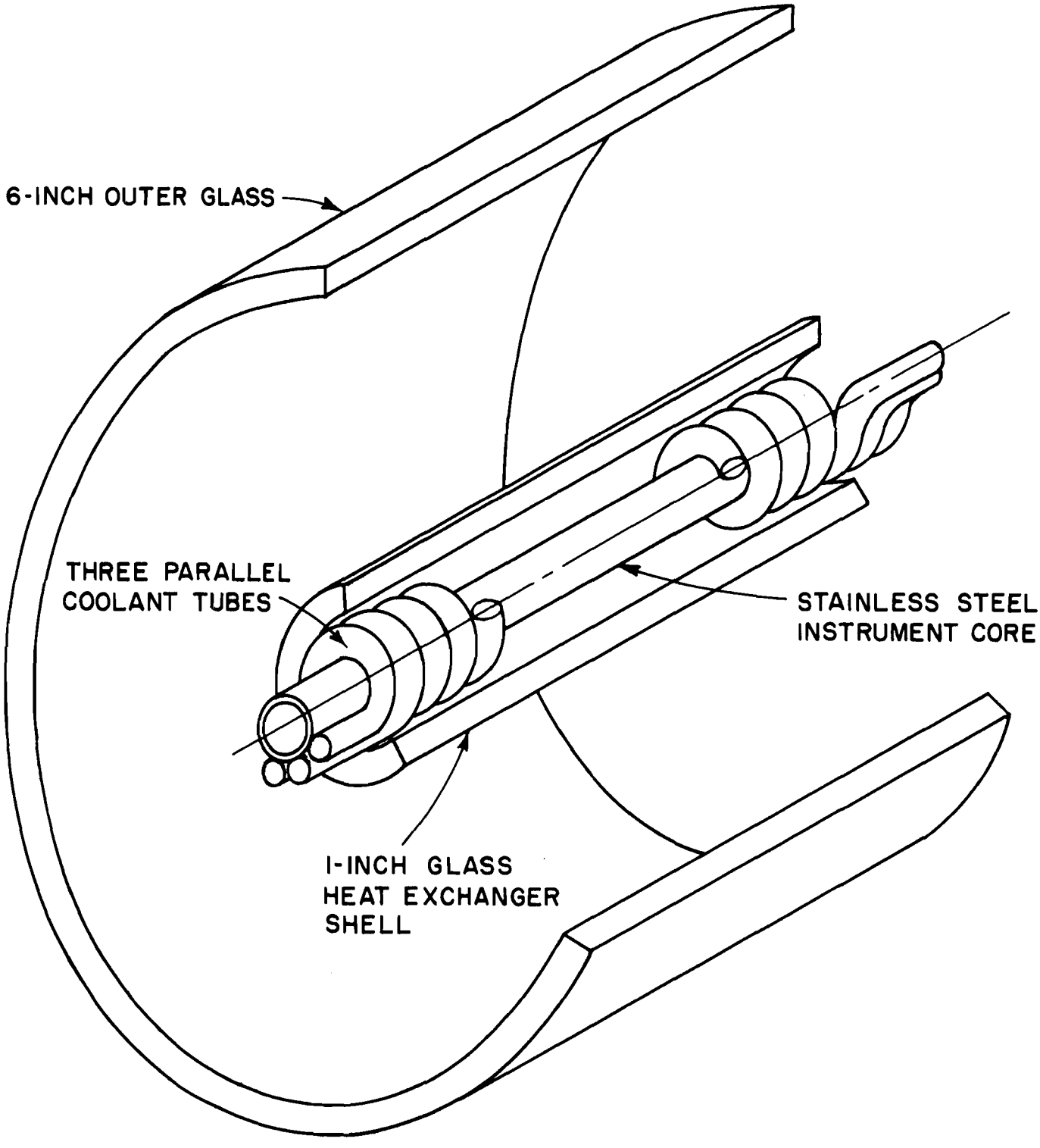

FIGURE 7 TEST CORE WRAP - UP

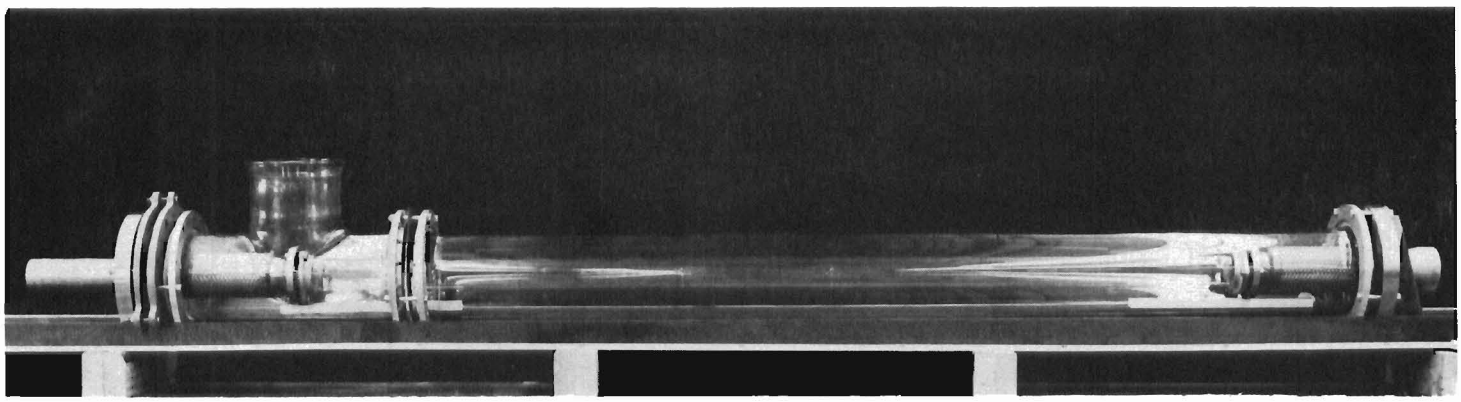

A. OUTER GLASS ON ALIGNMENT CHANNEL WITH FLANGES AND 2-INCH INNER GLASS INSTALLED.

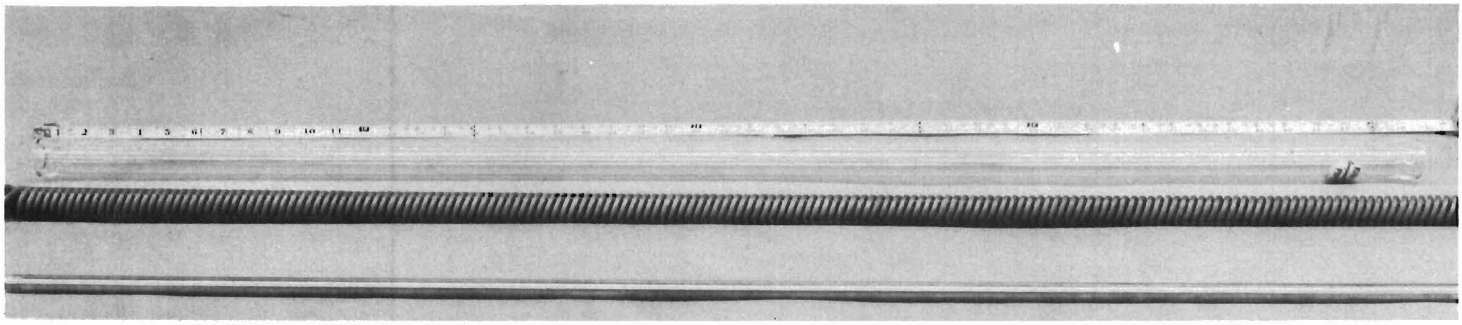

B. TEST CORE FOR 1-INCH SPIRAL HEAT TRANSFER SECTION (1-INCH SPIRAL COOLANT TUBES, WITH INSTRUMENTATION CORE AND TYPICAL 1-INCH INNER GLASS)

FIGURE 8 TEST HEAT EXCHANGER

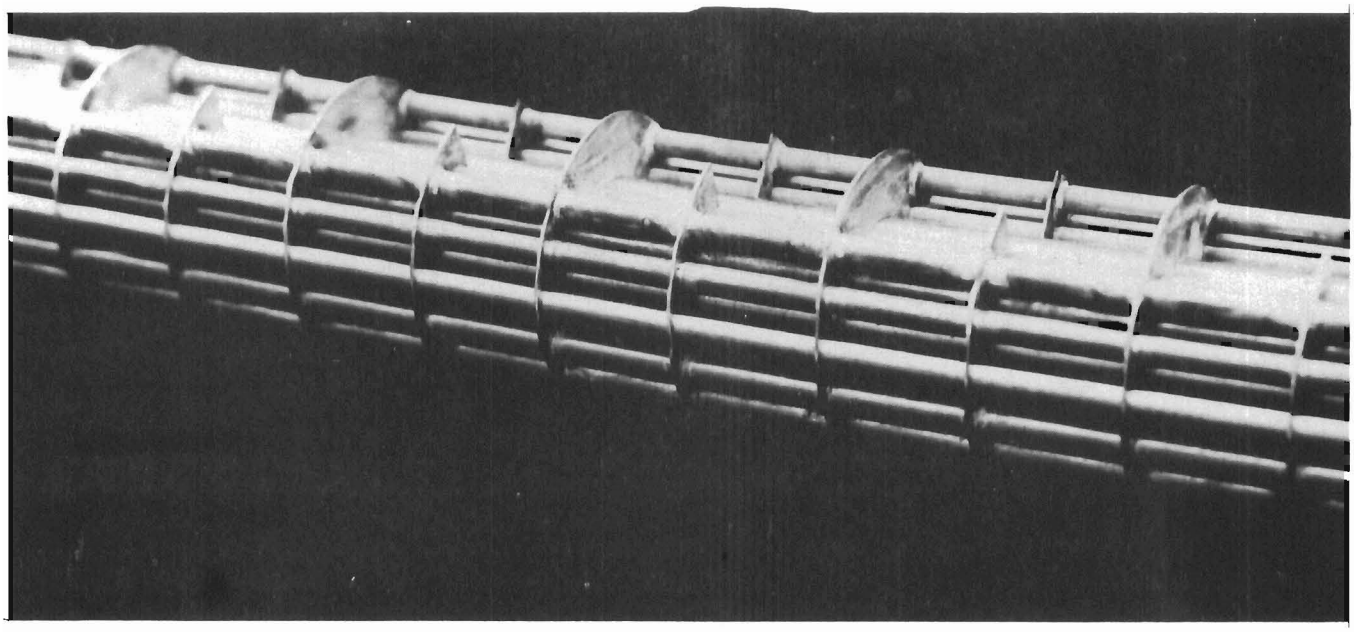

A 2-INCH STAGGERED TUBE BAFFLED HEAT EXCHANGER TUBE AND BAFFLE DETAILS

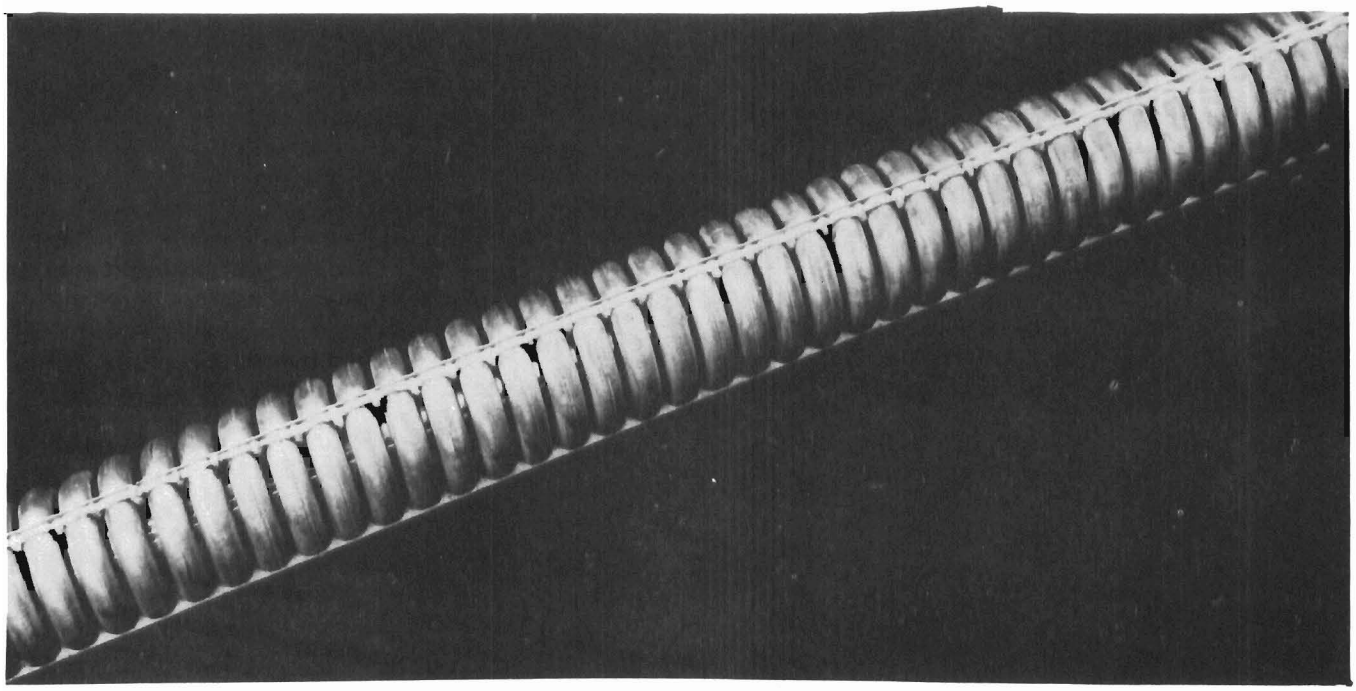

B 2-INCH SPIRAL TUBE HEAT EXCHANGER TUBE DETAILS

FIGURE 9 TEST HEAT TRANSFER SECTIONS

CLOSE-UP AT 21-29 INCHES

TEST F-17

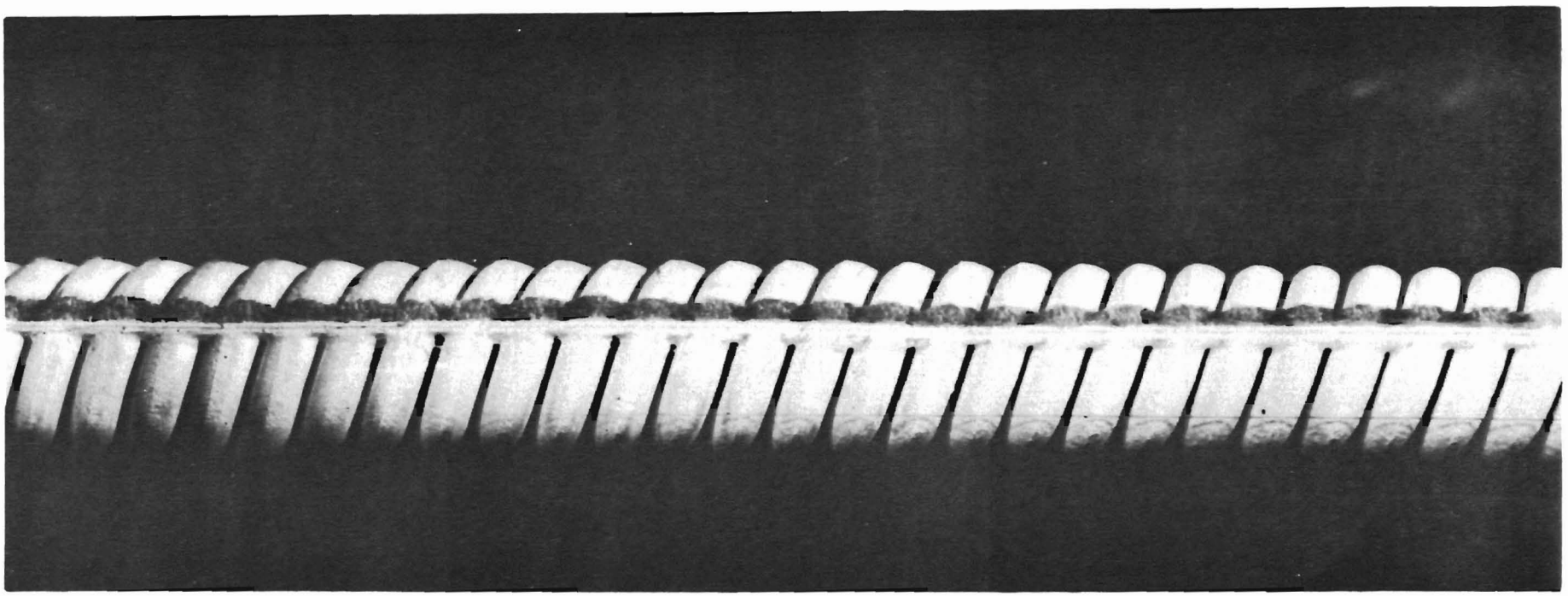

FIGURE 10 "MASS TRANSFER" DEPOSIT FORMATION

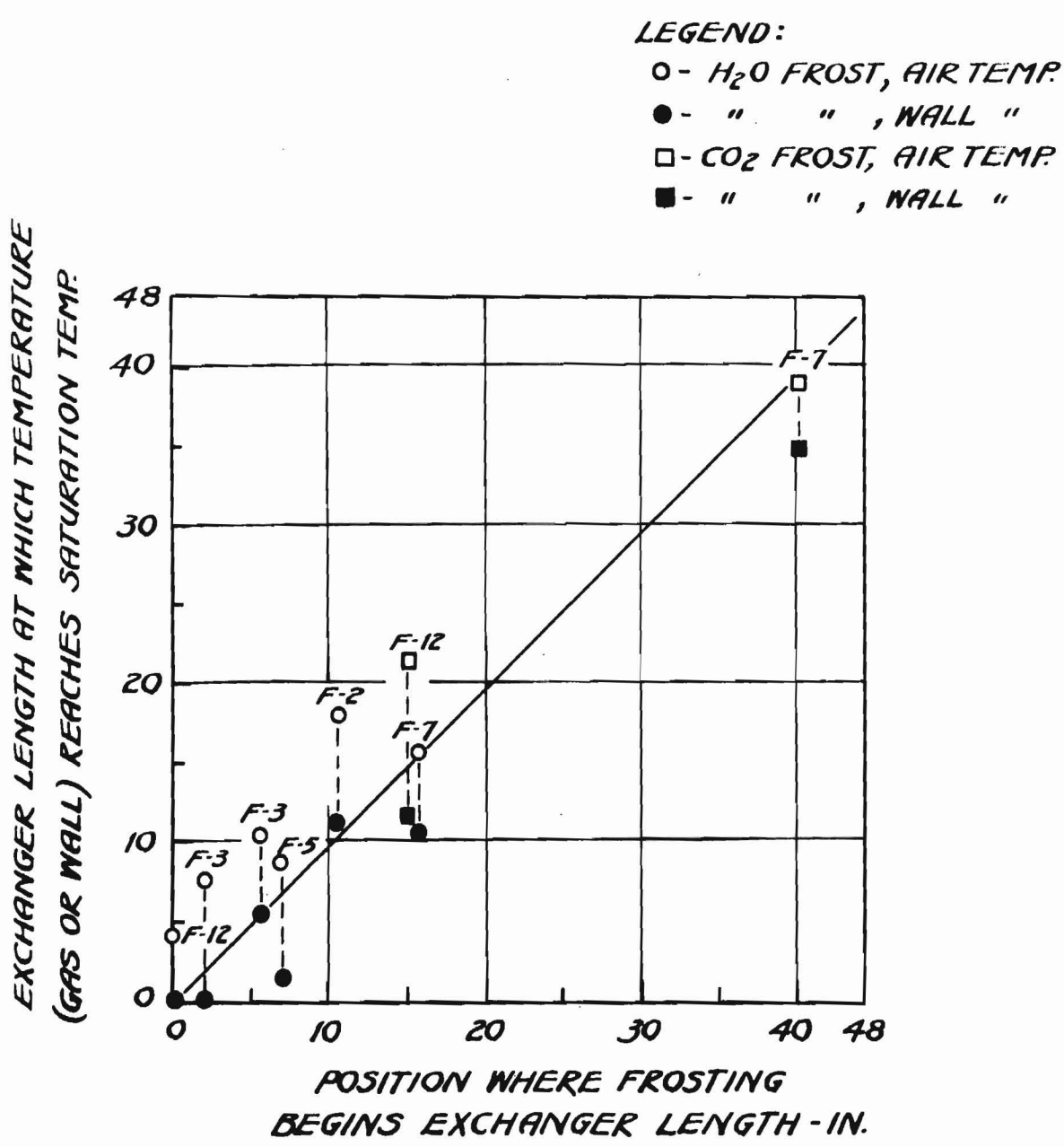

FIGURE 11 LOCATION OF FREEZE - OUT POINT

CLOSE-UP AT 2-10 INCHES

TEST F-13

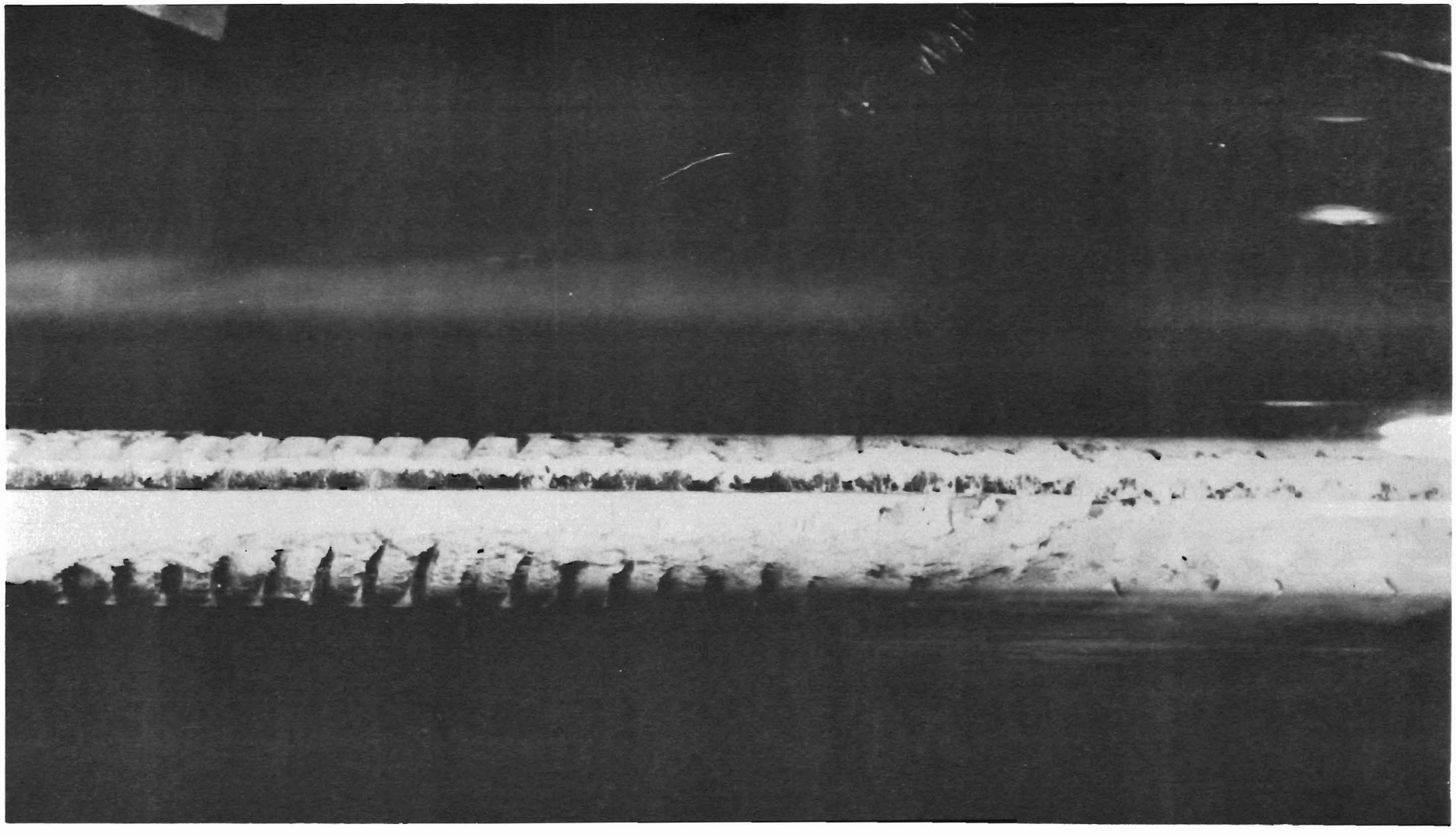

FIGURE 12 "LN_2 SPRAY" DEPOSIT FORMATION

CLOSE - UP AT 0-8 INCHES

TEST F-12

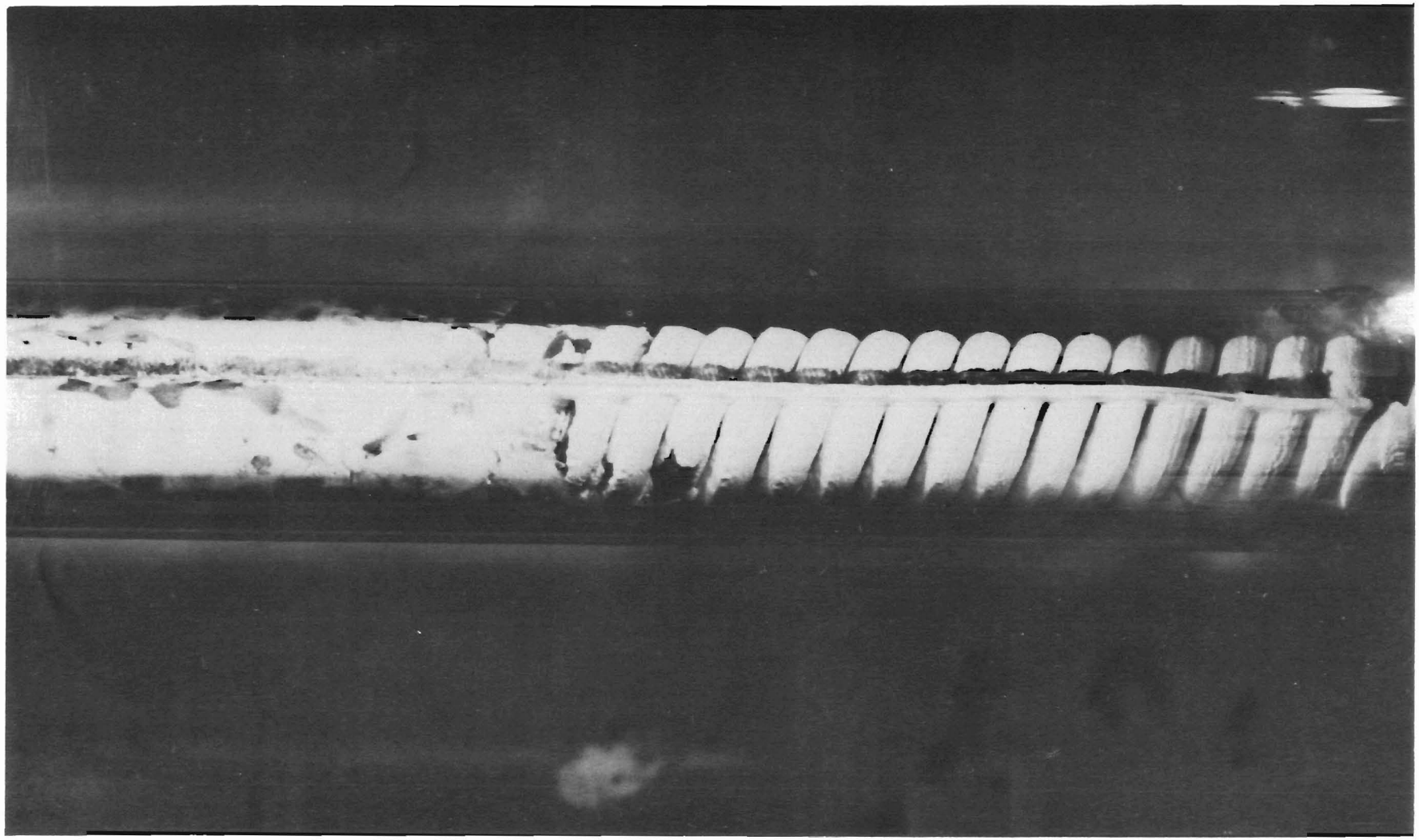

FIGURE 13 "HIGH ΔT" DEPOSIT FORMATION

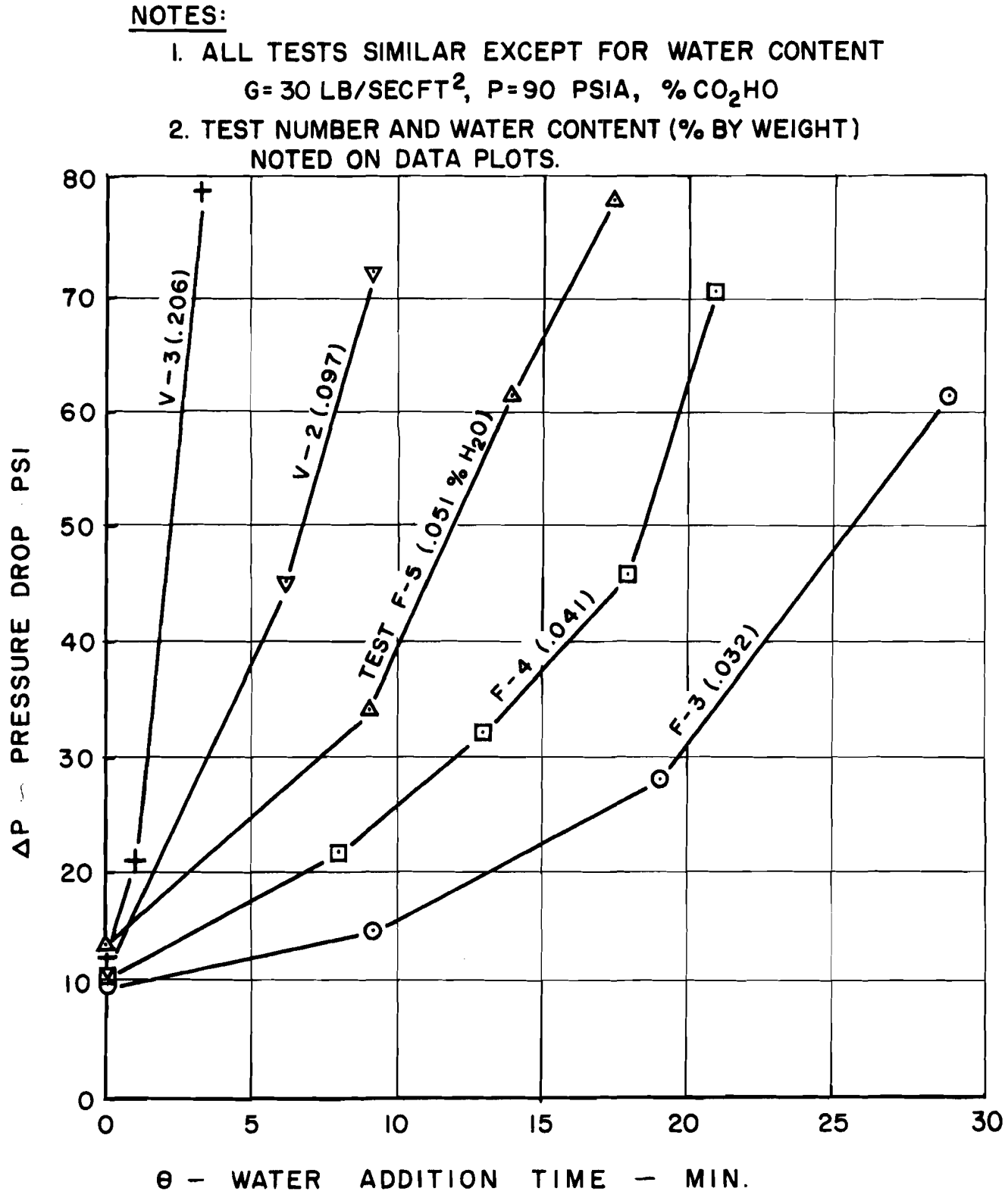

FIGURE 14 TYPICAL PRESSURE DROP DATA

SYMBOL	TEST	$\%H_2O$	G LB/SECFT^2	P PSIA	COOLANT INLET TEMP-°R	X/L
●	DATA of FIG. 11		30	90	300	.32-.37
▲	F-17	.017	100	300	150	.30
⊙	F-8	.016	30	90	170	.23
⊡	V-8	.025	15	90	170	.18
△	F-10	.018	50	90	170	.18
+	V-1	.025	10	30	190	.17
▽	V-5	.027	30	90	410	.44

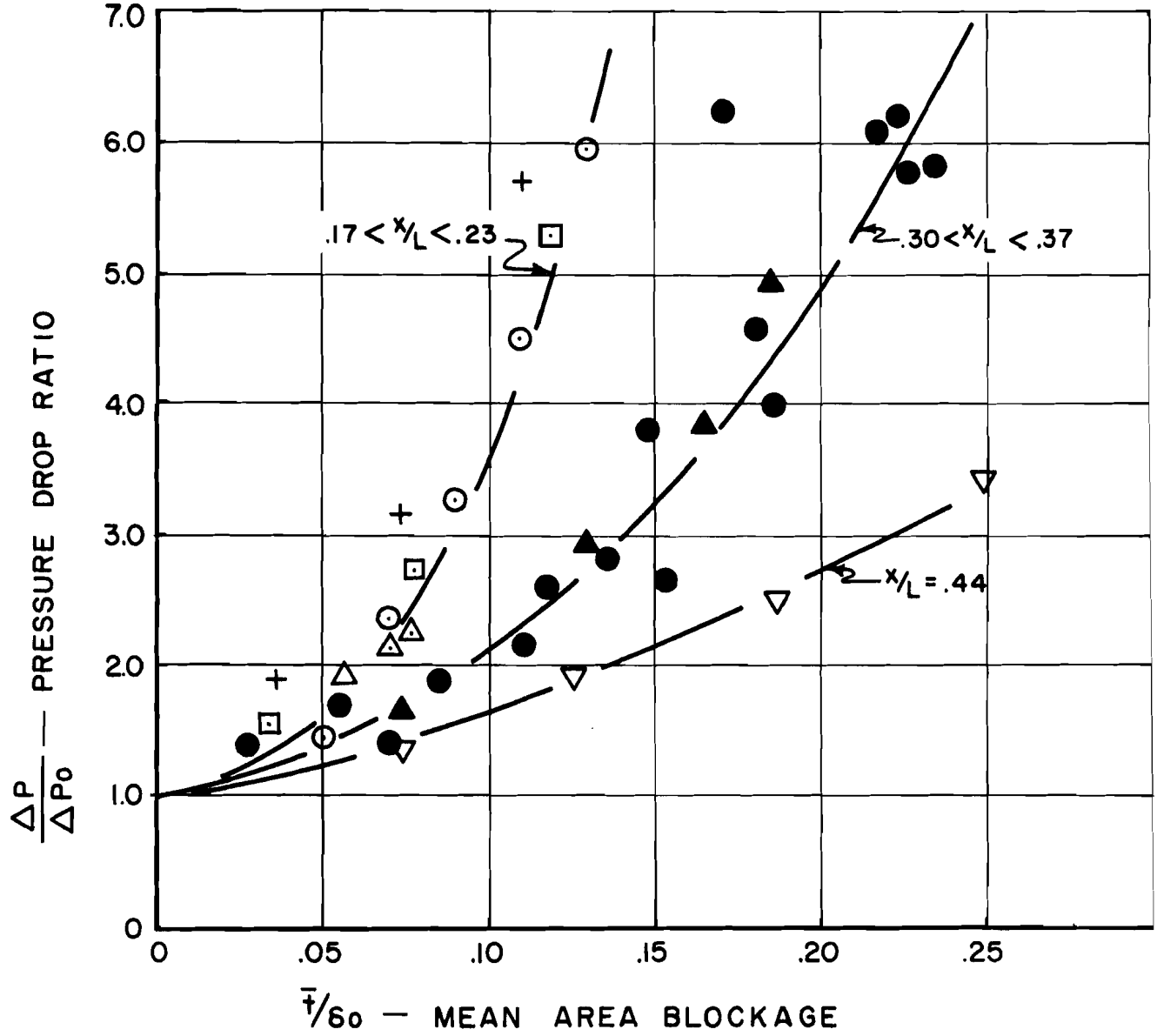

FIGURE 15 PRESSURE DROP CORRELATION

SYMBOL	TEST	$\frac{W_{SPRAY}}{W_{CARRIER}}$
■	F-14	.25
●	F-13	.33
▼	V-9	.46

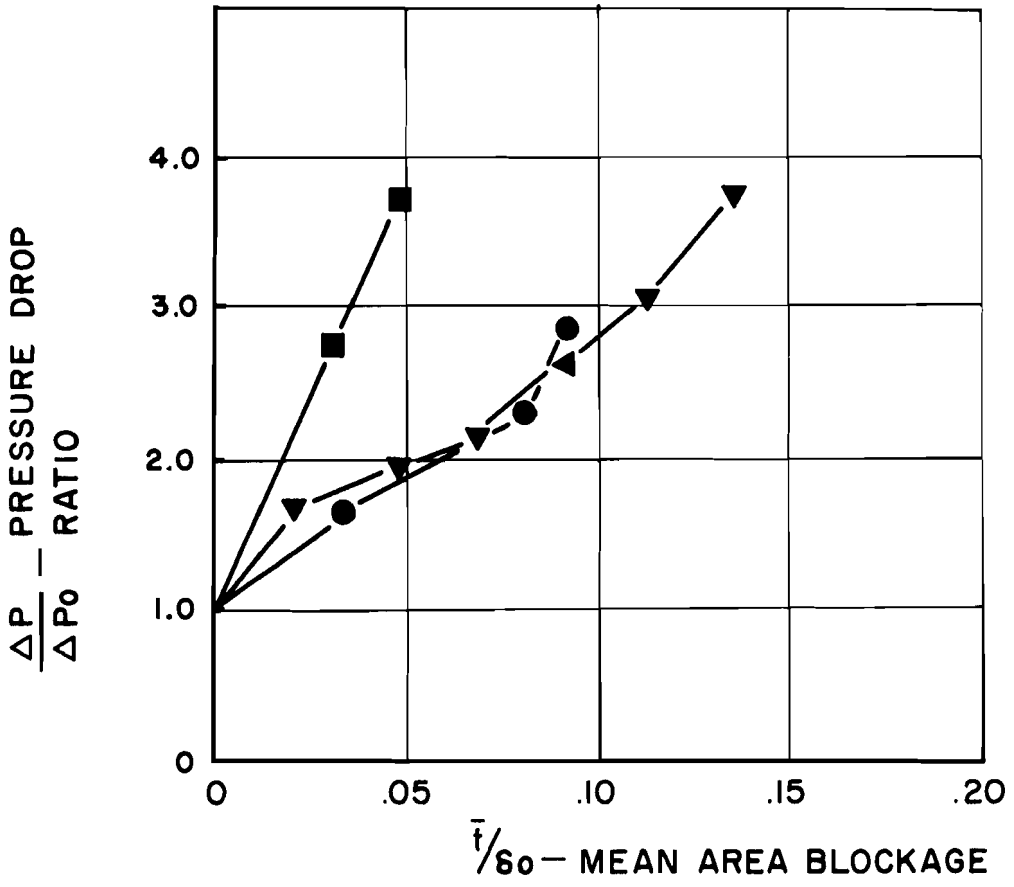

FIGURE 16 PRESSURE DROP CORRELATION LN_2 SPRAY TESTS

SYMBOL	TEST	% H_2O
+	F - 2	.006
⊙	F - 3	.032
⊡	F - 4	.041
△	F - 5	.051

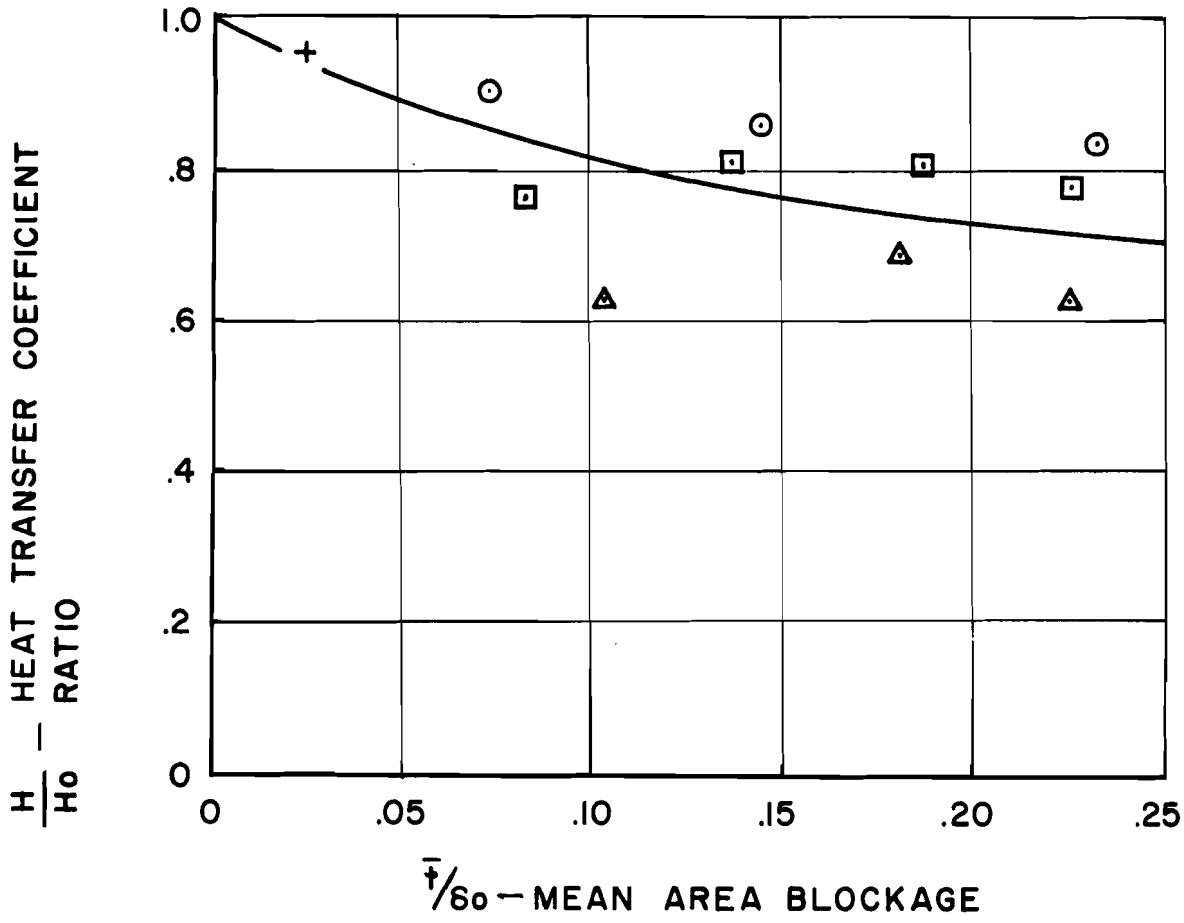

FIGURE 17 HEAT TRANSFER CORRELATION

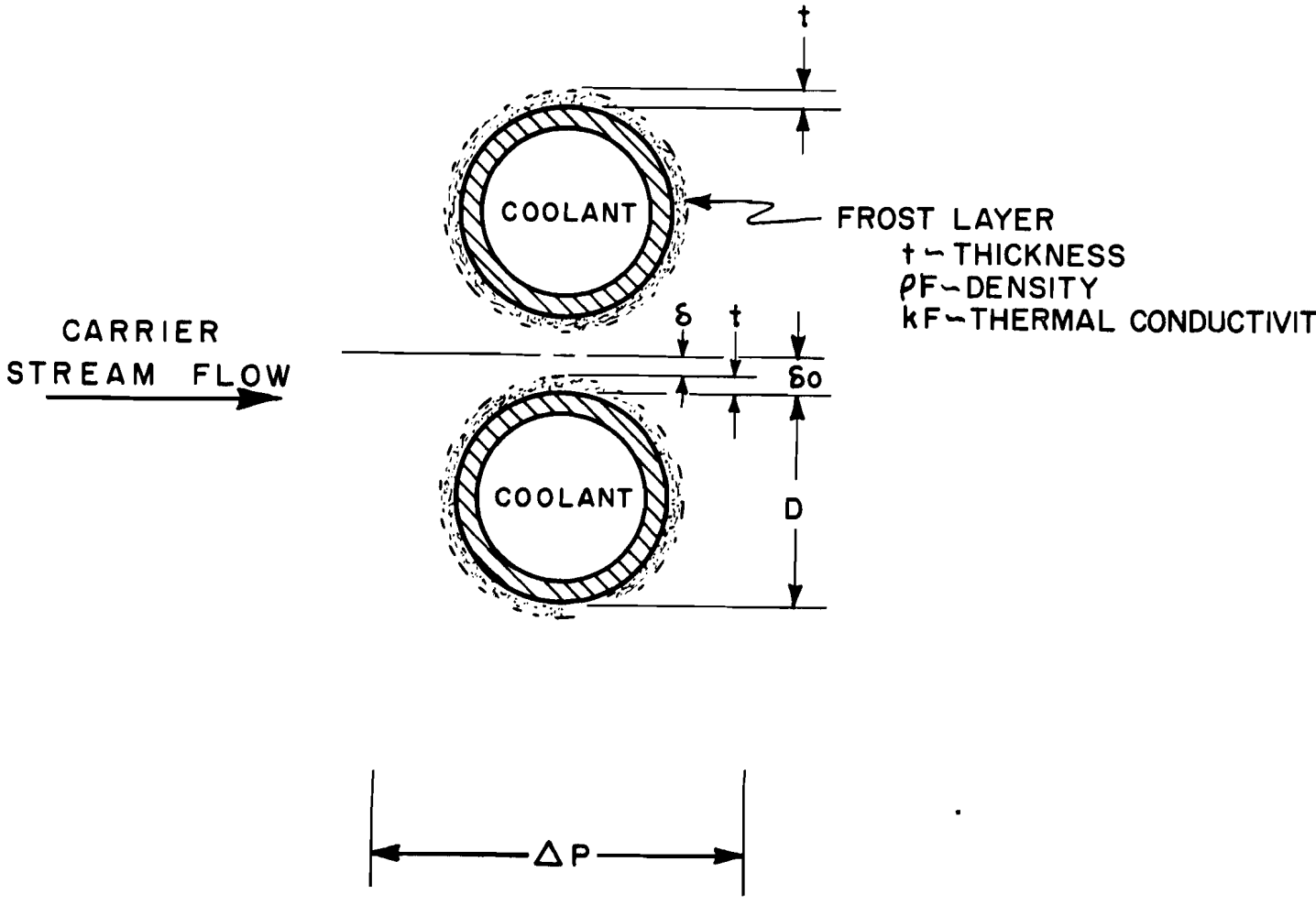

FIGURE 18 GEOMETRIC MODEL FOR SINGLE TUBE FLOW AND HEAT TRANSFER ANALYSIS

NOTES:

1. CONSTANT FLOW DENSITY
2. $\frac{\Delta P/\Delta P_o}{(W/W_o)^2} = \left[\frac{1}{1-t/\delta_o}\right]^2$
3. RESULTS APPLICABLE TO ANY SYSTEM OPERATING LINE (I.E. CONST. w or CONST. ΔP)

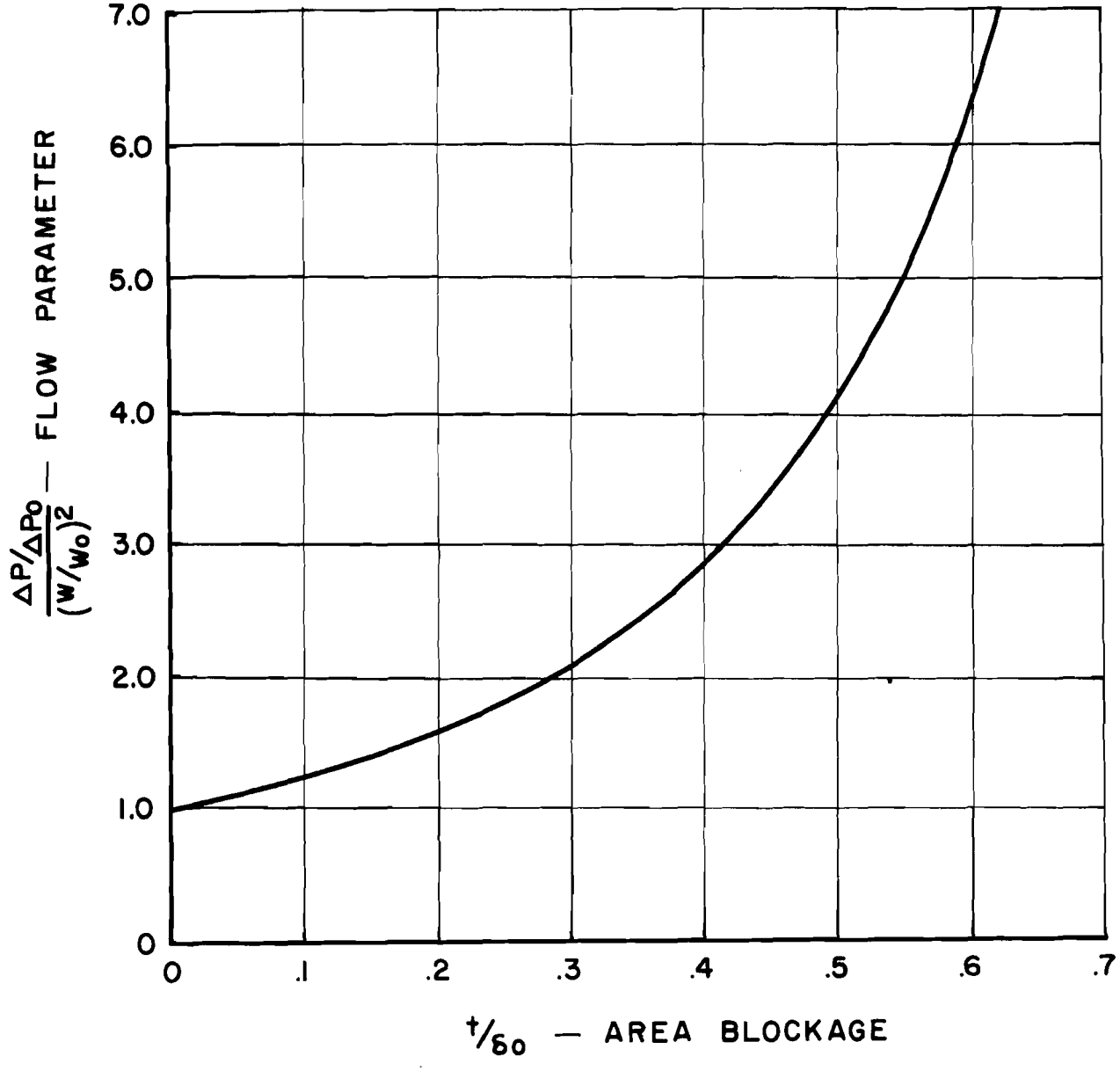

FIGURE 19 EFFECT OF AREA BLOCKAGE ON FLOW CAPACITY SINGLE TUBE ROW ANALYSIS

NOTES:

1. CLOSE PACKED TUBES ($\delta_o/\delta_o \ll 1$)
2. FOR CONST ΔP ——————
$$u_o/u = 1 + \left(\frac{h\delta_o}{RF}\right)\left(t/\delta_o\right)$$
3. FOR CONST w — — — — — — —
$$u_o/u = (1 - t/\delta_o)^{.6} + \left(\frac{h\delta_o}{RF}\right)\left(t/\delta_o\right)$$

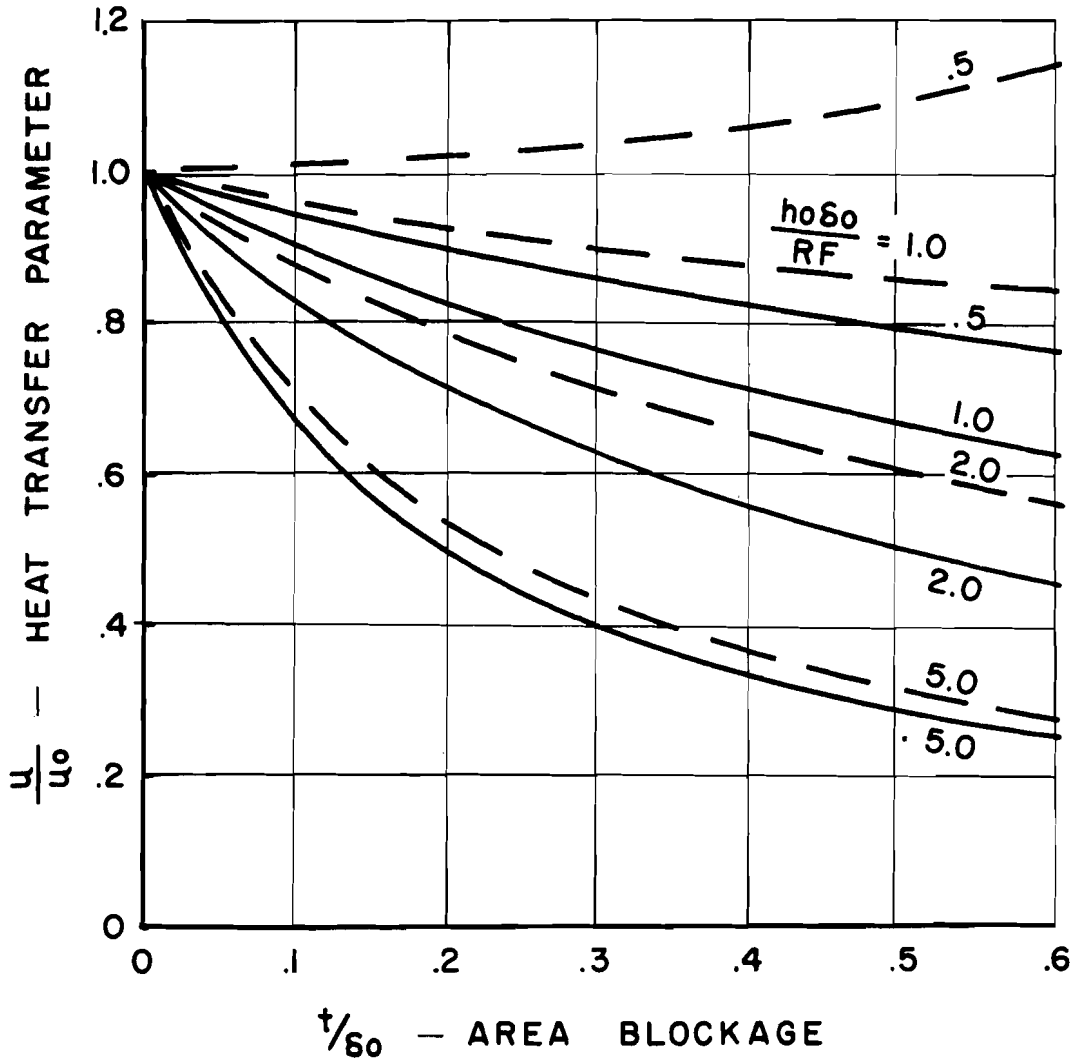

FIGURE 20 EFFECT OF FROST LAYER ON HEAT TRANSFER SINGLE TUBE ROW ANALYSIS

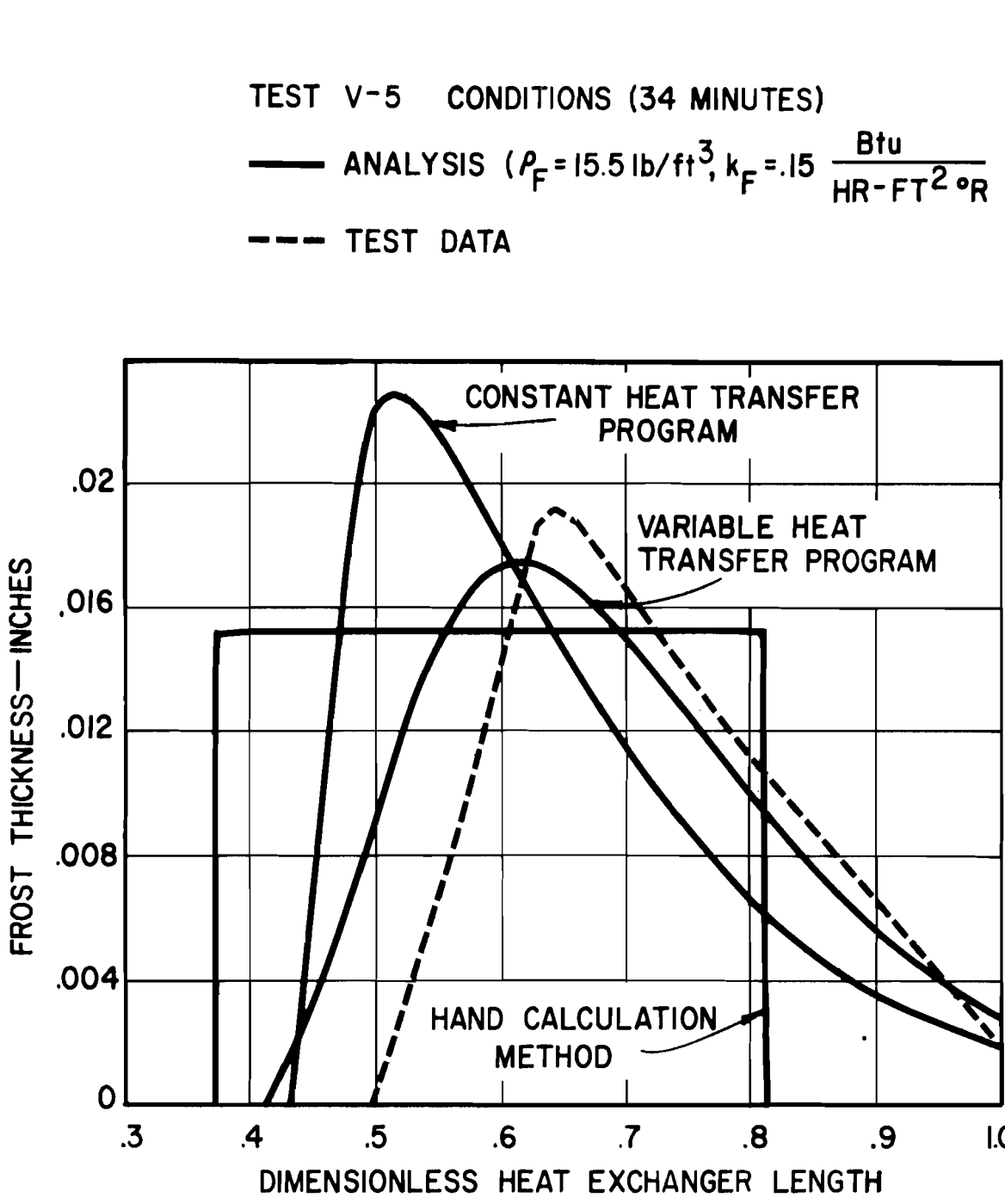

FIGURE 21 FROST THICKNESS PROFILES - COMPARISON OF ANALYTICAL METHODS

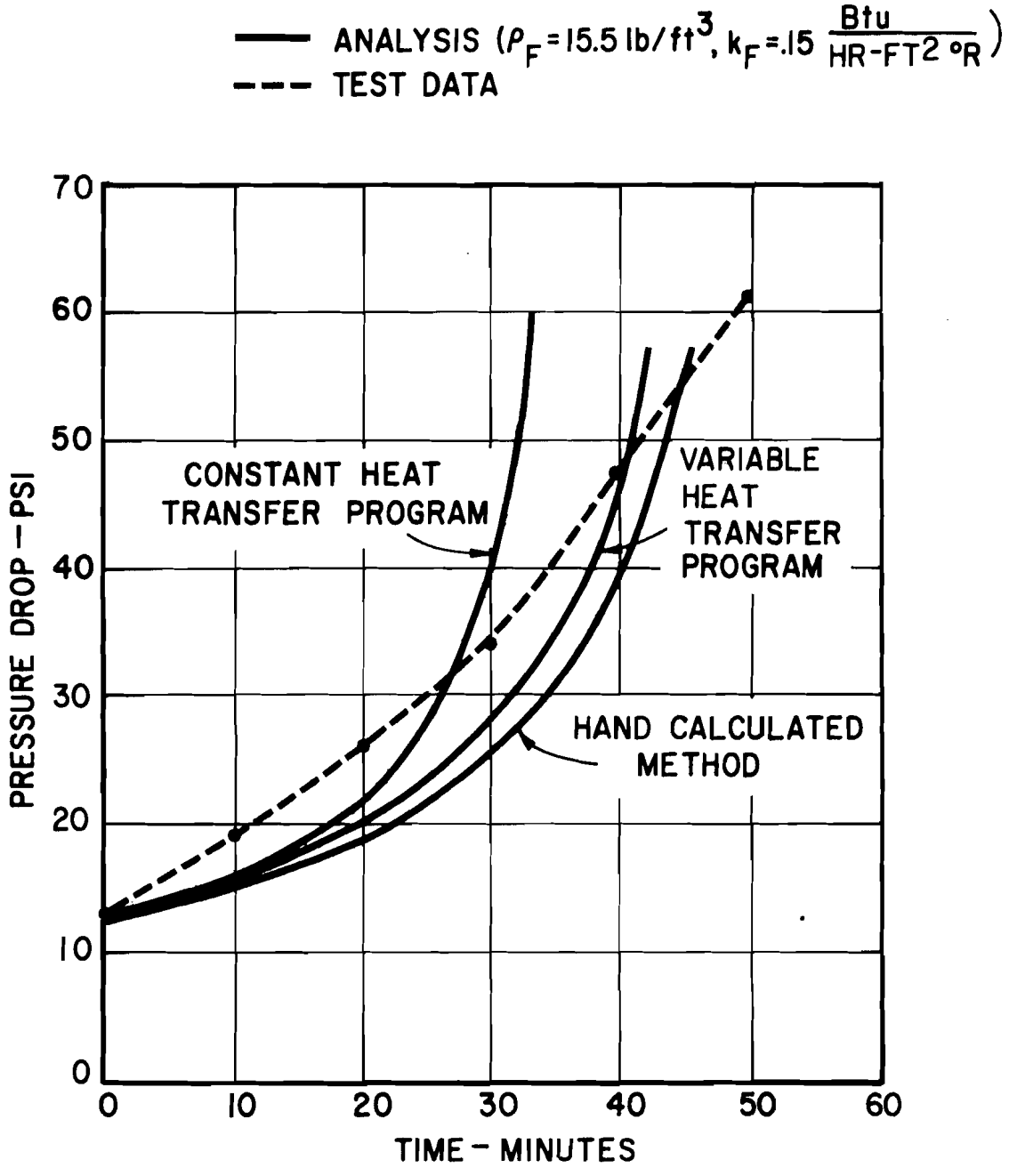

FIGURE 22 HEAT EXCHANGER PRESSURE DROP - COMPARISON OF ANALYTICAL METHODS

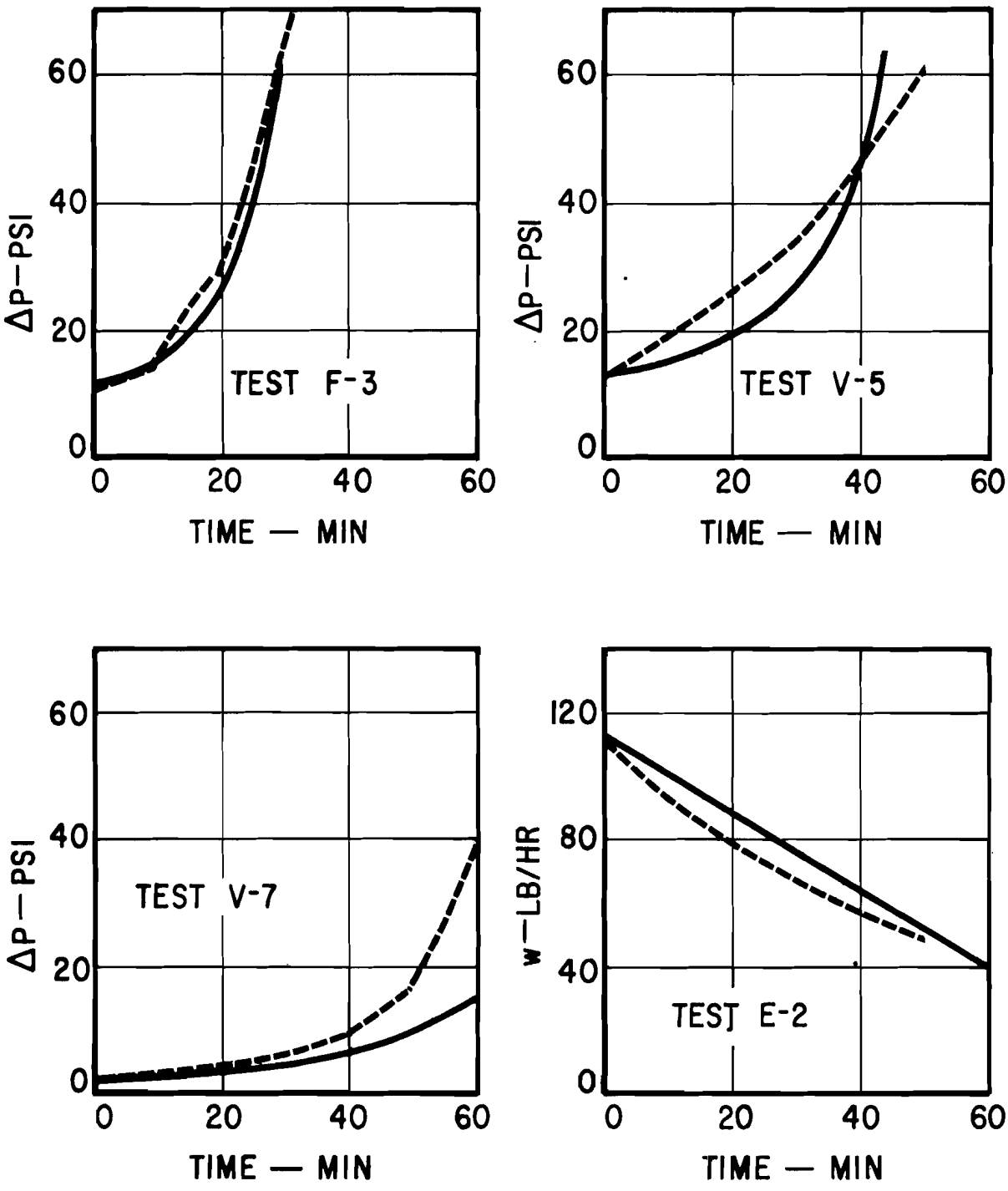

NOTES:

1. TESTS F-3 AND V-5 — CONST. FLOW — WATER FROST
2. TEST E-2 — CONST. ΔP — WATER FROST
3. TEST V-7 — CONST. FLOW — CO_2 FROST

——— VARIABLE HEAT TRANSFER COMPUTER PROGRAM

- - - - EXPERIMENTAL DATA

FIGURE 23 PRESSURE DROP AND FLOW COMPARISONS

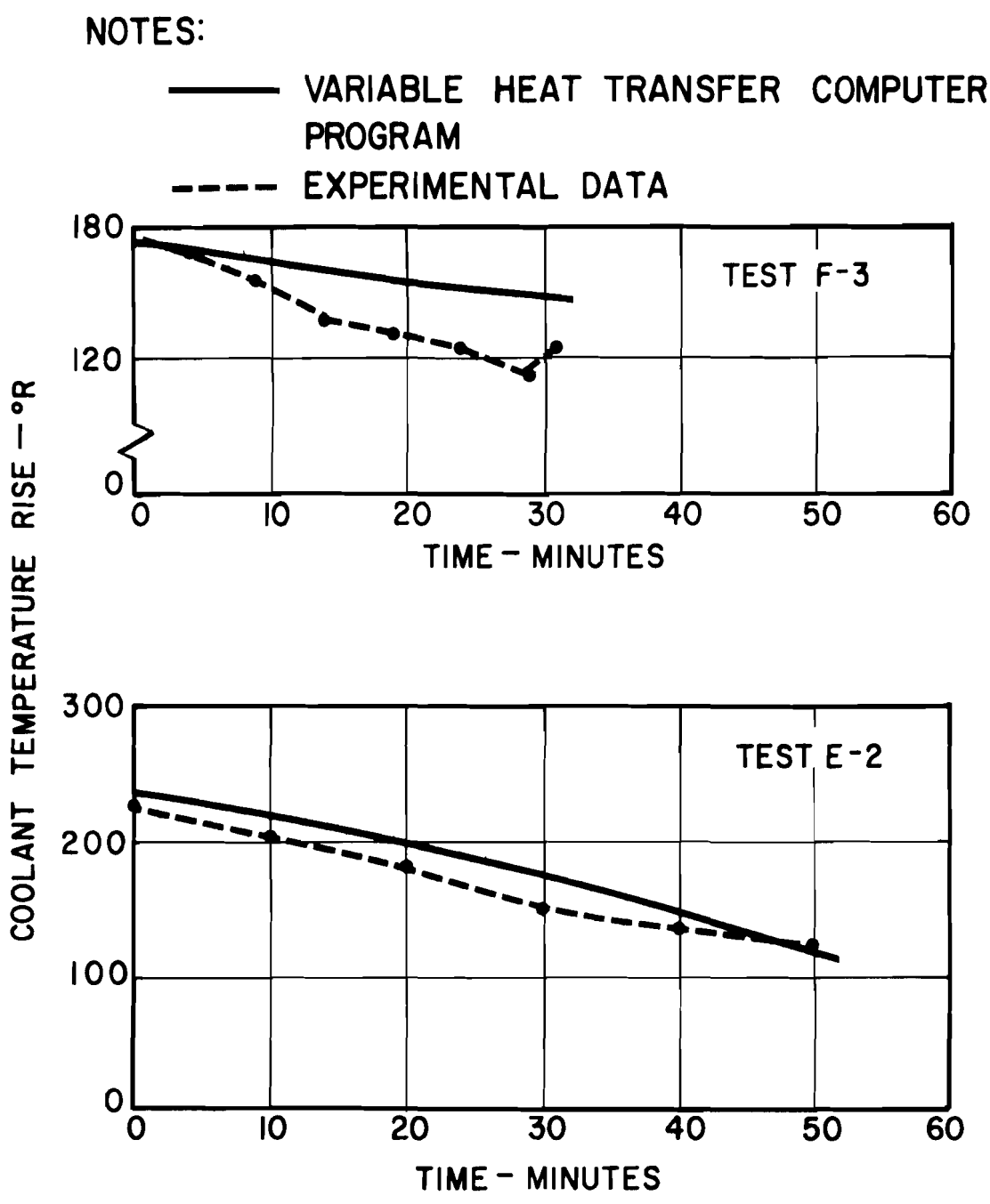

FIGURE 24 HEAT TRANSFER COMPARISONS

APPENDIX 1

REMOVAL OF WATER AND CARBON DIOXIDE FROM A TURBULENT AIR STREAM BY MASS TRANSFER TO THE COLDER TUBE WALL

TABLE OF CONTENTS

A. Heat and Mass Transfer Model

1. Qualitative Discussion

Let us assume that air containing water vapor and carbon dioxide is being cooled as it flows down the inside of a circular tube. As soon as the tube wall temperature drops below the saturation temperature corresponding to the partial pressure of the impurity (CO_2 or H_2O) in the air, mass transfer to the wall will begin. In addition, heat transfer to the wall continues to reduce the temperature of the air flow stream.

The degree of impurity saturation in the air stream will depend on the relative rates of heat and mass transfer. If no mass transfer occurred, the air would become supersaturated in the impurity. At high rates of mass transfer, the impurity would be depleted more rapidly than the decrease in vapor pressure of the impurity in the cooling bulk air, and the air would never become saturated.

By examining the basic heat and mass transfer relationships for the system, we may estimate the relative rates of heat and mass transfer for various conditions. Then the air stream saturation ratio;

$$S = \frac{P}{P_s} = \frac{\text{actual partial pressure of species in bulk air}}{\text{vapor pressure of species at bulk air temperature}}$$

may be evaluated as a function of air stream temperature in the exchanger. The value of S may then be used in conjunction with the results from our study of homogeneous and heterogeneous nucleation to predict the mechanism for freeze-out of water vapor and carbon dioxide for a specific system. This analysis allows us to estimate both the wall freeze-out due to mass diffusion and the bulk freeze-out due to heterogeneous and/or homogeneous nucleation.

2. Basic Equations

Heat transfer:

$$dq = mC_p dT = -hdA_s (T - T_w) \qquad (1)$$

m = mass flow of air, lbs/hr

q = heat flow rate, BTU/hr

C_p = heat capacity of air, BTU/lb ^oR

T = bulk temperature of air, ^oR

h = heat transfer coefficient, BTU/hr ft^2 ^oR

A_s = heat transfer surface area, ft^2

T_w = wall temperature, ^oR

or, $dq = 3600\ V_g\ \rho_g\ (\frac{\pi}{4}\ D^2)\ C_p\ dT = -h\ (\pi\ D dL)\ (T - T_w)$ (2)

V_g = air velocity, ft/sec

ρ_g = air density, lbs/ft^3

D = tube inside diameter, ft

L = tube length, ft

and finally,

$$dT = \frac{-h}{3600\ V_g\ \rho_g\ C_p}\ \frac{4}{D}\ (T - T_w)\ dL \qquad (3)$$

For mass transfer:

$$dw = mdH = -K_m dA_s\ \rho_g\ (H - H_w) \qquad (4)$$

w = impurity transfer rate, lbs impurity/hr

H = humidity, lbs impurity/lb air

H_w = humidity corresponding to saturation at T_w, lbs impurity/lb air

K_m = mass transfer coefficient, ft/hr

The mass transfer equation reduces to:

$$dH = \frac{-K_m}{3600\ V_g}\ \frac{4}{D}\ (H - H_w)\ dL \qquad (5)$$

and the relative rates of mass and heat transfer may be expressed as:

$$\frac{dH}{dT} = \frac{K_m}{(h/\ \rho_g C_p}\ \frac{(H - H_w)}{(T - T_w)} \qquad (6)$$

The mass transfer coefficient may be found from:

$$K_m = .023\ D_v/D\ (DV_g\ \rho_g/\mu_g)^{.83}\ (3600\ \mu_g/\ \rho_g D_v)^{.44} \qquad (7)$$

(from Sherwood & Pigford, "Absorption & Extraction", p. 77, eq. 108, McGraw-Hill, 1952)

D_v = diffusivity of impurity in air, ft^2/hr

μ_g = bulk air viscosity, lb/sec ft

The heat transfer coefficient may be found from:

$$\left(\frac{h}{\rho_g C_p}\right) = .023\ (3600\ V_g)\ \left(\frac{DV_g \rho_g}{\mu_g}\right)^{-.2}\ \left(\frac{3600\ \mu_g C_p}{k_g}\right)^{-.67} \qquad (8)$$

(From McAdams, "Heat Transmission", 3rd Edition, p. 219, eq. 9-10c, McGraw-Hill, 1954)

k_g = thermal conductivity of air, BTU/hr ft ^oR

Combining eqs. 6, 7, and 8, we obtain:

$$\frac{dH}{dT} = 2.47\ (DV_g \rho_g)^{.03}(\rho_g D_v)^{.56}\ \left(\frac{C_p}{k_g}\right)^{.67} \mu_g^{.08}\ \frac{(H - H_w)}{(T - T_w)} \qquad (9)$$

3. Parametric Equations

We select as parameters, D, V_g, P (Pressure in psia) and temperature, T.

The fluid properties may now be expressed as functions of P and T.

Over the range of interest (200 - 600° R, 30 - 300 psia) air may be considered as a perfect gas. Consequently, air density may be approximated by:

$$\rho_g = .77\ (P/100)\ (360/T) = 2.77\ \frac{P}{T} \qquad (10)$$

(air density at 100 psia, 360° R = .77 lbs/ft^3)

From Figure 1, it is evident that air viscosity closely equals:

$$\mu_g = 8.95 \times 10^{-5}\ T^{.85} \text{ centipoises} \qquad (11)$$

$$\mu_g = 6.02 \times 10^{-8}\ T^{.85} \text{ lb/sec ft}$$

(independent of pressure)

From Figure 2, we note:

$$k_g = 3.32 \times 10^{-5}\ T^{.95}\ \text{BTU/hr ft}\ ^{o}\text{R} \tag{12}$$

(independent of pressure)

Over the range of interest, we may assume:

$$C_p = .25\ \text{BTU/lb}\ ^{o}\text{R} \tag{13}$$

The values of D_v follow the relationship:

$$D_v \propto T^{1.5}/P \tag{14}$$

(from Sherwood & Pigford, op.cit., p. 10)

Values for the diffusivity of water vapor and carbon dioxide in air are given in the International Critical Tables:

For carbon dioxide, $D_v = .535\ \text{ft}^2/\text{hr}$ at 1 atm, 492^{o} R

$$D_{v_{CO_2}} = .721\ \frac{T^{1.5}}{P} \times 10^{-3}\ \text{ft}^2/\text{hr} \tag{15}$$

For water vapor, $D_v = .853\ \text{ft}^2/\text{hr}$ at 1 atm, 492^{o} R

$$D_{v_{H_2O}} = 1.15\ \frac{T^{1.5}}{P} \times 10^{-3}\ \text{ft}^2/\text{hr} \tag{16}$$

Combining the functional relationships with equation 9, we obtain:

$$\left(\frac{dH}{dT}\right)_{\substack{\text{water}\\\text{vapor}}} = 10.5\ (DV_gP)^{.03}\ \frac{1}{T^{.3185}}\ \frac{(H - H_w)}{(T - T_w)} \tag{17}$$

Values of $H_w = f(T)$ are tabulated in Perry's "Chemical Engineers Handbook", 3rd Edition, p. 760 ff. for air saturated with water vapor at 1 atm. Values at other pressures, neglecting "non-ideal gases" effects, may be found from:

$$\left[H_w \text{ at } P \right] = \left[H_w \text{ 1 atm} \right] \times \left(\frac{14.7}{P}\right) \tag{18}$$

If a value of $T - T_w$ is set, $H = f(T)$ can be found by a stepwise technique, assuming:

$$\Delta H = \frac{dH}{dT} \Delta T \tag{19}$$

where ΔT = incremental change in T. For our purposes, a 2° R temperature step should yield a fair approximation of $H = f(T)$. The stepwise calculations for several cases have been made.

Water Removal ($T_{\text{wall initial}} \geq T_{\text{sat'n initial}}$)

Case I: $P = 150$, $V_g = 100$, $D = .0104$ (1/8")

Air sat'd at 100° F, H - 4320 ppm

$T - T_w = 2^\circ$ R

Case II: Same as above, except $T - T_w = 20^\circ$ R

Case III: Same as above, except $T - T_w = 60^\circ$ R

Case IV: Same as above, except $T - T_w = 200^\circ$ R

Case V: Same as above, except $T - T_w = 20^\circ$ R and air sat'd at 460° R, H = 79 ppm

Carbon Dioxide Removal ($T_{\text{wall initial}} \geq T_{\text{sat'n initial}}$)

Case I: $P = 150$, $V_g = 100$, $D = .0104$

500 ppm CO_2 in air, $T - T_w = 2^\circ$ R

Case II: Same as above, except $T - T_w = 20^\circ$ R

Case III: Same as above, except $T - T_w = 50^\circ$ R

Case IV: Same as above, except $T - T_w = 200^\circ$ R

In all the above cases, it is assumed that the impure air stream enters the system in a region where the "hot end" wall temperature is above the saturation temperature corresponding to the initial air humidity. Therefore, mass transfer to the walls is initiated at the point along the exchanger where the wall temperature reaches the dew (or frost) point of the air. Considerable mass transfer can occur before the bulk air stream is cooled to a temperature corresponding to its initial dew point, for this reason.

However, one might encounter a situation in which saturated air is ingested by the system. Since the saturated inlet air immediately contacts a cold heat exchange surface, condensation or frosting will be initiated. However, the mass transfer rates will be different from those computed for the case where moist air enters the system at elevated temperatures:

$$(T_{wall}\ \underset{\text{initial}}{\geq}\ T_{saturation})_{\text{initial}}$$

The same mass and heat transfer model may be used to estimate the frosting rates for a saturated inlet air stream. Cases where the inlet wall temperature is below the initial dew point but the inlet air is not saturated will be somewhere between the two sets of calculated frosting rates. Carbon dioxide deposition is not affected in this manner, since inlet air temperatures will always be well above the ice point for carbon dioxide.

Water Removal (Inlet air saturated)

Case III': Same as Case III for water removal except initial air temp. = 560° R (sat'n) and heterogeneous nucleation centers are present ($S \leq 1$ at all times)

Case IV': Same as Case III' except $T - T_w = 200^\circ$ R

Case V': Same as Case III', except initial air temp. = 460° R (sat'n) (H_i = 79 ppm)

It is assumed that nucleation centers are present in the air and that particle formation will occur whenever the moisture content of the air exceeds saturation at the bulk air temperature. Once the bulk air becomes saturated it will remain at saturation during further cooling and excess moisture will result in particle growth. Mass transfer rates will then be determined by a driving force corresponding to the difference between saturation humidities at bulk air and wall temperatures.

4. Critical Gas-Wall ΔT for Nucleation

We can estimate a critical value for $(T - T_w)$ below which heterogeneous nucleation will not occur by comparing the slope of the mass transfer water vapor removal curve with the slope of the vapor pressure curve for water.

When the slopes are equal at equivalent temperatures and pressures, the air stream will be maintained at or below saturation by mass transfer. Below the "critical Δ T", no nucleation would occur; above the "critical Δ T", nucleation would be anticipated if nucleation centers are present in the vapor.

From eq. 17:

$$\frac{dH}{dT} = 10.5\ (DV_g P)^{.03}\ \frac{1}{T^{.3185}}\ \frac{(H - H_w)}{(T - T_w)} \tag{17}$$

Converting H to p (partial pressure of water vapor), assuming $H \gg H_w$, and substituting D = .0104' (1/8"), V_g = 100 ft/sec and P = 150 psia, we obtain:

$$\frac{dp}{dT} = \frac{12.2\ p}{T^{.3185}\ (T - T_w)} \tag{20}$$

From the Clausium-Clapeyron equation, the vapor pressure curve has a slope

$$\left(\frac{d\ln p}{dT}\right)_{\substack{\text{water}\\\text{vapor}}} = \frac{1}{p}\ \frac{dp}{dT} = \frac{L}{RT^2} = \frac{10^4}{T^2}\ * \tag{21}$$

L = latent heat of vaporization

We compute for water vapor:

$(T - T_w)_{critical}$ °R	T_{avg} °R
43°	500°
37°	460°
30°	410°

A ten-fold increase in $(DV_g P)$ will result in less than a 10% increase in $(T - T_w)_{crit}$ because of the small dependence of dp/dT on this factor.

The same comparison may be made for CO_2 removal. For CO_2, the vapor pressure curve was taken to have a slope:

$$\left(\frac{d\ln p}{dT}\right)_{CO_2} = \frac{1}{p}\ \frac{dp}{dT} = \frac{L'}{RT^2} = \frac{5400}{T^2} \tag{22}$$

L' = heat of sublimation

* 10^4 based on slope of actual vapor pressure curve. Theoretical value of $L/R \approx 9500°$ R.

The critical values for $(T - T_w)$ for carbon dioxide are:

$(T - T_w)_{crit.}$ °R	T_{avg} °R
21°	270°
15°	220°

B. Discussion of Results

1. Water Vapor Removal

We have considered two cases in which air, containing moisture, is cooled as it flows through a tube. In the first case, the initial moisture content in the air is 4320 ppm (.43% by weight) and in the second case the air initially contains 79 ppm. We have selected a system at

P = 150 psia

V_g = 100 ft/sec

D = 1/8 inch

so in the high moisture content example, the stream saturation temperature is 560° R and in the second case, saturation occurs at 460° R. We note that except for shifting the initial saturation temperature, total pressures have essentially no effect on the moisture removal rate. In the rate equation P, V_g, and D occur only to the .03 power and variation in these parameters over a very wide range produces only a minor variation in the moisture removal rate.

Examination of Figures 3 and 4 shows that the analytical moisture removal curves for mass transfer to the cold tube walls are strongly influenced by the temperature driving force between the bulk gas and the tube wall. For low values of $(T - T_w)$, the cooling air may never reach saturation. In the $T - T_w = 2°$ R example, S never reaches a value of one, so all moisture is removed by mass transfer. Since in an air-nitrogen exchanger, this would correspond to about a 4° R ΔT between streams, it is unlikely that a heat exchanger would be operated at this condition. However, the range of $(T - T_w)$ between 2° R and 20° R represents reasonable operating conditions. Even at $T - T_w = 20°$ R, the stream initially containing 4320 ppm of water is reduced to a water vapor concentration of $\lesssim$10 ppm before the stream reaches S = 1, and the stream initially at 79 ppm is reduced to $\lesssim$1 ppm.

Therefore, it is apparent that a significant amount of moisture removal will occur by a pure mass transport mechanism. As soon as the stream becomes slightly supersaturated, heterogeneous nucleation is possible and subsequent moisture removal can occur by a combination of mass transfer

and particle growth. We do note, however, that mass transfer, even for $T - T_w$ as large as 60° R reduces S to the point where homogeneous nucleation will not occur until after essentially all water vapor is removed from the stream. Even heterogeneous nucleation can not occur under these conditions until over 90% of the moisture is removed by mass transfer to the walls.

As a frost layer builds up on the wall, the initial value of $T - T_w$ will decrease and tend to make conditions even more favorable for mass transport. Maximum frost thickness occurs near the start of the freeze-out zone where $(H - H_w)$ is maximum.

Significant amounts of nucleation may be encountered, however, when the inlet air to the cooling system is initially saturated with water vapor. Figures 5, 6 and 7 show the calculated values for humidity vs air temperature for typical situations where the inlet air is initially at saturation. It is assumed that nuclei are present so that supersaturation results immediately in particle formation. The vapor humidity curve represents the actual vapor pressure of water in the bulk air and follows the saturation curve after the air stream becomes saturated. The total humidity curve represents the total moisture in the air stream. This is equal to the inlet humidity minus the moisture removed by mass transfer to the walls and also to the sum of vapor humidity and particle concentration. Therefore, the difference between total humidity and vapor humidity represents the particle concentration due to heterogeneous nucleation.

Figure 8 is a plot of percent nucleation vs $(T - T_w)$ for the case where the inlet air is saturated. Also shown for comparison is a curve for the case where air enters at an elevated temperature such that frosting is initiated when $T_w = T_{sat'n}$.

Heterogeneous nucleation is assumed to occur in this case, also. The 0% nucleation point was determined by the "critical ΔT" calculation described in Section A.

We observe that nucleation accounts for more than 50% of solids formation only when saturated air enters an exchanger having $(T - T_w)$ about 100° R. If 560° R, saturated air (H_i = 4320 ppm) enters a cooler having $(T - T_w) = 60^\circ$ R, only 25% nucleation will occur. The same air stream entering a cooler having $(T - T_w) = 200^\circ$ R will result in 75% nucleation.

Similar results are obtained for a stream initially saturated at 460° R (79 ppm), with somewhat greater percent nucleation than in the higher humidity case. However, if air containing the same amount of moisture is introduced to the system at a point above that where $T_w = T_{sat'n}$, nucleation becomes a minor effect in comparison to mass transfer to the exchanger walls.

Therefore, nucleation might predominate for inlet air at atmospheric pressure and saturated with water vapor if $(T - T_w) > 100^\circ$ R. However, as the pressure and temperature of the inlet air increase, mass transfer becomes the predominant freeze-out mechanism and remains so throughout the remainder of the mission.

The effect of other configurations, such as flow normal to tubes, has not been considered in this analysis, but since both mass and heat transfer are related to air turbulence in the same manner, we would not expect results for other configurations to be much different from this simple, single tube analysis. For the case of flow normal to a single cylinder, heat and mass transfer cylinder, heat and mass transfer rate equations are nearly identical in form. In fact, if we compare

$$j_D = \left(\frac{K_M}{V_g}\right)\left(\frac{\mu_g}{\rho_g D_v}\right)^{2/3} = f(Re)$$

and

$$j_H = \left(\frac{h}{C_p \rho_g V_g}\right)\left(\frac{C_p \mu_g}{K_n}\right)^{2/3} = f(Re)$$

(Sherwood & Pigford, p. 61)

for various configurations, we find them to be essentially identical functions of Re, Reynold's Number. These curves may be found in Sherwood & Pigford, normal to cylinder - p. 70; to single spheres - p. 74; packed granular beds - p. 86.

Although our analysis for flow within a single tube was based on slightly modified equations, both the Prandtl and Schmidt numbers are close to unity and variation in their powers causes little change in the basic rate equation developed.

2. Carbon Dioxide Removal

In Figure 9, curves are presented for carbon dioxide removal by mass transport. Again we observe that for $T - T_w = 2^\circ$ R, supersaturation (Figure 10) never occurs. For a $T - T_w = 20^\circ$ R, by the time S = 1, the initial 500 ppm of CO_2 is reduced to 20 ppm. At high values of $T - T_w$, up to 200° R, it is still evident that 70 - 80% or more of the carbon dioxide is removed by a mass transfer mechanism before even heterogeneous nucleation can occur. By the time supersaturation ratios are sufficient to promote homogeneous nucleation, essentially all the impurity has been removed by mass transfer to the walls.

Notes:

$$\mu_g = .0133 \left(\frac{T}{360}\right)^{.85}$$

Data per M.W. Kellogg Company
Technical Data Book, Curve G-815.90 3/42

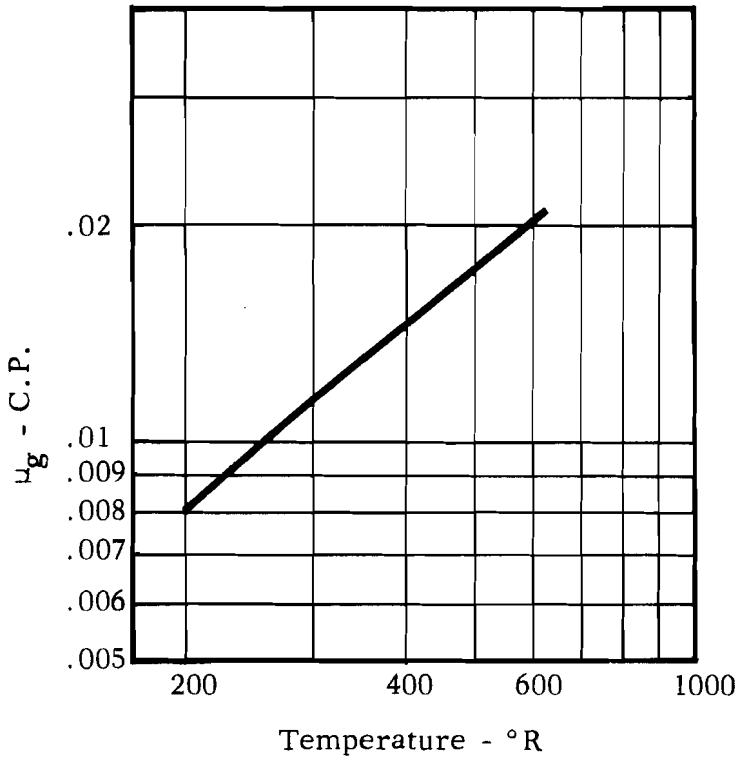

FIGURE 1 VISCOSITY OF AIR (FOR PRESSURES BELOW 300 PSIA)

Notes:

$$k_g = .0089 \left(\frac{T}{360} \right)^{.95}$$

Data per M.W. Kellogg Company
Technical Data Book, Curve G-815.65 9/42

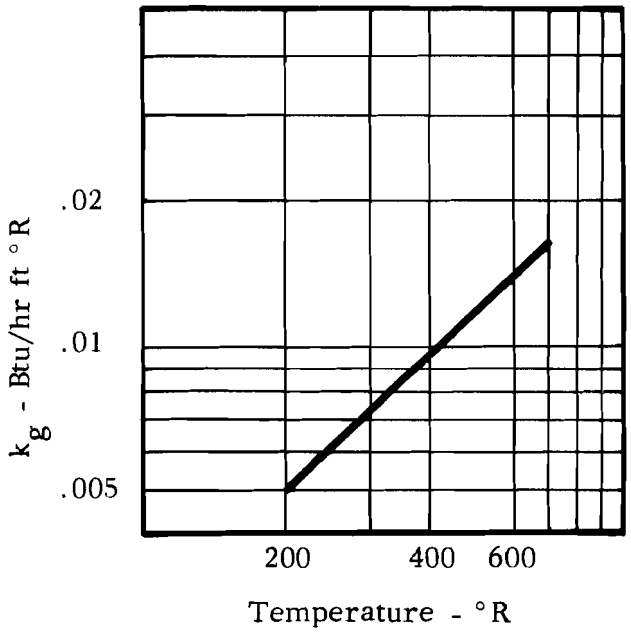

FIGURE 2 THERMAL CONDUCTIVITY OF AIR
(FOR PRESSURES BELOW 300 PSIA)

$$\frac{dH}{dT} = 10.5 \frac{(P\ V_g\ D)^{.03}}{T^{.3185}} \frac{(H - H_w)}{(T - T_w)}$$

P = 150 psia
V_g = 100 ft/sec
D = .0104 ft (1/8")
w denotes conditions at wall

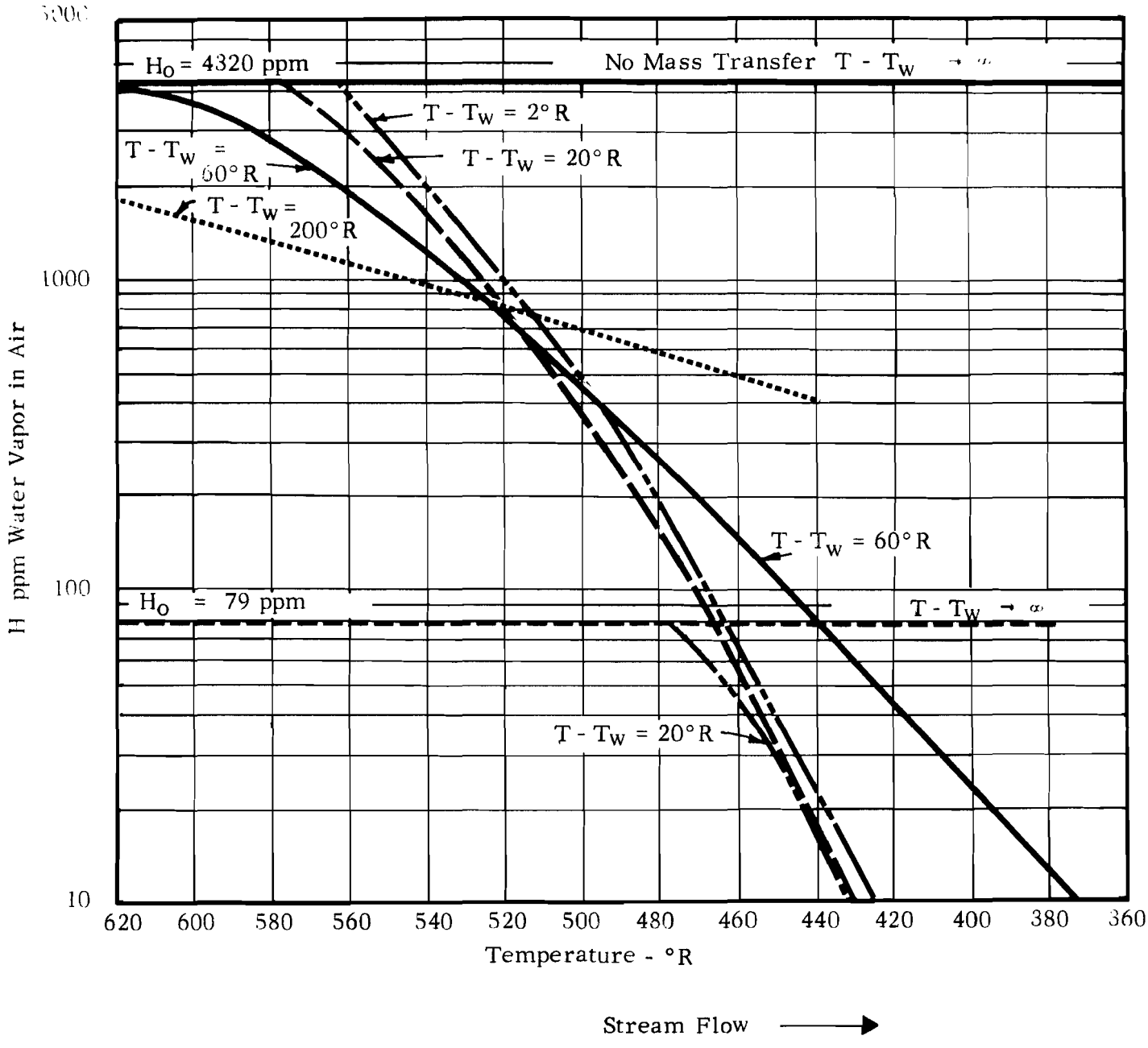

FIGURE 3 WATER VAPOR REMOVAL BY MASS TRANSFER TO TUBE WALLS IN A TURBULENT, COOLING, AIR STREAM

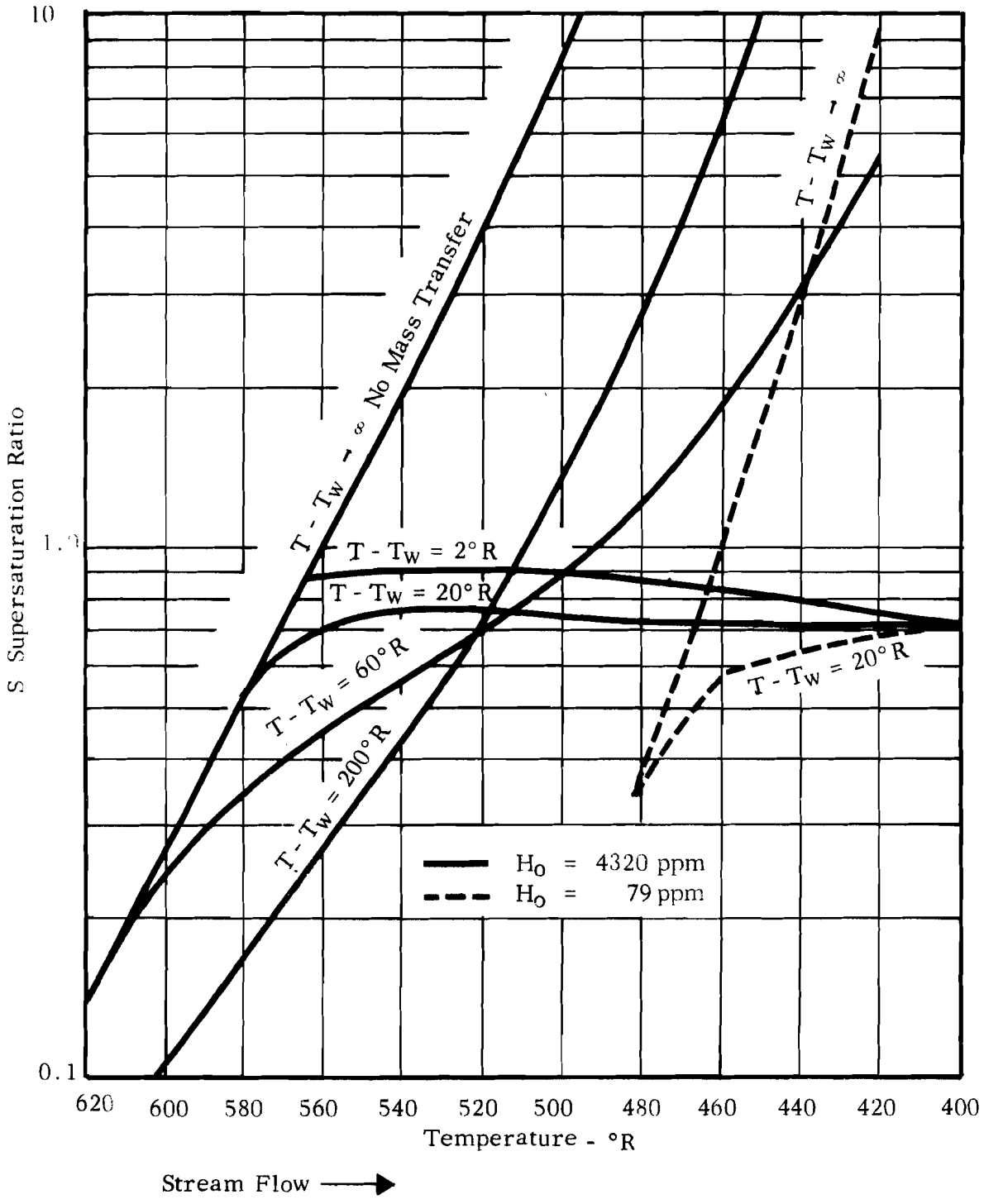

FIGURE 4 EFFECT OF WATER VAPOR REMOVAL BY MASS TRANSFER TO TUBE WALLS IN A TURBULENT COOLING, AIR STREAM ON SUPERSATURATION RATIO

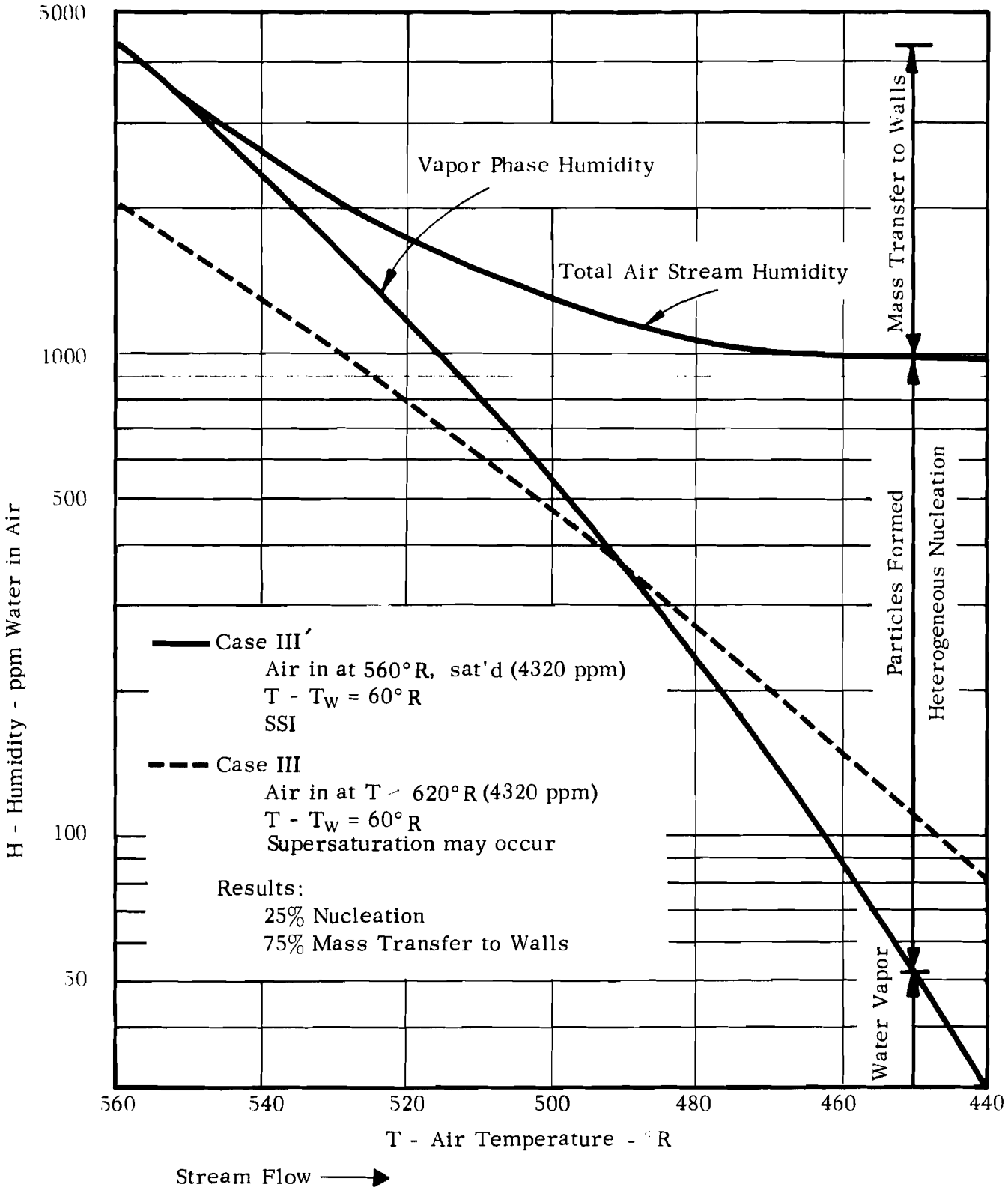

FIGURE 5 WATER REMOVAL FROM AIR STREAM IN COOLER WHEN INLET AIR IS AT SATURATION AT 560°R ($T - T_w = 60°R$)

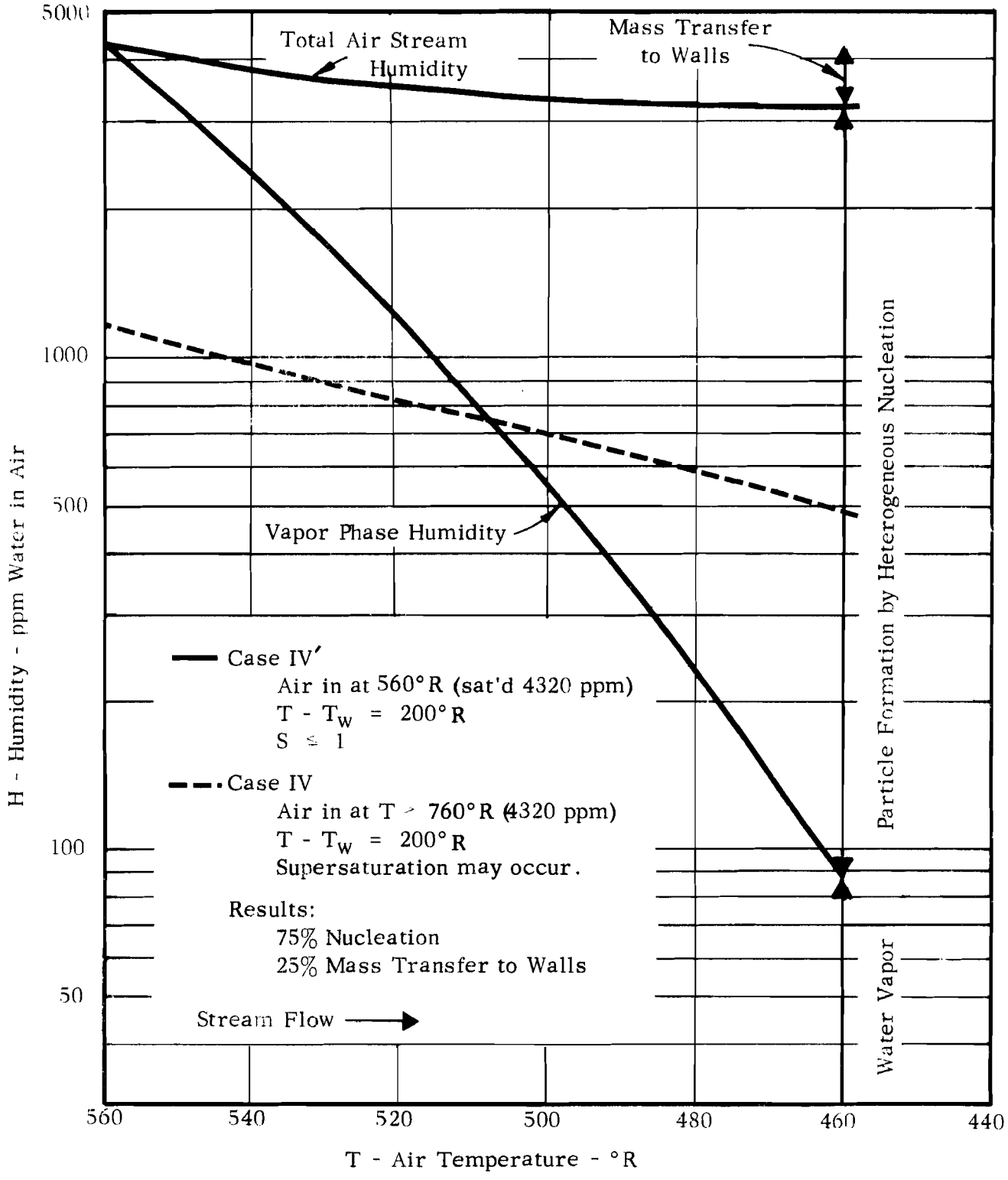

FIGURE 6 WATER REMOVAL FROM AIR STREAM IN COOLER WHEN INLET AIR IS AT SATURATION AT 560°R (T - T_w) = 200° R

Case V′

Air in at 460° R, sat'd (79 ppm)

$T - T_W = 60°R$

$S \approx 1$

Results:

38% Nucleation

62% Mass Transfer to Walls

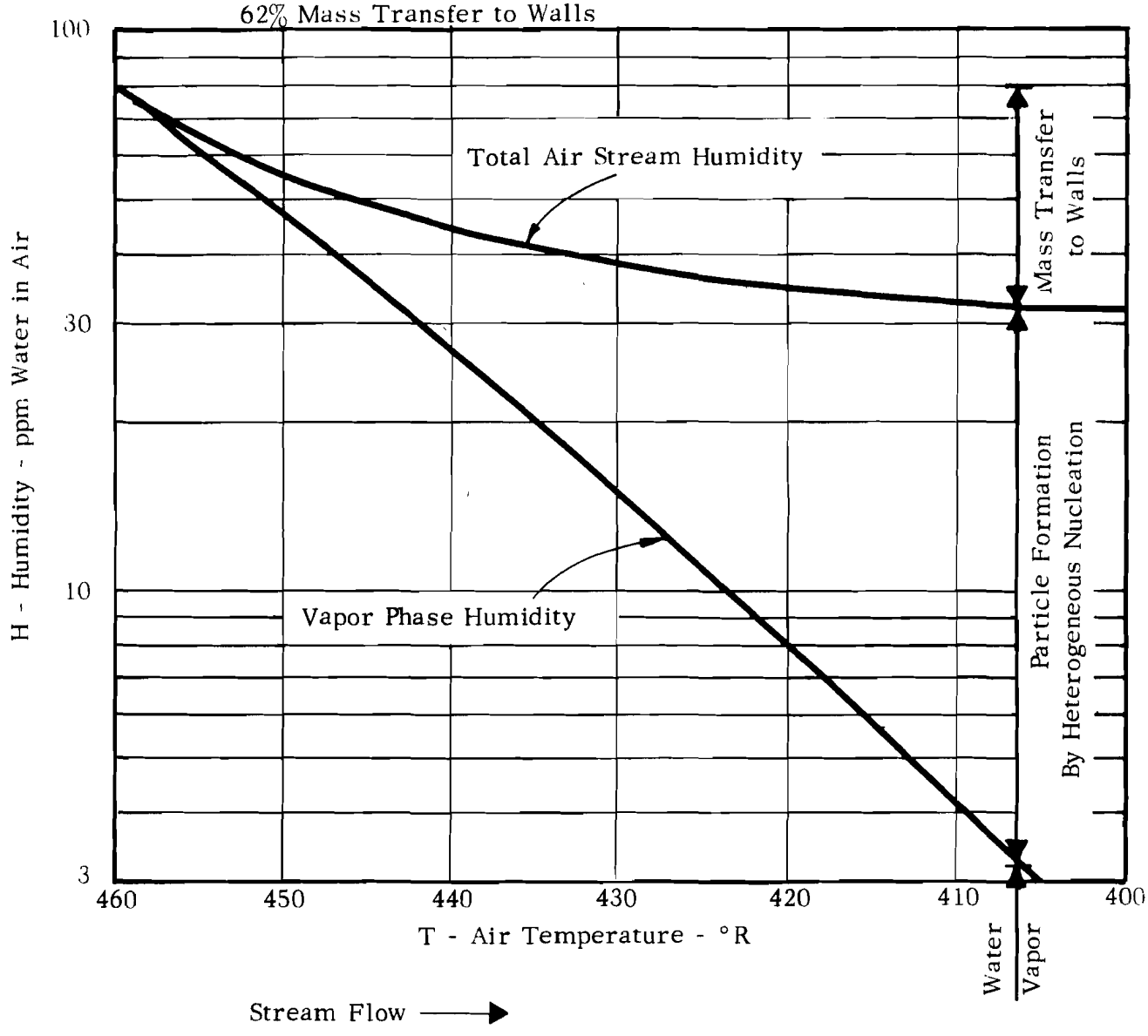

FIGURE 7 WATER REMOVAL FROM AIR STREAM IN COOLER WHEN INLET AIR IS AT SATURATION AT 460° R ($T - T_W$) = 60° R

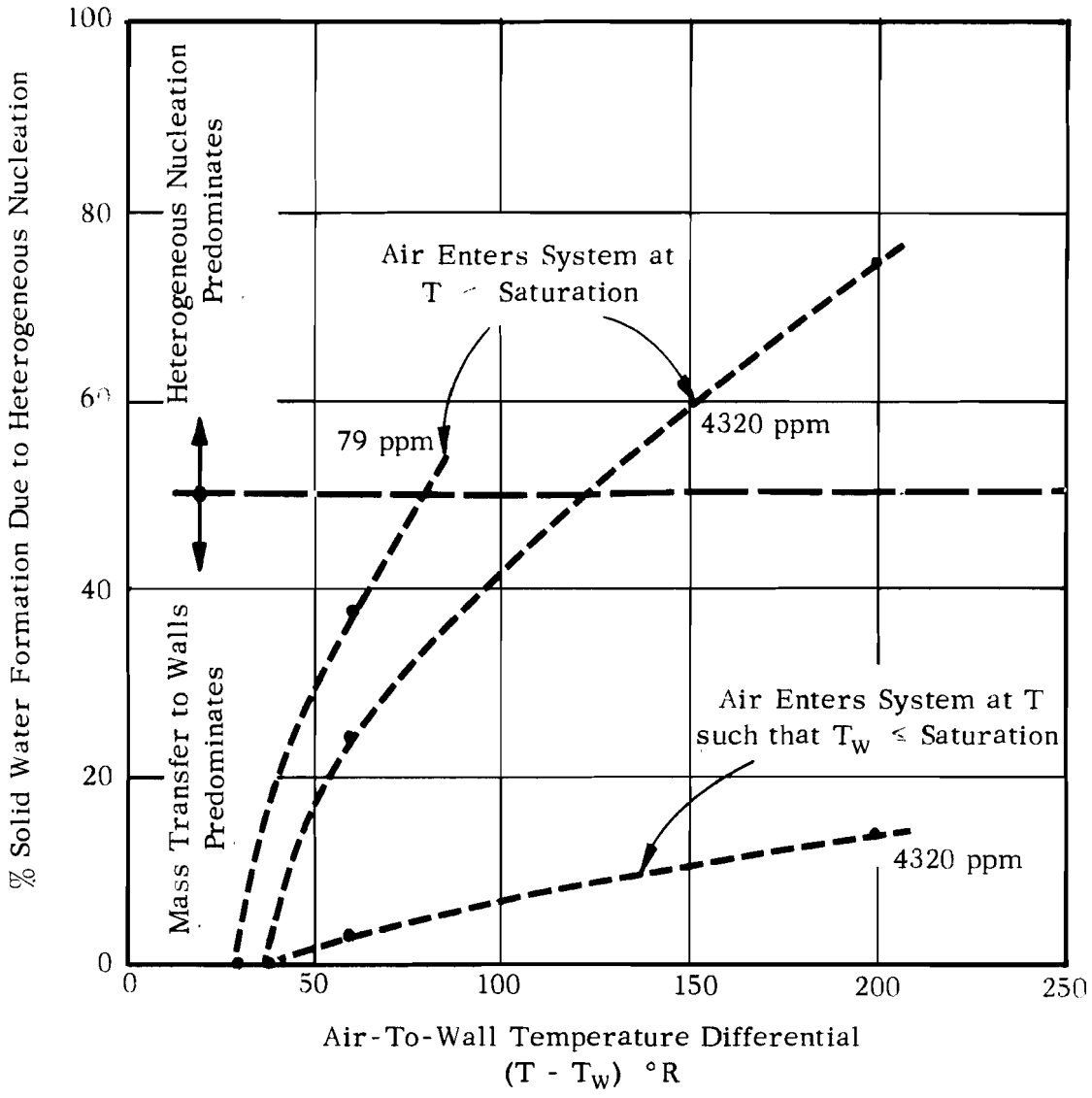

FIGURE 8 RELATIVE IMPORTANCE OF MASS TRANSFER TO WALLS AND HETEROGENEOUS NUCLEATION DURING FREEZE-OUT OF WATER VAPOR IN AIR COOLER

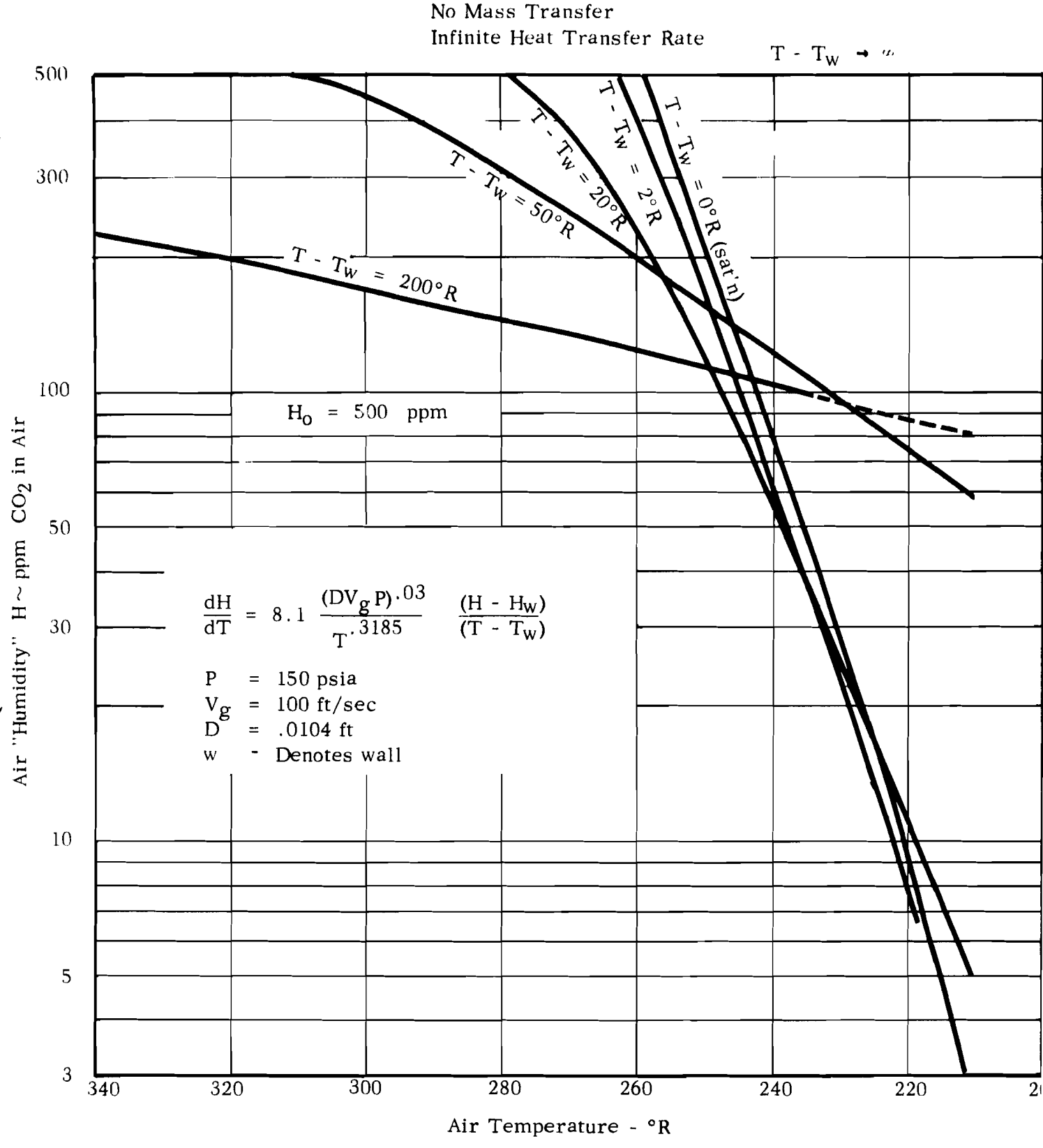

FIGURE 9 CARBON DIOXIDE MASS TRANSFER (HUMIDITY RESULTS)

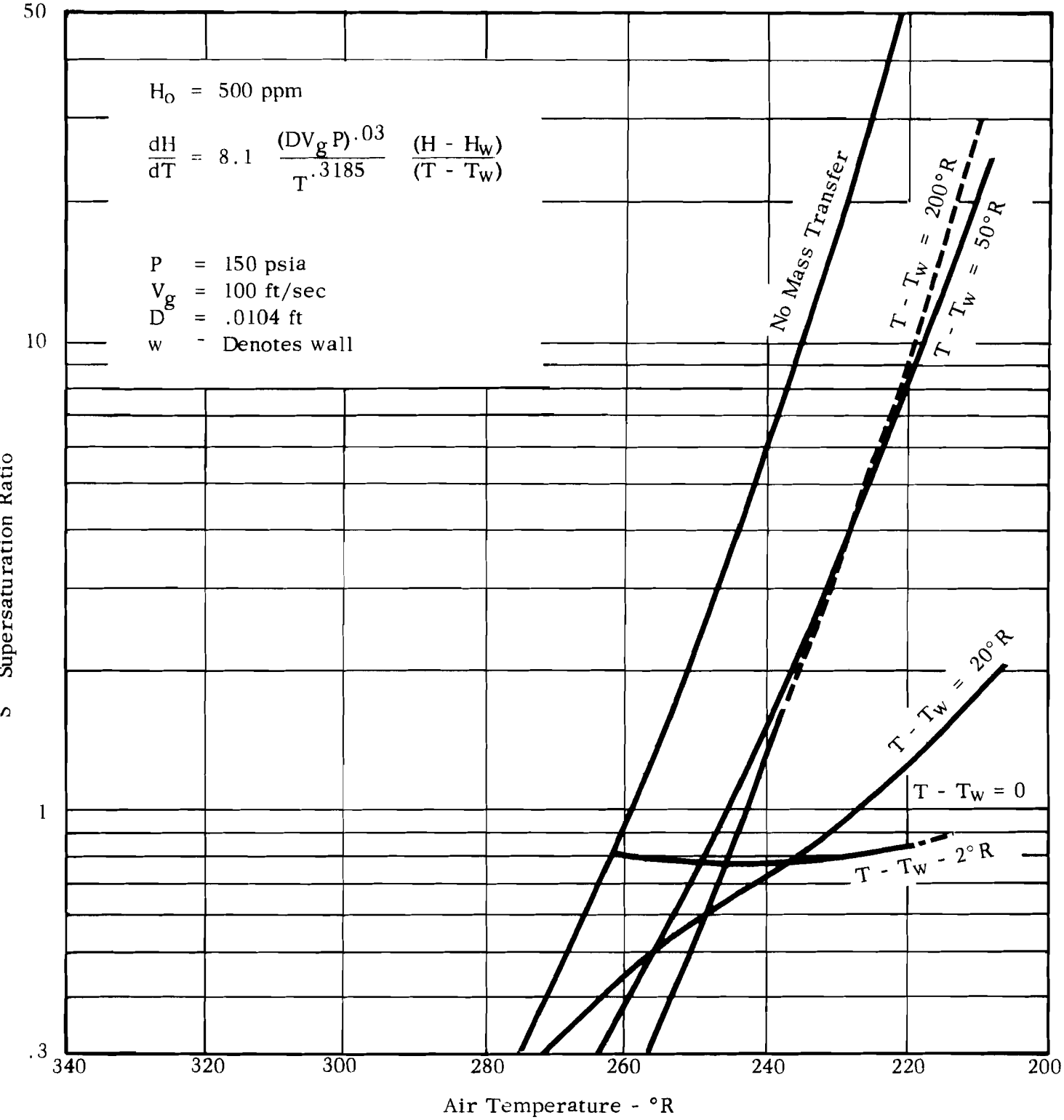

FIGURE 10 CARBON DIOXIDE MASS TRANSFER (SATURATION RATIO RESULTS)

APPENDIX 2

HOMOGENEOUS NUCLEATION AND GROWTH

TABLE OF CONTENTS

SUMMARY

A. Nucleation and Growth

We have examined the process of homogeneous nucleation of water and carbon dioxide in an air stream which is being rapidly cooled. For simplicity, to clarify the analyses, we have assumed that these condensible vapors do not coat out on any walls nor do heterogeneous nucleation processes play an important role. These phenomena have been studied separately.

Experimental studies of homogeneous nucleation reported in the literature fall into two general areas:

Cloud Chambers, wherein gas containing a condensible component is rapidly expanded in a piston and any mist, cloud, etc., studied by optical techniques. Heterogeneous nuclei are removed by preliminary expansions and removal of the "dirty" condensate. Data are sparce and not always meaningful since the observed fog droplets are much larger than the original nuclei and the analyses must include both nucleations and growth kinetics. It has, however, been quite well established that homogeneous nucleation requires the gas to be supersaturated; the level of supersaturation varies greatly depending upon conditions. For example, air-water systems expanded to $\sim$ 470°R require a value of S (saturation ratio P/P_{vp}) of $\sim$ 4-5 to form rapidly a fog. If the temperature investigated is near 420°R, values of 5 near 10 are required to produce similar fogging. For any inlet gas, increasing S (by rapid and larger expansion ratios) yields a fog with a greater number of particles but with a smaller particle size. These and other effects are discussed in detail later.

Expansion Nozzles - An alternative experimental procedure which offers some advantages over the cloud chamber is the expansion of the vapor through a nozzle. The history of the condensation process is spread out spacially rather than necessitating an examination of a rapid time sequence. Results obtained by this technique are similar in nature to those noted in the cloud chamber but somewhat more confidence is attached to the experimental results. The technique is discussed in some detail by Dunning (1).*

1. Summary of Mechanism

In a gas mixture containing the condensible component, there exist statistically random fluctuations resulting in the formation of dimers, trimers, ... These embryos may be examined from the elementary reactions forming them both kinetically and thermodynamically.

Thermodynamics indicates that for any given condition of temperature and concentration,

*Underlined numbers in parentheses refer to Bibliography on Page 31.

there exists only one given embryo size which is thermodynamically stable; those smaller in size tend to redisperse, those larger tend to grow. Pages 1 - 9 of the enclosed notes discuss the thermodynamics important in expressing quantitatively the concentration and size of such critical embryos. The number of molecules/ critical embryo is given by Eq. (23a) and the concentration by Eq. (24). For water, the number of molecules/critical nucleus ranges between 20-100, the lower range applicable at high values of S at low temperatures. For CO_2, the corresponding values are comparable.

2. Rates of nuclei formation are considered from two points of view.

a. Volmer (2), Becker - Doring (3) Frenkel (4) Theory

This theory has been discussed by many authors and expanded upon by most. The best review is given by Courtney (5) who has pointed out a few errors perpetuated by most previous authors.

Basically, the rate of formation of critical sized embryos is considered the rate controlling step and growth of smaller sized embryos is taken to be occurring almost instantaneously.

In simple terms, the formation rate is taken to be proportional to (a) the collision rate of monomer with embryos slightly smaller than the critical size, (b) the area of the critical embryo, (c) the concentration of the critical embryo, and (d) the concentration of monomer. The mathematics lead to Eq. (33) of this appendix which is of the form:

rate of formation of critical sized embryos $\sim C e^{\phi(\ldots)}$

The constants C and ϕ are functions of the physical properties of the system and somewhat of the system temperature and S. Many authors take $C \sim 10^{25}$. A plot of this rate vs. S for various temperatures for water-air is shown in Figure 5. Small changes in S greatly affect the rate. It is convenient to define a rate of $\sim 10^5$ as a "rapid" nucleation rate, i.e., a rate which appears instantaneous to visual observation.

b. Non-Steady State Approach

Courtney (5) has by-passed the Volmer et al approach and written the differential equations describing the rate of formation of dimers, trimers. He could then estimate the rate of formation of embryos of various sizes for a given T and S. The results are more difficult to describe here (see p. 10-14) but the net result does not differ qualitatively from (a) except that the constant C is $\sim 10^{21}$.

The examination of the question of nuclei rates of formation has shown that for any given system the formation of critical sized embryos is very slow until a critical value of S is attained. The dependence upon the value of S is very large (i.e., several orders of magnitude per unit change in S). Once this value of S is attained, nucleation is very fast, and of the order of a few microseconds.

3. Growth of Nuclei

After formation of the critical size embryo, growth occurs primarily by addition of monomer. The mathematics describing this process are given on pages 15 - 20 as suggested by Courtney. The end result is a rather complicated integral equation (Eq. 48) which expresses supersaturation ratio as a function of time. In addition, p. 21 - 22 show how the droplet size may be expected to vary as a function of time.

In a stagnant system starting with a given supersaturation ratio (S) and temperature (T), one may estimate the number and size distribution of particles at any time thereafter. In a heat exchanger, where T decreases with time the problem is much more difficult. Once homogeneous nucleation is initiated, S tends to decrease because of growth on the particles. However, if T drops so rapidly that the net value of S increases, then more nucleation results. If T drops very rapidly, then most of the condensible component is removed from the vapor by nucleation and the net result is a large number of very small nuclei. If, on the other hand, T drops slowly, then most of the condensible component is removed by growth mechanisms and the net result is fewer particles of larger size.

THERMODYNAMICS OF NUCLEATION

From a homogeneous phase, supersaturated with respect to some component A, small agglomerates of particles form. These agglomerates are the precursors of the stable phase tending to separate from the mother phase. These groups of molecules, appropriately termed embryos, are formed by successive reactions of the form:

$$\overline{A} + A \rightleftharpoons \overline{2A}$$
$$\overline{2A} + A \rightleftharpoons \overline{3A}$$
$$\cdots \qquad \cdots$$
$$\overline{(g-1)A} + A \rightleftharpoons \overline{gA} \text{ or } A_g$$

overall:

$$gA \longrightarrow A_g$$

This growth process is bimolecular in character and results from random fluctuations in the mother phase. As will be discussed below, all the embryos below a certain size are unstable and tend to decompose; however, at a certain size (noted here by A_g) a stable embryo is formed which tends to grow larger spontaneously. This critical sized embryo is termed the nucleus. The nucleus is capable of further growth while all those smaller are inherently unstable.

It is the purpose of this section to investigate the thermodynamic properties of the nucleus; the results will be used to allow one to model the kinetic process and allow a prediction of nucleation growth rates.

1. Size of Nucleus

System: gas A (monomer), 1 liquid (or solid) particle with area $4\pi R^2$. T, P = const.

The total free energy for this system is:

$$\underline{F} = N_A^m \mu_A^m + N_A^D \mu_A^D + 4\pi R^2 \sigma \quad (1)$$

where N_A = no. of moles

N_A^m - in mother phase

N_A^D - in drop

μ_A = chemical potential

μ_A^m - in mother phase

μ_A^D - in bulk liquid

but $N_A^m + N_A^D$ = constant (2)

and for a nucleus, we have an equilibrium situation where the Gibbs criterion is:

$$\delta \underline{F})_{T.P} \geq 0 \quad (3)$$

since the only independent variable is δN_A^D (or δN_A^m), then

$$(\delta \underline{F} / \delta N_A^D)_{T.P} = 0 \quad (4)$$

$$= (\mu_A^D - \mu_A^m) + 4\pi\sigma \frac{\partial R^2_D}{\partial N_A}_{T,P}$$

but $N_A^D = \frac{4}{3}\pi R^3 \times \frac{1}{\nu_A}$ (5)

where ν_A = molal volume of pure A in drop.

so $dN_A^D = \frac{4\pi R^2}{\nu_A} dR = \frac{2\pi R}{\nu_A} d(R^2)$ (6)

or $\frac{dR^2_D}{dN_A} = \frac{\nu_A}{2\pi R}$

and Eq. (4) becomes,

$$(\mu_A^D - \mu_A^m) + 2\sigma v_A / R_c = 0 \qquad (7)$$

Eq. (7) indicates that at large values of R, $\mu_A^D = \mu_A^m$, but at low values,

$$\mu_A^D < \mu_A^m$$

2. Free Energy Change in Nucleation

$$\Delta F = \underline{F} \text{ final} - \text{Finitial}$$

$$= (N_{A_f}^m \mu_{A_f}^m + N_{A_f}^D \mu_{A_f}^D + 4\pi R^2 \sigma) - N_{A_f}^m \mu_{A_i}^m - N_{A_f}^D \mu_{A_i}^m$$

assuming $\mu_{A_f}^m = \mu_{A_i}^m$

$$\Delta F = N_A^D (\mu_A^D - \mu_A^m) + 4\pi R^2 \sigma \qquad (8)$$

substituting from (7) and (5), where R in (7) is the critical nucleus radius, r_c,

$$\Delta F = -\frac{4}{3} \frac{\pi R^3}{v_A} \times \frac{2\sigma v_A}{r_c} + 4\pi R^2 \sigma$$

$$= 4\pi\sigma \left(R^2 - \frac{2}{3} \frac{R^3}{c}\right) \qquad (9)$$

when Eq. (9) is differentiated with respect to R,

$$\partial \Delta F / \partial R = 4\pi\sigma \left(2R - \frac{2R^2}{r_c}\right) = 8\pi\sigma R (1 - R/R_c) \qquad (10)$$

when	$R < R_c$	$\frac{\partial \Delta F}{\partial R}$	is > 0	and system is stable with respect to formation of new phase
	$R > R_c$	$\frac{\partial \Delta F}{\partial R}$	is < 0	and nucleation is spontaneous, i.e., phase change is favored thermodynamically
	$R = R_c$	$\frac{\partial \Delta F}{\partial R} = 0$		critical sized nucleus, could go either way

3. Note for Clarity:

The nomenclature in the literature is very confused and it is advisable to clarify a point of nomenclature here. The μ_A^m is the chemical potential of the homogeneous phase at some pressure P. The μ_A^D is the chemical potential of the

condensed phase but is taken to be at the pressure of the bulk phase at the temperature T, i.e., at P_{eq}. Now it was shown that at equilibrium

$$\mu^{m}_{A} - \mu^{D}_{A} = 2\sigma v_A/R_c \qquad \text{(Eq. 7)}$$

Now, of course, the condensed phase within the drop also has a chemical potential, let's call $\mu^{D'}_{A}$ which is not equal to μ^{D}_{A} but which is equal to μ^{m}_{A} if the drop and mother phase are in equilibrium, i.e.,

$$\mu^{m}_{A} = \mu^{D'}_{A} \qquad \text{so that}$$

$$\mu^{D'}_{A} - \mu^{D}_{A} = 2\sigma v_A/R \qquad (11)$$

Eq. (11) fits our concepts better than (7) since it is reasonable to expect the bulk μ to be less than μ at the higher pressure within the drop.

In fact, since the La place Eq.,

$$P_{\text{inside drop}} - P_{eq} = 2\sigma/R \text{ (for spherical drops)} \qquad (12)$$

then $$\mu^{D'}_{A} - \mu^{D}_{A} = v_A (P_{\text{inside drop}} - P_{eq.}) \qquad (13)$$

but this is just the isothermal work of compression in terms of μ.

4. Equilibrium Concentrations of Nucleus

from P 3

$$gA \rightleftarrows A_g$$

$$K = \exp\left[-\Delta F^{o}/kT\right] = (\bar{f}/f^{o})_{Ag}/(\bar{f}/f^{o})^{g}_{A} \qquad (14)$$

assuming $\mu_{A_g} = g\,\mu_A$

where μ_{A_g} = chemical potential for the nucleus /basis of molecules ~ μ^{D}_{A} using nomenclature above, i.e., at $P_{\text{inside drop}}$

μ_A = chemical potential of homogeneous phase per molecule

Choose standard state as pure component at pressure P. From the definition of fugacity,

$$\bar{f}_{Ag} \equiv (y\gamma f^{o})_{Ag} \qquad (15)$$

where f^{o} = fugacity for pure component

$$K = (y\,\delta)_{Ag}/(y\,\gamma)_A^g \tag{16}$$

Assume $\gamma \sim 1.0$ for both A_g and A, solving for Y_{A_g}

$$Y_{A_g} = Y_A^g\, K = Y_A^g \exp\left[-\Delta F^o/kT\right] \tag{17}$$

To estimate ΔF^o, consider the chart below:

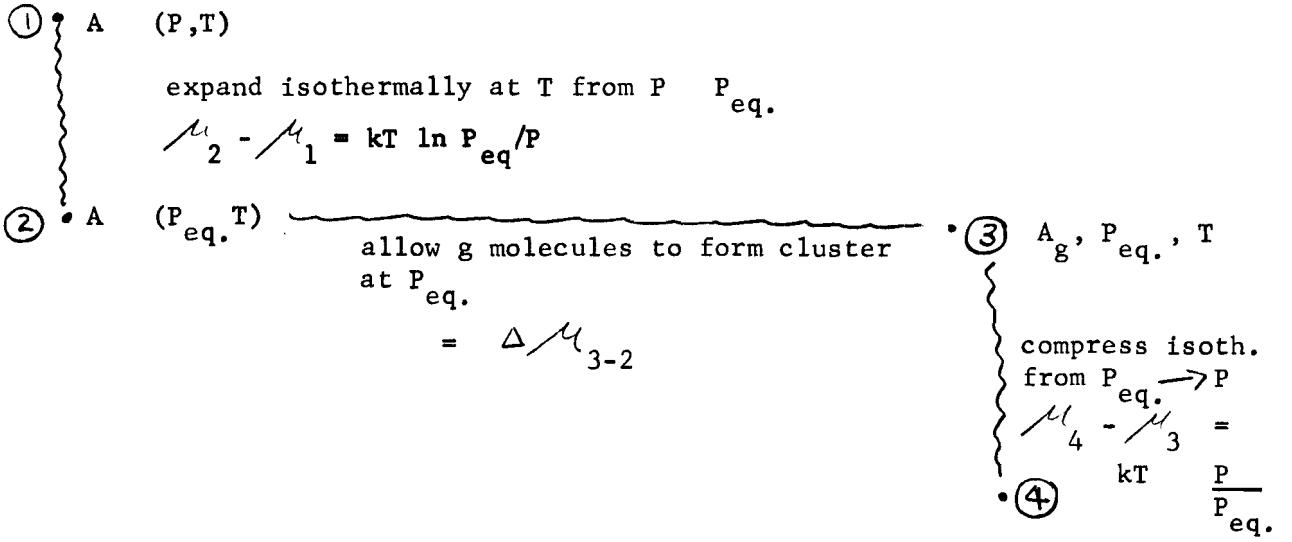

now $\Delta F^o = \mu_4 - g\mu_1$

$$= kT \ln \frac{P}{P_{eq}} + \Delta\mu_{3-2} + g\,kT \ln P_{eq}/P \tag{18}$$

$$= -(g-1)\,kT \ln P/P_{eq} + \Delta\mu_{3-2}$$

now $\Delta\mu_{3-2}$ is the same as ΔF in Eq. (8) except that the term $(\mu_A^D - \mu_A^m)$ is replaced by $(\mu_A^D - \mu_A^m$ (at $P_{eq}))$ and this is, of course, zero, so

$$\Delta\mu_{3-2} = 4\pi R^2 \sigma \tag{19}$$

Thus

$$\Delta F^o = -(g-1)\,kT \ln P/P_{eq} + 4\pi R^2 \sigma \tag{20}$$

and from (17),

$$Y_{A_g} = Y_A^g \exp \left\{ (g-1) \ln (P/P_{eq}) \frac{4\pi\sigma R^2}{kT} \right\} \qquad (21)$$

Now we perform the following rearrangements:

If C = concentrations / unit volume,

$$Y_{A_g} = C_{A_g}/C_{\text{Total}}$$

$$Y_A = C_A / C_{\text{Total}}$$

$$P = C_{\text{Total}}/kT$$

$$P_{eq} = C_{eq} / kT$$

$$\frac{C_{A_g}}{CT} = \frac{(C_A)^g}{CT} \left(\frac{C_T}{C_{eq.}}\right)^{3-1} \exp \left\{ \frac{-4\pi\sigma R^2}{kT} \right\}$$

$$C_{A_g} = C_{eq} \left(\frac{C_A}{C_{eq}}\right)^g \exp \left\{ \frac{-4\pi\sigma R^2}{kT} \right\}$$

$$C_{A_g} = C_{eq} \exp \left\{ g \ln S \; \frac{-4\pi\sigma R^2}{kT} \right\} \qquad (22)$$

Finally - to eliminate g from Eq. (22) we note that there is a critical sized radius with a nucleus containing gc molecules which is in a neutral equilibrium. Nuclei larger than R_c grow and those less decompose. It is reasonable therefore to suppose that the minimum concentration of C_{A_g} results when g = gc. Thus to to get the value of $C_{a_{g_c}}$ we differentiate (22) with respect to g and set equal to zero.

To eliminate R,

$$A = 4\pi R^2$$

$$V = \frac{4}{3}\pi R^3 = \nu_g g$$

where ν_g = volume/molecule in the cluster

$$R = (3\nu_g g/4\pi)^{1/3}$$

and $$C_{A_g} = C_{eq} \exp \left\{ g \ln S - \frac{4\pi\sigma}{kT} \left(\frac{3\nu_g g}{4\pi}\right)^{2/3} \right\} \qquad (23)$$

$$dC_{A_g}/dg = C_{eq}\left[\exp\left\{\right\}\right]\left[\ln S - \frac{8\pi\sigma}{3kT}\left(\frac{3v_g}{4\pi}\right)\left(\frac{3v_g g_c}{4\pi}\right)^{-1/3}\right] = 0$$

Since $C_{eq} \neq 0$

$$\exp\left\{\right\} \neq 0$$

then

$$\ln S - \frac{2\sigma v_g}{kT}\left(\frac{3v_g g_c}{4\pi}\right)^{-1/3} = 0$$

$$\left(\frac{3v_g g_c}{4\pi}\right)^{-1/3} = \frac{(\ln S)kT}{2\sigma v_g}$$

$$g_c = \left(\frac{2\sigma v_g}{kT \ln S}\right)^3 \left(\frac{4\pi}{3v_g}\right)$$

$$= \frac{32\sigma^3 v_g^2 \pi}{3(kT)^3(\ln S)^3} \qquad (23a)$$

and $$C_{A_{g_c}} = C_{eq} \exp\left\{g_c \ln S - \frac{4\pi\sigma}{kT}\left(\frac{3v_g}{4\pi} \times \frac{32}{3} \frac{\sigma^3 v_g^2 \pi}{(kT)^3 (\ln S)^3}\right)^{2/3}\right\}$$

$$= C_{eq} \exp\left\{\frac{32}{3} \frac{\sigma^3 v_g^2 \pi}{(kT)^3(\ln S)^2} - \frac{\sigma^3 \pi v_g^2}{(kT)^3 (\ln S)^2} \times 16\right\}$$

$$= C_{eq} \exp\left\{-\frac{16}{3} \frac{\sigma^3 v_g^2 \pi}{(kT)^3 (\ln S)^2}\right\}$$

$$C_{A_{g_c}} = C_{eq} \exp\left\{-\frac{16}{3} \frac{\sigma^3 v_g^2 \pi}{(RT)^3 (\ln S)^2}\right\} \qquad (24)$$

Eq. (24) is the final equation for the concentration of critical sized nuclei. It will be used later.

A final note regarding the numerical magnitude of g_c. From Eq. (23a),

$$g_c = \frac{\text{const}}{(\ln S)^3}, \qquad \text{const} = \frac{32}{3} \frac{\sigma^3 v_g^2 \pi}{(RT)^3}$$

Courtney (Texaco Exp. Inc. Report TM-1250, 7/61) calculates some typical values of g_c for water-air systems, shown in Figure 1.

NUCLEATION RATES - A NON-STEADY STATE APPROACH

In the thermodynamics section, we calculated the concentration of clusters with g molecules in equilibrium with the bulk monomer gas. This was Eq. (23). Also it was pointed out that clusters with less than g_c molecules (see Eq. 23a) were inherently instable and tended to decompose while those with $g > g_c$ tended to grow.

In this section we shall examine the growth rates of small clusters to give a better picture of the time scale required in homogeneous nucleation of liquids and solids from vapor streams.

One pictures the nucleating vapor as a mixture of monomers, embryos, clusters, etc., all in a process of dynamic motion, decomposing and growing depending upon the environment. If one would isolate a single cluster of g molecules but still allow access to monomer, it would spontaneously grow if $g > g_c$, decompose if $g < g_c$. The question is, how fast do critical nuclei form in a given situation. For example, take water vapor in air at 474°R with an initial supersaturation ratio of 4.5. Application of Eq. (23a) indicates that $g_c \sim 85$ molecules. How long does it take to form such nuclei at this T & S?

We will give below a possible method for estimating such nucleation times and it will be shown that they are in the order of 0.1 to 1 μsec for any reasonable value of S. Even with velocities of 100 ft/sec expected in the proposed exchanger, this corresponds to a travel distance of less than 0.001 inches.

A note regarding the value of S required for these rapid rates for homogeneous nucleation. Suppose the weight % of water in the air was 10^{-6}% (or a weight fraction of 10^{-4}) and an inlet pressure of 100 psia. Then the partial pressure of water in the inlet air is about $29/18 \times 10^{-4} \times 10^2 = .016$ psia. If no supersaturation occurred the gas becomes saturated at 457° R. A saturation ratio of ~ 8 may be required to nucleate rapidly so that

$$S = 0.016/P_{v_{P_{sat\ at\ T}}} = 8$$

$$P_{v_{P_{sat}}} = \sim .002 \text{ or } T \sim 420^\circ \text{ R}$$

i.e., a temperature of 420° R is required to make nucleation occur rapidly. This problem will be referred to again when particle growth is examined.

NUCLEATION KINETICS

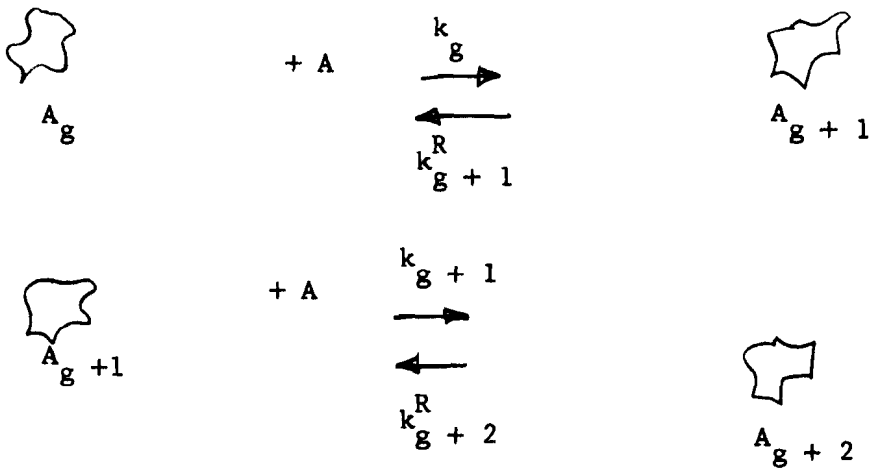

etc.

The rate of change of the concentration of the A_g cluster, C_{A_g} is given as,

$$\frac{dC}{d\theta}_{A_g} = k_{g-1} C_A C_{A_{g-1}} + k^R_{g+1} C_{A_{g+1}} - k_g C_{A_g} C_A - k^R_g C_{A_g} \qquad (25)$$

The actual concentrations of clusters are given by C_A C_{A_g} - 1, etc and the equilibrium value is designated by $C_{A_g}^{\#}$, $C_{A_{g-1}}^{\#}$, etc. From Eq. (23),

$$C_{A_g}^{\#} = C_{eq} \left\{ g \ln S - 4\pi\sigma/kT \, (3v_g/4\pi)^{2/3} \right\} \qquad (23)$$

Where, as before, C_{eq} = conc. of monomer in eq. with planar surface.

Several assumptions are made in the analysis:

1. Experimental and theoretical data seem to indicate that equilibrium concentrations of small clusters are built up extremely rapidly.

2. The forward rate constant k for addition of monomer to cluster is given by:

$$k_g = \alpha_g \omega A_g, \quad cm^3/sec \qquad (26)$$

where α_g = accomodation coef. for addition of monomer to cluster.

ν = collision rate of monomer with cluster

= $(kT/2\pi m)^{1/2}$, cm/sec (Note: To get correct units the constant 980 gm^{mass} - cm/gm^{force} - sec^2 has to be included in bracket).

A_g = surface area, cm^2

= $4\pi R_g^2$

but since $V_g = \frac{m}{\rho} g = v_g g = \frac{4}{3} \pi R^3$

$$R = (3v_g g/4\pi)^{1/3}$$

and

$$A_g = 4\pi(3v_g g/4\pi)^{2/3}$$

3. During the nucleation period, the concentration of the monomer, C_A, does not change appreciably.

4. The temperature is constant.

Now we have an expression for k_g, k_{g-1}, k_{g+1}, etc. from (26). To obtain an expression for k_g^R, assume that if equilibrium should be attained,

$$\frac{dC}{d\theta} A_g = \frac{dC}{d\theta} A_{g-1} = \frac{dC}{d\theta} A_{g+1} = \ldots = 0$$

Thus from (25),

$$k_g (C_{A_g}^{\#} C_A) = k_{g+1}^R C_{A_{g+1}}^{\#}$$

$$k_{g-1}(C_{A_{g-1}}^{\#} C_A) = k_g^R C_{A_g}^{\#} \qquad (27)$$

or $$k_{g+1}^R = k_g / C_{A_g}^{\#} C_A / C_{A\, g+1}^{\#}$$

$$k_g^R = k_{g-1} C_{A_{g-1}}^{\#} C_A / C_{A_g}^{\#} \qquad (28)$$

substituting into (25):

$$dC_{A_g}/d\theta = k_{g-1}\, C_A\, C_{A_{g-1}} - k_g\, C_{A_g}\, C_A + C_{A_{g+1}} \left(k_g C_{A_g}^{\#}\, C_A / C_{A_{g+1}}^{\#}\right)$$

$$- C_{A_g} \left(k_{g-1} C_{A_{g-1}}^{\#}\, C_A / C_{A_g}^{\#}\right) \qquad (29)$$

or

$$= k_{g-1} C_A\, C_{A_{g-1}} - C_{A_g}\, C_{A_{g-1}}^{\#} / C_{A_g}^{\#} - k_g\, C_A\, C_{A_g} - C_{A_{g+1}}\, C_{A_g}^{\#} / C_{A_{g+1}}^{\#} \qquad (30)$$

Next replace k_g and k_{g-1} from (26) and replace $C_{A_g}^{\#}$, etc., from (23) to give,

$$dC_{A_g}/d\theta = p_{g-1}\, C_{A_{g-1}} - q_g\, C_{A_g} + r_{g+1}\, C_{A_{g+1}} \qquad (31)$$

where

$$p_{g-1} = \alpha_{g-1}\, v\, 4\, (3v_{g-1}/4\pi)^{2/3}\, (g-1)^{2/3}\, C_A$$

$$r_{g+1} = \alpha_{g+1} v\, 4\pi (3v_{g+1}/4\pi)^{2/3}\, g^{2/3} C_{eq} \exp\left\{\psi\left[(g+1)^{2/3} - g^{2/3}\right]\right\}$$

$$\psi = 4\pi (3v_{g+1}/4\pi)^{2/3} \sigma/kT$$

$$q_g = r_g + p_g$$

$r_g \backsim r_{g+1}$ with all terms containing g reduced by one

$p_g \backsim p_{g-1}$ with all terms containing g increased by one

Equation (31) is a differential equation which may be solved given the boundary conditions and values of C_A, C_{eq}, T, α, v, v_g, σ. Courtney (Texaco Exp. Inc., TM-1250, 7-15-61) has solved for C_{A_g} for water-air systems using various boundary conditions. For example, if

$$C_{19} = C_{19}^{\#} \qquad \theta > 0$$

$$C_{20} = C_{21} = \ldots = 0 \qquad \theta = 0$$

A typical plot is given in Figure 2. For values of S higher than 4.5 at 455° R, 10 at 420° R, 20 at 385° R, the values of C_{A_g} (g up to 100) have stabilized and show no more rapid growth (in μsec range). Below these values of S, no data are available. For these values of S, no appreciable time is required to nucleate.

ESTIMATION OF SUPERSATURATION TO OBTAIN RAPID HOMOEGENOUS NUCLEATION RATES

In pages 10-13 we found that nucleation rates could be very rapid if high supersaturations were employed. Since the equations used to determine C_g as a f(θ), Eq. (31), are difficult to solve and answers are available from a computer at only a very few values of S and T for water vapor-air cases, one may advantageously look at other theories of nucleation rates. These other theories are highly simplified but yield "ball-park" estimates.

One of the simplest is due to Volmer. Noting as before that the size of the critical nucleus is A_{g_c}, Volmer assumes that all nuclei up to size g_c are formed very rapidly and that the step,

$$A_{g_c} + A \longrightarrow A_{g_c+1}$$

is the rate controlling step.

The "rate of nucleation" is thus defined as the formation rate of the A_{g_c+1} nucleus.

Call this rate R. Then,

$$R = k\, C_{A_{g_c}}\, C_A \tag{32}$$

Where k is given by Eq. (26) and since $C_{A_{g_c}}$ is present in an equilibrium concentration, $C_{A_{g_c}} = C_{A_{g_c}}^{\#}$ and is given by Eq. (24). Inserting these values,

$$R = \alpha_{g_c} (RT/2\pi M)^{1/2} \times 4\pi (3v_{g_c}/4\pi)^{2/3} g_c^{2/3} C_{eq}\, C_A$$

$$\exp\left\{-16/3\ \sigma^3 v_{g_c}^2 \pi/(RT)^3 (\ln S)^2\right\} \tag{33}$$

A similar expression is derived by Becker-Doring who assume that there are several slow rate steps near the critical nucleus (rather than one in Volmer's theory).

Now in Eq. (33), the pre-exponential factor for water-air does not vary appreciably and many authors assume that a value of 10^{25} is reasonable. Thus,

$$R \cong 10^{25}_{\exp}(-\phi/(\ln S)^2) \tag{34}$$

where $\phi = \frac{-16}{3} \sigma^3 v_g^2 \pi/(RT)^3$

A plot of ϕ is shown in Figure 3 a function of temperature for the water-air system. The vapor pressure of water is given in Figure 4.

In Figure 5 is shown a plot of R vs S from Eq. (34) for three temperatures. If we say arbitrarily that a Rate of 10^5 clusters/cm^3-sec corresponds to a rapid rate of nucleation that at

T °R	A value of S required to give R = 10^5
473	5
420	10.2
384	19

A value of S which yields (visually) a very rapid fogging rate at room temperature is quoted in the literature as 4.2. This agrees well with the above values.

We will evaluate the above results as regards the proposed heat exchangers after we discuss the growth process.

GROWTH OF PARTICLES AND THE SIMULTANEOUS DECREASE IN THE SUPERSATURATION OF VAPOR

The Growth of a Single Particle

If we focus on some single nuclei which may be larger or smaller than one of critical size (although the larger ones are of more interest here), the nucleus will suffer collisions from the monomer and grow:

The number of such collisions is given by Eq. (26).

$$\text{eff. coll./sec} = \alpha U A C_A, \text{ molecules/sec}$$

The right hand side gives the rate of increase in the number of molecules of the nucleus. Thus, the rate of increase in mass of this particle is:

$$= m\alpha u A\, C_A$$

Of course, simultaneously, the nuclei is evaporating at a rate of:

$$= \alpha^R u^R A$$

This group, multiplied by C_{eq}, would yield the growth rate (= evaporation rate/C_{eq}) at equilibrium. Assuming, the accomodation coef. $\alpha^R = \alpha$ (i.e., α = f(size of nuclei)) and that

u^R = coll. rate at eq.

$A = 4\pi(3v_g/4\pi)^{2/3}$

see page 12

$$C_{eq} = \alpha^R u^R / \alpha u$$

Then $(dM/d\theta)_{\text{single particle}} = \alpha u\, m(C_A - C_{eq})A$ (35)

where $dM/d\theta$ = mass rate of change for particle under consideration, i.e., containing g molecules.

The Growth of Groups of Molecules with g Molecules

The total mass rate of growth of all particles with g molecules is just Eq. (35) multiplied by N_g, the total number of particles with g molecules,

$(dM/d\theta)$ all particles with g molecules

$$= \alpha u m\,(C_A - C_{eq})A\, N_g \quad (36)$$

If a unit volume is taken as a base, then dividing by this V (V = const., i.e., 1 cm^3 or 1 ft^3.).

$d(M/V)/d\theta$ all particles with g molecules

$$= \alpha u m\,(C_A - C_{eq})\, A\, C_{A_g} \quad (37)$$

The Growth of All Particles

Eq. (37) summed over all particles gives the total mass rate increase in our volume, i.e.,

$$d(M/V)/d\theta \text{ all particles} = \sum \alpha u_m (C_A - C_{eq}) A \, C_{A_g}$$

$$= \alpha u_m (C_A - C_{eq}) A_T \tag{38}$$

$$A_T = \sum_g A \, C_{A_g}$$

Material Balance for System

Since C_A = molecules of A/unit volume,

$$d(M/V)/d\theta \text{ all particles} = -m \frac{dC_A}{d\theta} \tag{39}$$

or

$$-dC_A/d\theta = \alpha u (C_A - C_{eq}) A_T \tag{40}$$

Determination of A_T

Rate of Change of Radius

$$\text{Mass of particles} = \frac{4}{3} \pi R^3 \rho = M \tag{41}$$

$$dM/d\theta = 4 \pi R^2 \rho \frac{dR}{d\theta} \tag{42}$$

$$= \alpha u_m (C_A - C_{eq}) A \text{ by Eq. (35)}$$

$$\therefore \quad dR/d\theta = \frac{\alpha u_m}{\rho} (C_A - C_{eq}) \tag{43}$$

The change in radius from a critical nuclei size ($R \sim 0$) to some value R is followed over a time $\theta = \theta'$ (when the critical size is first reached) to any time θ, i.e.,

$$R_\theta = \int_{\theta'}^{\theta} \frac{\alpha u_m}{\rho} (C_A - C_{eq}) d\theta \qquad (44)$$

Nucleation Rate

In a small time interval around θ', the number of new nuclei being formed is R(see page 14). These change in size by Eq. (44). The total area present at any time θ is A_T where,

$$A_T = \int_0^{\theta} (4\pi R_\theta^2)\, R\, d\theta' \qquad (45)$$

$$= \int_0^{\theta} (4\pi) \left[\int_{\theta'}^{\theta} \frac{\alpha u_m}{\rho} (C_A - C_{eq}) d\theta \right]^2 R\, d\theta' \qquad (46)$$

Substituting Eq. (46) in Eq. (40) and integrating between 0 and θ,

$$C_{A_{initial}} - C_A = \int_0^{\theta} 4\pi(\alpha u)^3 \frac{m^2}{\rho^2} (C_A - C_{eq}) \left\{ \int_0^{\theta} R \left[\int_{\theta}^{\theta} (C_A - C_{eq}) d\theta \right]^2 d\theta' \right\} d\theta \qquad (47)$$

Finally, substituting R from Eq. (33), g_c from (23a), and letting

$S = C_A/C_{eq}$ = supersaturation ratio at θ

$S_o = C_{A_{initial}}/C_{eq}$ = supersaturation ratio at $\theta = 0$

then,

$$S = S_o - K_2 C_{eq}^4 \int_0^{\theta} (S-1) \left\{ \int_0^{\theta} S \exp\left[-K_1/(\ln S)^2 \right] \left[\int_{\theta'}^{\theta} (S-1) d\theta \right]^2 d\theta' \right\} d\theta \qquad (48)$$

where

$$K_1 = 16\pi\sigma^3 v^2/3(RT)^3$$

$$K_2 = \frac{4\pi m^2}{\rho^3} \alpha^4 (2m\sigma/\pi)^{1/2} (kT/2\pi m)^{3/2}$$

Courtney (5) solved this integral equation for water vapor-air at several temperatures and gives plots of S vs. θ. α was assumed to be unity.

Examination of Rate of Radius Growth

Since nucleation rates are so rapid at values of S larger than some lower limit (see Figure 5), let us look further at Eq. (44) and try and estimate a value of $dR/d\theta$ and R_θ.

$$dR/d\theta = \alpha u \frac{m}{\rho} (C_A - C_{eq}) = \alpha u \frac{m}{\rho} C_{eq} (S-1) \qquad (49)$$

let $\alpha = 1.0$
and $u = (kT/2\pi m)^{1/2}$

$k = 1.38 \times 10^{-16}$ ergs/molecule - ^oK

$m = 2.99 \times 10^{-23}$ gms/molecule of H_2O

Note this checks because:

$$k/m = \frac{1.38 \times 10^{-16} \text{ ergs} \times 10^{23}}{2.99 \text{ gms mol}/^oK} \quad 1 \text{ erg} \times .9869 \times 10^{-9} \text{ liter - atm} \times 18 \text{ gms/mole}$$

$$= .08207 \text{ liter - atm/mole } ^oK$$

$$\therefore \quad u = \left(\frac{1.38 \times 10^{-16}}{2.99 \times 10^{-23}} \quad \frac{T}{2\pi}\right)^{1/2}$$

let $T \sim 420^o$ R = $40^oC = 233^o$ K

$$u = \left(\frac{1.38 \times 10^{7} \times 233}{2.99 \times 2 \times 3.14}\right)^{1/2} = (1.7 \times 10^{8})^{1/2}$$

$$= 1.3 \times 10^{4} \text{ cm/sec}$$

$$m = 2.99 \times 10^{-23} \text{ gm}^M/\text{molecule}$$

$$\rho = 1 \text{ gm}^M/\text{cm}^3$$

C_{eq} is a f(T),

T (^oR)	C_{eq} molecules/cm^3
473	7.89×10^{16}
420	5.8×10^{15}
384	6.8×10^{14}

$$dR/d\theta = \frac{1.3 \times 10^4 \times 2.99 \times 10^{-23}}{1} (S-1) C_{eq}$$

$$= 3.9 \times 10^{-19} C_{eq} (S-1)$$

For example, at 420^o R,

$$dR/d\theta = 3.9 \times 10^{-19} \times 5.8 \times 10^{15} (S-1)$$

$$= 2.26 \times 10^{-3} (S-1) \text{ cm/sec}$$

$$R_\theta = 22.6 \int^\theta (S-1)\, d\theta \text{ microns}$$

If liquid drops are nucleated, we know that at values of S $\sim$ 10, (see page 15), nucleation rates are very rapid. Using Courtney's values of S vs. θ (calculated from Eq. (48)), the approximate values of R as a f(θ) for T = 420^o R and $S_{initial} \sim 10$ are:

R (microns)	Time (sec)
0	0
0.2	.001
1	.005
2	.01
8	.04
20	0.1
38	0.2
63	0.4
74	0.6

Next lets look at the situation where the nucleation rate reaches 10^5 clusters/cm^3-sec at $\sim 476^o$ R. $S \sim 5$ at $\theta \sim 0$. $C_{eq} \sim 7.9 \times 10^{16}$ so approximately

$$R_\theta = 22.6 \times \frac{7.9 \times 10^{16}}{5.8 \times 10^{15}} \int^{\theta} (S-1)\, d\theta$$

$$R = 310 \int^{\theta} (S-1)\, d\theta \text{ microns}$$

R (microns)	Time (sec)
0	0
1.2	.001
6.2	.005
12	0.01
24	0.02
60	0.05

and finally at 384° R, S (to cause nucleation $\simeq$ 19) and $C_{eq} = 6.8 \times 10^{14}$.

$$R_\theta = 22.6 \times \frac{6.8 \times 10^{14}}{5.8 \times 10^{15}} \int^{\theta} (S-1)\, d\theta$$

$$= 2.64 \int^{\theta} (S-1)\, d\theta \text{ microns}$$

R (microns)	Time (sec)
0	0
.05	.001
.24	.005
.48	0.01
2.40	.05
4.8	0.1
24	.5
45	1

To interpret these results, lets go back to the 420° R case. Suppose the N_2 entering the exchanger has a dew point of 462° R. This corresponds to a partial pressure of 0.02 psia. The conditions for the entering gas could be any of the following,

240 ppm at 50 psia

120 ppm at 100 psia

40 ppm at 300 psia

The gas is cooled in the exchanger. Assume for the moment that there is no change in the pressure and all nucleation is homogeneous.

As the nitrogen cools to 2° F the gas becomes saturated with water vapor but the nucleation rate is vanishingly small. If we take 10^5 nuclei (of critical size) formed /cm^3-sec as our criterion, then figure 6 shows that this

nucleation rate is achieved at T $\backsim 420^{\circ}$ R. If the temperature could be held at this level then the growth rates of particles would be given as on page 21 , and the S would drop. If, however, the gas were to continue to cool rapidly, this would over-ride the decrease in S due to particle growth and more nuclei would be released until there were sufficient nuclei growing to cause the net value of S to decrease.

How fast does the temperature drop? Lets consider the case with the lowest velocity, i.e., P_{inlet} = 300 psia and G = 10 lb/hr-ft^2. Then since $T_{in} = 560^{\circ}$ R, ρ_{in} = 1.4 lb/ft^3, and V_{in} = (10 lb/sec-ft^2)/(1.4 lb/ft^3) = 7.2 ft/sec.

$$V_{out} = (10)/(4.7) = 2.1 \text{ ft/sec at T = sat.}$$

and

$$V = aL + b$$

$$7.2 = 0 + b$$

$$2.1 = aL_T + b$$

$$a = -5.1/L_T \qquad b = 7.2$$

$$V = 7.2 - 5.1\ (L/L_T)$$

In the same way,

$$T = B\ L + C$$

$$\left.\begin{aligned} T_{in} &= B\ 0 + C \\ T_{out} &= B\ L_T + C \end{aligned}\right\} \quad C = T_{in} \qquad B = T_{out} - T_{in}/L_T$$

$$T - T_{in}/T_{out} - T_{in} = L/L_T$$

so

$$V = 7.2 - 5.1\ (T - T_{in}/T_{out} - T_{in})$$

now $V = dL/d\theta$

in terms of T,

$$7.2 - 5.1\ (L/L_T) = L_T\ dT/(T_{out} - T_{in})\ d\theta$$

$$dT/d\theta = (T_{out} - T_{in})/L_T \left[7.2 - 5.1\ (L/L_T) \right]$$

Typical values of $T_{out} - T_{in}/L_T \sim 70^{\circ}$ R/ft

and a value of L/L_T when the temperature is 420° R = 0.4, so,

$$(dT/d\theta)_{T \sim 420^{\circ} R} = (70)\ (7.2 - 5.1 \times .4)$$

$$= 70 \times (7.2 - 2.04)$$

$$= 70 \times 5.2 = 364\ ^{\circ}R/sec$$

Referring back to page 21 , we see that in 10 milliseconds a particle is $\sim 2\ \mu$ in size but the temperature has dropped ~ 3 or 4° R. How does this affect the rate of growth? We cannot be sure but for an approximation refer to Eq. (49). Note that if $C_A \gg C_{eq}$, i.e., $S \gg 1$, then when the temperature is changed, if μ us assumed to be only a weak function of temperature, we can say that,

$$dR/d\theta = \alpha\, u\, \frac{m}{\rho}\, C_A \qquad (49a)$$

so the rate of change of R is almost constant until C_A begins to drop. Of course, while the cooling is going on the gas is becoming more supersaturated. In fact, in this example, a Δ T of 4° R would raise the S from 10 to over 13. This increase in S causes an enormous increase in the nucleation rate (by x 10^3 or thereabout). These new nuclei tend to grow but some time in this immediate region the increased number of nuclei (all starting to grow) will result in a decreasing value of S, over-riding the tendency of S to increase due to temperature decreasing. Courtney's theoretical plots indicate that around 420° R, with S values somewhat over 15, nucleation and growth will drop S to ~ 1 to 3 in 10 milliseconds. With this precipitious drop in S, growth essentially stops and we are left with many particles in the 0 - 2 μ range and a few of larger dimensions.

In summary, then, for this case, assuming no heterogeneous nucleation, the gas supercools from a theoretical saturation temperature of 462° R to around 420°R wherein nucleation is noted to initiate a cloud of very small nuclei. Within a temperature range of $\sim 470^{\circ}$ R or ~ 30 milliseconds (about 1.5 - in) the number of nuclei have increased enormously and the saturation level has fallen to near unity. The particle range is 0.1 - 2 μ for most particles with a few $> 10\ \mu$.

One is struck by the rapidity of nucleation and decrease in supersaturation level in the case chosen. If the inlet humidity had been different from that assumed, the results would not have been qualitatively much different; i.e., only a different point in the exchanger would have comprised the nucleation region (with, of course, different T's and S's).

If the flow rate had been increased, we would anticipate nucleation at about the same point, but since $dT/d\theta$ is much larger, then most of the water would be removed by formation of very small particles and few particles greater than 0.1 - 1.0 μ would be formed.

On the other hand, if much lower flow rates were reached the decrease in S would be due primarily to growth rather than from new nuclei and most particles would be large ($>10\mu$).

Carbon Dioxide

The discussion before this point has dealt primarily with the water-air system. Since carbon dioxide may also be present, it is interesting to consider the nucleation and growth of it.

Properties

Surface Tension (LIQ)

ICT 4:447

$$\sigma = 75(1-T_R)^{1.25} \text{ ergs/cm}^2$$

$T_c \sim 547^\circ$ R

$T_{\text{triple point}} = 390^\circ$ R

$T_{R_{\text{triple point}}} = 390/547 - 0.72$

$$\sigma_{\text{triple point}} = 75\ (1-.72)^{1.25} = 75\ (.28)^{1.25} = 75 \times .2 = \underline{15}$$

approximate

$$\sigma_{\text{solid } CO_2} = \sigma_{\text{liq. } CO_2 \text{ at TP}} \times \frac{\sigma \text{ solid } H_2O}{\sigma_{\text{liq. } H_2O \text{ at TP}}}$$

$$= 15 \times 90/76 \simeq 18 \text{ ergs/cm}^2$$

Vapor Pressures-Solid - see Figure 7.

Molecule concentration at equilibrium -

$$C_{eq} = \frac{P_{vp}}{RT_{sat}} = \frac{P_{MM}}{T^{o}K} \times \frac{^{o}K - mole}{82.07\ cc\text{-}atm} \times \frac{1a\ tm}{760\ MM} \times 6.03 \times 10^{23}\ \frac{mol/cc}{mole}$$

$$= .97 \times 10^{19}\ P/T\ molecules/cm^{3}$$

$T^{o}R$	$T^{o}K$	P_{MM}	P/T	C_{eq}(solid) molecules/cm^3
391 (T.P)	217	3885	17.9	1.6×10^{20}
384	213	3073	14.4	1.3×10^{20}
366	203	1486	7.4	7.3×10^{19}
348	193	672	3.5	3.4×10^{19}
330	183	279	1.6	1.5×10^{19}
312	173	104	0.60	5.9×10^{18}
294	163	34.6	0.21	2.0×10^{18}
276	153	9.8	0.064	6.3×10^{17}
258	143	2.3	0.016	1.5×10^{17}
240	133	.43	3.2×10^{-3}	3.1×10^{16}
221	123	.061	5.0×10^{-4}	4.9×10^{15}
204	113	.0059	5.2×10^{-5}	5.1×10^{14}

density of solid CO_2 = 95 lbs/ft^3 = 1.5 gms/cm^3

$$v = 44\ \frac{gms}{gmole} \times 1\ cm^3/1.5\ gms \times mole/6.03 \times 10^{23}\ molec = 49 \times 10^{-23} cm^3/molec$$

Boltzmann's constant = 1.38×10^{-16} ergs/molec ^{o}K

$$\phi = \frac{-16\pi\sigma^3}{3} /(kT)^3$$

$$= \frac{-16}{3} \times (18)^3 \times \frac{(4.9 \times 10^{-23})^2 \times 3.14}{(1.38)^3 \times 10^{-48}\ T^3}$$

$$= -16.7 \times \frac{5800 \times 24 \times 10^{-46}}{2.6 \times 10^{-48}\ T^3} = \frac{-8.9}{T^3} \times 10^7$$

T ^{o}R	T ^{o}K	T^3 $(^{o}K)^3$	$-\phi$	T ^{o}R	T ^{o}K	T^3 $(^{o}K)^3$	$-\phi$
391	217	10^7	8.9	294	163	4.3×10^6	20.5
384	213	9.8×10^6	9.1	276	153	3.6×10^6	25
366	203	8.2×10^6	10.8	258	143	2.9×10^6	31
348	193	7.2×10^6	12.4	240	133	2.3×10^6	38
330	183	6.1×10^6	14.6	221	123	1.85×10^6	48
312	173	5.2×10^6	17.0	204	113	5×10^5	180

Estimation of g_c

$$g_c = \frac{32}{3} \frac{\sigma^3 v^2 \pi}{(kT)^3 (\ln S)^3}$$

$$= -2\phi/(\ln S)^3 \quad \text{where } \phi \text{ is tabulated above.}$$

Now to consider what temperature range is of most interest. The inlet CO_2 0.05 wt. percent,

$$= 0.0005 \times 29/44 = 0.00033 \text{ mole. per cent}$$

Inlet pressures range between 300 to 50 psia so inlet partial pressures

$3.3 \times 10^{-4} \times 760/14.7 \times 300 = 5.1$ mm

to $3.3 \times 10^{-4} \times 760/14.7 \times 50 = .85$ mm

For the former $T_{SAT} \backsim 266^{\circ}$ R

and for the latter $T_{SAT} \backsim 246^{\circ}$ R

Lets call T const $\sim 257^{\circ}$ R for those calculations where there is not a strong dependence on T, i.e.,

$\phi \sim -31$

$g_c \sim 62/(\ln S)^3$

and the pre-exponential factor in Eq. (33),

$$\propto (RT/2\pi M)^{1/2} \times 4\pi (3v/4\pi)^{2/3} g_c^{2/3} C_{eq} C$$

Now

$$RT/2 M = 1.987 \text{ cal/mole } ^{\circ}K \times T^{\circ}K/2 \times 3.14 \times 107.5 \text{ kg-meter/252 cal}$$

$$\times 100 \text{ g}^F/1 \text{ kg} \times 100 \text{ cm}/1M \times 1 \text{ gmole}/M_{gm} s^m \times 980 \text{ gm}^m \text{ cm/gm}^F \text{sec}^2$$

$$= \frac{1.987 \times 107.5 \times 10^5 \times 9.8 \times 10^2}{6.28 \times 252} \frac{T}{M}$$

$$= 13.2 \times 10^6 \, T/M$$

If $T \sim 257^{\circ}$ R, M = 44,

$$(RT/2\pi M)^{1/2} = 10^3 (13.2 \times 143/44)^{1/2} = 10^3 \times 6.6 \text{ cm/sec}$$

and

$$(4\pi)^{1/3}(3v)^{2/3} = (12.5)^{1/3} (3 \times 4.9 \times 10^{-23})^{2/3}$$

$$= 2.32 \times 28 \times 10^{-16} = 65 \times 10^{-16} \frac{\text{cm}^2}{(\text{molec})^{2/3}}$$

and

$$g_c^{2/3} = 31^{2/3} = 9.8 \text{ molec}^{2/3}$$

and

$$C_{eq}\, C = (C_{eq})^2\, S \text{ but at} \sim -130^\circ \text{ C, } C_{eq} = 1.5 \times 10^{17} \text{ molec/cm}^3$$

$$C_{eq}^2\, S = S\ 2.25 \times 10^{34} \text{ molec}^2/\text{cm}^6$$

and

$$\alpha \sim 1$$

$$\therefore\ \alpha\ (RT/2\pi M)^{1/2} \times 4\pi (3v/4\pi)^{2/3}\, g_c^{2/3}\, C_{eq}\, C$$

$$= (1)\ (6.6)(10^3\quad 65\quad 10^{-16})(9.8)(2.25)(10^{34})(S)$$

$$= 9.5\ S \times 10^{24} = \sim 10^{25}\ S$$

The rate of nucleation at $\sim 257^\circ$ R is then,

$$R = 10^{25} \times S \times e^{-31/(\ln S)^2}$$

S	lnS	$(\ln S)^2$	$-31/(\ln S)^2$	$e^{-31/(\ln S)^2}$	R
2	.69	.48	-65	10^{-28}	2×10^{-3}
3	1.1	1.2	-26	10^{-11}	2×10^{14}
2.5	.92	.84	-37	10^{-16}	2×10^{9}
2.3	.83	.69	-45	10^{-19}	2×10^{6}
2.2	.79	.63	-49	10^{-22}	2×10^{3}

at 257° R.

A value of S = 2 corresponds to 500° R from S = 1 to S = 7.

A value of S = 3 corresponds to 500° R from S = 2 to S = 3.

Nucleation begins very rapidly with CO_2 and it appears that it will be easy to fog without much growth.

For example, using the inlet P = 300 psia 0.05 wt.percent gas becomes saturated with CO_2 at 260° R and in $\sim 14^{\circ}$ R (14/400 = 0.035 a 3% of length or $\backsim$ 2 inch). The nucleation rate has increased from zero to a <u>very</u> large value.

BIBLIOGRAPHY OF MAJOR REFERENCES

1. "Nucleation Processes and Aerosol Formation", W. J. Dunning, "The Physical Chemistry of Aerosols", Disc. of the Faraday Soc., No. 30, 1960, p. 9-19.

2. "Kinetik der Phasenbildung", M. Volmer, Ann Arbor, Edwards Bros., 1945.

3. Becker, R. and Doring, W., Ann. Physik, 24, 719 (1935).

4. "Kinetic Theory of Liquids", J. Frenkel, Dorier Pub., Inc., New York.

5. "Kinetics of Condensation from the Vapor Phase", W. G. Courtney and W. J. Clark, Texaco Exp. Inc., TM-1250, July 1961, TM-1340, April 1962.

6. General References

   a. Reference 1

      "Nucleation of Water Aerosols", B. J. Mason, P. 20-38.

      "Ice Crystal Nucleation by Aerosol Particles", N. H. Fletcher, p. 39-45.

   b. "Symposium on Nucleation Phenomena", Ind. Eng. Chem. 1270-1338 June 1952.

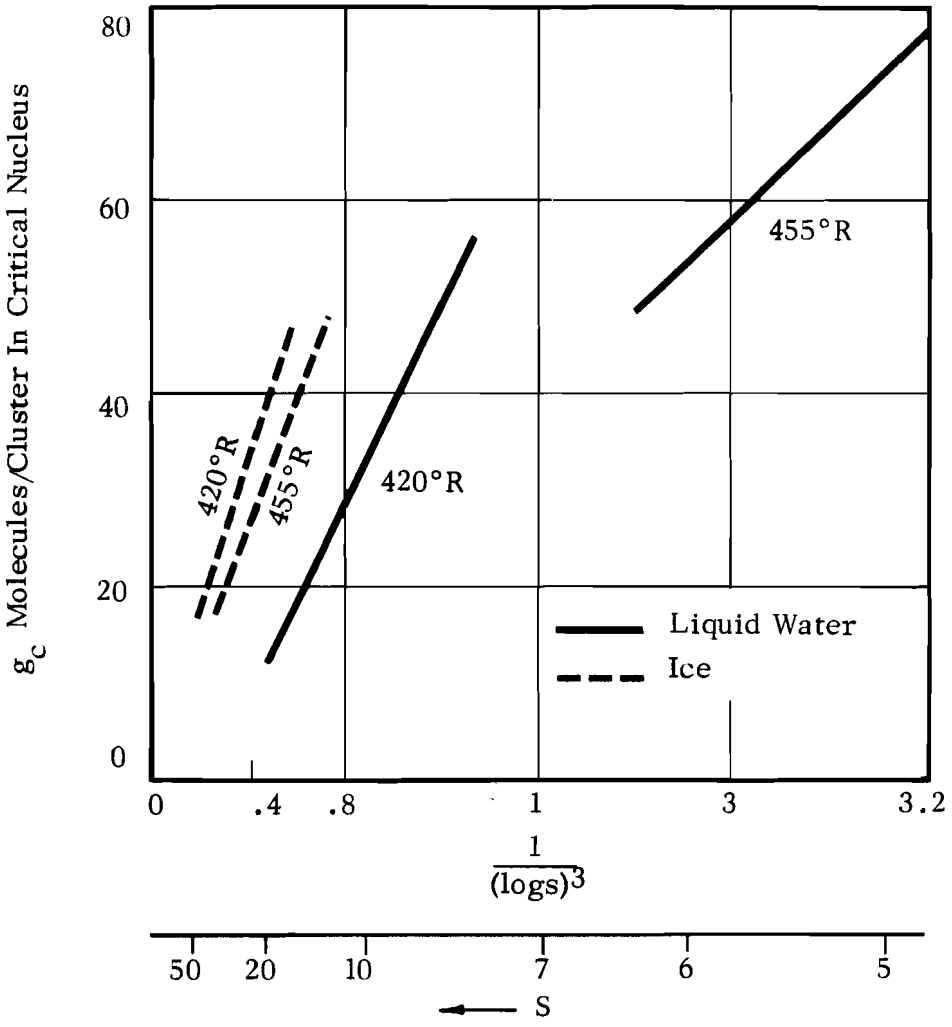

FIGURE 1 TYPICAL VALUES OF g_c FOR WATER - AIR SYSTEMS

Data Per Courtney
(Texaco Exp. Inc.
Report TM-1250
7/15/61)

$g_c = 43$
$T = 420°R$
$S_o = 10$

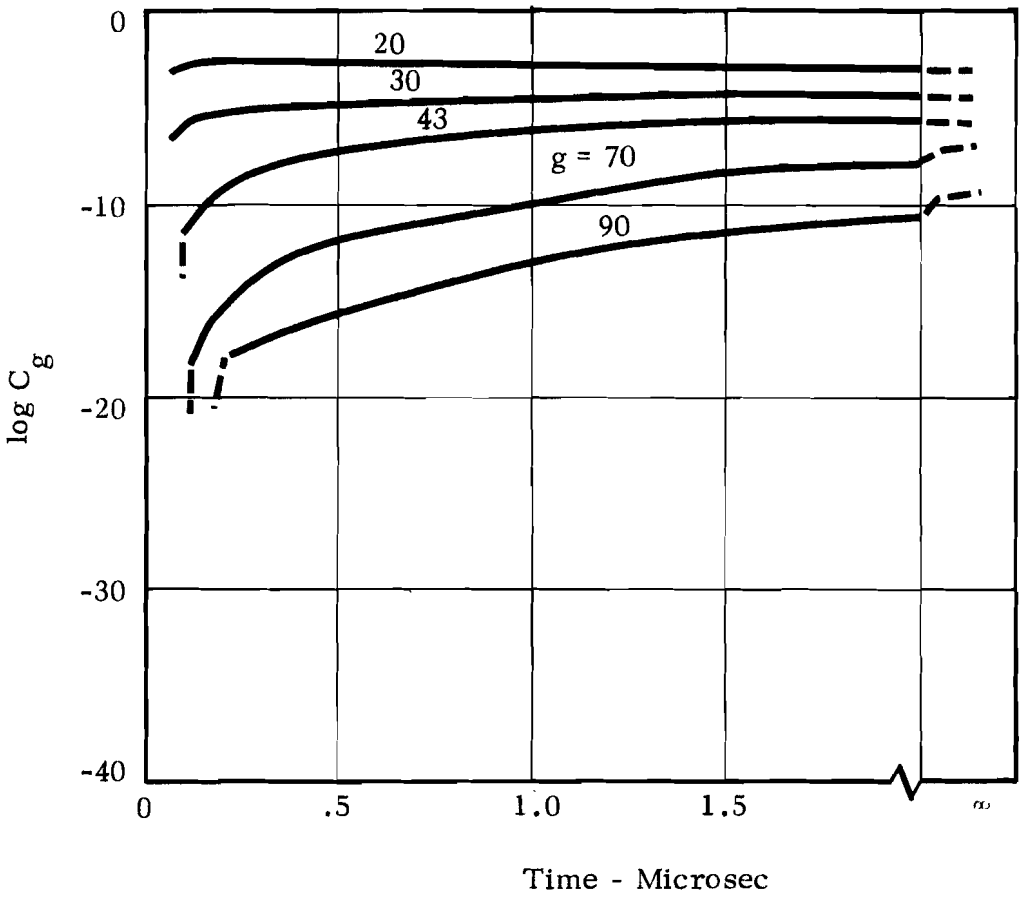

FIGURE 2 GROWTH RATES OF SMALL CLUSTERS OF MOLECULES IN WATER - AIR SYSTEMS

Data Per Courtney
(Texaco Exp. Inc.
TM-1250 7/15/61)

$$R \leq 10^{-5} e^{-\left(\frac{\phi}{lws}\right)^2}$$

$$\phi = \frac{-16}{3} \quad ^3 \quad V_g^2 \quad \pi/(RT)^3$$

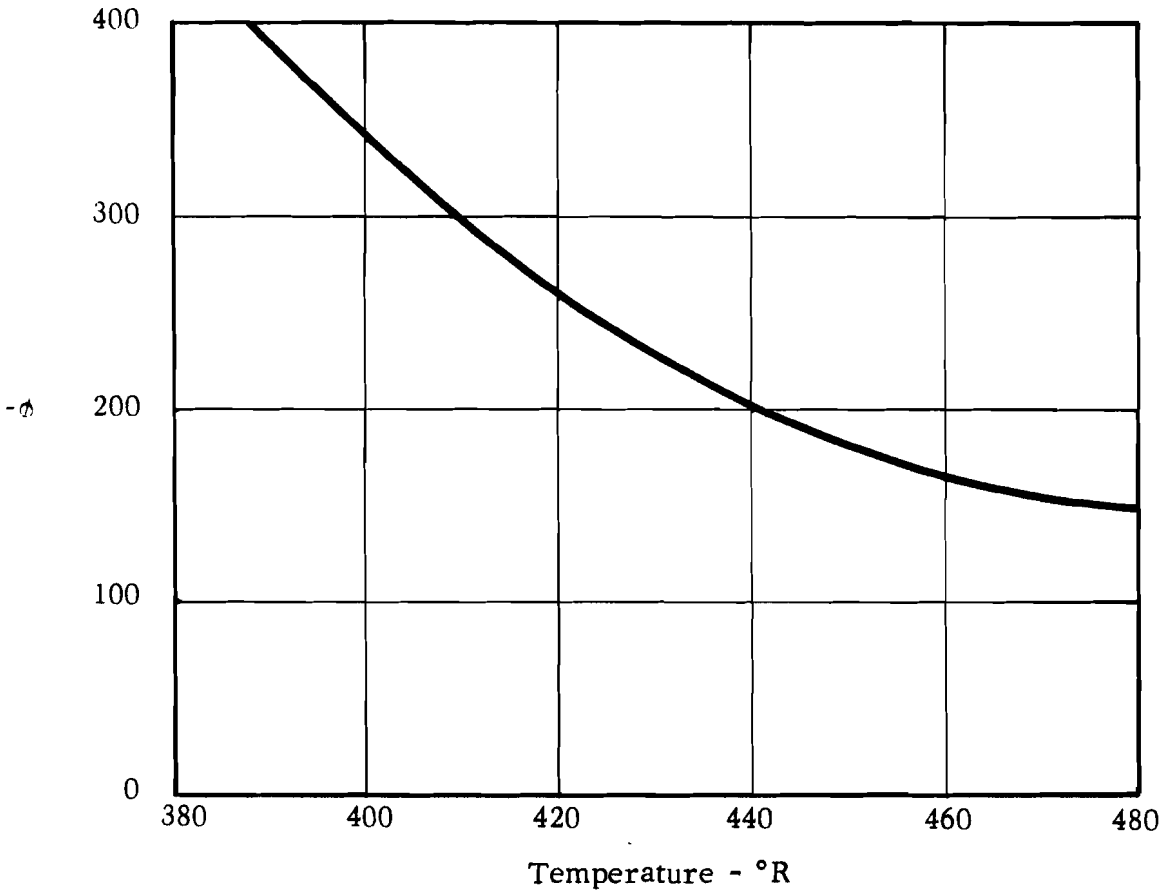

FIGURE 3 EXPONENTIAL FACTOR, ϕ, VS TEMPERATURE

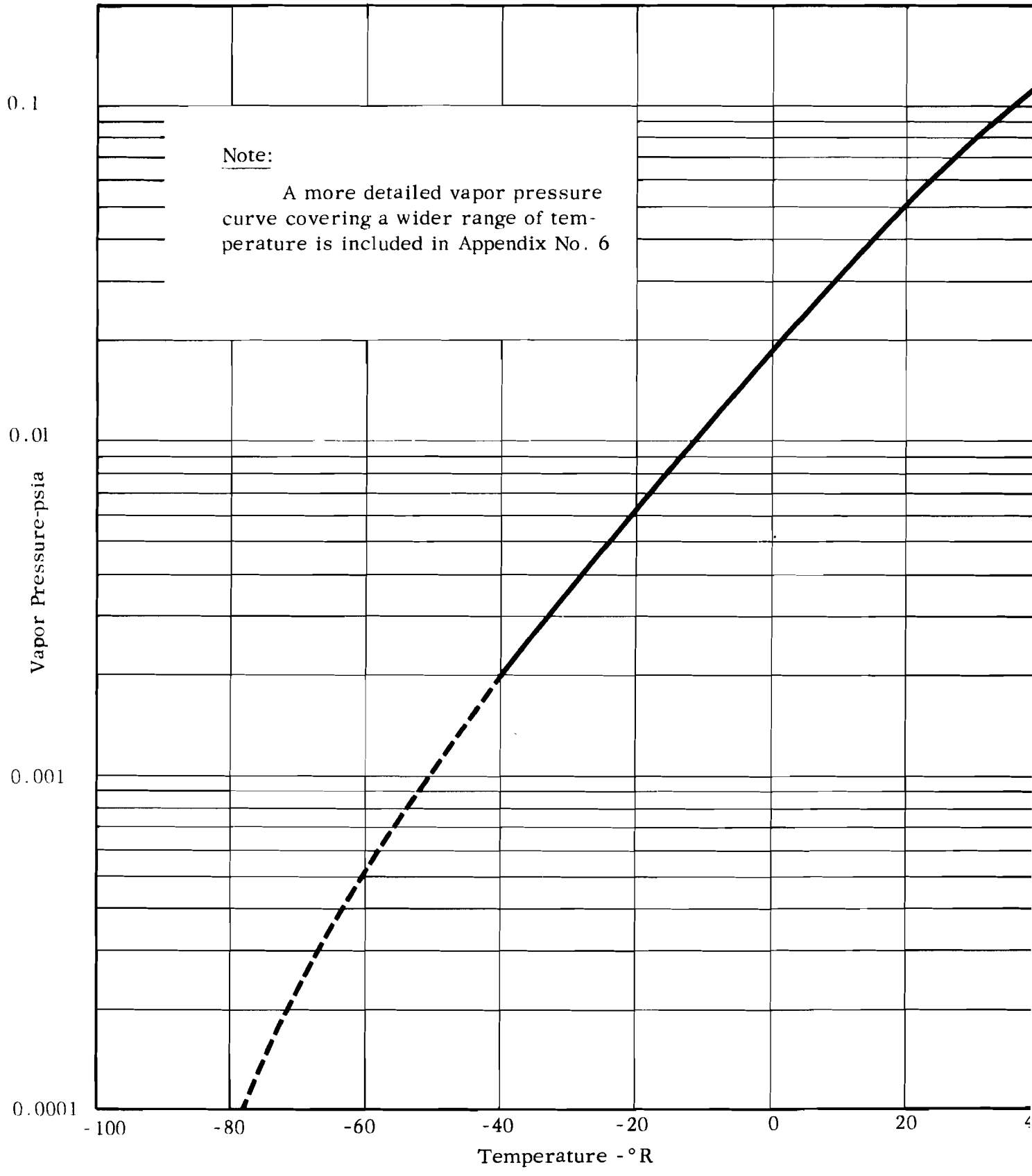

FIGURE 4 VAPOR PRESSURE OF WATER AS A FUNCTION OF TEMPERATURE

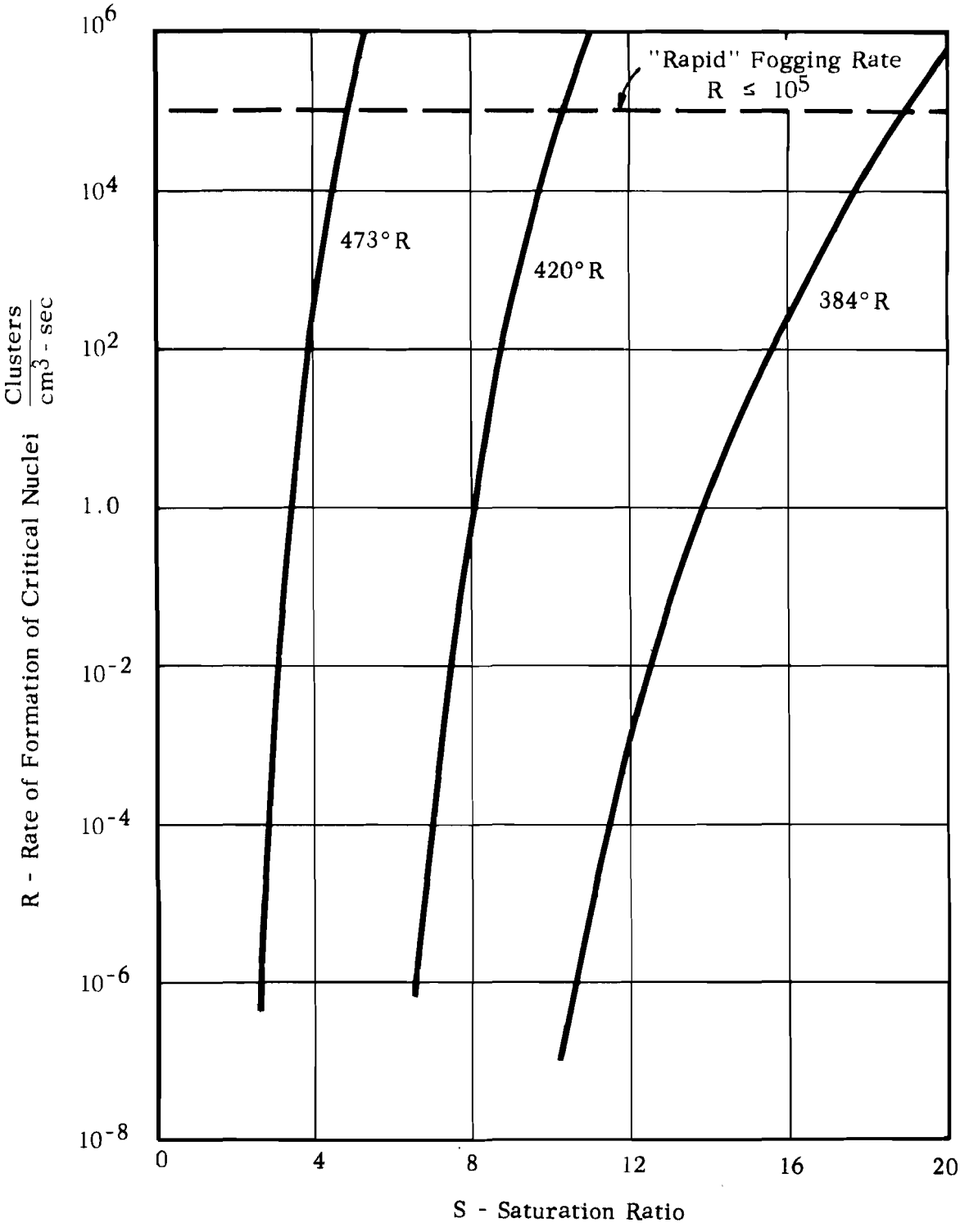

FIGURE 5 HOMOGENEOUS NUCLEATION RATES FOR AIR - WATER SYSTEMS

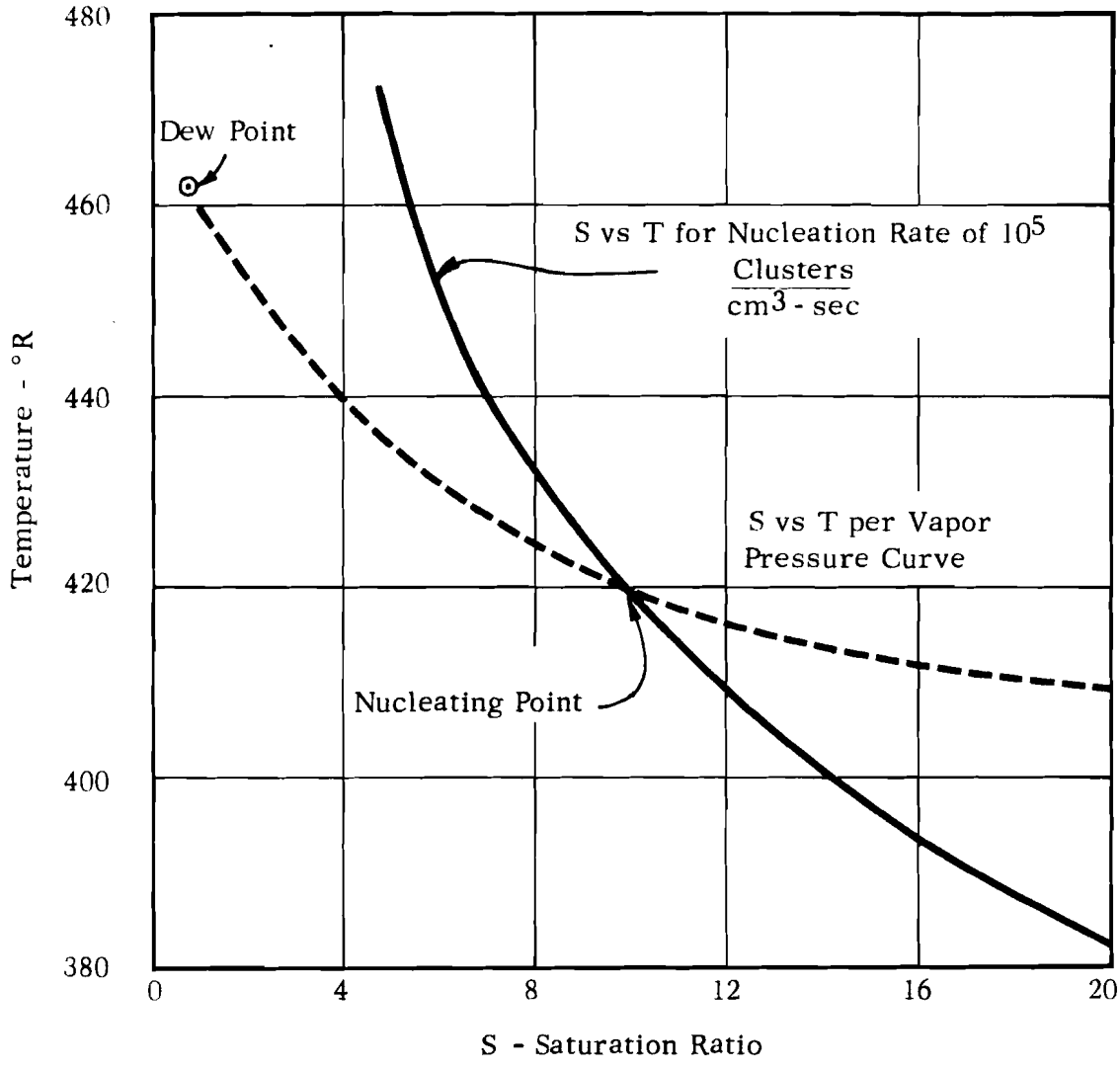

FIGURE 6 ESTIMATION OF "NUCLEATING POINT" HOMOGENEOUS NUCLEATION IN TYPICAL WATER-AIR SYSTEM

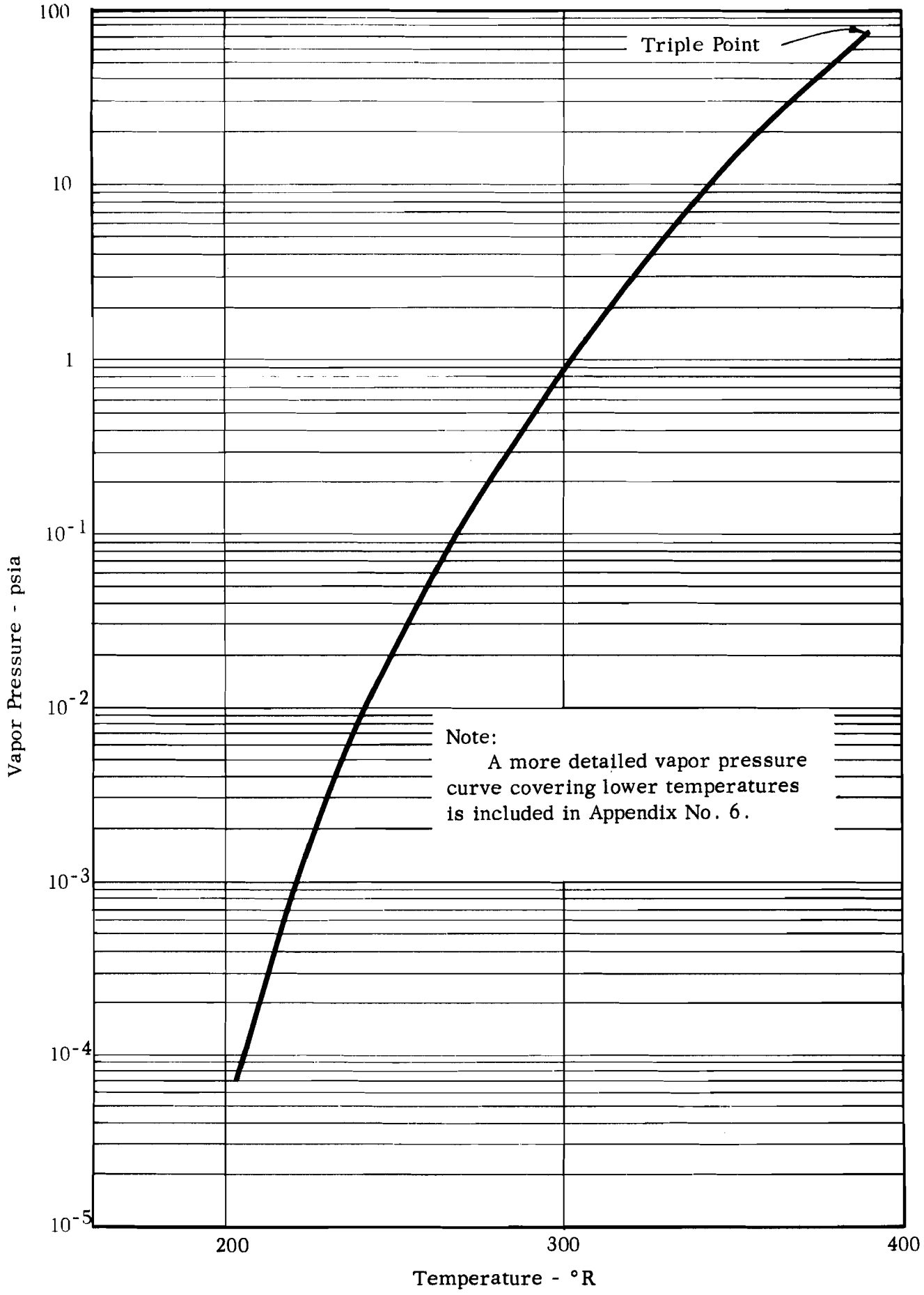

FIGURE 7 VAPOR PRESSURE OF SOLID CARBON DIOXIDE

APPENDIX 3

HETEROGENEOUS NUCLEATION

TABLE OF CONTENTS

INTRODUCTION

In Appendix No. 2, we have derived many of the basic equations to estimate the rate of homogeneous nucleation for water and CO_2 from air at low temperatures. The equations derived are certainly not quantitatively correct but they predict the approximate effects of most of the pertinent variables. Reference to the above noted attachment, we concluded that, if the homogeneous mechanism prevails, large supersaturations are required to initiate nucleation.

On the other hand, if the air has a sufficient number of the right kind of impurity particles, then it is quite possible to have nucleation proceed in a heterogeneous route. Mason (5)* expresses these ideas in a cogent manner:

"The presence of impurities in the vapor may greatly facilitate condensation. In the atmosphere there is an abundance of particles having a wide variety of size and constitution, their size and number concentration usually being such that even the most rapid cloud formation is associated with very small values of supersaturation, usually less than 1%."

These notes attempt to summarize the existing concepts of heterogeneous nucleation and point out those important points applicable to frosting heat exchangers. Many of the results derived in the homogeneous nucleation notes will be used without additional justification. In the following development, equations taken from Appendix No. 2 will be identified by the prefix **M** in the equation number.

REVIEW OF THE IMPORTANT HOMOGENEOUS EQUATIONS

Equation M-33 describes the rate of homogeneous nucleation of a condensible component in an inert gas. It may be written as:

$$R = K \exp\left[-\Delta F^{o}/kT\right] \qquad (1)$$

R = rate of formation of critical sized nuclei /cm^3-sec.

ΔF^{o} = the free energy change associated with the reaction of g_c molecules at P, T to form a nuclei of g_c molecules at P, T

The change is worked out in detail in Appendix No. 2 and given analytically in Eq. M-20

$$= -(g_c - 1)\, kT \ln S + 4\pi R_c^2 \sigma$$

where g_c = number of molecules in the critical sized nucleus

$$= 32\, \sigma^3 v^2 \pi / 3\, (kT)^3 (\ln S)^3 \text{ by M-23a}$$

---

* Underlined numbers in parentheses refer to Bibliography on Page 11.

$$R_c = (3\ v\ g_c/4\ \pi)^{1/3} \text{ by a volume balance}$$

Substituting these values into (1), simplifying, we obtain (using the K value from Eq. M-33),

$$R = \left[\frac{RT}{2}\right]^{1/2} \left[\frac{1}{M}\right]^{1/2} \times 4\pi \left[\frac{3v}{4}\right]^{2/3} g_c^{2/3}\ C\ Ceq$$

$$\exp\left[\frac{16}{3}\ \frac{\sigma^3 v^2 \pi}{(RT)^3 (\ln S)^2}\right] \qquad (2)$$

The pre-exponential factor may be slightly different in other derivations but in most cases the differences are small and it is within reason to take it to be $10^{25} \pm$ a few orders of magnitude. Thus equation (2) becomes

$$R_{HO} = 10^{25} \exp\left\{\frac{-16}{3}\ \frac{\sigma^3 v^2 \pi}{(RT)^3 (\ln S)^2}\right\} \qquad (3)$$

The designation R_{HO} indicates the rate of nucleation by homogeneous mechanisms. As before,

σ = surface tension

v = specific volume of phase in the nuclei

RT = energy/mole

S = supersaturation ratio

The other relation we need is an expression for the radius of a critical sized nuclei. This is easily obtained from the relations involving g_c and r_c on the previously presented. Eliminating g_c,

$$R_c = 2\sigma v/kT \ln S \qquad (4)$$

MODEL FOR HETEROGENEOUS NUCLEATION

Let 1 refer to the medium, 2 to the nucleating phase, and 3 the foreign nucleating particle. For convenience of calculation let us assume that 3 is a spherical particle. (If it is not, the geometry is more complex but the general result is not appreciably affected). The derivation follows that developed by Fletcher (1).

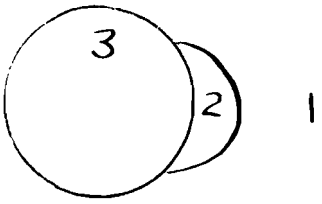

Again g_c represents the number of molecules in 2 when a critical nuclei radius is formed and spontaneous growth starts.

On the basis of this model, the free energy change going from monomer to the critical nuclei size is not given by Eq. (M-20), but rather

$$\Delta F^{o} = -(g_c - 1)\, kT \ln S + \sigma_{12} A_{12} + (\sigma_{23} - \sigma_{13}) A_{23} \qquad (5)$$

In homogeneous nucleation $A_{23} \rightarrow 0$, $A_{12} \rightarrow 4\pi R_c^2$ and Eq. M-20 results. In heterogeneous nucleation the free energy is decreased by the amount $\sigma_{13} A_{23}$ when nucleation occurs.

The terms σ_{12}, . . . refer to surface or interfacial tensions between phases and

A_{12}, . . . the areas of contact.

As before we wish to substitute ΔF^{o} into Eq. (1) but to accomplish this, the complex geometry must be analyzed.

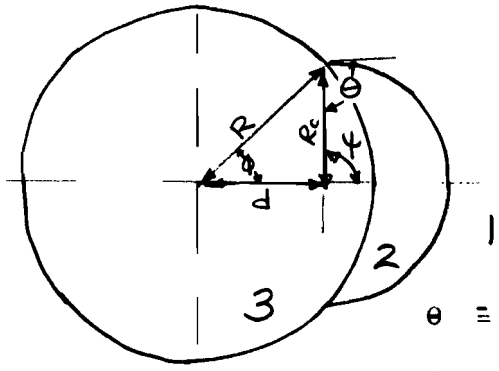

R_c = radius of critical sized nuclei

R = radius of foreign nucleating particle

d = center-to-center distance of 2 and 3

$\theta \equiv$ contact angle

$$\cos\theta \equiv m = (\sigma_{13} - \sigma_{23})/\sigma_{12}$$

$$-1 \leq m \leq 1$$

The areas of contact may now be expressed:

$$A_{12} = 2\pi R_c^2 (1 - \cos\psi) \qquad (6)$$

$$A_{23} = 2\pi R_c^2 (1 - \cos\phi) \qquad (7)$$

$$V_2 = g_c v_2 \tag{8}$$

$$= 1/3\ \pi R_c^3 [2-3\cos\ + \cos^3\psi] - 1/3\ R^3(2-3\cos\phi + \cos^3\phi)]$$

$$\cos\phi = (R-R_c\cos\theta)/d = (R-R_c m)/d$$

$$\cos\phi = -(R_c-R\cos\theta)/d = -(R_c-Rm)/d$$

$$\phi = (R^2 - 2\ R_c\ Rm)^{1/2} \tag{9}$$

Following the same procedure as given in detail in Appendix No. 2 one finds that (instead of Eq. M-24)

$$C_a = C\ eq\ \exp\left\{-\frac{8}{3}\ \frac{\sigma^3 v^2 \pi f(m,x)}{(RT)^3(\ln S)^2}\right\} \tag{10}$$

$$\text{or } \Delta F_{HOMO} \times \frac{f(m,x)}{2} = \Delta F_{HETERO} \tag{11}$$

$$\text{and where } \chi = R/R_c \tag{12}$$

and Fletcher gives for the function f (m,x),

$$f(m,x) = 1 + \left[\frac{1-mx}{\beta}\right]^3 + x^3\left[2-3\ \left(\frac{x-m}{\beta}\right) + \left(\frac{x-m}{\beta}\right)^3\right] + 3\ mx^2\ \left(\frac{x-m}{\beta}\right) - 1 \tag{13}$$

This function is plotted in Figure 1 as given by Fletch. As R 0, f(m,x) 2, and $\Delta F_{HETERO} \rightarrow \Delta F_{HOMO}$, i.e., the resultant equation 10 approaches the homogeneous case. The other limit, as $R \rightarrow \infty$ (i.e., a plane surface), then f(m,x) approaches the limit,

$$f\ (m,x)_{x \rightarrow \infty} \rightarrow \frac{(2+m)(1-m)^2}{2} \tag{14}$$

Eq. (14) agrees with the results of Turnbull and Vonnegut (2) where their

$$f(\theta) = (1/2)\ f\ (m,x)_{x \rightarrow \infty} \tag{15}$$

The rate of nucleation, expressed as nuclei formed per particles per second, R_{HETRO},

$$R^1_{HETRO} = K^1_{HETRO} \exp \frac{\phi f(m,x)}{2 (\ln S)^2} \quad (16)$$

where ϕ is given in Eq. M-34 as

$$\phi = \frac{-16}{3} \sigma_{12}^3 v^2 \pi / (RT)^3$$

and is plotted as a function of T in Appendix No. 2.

If we wish to express the rate of nucleation /cm^3 -sec, then

$$R_{HETRO} = K_{HETRO} \times 4\pi R^3 \times N_H \exp \left\{ \frac{\phi(f1m,x)}{2(\ln(S))^2} \right\} \quad (17)$$

Now in many cases $K_{HETRO} \sim 10^{25}$ $\frac{\text{nuclei}}{cm^3\text{-sec}}$

$4 \pi R^2$ = area/foreign particle, $\frac{cm^2}{\text{particle}}$

N_H = number of foreign particles/cm^3.

All of our results are thus expressed semi-quantitatively in Eq. (17). Let us now examine some of the terms.

PARTICLE CATALYSIS

To cause hetrogeneous nucleation, a particle must have certain properties.

a. Particle Size

Obviously the particle to be active must be larger than the size of the critical nucleus (4). If smaller, then growth would tend to be somewhat easier than that for pure homogeneous nucleation, but the predominent effects occur when the initial foreign particle size is equal to or greater than R_c. Eq. (4) indicates the range of R_c,

$$R_c = 2 \sigma v/kT \ln S$$

As an example, for water at 420°R

σ 83.6 ergs/cm^2 (liq. water)

$v \sim 3 \times 10^{-23}$ cm^3/molecule

$k \sim 1.38 \times 10^{-16}$ ergs/°K - molecule

T = 420°R = 233°K

$$R_c = \frac{(83.6)(3)(10^{-23})(2)}{(1.38)(10^{-16})(233)} \times \frac{1}{P_n S} \text{ cm}$$

if $S \sim 10$

$$R_c \sim 6 \times 10^{-8} \text{ cm} \quad 6 \times 10^{-4} \mu \sim 6^{\circ}A$$

if $S \sim 1.1$

$$R_c \sim 1.5 \times 10^{-6} \text{ cm} \sim 150 \times 10^{-4} \mu \sim 150^{\circ}A$$

For high values of S, particles of molecular size could be active. For values of $S \searrow 1.0$, much larger particles are necessary. For most atmospheric particles, the sizes are $> .05\mu$ so that size should present no problem. We will discuss size of "expected" particles more later.

b. Composition

Much has been written concerning the effect of chemical structure on nucleating activity of foreign particles. There seems to be general agreement that a low contact angle (i.e., $\theta \searrow 0^{\circ}$, $m \rightarrow +1$) or a good wetting is most desirable. (See Eq. 17, f (m,x) increases as m decreases). This indicates that probably the best agent would be the material itself. It is well known that materials with a structure similar to ice are good "ice" nuclei, e.g., silver iodides. Turnbull and Vonnegut discuss such catalytic foreign agents (2). Fletcher (3) considers the possibility that the better nucleating agents have strong electric fields near the surface but notes that dislocations or strains on such an agent are not of much importance.

In very clean air, nucleation occurs to some degree on ions of a very small radius (thus with small R, high S, see preceeding page). Near oceans, the air is often contaminated with salt particles which act as very efficient nuclei (5). In fact, due to their hydroscopic nature, these salt drops can actually cause nucleation at supersaturation values less than unity. Mason discusses the extreme difficulty to supersaturate a water-air mixture in the presence of salt (5).

A note of caution is indicated by Bustein (9) who found that nucleating agents coated with paraffine (to give a large θ, non-wettable surface) were still reasonably effective nucleating materials. Many other authors (10, 12, 13) have also considered the problem.

In summary, for nuclei to be effective, they must be at least a large as R_c, preferably polar in nature, wettable by the condensing material. Good examples are salts, acids, combustion products, etc.

c. Number of Nuclei

Obviously, from Eq. 17, it is apparent that the larger the number density, the larger the effect. One interesting way to look at this problem involves a technique to be utilized later so development here is appropriate.

In the homogeneous nucleation notes, we chose the somewhat arbitrary level of 10^5 new nuclei formed per cc per sec to represent the condition of rapid nucleation. Using the same value here, from Eq. 17

$$10^5 = 10^{25}\, 4\pi R^2 N_H \exp\left\{\frac{\Phi}{2} \quad \frac{f(m,x)}{(\ln S)^2}\right\} \tag{18}$$

rearranging and taking natural logs,

$$0 = 48.7 + 2 \ln R + \ln N_H + \left\{\frac{\phi}{2(\ln S)^2} \quad f(m,x)\right\}$$

Assuming R, σ, v as reasonably constant, then

$$\ln N_h = C_1 + \frac{C_2}{T^3(\ln S)^2} \tag{19}$$

Dunning (4) discusses some experiments of Willmerth and Nagamatsu who carried out a series of seeding experiments with CO_2 in air to varify Eq. 19. It might be expected to fit well when N_H was large but to fail for low values of N_H. Their plot shown below appears to verify this conclusion. At concentrations of CO_2 greater than 70 ppm, heterogeneous nucleation resulted. At lower quantities, nucleation was predominantly homogeneous. These results show qualitatively that there is a minimum concentration of foreign particles which affect significantly the nucleation process.

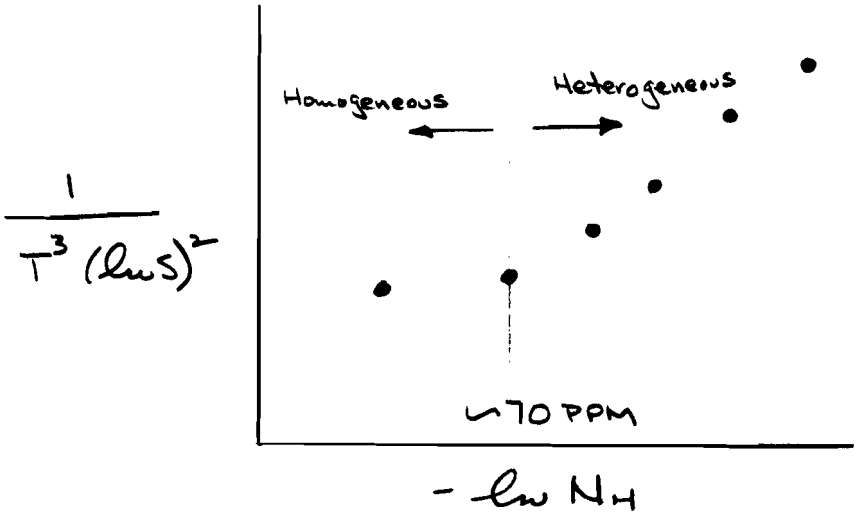

NUCLEI IN ATMOSPHERIC AIR

Mason in his book "Physics of Clouds" (6) gives a good discussion of atmospheric nuclei.

Particles range from 10^{-7} cm for small ion groups to more than 10 μ for the larger salt and dust particles. Near ground level above industrial centers, concentrations up to $10^6/cm^3$ have been reported. For convenience, the nuclei have been roughly classed:

1. Aitken nuclei, 0.005 μ to 0.2 μ
2. Large nuclei, 0.2 μ to 1 μ
3. Grant nuclei, >1 μ

Aitken nuclei usually occurs in much larger numbers than either of the other two. The often-quoted ratios between the three, starting with Aitken are 10^6: 10^3: 1. These Aitken types usually result from smoke, gas phase chemical reactions, wind-blown dust, etc. The other two types usually are formed from some kind of mechanical action or spray.

In a preminary survey of variation with height, a number of balloon ascents have shown that as an average,

Height, meters	Number of Aitken Nuclei per cc.
0 - 500	2×10^4
500 - 1000	1×10^4
1000 - 2000	2.5×10^3
2000 - 3000	8×10^2
3000 - 4000	3×10^2
4000 - 5000	2×10^2
>5000	1×10^2

For larger nuclei

Height, meters	Number/cm^3 >		
	10 μ	5 μ	1 μ
1000	10^{-2}	10^{-1}	1
1500	10^{-3}	10^{-2}	1
2000	10^{-6}	10^{-4}	10^{-2}

Grant nuclei are not found at high altitudes.

It appears that at high altitudes, the number of nuclei decreases regularly. Certainly only a few nuclei /cc will not greatly affect nucleation rates.

SATURATION LEVELS EXPECTED IF HETEROGENEOUS NUCLEATION PREDOMINATES

Using the criterion $R \sim 10^5$ nuclei 1cc-sec, from Eqs. 18 and 19, rearranged,

$$S = \exp \left\{ \frac{-\phi\, f(m,x)}{2\ 48.7 + 2\ \ln R + \ln N_H} \right\}^{1/2} \qquad (20)$$

For example if $T = 420^{\circ}R$, $\phi = -260$ (from p. 17 of the homogeneous notes), and if $X \to 0$ (i.e., homogeneous nucleation),

$$S = \exp \left[(-X-260)/48.7 \right]^{1/2} = e^{(5.38^{1/2}} = 10$$

which is the same as we got before on p. 19 of the homogeneous notes*.

To determine S for the heterogeneous case, Eq. 20 cannot be solved directly for S since X contains R_c and R_c is also a function of S. It is a trial and error solution. To see how Eq. 20 varies with R, we can choose a particular example and let R and m vary. For convenience choose a "dirty" gas with $N_H \cong 10^5$ nuclei/cc and calculate the value of S which will cause <u>one new nuclei formed per particle per second</u>, 1.e., from Eq. 17.

$$R_{HETRO} \cong 10^5$$

$$K_{HETRO} \cong 10^{25}$$

$$N_H \cong 10^5$$

$$\therefore\ 10^5 = 10^{25} \times 4\pi R^2 \times 10^5 \exp \left\{ \frac{\phi\, f(m,x)}{2(\ln S)^2} \right\} \qquad (21)$$

This relation has been plotted by Fletcher (<u>1</u>) and is shown in Figure 2.

For values of $m \sim 1$ and for reasonably sized particles, the supersaturation level to cause appreciable nucleation is nil. For higher values of θ, (lower values of m) higher supersaturations are required, but less than for homogeneous mechanisms. At these conditions, if S exceeds 4.2-4.5 homogeneous nucleation predominates.

*Strictly speaking $R \to 0$, $\ln R \to -\infty$ so this is a poor example. Actually Eq. 20 is not applicable to homogeneous nucleation. This will be discussed later.

ICE OR WATER NUCLEATION

For reasons not apparant at this time, the general consensus of investigators in the field is as follows:

In homogeneous nucleation, the nuclei first appears as water but change to ice if the ambient temperature is below freezing. This seems to hold down to 420°R. At temperatures below 386°R, ice particles appear preferentially. These facts are disputed by Courtney. Mason (5) and Schaefer (12) discuss these points.

For heterogeneous nucleation, ice particles may form initially if the crystal structure of the foreign material is such as to promote it. In many cases, the behavior is similar to that for homogeneous nucleation.

REFERENCES

1. "Size Effect in Heterogeneous Nucleation," N. H. Fletcher, J. Chem. Phys., 29, 572 (1958).

2. Turnbull, D. and Vonnegut, B., Ind. Eng. Chem. 44, 1292 (1952).

3. "Ice Crystal Nucleation by Aerosol Particles," N. H. Fletcher, "The Physical Chemistry of Aerosols," Gen Disc of the Fairday Soc., 1960. p 39.

4. "Nucleation Processes," W. J. Dunning, Ibid, p. 9.

5. "Nucleation of Water Aerosols," B. J. Mason, Ibid, p. 20.

6. "The Physics of Clouds," B. J. Mason, Oxford, The Clarendon Press, 1957.

7. "Distribution in the Atmosphere of Certain Particles Capable of Serving as Condensed Nuclei", H. B. Byers, J. R. Sievers, and B. Tufts, "Artificial Stimulation of Rain," Proc. Conf. Physics and Cloud Precipitation Particles, Woods Hole, Mass., 1955, p. 47.

8. "Recent Measurements of the Vertical Distributions of Aitken Nuclei," H. Weickmann, Ibid, p. 81.

9. "The Role of Adsorption in Water Condensation," S. J. Bustein, Ibid, p. 145.

10. "Studies of the Effects of Certain Chemicals on the Inhibition of Nucleation," S. J. Bustein, Ibid, p. 376.

11. "Liquid and Crystal Nucleations," G. M. Pound, Ind. Eng. Chem. 44, 1278 (1952).

12. "Formation of Ice Crystals in Ordinary and Nuclei-Free Air," V. J. Schaefer, Ind. Eng. Chem. 44, 1300 (1952).

13. "The Possibility of Surface Activation and Passivation of Nuclei in Water Vapor Condensation," G. I. Izmailova, P. S. Prokhorov, and B. V. Peryagen, Call. J. (U.S.S.R.) 19, 557-611 (1957).

14. Willmerth and Nagamatsu, J. App. Phys. 23, 1089 (1952).

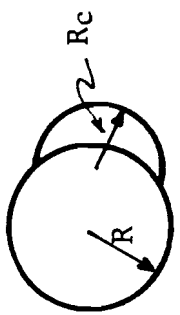

From
N.H. Fletcher
J. Chem. Phys.
29, 572 (1958)

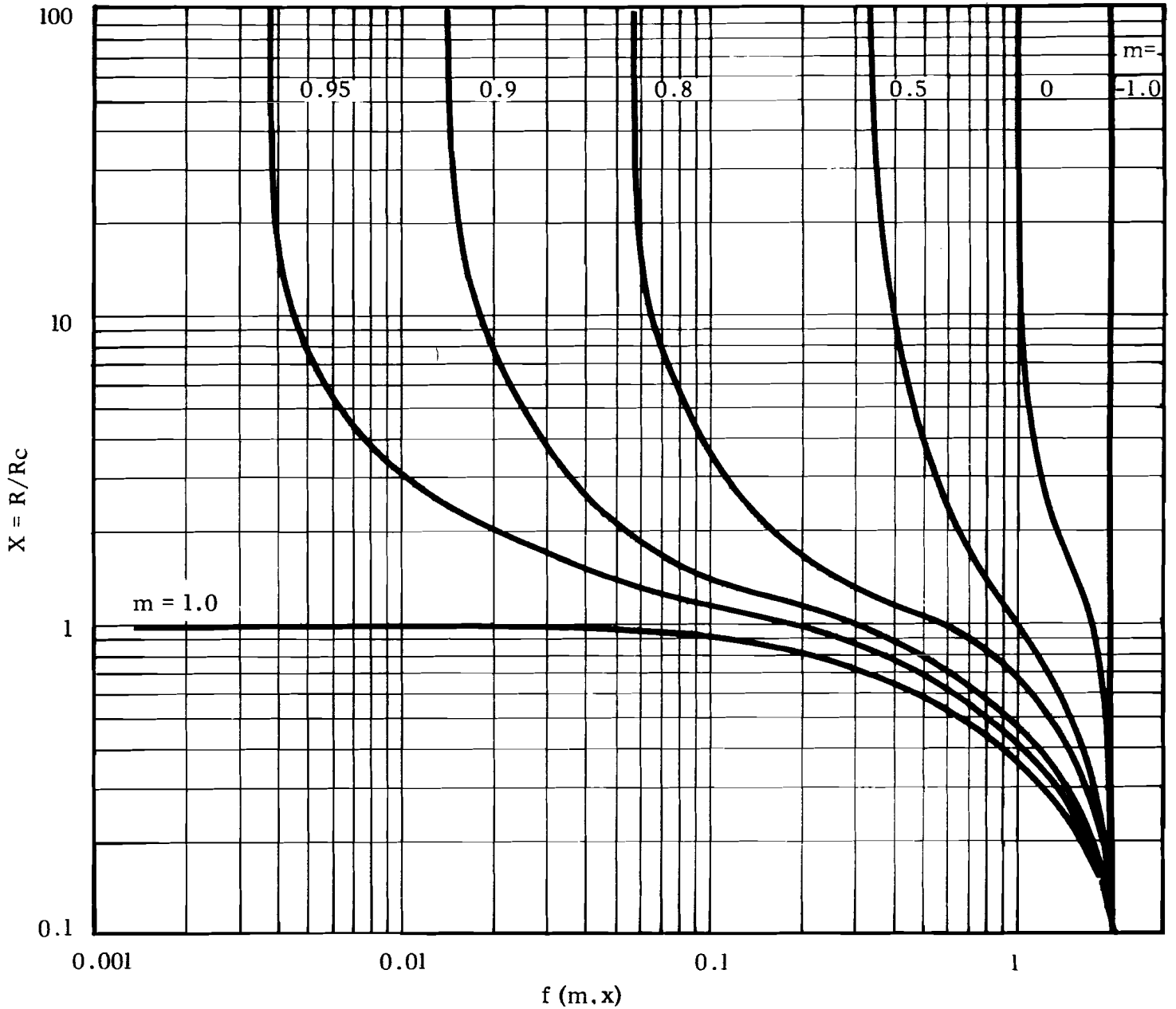

FIGURE 1

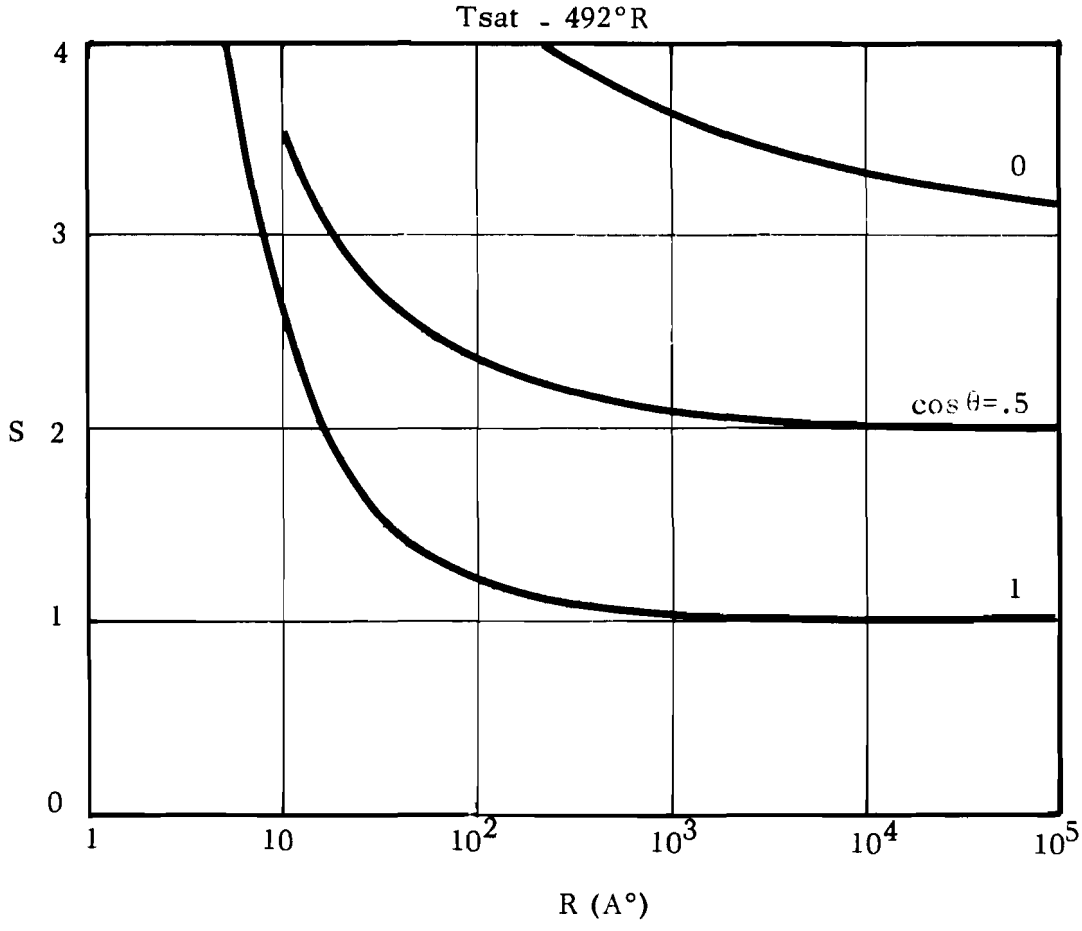

FIGURE 2 SATURATION RATIO (S) AS A FUNCTION OF RADIUS OF FOREIGN NUCLEATING PARTICLE (R) AND CONTACT ANGLE (θ)

APPENDIX 4

LIQUID NITROGEN INJECTION

TABLE OF CONTENTS

SUMMARY

Injection of liquid nitrogen drops into a moving, warm, humid air stream is analyzed to allow a prediction of the rate of drop vaporization and temperature drop of the air. The principal variables considered are inlet water concentration, ratio of injected liquid nitrogen stream-to-air stream, drop diameter, and inlet air temperature. The results are plotted in generalized curves and specific examples shown in detail. The results are useful to predict the relative rates of ice nuclei formations relative to nuclei growth to allow an estimation of the particle size of the ice particles frozen out by such a process.

The injection of liquid nitrogen into an air stream results in a rapid chilling of the air and encourages the condensation or solidification of contaminants if the dew point of the contaminant is reached. An analytical study of the problem of how rapidly does the air cool is conveniently resolved into energy and material balances and rates of heat transfer, the latter being important since the rate of air cooling is controlled by the rate of heat transfer to the liquid nitrogen. The results of any such analyses are then a prediction of the evaporation rate and temperature drop of the air as a function of time.

ENERGY AND MATERIAL BALANCES

A basis of one lb of air is chosen. To this air, ψ lbs of liquid nitrogen are added. It is assumed that no flashing occurs during the spray operation. Should there be flashing, the analyses to follow are not affected since we make the reasonable assumption that the mixing of gas streams occurs rapidly compared to vaporization. For example, if during flashing, 50% of the liquids were to be vaporized, we can mix this vapor with the inlet air stream to determine the effective gas inlet temperature, and this mixture then becomes the basis upon which the 1 lb of air is chosen; the unvaporized liquid nitrogen then becomes the ψ lbs.

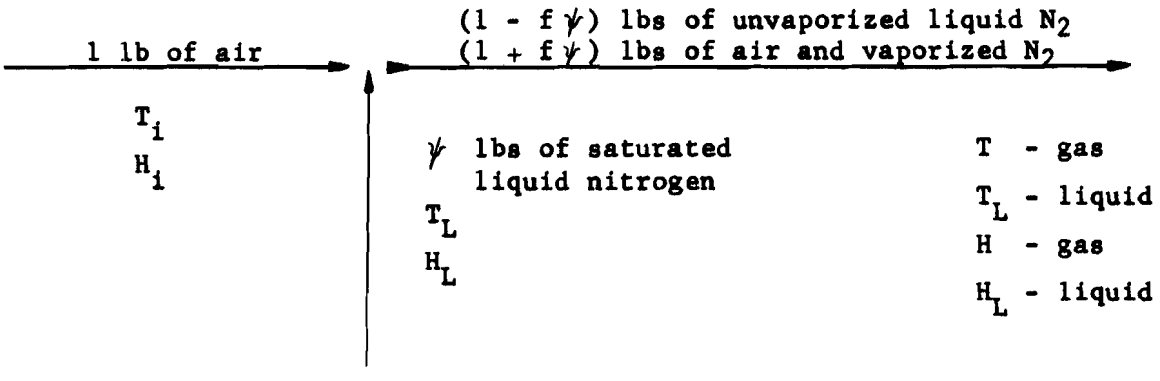

The liquid nitrogen is assumed to enter as a spray of small droplets with a narrow distribution of sizes and with an initial diameter D_o. There are N_D drops associated with the ψ lbs of liquid nitrogen. N_D, D_o and ψ are related as:

$$(4/3)\pi(D_o/2)^3 N_D \rho_L = \psi \qquad (1)$$

where ρ_L = liquid nitrogen density.

Energy Balance

In: $\psi H_L + H_i$

Out: $H + \psi f H + (1 - f) H_L \psi$

where f = fraction of liquid nitrogen vaporized by heat transfer from the air (not by flashing).

Assuming steady state, negligible heat transfer to walls, and that the properties of the vaporized nitrogen are identical to the air, and finally that the vaporized nitrogen mixes instantaneously with the air to give some final average temperature T and enthalpy H, then:

In = Out

or

$$H_i + f \psi H_L = H(1 + f \psi) \qquad (2)$$

RATES OF HEAT TRANSFER

When the drops of liquid nitrogen are injected into the moving air stream, they tend to accelerate rapidly to the main stream velocity; the smaller the drop, the more rapid the acceleration. The controlling factor in the rate of heat transfer is undoubtedly the energy transfer through the boundary layer of relatively stagnant air surrounding the drop. For small drops, the gas phase heat transfer coefficient h is estimated as

$$\frac{hD}{k} = 2\left[1 + \left(\frac{Dv\rho}{\mu}\right)^{0.5} \times 0.276\right] \qquad (3)$$

where the Prandtl number is assumed to be near unity.

k = thermal conductivity of the gas in the boundary layer.
μ = viscosity of the gas in the boundary layer.
ρ = density of the gas in the boundary layer.
D = drop diameter.
v = relative velocity between drop and air.

Immediately upon injection, the group (hD/k) will be a maximum; the relative drop velocity and drop diameter both decrease to yield the limit of $hD/k \rightarrow 2$ when the drop is moving essentially at stream velocity. To show the importance of the bracketed term, the table below lists hD/2k for various values of D and v.

	D (microns)		
v = 1 ft/sec	1	10	100
hD/2k	1.15	1.47	2.5
v = 10 ft/sec			
hD/2k	1.47	2.5	5.7

For purposes of the analyses to follow, let

$$hD/2k = \beta \tag{4}$$

where $\beta > 1$ but rapidly decreases and approaches 1 as a limit.

COMBINATION OF THE ENERGY BALANCE AND HEAT TRANSFER RATES

In a time $d\theta$ the heat transferred dQ evaporates a mass fraction df of the original drop mass $(\pi D_o^3/6)\rho_L$, i.e.,

$$dQ = \frac{\pi D_o^3}{6} \rho_L N_D \Delta H_v \, df = h N_D 4 \pi (D/2)^2 (T - T_L) \, d\theta \tag{5}$$

where all the terms except ΔH_v, T, T_L and D have been defined previously and

ΔH_v = heat of evaporation of liquid nitrogen
T = gas temperature
T_L = liquid nitrogen temperature
D = drop diameter.

The fraction evaporated f is related to D as,

$$f = 1 - (D/D_o)^3 \tag{6}$$

so

$$df = -\frac{3D^2}{D_o^3}\, dD \tag{7}$$

Inserting (7) into (5) and using (4) to determine h,

$$\frac{DdD}{d\theta} = -\frac{4\beta k\,(T - T_L)}{\rho_L\, \Delta H_v} \tag{8}$$

Equation (8) may be non-dimensionalized conveniently by defining

$$D^* = D/D_o$$

$$\theta^* = \theta/\theta_o \quad (\text{where } \theta_o \equiv (\text{sec}))$$

$$T^* = (T - T_L)\Big/(T_i - T_L)$$

to give

$$-D^*\, dD^* = \eta\, \Delta T^*\, d\theta^* \tag{9}$$

where

$$\eta = \frac{4k\beta\theta_o\,(T_i - T_L)}{\rho_L\, \Delta H_v\, D_o^2} \quad (\text{dimensionless}) \tag{9a}$$

Take enthalpy base as $H_L = 0$.

Assume that the gas enthalpy is a linear function of temperature,

$$H = C_p T + b$$

$$H_i = C_p T_i + b$$

Equation (2) then becomes

$$b + C_p T_i = (C_p T + b)(1 + f\psi)$$

$$T = \frac{b + C_p T_i - b - bf\psi}{(1 + f\psi)\, C_p} = \frac{C_p T_i - bf\psi}{(1 + f\psi)\, C_p} \tag{10}$$

subtract T_L and divide by $T_i - T_L$

$$T^* = \frac{T - T_L}{T_i - T_L} = \frac{C_p T_i - bf\psi}{C_p (T_i - T_L)(1 + f\psi)} - \frac{T_L}{(T_i - T_L)}$$

$$= C_p T_i - \frac{bf\psi - C_p T_L - C_p T_L f}{C_p (T_i - T_L)(1 + f\psi)} \qquad (11)$$

$$T^* = \frac{1}{1 + f\psi} - \frac{f\psi (b + C_p T_L)}{C_p (T_i - T_L)(1 + f\psi)}$$

Substituting Equation (11) into (9) yields

$$- \frac{(1 + f\psi) D^* dD^*}{(1 - f\psi)\left[\frac{C_p T_L + b}{C_p (T_i - T_L)}\right]} = \eta \, d\theta^* \qquad (12)$$

where from Equation (6), $f = 1 - D^{*3}$.

Equation (12) contains two variables, D^* and θ^*, and a relation between them may be obtained once ψ, C_p, b and η are specified.

TYPICAL VALUES OF ψ, C_p, b AND η

ψ

From Equation (10)

$$\psi = \frac{(T_i - T)}{f(T - b/C_p)} \qquad (13)$$

To determine a range of expected values of ψ, consider the case where the drop is essentially vaporized completely, i.e., $f \sim 1$. Also for purposes of discussion, let $T_i \sim 520^\circ R$ (obviously larger values of T_i would lead to larger values of ψ and visa-versa; the calculated value of ψ is, however, not particularly sensitive to reasonable perturbations in T_i). We consider also that the system pressure is about 100 psia and ask what values ψ will reduce the equilibrium concentration of water vapor to 1/10, 1/100 and 1/1000 of the original value.

Inlet Wt. % water	Value of ψ (lbs Liq. N_2/lb air) to reduce inlet water concentration by -		
	1/10	1/100	1/1000
0.100	0.11	0.19	0.165
0.050	0.13	0.21	0.285
0.025	0.155	0.235	0.31
0.010	0.19	0.27	0.335

If these values of pressure and inlet water concentration are realistic, then values of $\psi \sim 0.15$ to 0.35 must be considered.

C_p, b

The heat capacity of air (or nitrogen) vapor in the temperature and pressure range of interest here is about 0.25 Btu/lb-^oR.

The value of b for air (or nitrogen) vapor with a base of H (sat. liq., 100 psia) = 0 is about 32.2 Btu/lb.

η

The parameter η is defined by Equation (9a). None of the terms except D_o may be varied widely.

$\underline{k}$ is the thermal conductivity of nitrogen gas in the boundary layer around the evaporating drop. If one chooses the arithmetic average temperature to be the film temperature, then

$$\underline{k} = \frac{k_t + k_{177^oR}}{2} \sim 0.011 \text{ Btu/hr-ft}^2\text{-}^oR/\text{ft};$$

β is defined in Equation (4) and ranges upwards from one;

θ_o is defined as 1 sec;

$(T_i - T_L)$ depends upon the inlet temperature; a value of $T_i \sim 520^oR$ is reasonable, so $(T_i - T_L) \sim (520\text{-}177) = 343^oR$;

ρ_L is the density of liquid nitrogen, = 44 lbs/ft^3;

ΔH_v is the latent heat of vaporization of the liquid nitrogen, = 71 Btu/lb;

D_o is the original drop diameter, ft; a more convenient unit is the micron, 10^{-4} cm.

$$\text{thus, } \eta = \frac{\beta}{D_o^2} \times \frac{4\, k\, \theta_o (T_i - T_L)}{\rho_L\, \Delta H_v}$$

$$= \frac{\beta}{D_o^2} \times 4 \times 0.011 \times \frac{1}{3600} \times \frac{343}{44} \times \frac{1}{71} \times \frac{1}{(3.3)^2 \times 10^{-12}}$$

where D_o is in microns

$$= 1.3 \times 10^5 \frac{\beta}{D_o^2} \qquad (14)$$

FINAL RESULTS

Equation (12) has been integrated numerically for three values of ψ, and the results are shown in Figure 1. Using the same figures, Equation (11) allows one to determine ΔT^*, the fractional decrease in temperature, to be determined as a function of D^*. These results are shown on Figure 2. From the values of $\eta\theta^*$ in Figure 1, the value of D^* for various times may be determined using η from Equation (14). These curves are shown in Figure 3. Figure 3 allows for different values of D_o, ψ and β by simple ratios, e.g., suppose one wished to determine the time required to decrease the initial drop diameter by 20% using $\psi = 0.35$ and with an estimate of $\beta = 2$; the original drop diameter is 20 μ. From Figure 3 at $D_o = 100\,\mu$, $\beta = 1$, $\psi = 0.35$, $\theta = 1.4 \times 10^4$ microseconds. To change to $\beta = 2$, $D_o = 20$, then

$$\theta = 1.4 \times 10^4 \times \frac{(20)^2}{(100)^2} \times \frac{1}{2} = 1.4 \times 10^4 \times 2 \times 10^{-2}$$

$$= 2.8 \times 10^2 \text{ microseconds.}$$

For this same value of $D^* = 0.8$, $\Delta T^* = 0.72$ and

$$T = 0.72\,(T_i - T_L) + T_L = 0.72\,(520 - 177) + 177$$

$$= 247 + 177 = 424^\circ R.$$

Thus the temperature has dropped from 520°R to 424°R in about 280 microseconds.

Another example is worked out and shown in Figure 4 for the case of $\beta = 1$, $D_o = 100\,\mu$, $T_i = 520^\circ R$, $\psi = 0.25$, P = 100 psia and shows the fraction

vaporized and temperature as a function of time. The rates of freeze-out depend upon the supersaturation. In the case demonstrated in Figure 4, the supersaturation ratio is plotted as a function of time in Figure 5. Two inlet water concentrations are shown, one corresponding to inlet gas being saturated at 520°R (0.25 wt %) and another where the inlet gas is still at 520°R but with a dew point of 462°R (0.02 wt % H_2O).

These results show the best calculated values of the effect of liquid nitrogen addition to a humid air stream. The decrease in air temperature and increase in supersaturation ratio affect the rates of nucleation and growth, and this is discussed further in the next section.

HOMOGENEOUS NUCLEATION IN A HUMID AIR STREAM AFTER LIQUID NITROGEN INJECTION

The problem of estimating an average particle size of water ice particles after injection of liquid nitrogen is an extremely complex one. We discussed the general problem in Appendix No. 2, Eq. 44 and Eq. 48 for isothermal cases; in this instance the temperature is changing rapidly with time, and without considerable additional work, only approximate answers are possible.

An engineering approach to the problem makes use of the temperature-time relations developed above along with computer solutions of Eq. 48 Appendix 2. We consider first two extreme cases and then discuss briefly the ill-defined middle region.

Very Small Diameter Spray

Consider sprays in the range of 10 microns original diameter. Figures 2 and 3 indicate that the temperature drop of the air is extremely rapid and all vaporization is essentially completed in some 500 microseconds. Typically an inlet humid air stream might have a water content such as to give a dew point near 462°R, i.e., the partial pressure of water is about 0.02 psia. The inlet air temperature is 520°R, the liquid nitrogen saturated at 100 psia (177°R), and ψ (the lbs of liquid nitrogen/lb inlet air) about 0.25 (Choices of somewhat different inlet temperatures and humidities and ψ's will not affect the conclusions developed below). Referring to Figures 2 and 3, the following table is developed.

$D^* = D/D_o$	$\Delta T^* = (T-T_L)/(T_i-T_L)$	T, °R	θ(microseconds)	S
1	1	520	0	< 1
0.9	0.89	480	78	< 1
0.8	0.79	449	155	2
0.7	0.73	427	230	6.7
0.66	0.71	420	280	10
0.6	0.69	413	300	15
0.5	0.66	403	370	31
0.4	0.64	397	430	50

From the examples in Appendix No. 2, a "rapid" rate of homogeneous nucleation is achieved at $\sim 420^{o}R$, where S = 10. This rapid rate corresponds to about 10^5 nuclei formed per cc-sec. Radial growth rates at this value of S and T were shown to be about 0.22 microns/microsecond so that any real growth is almost non-existent in the short time interval possible in the realm of $420^{o}R$. The table shows that within 20 microseconds after S = 10, the temperature has dropped from $420^{o}R$ to $413^{o}R$ and S increased to 15. This corresponds to the almost unbelievable increase in nucleation rate from 10^5 to 10^9; obviously most of the water comes out as sub-micron particles.

Large Diameter Spray

Next consider a large diameter spray but under conditions as described above; as before we can make the following table.

$D^* = D/D_o$	$\Delta T^* = (T-T_L)/(T_i-T_L)$	T, ^{o}R	θ(seconds)	S
1	1	520	0	< 1
0.9	0.89	480	0.78	< 1
0.8	0.79	449	0.155	2
0.7	0.73	427	2.3	6.7
0.66	0.71	420	2.8	10
0.6	0.69	413	3.0	15
0.5	0.66	403	3.7	31
0.4	0.64	397	4.3	50

As before, nucleation becomes rapid (10^5 nuclei/cc-sec) at $420^{o}R$, S = 10, but the time scale is 10^4 longer than for the D_o = 10 micron case. Courtney's calculations indicate that for these conditions (i.e., some 0.1 sec in the S = 10-12 range), the particles nucleated may grow in radius to 10-20 microns, and such growth will prevent any important rise in the nucleation rate; in fact a decrease will usually result. The best estimate is that near S = 10, a large number of nuclei form and subsequent growth is important, S decreasing to about unity in 0.2 seconds with most particles in the 20-40 micron (radius) range.

Intermediate Range Spray

For sprays in the intermediate range, around 100 micron drops, a similar table could be prepared with the time scale 10^{-2} x the 1000 micron spray scale. It is in this range that both nucleation and growth are important. Very approximate estimates indicate that nucleation is probably the more important, and the radius of the particles would probably be in the micron range, i.e., 0.5 to 5. It is just such a range that is difficult to separate by standard centrifugal separators.

None of the calculations take the particle-particle agglomeration processes which will operate to give a distribution of larger particle sizes.

C_p = 0.25 Btu/lb - °R

b = 32.3 Btu/lb

$(T_i - T_L)$ = 343°R

T_L = 177°R = Sat at 100 psia

$\Psi = \frac{\text{lb } N_2 \text{ (Liq)}}{\text{lb air}}$

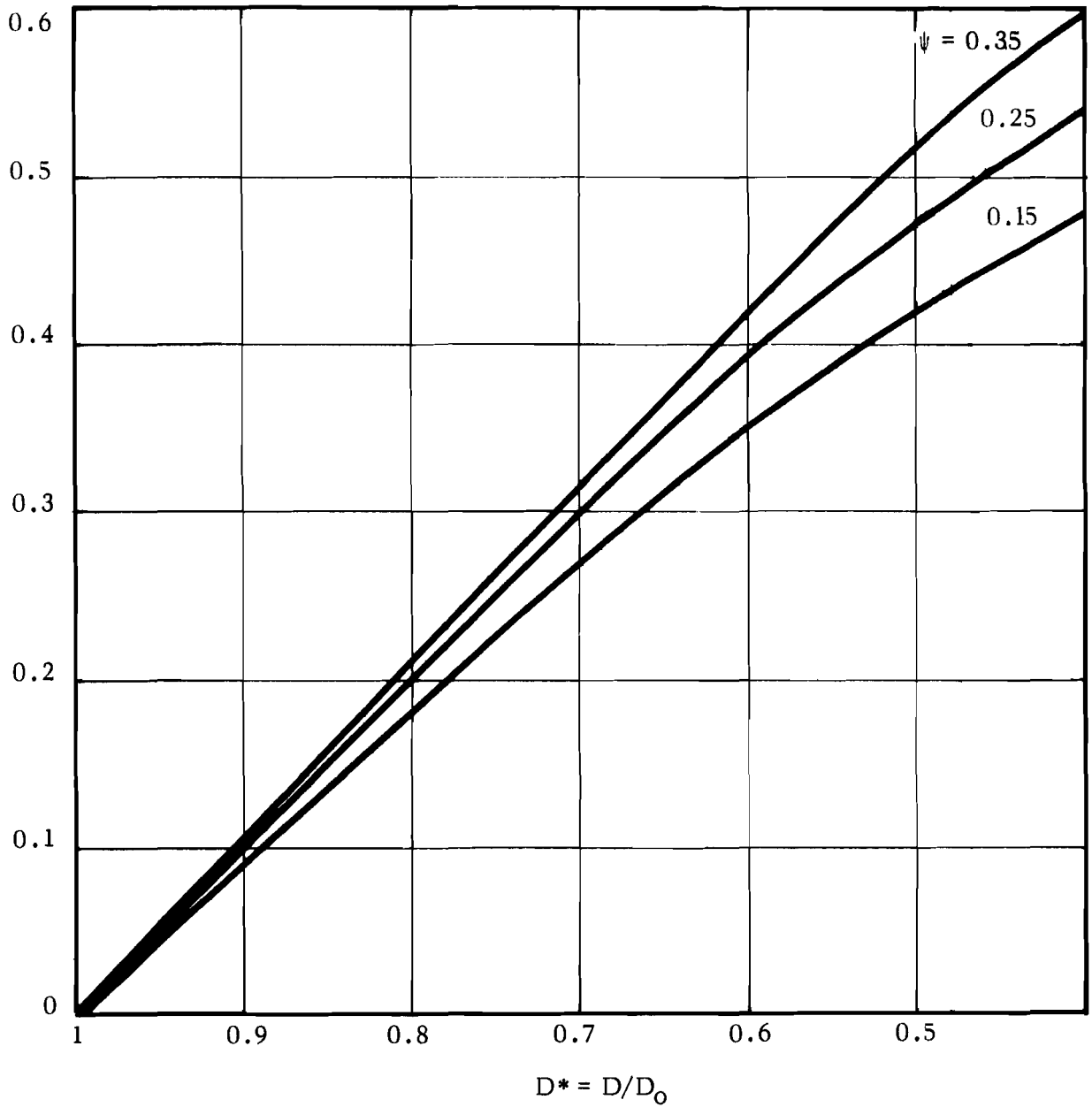

FIGURE 1 SOLUTION OF EQUATION (12)

$$\Psi = \frac{\text{lb of liquid nitrogen}}{\text{lb of Inlet Air}}$$

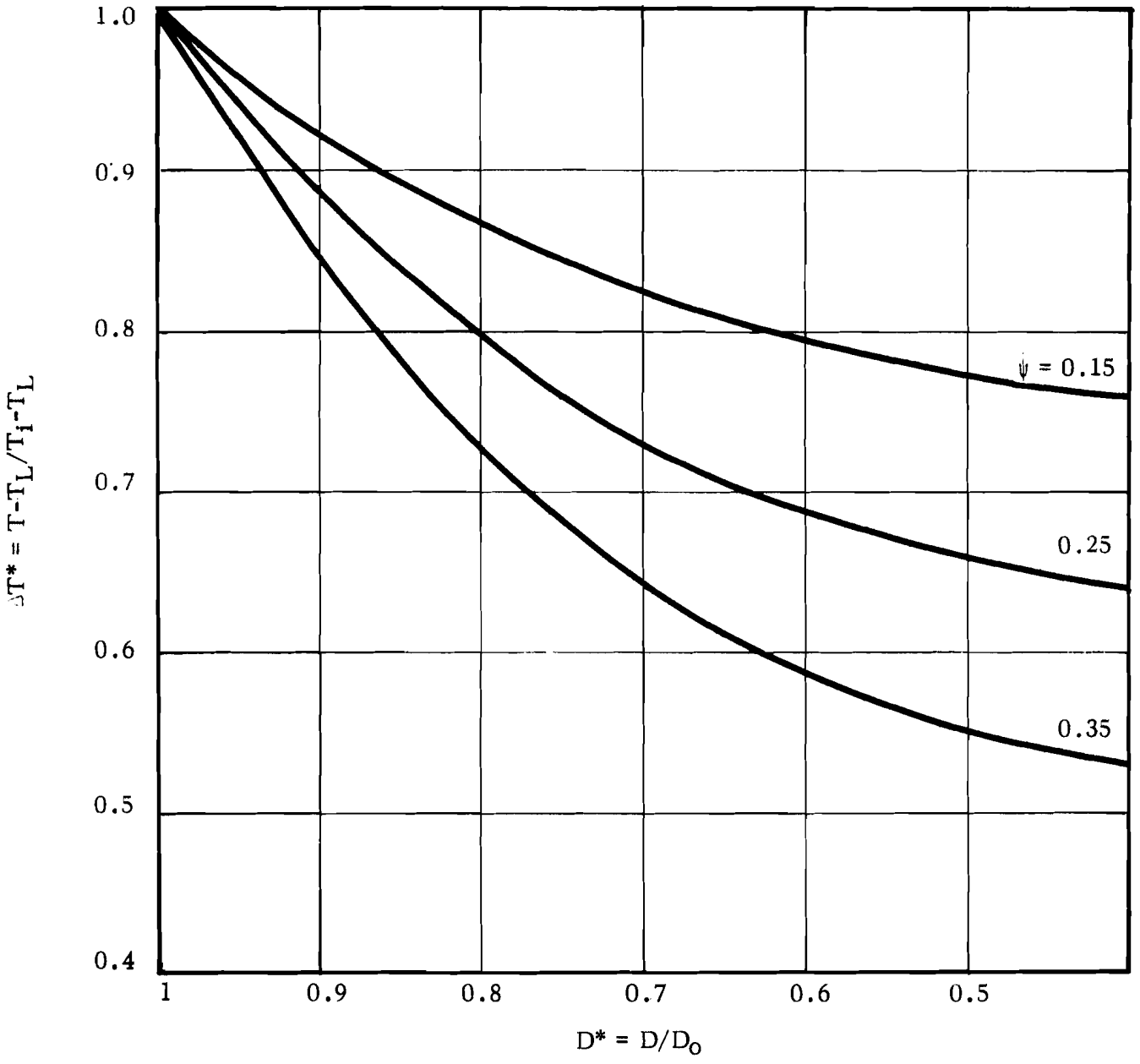

FIGURE 2 AIR TEMPERATURE DROP AS A FUNCTION OF THE DROP DIAMETER

Notes:

D_o = 100 μ, β = 1

1. For any other value of D_o, multiply plotted time by $(D_o/100)^2$
2. For any other value of β multiply plotted time by 1/β

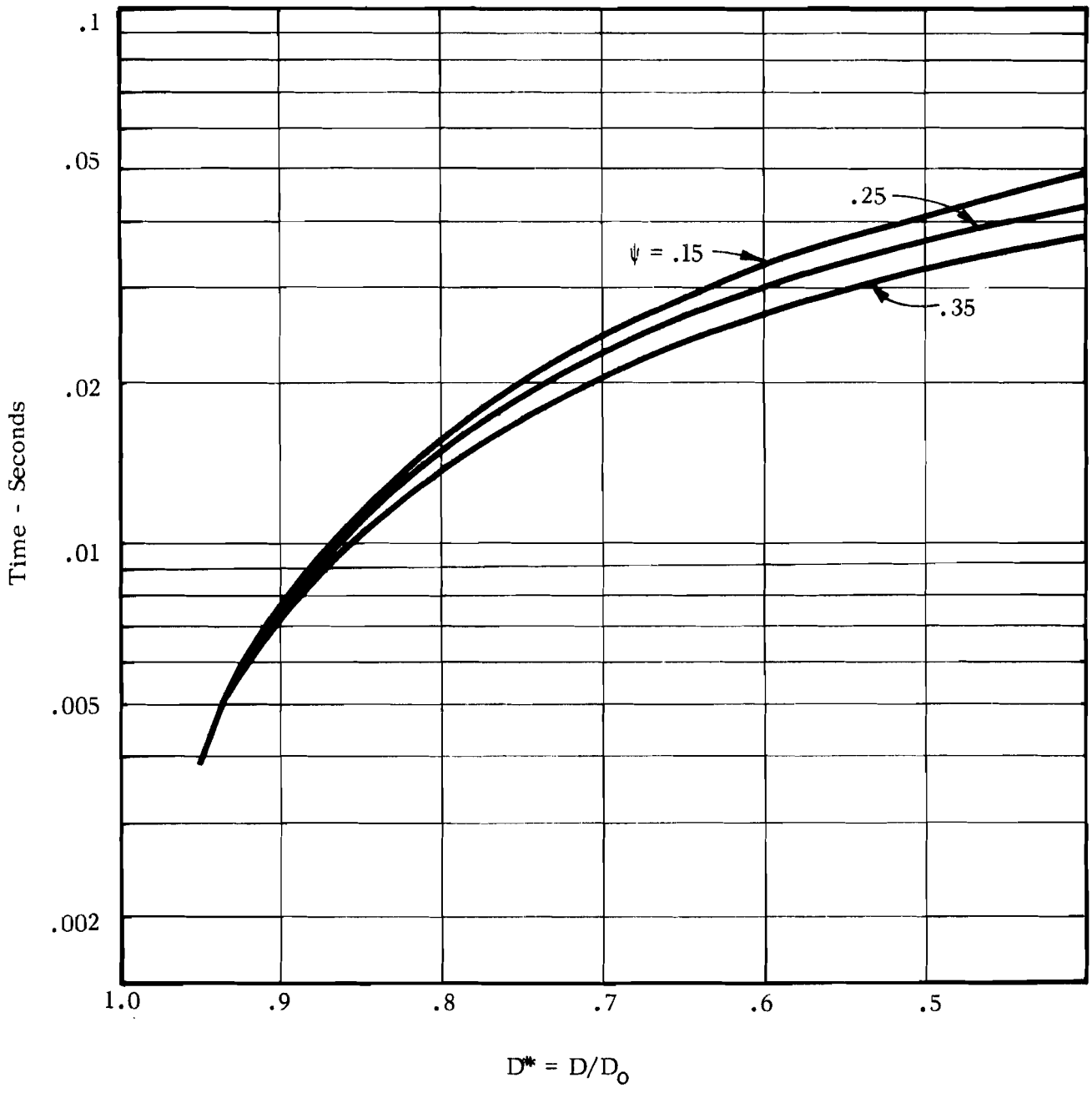

FIGURE 3 RATE OF DROP VAPORIZATION

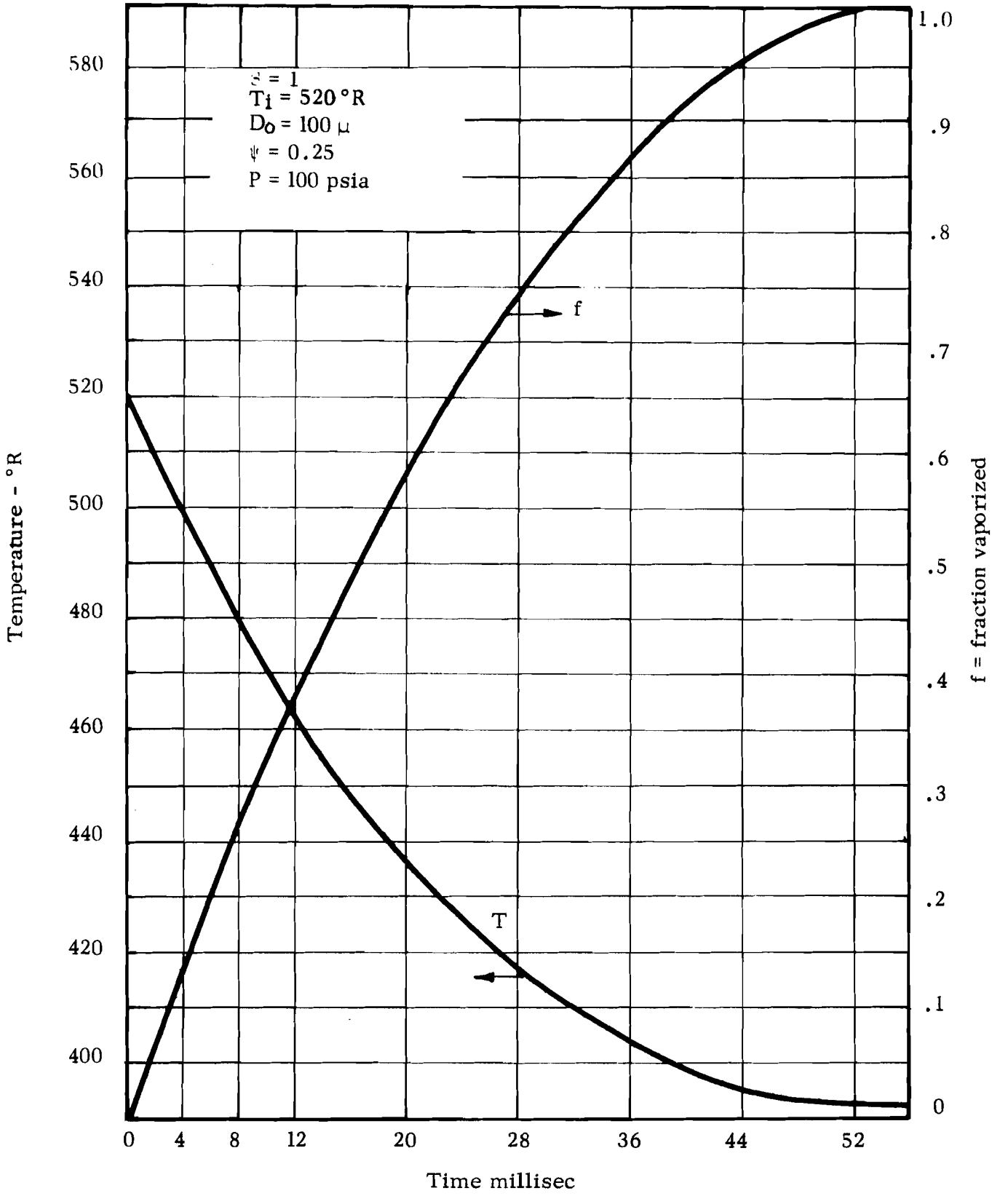

FIGURE 4 RATE OF TEMPERATURE DROP AND VAPORIZATION

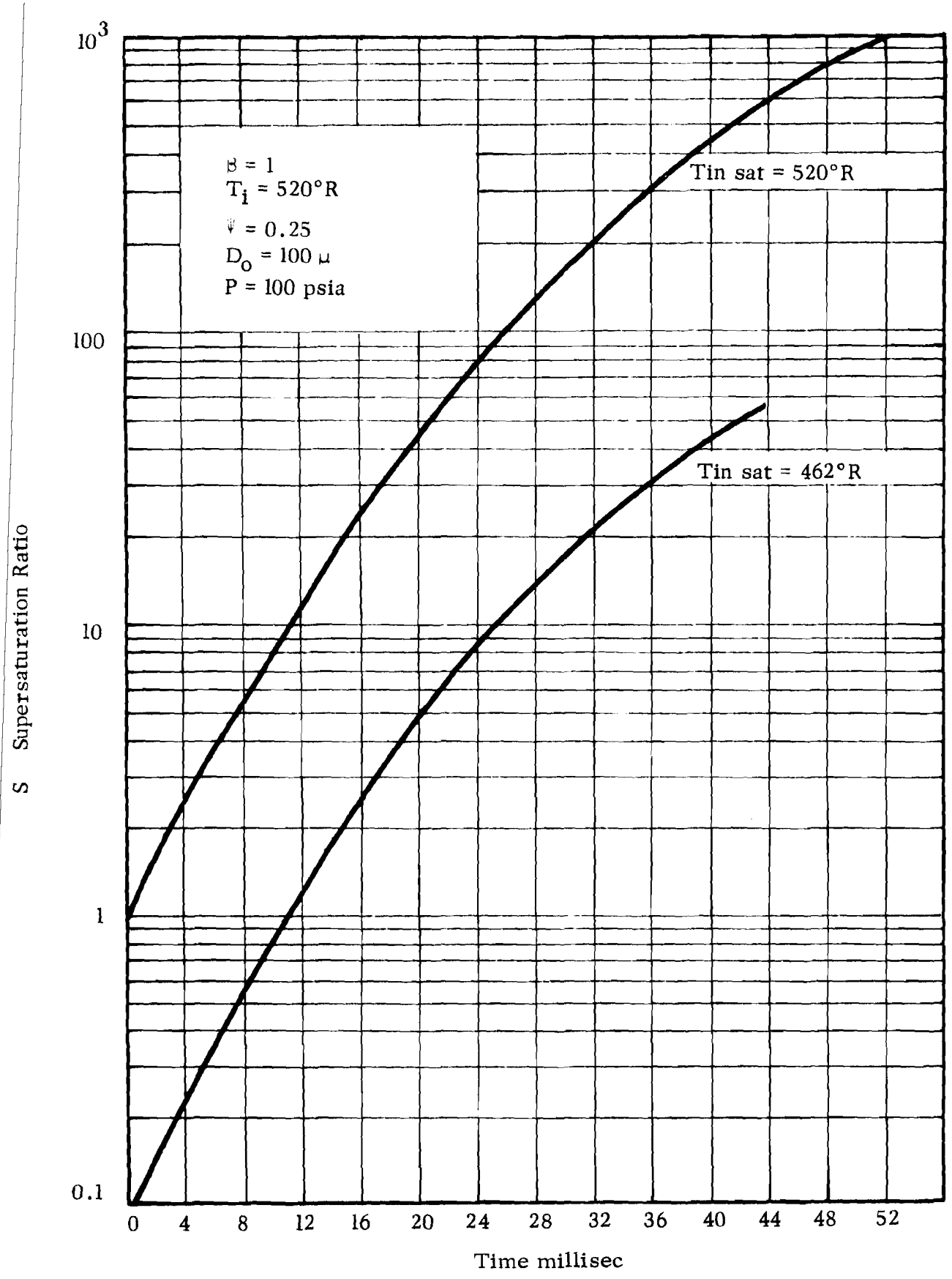

FIGURE 5 SUPERSATURATION RATIO AS A FUNCTION OF TIME

APPENDIX 5

SURFACE EFFECTS IN FROSTING MECHANISMS

TABLE OF CONTENTS

A. SELECTED REFERENCES

1. Effect of Surfaces on the Adherence of Ice and Frost

Thomas Brunner
Z. Angew Mathematik u. Physik 3; 460-466 15 Nov. 1952
(Text in German with English Summary)
Tables, graphs, diagrs., 5 refs.

SOME OBSERVATIONS ON THE ADHESION OF ICE TO SURFACES

The adhesion of ice to clean, oxidized, and commercial metals and to surfaces covered with silicone grease, paraffin, artificial resin, and ski wax was studied by means of a statistical shearing experiment. Distilled water was frozen on metal blocks at 485°R which were submitted to a tensile load exerted by means of a spring balance. The mean adhesion of ice to the mechanically treated surface is 8.7 kg/sq cm on the basis of 324 samples tested under similar conditions. The apparent shearing strength of ice is found to behave in approximately the same proportions. The effect is attributed to a reduction in the true surface of the sample as a result of the film covering.

Wm. C. Geer, Merit Scott
NACA Tech. Note 345 July 1930
23 p., illus., diagrs., 4 refs.

THE PREVENTION OF THE ICE HAZARD ON AIRPLANES

The formation and adhesion of ice on small airfoils were observed in a wind tunnel. The ice becomes cloudy and more snowy with decreasing temperatures, the hardness does not decrease appreciably, and the adhesion to any given surface increases. Possible means of preventing ice include the use of exhaust engine heat, application of substances which lower the freezing point of water, substances which lower the interfacial adhesion tension, lubricants, and the ice-removing overshoe. Experiments and results obtained with various substances are described. Varnishes containing calcium stearate and calcium oleate gave the best results. Rubber overshoes containing one or more expansion tubes are effective in removing ice from wings, struts, wires, and other parts.

General Electric Co.
Rept. 5539, "Basic Icing Res. by Gen. Elec. Co. for Fiscal Year 1946"
p. 149-91, Ed. by R. D. Bowers, Jan. 1947
by Robert Smith-Johannsen
10 refs.

THE EFFECT OF IMPURITIES IN WATER ON ICE ADHESION

Impurities in water reduce the adhesion of ice formed from it as compared to the adhesion of ice from distilled water. This reduction was noted on both hydrophilic and hydrophobic surfaces. A 0.001 M. $Th(NO_3)_4$ reduced adhesion 97% on Al. The rate of freezing at the interface influences the resultant adhesion of the ice. Small grains develop under quick freezing and large grains under slow freezing. The log of the ice adhesion varies inversely with the concentration of the solute. Tests with surface coating materials to which ice has very low adhesion and which show good resistance to weathering are described. The reduction in adhesion is an adsorption phenomenon. Experiments with numerous salts in various lacquer materials show that the salts most effective as impurities are also most effective when incorporated in a lacquer film. The degree of hygroscopy of the salt influences the behavior of the coating material.

Interchemical Corp.
Complete Final Report, Proj. No. 1212-321 23 Feb. 1954
by C. J. Rolle, John J. Godfrey and others.

FORMULATION OF COATING MATERIALS WITH OPTIMUM DE-ICING OR ANTI-ICING PROPERTIES

Describes apparatus and technique for measuring ice adhesion to coated panels in which ice is frozen to the sample surface in a cylindrical holder and torque applied until separation occurs. A wide variety of lacquer compositions were formulated and tested. Formulae are given. A lacquer exhibiting very low adhesion to ice is recommended.

Mass. Inst. of Tech., De-Icing Res. Lab.
Rept. #1 to Nat'l Academy of Sci. 23 Feb. 1940

AN INVESTIGATION OF METHODS FOR THE DE-ICING OF AIRCRAFT

The methods and apparatus developed for measuring the adhesion of ice to different materials are described. Data on the adhesion of ice to brass at different temperatures are tabulated and compared with the results of earlier investigations. Similar data are given for Al, Fe, and Lucite. Results are given for brass coated with different materials. The least adhesion was obtained with Bakelite lacquer. The adhesive forces appear to be of chemical nature rather than physical. De-icing of airplane antennas and windshields is discussed. The use of deflectors to prevent windshield icing is suggested.

Mass. Inst. of Tech., De-Icing Res. Lab.
Final Report to USAAF 30 June 1943
47 p., illus., diagr., tables, photos

AN INVESTIGATION OF METHODS FOR THE DE-ICING OF AIRCRAFT

A number of coatings were tested on a model propeller operating in a cold room with a water spray. None gave protection against ice for more than a few minutes. Tests of a propeller with the leading edge shingled with rubber strips (Shere-Khan) were more successful. The use of water-repellent coatings to prevent run-back ice appears promising. Anti-fogging preparations for windshields were tested. All provided temporary protection. Preliminary tests of a mechanical scraper for ice removal on windshields appeared promising. Different designs of air rams intended to remove water droplets from the air have been worked out and an instrument to measure their efficiency has been built and calibrated. Electrical heating systems for the protection of antennae and antennae masts were evaluated.

Nat'l Security Indust. Assoc.
Prog. Rept. #1 20 May 1950
19 p., 5 refs.

NSIA ICE-PHOBIC COATING TASK COMMITTEE

A research program was initiated for the development of a paint of low ice adhesion to be applied to ships and aircraft. A review of available data on the subject is presented for submission to the NSIA Ice-Phobic Coatings Task Committee Meeting on 2 June 1950. Previous investigations included the testing of f.p. depressants, coatings of low ice adhesion, thermal methods, and mechanical means. Industrially tested coatings recommended for further investigations include silicones and glass beads, hydrophobic plastics such as polyethylene and Teflon, and a wax-like compound, Antice. A list of 28 abstracts of patents and a bibliography consisting of approximately 100 entires of published journal articles, patents, and reports are included.

W. L. Sibbitt, W. E. Fontaine, J. P. Dotson
Refrig. Eng. 62, #12; 49-51, 92, 94 Dec. 1954
Graphs, diagrs.

ICE FORMATION ON METAL SURFACES

The shear and tensile strengths were measured for pure ice as well as for adhesion of ice frozen to clean metal surfaces and metal surfaces coated with a variety of oils, greases, waxes and silicone compounds. The apparatus and experimental procedure are described. Most strength measurements were made at about 20°R. Experimental values of the ice strengths varied over a considerable range. The average tensile strength of ice in layers greater than 1/8 in. thick was about 105 lb/sq in which increased to 300 lb/sq in. for layers 1/64-in. thick. The tensile strength of adhesion of ice on clean metal surfaces was greater than 160 lb/sq in. which was reduced to 2-4 lb/sq in. for metals coated with effective materials such

as the silicone compounds. The shear strength of pure ice varied from 100-115 lb/sq in. depending upon the orientation of the crystal planes of the ice. The shear strength of adhesion of ice on clean metal surfaces was about 65 lb/sq in. which was reduced to 0.5-2 lb/sq in. for metals coated with effective materials. The surface coatings providing the lowest adhesion of ice also provided the maximum inhibition to ice formation.

U. of Cincinnati, App. Sci. Res. Lab.
Tech. Rept. # WADC TR 55-44 Feb. 1955
Rept. on Operational and Physical Investigations of Aircraft Environmental Protection
by Philip E. Berghausen, Robert J. Good and others
172 p., illus., tables.

FUNDAMENTAL STUDIES OF THE ADHESION OF ICE TO SOLIDS

A theory is presented by which the energy of adhesion between ice and a solid can be calculated from the heats of immersion and adsorption. The surface energy of ice at -22.2°C (451°R) is reported as 243 ergs/cm.^{2}. The energy of adhesion of ice has been measured for six solids, and ranges from 209 ergs/cm.^{2} for Graphon to 768 ergs/cm.^{2} for barium sulphate. It is concluded that only coatings in which the surface atoms are bound by nonpolar covalent forces will, be useful in promoting the release of ice. A flaw mechanism has an important effect on ice adhesion in practical instances.

Tamakichi Takano
Teion-kagaku 5; 21-36 1950
Illus., tables, graphs, diagrs., 1 ref. (Eng. Summary)

STUDIES ON ICE FORMATION IN A WINDTUNNEL. III DIFFERENCE OF MATERIAL

Copper, iron, brass, duralumin, wood, glass, and ebonite were used to study their effect on the nature of the ice formed. The importance of the thermal conductivity of the materials tested was noted. It was found that the amount of icing formed on metals was in the main inversely proportional to their thermal conductivities. Among non-metals, glass accumulates the largest amount of ice, ebonite the least and wood a medium amount. Clear ice forms more readily on metals than on non-metals near 492°R. Translucent ice followed by sublimation ice occurs on the leading edges near 473°R. Ice formation may be classified according to density. The density of ice deposits is readily measured by immersing samples in CCl_4. Shear strength of ice on various materials was measured. Ice formed on a glass rod had a shear strength of 1.10 kg/sq cm; ebonite, 1.62 kg/sq cm. and copper, 2.14 kg/sq cm.

Anon.
Chem. Inds. 67; 559-60 Oct. 1950
Illus.

ICEPHOBIA

The need for coatings to prevent or lessen adhesion of ice to various kinds of surfaces is pointed out. Kel-F, monochlorotrifluoroethylene, is a plastic material which has shown the best anti-icing properties. Other materials include silicone coating, Teflon, polyethylene and polystyrene. Freezing point depressants, parting compounds, adhesion depressants and nucleated surfaces also facilitate ice removal in addition to mechanical and thermal systems.

Montogomery Knight, Wm. C. Clay
NACA Tech. Note 339 May 1930
21 p., illus., table, diagrs, 12 refs.

REFRIGERATED WIND TUNNEL TESTS ON SURFACE COATINGS FOR PREVENTING ICE FORMATION

General atmospheric conditions which cause various types of ice formations on airplanes are discussed. Ice formations were artificially produced in a wind tunnel and tests were made on various surface coatings to find their effect in preventing or delaying ice formation. Water insoluble compounds used included light and heavy lubricating mineral oil, cup grease, vaseline, paraffin, and Simonize Wax. Water soluble compounds tested were glycerine, glycerine and $CaCl_2$, molasses and $CaCl_2$, hardened sugar solution, and hardened glucose solution. None of the compounds showed any appreciable preventive action with a heavy spray of cold water directed at a model airfoil surface. Results of tests with a lighter spray indicate the ineffectiveness of the insoluble compounds, while a hardened syrup solution provided good prevention for short periods of time in light spray at temperatures just below freezing.

B. Heterogeneous Nucleation

S. J. Birstein, C. A. Anderson
J. Meteorology 12; 68-73 Feb. 1955
Tables, graphs, diagrs., 24 refs.

THE MECHANISM OF ATMOSPHERIC ICE FORMATION, I: THE CHEMICAL COMPOSITION OF NUCLEATING AGENTS

The nucleating ability of a number of chemicals was studied. The nuclei were prepared in a nitrogen atmosphere rather than air in order to prevent a reaction at the hot filament with atmospheric oxygen. Numerous materials previously reported as effective nucleating agents, were found to be relatively ineffective. The results indicate that the manner of preparation of the various chemicals affects to a large degree their nucleating effectiveness.

B. J. Mason, J. **Hallett**
Nature 177; 681-683 14 April 1956
Illus., table, diagr., 9 refs.

ARTIFICIAL ICE-FORMING NUCLEI

Results of earlier investigations on nucleating ability of several substances are reviewed and criticized, and new tests on many of these substances are described. The great majority of substances reported as active by other workers failed to produce ice crystals in a supercooled cloud at temperatures above 420°R if spectroscopically pure materials were used and great care taken to exclude all traces of iodine and silver from the air in the experimental chamber.

Hans Rudolf Pruppacher, Raymund Sanger
Z. angew. Math. Phys. 6; 485-493 25 Nov. 1955
Table, diagr., 17 refs., (Text in German w/Eng. Summary)

THE MECHANICS OF FREEZING SUPERCOOLED WATER DROPS THROUGH DISPERSED NUCLEI (II)

Results of experiments on the relation between the crystallographic properties of substances and their nucleating ability are discussed in the light of existing theories. Weyl's hypothesis appears to agree best with observations. In the case of two-atomic seeding substances, one of the elements (the one on the left-hand side of the periodic system) must be much less polarizable than the partner (on the right-hand side). Another property of the seeding substances is their non-solubility in water. The forces responsible for the nucleability of substances are those which also determine the surface structure of the seeding particles and water droplets.

General Electric Co. Res. Lab.
Final Rept. to 1 July 1945 Oct. 1945
by Irving Langmuir
Cont. W 33-038-AC-9151(14006)

FINAL REPORT ON ICING RESEARCH UP TO 1 JULY 1945

A final report is given on ice research conducted by the General Electric Company. It contains a brief description of the time and rise theory, and it is suggested that this theory be extended to consider the formation of drizzle and rain. Formation of water droplets in clouds, ice crystals in clouds, and phenomena of ice deposition are considered. A brief summary is given of the results obtained with G. E. differential analyzer which involved the study of trajectories of water droplets of several sizes near cylinders, ribbons and spheres for a wide range of wind velocities. Ice deposition near the freezing point and at high air velocities, and anti-icing coatings for propellers, airfoils and skis were studied. The development of a heated mast of glasscloth and Permafil containing heated wires or covered with conducting coatings is also discussed.

REFERENCE: Bibliography of Ice and Frost Control
WADC 56-338
ASTIA AD 142317
January 1958

B. DEPOSIT ADHESION "BREADBOARD" TEST

We have conducted some qualitative "breadboard" tests of deposit adhesion. The objectives of this work were to determine if surface coatings had marked influence on deposit formation and also to determine if the deposit could be easily removed by mechanical means such as vibration, scraping, and high velocity air jets. The results of this work are summarized below.

1. Test Apparatus

For these tests, the heat transfer surfaces consisted of three coils of 1/4" O.D. tube in parallel. Each coil had an outer diameter of approximately 1 3/4" and consisted of seven turns. The spacing between adjacent turns was about 1/4". This heat transfer surface was cooled to approximately 160° R by passing liquid nitrogen through the coils from a pressurized "Loxette" type dewar. The air stream, at approximately ambient temperature, was provided by a plant air hose. During the course of deposit build-up, the air hose was directed so as to simulate cross flow conditions on the heat exchanger surfaces. A schematic of this test apparatus is shown in Figure 1.

It should be emphasized that the control and measurement of conditions was strictly qualitative. We did not provide instrumentation for the measurement of temperatures, air stream contaminant concentrations or flow velocity. The comparative rates of deposit build-up were judged by visual observation.

2. Coatings

Each of the three heat transfer coils was coated with a different surface coating. The three coatings used were as follows.

a. Enamel Spray Paint

b. Spray Teflon

c. Sodium Silicate

In addition, in some of the latter tests, silicone oil was applied over portions of the coil surface.

3. Results

a. None of the three basic coatings (i.e., spray enamel, teflon or sodium silicate) seemed to have much effect on deposit formation.

b. Silicone oil did seem to inhibit the initial formation of deposit. With silicone oil, as with other test work, the initial formation of deposits occurred as scattered tufts on the heat transfer surface. However, after these tufts or islands achieved coverage of the surface, deposit formation seemed to proceed at about the usual rate.

c. The deposit which formed appeared to be easily removeable by mechanical means. It was possible to shake loose some of the deposit by tapping the tube. It was quite easy to blow away the deposit by directing a high velocity jet of air on the tube. It was also possible to remove the deposit with a brush.

d. As a matter of interest, it was noted that the spray teflon tended to crack when the heat transfer coils were cooled down.

4. Tentative Conclusions

Although the tests were not conducted under conditions closely simulating those in the heat exchangers, we feel it is possible to draw two tentative conclusions from the results.

a. Surface coatings are not particulary effective in reducing deposit formation.

b. The deposit formation appears to be a fairly porous, weak structure which may be easily removed by mechanical techniques. Methods such as vibration, scraping, or air jet impingement may be effective.

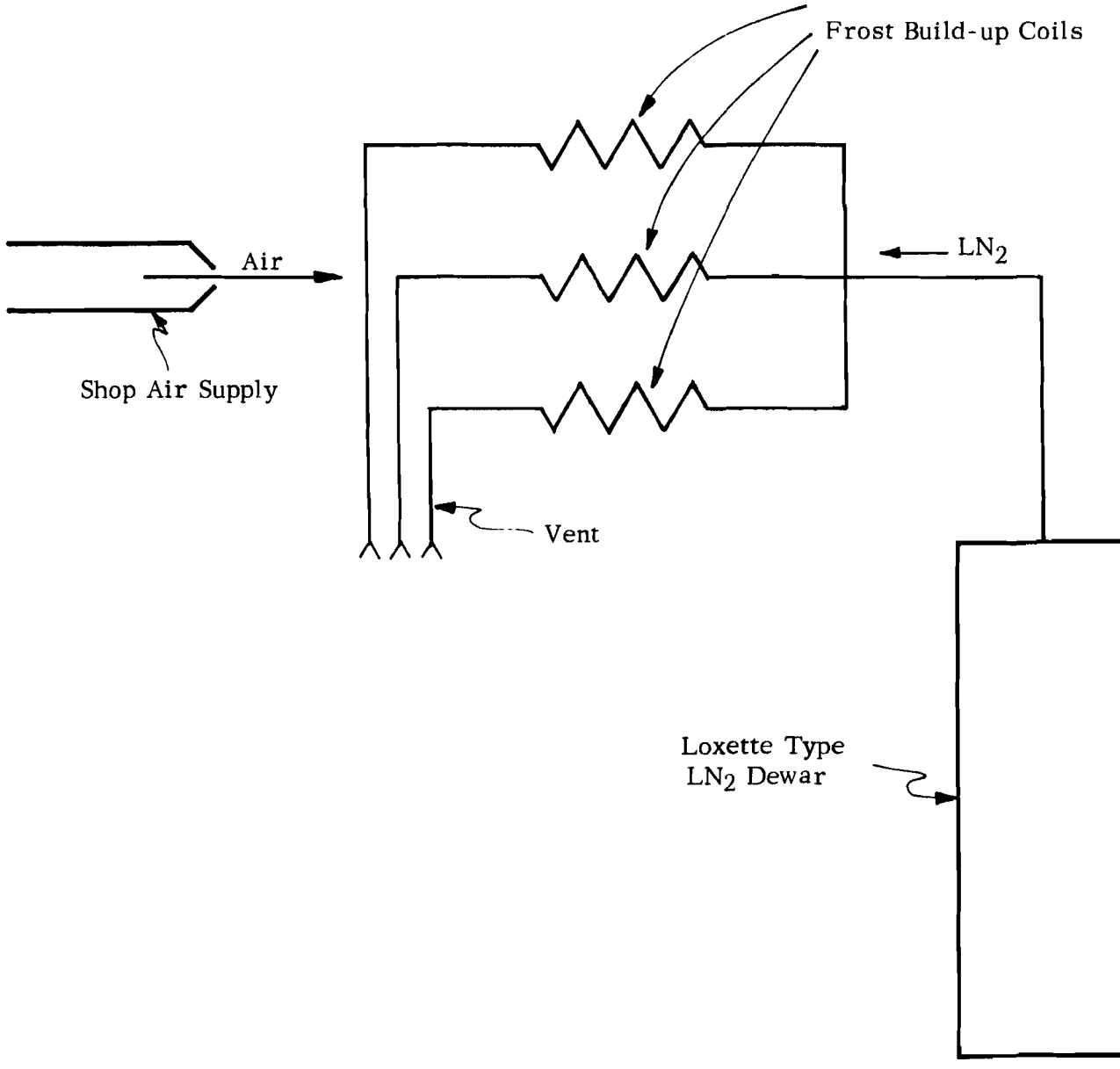

FIGURE 1 SCHEMATIC OF TEST APPARATUS

APPENDIX 6

FROST PROPERTIES

TABLE OF CONTENTS

A. PROPERTIES OF DRY AIR AND (AIR-FREE) WATER AND CARBON DIOXIDE

In the discussion pertaining to the properties of water and carbon dioxide frosts, the properties of the pure materials are often used. For convenience, the best estimate of these values are given below:

1. Density

a. Carbon Dioxide

Solid carbon dioxide densities are essentially independent of pressure and only a weak function of temperature. The temperature variation is given in Table I but in most of the calculations, a value of 1.6 gms/cm^3 was taken to be a representative average.

TABLE I

SOLID DENSITY OF CARBON DIOXIDE (1)*

T^oR	ρ gm/cm^3	ρ lb/ft^3
350	1.53	95.4
348	1.565	97.5
330	1.581	98.6
312	1.594	99.5
294	1.607	100.0
276	1.618	100.8
258	1.627	101.2
163	1.665	103.8

b. Water

The density of water-ice is given in Table II as a function of temperature. For our calculations we chose a value of 0.92 gm/cm^3 to be representative.

TABLE II

SOLID DENSITY OF WATER ICE (8)

T^oR	ρ gm/cm^3
492	0.918
490	0.918
480	0.919
470	0.920
460	
450	0.921
440	0.922
430	0.923
420	0.924

*Underlined numbers in parentheses refer to Bibliography on Pages 12 and 13.

2. Thermal Conductivity

a. Carbon Dioxide

A literature search indicated only two references of the thermal conductivity of solid carbon dioxide (3, 4). Unfortunately, they are in poor agreement. The values are given in Figure 1.

Eucken and Engleit's data cover a wider range of temperature and have been chosen when numerical values are required. There still appears to be no good reason to select one set of data in preference to the other and this is an area requiring further work.

The data of Eucken and Engleit have been extrapolated to lower temperatures by the empirical relation:

$$k = A/T^n \qquad (1)$$

where k = solid conductivity, Btu/hr-ft^2-of/ft

T = temperature $^\circ R$

$A = 325$

$n = 1.22$

b. Water

In contrast to the paucity of data for carbon dioxide, ice thermal conductivities have been thoroughly studied. Three of the best sets of data, (5, 6, 7), are shown in Figure 2. The agreement is excellent; no equation of the form of (1) appears to fit the data accurately over this wide temperature range. Figure 2 does not show the very low temperature data (40 to 60°R) of Dean and Timmerhaus but these data do not fall on the extrapolated curve.

c. Air (see Figure 3.)

3. Heat of Sublimation

The heat of sublimation is only required for calculation of $k^{\epsilon X}$ at temperatures near the triple point. We have used the values:

Carbon Dioxide: $\Delta H_s = 233.8$ Btu/lb (8)

Water: $\Delta H_s = 1190$ Btu/lb (9)

4. Vapor Pressures

Vapor pressures of water-ice and solid carbon dioxide are plotted as a function of temperature in Figures 4 and 5. (8)

B. FROST DENSITY

It is impossible at this time to delineate with any degree of assurance the quantitative effect of the system indepedent variables upon the density of deposited frost. No definitive studies have yet been made to clarify this area; we present below some tentative conclusions inferred from the studies on water frost thermal conductivity and propose a rough correlation.

1. Water Frost

The fluid mechanics of the water-air stream and the temperature level of the frost are the most important independent variables.

Temperature of Frost

Temperature per se has little to do with the density of frost; as we have seen, the individual ice particle density is not affected strongly by temperature. However, if the temperature level is near the triple point and if there is a temperature gradient across the frost, then the warmer layers tend to evaporate and deposit on the colder layer. This "distillation" effect is what leads to the concept of "excess thermal conductivity" discussed later. At the present time, it is sufficient to note that the effect is to increase gradually the bulk frost density with time. If the temperature level is low, then the driving force for the evaporative transfer is small and time has little effect on the density. Many investigators studying frost properties have noted this transient effect; however, these studies were, in general, made near the triple point where the highest solid vapor pressures are noted. In the present investigation, most of the frost was deposited at temperatures well below the triple point and in such cases we would expect little change in frost density with time. (See, however, comments of Section B below).

Fluid Mechanics

It is well known that frosts formed by natural convection mechanisms are loose and porous with low densities in the range of 0.02 to 0.04 gm/cm^3 when freshly formed. (10)

Contrasted with this are the studies made with forced convection. In such studies frost densities from 0.1 to nearly 0.5 gm/cm^3 have been reported. (In a few cases the density even exceeded 0.5). It would be convenient to relate the frost density to the Reynold's number, but as yet there are insufficient data to warrant such a conclusion. The data do indicate, however, that density increases with flow velocity in some manner. We present in Figure 6 a plot showing experimental values of water frost density as a function of velocity for three independent studies (none of which were, however, designed primarily to study frost density). The low velocity data of Brazinsky (12) and the high velocity data of Coles (11) were taken in similar pieces of apparatus -- essentially a flat, cooled plate with humid air flowing over it. The Arthur D. Little, Inc., data resulted from experiments in in-line tubular exchanges (described elsewhere in this report). The straight line in Figure 6, drawn for convenience of interpolation, is not to be construed as necessarily representing a reliable correlation.

The temperature level of all these investigations was sufficiently low to minimize evaporation transfer within the frost, i.e., Brazinsky, 140°R; Coles, 455 to 460°R; Arthur D. Little, Inc., variable but usually around 460°R.

A somewhat similar trend in benzene frost density was noted by Rische (2) when benzene was frosted from nitrogen. Rische's data shows an appreciable time effect (i.e., density increased with time) but the temperature level of the frost was near that of the triple point of benzene (500°R) so that evaporative effects were important.

Almost all the water frost data taken to date all indicate that the frost density is less than half the density of solid ice. We classify such a frost as a "low-density" frost. The reason for such a classification will be apparent when we discuss frost conductivity correlations.

2. Carbon Dioxide Frost

No data could be found in the literature for carbon dioxide frost densities. The Arthur D. Little, Inc., tests indicated that a value of about 1 gm/cm^3 would be representative at velocities near 60 ft/sec and at temperatures well below the triple point. Presumably, different values would be obtained at different flow velocities.

The value of 1 gm/cm^3 for density indicates that carbon dioxide frost formed in forced convection heat transfer is over 50% of the solid density and we classify such frosts as "high density" frosts.

3. Arthur D. Little, Inc., Studies on the Effect of Time on Frost Density

We have noted above that frost formed at the low temperatures and high pressures used in the present study should exhibit no appreciable distillation effect and thus the frost density should be time and thickness independent. However, some few data points (presented in Appendix No. 9) have indicated that, as the frost thickness increases during a run, there is a significant increase in the density; there is, however, some limiting asymptote of density close to that predicted in Figure 6. It is difficult to delineate a specific reason for this effect. Possibly the thin frost layer is sufficiently porous (e.g., suppose the frost was primarily formed from dendrites vertical to the surface) that contaminant deposition occurs to some degree within the existing frost - and causes an increase in apparent density. However, for thick frosts, the structure is less porous and the majority of contaminant now deposited is limited to the surface or just below. This tentative explanation is open to some question and more experimental work would be needed to confirm completely the range of thickness and time over which the density varies.

C. THEORETICAL CONSIDERATIONS IN FROST THERMAL CONDUCTIVITY

1. Literature Survey

Gorring and Churchill have summarized and evaluated available methods for predicting the conductivities of heterogeneous materials (13). Of the three modes of energy transfer, natural convection, radiation, and conduction, only the last appears to be of any significance in cryogenic frosts. Natural convection is usually

unimportant because of the interlocking type of frost structure producing small diameter connecting pores. Radiation is only important at high temperatures.

It is convenient to classify heterogeneous materials into three categories: (1) dispersions, (2) packed beds, and (3) continuous pairs. Dispersions are defined as a discontinuous phase dispersed in a continuous phase; continuous pairs refer to materials where both phases are significantly continuous. Packed beds are limiting cases between dispersions and continuous pairs; e.g., dispersions with point contacts.

There is a limiting density for dispersions; i.e., when all particles of the discontinuous phase are in the tightest packing arrangement. If the model postulates the discontinuous phase to be composed of spheres, then the value of

$$S \leq 0.524$$

where $$S = \frac{\rho_F - \rho_g}{\rho_S - \rho_g}$$

ρ = density

subscripts F - frost

g - gas

S - solid

It was noted before that water frost densities were usually found experimentally to have values of S less than 0.5 so that one might model these water frosts in the form of dispersions. However, it was also noted that carbon dioxide frosts were more dense and $S_{CO_2} > 0.5$ so that one may model carbon dioxide frosts as a continuous-pair type. We make these observations because the correlation techniques chosen depend upon the type of structure of the frost. We discuss low-density frosts below and develop general relations applicable to low-density water frosts; following this we develop a similar relation for high-density frosts and apply this to carbon dioxide and high-density water frosts.

The final results in any case may be expressed in such a way that the frost thermal conductivity depends only upon the frost structure and the conductivities of the solid and gas phase; i.e.

$$k_F = f\ (k_s, k_g, \text{structure}) \qquad (2)$$

k_F = frost thermal conductivity

k_s = solid thermal conductivity

k_g = gas thermal conductivity

2. Low-Density Frosts

One may visualize an infinite number of geometrical arrangements of solids present in a continuous phase as a dispersion. Raleigh (14) has developed rigorous solutions

for many simple geometrical arrangements. For example, for a regular array of uniformly-sized non-touching spheres,

$$\frac{k_F}{k_g} = 1 - \frac{3S}{\frac{2+V}{1-V} + S - \alpha\frac{(1-V}{(1.33+V} S^{10/3} - \cdots + \cdots} \qquad (3)$$

where all terms have been defined before except:

$V = k_s/k_g$

α = constant depending upon the exact structure of the frost. Suggested values are 1.31, 0.29 and 0.0752 for simple cubic body-centered cubic, and face-centered cubic arrays respectively. (13, 15)

Other models have been suggested but we have found that the model developed by Woodside (16) gives results which fit well for water frosts near 32°F. A simple cubic array of spheres was chosen and infinite conductivity assumed in all directions other than that in the direction of energy transport. The final equation is*:

$$\frac{k_F}{k_g} = \left\{ 1-\left(\frac{6S}{\pi}\right)^{1/3} \left[1 - \frac{(a^2-1)}{2a} \ln \frac{a+1}{a-1} \right] \right\}^{-1} \qquad (4)$$

where $a = \left[1 + \frac{4}{\pi \Psi (6S)^{2/3}} \right]^{1/2}$

$\Psi = (k_s - k_g)/k_g \frac{\pi}{}$

The assumption that the isotherms are non-curved in the frost is a good assumption for values of Ψ less than about 30. At higher values, the isotherms should bend sharply about the spheres, emphasizing the important contribution of the solid. Equation (4) is not applicable if S is greater than 0.524 and probably should not be used for S greater than about 0.5; i.e., for high-density frosts. Dressler (17) has calculated the conductivity of a similar cubic array by an accurate relaxation technique for S = 0.524.

The value of k_g contains as a sum, the conductivity due to the air itself and one for a contribution due to evaporative transport. This subject is discussed fully in the section entitled, "excess conductivity."

Equation (4) may be generalized as:

$$k^* = k_F/k_g = f(S, \Psi) \qquad (5)$$

and a plot of this function is given in Figure 7. Examples using such a plot are given in a later section.

3. High-Density Frosts

High-density frosts such as carbon dioxide have apparently a continuous-pair type of

*In the original article the equation given is incorrectly printed; the graphs and tables are, however, correct.

structure. One of the most successful models to treat this type of matrix is the truncated-sphere model developed by Riemann (18) and tested extensively by Gorring and Churchill (13). The solid phase is assumed to be composed of spheres of diameter 2R with common intersecting circles of diameter 2r. The derivation is neatly summarized by Gorring and Churchill (19).

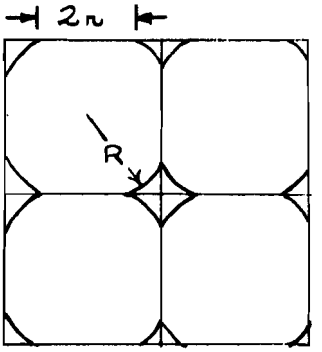

Riemann Truncated
Sphere Model

The final result is given by:

$$\frac{k_{F_1}}{k_s} = \left(\frac{R}{r} + \frac{1}{\pi} \ln\left(\frac{2R}{r}\right) \right)^{-1} \qquad (6)$$

where k_{F_1} is the contribution to the frost conductivity due to solid spheres.

The ratio (R/r) is related to the density parameter

$$S = (\rho_F - \rho_g) / (\rho_s - \rho_g)$$

by a material balance,

$$S = \frac{\pi}{6\left[1 - \left(\frac{r}{R}\right)^2\right]^{3/2}} \left\{ 1 - \frac{3}{2}\left[\left(\frac{r}{R}\right)^2 + 1 - \left[1 - \left(\frac{r}{R}\right)^2\right]^{1/2} \right] \left[1 - \left[1 - \left(\frac{r}{R}\right)^2 \right]^{1/2} \right] \right\} \qquad (7)$$

Obviously Equation (6) is not applicable for dispersions; i.e.,

where $r > R$.

Solving equations (6) and (7) simultaneously k_{F_1}/k_s is plotted as a function of S in Figure 8.

Now equation (6) allows only for the contribution due to the solid phase. Some heat flow will be due to the interstitial air and this contribution, k_{F_2}, is estimated approximately as (13),

$$k_{F_2}/k_g = 2\,(1-S)/(2+S) \qquad (8)$$

where k_g is given by equation (11). This relation is plotted in Figure 9 or given approximately as

$$\frac{k F_2}{k_g} = 0.82 - 0.855 \qquad (9)$$

Finally, the total frost conductivity is determined as

$$kF = kF_1 + kF_2 \qquad (10)$$

and is believed applicable for high-density frosts where $S > 0.524$ but less than about 0.9.

4. Excess Thermal Conductivity

The contribution of trapped air to the frost thermal conductivity is two-fold. First there is the usual conductivity of the dry gas as given for air in Figure 3. Second, since there is a temperature gradient across the frost layer, evaporation takes place at the warmer sections and desublimation at the colder. Any vapor flux occurs by a diffusional mechanism and is associated with the transport of energy. It is convenient to account for such a phenomena by increasing the dry gas conductivity by an amount equal to this excess; i.e.,

$$k_g = k_g' + k^{ex} \qquad (11)$$

where k'_g = dry gas conductivity from Figure 3.

k^{ex} = excess thermal conductivity due to this evaporative transport.

To obtain a relation for k^{ex}, which we have implicitly defined as:

$$q_g^{ex} = k^{ex}\, dT/dx \qquad (11a)$$

We consider the total mass flux occurring as a result of the concentration difference in the frost layers, i.e.,

$$N = D_v\, dc/dx \; * \qquad (12)$$

where N = mass (or moles) of material diffusing over a length dX due to a concentration difference dC.

D_v = diffusion coefficient

*We have neglected mass transferred by bulk motion of the vapor. If the latter is considered, the final value of k^{ex} is multiplied by the factor $(P/_{(P-P_{vp})})$, a number very close to one for the small values of P_{vp} considered here.

Assuming ideal gases, $C = P_{vp}/RT$ where P_{vp} the vapor pressure. Also $P_{vp} = f(T)$, so

$$N = D_v \frac{dc}{dx} = D_v \frac{d}{dx} (P_{vp}/RT) = D_v \frac{d}{dt} (P_{vp}/RT) \frac{dt}{dx} \quad (13)$$

$$\text{and} \quad N = \frac{D_v}{R} \left[\frac{1}{T} \frac{dP_{vp}}{dt} - \frac{P}{T^2} \right] \frac{dt}{dx} \quad (14)$$

$$\text{also} \quad (N)(\Delta H_{sub}) = q^{ex} \quad (15)$$

where ΔH_{sub} = heat of sublimation

and by the Clapeyron - Eq.

$$\frac{1}{T} \frac{dP_{vp}}{dt} = \frac{P_{vp}}{T^3 R} \Delta H_{sub} \quad (16)$$

$$\text{Combining} \quad k^{ex} = \frac{D_v}{R} \frac{P_{vp}}{T^2} \Delta H_{sub} \left(\frac{\Delta H_{sub}}{RT} - 1 \right) \quad (17)$$

Usually Equation (17) is simplified by assuming $\frac{\Delta H_{sub}}{RT} >> 1$ so

$$k^{ex} = \frac{D_v}{R^2 T^3} P_{vp} \Delta H_{sub}^2 \quad (18)$$

Now D_v is a function of temperature and pressure as,

$$D = D_o (T/T_o)^{3/2} (P/P_o) \quad (19)$$

where the subscript o refers to some standard condition. Thus $k^{ex} = f(T,P)$ for any given air frost. We have plotted k^{ex} for water and carbon dioxide frosts in Figures 10 and 11. It is readily apparent that k^{ex} is only important for high temperature, low pressure frosts.

D. EXPERIMENTAL FROST THERMAL CONDUCTIVITY DATA

Table 3 presents a summary of the published investigations on the thermal conductivity of water frost. The data given in these studies is shown in Figure 12 as a function of frost density. A good mean of the data for densities greater than 0.1 gm/cm^3 appears to be given by Devaux (23) for temperatures near 32°F. For low temperature experiments (10, 12) the conductivities are much lower and the scatter much greater.

E. COMPARISON OF CALCULATIONS WITH EXPERIMENTAL VALUES

Figure 12 which shows the experimental values of water frost conductivity has also superimposed the calculated values of kF for the same density. Curve A was determined for water frost at 492°R from equation (14) and Figure 7 for values of density less than 0.5 gm/cm^3 (low-density) and from Figures 8 and 9 at values of density greater than 0.45. Curve B is determined from equation (14) and Figure 7 for water-frost at 250°R to determine the closeness of agreement with the 250°R F data of Brazinsky (12). Agreement is reasonable considering the scatter of the experimental data.

F. WORKING CURVES

The previous discussion has been summarized into three curves in Figures 13, 14 and 15.

Figure 13 - Water-Air Frost, density less than 0.5 gm/cm^3

Figure 14 - Water-Air Frost, density between 0.5 and .75 gm/cm^3

Figure 15 - Carbon Dioxide-Air Frost, density greater than 0.8 gm/cm^3

These curves may be used to estimate the various frost conductivities once the temperature level and density of the frost have been specified.

TABLE 3

SUMMARY OF WATER FROST EXPERIMENTS

Ref. No.	Temp. Range of Frost	Geometry of Eq.	Type of Flow of Humid Gas	Remarks
10	160 to 400°R	5 3/8 Sphere with Liq. Oxy.	Natural Convection	ρ meas exp. k calc. from est. surface temp. and heat flux
20	492°R			Packed Snow
21	450 to 470°R	Vertical Tube Frost Outside	Forced Conv. V = 16-40 ft/sec	ρ meas. exp. from thickness and total wt. readings. Average k calc.
22	492°R	Horizontal Tube Bundle, Frost on Outside	Cross Flow, Baffled, 2 - 6 ft/sec	Tube Dia 1.5 in. Tube Sp. 1.9-in. Re 2700 to 9300 Bundle 69 in. long, 35 in high
23	492°R			Packed Snow
11	440 to 480°R	Flat Plate	Forced Conv. V up to 800 ft/sec	Prob. best work
20	492°R			Packed Snow
12	250°R (Average)	Flat Plate	Forced Convection V around 20 ft/sec	ρ meas. experimentally k calculated from Temp. Gradient in Frost

BIBLIOGRAPHY

1. International Critical Tables, McGraw-Hill Book Company, Inc., New York, 1928; I, 112; III, 43.

2. Rische, Chem. Ing. Tech. 29, 603 (1957).

3. "The Experimentelle Bestimmung des Warm leit vermogens einger Gase und Flussig keiten", Eucken, O., and H. Engleit, Feit fur die gesamte Kalte - Ind. 45, 109 (1938)

4. "The Kellog Charts", Kellog Company

5. Jakob, M. and S. Erk, Feit. tech. Physik. 10, 623 (1929)

6. Ratcliffe, E. H., Phil. Mag. 7, 1197 (1962)

7. "Thermal Conductivity of Solid H_2O and D_2O at Low Temperatures"
   Dean, J. W., and K. D. Timmerhaus, Paper E-5, 1962 Cryogenic Eng. Conf., Los Angeles, Aug. 14-16, 1962.

8. Handbook of Chemistry and Physics, Chem. Rubber Pub. Company.

9. "Steam Tables", Keenen, J. and E. Keyes, Wiley, New York, 1936.

10. "Heat and Mass Transfer to Uninsulated Oxygen Containers", Holten, D.C., B. S. Thesis, Univ. of Colo., 1957.

11. "Experimental Determination of the Thermal Conductivity of Low Density Ice", Coles, W. D., NACA TN 3143, 3-54.

12. Brazinsky, J., M.I.T., Private Communication. Unpublished results of some recent research work.

13. Gorring, R. L. and Churchill, S. W., Chem. Eng. Prog., 57, 53 (1961).

14. Rayleigh, L., Phil. Mag. V, 34, 481 (1892).

15. DeVries, D. A., Bull. Intern. Inst. Refrig. Annexe, 1952, 32, 115 (1952).

16. Woodside, W. Can. J. Phys. 36, 815 (1958)

17. Deissler, R. G., Trans. A.S.M.E. 80, 1417 (1958).

18. Riemann, G. H. M. Weber, "Die Partiellen Differential - Gleichunger der Mathematischen Physik", Band 1, p. 474, F. Vieweg and Sohn, Braunschweig (1919).

19. Gorring, R. L. and S. W. Churchill, ADI 6754, June 1961.

20. See Ref. 1, Vol. II, 313

21. "Research on Frost Formation in Low Temperature Dehumidifier", Kamer, S., et al, Kyoto Univ., Japan.

22. Prens, L. Kaltetechnik 8, 160, 182 (1956).

23. Devaux, J., Sci. Abs. Series A, Vol. 36, 980 (1933)

24. "A Compendium of the Properties of Materials at Low Temperature (Phase 1), Part 1. Properties of Fluids" WADD TR 60-56, Table 3.006.

Note That The Two Sets Of Data Disagree

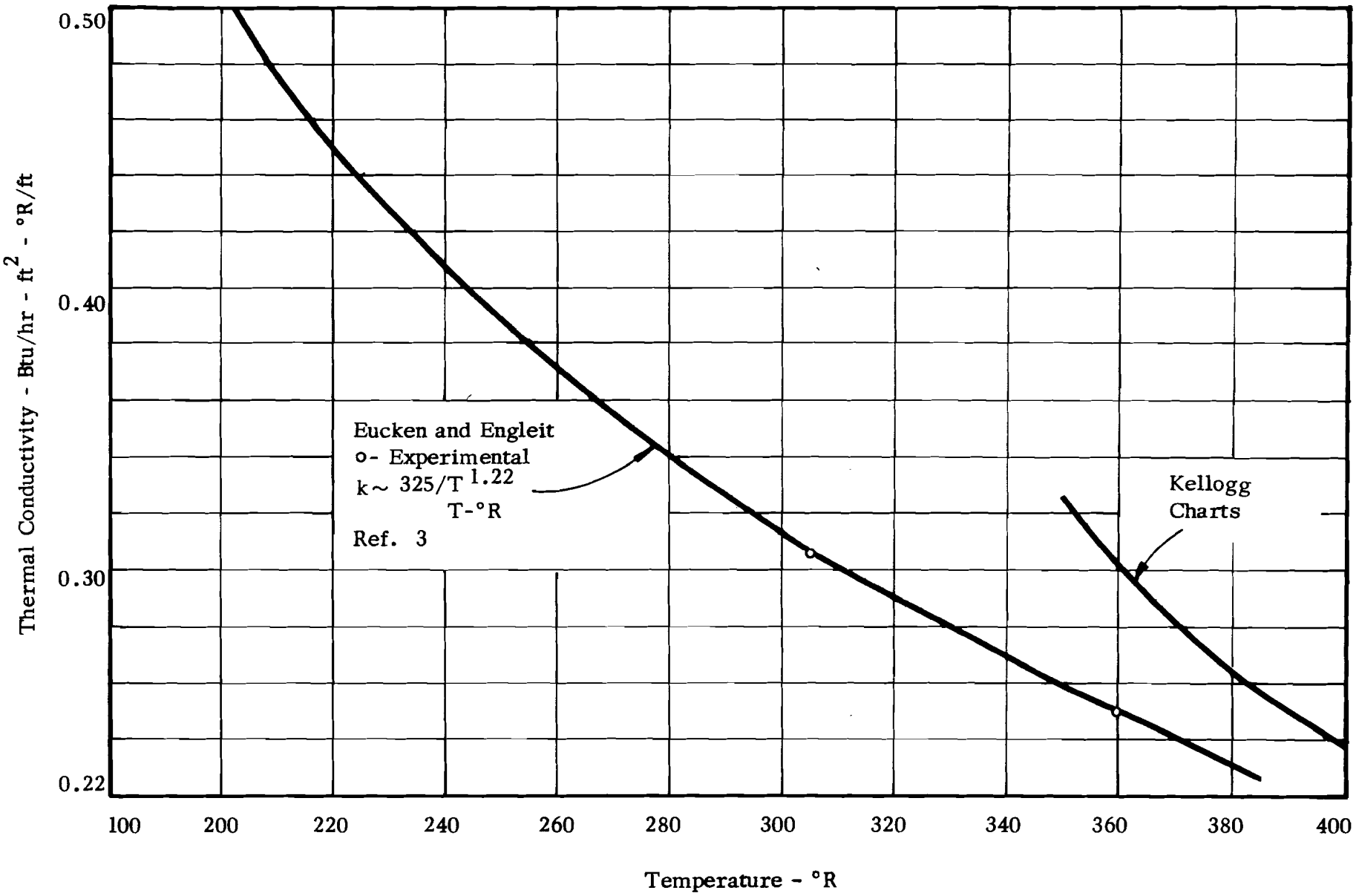

FIGURE 1 ESTIMATED THERMAL CONDUCTIVITY OF SOLID CARBON DIOXIDE

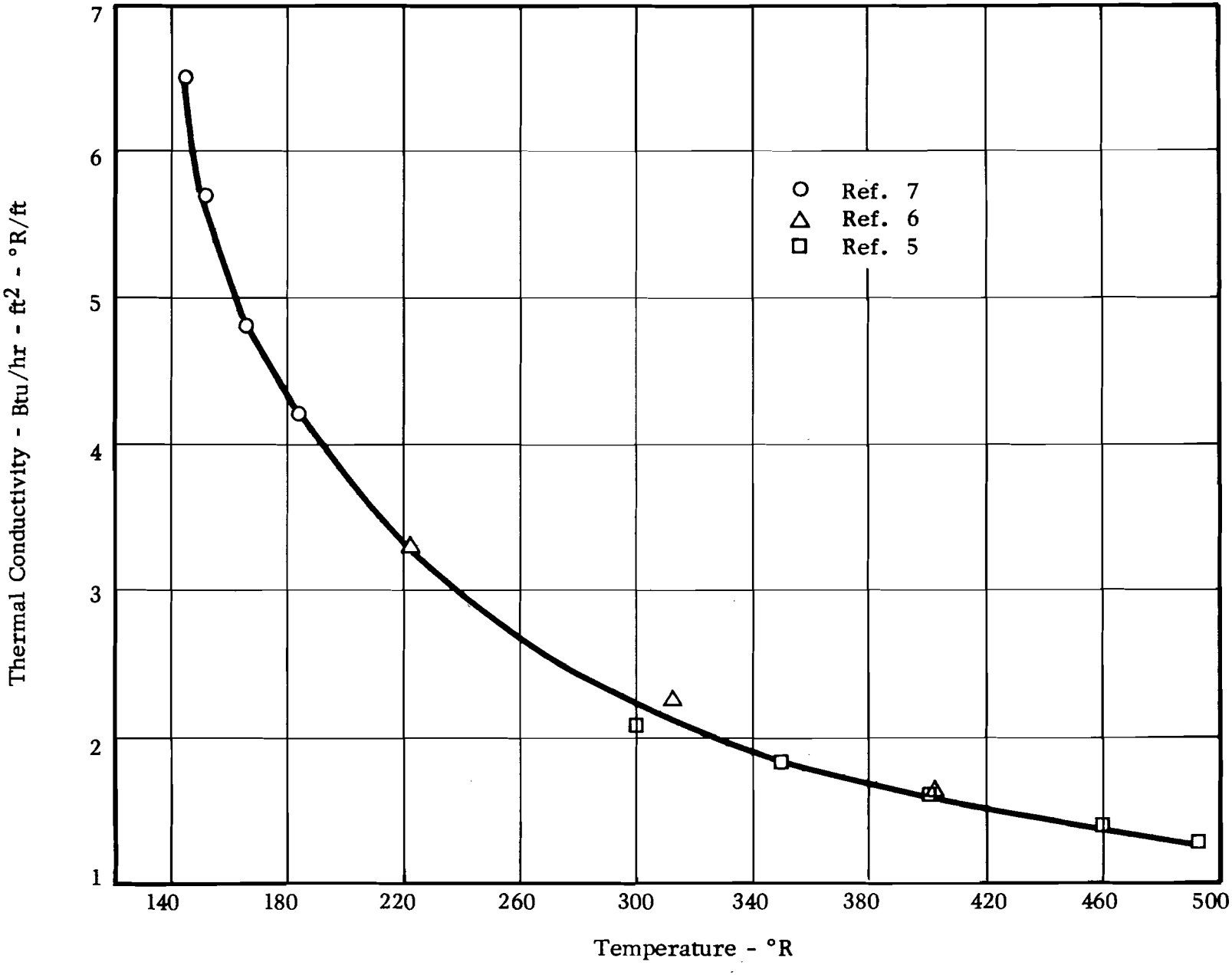

FIGURE 2 THERMAL CONDUCTIVITY OF WATER-ICE

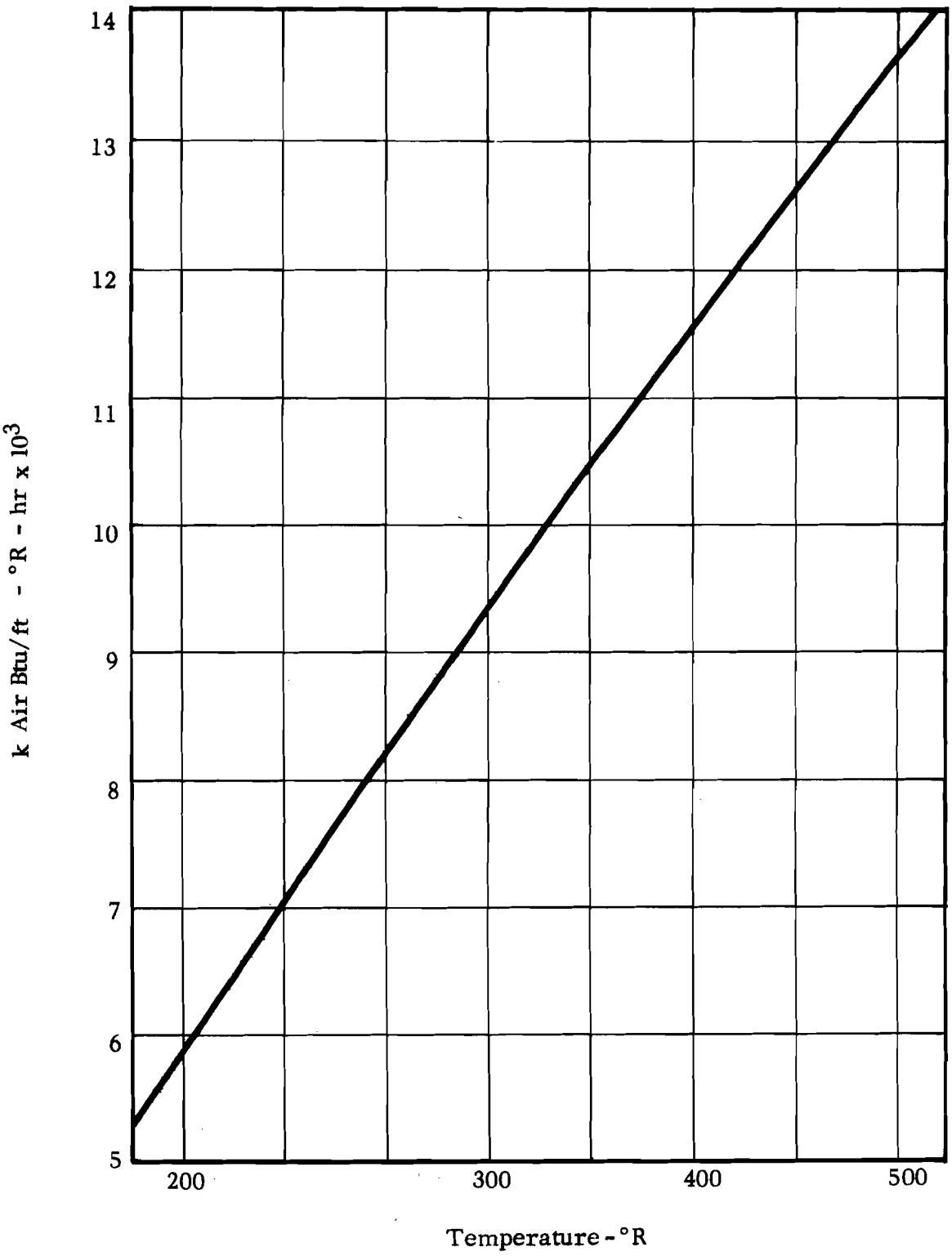

FIGURE 3 THERMAL CONDUCTIVITY OF DRY AIR (24)

A. High Temperature Range

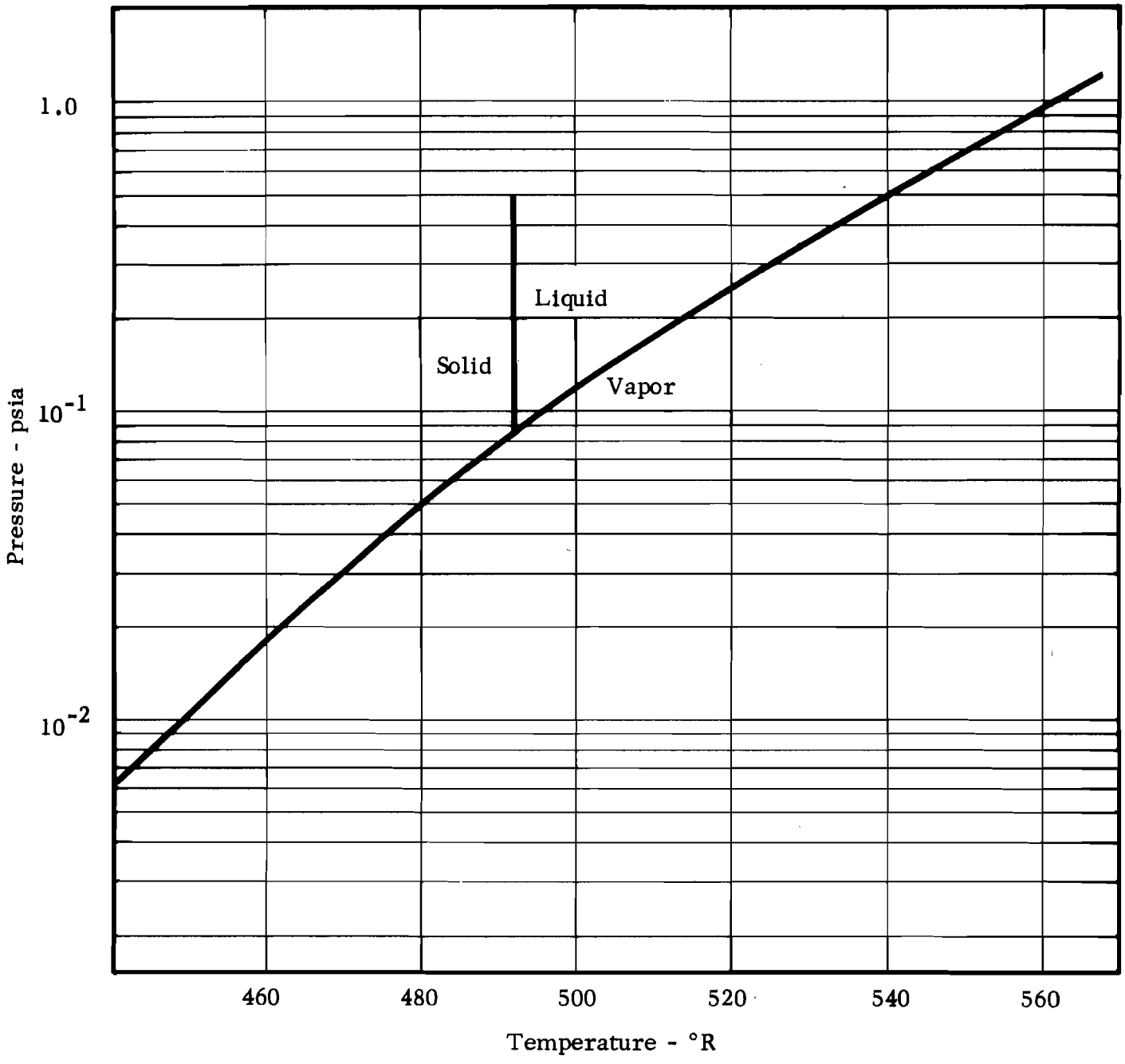

FIGURE 4 VAPOR PRESSURE OF WATER

B. Low Temperature Range

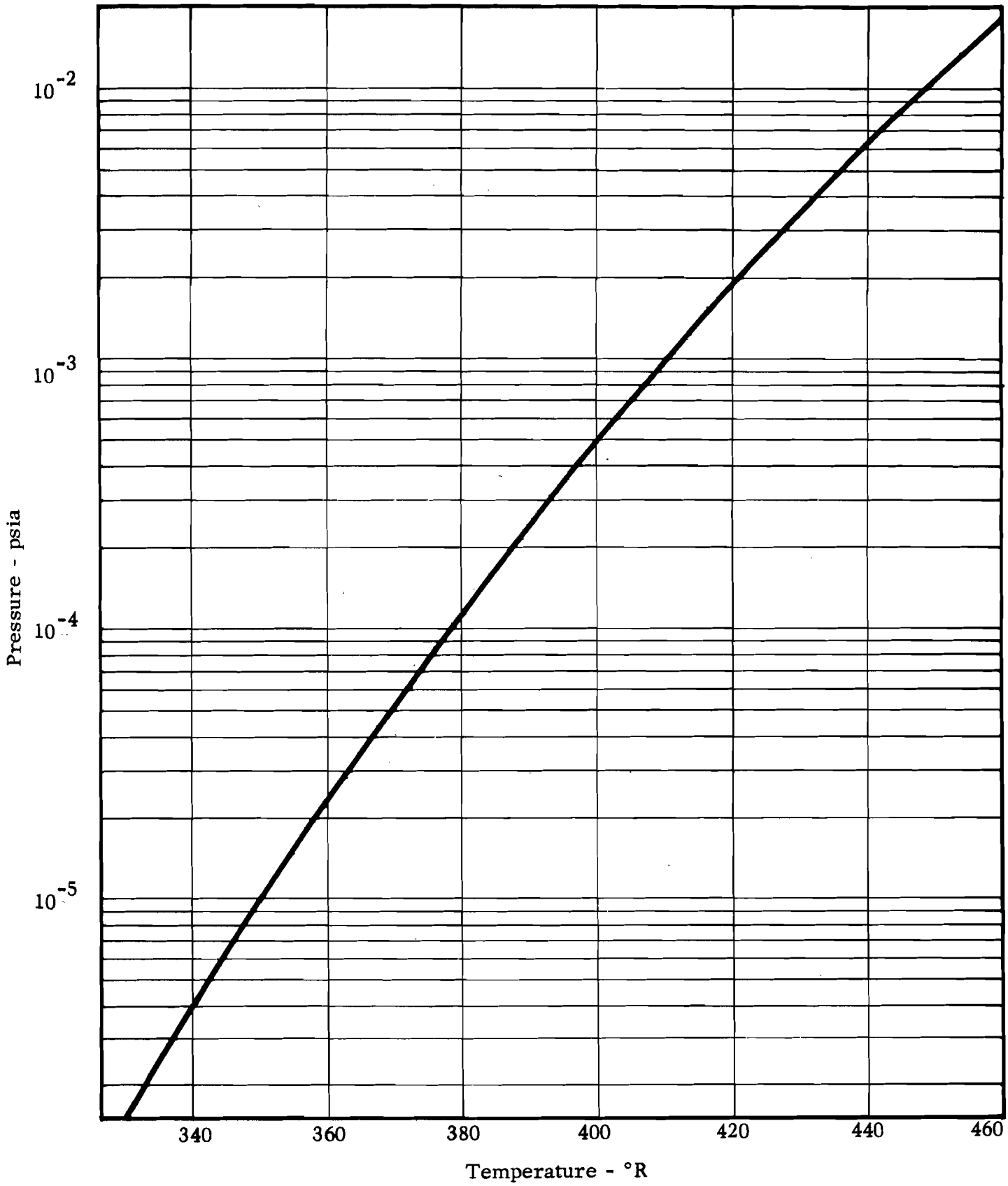

FIGURE 4 (Cont'd) VAPOR PRESSURE OF WATER

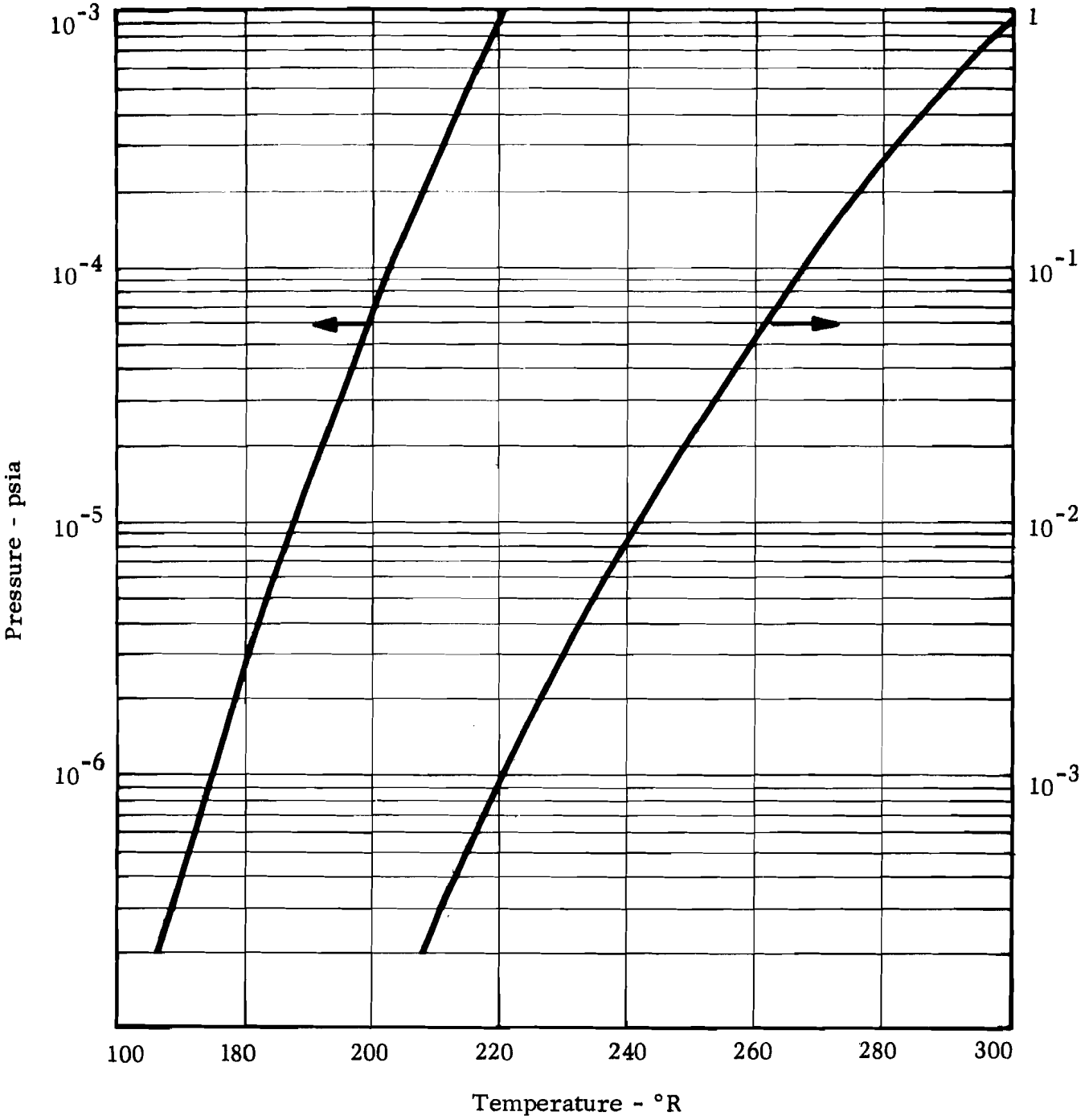

FIGURE 5 VAPOR PRESSURE OF SOLID CARBON DIOXIDE

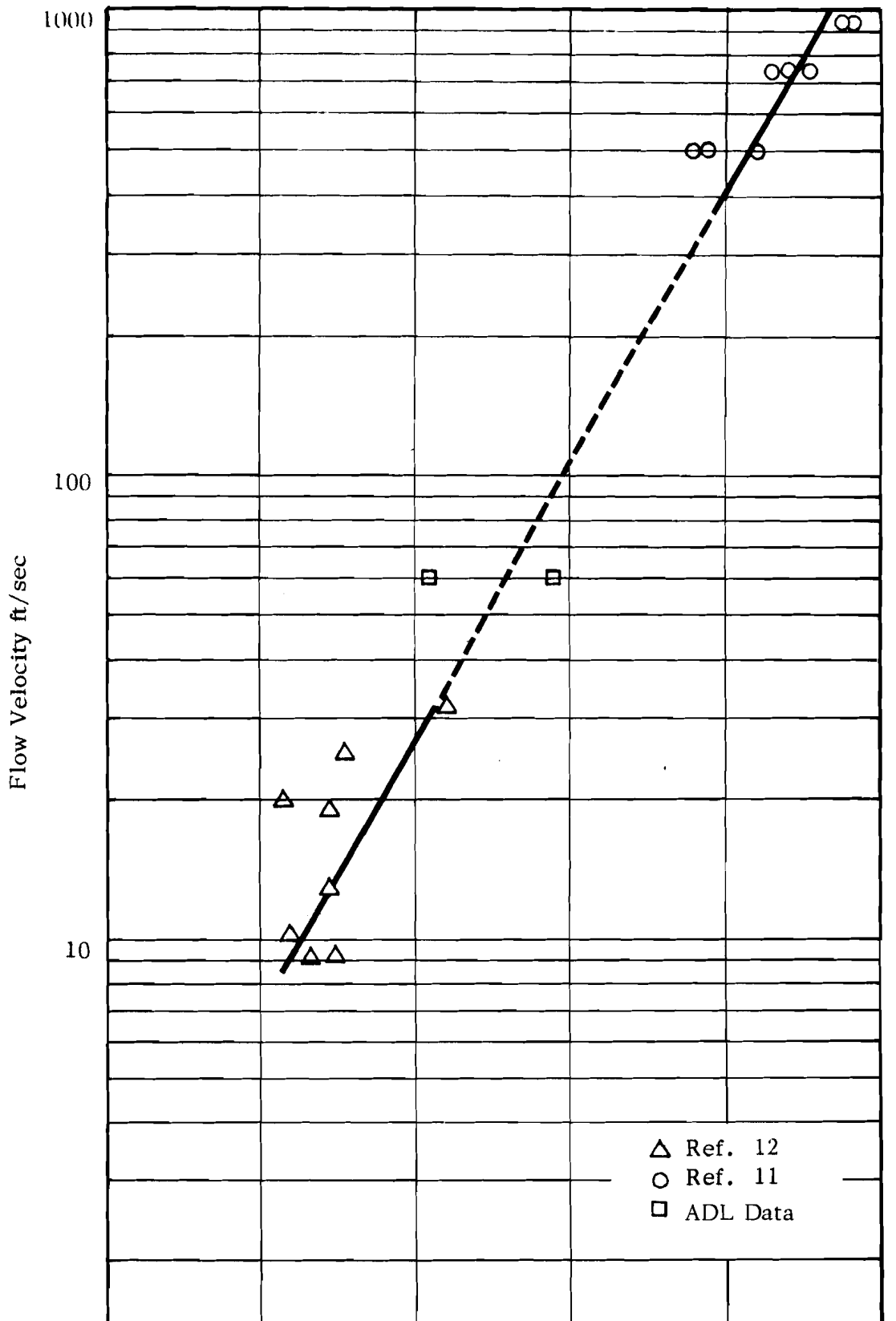

FIGURE 6 EFFECT OF FLOW VELOCITY ON WATER-FROST DENSITY

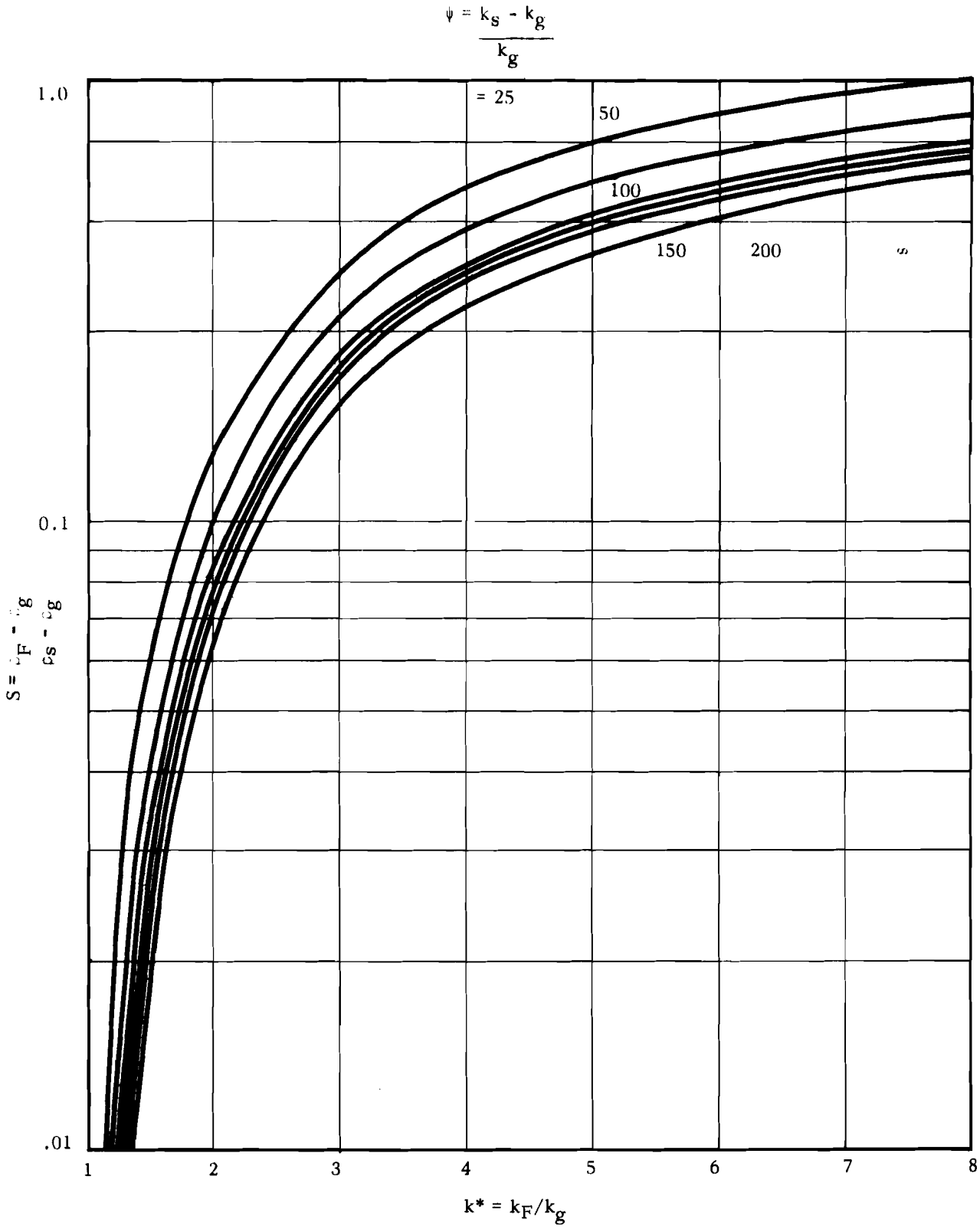

FIGURE 7 EFFECT OF ψ AND S ON k^* FROM EQUATION 5

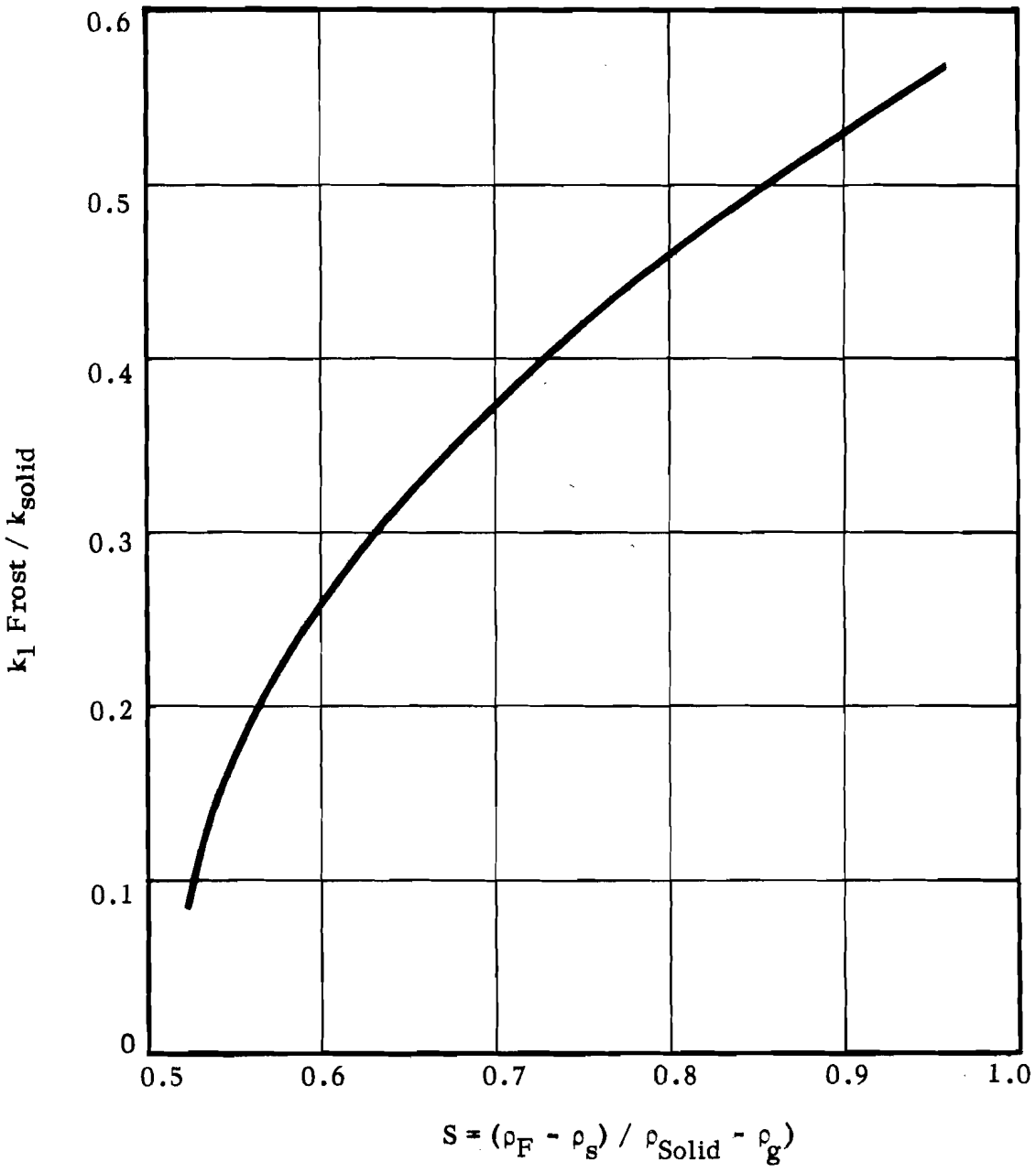

FIGURE 8 k_1 Frost/k_{Solid} VS S FROM EQUATION 6 & 7

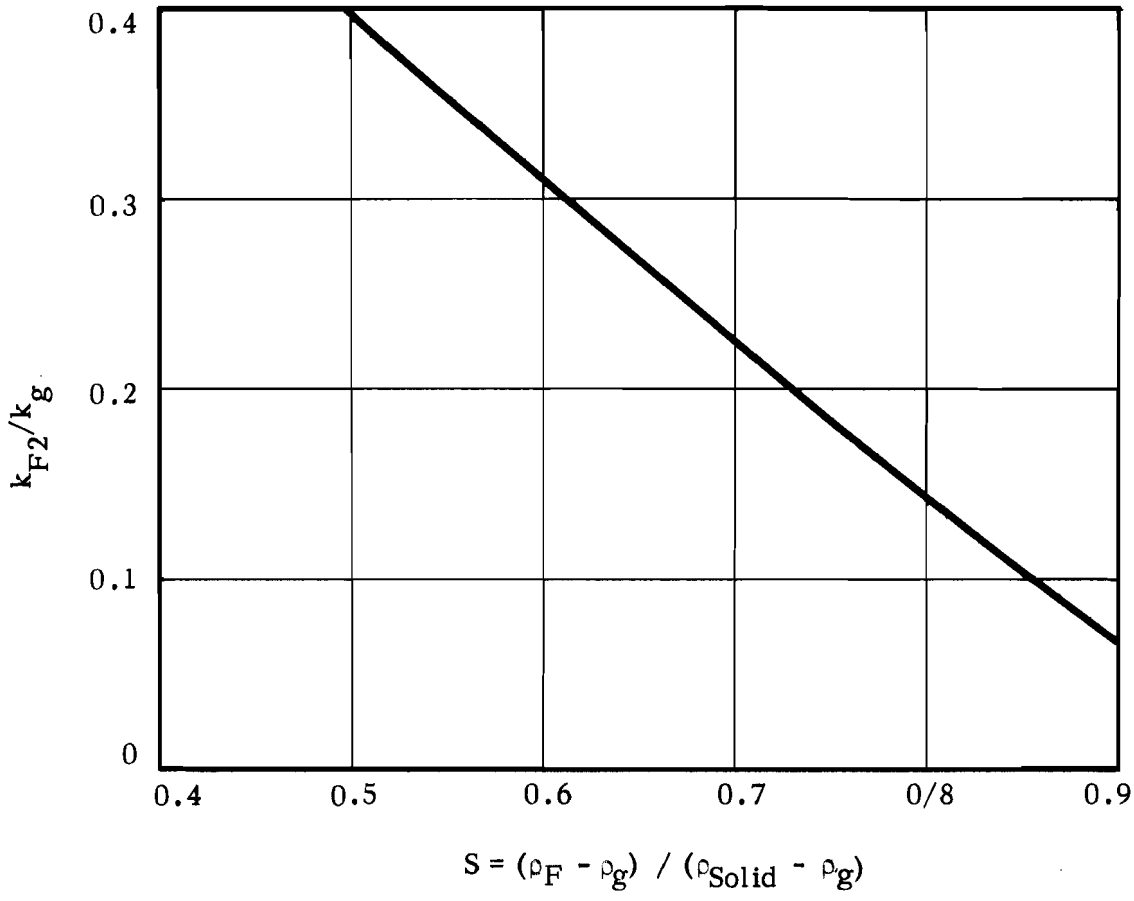

FIGURE 9 $\frac{k_{F2}}{kg}$ FROM EQUATION 9

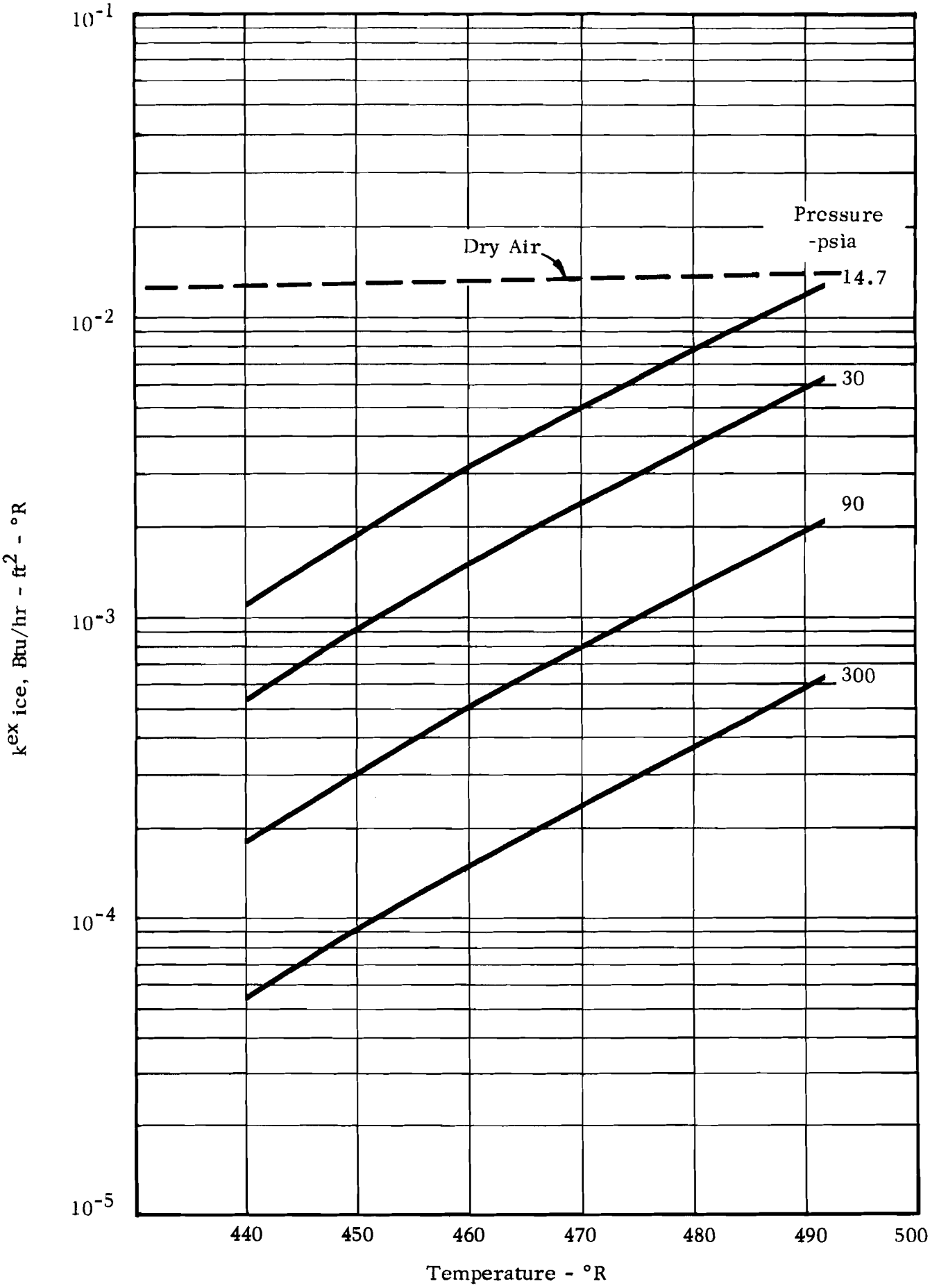

FIGURE 10 EXCESS THERMAL CONDUCTIVITY OF WATER ICE

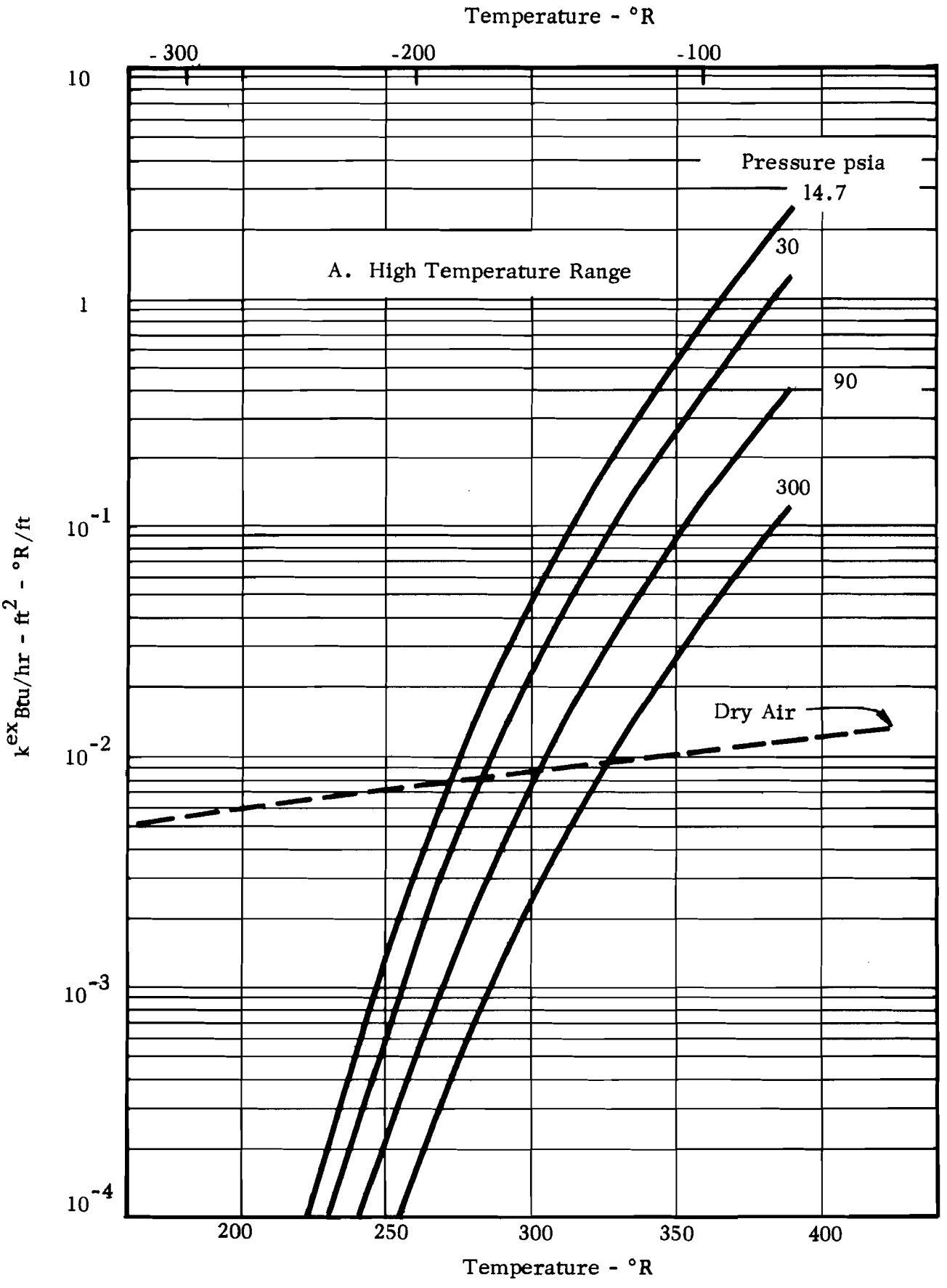

FIGURE 11 EXCESS THERMAL CONDUCTIVITY OF CARBON DIOXIDE 'ICE'

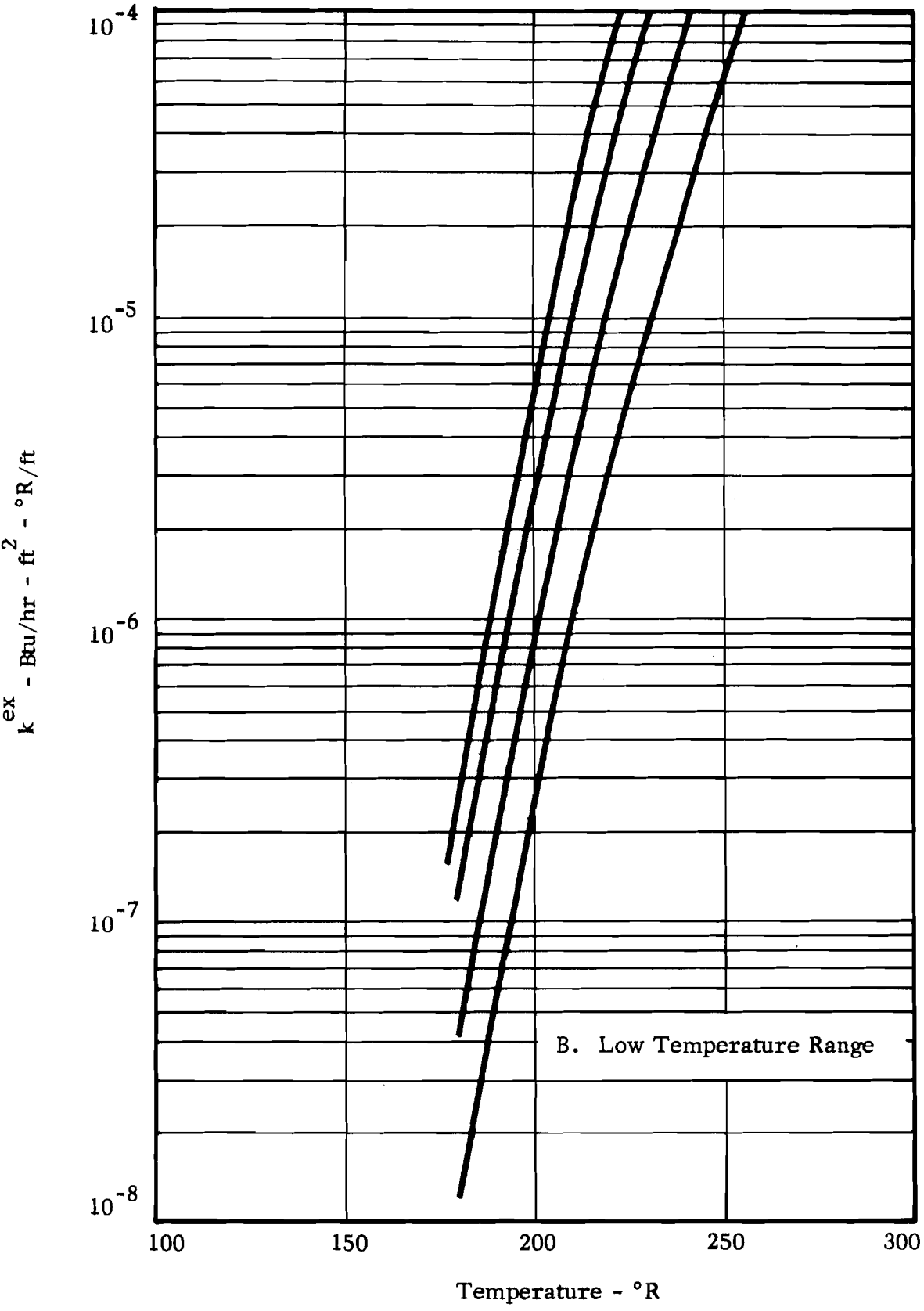

FIGURE 11 (Cont'd) EXCESS THERMAL CONDUCTIVITY OF CARBON DIOXIDE ICE

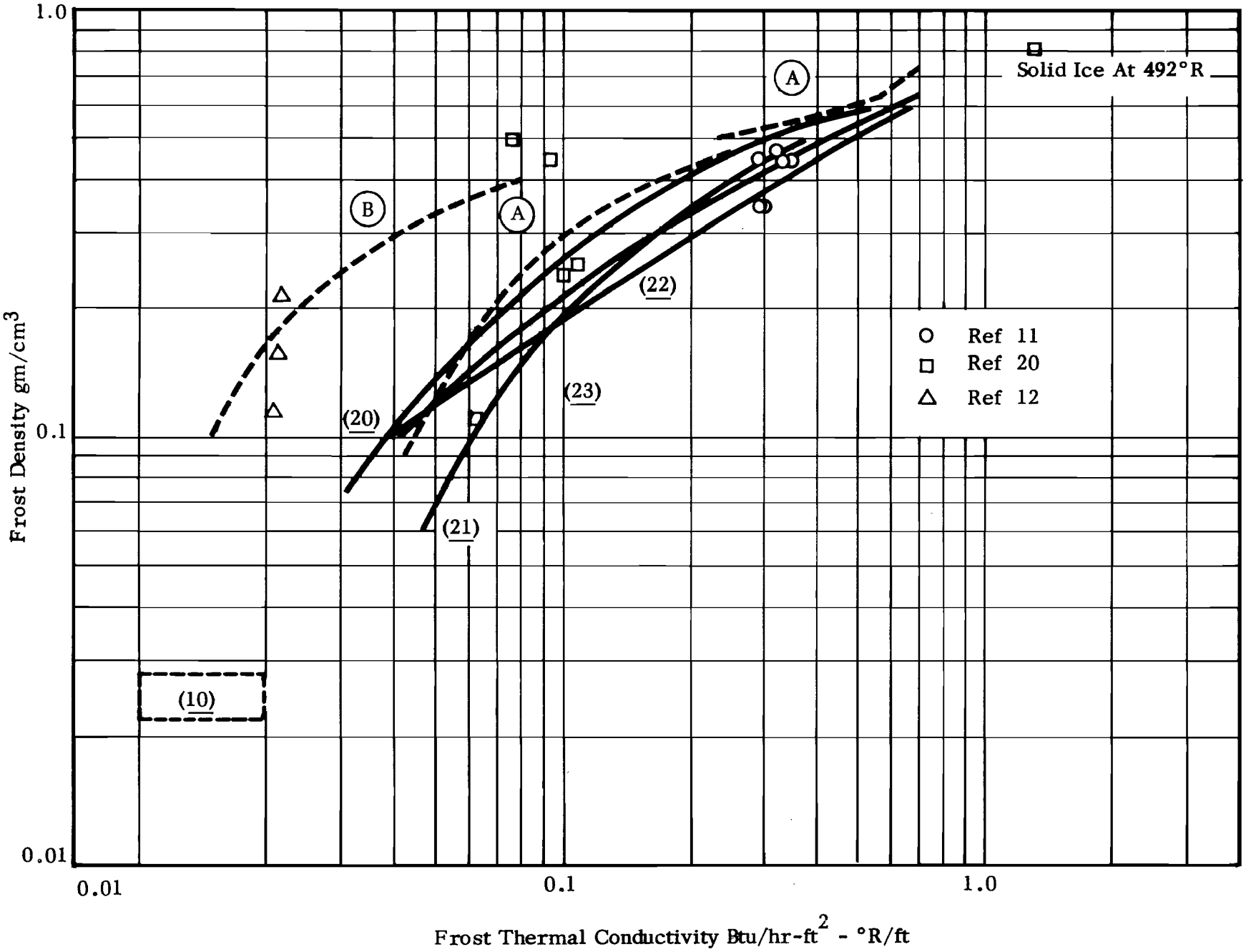

FIGURE 12 EXPERIMENTAL AND CALCULATED VALUES OF WATER-FROST CONDUCTIVITY

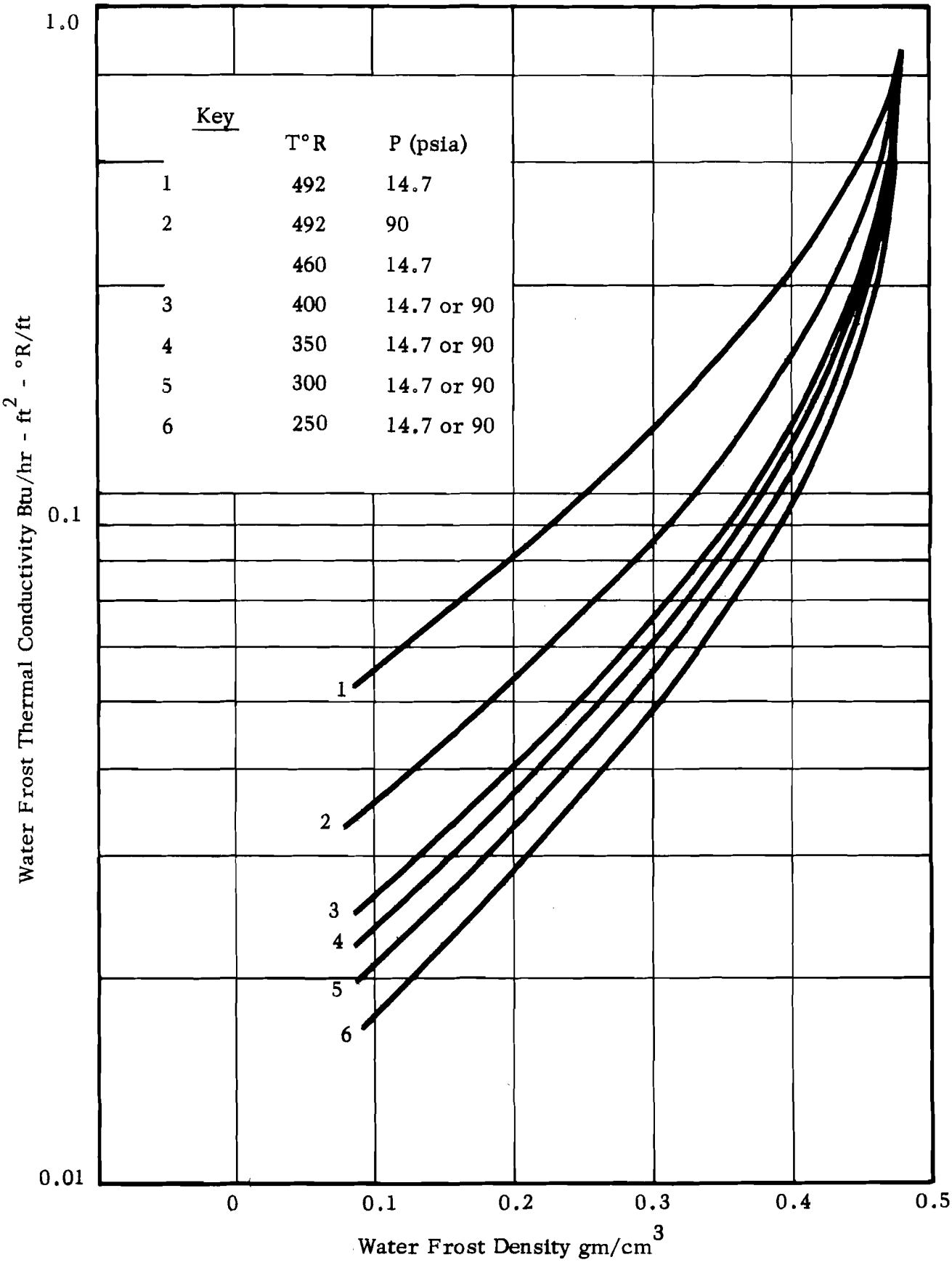

FIGURE 13 LOW-DENSITY WATER FROST THERMAL CONDUCTIVITY
(Calculated by Woodside Model)

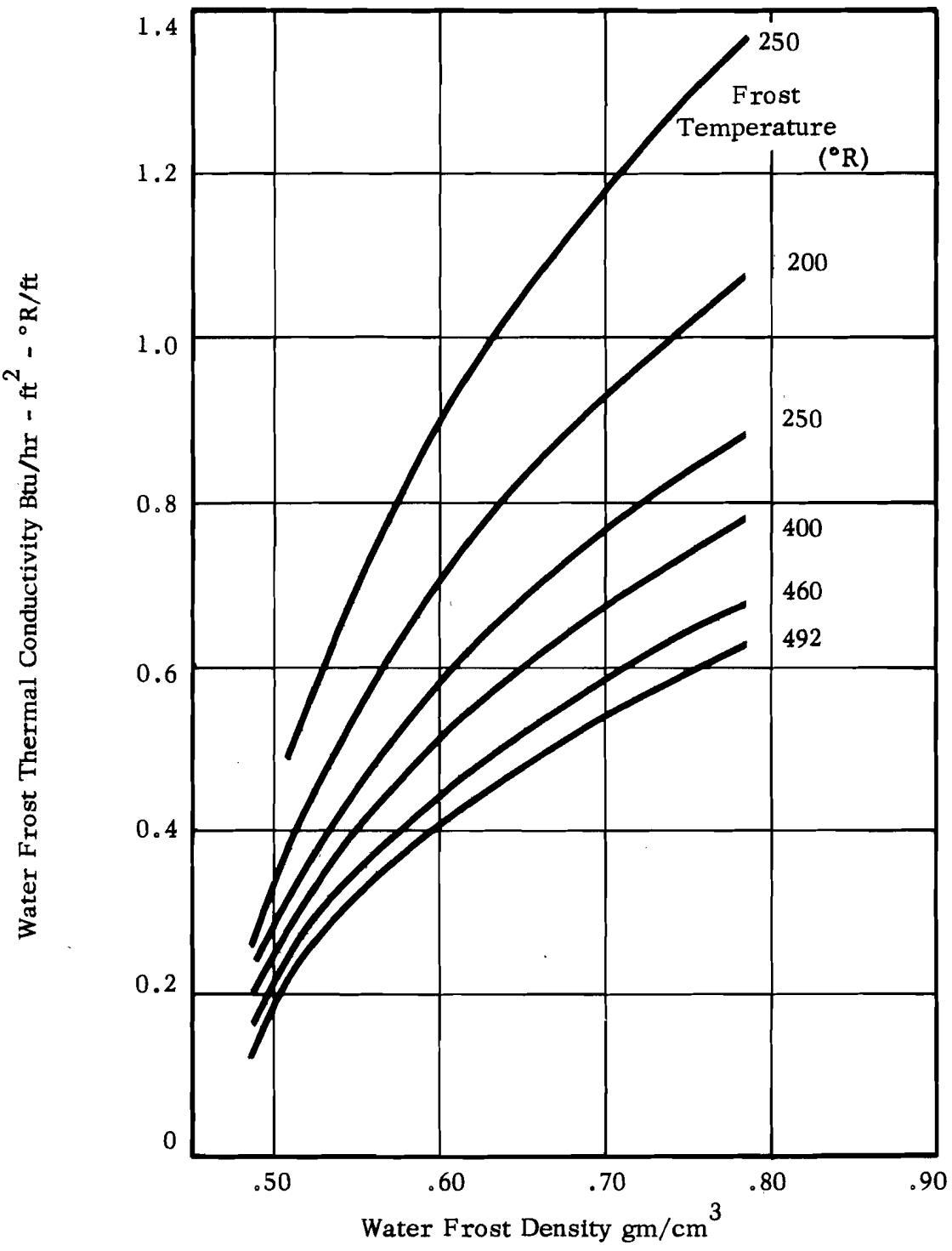

FIGURE 14 HIGH DENSITY WATER FROST THERMAL CONDUCTIVITY

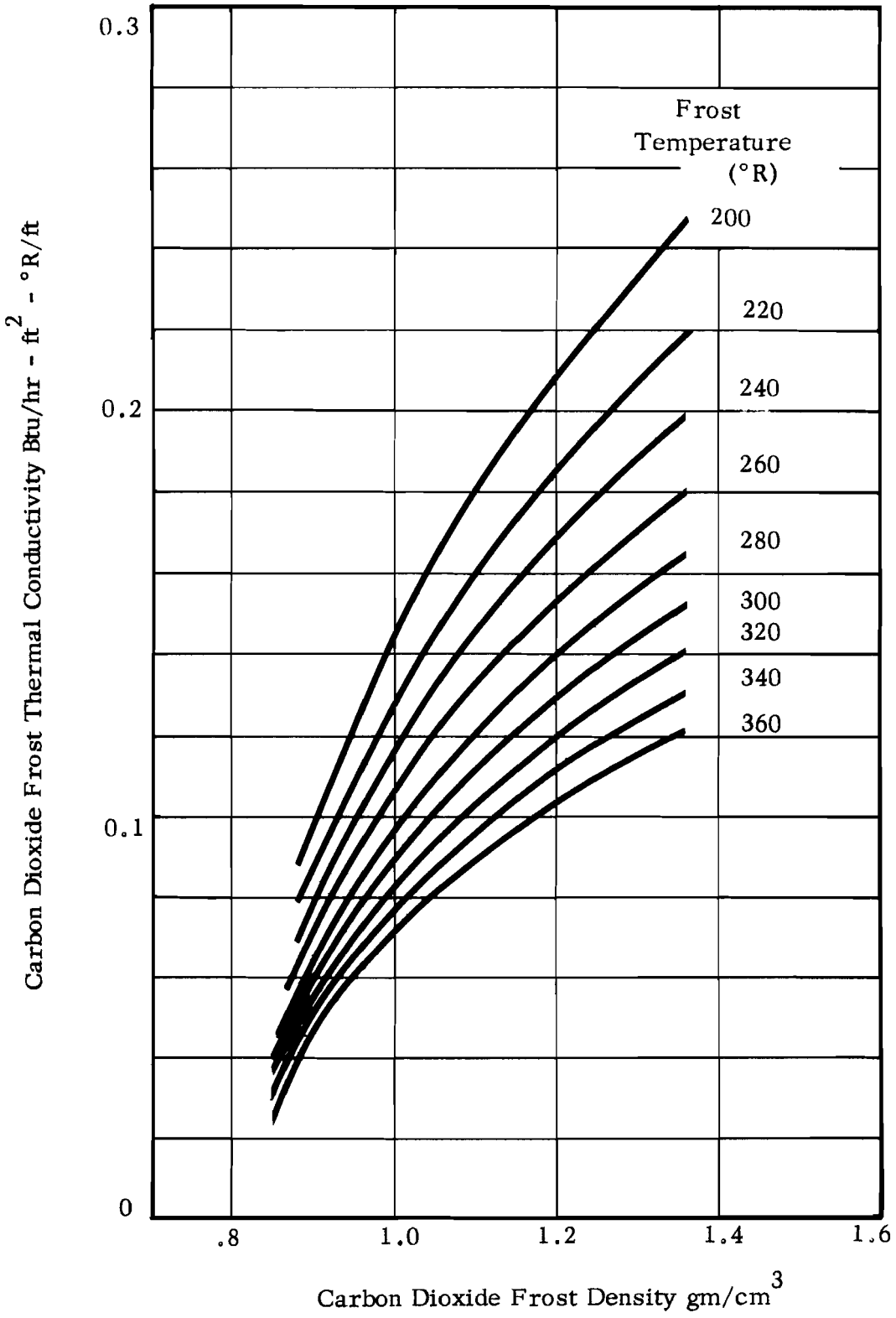

FIGURE 15 THERMAL CONDUCTIVITY OF CARBON DIOXIDE FROST

APPENDIX 7

PHOTOGRAPHS AND DRAWINGS

OF TEST EQUIPMENT

TABLE OF CONTENTS

Photographs and Drawings of Test Equipment

These photographs and drawings supplement the description of the test equipment presented in the main body of this report.

All equipment required for control and instrumentation of the facility is mounted on a test skid. This skid is shown in Photo No. 1. The test skid is 13 feet long - 4½ feet high and 3 feet wide. The top of the skid serves as a platform for the test heat exchanger and photographic equipment. Referring to photo No. 1A, the pressure gauges and temperature recorders are mounted on the instrumentation side of the test skid. The Consolidated Electrodynamics Corporation humidity meter for measurement of water content is mounted on the lower portion of the test heat exchanger protective hood. Mounted on a shelf above the humidity meter, is a Beckman infrared analyzer which was used for the measurement of carbon dioxide concentration in the inlet and exit streams. The small high pressure manifold in the right of this photo is for the liquid nitrogen spray stream. Photo No. 1B shows the viewing side of the test skid. The test heat exchanger is located behind a pane of 1-inch bullet-proof glass located in the lower portion of the protective hood on top of the test skid. In the foreground of this photograph are high-pressure bottles used for instrument air and a high-pressure bottle used for the addition of carbon dioxide to the air stream. The tank insulated with glass wool blanket insulation, just visible behind the high-pressure bottles, is the coolant heat exchanger.

Photo No. 2 presents a close-up view of the gas stream flow control. Flow control for the air coolant and spray streams is accomplished with a choked

orifice preceded by a pressure regulator. The insulated line shown in this photo is a liquid nitrogen supply to coolant heat exchanger. It may be noted that the high-pressure gas lines and the liquid nitrogen supply enter through a small aperture in the wall of the test cell.

Photo No. 3 illustrates the high-pressure gas supply and liquid nitrogen supply for the test facility. The manifolds for the air and coolant stream are shown in this photo. As previously mentioned, the spray stream manifold is located inside the test cell.

Figure 1 is a flow sheet of the freeze-out test facility. This flow sheet indicates the location of all valves, controls, and measuring points.

Figure 2 is an assembly drawing of the test heat exchanger. This drawing shows the details of construction of the test heat exchanger including the method of support of the test heat transfer section and the connections for the air, coolant, and liquid nitrogen spray streams.

Figures 3, 4 and 5 present geometric details of the test heat transfer sections. These drawings indicate the location of measuring points along the test heat transfer sections and include data on tube clearance as well as the flow and heat transfer areas for the air and coolant streams.

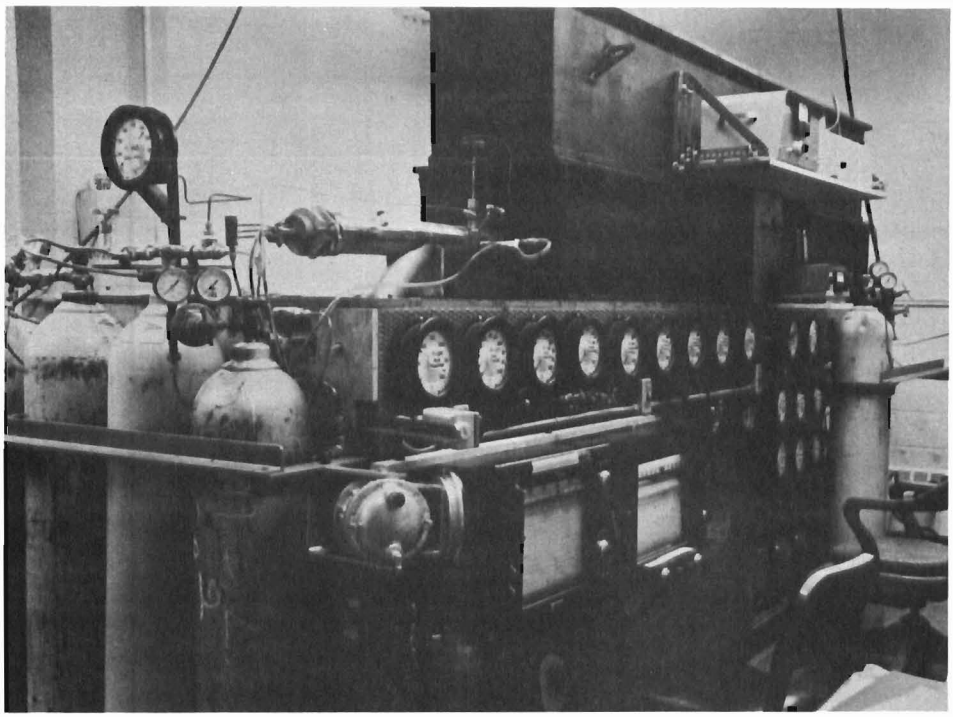

A. Instrumentation Side - System operation control and data read-out.

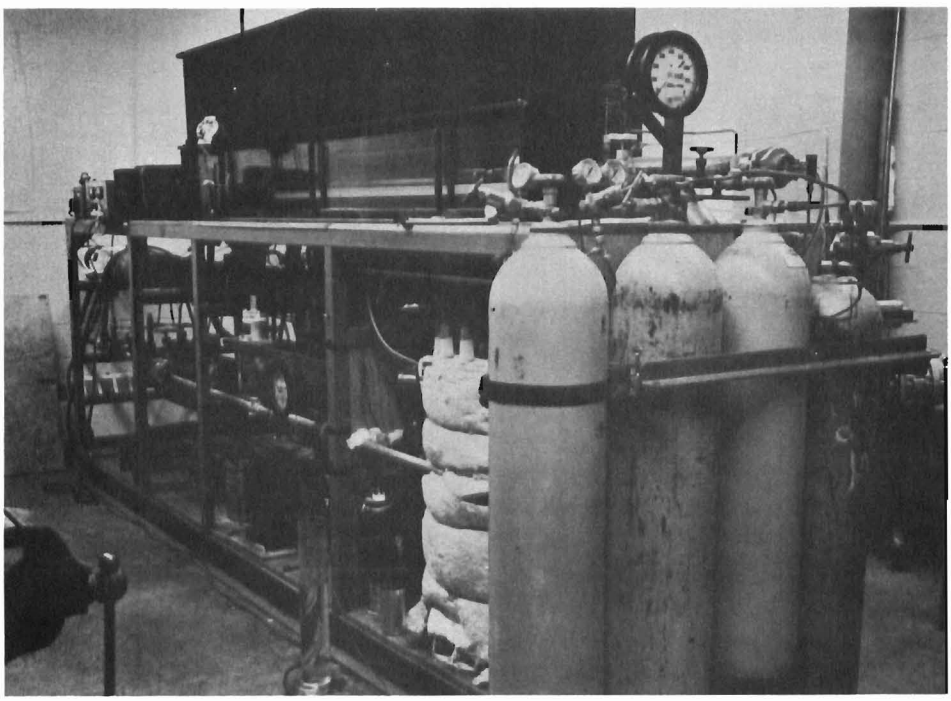

B. Test Heat Exchanger Viewing Side - Air, coolant and spray stream piping, water proportioning pump, coolant and spray heat exchanger.

PHOTO NO. 1 TEST EQUIPMENT SKID

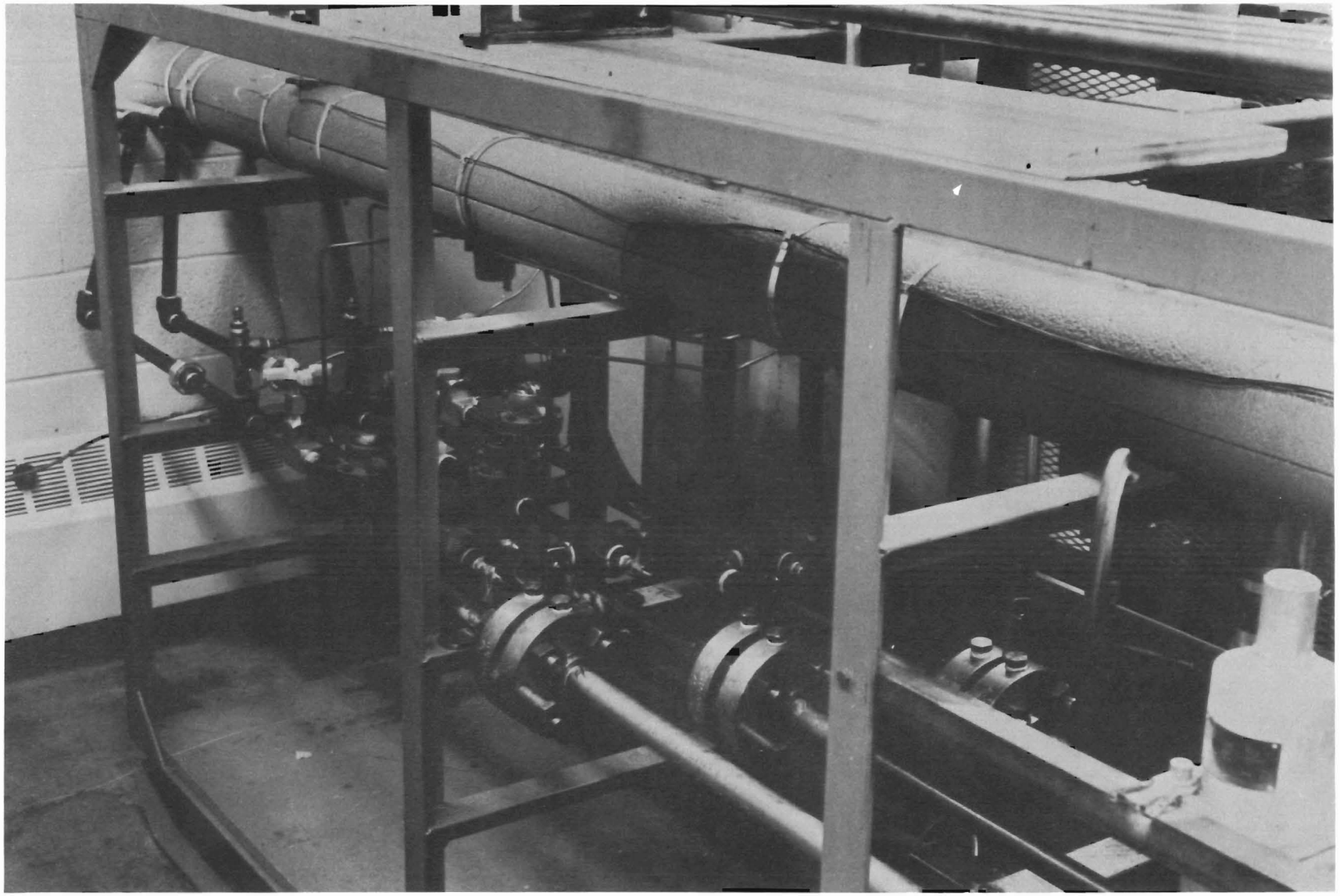

Pressure control stations and flow control orifices for air, coolant and spray streams.

PHOTO NO. 2 GAS STREAM CONTROL

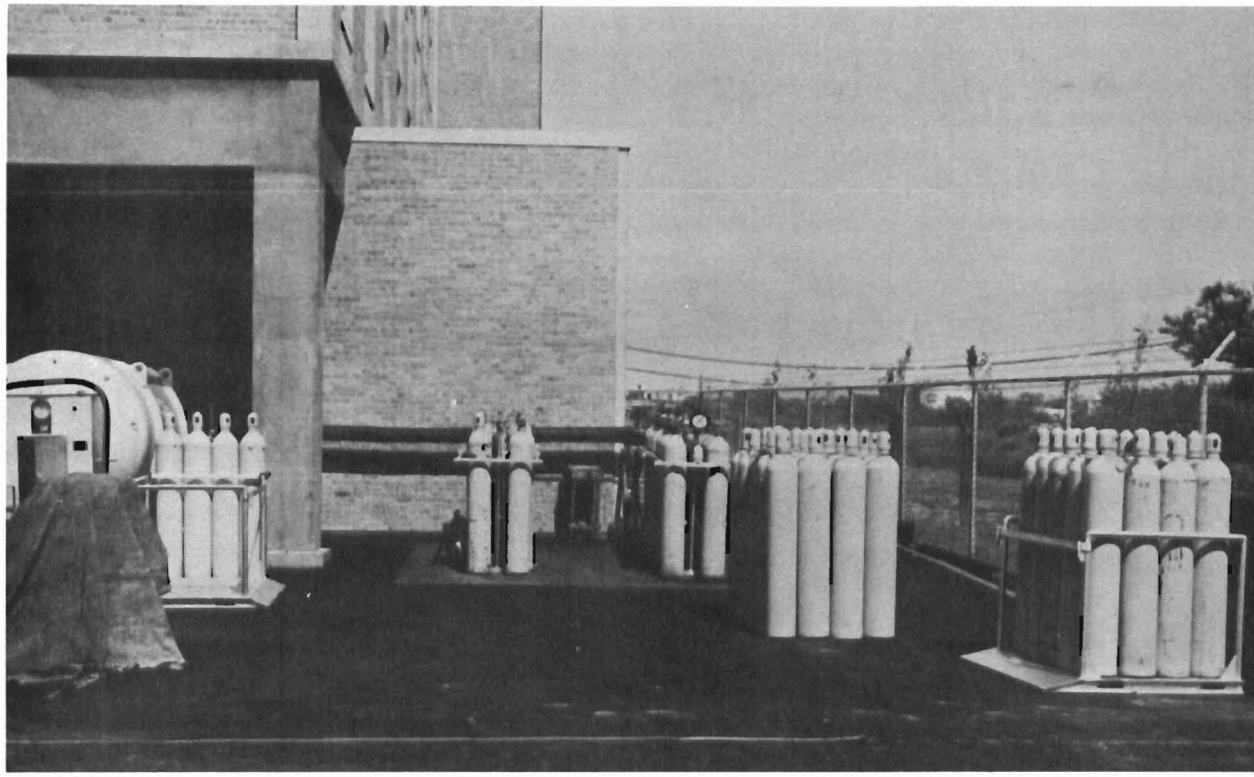

A. Liquid nitrogen storage tank, air and coolant stream manifolds and reserve high pressure bottles.

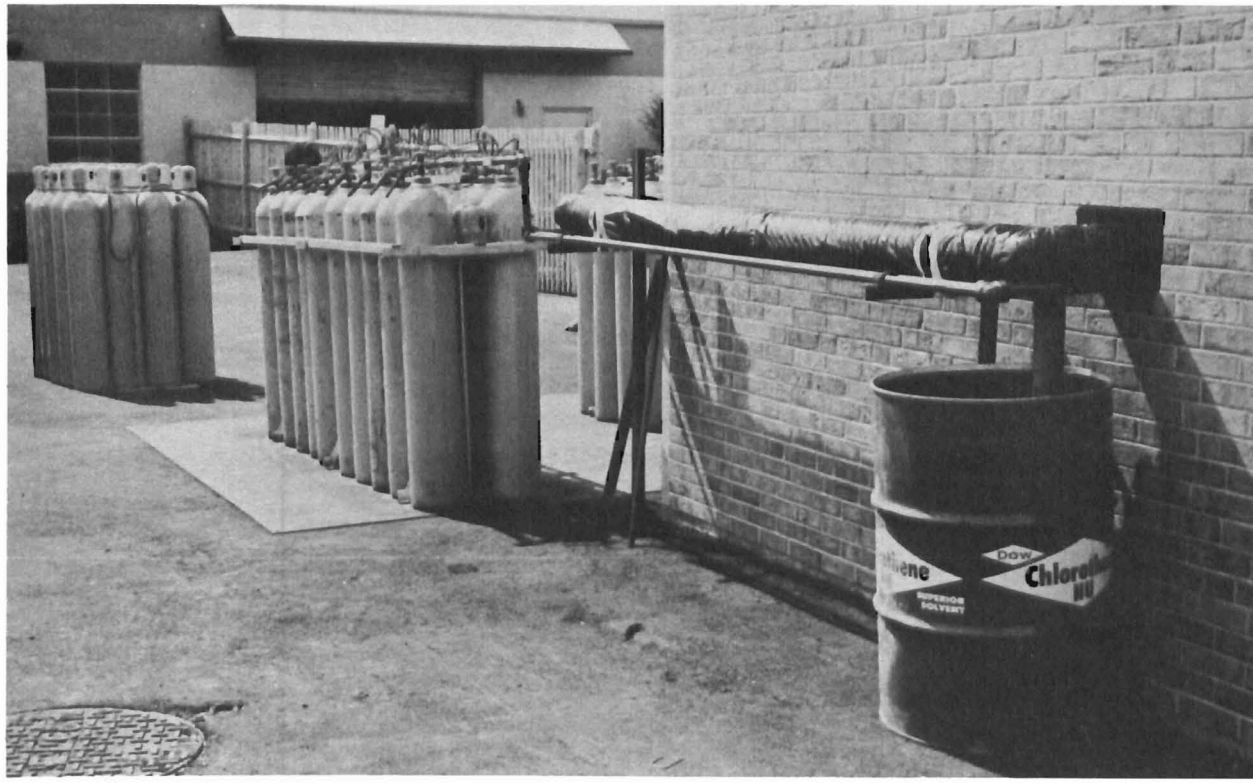

B. Air stream manifold, line feed-through to test skid, and 3-inch vent line catch tank.

PHOTO NO. 3 TEST FACILITY - LIQUID AND GAS SUPPLY

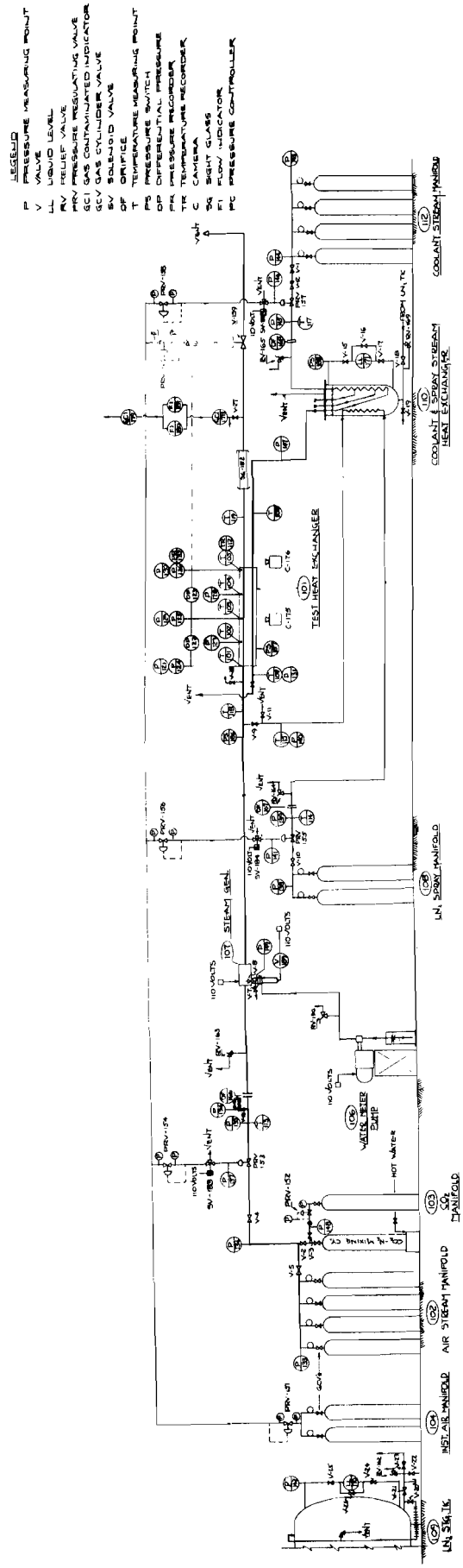

FIGURE 1 FLOW SHEET - FREEZE-OUT TEST FACILITY

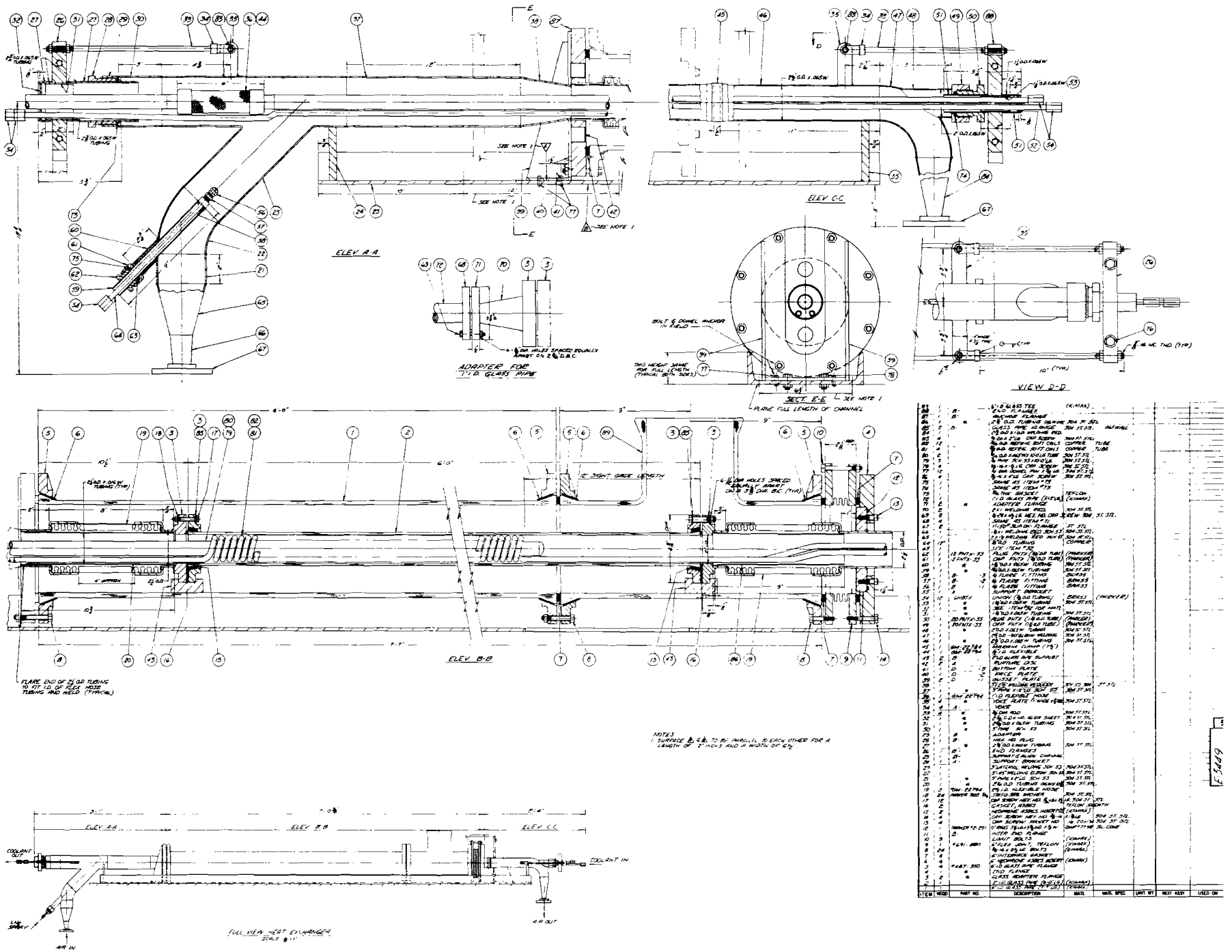

FIGURE 2 TEST HEAT EXCHANGER ASSEMBLY

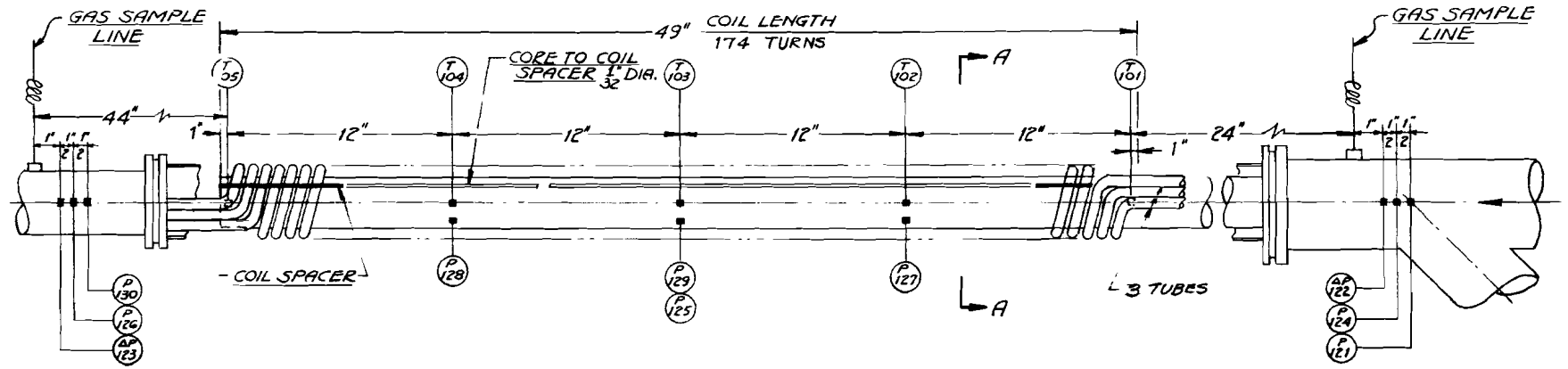

HEAT EXCHANGER DATA:

TUBE SIZE: 3/16" O.D. × .030 WALL, ANNEALED COPPER ,

TOTAL AIR SIDE SURFACE AREA: 1.76 FT.²

AIR TO COOLANT SURFACE AREA RATIO: 1.472

AIR SIDE FLOW AREA: .150 IN.²
.00104 FT.²

COOLANT SIDE FLOW AREA: .0379 IN.²
.000263 FT.²

AIR TO COOLANT - FLOW AREA RATIO: 3.96

δ - HALF CLEARANCE: .031 IN.

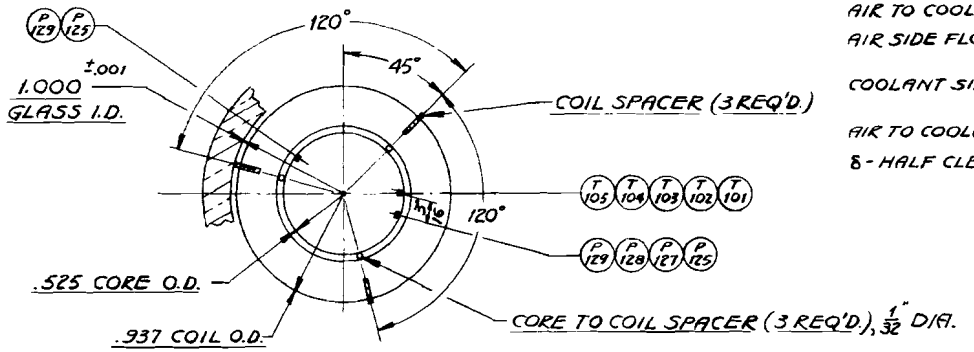

SECT. A-A

NOTES:

1. PRESSURE GAGE P-129 AND TRANSDUCER P-125 ARE CONNECTED TO A COMMON SENSE LINE. THIS SENSE LINE IS FOR REASONS OF RELIABILIT FED BY DOUBLE PNEUMATIC LEADS FROM THE TEST CORE.
2. 94% OF TUBE SPACES ARE BETWEEN .055" AND .070"

FIGURE 3 TEST HEAT TRANSFER SECTION DETAILS - 1-INCH SPIRAL CONFIGURATION

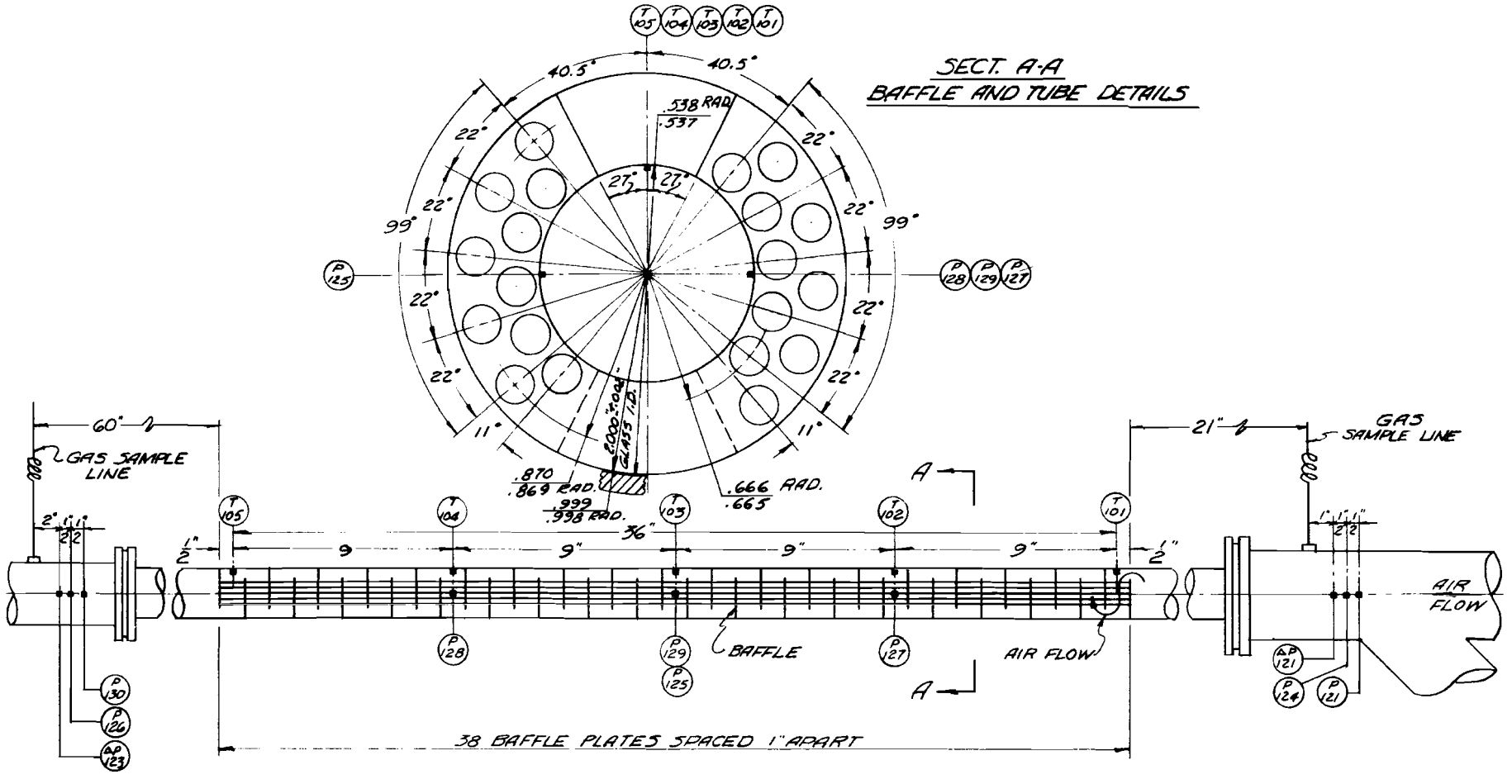

HEAT EXCHANGER DATA

1. TUBE SIZE: 3/16 O.D. X .032 WALL, HARD DRAWN COPPER.
2. TOTAL AIR SIDE SURFACE AREA: 30 FT^2
3. RATIO AIR TO COOLANT SURFACE AREA: 1.535
4. AIR SIDE FLOW AREA: .278 $IN.^2$ / .00193 $FT.^2$
5. COOLANT SIDE FLOW: .234 IN^2 / .00625 $FT.^2$
6. AIR TO COOLANT-FLOW AREA RATIO: 1.19
7. S-HALF CLEARANCE: .035 IN.

FIGURE 4 TEST HEAT TRANSFER SECTION DETAILS - 2-INCH BAFFLE CONFIGURATION

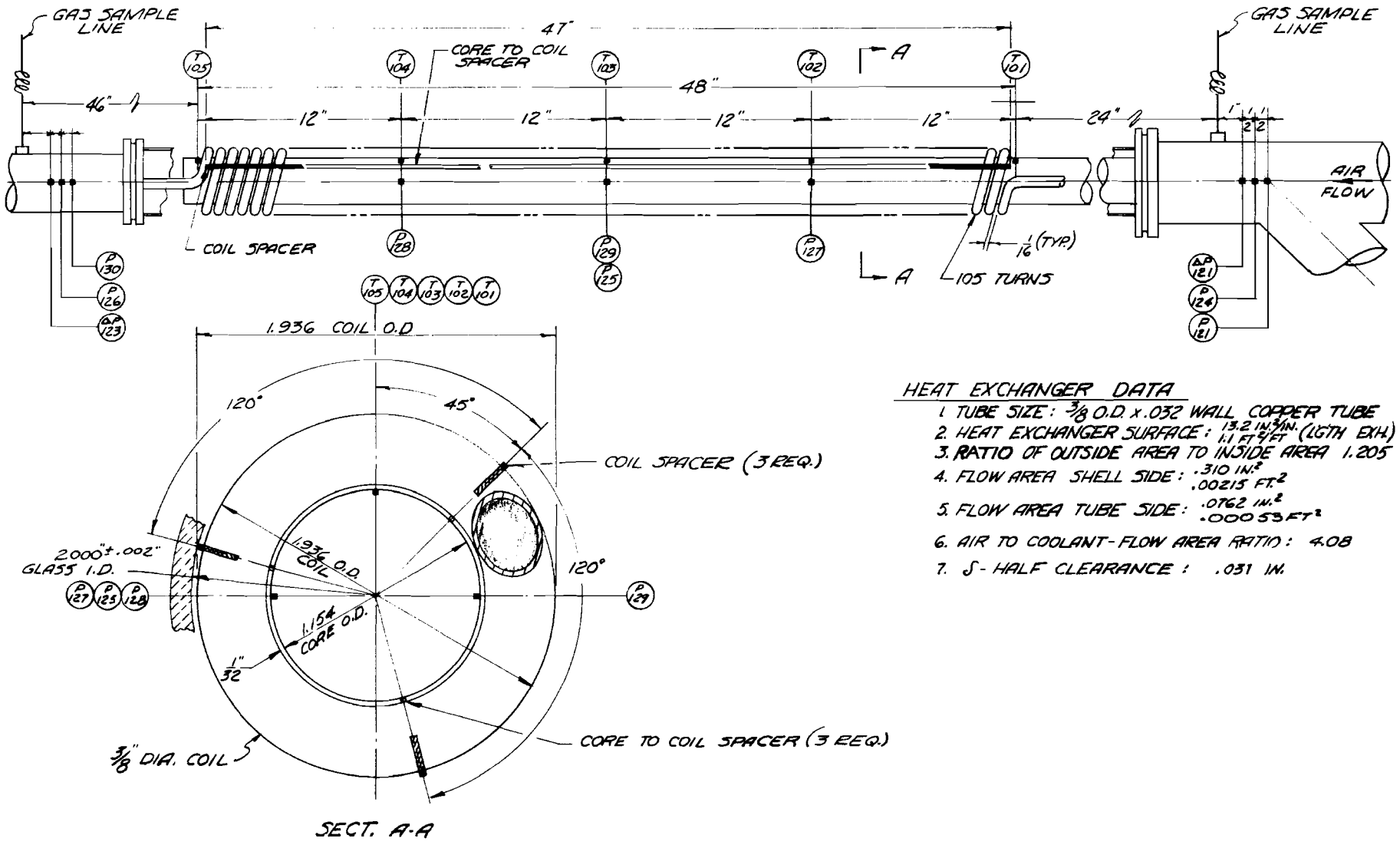

FIGURE 5 TEST HEAT TRANSFER SECTION DETAILS - 2-INCH SPIRAL CONFIGURATION

APPENDIX 8

PHOTOGRAPHS OF TYPICAL

FROST FORMATION

TABLE OF CONTENTS

PHOTOGRAPHS OF TYPICAL FROST FORMATION

The photographs in this Appendix are presented to supplement the photographic data presented in the main body of the report.

We have chosen to represent a rather extensive coverage of test F-17 which was typical of the performance of the one-inch spiral configuration when mass transfer was the primary mode of contaminant deposition. In addition, photographs are included showing the performance of the one-inch spiral configuration in the presence of nucleation due to both liquid nitrogen spray and a high gas-wall ΔT. Photos of the baffled heat exchanger operating under both mass transfer conditions and bulk stream nucleation are also presented.

Since the photographic coverage of F-17 is relatively extensive, it is pertinent to summarize the test conditions and present a brief synopsis of the sequence of events during the test. Test F-17 was performed under the following conditions:

1. Air Stream.

   a. Mass velocity: 100 lb/sec-ft^2.
   b. Mass flow rate: .104 lb/sec.
   c. Inlet pressure: 300 psig.
   d. Velocity: 58 Ft/sec (Nominal)
   e. Water concentration: .025%.
   f. Carbon dioxide concentration: .05%.

2. Coolant Stream.

   a. Mass flow rate: .052 lb/sec.
   b. Stream pressure: 625 psig (nominal).
   c. Inlet temperature: 150°R.

The total duration of test F-17 was 27¼ minutes. The air stream and carbon dioxide contaminate were established at rated flow in approximately one minute after the start of the test. At about six minutes of test time the CO_2 frost becomes evident to the cold section of the heat exchanger. Contamination of the air stream with water was initiated at 15-3/4 minutes and was measured at the heat exchanger inlet gas sample tap at 18 minutes. A stable maximum water concentration was achieved at 22 minutes and the pressure drop was 230 psi at 26¼ minutes. The test was concluded at 27¼ minutes of test time. Photographs of the frost distribution during the performance of the test are shown in Photos 1 through 5. Photos 6 through 12 are close-up which show the appearance of the frost over the entire heat exchanger immediately after the conclusion of the test.

Photo 13 presents an overall view of the 1" spiral test heat exchanger near the conclusion of the test in which nucleation was induced by spraying liquid nitrogen into the inlet air. In this test, V-9, a fairly high saturation ratio was obtained in the bulk stream by chilling the inlet air to about 390°R with a liquid nitrogen stream. As a result, nucleation proceeded in the direction of a large number of very small particles which were distributed fairly uniformly throughout the length of the test heat exchanger.

Photo 14 presents an overall view of the 1" spiral test heat exchanger near the

conclusion of the high gas-wall ΔT test. In this test, F-12 a gas wall ΔT of the order of 108° R was achieved at the warm end of the heat exchanger by unbalancing the heat exchanger with excess coolant flow. This technique results in a large ΔT at the warm end and a relatively small ΔT at the cold end of the test heat exchanger. The photograph shows that nucleation freeze-out of water was apparent in the region 6 to 12 inches. Prior to the 6-inch point, water freeze-out occurred by mass transfer. In this region the bulk stream saturation ratio, although increasing, had not yet reached a level high enough to "trigger" nucleation. In the region downstream of 12 inches, the frost formation is due to the "mass transfer" deposition of carbon dioxide.

Photo 15 presents an overall view of the baffled heat exchanger in which the tubes are arranged in a staggered array during a test in which the contaminate deposition was primarily by mass transfer. The two zones of frost, i.e., water frost and carbon dioxide frost are quite evident in this photograph.

Photo 16 presents an overall view of the baffled heat exchanger during a test in which nucleation was induced by liquid nitrogen spray. As in the case of V-9 a high saturation ratio was achieved favoring the formation of small particles and the contaminant deposition seems to be reasonably well distributed through the test heat exchanger.

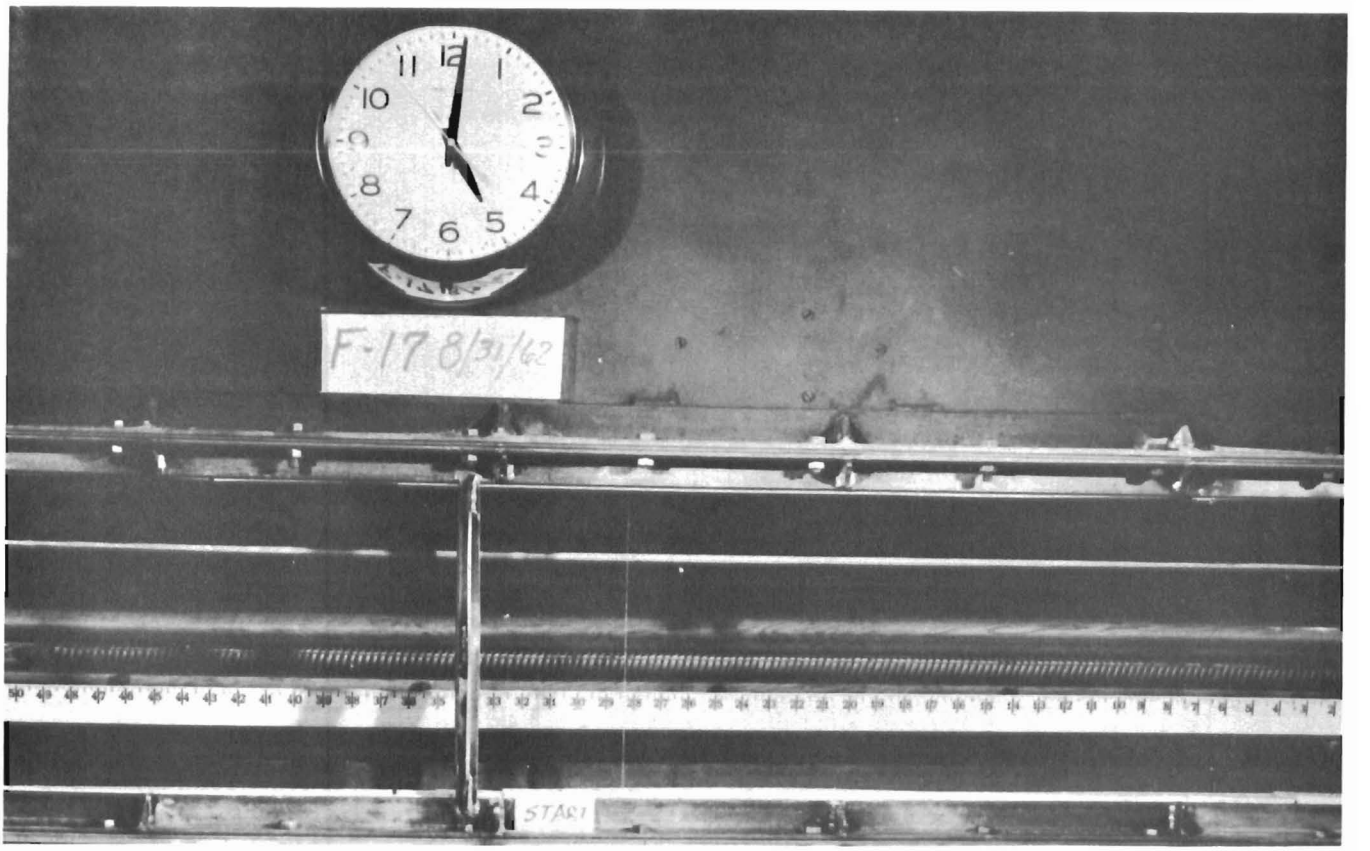

PHOTO NO. 1 TEST F-17 - CLEAN HEAT EXCHANGER AT START OF TEST
TIME: 0 min - 53 sec

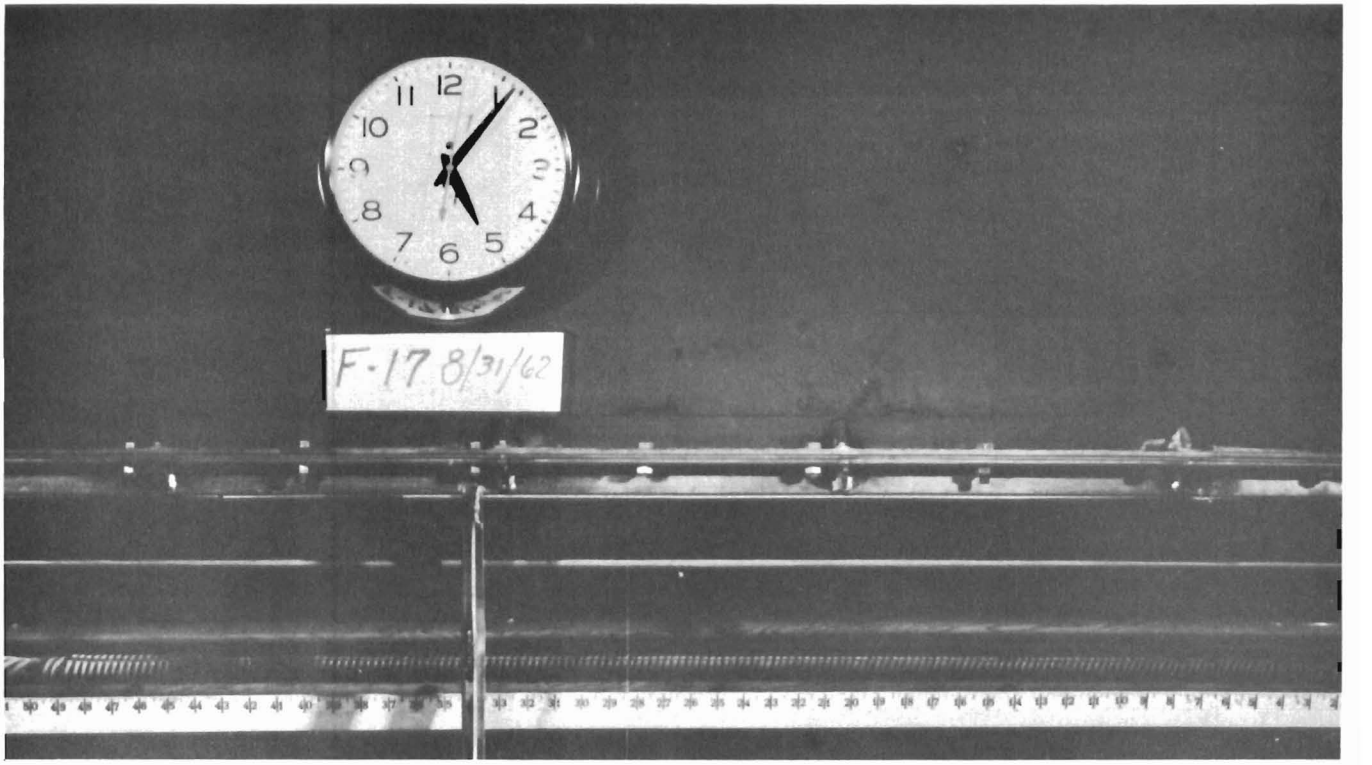

PHOTO NO. 2 TEST F-17 - BEGINNING OF CARBON DIOXIDE FROST FORMATION
45-48 INCH REGION (TIME: 6 min - 0 sec)

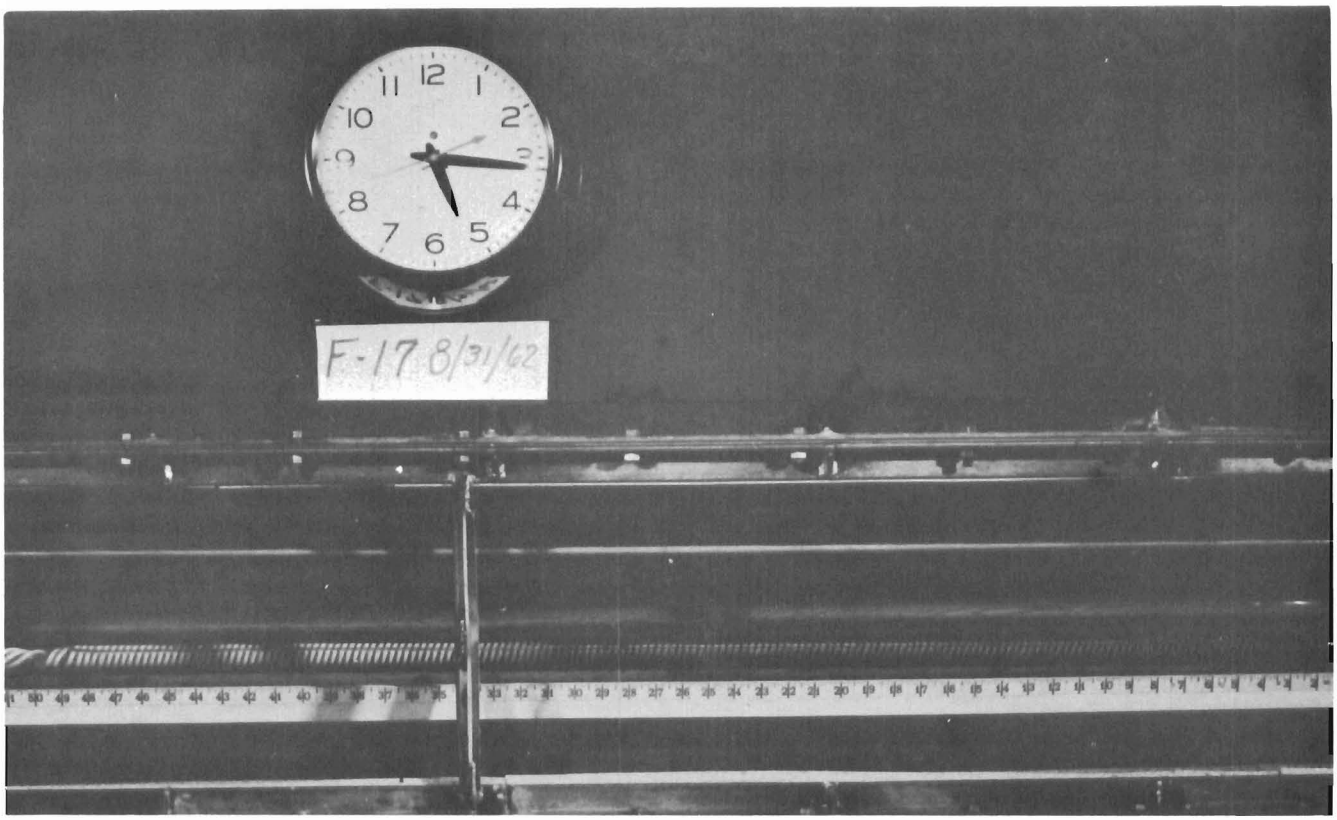

PHOTO NO. 3 TEST F-17 - CARBON DIOXIDE FROST ACCUMULATION IN 31-48 INCH REGION AT TIME WHEN HUMIDIFICATION OF AIR STREAM WAS INITIATED (TIME: 15 min - 40 sec)

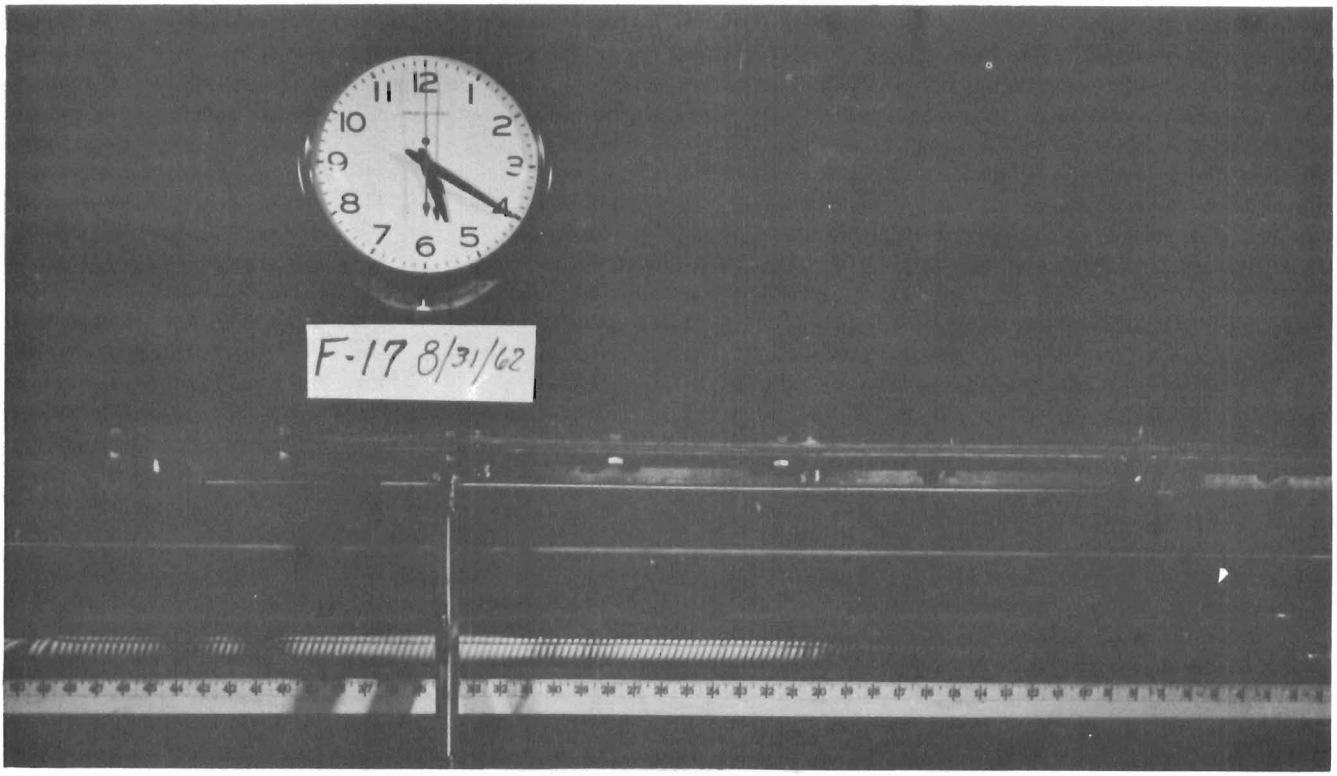

PHOTO NO. 4 TEST F-17 - CARBON DIOXIDE ACCUMULATION 31-48 INCH REGION WATER FROST ACCUMULATION 25-30 INCH REGION TIME: 20 min - 0 sec

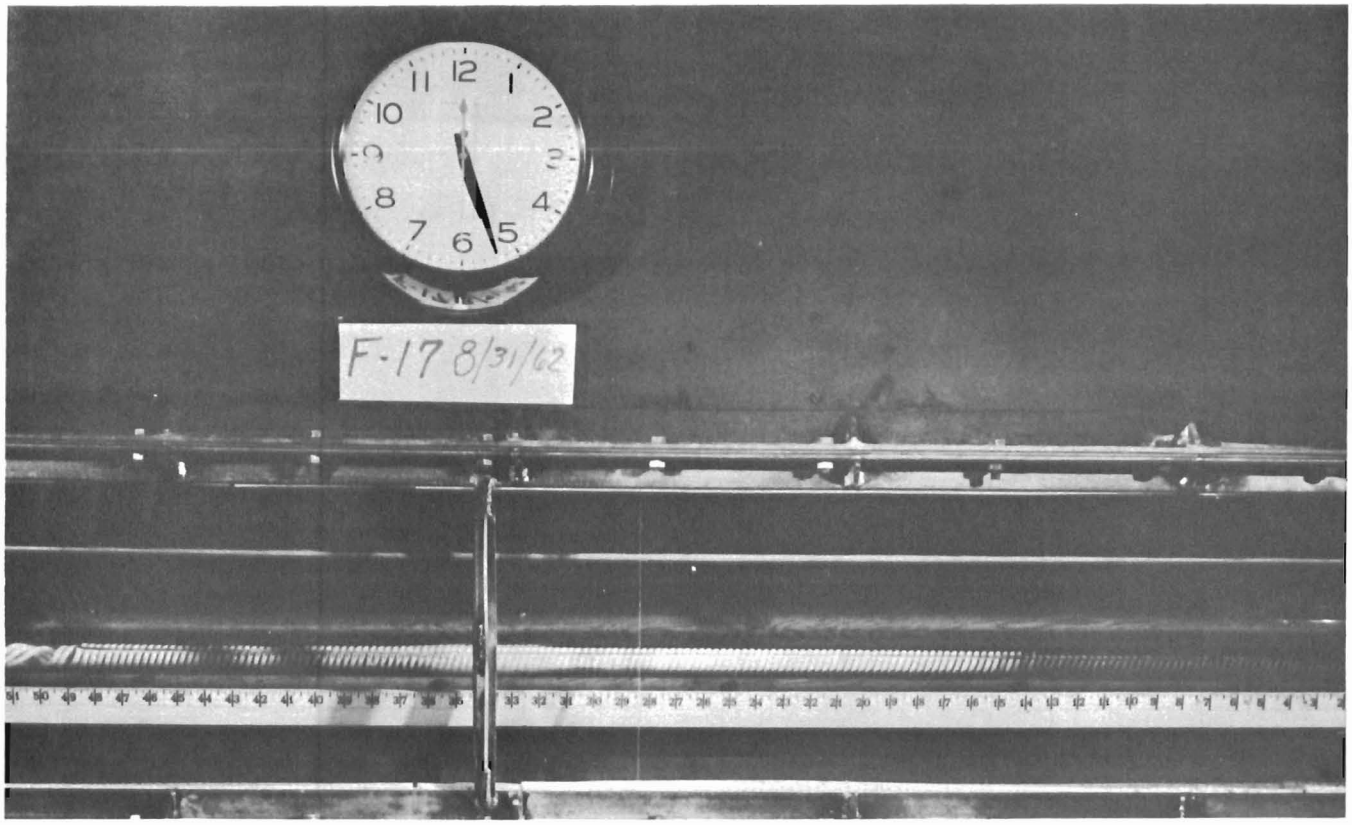

PHOTO NO. 5 TEST F-17 - CARBON DIOXIDE FROST ACCUMULATION IN 31-48 INCH REGION WATER FROST ACCUMULATION IN 14-30 INCH REGION
TIME: 26 min - 30 sec

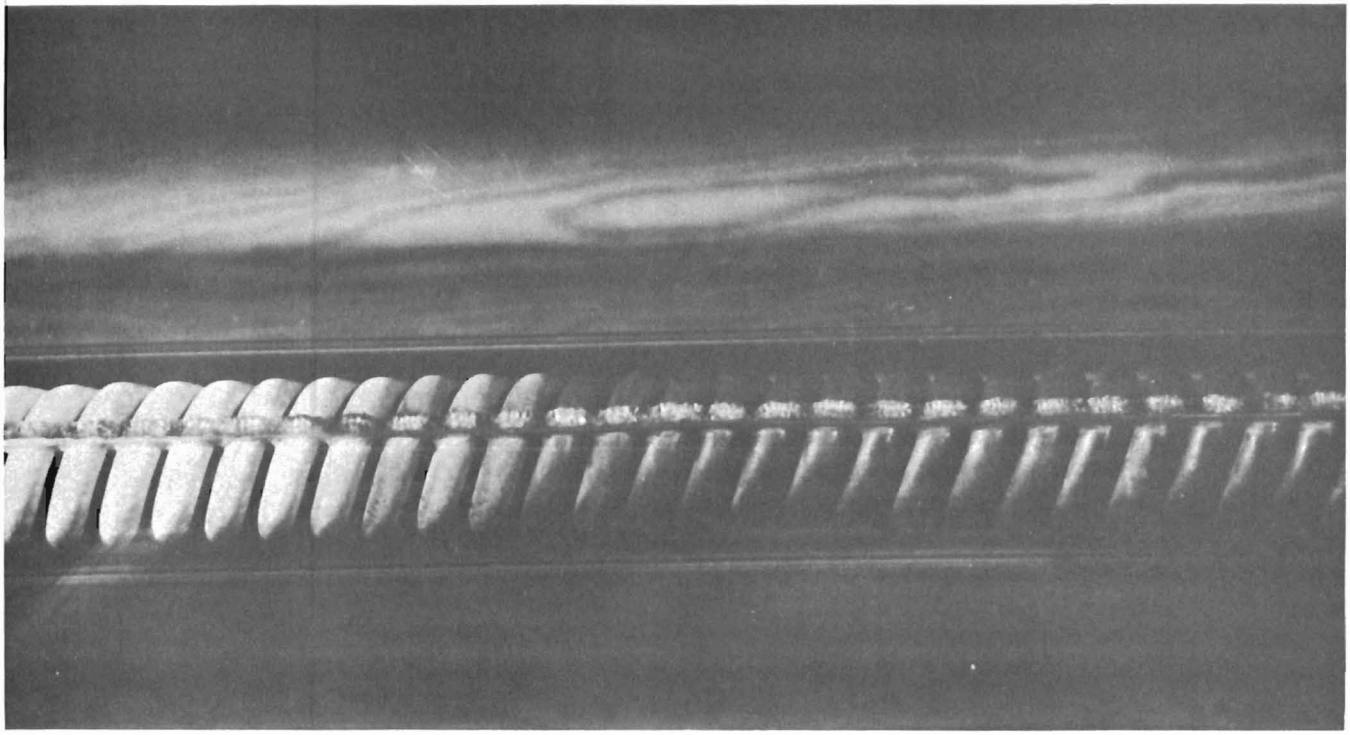

PHOTO NO. 6 TEST F-17 - WATER FROST IN REGION 7-15 INCHES
TIME: 31 min - 0 sec

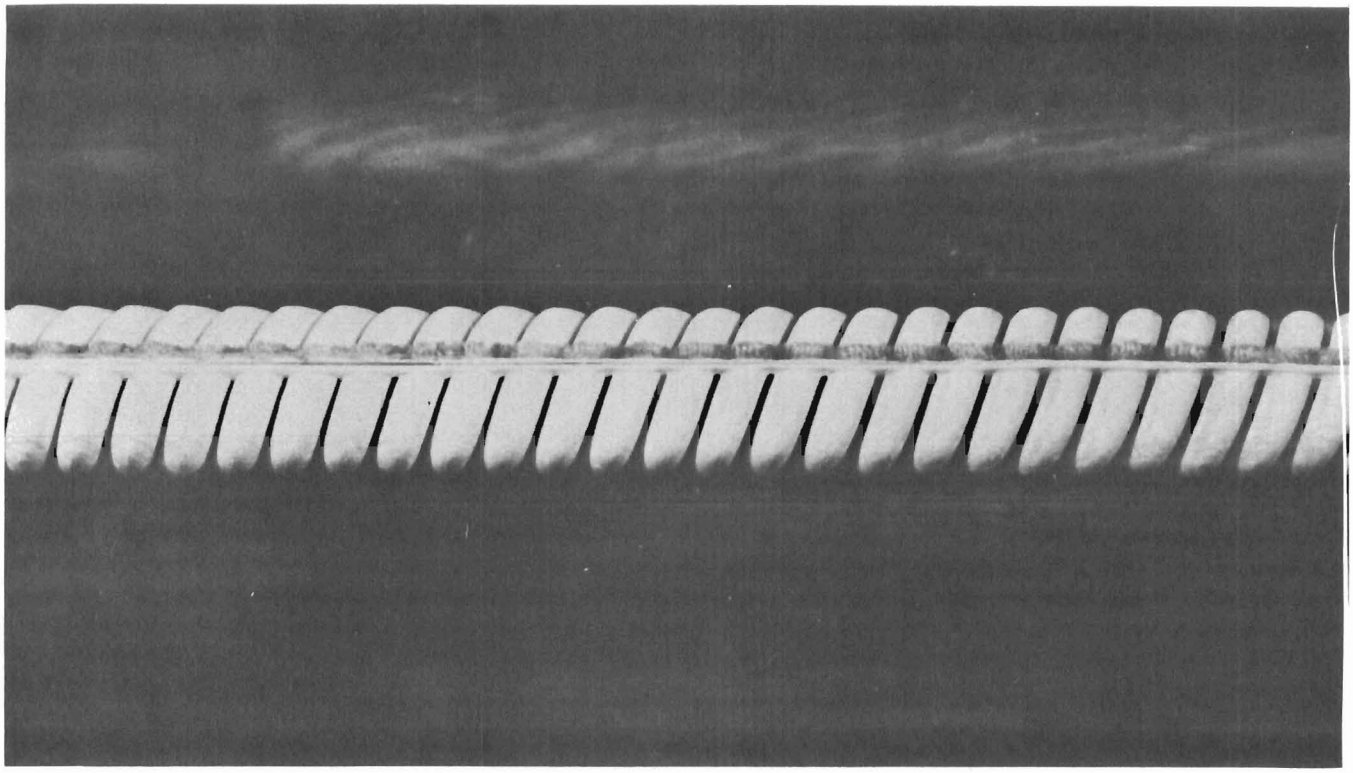

PHOTO NO. 7 TEST F-17 - WATER FROST IN REGION 14-22 INCHES
TIME: 32 min - 0 sec

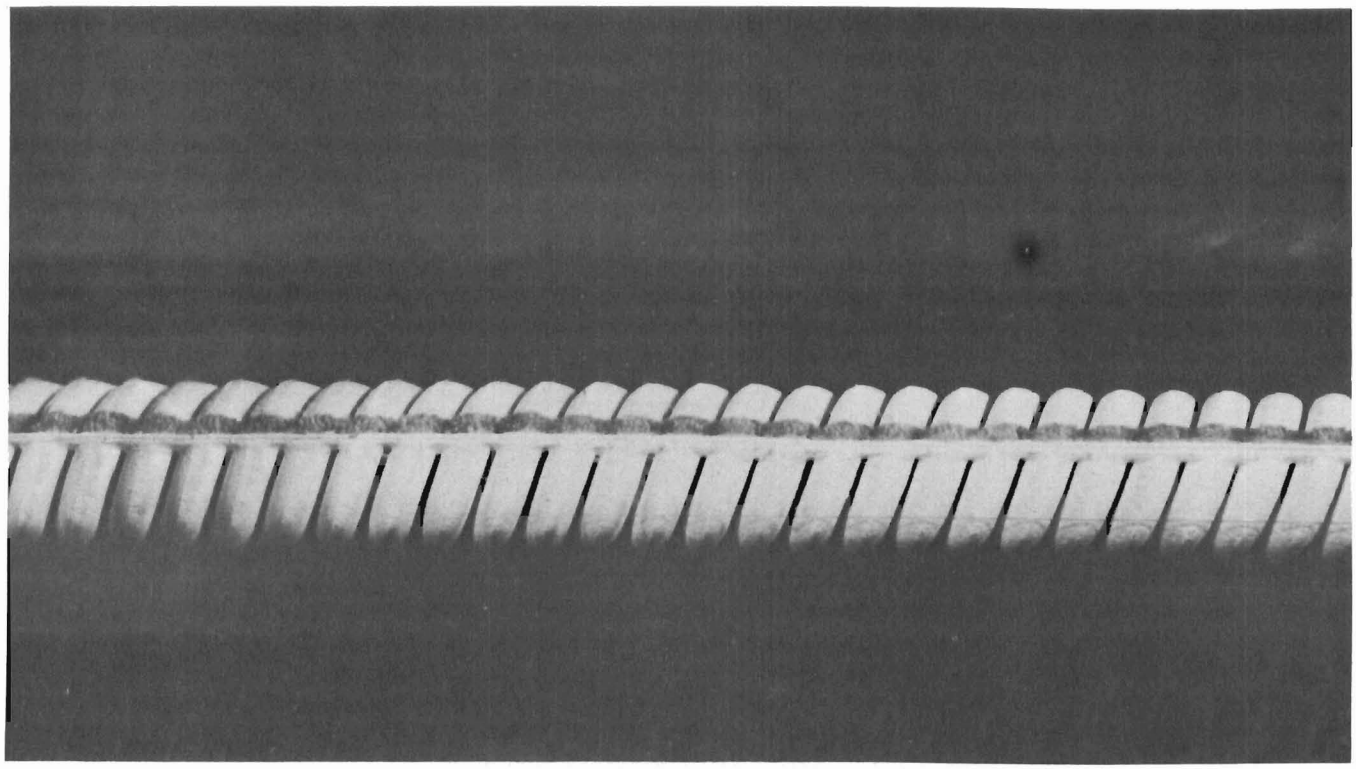

PHOTO NO. 8 TEST F-17 - WATER FROST IN REGION 21-29 INCHES
TIME: 32 min - 15 sec

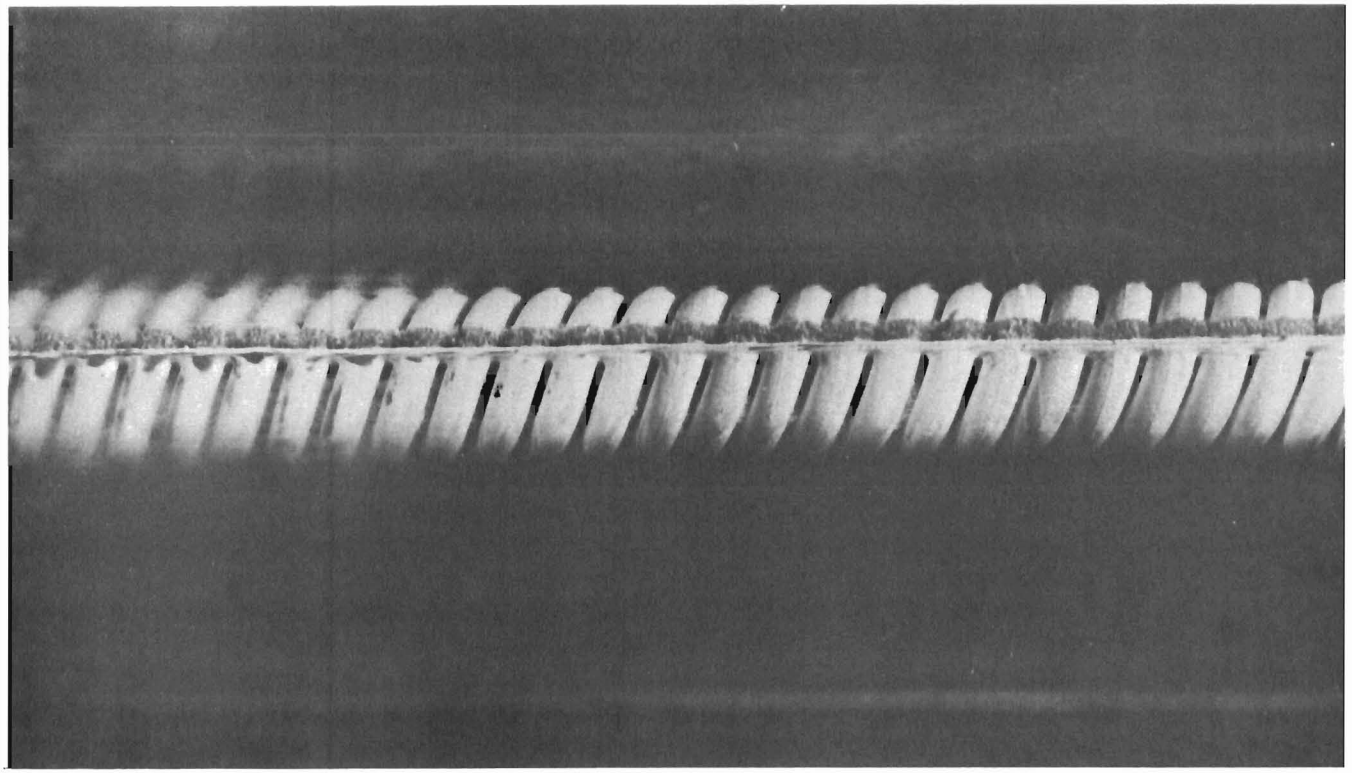

PHOTO NO. 9 TEST F-17 - WATER FROST IN REGION 27-31 INCHES (RIGHT)
CARBON DIOXIDE FROST IN REGION 31-35 INCHES (LEFT)
TIME: 32 min - 45 sec

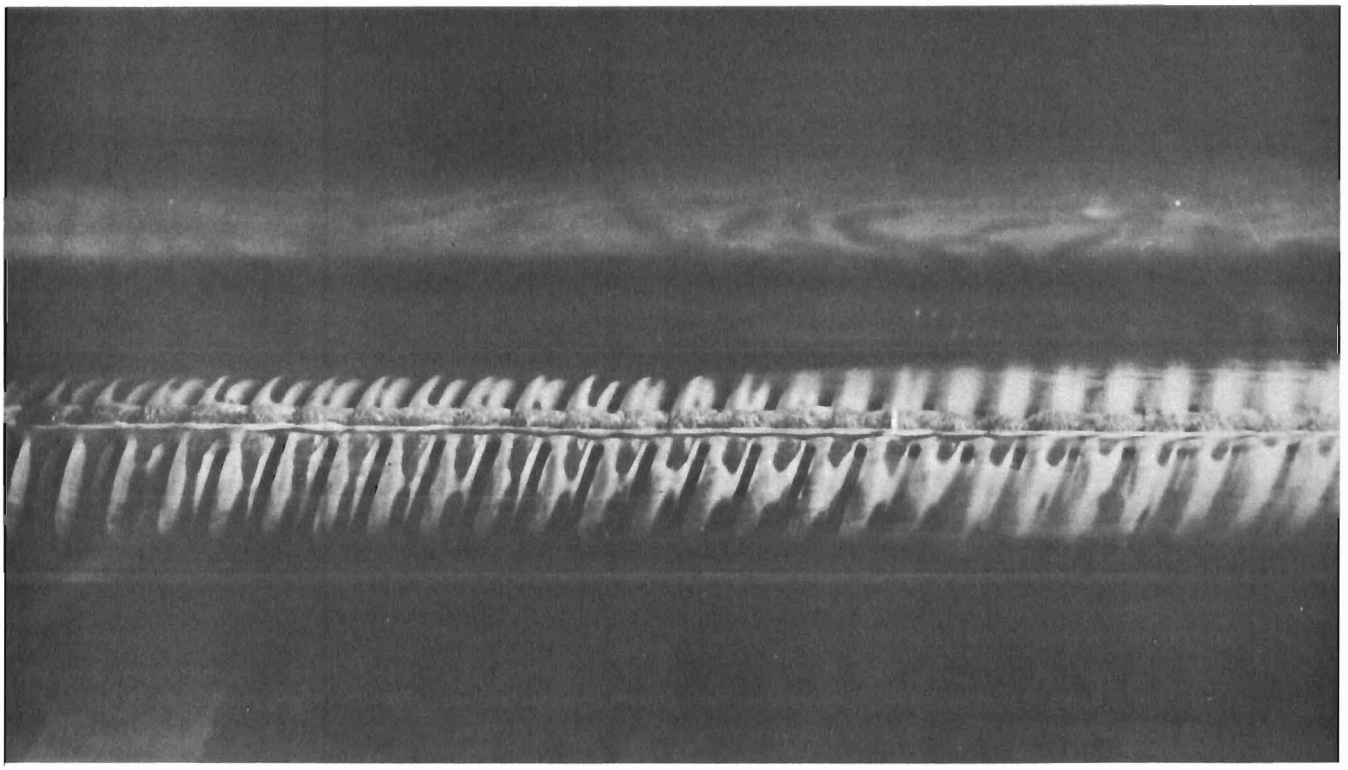

PHOTO NO. 10 TEST F-17 - CARBON DIOXIDE FROST IN REGION 33-41 INCHES
TIME: 33 min - 45 sec

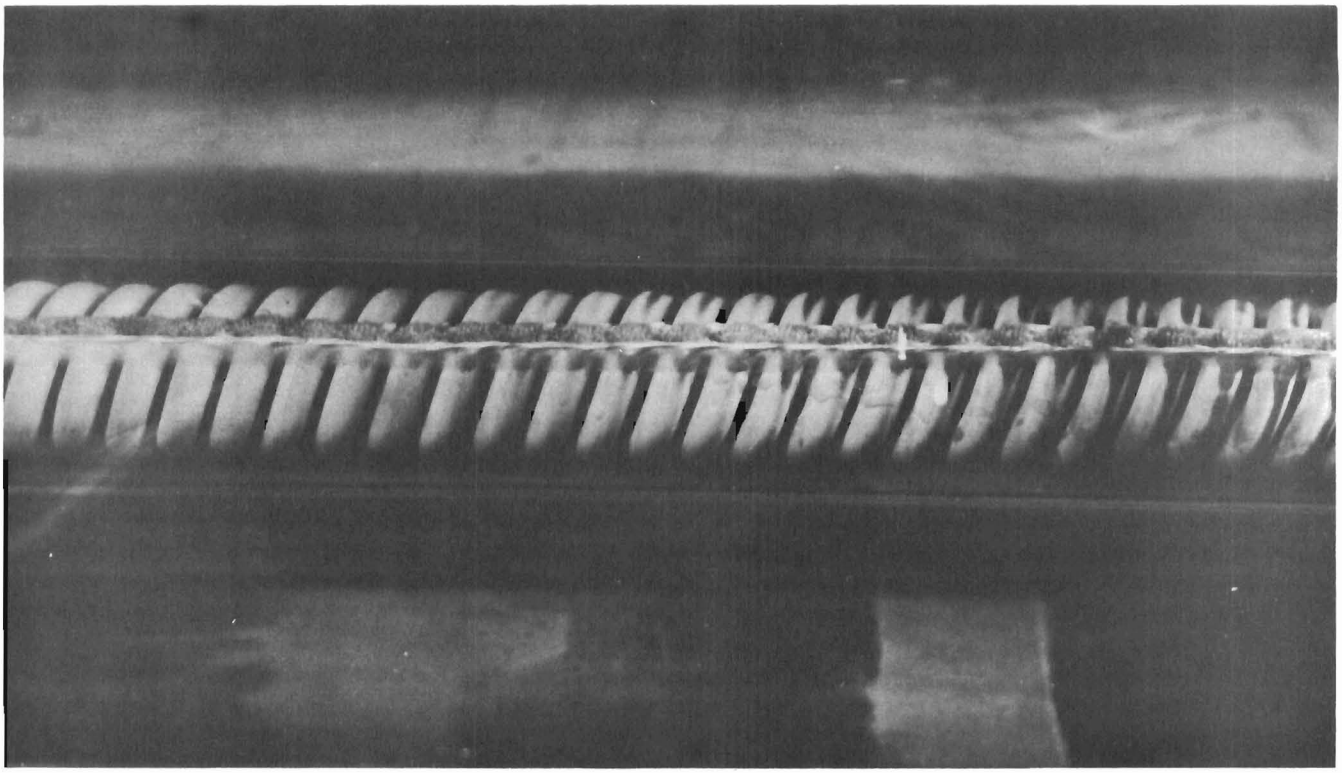

PHOTO NO. 11 TEST F-17 - CARBON DIOXIDE FROST IN REGION 39-47 INCHES
TIME: 34 min - 30 sec

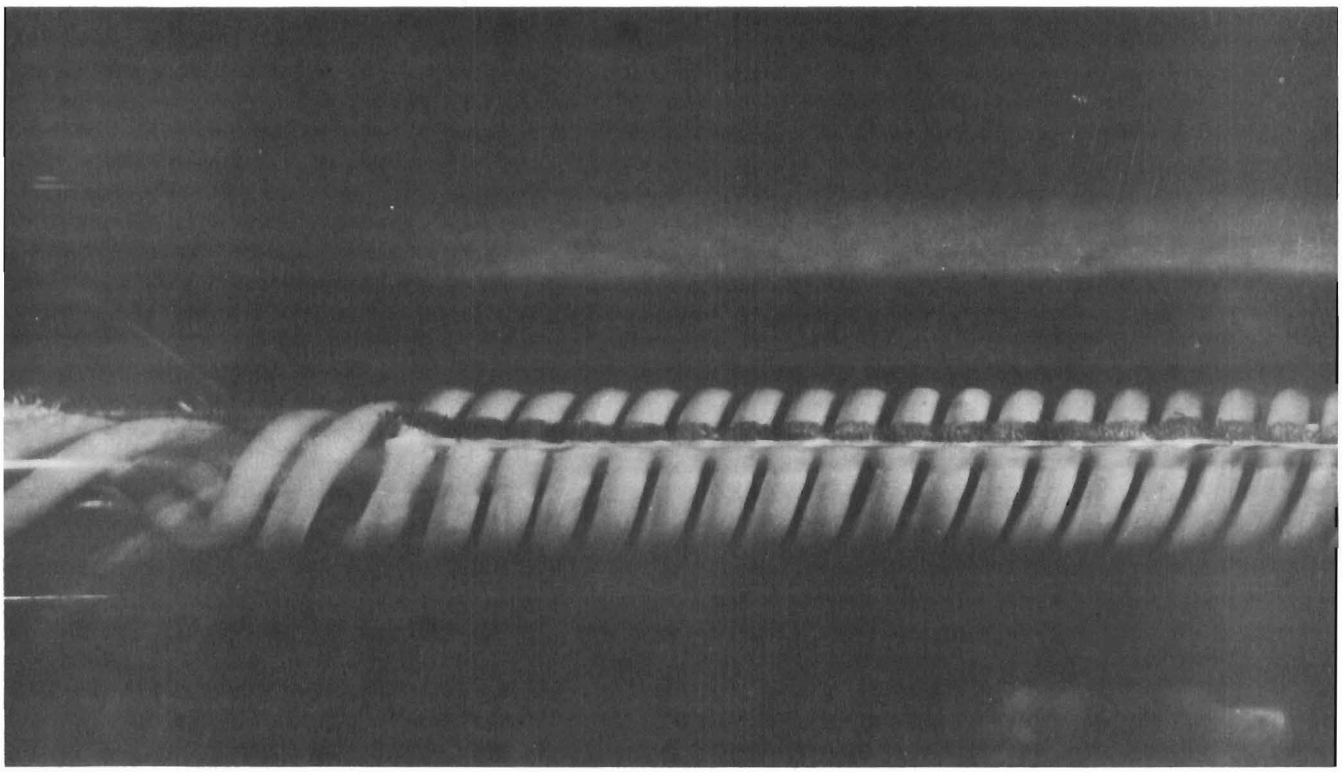

PHOTO NO. 12 TEST F-17 - CARBON DIOXIDE FROST IN REGION 44-52 INCHES
TIME: 35 min - 30 sec

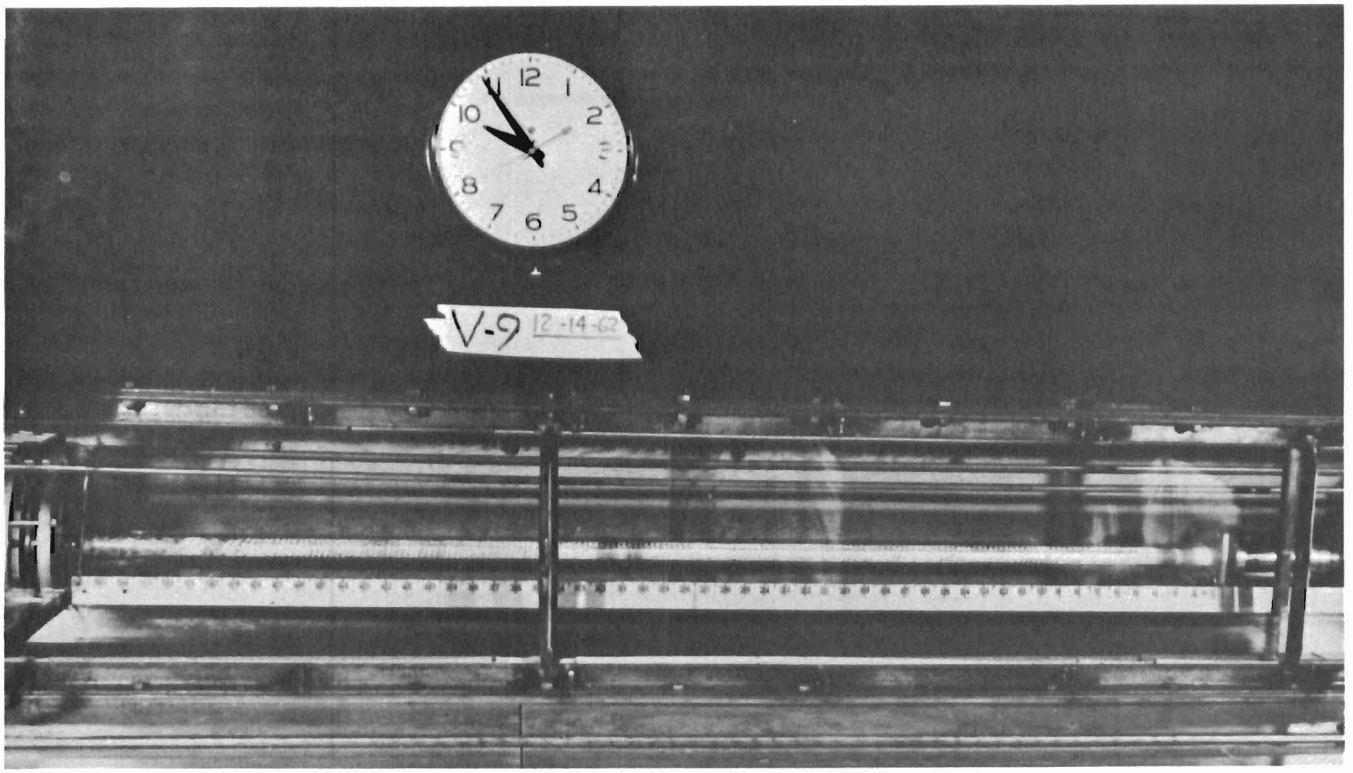

PHOTO NO. 13 OVERALL VIEW OF LN_2 SPRAY FROST FORMATION
TEST V-9 1-INCH SPIRAL

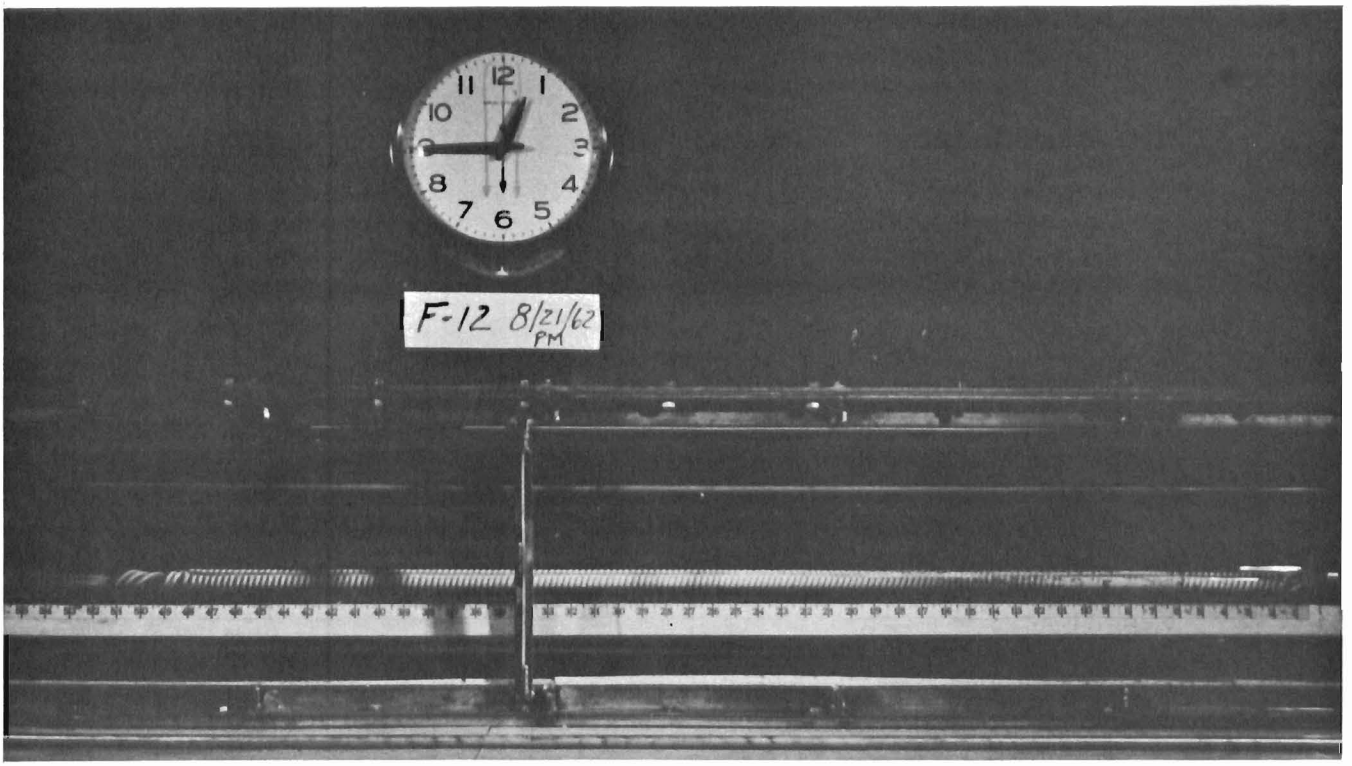

PHOTO NO. 14 OVERALL VIEW OF HIGH GAS-WALL ΔT FROST FORMATION
TEST F-12 1-INCH SPIRAL

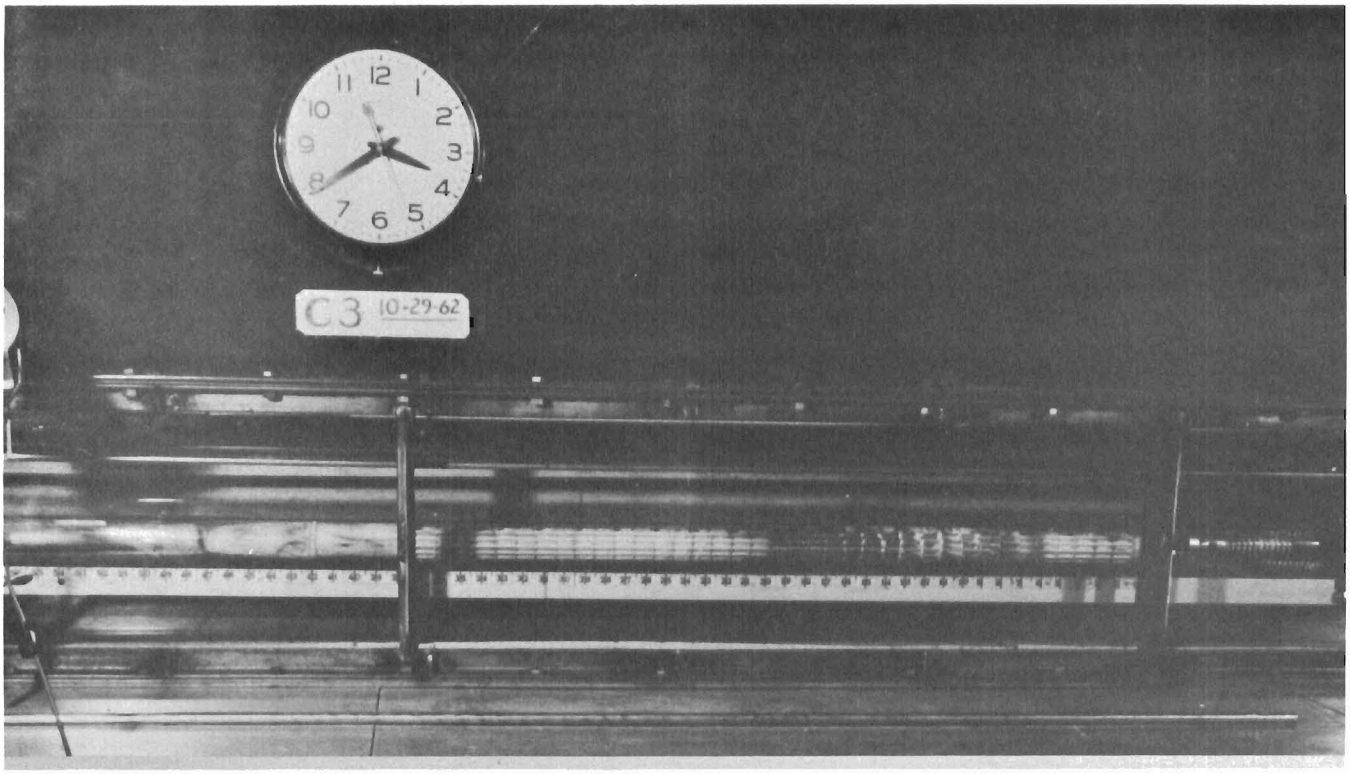

PHOTO NO. 15 OVERALL VIEW OF MASS TRANSFER FROST DEPOSITION TEST C-3 2-INCH BAFFLE

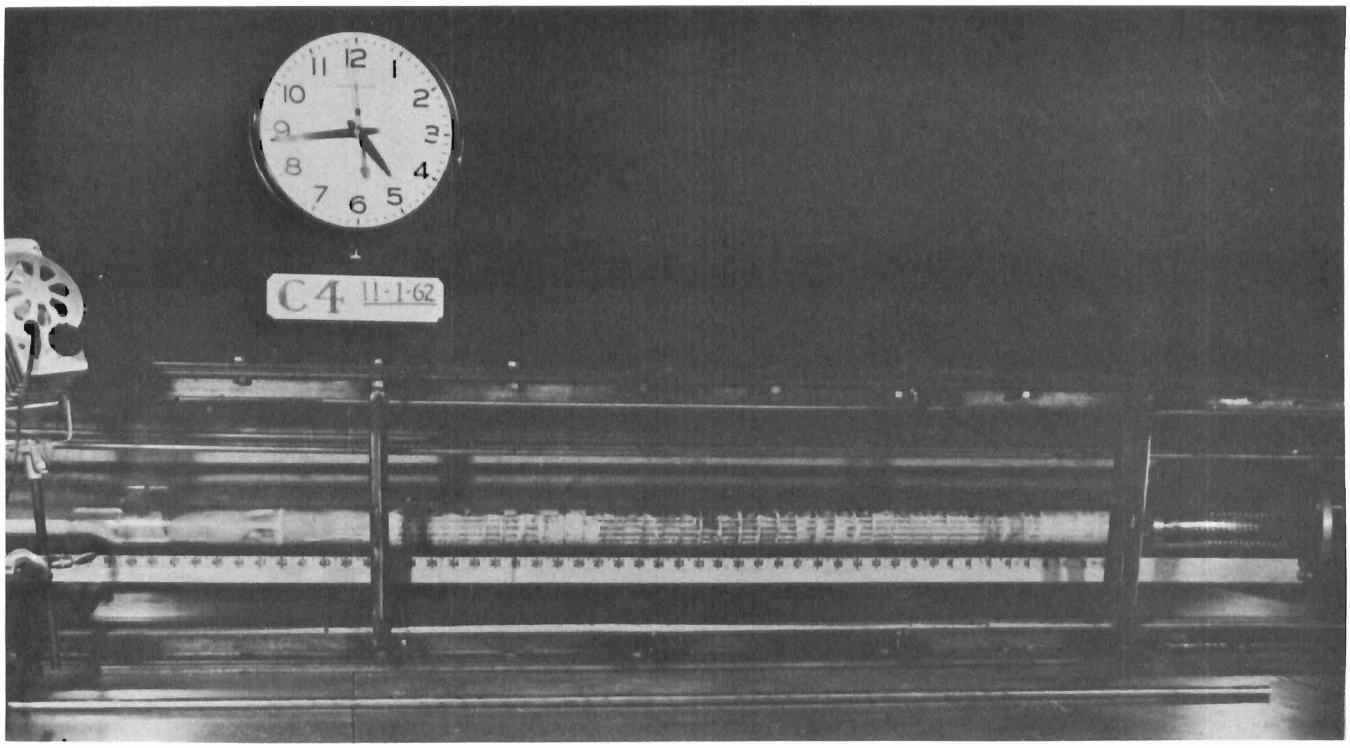

PHOTO NO. 16 OVERALL VIEW OF LN_2 SPRAY FROST FORMATION TEST C-4 2-INCH BAFFLE

APPENDIX 9

EXPERIMENTAL MEASUREMENT OF FROST THICKNESS AND DENSITY FOR MASS TRANSFER FROST DEPOSITION

TABLE OF CONTENTS

EXPERIMENTAL MEASUREMENT OF FROST THICKNESS AND DENSITY FOR MASS TRANSFER FROST DEPOSITION

For tests in which mass transfer governed frost deposition, the frost was almost entirely concentrated on the coolant tubes. At any given axial location, the frost thickness around the tubes appeared to be reasonably uniform. Therefore, since the geometry of the frost layer was regular, a meaningful frost thickness could be determined as a function of axial position from photographs of the frost formation. This thickness data could be used in conjunction with contaminant "hold up" data to determine the mean density of mass transfer frost deposition.

Similar techniques could not, without great difficulty, be applied to nucleation frost formation, since the irregular nature of the frost formation prevented any reasonable estimates of frost thickness and volume.

1. Frost Thickness Measurements

Frost thickness measurements were obtained from close-up photos similar to those presented in Appendix 8. After enlargement the resulting photos were approximately 1 1/2 times actual size and showed about a 4" length of heat exchanger. The magnification factor was determined from the distance occupied by four tubes in the photograph compared to the known average distance for the same number of tubes.

The actual tube spacings were measured with thickness gauges prior to performing the tests. The average of all readings resulted in tube spacing of .065" for clean heat exchangers. As the frost accumulates on the tubes the spacing decreases.

Frosted spacing was measured at every fourth tube shown in the frost photographs to a reading accuracy of about .1 mm (.004 in) through use of a Bausch & Lomb optical measuring magnifier. These measurements were corrected for the photomagnification to determine an actual spacing. The frost thickness is one-half the clean tube spacing minus the frosted spacing.

A plot of frost thickness versus heat exchanger location is presented in Figure 1 for Test F-17. This profile was obtained from enlarged versions of the close-up photos shown in Appendix 8. Figures 2 and 3 present composite curves showing frost profiles at various times during the course of tests V-5 and V-7. The F-17 and V-5 test data is for water frost. The data shown for test V-7 is for carbon dioxide frost.

2. Frost Density Determination

Frost volume was obtained from curves of frost thickness versus length such as those shown in Figures 1, 2 and 3. In obtaining the frost volume it was assumed that the frost was distributed uniformly around the tubes of the heat exchanger, at any given axial location. The frost volume per unit heat

exchanger length, at any location, could readily be determined from frost thickness and heat exchanger surface geometry. Total frost volume was obtained by numerically integrating the frost volume per unit length over the frost zone.

The total mass of contaminant deposited on the heat exchanger surfaces was computed from the inlet and outlet concentrations, the time interval from the start of contaminant flow and the air stream flow rate. The inlet and outlet contaminant concentrations were measured with the water and carbon dioxide gas analyzers. Zero time for water addition was generally taken at the point at which the humidity meter had achieved 63% of the steady state humidity rating. For tests V-5, F-17 and V-2 these times were approximately 41, 18 and 14 minutes respectively. For the carbon dioxide contaminant deposition test, V-7, zero time for contaminant deposition was taken at the time at which the heat exchanger had achieved near steady state temperature conditions. This time was estimated to be 5 minutes for test V-7.

Mean frost density for either water or carbon dioxide was obtained by dividing the contaminant hold-up mass by the total frost volume of that contaminant.

The results obtained are tabulated below. In this tabulation the test times for the start of contaminant deposition and the test times for the heat exchanger plug-up are presented for reference to the times at which the density determinations were made.

FROST DENSITY DATA

Test	Contaminant	Start Contaminant Deposition (min)	Heat Exchanger Plug-up (min)	Density Determination (min)	Frost Density lb/ft^3	gm/cc
F-17	H_2O	18	27	31	11	.176
V-2	H_2O	14	26.5	28	16.8	.27
V-5	H_2O	41	94	60	12.5	.20
	H_2O	41	94	74	18.5	.296
	H_2O	41	94	86	19.5	.312
V-7	CO_2	5	72	32	43	.69
V-7	CO_2	5	72	50	65	1.04
V-7	CO_2	5	72	61	64	1.03
V-7	CO_2	5	72	67	71	1.12

3. Discussion of Results

The frost thickness profiles are in general agreement with mass transfer theory. The beginning of the frost generally correlates reasonably well with the point at which the tube wall temperature has dropped to saturation. The initial rise in thickness results from the increased humidity driving force as the wall saturation humidity drops off much more rapidly than the stream humidity. The decreasing frost thickness in the trailing edge of the frosted zone reflects the fact that the stream humidity has been greatly decreased by prior mass transfer. A more detailed discussion of the comparison between these experimental results and frost profiles predicted by a computer solution based on mass transfer theory is given in Appendixes 12 and 13 to this report.

The water frost density appears to be in reasonably good agreement with the correlation presented in Appendix 6. For all the tests considered here nominal air velocity (based on a nominal air temperature of 460° R) was approximately 60 feet a second. For this air velocity the correlation of Appendix 6 would indicate a frost density of .26 gm/cc or 15.5 lb/ft^3. All of the experimental data is within about 25% of this value. It is believed this variation is not excessive in terms of the possible errors in air flow, contaminant concentration and experimental measurement of frost thickness.

It is interesting to note that in both test V-5 (water frost) and test V-7 (carbon dioxide frost) there is an apparent increase in frost density with time. As discussed in Appendix 6 such an increase would appear unlikely based on the results of other experimentors. However, it is at least conceivable that with time the porosity of the frost might be reduced by additional deposition within the pores of the frost structure. However, we do not believe the data is sufficiently definitive to establish a working curve of frost density versus time.

The carbon dioxide frost density as determined in V-7 is considerably greater than the water frost density. As discussed in Appendix 6, our literature search did not yield any data on the density of carbon dioxide frost. Hence, we will assume that a value of 65 pounds per cubic foot which is representative of the V-7 test results, will be adequate for our subsequent analytical studies.

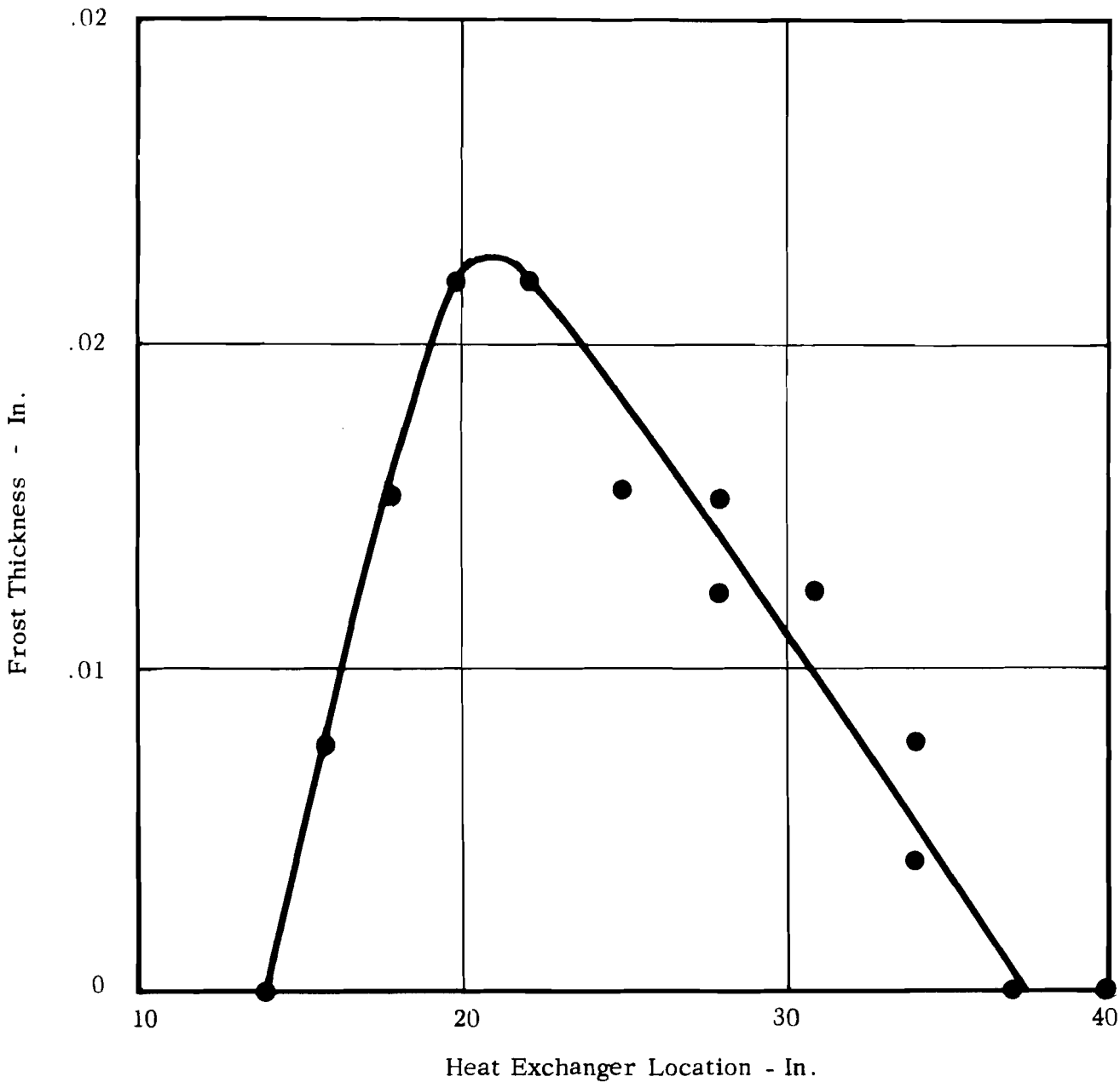

FIGURE 1 H_2O FROST THICKNESS PROFILE
TEST F-17 θ - 31 MINUTES

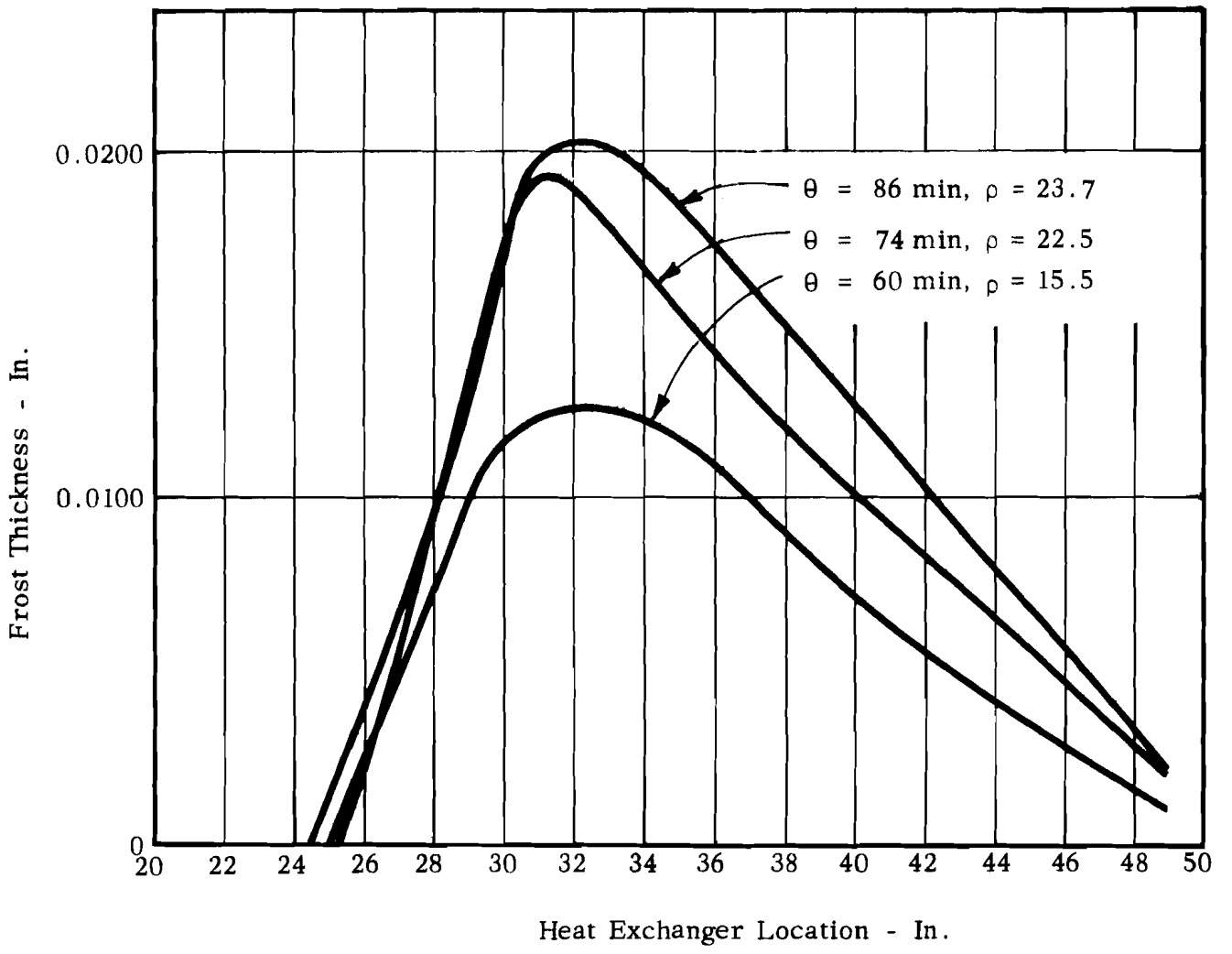

FIGURE 2 H_2O FROST THICKNESS PROFILES
TEST V-5

ϕ = 32 min.
ϕ = 50 min.
ϕ = 61 min.
ϕ = 67 min.

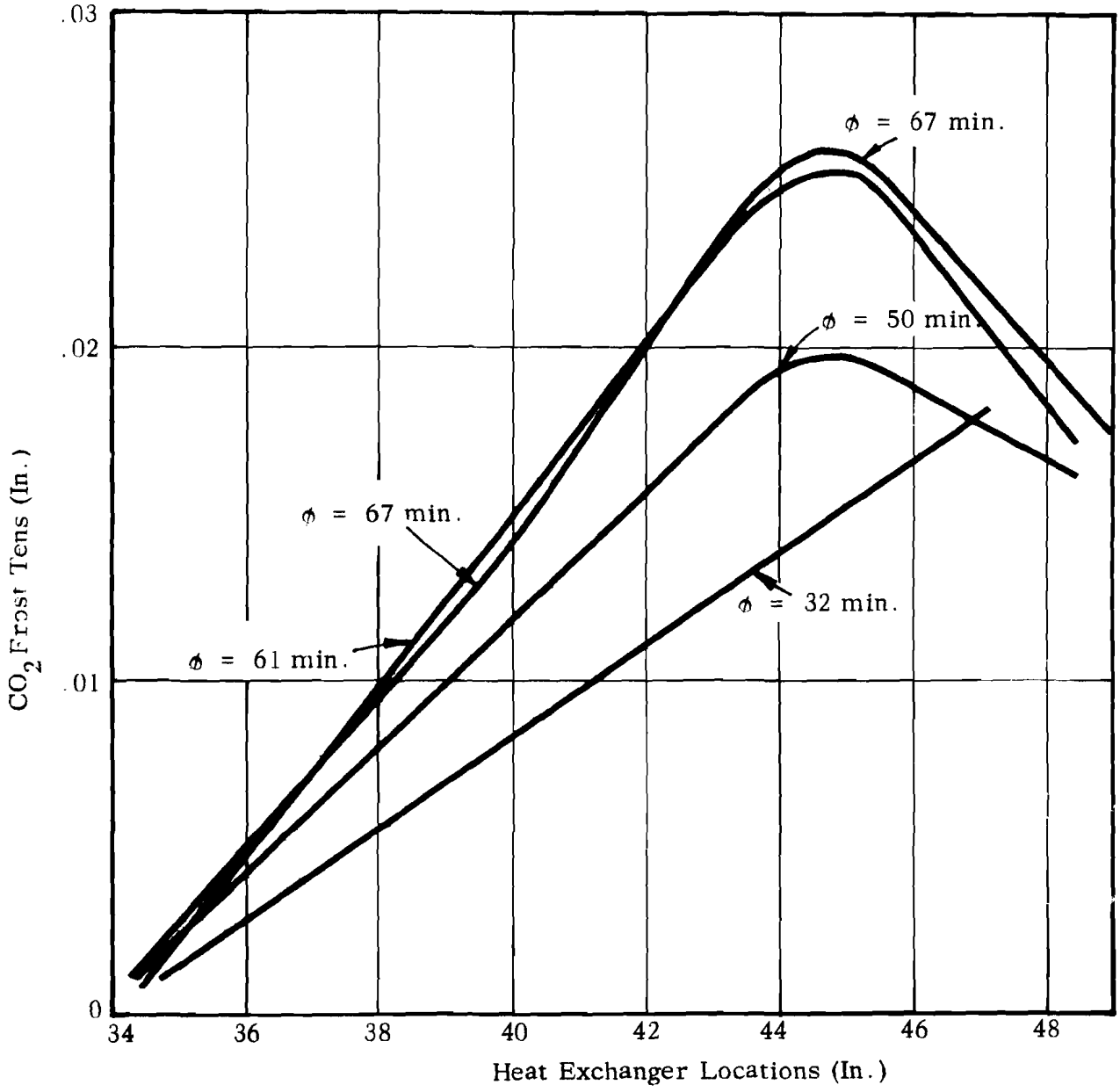

FIGURE 3 CO_2 FROST THICKNESS PROFILES
TEST V-7

APPENDIX 10

PRESSURE DROP AND FLOW DATA CORRELATION

TABLE OF CONTENTS

PRESSURE DROP AND FLOW DATA CORRELATION - PRELIMINARY VERSION

A. Analytical Basis

Analysis of the effect at a given frost layer on the flow characteristics of a single tube row, or a series of tubes having uniform frost thickness, has indicated that the flow parameter

$$\frac{\Delta P/\Delta P_o}{(W/W_o)^2}$$

is a direct function of the area blockage (t/δ_o). Per equation (1) of Appendix 11

$$\frac{\Delta P/\Delta P_o}{(W/W_o)^2} = \left[\frac{1}{1-t/\delta_o}\right]^2 \frac{\rho_o}{\rho} \quad (1)$$

where:

ΔP - pressure drop

W - flow

t - frost thickness

δ - tube half clearance

ρ - flow density

subscript o - denotes clean condition

When analyzing a finite heat exchanger in which both frost thickness and density may vary with length, the integration of equation (1) along the heat exchanger may become fairly complex. It is possible, however, to achieve a very simple expression for the over-all effects of frost on heat exchanger flow performance by making the following approximations:

1. Assume uniform frost thickness in a frosted zone of length (X).

2. Neglect variations in flow density.

3. Assure the clean pressure drops of the frosted and unfrosted zones are proportional to the lengths of these zones.

As shown in Appendix 11 (Equation 8A) the variation in the over-all flow parameter for the above simplified model may be described by the following equation:

$$\frac{\Delta P_L/\Delta P_{Lo}}{(W/W_o)^2} = \frac{X}{L}\left[\frac{1}{1-\bar{t}_x/\delta_o}\right]^2 + \frac{1-X}{L} \quad (2)$$

where:

ΔP_L - over-all heat exchanger pressure drop

$\bar{t}x/\delta_o$ - mean area blockage in frosted zone

X - length of frosted zone

L - total heat exchanger length

If we further define an over-all mean area blockage $(\bar{t}/\delta_o)$ based on the frost being uniformly distributed over the total heat exchanger, area then $\bar{t}/\delta_o$ can be related to $\bar{t}x/\delta_o$ as follows:

$$\bar{t}x/\delta_o = (\bar{t}/\delta_o)(L/X) \quad (3)$$

From equations 2 and 3 above, it is possible to plot

$$\frac{\frac{\triangle PL}{\triangle PL_o}}{(W/W_o)^2}$$

as a function of $\bar{t}/\delta_o$ for specified values of X/L.

The results are plotted in Figure 1. It is apparent from this plot that for extremely small amounts of mean area blockage the frosted length fraction is quite unimportant. However, as mean area blockage increases, the importance of the frost length fraction increases greatly. At equal mean area blockage the pressure drop ratio is much higher when the frosted length fraction is small.

We would not expect the plot of Figure 1 to accurately predict the heat exchanger performance, in that the assumption of constant frost thickness in the frosted area is quite unrealistic. However, this plot does illustrate the relative effects of mean area blockage and frosted length fraction on heat exchanger flow performance and does suggest a method for correlating the test data.

B. Constant Flow Tests

Figure 2 is a plot of pressure drop vs. water addition time for several tests which are similar in all respects except for the quantity of water in the inlet air. It is noted from this plot that percent of water in the inlet air has a marked effect on the rate of pressure drop increase.

In Figure 3, the data previously presented in Figure 2 is replotted in the form of pressure drop ratio vs. computed area blockage. For all of these tests, the frosted length fraction is quite similar. Therefore, the majority of data points plot quite close to a single correlation curve. It should be noted at this time that the mean area blockage is computed from the measured water flow, known heat exchanger geometry, and frost density estimated from a correlation plot of water frost density vs. flow velocity. The following relationship is used:

$$\bar{t}/\delta_o = \frac{\int_o^\theta wcd\theta}{\rho_F A_S \delta_o}$$

where:

$\bar{t}$ - mean frost thickness

δ_o - tube half clearance

$\int_o^\theta wcd\theta$ - total water addition

θ - water addition time

ρ_F - frost density

A_S - total heat exchanger surface area

In computing the frosted length fraction (X/L), it was assumed that the start of frosting corresponded to the point at which the wall temperature reached the inlet contaminant saturation temperature. The end of the frosted length was defined as the location at which the carrier gas temperature had dropped to saturation at 10% of the inlet contaminant concentration.

Figure 4 presents a plot of pressure drop ratio vs. mean area blockage for several tests in which the frosted length fraction varies markedly due to changes in coolant inlet temperature. It may be noted that, for equal area blockage, the pressure drop ratio increases as X/L decreases. Qualitatively at least, this effect is very similar to that illustrated by the simplified analytical model of Figure 1.

Figure 5 presents a plot of pressure drop ratio vs. area blockage for three tests in which the flow rate per unit area varied. However, since the frosted length for all three tests was similar, the data plots close to a single line.

In Figure 6, three tests at various pressure levels are compared. In these tests, the curves tend to fan out somewhat. However, the differences appear to result primarily from differences in frosted length. In particular, it may be noted that high pressure test, F-17, which shows a much lower rate of pressure rise than the lower pressure tests, and also has a larger frosted length, agrees quite well with the data of Figure 3 in which tests of comparable frosted length are considered.

Figure 7 presents a comparison of the three heat exchanger configurations used in this program. In general, the differences between these three configurations do not seem to be large.

Figure 8 presents pressure drop data on the liquid nitrogen spray tests. For these tests a frosted length based on heat exchanger temperature profiles has no real significance since the mechanisms of deposition is one of nucleation in the bulk stream rather than mass transfer. On this plot, data for both the one-inch spiral and two-inch baffle configuration is presented. The results indicated that pressure drop increase is reduced by increasing liquid nitrogen spray rate up to a point (i.e., a spray ratio of about 33%) beyond that point increasing spray ratio does not seem to help. No real differences in performance here can be attributed to the two different configurations. It is our belief that the dependence of pressure drop on spray ratio is associated with the particle size resulting from nucleation. A high spray rate results in high bulk stream saturation ratios and the formation of an extremely large number of small particles which are not readily separated by impingement on heat exchanger drop walls and which, therefore, are distributed fairly uniformly throughout the heat exchanger. Low spray rates on the other hand favor the formation of large particles which tend to be readily trapped in the inlet of the heat exchanger.

Figure 9 presents a comparison between high gas to wall Δ T tests and normal gas to wall Δ T tests. The results are somewhat scattered. For the case of the one-inch configuration, the pressure drop at high Δ T is actually somewhat less than it was under normal Δ T conditions. With the two-inch spiral, the opposite effect is observed. The interpretation of this data is not clear.

C. Constant Pressure Drop Tests

Figure 10 is a plot of air flow vs. time for two constant pressure tests in which deposit accumulation results in a decrease in air flow. The results indicate, naturally, that increasing the water content has a large effect on the decrease in air flow.

Figure 11 presents the same data with the square of the flow ratio plotted against mean area blockage. From the analytical curve of Figure 1, we would expect the square of the flow ratio (for constant pressure drop tests) to vary in manner similar to the pressure drop ratio (for constant flow tests), when plotted against mean area blockage. The results are in qualitative agreement with the correlation curve developed in Figure 3 for similar tests. It appears that the differences that do result are due to the shifting temperature gradients which exist in the constant pressure drop tests and which have the effect of varying the effective frosted length.

D. Carbon Dioxide Deposit Effects

For the tests considered in sections B and C above, the area blockage due to carbon dioxide was small compared to that due to water. Therefore, carbon dioxide frost was neglected in computing area blockage and no attempt was made to separate out the small pressure drop effect due to carbon dioxide frost.

However, in a few tests, such as V-7, when water content was held to a minimum, carbon dioxide area blockage was predominant and in these cases, the pressure drop effects are similar to those due to water when pressure drop ratio is plotted against area blockage.

In Figure 12, the pressure drop ratio vs. area blockage for test V-7 is compared with comparable results for water frost. The results indicate similar performance, although the carbon dioxide pressure drop effect seems to be slightly lower in the early stages of frost build-up, and then increase somewhat faster near plug-up, than is the case with water frost.

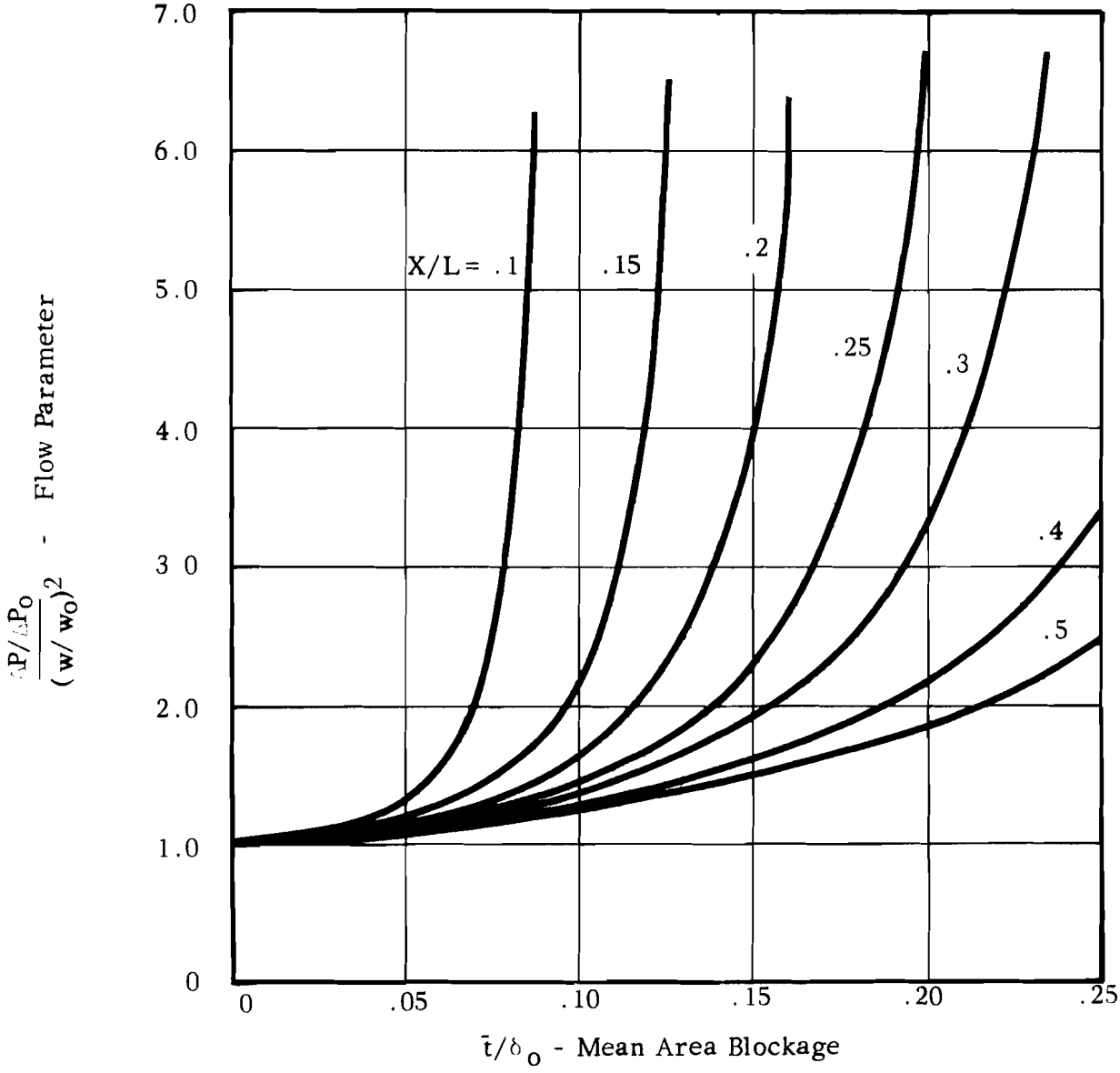

FIGURE 1 PRESSURE DROP RATIO VS AREA BLOCKAGE
SIMPLIFIED ANALYTICAL SOLUTION

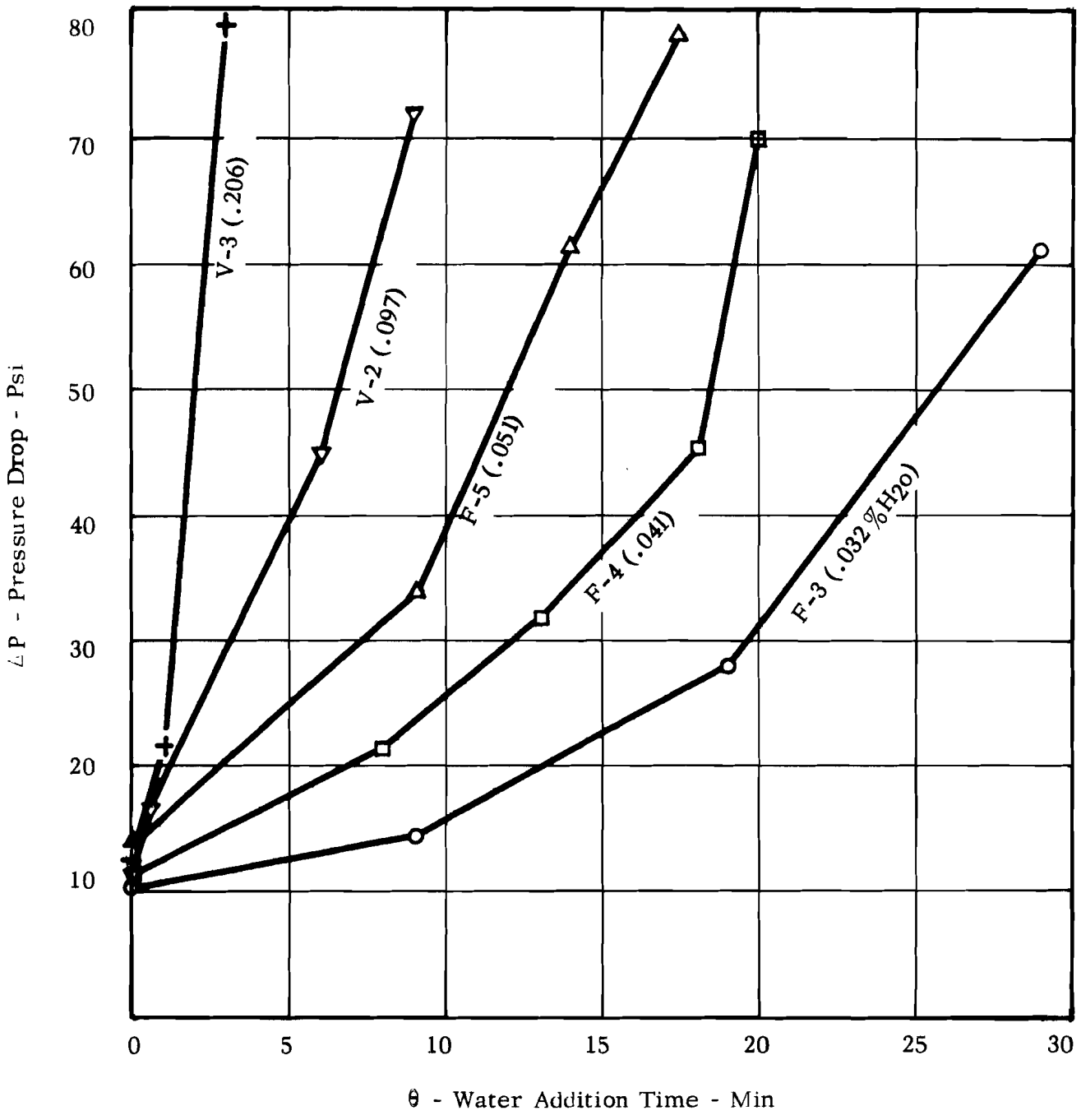

FIGURE 2 EFFECT OF WATER ADDITION ON HEAT EXCHANGER PRESSURE DROP (RAW DATA)

Notes:

1. Symbol Identification:
   ▽ - Verification Test Series
   ○ - Flow Test Series
   Test Numbers Within Symbols
2. $.32 < x/_L < .37$ For All Tests

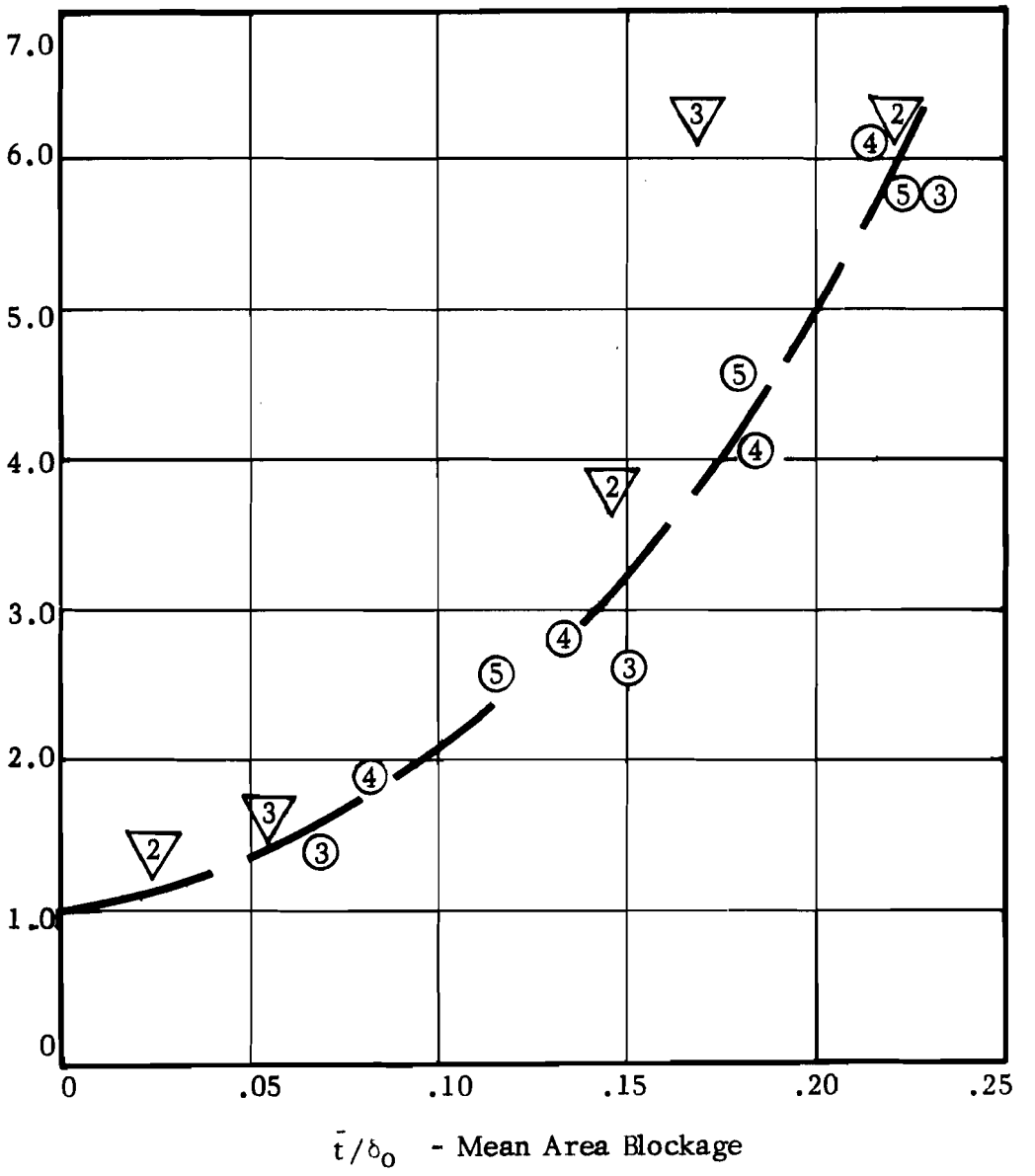

FIGURE 3 EFFECT OF WATER ADDITION ON HEAT EXCHANGER PRESSURE DROP (CORRELATION PLOT)

Symbol	Test	Coolant Inlet-°R	x/L
●	H-6	52	.11
○	F-8	200	.23
□	F-3	330	.33
△	V-5	400	.44

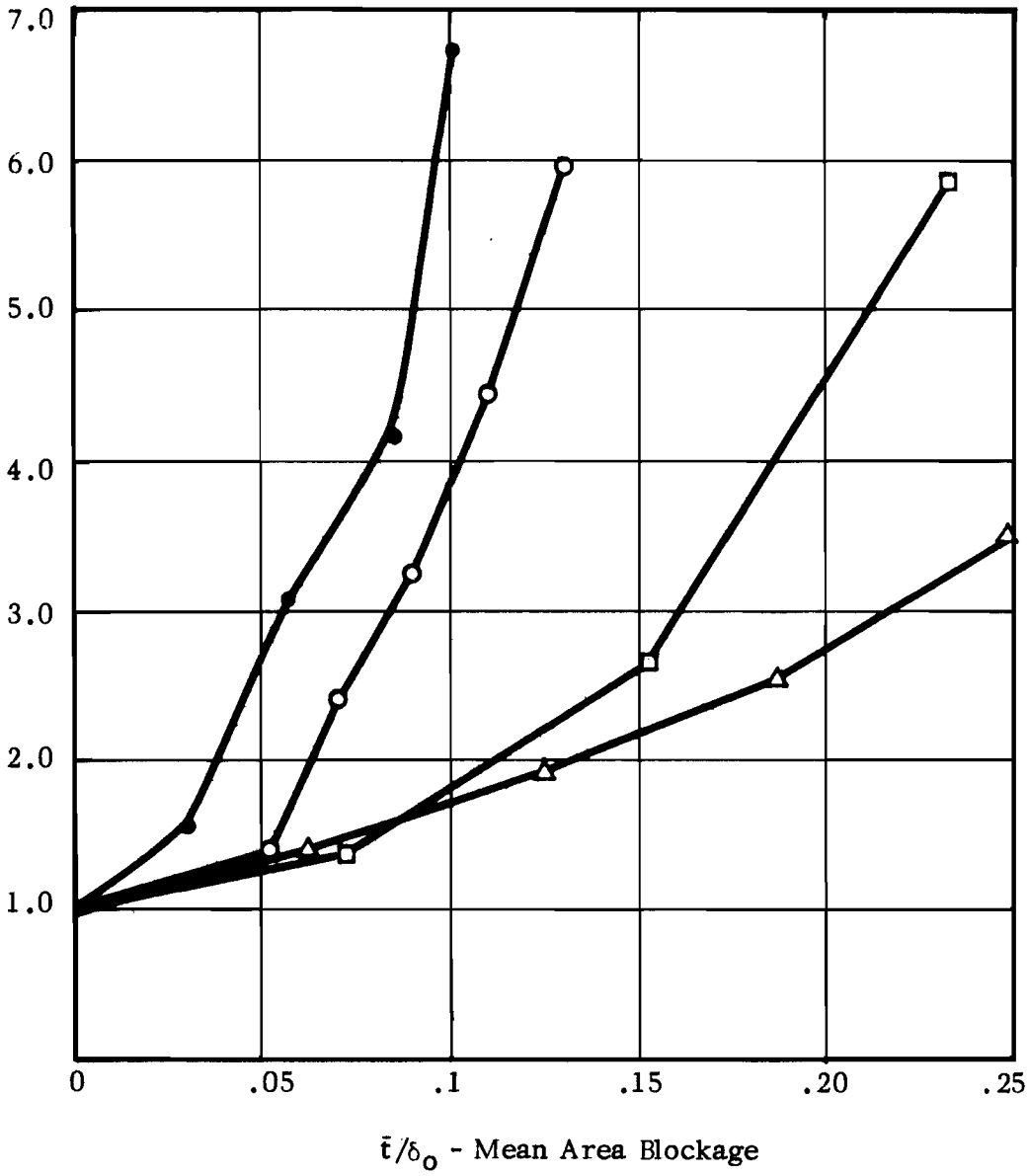

FIGURE 4 PRESSURE DROP RATIO VS AREA BLOCKAGE
VARIABLE COOLANT INLET TEMPERATURE

Symbol	Test	G (lb/sec ft^2)	x/L
○	F-8	29.3	.23
▲	F-10	47.9	.18
●	V-8	15.3	.18

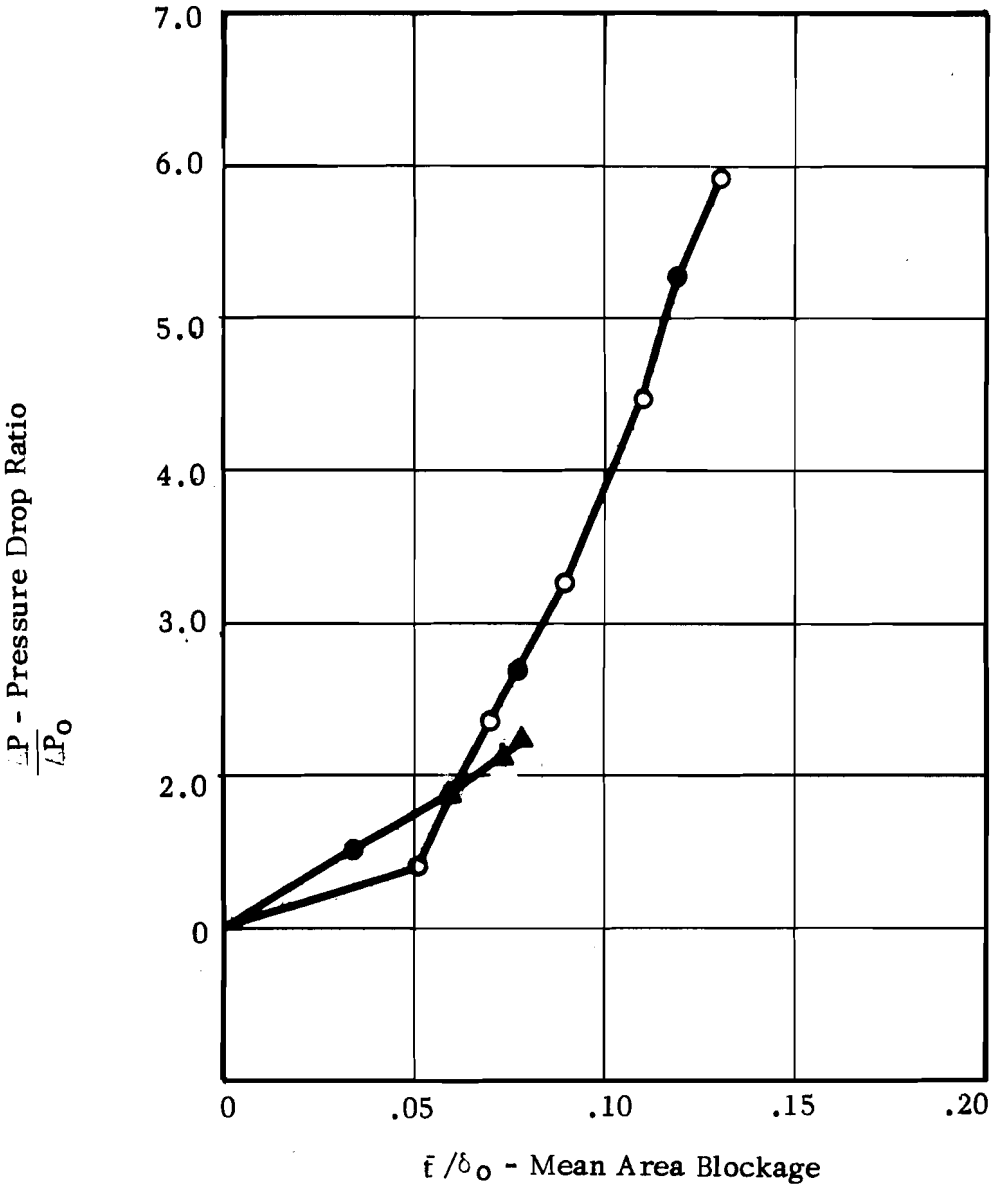

FIGURE 5 PRESSURE DROP RATIO VS AREA BLOCKAGE VARIABLE FLOW

Symbol	Test	Pa (Psia)	x/L
○	F-8	88	.23
●	V-1	30	.17
▲	F-17	298	.30

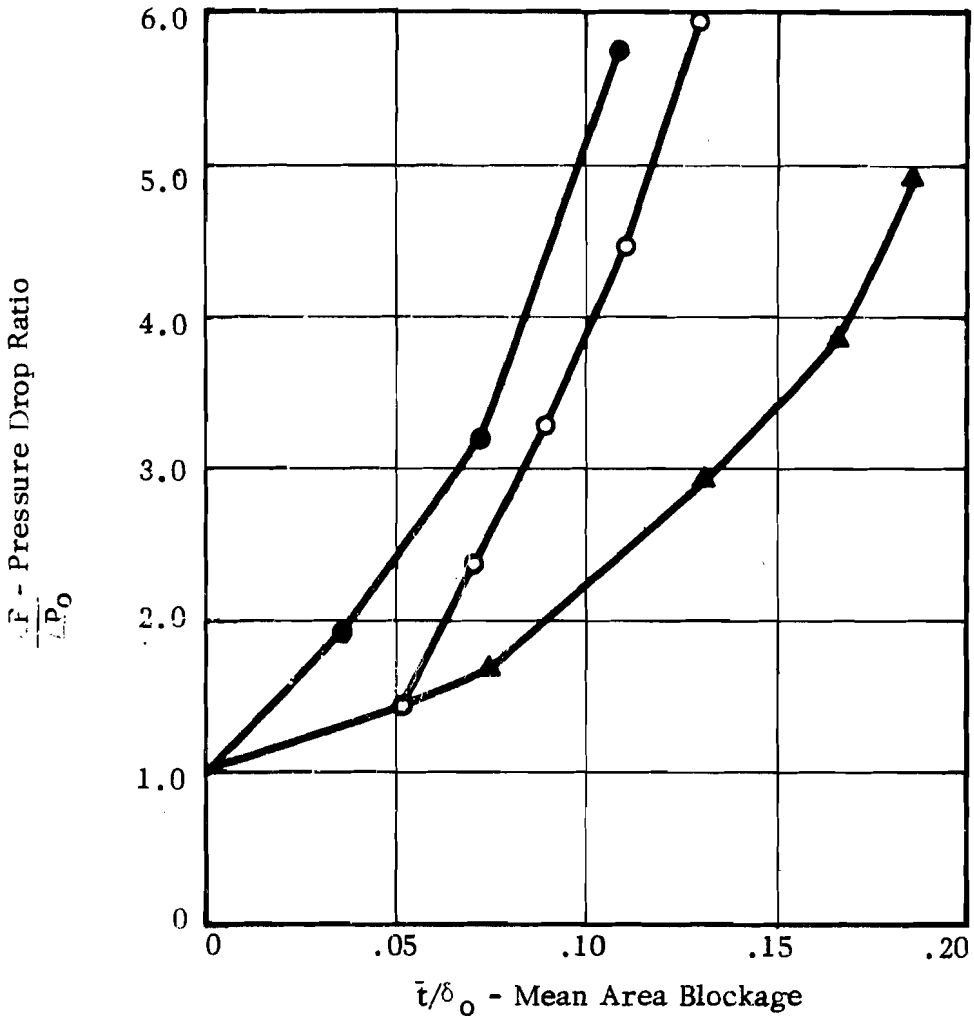

FIGURE 6 PRESSURE DROP RATIO VS AREA BLOCKAGE VARIABLE PRESSURE

Symbol	Test	Configuration	x/L
○	F-8	1" Spiral In-Line	.23
●	C-5	2" Spiral In-Line	.27
□	C-1	2" Baffle Staggered	.21

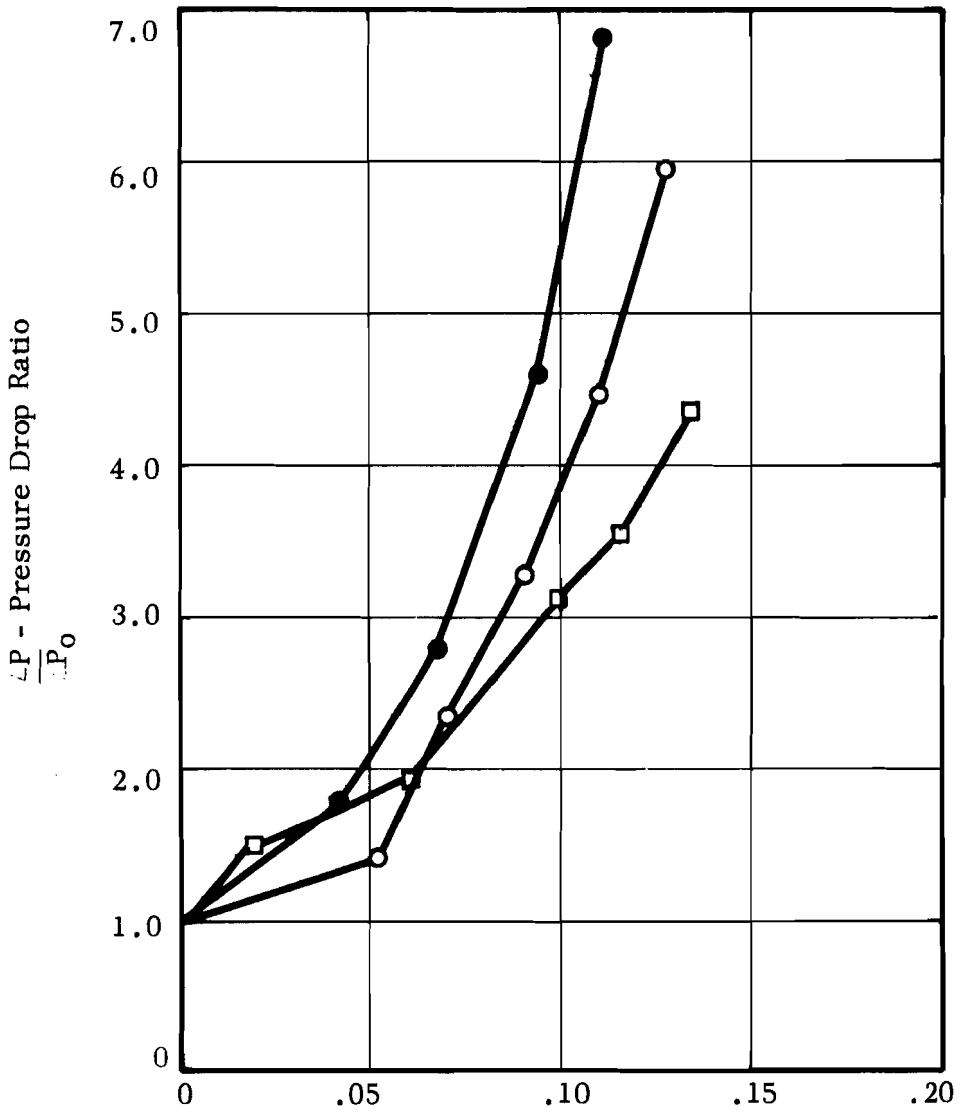

FIGURE 7 PRESSURE DROP RATIO VS AREA BLOCKAGE COMPARISON OF HEAT EXCHANGE CONFIGURATIONS

Symbol	Test	Configuration	W Spray / W Air
	F-14	1" Spiral	.25
	F-13	1" Spiral	.33
	V-9	1" Spiral	.46
	C-2	2" Baffle	.18
	C-4	2" Baffle	.35

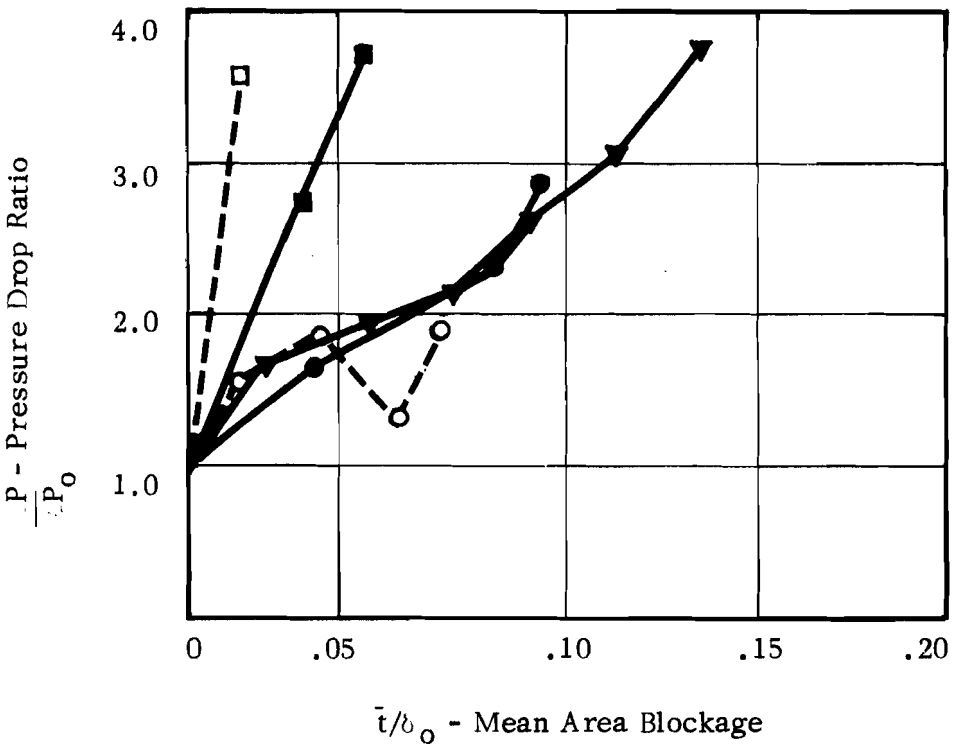

FIGURE 8 PRESSURE DROP VS AREA BLOCKAGE
LN_2 SPRAY TESTS

Symbol	Test	Configuration	ΔTmax (°R)	x/L
○	F-8	1" Spiral	80	.23
●	F-12	1" Spiral	180	.10
□	C-5	2" Spiral	100	.27
■	C-6	2" Spiral	240	.10

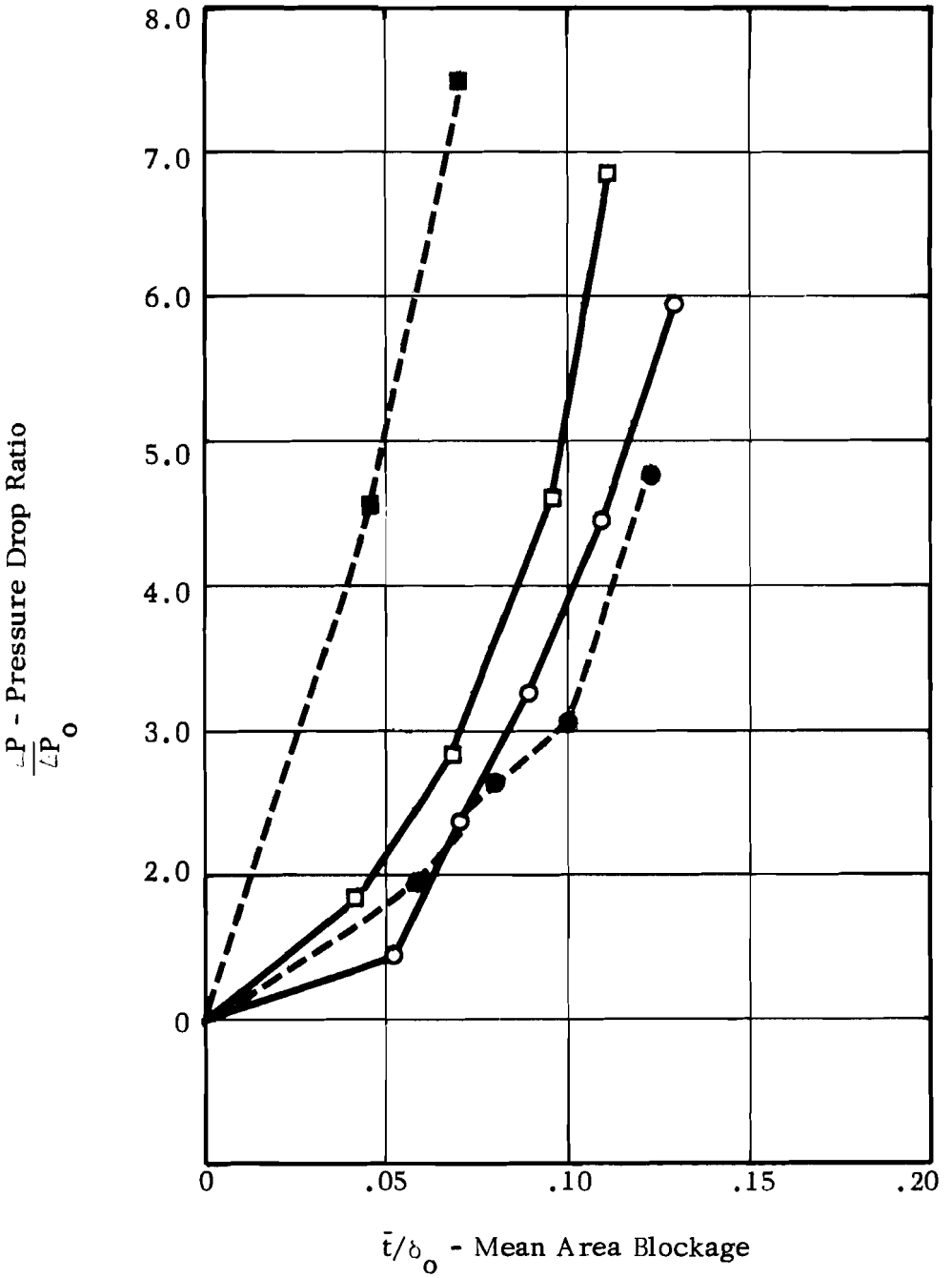

FIGURE 9 PRESSURE DROP RATIO VS AREA BLOCKAGE GAS-WALL ΔT

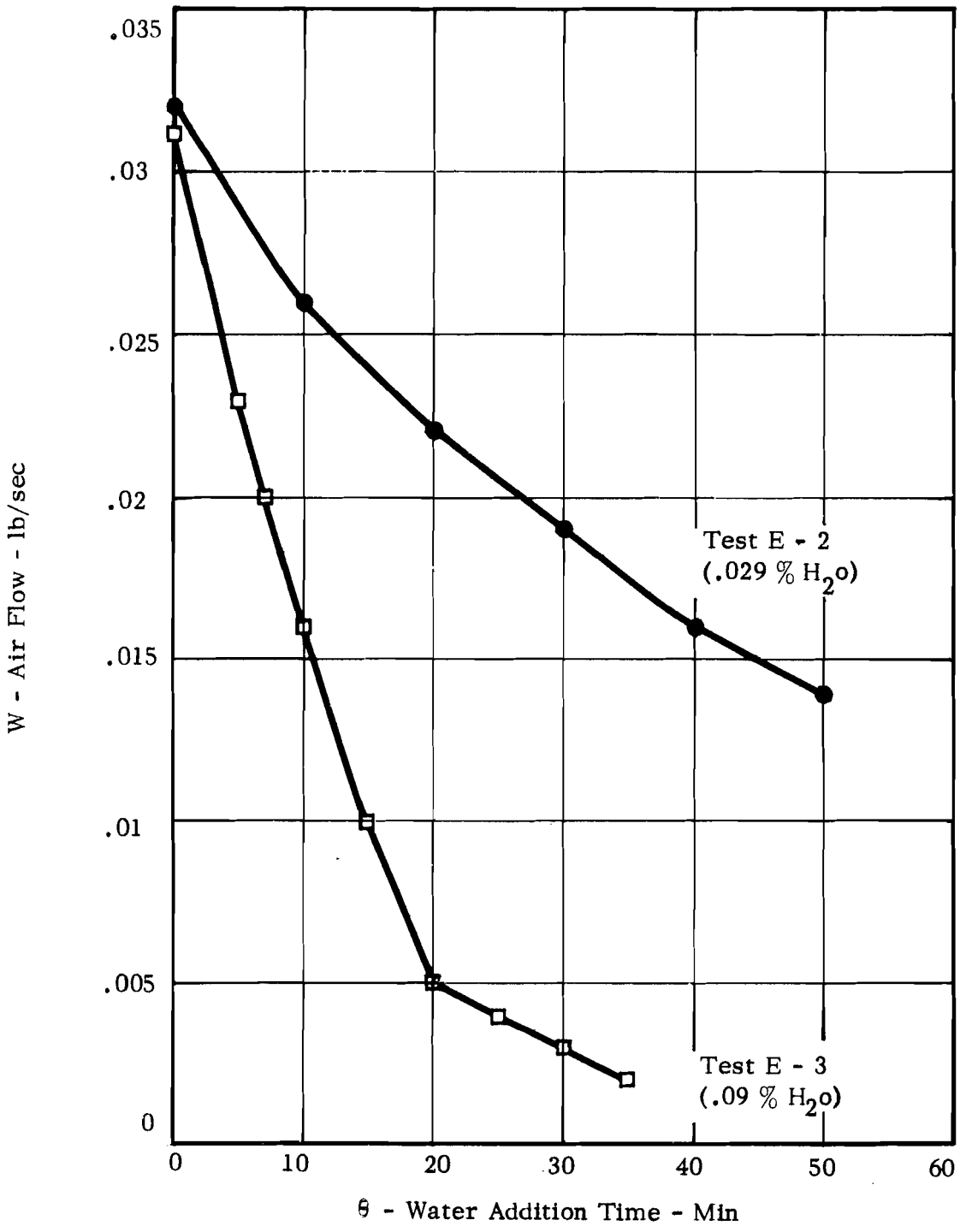

FIGURE 10 EFFECT OF WATER ADDITION ON HEAT EXCHANGER AIR FLOW

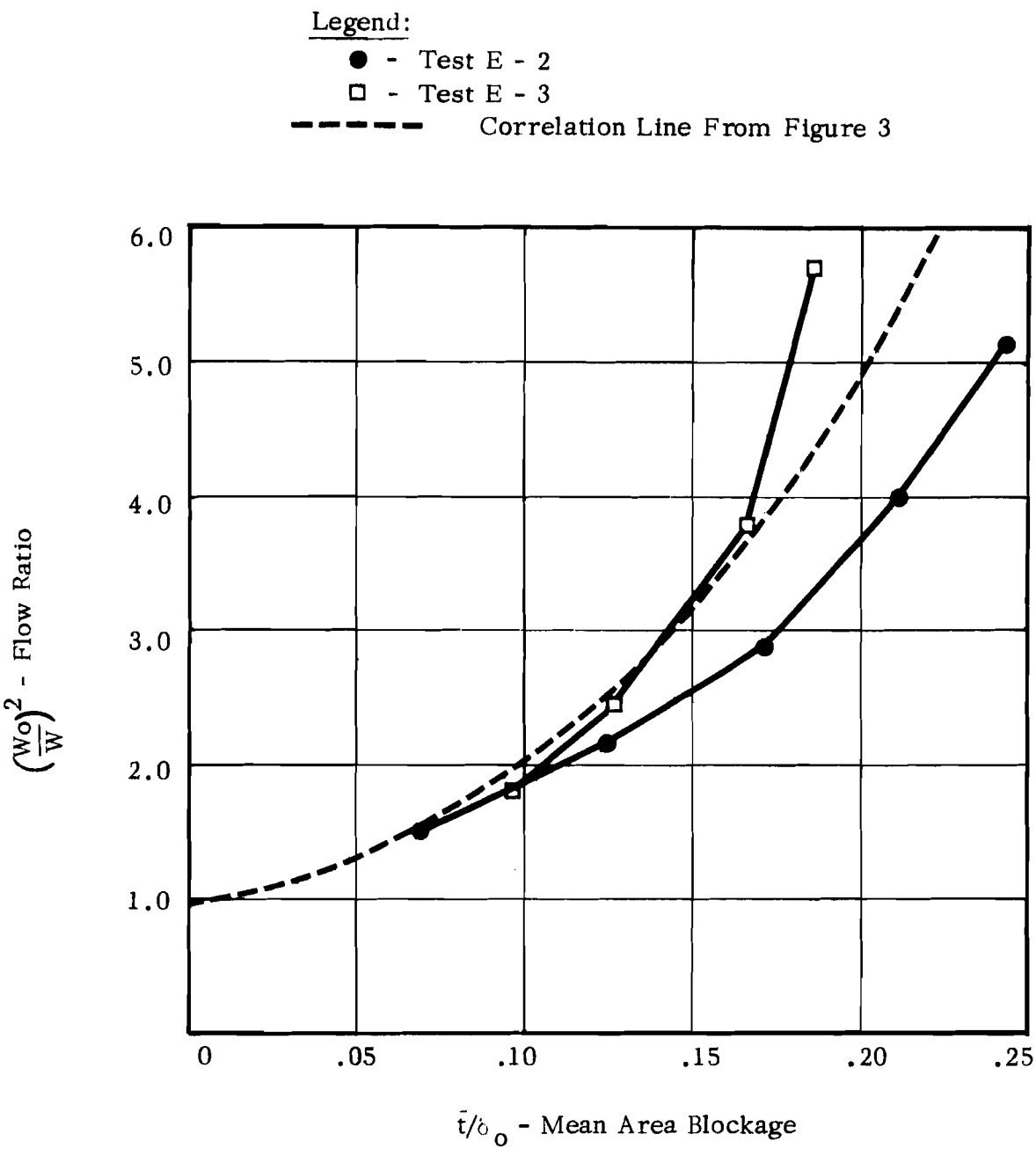

FIGURE 11 EFFECT OF AREA BLOCKAGE ON HEAT EXCHANGER AIR FLOW

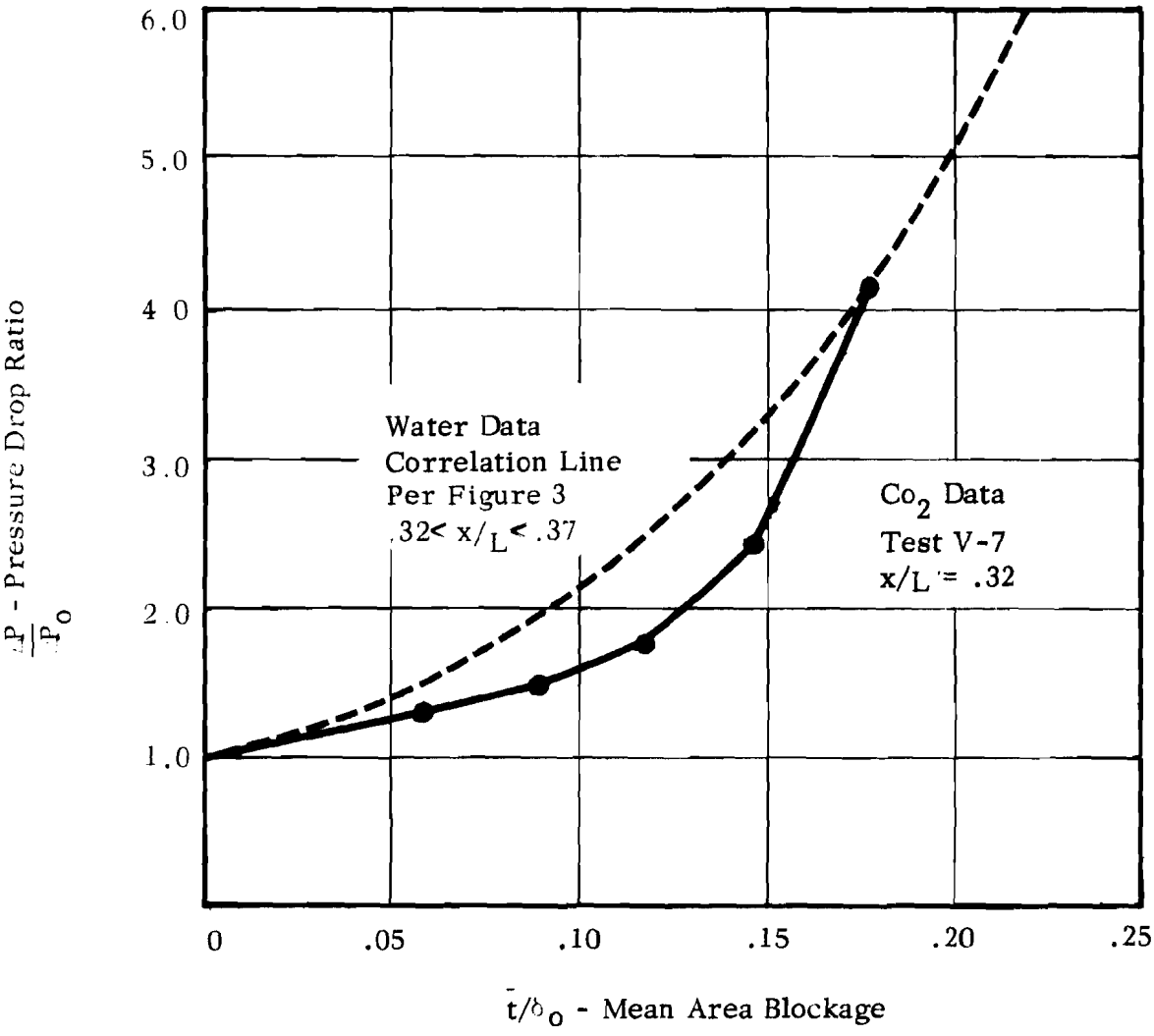

FIGURE 12 PRESSURE DROP RATIO VS AREA BLOCKAGE
COMPARISON OF WATER AND CARBON DIOXIDE

APPENDIX 11

HAND CALCULATION METHOD FOR PREDICTING EFFECTS OF CONTAMINANT DEPOSITION ON HEAT EXCHANGER PERFORMANCE

TABLE OF CONTENTS

I. INTRODUCTION

The overall problem of contaminant freeze-out in heat exchangers involves both the deposition of contaminant within the heat exchanger and the contaminant concentration and particle size in the exit stream. The contaminant deposited in the heat exchanger will cause flow area blockage and insulation on the frosted areas which will degrade the heat transfer and flow performance of the heat exchanger. The contaminant remaining in the exit stream may cause plugging in the downstream system components. The analytical methods discussed in the following report will be primarily concerned with the effects on heat exchanger, heat transfer and pressure drop caused by the accumulation of contaminants within the heat exchanger.

Analytical and experimental results indicate that mass diffusion is the most important mechanism governing the deposition of contaminants in heat exchangers. This admitted generalization is most valid when the heat exchanger ΔT between air and coolant is small. However, test results have indicated that even with quite large ΔT's in the order of 200°F, the deposition of contaminants in the heat exchanger is not greatly different and the pressure drop not substantially different than would result from mass diffusion. Surprisingly enough, even in the presence of nucleation due to liquid nitrogen spray which does make a substantial difference in the texture and distribution of deposits, the pressure drop effect does not appear to be grossly different than that which would exist in the presence of a mass diffusion type of deposit. Therefore, we have concluded that the mass diffusion mechanism is the most practical mechanism to serve as a basis for an analytical model of contaminant deposition.

We have considered both a computer solution and a simplified hand calculation approach to the problem of predicting deposit accumulation and the resultant effect on heat exchanger performance. Both approaches require prior knowledge of water and carbon dioxide density and thermal conductivity. The computer solution is potentially capable of developing both the frost profiles and the resulting effects on heat exchanger performance as part of an integrated calculation procedure with a minimum of simplifying assumptions. The computer solution is required for maximum accuracy and is well suited for the consideration of varying heat exchanger operating conditions. The simplified hand calculation approach, which will be the subject of the present discussion, requires some rather severe limitations on the choice of a frost distribution profile which limits its accuracy. Also, the hand calculation approach is not well adapted to the consideration of varying heat exchanger inlet conditions. Perhaps the greatest value of the hand calculation solution is that it provides a simple, flexible method of estimating the approximate effects of contaminant deposition on heat exchanger flow and heat transfer. The hand calculation method also serves to illustrate the relative importance of various parameters on heat exchanger performance. It may also be used to provide a rough independent check on the credibility of either experimental data or computer solutions.

II. SUMMARY

As a first step in estimating the effect of contaminant deposition on heat exchanger performance, we have considered the effect of a frost layer of given thickness and thermal conductivity on the flow and heat transfer capacity of a single tube row. In Section III, relationships are developed relating frost area blockage and thermal conductivity to the pressure drop and overall air-side heat transfer coefficient for a single tube.

We next considered the means of estimating the thickness and thermal conductivity of the frost layer for given heat exchanger operating conditions. A procedure was developed for estimating the effective frosted length in the heat exchanger area in which the frost would be deposited. Methods were reviewed for estimating the mean density and thermal conductivity of the frost as deposited in the heat exchanger. Detailed discussion of this work is contained in Sections IV and V of this report.

In the discussion above, we have mentioned the more basic aspects of the calculation model; namely, the estimation of the thickness and thermal conductivity of the frost layer as deposited in the heat exchanger and the determination of the effect of a given frost layer on the heat transfer and flow performance of a single tube row. In applying these results to an actual heat exchanger, it is necessary to develop procedures for applying the single tube row to finite length heat exchangers having both clean zones and frosted zones of varying frost thickness. Analytical procedures for determining the effects of contaminant deposition on overall heat exchanger performance are discussed in Section VI. One of the aspects of this analysis is the use of a distribution function to account for the effects of non-uniform frost thickness on pressure drop and heat transfer. The evaluation of distribution functions for an arbitrary triangular frost distribution is presented in Section VIII.

We have applied the analytical relations to specific test conditions and have used the comparison between analytical and experimental results as a check on the basic validity of the hand calculation model in Section VII. The tests F-2 through F-5 figure heavily in this comparison. We have prepared plots of pressure drop ratio and overall heat exchanger/heat transfer coefficient as functions of water addition for this series of tests. The experimental and analytical results were in general qualitative agreement. It is felt that the rather crude approach to frost distribution used in the hand calculation model was responsible for most of the discrepancies which did exist between the calculated and experimental results. Other factors which might have influenced the results were the apparent increase in frost density with time and the possibility of the heat transfer being influenced by the surface roughness of the deposits. The analytical procedure was also applied to test V-7, an extended length of carbon dioxide deposition test. The agreement between the experimental and analytical pressure drop results for this test were extremely good.

On an overall basis, we feel the hand calculation model has value as a rough guide as to the effect of contaminant deposition on heat exchanger performance. However, in many instances, computer solutions will be required both for improved accuracy and for coping with situations in which the heat exchanger inlet conditions are varying.

III. SINGLE TUBE ROW ANALYSIS

The presence of a frost layer degrades heat exchanger flow capacity by reducing the free flow area. The effect of the frost layer on heat transfer depends on both the area blockage and thermal insulation of the deposits. The thermal insulation of the frost tends to reduce heat transfer. The area blockage effect, however, tends to increase the air-side film heat transfer coefficients by increasing flow velocities.

Consideration of the effects of a given thickness and thermal conductivity of a frost layer on a single tube row illustrates the effects of frost on heat exchanger performance. For this analysis, the heat transfer and flow geometry are defined in Figure 1.

A. Flow and Pressure Drop

For a single tube row, the flow-pressure drop relationship, MacAdams "Heat Transmission", 3rd Edition, p. 162, may be expressed as:

$$\Delta P = 4f'' \frac{(\omega/A)^2}{\rho}$$

Neglecting variations in friction factors, the ratio between frosted pressure drop and clean pressure drop may be written as:

$$\frac{\Delta P}{\Delta P_o} = \left(\frac{\omega}{\omega_o}\right)^2 \left(\frac{A_o}{A}\right)^2 \frac{\rho_o}{\rho}$$

The above equation shows that the air pressure drop is directly proportional to the square of the flow rate, inversely proportional to the square of the free area, and inversely proportional to the fluid density. Since, referring to Figure 1, it is seen that free area is proportional to the available "half clearance" between tubes ($\delta = \delta_o - t$); the flow-pressure drop relationship also may be expressed as:

$$\frac{\Delta P/\Delta P_o}{(\omega/\omega_o)^2} = \left[\frac{1}{1 - \frac{t}{\delta_o}}\right]^2 \frac{\rho_o}{\rho} \qquad (1)$$

where:

ΔP = pressure drop
ω = flow rate
t = frost thickness
δ = tube half clearance
ρ = fluid density
subscript $_o$ represents clean conditions

A plot of the above relationship, for constant flow density, is presented in Figure 2. This plot indicates that an area blockage of 10% at a tube row would either increase the pressure drop across the tube row by 25%, for a constant flow system, or reduce the flow by 10%, for constant pressure drop across the tube row. The stipulation of constant flow density is probably valid for most practical applications in which substantial pressure or density variations due deposit formation could not be tolerated. However, as will be discussed later, the density variations in our test programs due to deposit formation were frequently quite substantial.

B. Heat Transfer

The overall air-side* heat transfer coefficient u, including air-side film resistance and the deposit insulation, for the single tube row of Figure 1, may be written as:

$$\frac{1}{u} = \frac{1}{h} + \frac{t}{k_F}$$

where:

u = overall air-side heat transfer coefficient
h = air-side film heat transfer coefficient
t = frost thickness
k_F = frost thermal conductivity

For the "clean" tube row (t = o) this equation reduces to $u_o = h_o$. Therefore, the ratio of clean to frosted overall heat transfer coefficient may be written as:

$$\frac{u_o}{u} = \frac{h_o}{h} + \frac{h_o t}{k_F}$$

The air-side film heat transfer coefficient (h) may be related to flow, tube diameter and fluid properties by the following equation valid for flow normal to tubes. (See MacAdams "Heat Transmission" 3rd Edition, p. 272.)

*In this Appendix, the term "air" is used to designate the carrier gas stream.

$$\frac{hD}{k} = .33\left(\frac{D\,\frac{\omega}{A}}{u}\right)^{.6}\left(\frac{C_p u}{k}\right)^{1/3}$$

Neglecting variations in air stream thermal conductivity, viscosity or Prandtl number during the frosting process, we may express the ratio of clean to frosted air-side film coefficients as:

$$\frac{h_o}{h} = \left(\frac{D}{D_o}\right)^{.4}\left(\frac{\omega_o}{\omega}\right)^{.6}\left(\frac{A}{A_o}\right)^{.6}$$

The tube diameter ratio (D/D_o) and free flow area ratio (A/A_o) may be written as:

$$\frac{D}{D_o} = \frac{D_o + 2t}{D_o} = 1 + 2\left(\frac{t}{D_o}\right) = 1 + 2\left(\frac{t}{\delta_o}\right)\left(\frac{\delta_o}{D_o}\right)$$

$$\frac{A}{A_o} = \frac{\delta}{\delta_o} = \frac{\delta_o - t}{\delta_o} = 1 - \frac{t}{\delta_o}$$

It is also convenient to rewrite the parameter $h_o t/k_F$ as $\left[(h_o\delta_o)/k_F\right](t/\delta_o)$.

Therefore, the ratio of clean to frosted overall air-side heat transfer coefficient may now be written as:

$$\frac{u_o}{u} = \left[1 + 2\left(\frac{t}{\delta_o}\right)\left(\frac{\delta_o}{D_o}\right)\right]^{.4}\left(1 - \frac{t}{\delta_o}\right)^{.6}\left(\frac{\omega}{\omega_o}\right)^{.6} + \left(\frac{h_o\delta_o}{k_F}\right)\left(\frac{t}{\delta_o}\right) \qquad (2)$$

This equation shows the variation in overall air-side heat transfer coefficient is a function of δ_o/D_o, t/δ_o, ω/ω_o and $h_o\delta_o/k_F$. For close packed tubes, little error results if we assume that $\delta_o/D_o = 0$ or more specifically that $(1 + (t/\delta_o)(\delta_o/D_o))^{.4} = 1.0$. As a test of this assumption, assume a pitch to diameter ratio of 1.4 (or $\delta_o/D_o = 0.2$) and compare the term $(1 + 2(t/\delta_o)(\delta_o/D_o))^{.4}$ with the term $(1 - (t/\delta_o))^{.6}$ as a function of t/δ_o.

t/δ_o	$\left[1 + 2(t/\delta_o)(\delta_o/D_o)\right]^{.4}$	$\left[1 - (t/\delta_o)\right]^{.6}$
.1	1.016	.9385
.2	1.031	.875
.5	1.076	.66

This comparison shows that for close packed tubes, the term $(1 + 2(t/\delta_o)(\delta_o/D_o))^{.4}$ is very nearly equal to unity. Therefore, the ratio of clean to frosted air-side overall heat transfer coefficients may be approximated with relatively little error as:

$$\frac{u_o}{u} = \left(1 - \frac{t}{\delta_o}\right)^{.6}\left(\frac{\omega_o}{\omega}\right)^{.6} + \left(\frac{h_o\delta_o}{k_F}\right)\left(\frac{t}{\delta_o}\right) \qquad (3)$$

The above relationship is valid for constant pressure drop, constant flow or any immediate operating lines. Certain simplifications can be made, however, for the specific cases of constant flow or constant pressure drop across a single tube row. For constant flow ($\omega/\omega_o = 1.0$)

$$\frac{u_o}{u} = \left(1 - \frac{t}{\delta_o}\right)^{.6} + \left(\frac{h_o\delta_o}{k_F}\right)\left(\frac{t}{\delta_o}\right) \qquad (3A)$$

For constant pressure drop, we note from equation 1 that $\omega/\omega_o = 1 - t/\delta_o$. Therefore, for constant pressure drop across a single tube row

$$\frac{u_o}{u} = 1 + \left(\frac{h_o\delta_o}{k_F}\right)\left(\frac{t}{\delta_o}\right) \qquad (3B)$$

A plot of equations 3A and 3B is presented in Figure 3. This plot illustrates the effects of frost thickness and thermal conductivity on the overall air-side heat transfer coefficient. This plot shows that for values of $h_o\delta_o/k_F < .7$ (high frost thermal conductivity for instance), the overall air-side heat transfer coefficient for constant flow actually increases with frost thickness. For higher values of $h_o\delta_o/k_F$ (low frost thermal conductivity), the overall air-side heat transfer coefficient is reduced as frost accumulates.

For water frost formation in our test heat exchanger at G = 30 lb/ft^2-sec, we would approximate $h_o\delta_o/k_F$ as 5.0.

Therefore, $h_o\delta_o/k_F$ is high enough so that frost accumulation reduces, rather than increases, the overall air-side heat transfer coefficient. It also may be noted from Figure 3, that for $h_o\delta_o/k_F = 5.0$, the loss in overall air-side heat transfer coefficient is about the same for either constant flow or constant pressure drop operation.

The analysis above has illustrated the effects of frost thickness and thermal conductivity on the flow and heat transfer characteristics of a single tube row. It will be noted here, and discussed in more detail later, that the frost density is required in order to determine the frost thickness. Hence, it is necessary to know the frost density and thermal conductivity in order to apply the above results to specific heat exchanger operating conditions.

The analysis above is restricted to a single tube, or to a short length of heat exchanger in which the frost thickness may be considered uniform. In considering an actual heat exchanger in which the frost thickness varies, it is necessary to know the distribution of frost thickness. From the distribution of frost thickness and the frost thermal conductivity, it is possible to calculate the overall effects of frost deposition on the performance of finite heat exchangers.

Therefore, in the sections below, we will first discuss frost properties and frost distribution and then present methods for applying this information to finite length heat exchangers.

IV. FROST PROPERTIES

The water and carbon dioxide frosts formed in heat exchangers are porous materials whose densities and thermal conductivities differ from those of the pure solids. For materials of this sort, many analytical and experimental correlations are presented in the literature for relating thermal conductivity to density. Data on frost density is much less plentiful.

We have made a rather thorough search of the literature to determine the most appropriate methods to relate frost thermal conductivity to the frost density, structure and properties of the constituents making up the frost. We have concluded that for reasonably low density frosts (i.e., $\rho F < 0.5\ \rho$ solid) that Woodside's model yields the best agreement with experimental data. For high density frosts, Riemann's truncated sphere model seems appropriate. Using these models, we have prepared generalized plots for determining water and carbon dioxide frost thermal conductivities from given frost density values. These plots are presented in Appendix 6.

We have obtained some information from the literature on water frost density. This data indicates that at temperatures well below 32°F (say 0°F), when the distillation effect is small, water frost density is primarily dependent on flow velocity. A correlation plot of water frost density versus flow velocity has been prepared based on a limited amount of literature data and including some data obtained in our experimental facility. This correlation, which we will use as a basis for determining water frost density, is presented

in Appendix 6. This plot indicates that at an air velocity of 60 ft/sec, the density of water frost will be about .25 gm/cc.

Our experimental measurements of carbon dioxide frost density included in Appendix 9 indicate a density of about 1 gm/cc at a nominal heat exchanger air velocity of 60 ft/sec. For lack of more extensive information, we will assume this value is typical for the range of operating conditions envisioned in this program.

V. FROST DISTRIBUTION

Mass diffusion theory indicates that the start of frosting in a heat exchanger should coincide with the point at which the surface temperature drops to the contaminant inlet saturation temperature. Proceeding downstream from the point of initial frosting, the thickness increases to a maximum and then tapers off thereafter. The shape of the frost thickness profile is related to the partial pressure driving force for mass diffusion between the bulk gas and the cold surface. The initial increase in frost thickness is due to the decrease in surface temperature at near constant bulk stream humidity; the subsequent decrease in frost thickness is associated with the decrease in bulk stream humidity due to prior freeze-out. Frost thicknesses measured in our test heat exchanger are consistent with the distribution indicated by mass diffusion theory.

We have found that a rough approximation for the effective length of the frosted area can be made by assuming that the start of frosting coincides with the point at which the surface reaches the contaminant inlet saturation temperature, and that the end of frosting coincides with the point at which the air temperature reaches saturation at 10% of the inlet contaminant concentration. This procedure is illustrated in Figure 4.

The concept of an effective frosted length permits quick estimation of a mean frost thickness. If we assume that all of each contaminant is distributed uniformly as frost throughout its frosted length, we can compute the mean frost thickness from the following relation:

$$\bar{t}_x = \frac{\int_o^\theta \omega_c d\theta}{\rho_F A_F} \qquad (4)$$

where

ω_c = contaminant flow rate
θ = time from start of frosting
ρ_F = frost density
A_F = heat transfer surface area in frosted length.

More realistic frost distribution might be obtained by assigning an arbitrary variation in frost thickness within the frosted length of the form $t/\bar{t}_x$ = f (fraction of frosted length). The type of distribution used would be based on experience obtained both from our initial computer studies and measurements of frost thickness from photographs of the test heat exchanger. For instance, a simple "right triangle" distribution of the form $t/\bar{t}_x = 2$(1 - fraction of frosted length) would account for the fact that the maximum frost thickness is generally of the order of twice the integrated mean thickness.

Additional accuracy in establishing frost distribution might be achieved by abandoning the effective length concept and computing frost thickness from the "zero time" rates of frost deposition along the heat exchanger. This method would be expected to be more responsive to the actual conditions existing for specific situations than would an effective mean thickness or an arbitrary distribution based on the effective mean thickness.

The degree of complexity which should be employed in establishing a frost distribution for use in hand calculation techniques depends on the balance between the required accuracy of the particular calculation and the investment in manpower required to implement the calculation.

The correlation between the accuracy of the frost distribution and the heat transfer and flow results depends to a large part, as will be discussed later, on the extent of frosting. When the frost layer is very thin, the use of an effective mean thickness is adequate for predicting heat transfer and pressure drop effects. However, as the heat exchanger approaches plug-up, frost distribution is very important. In considering the simplicity of the calculation, it should be recognized that the effective mean thickness, perhaps combined with an arbitrary thickness distribution, results in technique which is practical for hand calculation. The use of a more detailed procedure such as the "zero time" distribution results in a fairly tedious calculation procedure for determining the effects of contaminant deposition on heat exchanger performance. The general subject of the trades between calculation accuracy and calculation effort will be treated in more detail in the following sections.

VI. EFFECT OF CONTAMINANT FREEZE-OUT ON THE FLOW AND HEAT TRANSFER PERFORMANCE OF A FINITE LENGTH HEAT EXCHANGER

In the sections above, we have discussed the effects of frost thickness and thermal conductivity on the performance of a single tube row and have presented methods for estimating frost properties and frost distribution within a heat exchanger. It is the purpose of this section to consolidate this information into an analytical procedure which can be applied to actual heat exchangers. In essence, this discussion will be primarily concerned with "integrating" the single tube results throughout a heat exchanger having both frosted and non-frosted areas.

To develop this analysis, we will use the simple heat exchanger model shown is Figure 5. This heat exchanger, of total length L, consists of an effective frosted length X, and a clean length Z. The effective frosted length is determined by the method discussed above and illustrated in Figure 4. The techniques developed with this model can easily be applied to a heat exchanger having two frosted sections and one or more clean sections.

A. Flow and Pressure Drop

Referring to Figure 5, the overall pressure drop for the heat exchanger may be written:

$$\Delta P_L = \Delta P_X + \Delta P_Z$$

The ratio of frosted to clean overall pressure drop may be written:

$$\frac{\Delta P_L}{\Delta P_{Lo}} = \frac{\Delta P_X}{\Delta P_{Lo}} + \frac{\Delta P_Z}{\Delta P_{Lo}}$$

The terms on the right hand side of the above equation may be expanded, and the equation rewritten as:

$$\frac{\Delta P_L}{\Delta P_{Lo}} = \left(\frac{\Delta P_{Xo}}{\Delta P_{Lo}}\right)\left(\frac{\Delta P_X}{\Delta P_{Xo}}\right) + \left(\frac{\Delta P_{Zo}}{\Delta P_{Lo}}\right)\left(\frac{\Delta P_Z}{\Delta P_{Zo}}\right) \qquad (5)$$

The ratios $(\Delta P_{Xo}/\Delta P_{Lo})$ and $(\Delta P_{Zo}/\Delta P_{Lo})$ are "clean heat exchanger" parameters representing the proportion of total pressure drop occurring in the two sections. These rates can be readily calculated from the initial flow rate, fluid densities and the impedances of the two sections in the clean condition.

The term $\Delta P_Z/\Delta P_{Zo}$ represents the pressure drop ratio in the clean section. The pressure drop in this section may vary due to changes in flow density and flow rate resulting from deposit formation in the frosted section. In accordance with the pressure drop equation for flow normal to tubes,

$$\frac{\Delta P_Z}{\Delta P_{Zo}} = \frac{\bar{\rho}_{Zo}}{\bar{\rho}_Z}\left(\frac{\omega}{\omega_o}\right)^2 \qquad (6)$$

The term $\Delta P_X/\Delta P_{Xo}$ represents the pressure drop ratio in the frosted section. Referring to equation 1 in Section III above, we see that if we assume a

constant frost thickness within the frosted length ($\bar{t}_X$)

$$\frac{\Delta P_X}{\Delta P_{Xo}} = \left[\frac{1}{1 - \bar{t}_X/\delta_o}\right]^2 \left(\frac{\bar{\rho}_{Xo}}{\bar{\rho}_X}\right)\left(\frac{\omega}{\omega_o}\right)^2 \qquad (7A)$$

If, on the other hand, we assume an arbitrary frost distribution within the frosted length

$$\frac{\Delta P_X}{\Delta P_{Xo}} = F_P \left[\frac{1}{1 - \bar{t}_X/\delta_o}\right]^2 \left(\frac{\bar{\rho}_{Xo}}{\bar{\rho}_X}\right)\left(\frac{\omega}{\omega_o}\right)^2 \qquad (7B)$$

The distribution function F_P is <u>defined</u> merely as the ratio of pressure drop resulting from an arbitrary thickness distribution to the pressure drop for constant frost thickness. The distribution function is <u>evaluated</u> by integrating the thickness function $(1/(1 - t_X/\delta_o)^2$ along the frosted length. Expressed algebraically:

$$F_P \equiv \frac{\int \left[\frac{1}{1 - t_X/\delta_o}\right]^2 dy}{\left[\frac{1}{1 - \bar{t}_X/\delta_o}\right]^2}$$

where

t_X = local thickness at y
y = fraction of frosted length
$\bar{t}_X$ = integrated mean thickness

An integration of this type is performed, and the results presented for a "triangular" frost distribution in Section VIII of this Appendix. The expression for the overall flow characteristics of the heat exchanger may now be written by combining equations 5, 6 and 7B.

$$\frac{\Delta P_L}{\Delta P_{Lo}} = \left(\frac{\Delta P_{Xo}}{\Delta P_{Lo}}\right) F_P \left[\frac{1}{1 - \bar{t}_X/\delta_o}\right]^2 \left(\frac{\bar{\rho}_{Xo}}{\bar{\rho}_X}\right)\left(\frac{\omega}{\omega_o}\right)^2 + \left(\frac{\Delta P_{Zo}}{\Delta P_{Lo}}\right)\left(\frac{\bar{\rho}_{Zo}}{\bar{\rho}_Z}\right)\left(\frac{\omega}{\omega_o}\right)^2$$

or

$$\frac{\Delta P_L/\Delta P_{Lo}}{(\omega/\omega_o)^2} = F_P \left(\frac{\Delta P_{Xo}}{\Delta P_{Lo}}\right) \left[\frac{1}{1 - \bar{t}_X/\delta_o}\right]^2 \left(\frac{\bar{\rho}_{Xo}}{\bar{\rho}_X}\right) + \left(\frac{\Delta P_{Zo}}{\Delta P_{Lo}}\right) \left(\frac{\bar{\rho}_{Zo}}{\bar{\rho}_Z}\right) \qquad (8)$$

It should be noted that this equation is applicable to either constant flow or constant pressure drop operation (or any intermediate operating line for which the "system imposed" relationship between ΔP_L and ω is known). In applying this equation, certain points should be noted:

1. The ratios $\Delta P_{Xo}/\Delta P_{Lo}$ and $\Delta P_{Zo}/\Delta P_{Lo}$ are clean heat exchanger parameters calculated as discussed above.

2. The mean frost thickness in the frosted zone $\bar{t}_X$ is determined from equation 4 of Section V above. In variable flow systems, it may be necessary to solve equation 8 in steps so that the contaminant flow variation may be accounted for in equation 4. δ_o, the tube half clearance, is, of course, a heat exchanger geometry parameter.

3. The distribution function F_P is a somewhat arbitrary parameter. For uniform frost thickness in the frosted area, $F_P = 1.0$. Values of F_P as a function of $\bar{t}_X/\delta_o$ are presented in Section VIII for a triangular frost distribution. It is suggested that the calculation be performed for both $F_P = 1.0$ and F_P per Section VIII. The difference in the results will be an indication of the basic error introduced by non-exact knowledge of the frost distribution. As shown in Section VIII, the distribution function is close to unity for low area blockages (i.e., $F_P < 1.1$ for $\bar{t}_X/\delta_o < .2$). However, as the heat exchanger approaches plug-up, F_P becomes a substantial multiplier and the error associated with frost distribution becomes large.

4. The density ratio terms ($\bar{\rho}_{Xo}/\bar{\rho}_X$ and $\bar{\rho}_{Zo}/\bar{\rho}_Z$) are somewhat tedious to evaluate and fortunately may be neglected in most practical systems in which sufficient contaminant deposition to markedly alter flow density would be intolerable. When these terms need be evaluated, the pressure drop equations must be solved in an iterative manner. The general procedure for accounting for density variations would be as follows:

(a) First solve equation 8 for $\bar{\rho}_o/\bar{\rho} = 1.0$ (This is required to estimate flow rate variation, if any).

(b) Solve equations 6 and 7B assuming $\bar{\rho}_o/\bar{\rho} = 1.0$ to estimate altered distribution of pressure in heat exchanger.

(c) Estimate altered flow temperature profile from methods of Section B below.

(d) Estimate the density ratios from the temperature and pressures computed in (b) and (c) above.

(e) Repeat steps (a) - (d) until convergence is obtained.

It should be noted that the evaluation of equation 8 is greatly simplified if we make the following approximations:

1. Assume uniform frost thickness in frosted zone. Therefore:

$$F_P = 1.00$$

2. Neglect variations in flow density. Therefore:

$$\bar{\rho}_{X_o}/\bar{\rho}_X = \bar{\rho}_{Z_o}/\bar{\rho}_Z = 1.0$$

3. Assume clean pressure drops are proportional to length. Therefore:

$$\Delta P_{X_o}/\Delta P_{L_o} = X/L$$

$$\Delta P_{Z_o}/\Delta P_{L_o} = Z/L = (1 - X)/L$$

Equation 8 now is reduced to:

$$\frac{\Delta P_L/\Delta P_{L_o}}{(\omega/\omega_o)^2} = \frac{X}{L}\left[\frac{1}{1 - \bar{t}_X/\delta_o}\right]^2 + \frac{1 - X}{L} \qquad (8A)$$

This form of the equation has been found to be convenient as a basis for correlating experimental data in Appendix 10.

Before concluding this section, it should also be noted that equation 8 can easily be modified to include additional frosted zones and clean zones. For instance, if the heat exchanger has two frosted zones X_1 and X_2 and three clean zones Z_1, Z_2 and Z_3, the resulting equation would be:

$$\frac{\Delta P_L/\Delta P_{L_o}}{(\omega/\omega_o)^2} = F_{P1}\left(\frac{\Delta P_{X_{1o}}}{\Delta P_{L_o}}\right)\left[\frac{1}{1 - \bar{t}_{X_1}/\delta_o}\right]^2\left(\frac{\bar{\rho}_{X_{1o}}}{\bar{\rho}_{X_1}}\right) + F_{P_2}\left(\frac{\Delta P_{X_{2o}}}{\Delta P_{L_o}}\right)\left[\frac{1}{1 - \bar{t}_{X_2}/\delta_o}\right]^2$$

$$\left(\frac{\bar{\rho}_{X_{2o}}}{\bar{\rho}_{X_2}}\right) + \left(\frac{\Delta P_{Z_{1o}}}{\Delta P_L}\right)\left(\frac{\bar{\rho}_{Z_{1o}}}{\bar{\rho}_{Z_1}}\right) + \left(\frac{\Delta P_{Z_{2o}}}{\Delta P_L}\right)\left(\frac{\bar{\rho}_{Z_{2o}}}{\bar{\rho}_{Z_2}}\right) + \left(\frac{\Delta P_{Z_{3o}}}{\Delta P_L}\right)\left(\frac{\bar{\rho}_{Z_{3o}}}{\bar{\rho}_{Z_3}}\right)$$

B. Heat Transfer

Referring to Figure 5 as a model of a simple finite length heat exchanger, we can use the heat transfer relations of Section III above to express the variation in overall air-side heat transfer coefficient for the frosted and clean zones of the heat exchanger.

For the clean section, in which changes in heat transfer coefficient result only from changes in flow, the ratio of clean to frosted overall air-side heat transfer coefficient is as follows:

$$\frac{u_{oZ}}{u_Z} = \left(\frac{\omega_o}{\omega}\right)^{.6} \qquad (9)$$

In the frosted zone, changes in flow, free area and deposit thermal insulation must be considered. If we assume a uniform frost thickness within the frosted area, we may express the ratio of frosted to clean overall air-side heat transfer coefficient as:

$$\frac{u_{oX}}{u_X} = \left(1 - \frac{\bar{t}_X}{\delta_o}\right)^{.6} \left(\frac{\omega_o}{\omega}\right)^{.6} + \left(\frac{h_o \delta_o}{k_F}\right)\left(\frac{t_X}{\delta_o}\right)$$

As in the case of the pressure drop equations, the effect of an arbitrary frost thickness distribution can be included. The resulting equation would then be:

$$\frac{u_{oX}}{u_X} = \frac{1}{F_t}\left[\left(1 - \frac{\bar{t}_X}{\delta_o}\right)^{.6} \left(\frac{\omega_o}{\omega}\right)^{.6} + \left(\frac{h_o \delta_o}{k_F}\right)\left(\frac{t_X}{\delta_o}\right)\right] \qquad (10)$$

In the case of heat transfer, this distribution function (F_t) corresponding to a given frost thickness profile will be a function of ω_o/ω and $h_o\delta_o/k_F$ as well as $\bar{t}_X/\delta_o$. A sample calculation for a heat transfer distribution function is included in Section VIII. It will be noted that the effect of a non-uniform distribution tends to retard the rate of heat transfer decay; whereas in the case of pressure drop, a non-uniform distribution tended to increase the decay in flow capacity.

Equations 8 and 9 above allow for the calculation of the decay in overall air-side heat transfer coefficients in the frosted and clean zones of the heat exchanger. The total coefficient (H) between air and coolant in each zone can then be computed with standard techniques using the known coolant-side coefficient (h_c)

$$\frac{1}{H} = \frac{1}{u} + \frac{1}{h_c}$$

From this point on, calculation of the effects on air and coolant temperature becomes quite specific to the particular heat exchanger under consideration and is generally amenable to standard heat exchanger calculation procedures. Examples of this method as applied to our heat exchanger configuration are included in the next section.

VII. APPLICATION OF ANALYTICAL METHODS TO EXPERIMENTAL SYSTEM AND COMPARISON WITH EXPERIMENTAL DATA

The low pressure coolant tests (F-2, F-3, F-4, F-5) of the flow test series provide a good basis for testing the analytical methods developed above. Many aspects of these tests, such as the presence of only one contaminant and the constant specific heat, balanced flow, coolant, allow for a reasonably simple application of the analytical method. Also, as will be shown below, the data from all four tests fall on a single correlation plot which can be compared with a common analytical result rather than the more tedious process of comparing each test with analytical results specifically prepared for that condition.

A. Pressure Drop

In Appendix 10, a correlation of overall heat exchanger pressure drop ratio (frosted to clean) versus the computed overall mean area blockage has been prepared. The test data for tests F-2, F-3, F-4, F-5 fall close to a single curve on this basis. We will use our analytical methods, in the following paragraphs, both to corroborate the feasibility of a single experimental correlation curve of pressure drop ratio versus overall mean area blockage and to develop this curve from analysis.

The parameters which are common for tests F-2, F-3, F-4 and F-5 are:

Inlet Air Pressure	90 psia $\pm$ 3%
Flow Rate/Unit Free Area	30 lb/sec ft^2 $\pm$ 5%
Mean Air Velocity (@ 0°F and 80 psia)	64 ft/sec $\pm$ 5%
ΔP_o Clean Pressure Drop	12.5 psi $\pm$ 10%
δ_o - Nominal Tube Half Clearance	.031 in.*
Total Heat Exchanger Surface Area	1.76 ft^2 $\pm$ 2%

* 94% of the tube half clearances fall between .028 and .035.

Inlet Air Temperature	$525^{o}R \pm 10^{o}R$
Coolant Inlet Temperature	$321^{o}R \pm 6^{o}R$

Using the test values of inlet water content and the axial temperature plots, the lengths of the frosted zones for these tests are established using the methods outlined in the above sections and illustrated in Figure 4. These results are tabulated below.

		Start of Frosting			End of Frosting			
Test	Water Content (PPM-Vol)	P_{H_2O} (psia)	Tw (^{o}R)	Relative Location	P_{H_2O} (psia)	Ta (^{o}R)	Relative Location	X/L
F-2	80	.007	447	.25	.0007	408	.56	.31
F-3	500	.045	478	.14	.0045	435	.46	.31
F-4	640	.0575	485	.05	.00575	439	.38	.33
F-5	790	.0710	489	.12	.00710	440	.45	.33

As shown above, a common frosted length (X/L = .32) can be used for all four tests with little error.

The surface area in the frosted zone is now determined as $A_F = (.32)(1.76) = .565\ ft^2$. Using the plot of water frost density versus velocity in Appendix 6, we see that $\rho_F \approx .25\ gm/cm^3$.

Likewise the mean area blockage in the frosted zone ($\bar{t}_X/\delta_o$) may be related to the overall mean area blockage ($\bar{t}/\delta_o$) by the equation:

$$(\bar{t}_X)(X) = (\bar{t})(L)$$

or

$$\frac{\bar{t}_X}{\delta_o} = (\frac{\bar{t}}{\delta_o})(\frac{L}{X}) = 3.13\ (\frac{\bar{t}}{\delta_o})$$

Referring to equation 8 in Section VI above, we see that certain pressure drop ratios and density ratio are required to compute the variation in overall pressure drop due to deposit formulas.

Examination of the mean air densities in the frosted and unfrosted lengths shows that $\bar{\rho}_{oZ} \approx \bar{\rho}_{oX}$. Therefore, the clean heat exchanger pressure drops may be apportioned in accordance with length.

$$\frac{\Delta P_{Xo}}{\Delta P_{Lo}} = \frac{X}{L} = .32$$

$$\frac{\Delta P_{Zo}}{\Delta P_{Lo}} = \frac{Z}{L} = .68$$

In estimating the density ratios in the clean and frosted section, we make use of two conditions characteristic of these tests. First, air temperature changes are quite small; therefore, flow density changes result only from pressure changes. Secondly, the frosted zone is near the high pressure end of the heat exchanger. Therefore, we may assume the mean density in the frosted zone is proportional to mean heat exchanger pressure; the mean density in the clean section is proportional to downstream heat exchanger pressure. Expressed algebraically:

$$\frac{\bar{\rho}_{Xo}}{\bar{\rho}_{X}} \qquad \frac{P_1 - \frac{\Delta P_{Lo}}{2}}{P_1 - \frac{\Delta P_L}{2}} \tag{11A}$$

$$\frac{\bar{\rho}_{Zo}}{\bar{\rho}_{Z}} \qquad \frac{P_1 - \Delta P_{Lo}}{P_1 - \Delta P_L} \tag{11B}$$

where P_1 is the heat exchanger upstream pressure.

It should be noted that the above estimation technique for mean density is not generally applicable for all conditions but is roughly correct for the tests under consideration.

At this point, we have assembled all the information required to compute the pressure drop ratio from equation 8. In order to gain some insight into the independent effects of frost distribution and flow density, we will develop analytical curves of $\Delta P_L/\Delta P_{Lo}$ versus t/δ_o for the three cases described below:

Case	F_P	$\bar{\rho}_{Xo}/\bar{\rho}_X$ and $\bar{\rho}_{Zo}/\bar{\rho}_Z$
1	1.0	1.0
2	Triangular Distribution per Section VIII	1.0
3	1.0	per equations 11A & 11B

The applicable forms of equation 8 and the numerical results for these three cases are as follows:

Case 1

$$\frac{\Delta P_L}{\Delta P_{Lo}} = .32 \left[\frac{1}{1 - \bar{t}_X/\delta_o}\right]^2 + .68$$

$\bar{t}/\delta_o$	$\bar{t}_X/\delta_o$	$\left[\frac{1}{1 - \bar{t}_X/\delta_o}\right]^2$	$\Delta P_L/\Delta P_{Lo}$
0	0	1.0	1.00
.0297	.0928	1.21	1.07
.0595	.186	1.51	1.16
.0890	.278	1.91	1.29
.119	.371	2.54	1.49
.148	.464	3.46	1.78
.178	.556	5.10	2.31
.208	.65	8.20	3.30
.237	.741	14.9	5.44

Case 2

$$\frac{\Delta P_L}{\Delta P_{Lo}} = .32\, F_P \left[\frac{1}{1 - \bar{t}_X/\delta_o}\right]^2 + .68$$

$\bar{t}/\delta_o$	$\bar{t}_X/\delta_o$	F_P	$\left[\frac{1}{1 - \bar{t}_X/\delta_o}\right]^2$	$\Delta P_L/\Delta P_{Lo}$
0	0	1.0	1.0	1.0
.0297	.0928	1.02	1.21	1.08
.0595	.186	1.07	1.51	1.20
.0890	.278	1.20	1.91	1.41
.119	.371	1.70	2.54	2.06
.148	.464	4.65*	3.46	5.79

* Extrapolated value.

Case 3

$$\frac{\Delta P_L}{\Delta P_{Lo}} = .32 \left[\frac{1}{1 - \bar{t}_X/\delta_o}\right]^2 \frac{\bar{\rho}_{oX}}{\bar{\rho}_X} + .68 \frac{\bar{\rho}_{oZ}}{\bar{\rho}_Z}$$

$\bar{t}/\delta_o$	$\bar{t}_X/\delta_o$	$\left[\frac{1}{1 - \bar{t}_X/\delta_o}\right]^2$	$\bar{\rho}_{oX}/\bar{\rho}_X$*	$\bar{\rho}_{oZ}/\bar{\rho}_Z$*	$\Delta P_L/\Delta P_{Lo}$
0	0	1.0	1.0	1.0	1.0
.0297	.0928	1.21	1.00	1.00	1.16
.0595	.186	1.51	1.01	1.04	1.20
.0890	.278	1.91	1.03	1.07	1.36
.119	.371	2.54	1.05	1.11	1.60
.148	.464	3.46	1.08	1.18	2.00
.178	.556	5.10	1.15	1.39	2.83

* Computation of the density ratios using equations 11A and 11B requires a iteration procedure. $\Delta P_L/\Delta P_{Lo}$ is initially assumed, to estimate density ratios, and then checked by applying equation 8.

The results of this analysis are plotted in Figure 6. This plot illustrates the effects of frost distribution and varying flow density on the analytical results - and presents a comparison between these results and test data. This plot shows that frost distribution had a very pronounced effect on the analytical pressure drop result, after the ratio of frosted heat exchanger pressure drop to clean heat exchanger pressure drop exceeded about 1.5. Flow density variation has a similar but much less pronounced effect, A characteristic of the analytical curves for all three cases shown is that initially the analysis tends to underestimate the pressure drop ratio - but that the rate of pressure rise increases tends to increase faster for the analytical solutions than for the experimental curve. This result might be caused by a progressively increasing frost density under test conditions - whereas the analytical results are based on constant frost density. This effect will be studied further with the aid of computer solutions.

B. Heat Transfer

Experimental measurements of air and coolant temperatures, and mass flow rates for tests F-2 through F-5 allow us to compute the overall heat transfer coefficient for the test heat exchanger as a function of water addition. The overall heat transfer coefficient (H) is computed as follows:

$$H = \frac{W_a C_{pa} \Delta T_a}{A \Delta T_m}$$

where:

W_a = air flow
C_{pa} = specific heat of air (.246 Btu/lb ^oF)
ΔT_a = total air temperature drop
A = total heat exchanger air-side heat transfer area (1.76 ft^2)
ΔT_m = mean temperature difference between air and coolant

The overall mean area blockage ($\bar{t}/\delta_o$) for the various test points is calculated using the methods of Appendix 10. The pertinent results are tabulated below:

Test	Test Time (min)	$\bar{t}/\delta_o$	ΔT_a (^oF)	W_a (lb/sec)	ΔT_m (^oF)	H Btu/hr ft^2 ^oF
F-2	30	.0234	178	.0307	22	125.3
F-3	25	.072	186	.0304	24	118.5
	35	.152	183		25	112.0
	45	.23	182		25.5	109
F-4	25	.0815	177	.0304	27.5	98.4
	30	.133	175		25.5	105
	35	.185	175		25.5	105
	39	.225	170		26.0	100
F-5	29	.105	186	.0307	35	82
	35	.179	184		32.5	90
	38.5	.224	186		34.5	84.2

For an analytical representation of the effect of water addition on heat transfer, we will assume a uniform frost thickness in the frosted length $t_x = t_x$. Therefore, equation 10 or Figure 3, for $h_o\delta_o/k_F = 5.0$, can be used to determine the variation in overall air-side coefficient in the frosted length (U_X) as a function of area blockage in the frosted length ($\bar{t}_X/\delta_o$). (It may be noted that the relationship between mean area blockage in the frosted length (t_X/δ_o) and overall mean area blockage has been previously established as $\bar{t}_X/\delta_o = 3.13\ \bar{t}/\delta_o$ for this series of tests.)

Having arrived at the percentage variation in overall air-side coefficient (U_X) from Figure 3, the variation in overall air-to-coolant heat transfer coefficient (H_X) in the frosted length can be calculated by introducing absolute values of the clean air-side coefficient and the coolant-side coefficient. Making use of the equations for flow normal to tubes (for the

air-side) and flow within tubes (for the coolant-side), the heat transfer coefficients are estimated as:

$$U_o = 114 \text{ Btu/hr ft}^2 \text{ }^oF$$

$$h_c = \begin{matrix} 715 \text{ Btu/hr ft}^2 \text{ }^oF \text{ (based on coolant area)} \\ 486 \text{ Btu/hr ft}^2 \text{ }^oF \text{ (based on air-side area)} \end{matrix}$$

The detailed calculations of these coefficients are presented in Reference 3.

From the above, it follows that the clean air-to-coolant heat transfer coefficient for the total heat exchanger or any section, H_o, is:

$$\frac{1}{H_o} = \frac{1}{U_o} + \frac{1}{h_c} = \frac{1}{114} + \frac{1}{486}$$

$$H_o = 92.2 \text{ Btu/hr ft}^2 \text{ }^oF$$

Finally, the overall frosted heat exchanger heat transfer coefficient (H_L) can be calculated by averaging the clean and frosted coefficients on the basis of area. As previously calculated, the frosted area for tests F-2 through F-5 is approximately 32% of the total heat exchanger. Therefore, in the presence of frosting, the overall heat exchanger coefficient (H_L) may be written as:

$$H_L = H_Z (Z/L) + H_X (X/L)$$

$$H_L = .68 H_Z + .32 H_X$$

$$H_L = (.68)(92.2) + .32 H_X$$

where:

L = total heat exchanger length
X = frosted length
Z = clean length

The pertinent numerical results are tabulated below:

$\bar{t}/\delta_o$	$\bar{t}_x/\delta_o$	U_x Btu/hr ft^2 °F	H_x Btu/hr ft^2 °F	H_L Btu/hr ft^2 °F
0	0	114	92.2	92.2
.0595	.186	63.1	56.0	80.6
.119	.371	43.5	40.0	75.2
.178	.556	33.0	30.8	72.5
.237	.741	25.6	24.4	70.0

where:

$\bar{t}/\delta_o$ = overall mean area blockage

$\bar{t}_x/\delta_o$ = mean area blockage in frosted lengths

U_x = overall air-side heat transfer coefficient in frosted length (includes air film and frost resistance)

H_x = overall air-to-coolant heat transfer coefficient in frosted length

H_L = overall air-to-coolant heat transfer coefficient for total heat exchanger

The overall heat exchanger heat transfer coefficients are plotted as a function of water addition in Figure 7. This plot presents the experimental and analytical results discussed in the paragraphs above. The main features of this comparison are:

1. The experimental data of tests F-2 through F-4 appear to define a curve having about the same rate of decay as the analytical curve; however, the absolute values of experimental heat transfer coefficients are about 40% higher than the analytical results.

The 40% discrepancy is somewhat higher than we would normally expect from the intrinsic accuracy of the literature heat transfer correlations.

In this specific instance, however, we might expect the experimental coefficients to be somewhat higher than the calculated values due to the helical flow on the coolant-side and the surface roughness effect on the air-side. (Subsequent investigation of effect of curved flow on heat transfer coefficients indicate that by neglecting this factor, we may have underestimated the coolant-side coefficient by about 50% -- or the overall coefficient by about 7%.

2. The data of test F-5 is appreciably lower (say 15%) than that of tests F-2 through F-4. It is likely that the lower heat transfer coefficients in test F-5 result from the water injection starting prior to the

completion of heat exchanger cooldown - with the resultant spreading of the frost layer. Presumably the "spread" frost layer is too thin to markedly influence pressure drop but does have an effect on heat transfer.

3. In tests F-4 and F-5, there appears to be a tendency for the coefficient to initially rise and then decline. This effect may be due to the surface roughness effect.

4. It should be emphasized that the heat transfer coefficient experimental results are very sensitive to slight errors in the air-coolant temperature difference. An error of $3^{o}F$ in this temperature differential is equivalent to a 10% error in heat transfer coefficient.

In summary, the analysis seems to predict the general trend of the heat transfer decay due to water addition. However, at this point, we cannot rule out the possibility that some effects, such as surface roughness, which have not yet been considered in the analysis, may be important.

The test Data of V-7 provides an excellent opportunity to compare the analytical techniques with carbon dioxide pressure drop data. For this test, the effective length of the frosted zone, as defined in Section V above, turns out to be just slightly larger than the last quarter of the test heat exchanger. Experimentally, the pressure drop increase was found to be almost entirely confined to the last quarter of the test heat exchanger. Therefore, the measured pressure drops in the last quarter of the test heat exchanger can be compared directly with the frosted length pressure drop ratio of equation 7B. Also, since the "clean" pressure drop in this section is quite small (approximately 2.2 psi), we can develop a large pressure drop ratio without markedly altering flow density.

In developing an analytical plot of pressure drop ratio versus time, we have assumed uniform frost thickness and constant flow density. Therefore, Figure 2 can be used directly to relate pressure drop ratio to area blockage. In computing mean area blockage in the frosted length versus time, we have assumed $X/L = .25$. We have used a frost density of 65 lb/ft^3 which is in accord with recent experimental measurements.

A plot of the results is shown in Figure 8. The agreement between the experimental data and analytical curve is surprisingly good.

VIII. EVALUATION OF DISTRIBUTION FUNCTIONS FOR PRESSURE DROP AND HEAT TRANSFER

This section is presented to illustrate the evaluation of distribution functions for pressure drop and heat transfer. For the purposes of this illustration, we shall choose the triangular frost distribution profile shown below.

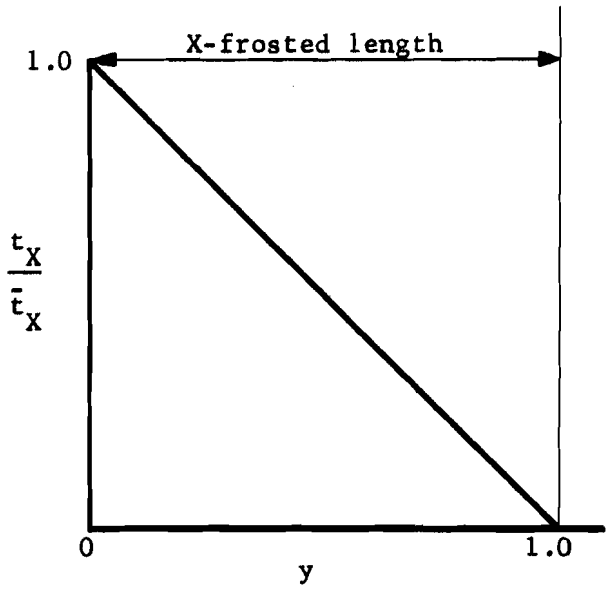

A. Pressure Drop

In accordance with the development of Section VIA:

$$F_P \equiv \frac{\int_o^1 \left[\frac{1}{1 - (t_X/\delta_o)}\right]^2 dy}{\left[\frac{1}{1 - \bar{t}_X/\delta_o}\right]^2}$$

If we define:

$$\beta = \left[\frac{1}{1 - t_X/\delta_o}\right]^2$$

$$\bar{\beta} = \left[\frac{1}{1 - \bar{t}_X/\delta_o}\right]^2$$

then

$$F_P = \frac{\int_o^1 \beta \, dy}{\bar{\beta}} = \int_o^1 (\beta/\bar{\beta}) \, dy$$

To evaluate F_P as a function of $\bar{t}_X/\delta_o$, the following operations are performed:

1. Compute $\beta/\bar{\beta}$ as a function of y for various values of $\bar{t}_X/\delta_o$ using the sketch above to establish t_X.

2. Numerically integrate plot of $\bar{\beta}/\beta$ versus y for each value of $\bar{t}_X/\delta_o$.

The results of this procedure are plotted in Figure 9.

B. Heat Transfer

In accordance with the development of Section VIB, the heat transfer distribution function may be defined as:

$$F_t = \frac{\int_o^1 U_X \, dy}{\bar{U}_X} = \int_o^1 \frac{U_X}{\bar{U}_X} \, dy$$

Using Figure 3, we can determine U_X/U_{Xo} as a function of t_X/δ_o and $\bar{U}_X/U_{Xo}$ as a function of $\bar{t}_X/\delta_o$. For our specific example, we will consider a constant flow system and assume $h_o\delta_o/k_F = 5$. (Note that the heat transfer results are in general a function of $h_o\delta_o/k_F$ and the system operating line, as well as area blockage; whereas, per Figure 1, the flow parameter is a function of area blockage only.)

From this point on, the procedure is similar to that used for the pressure drop function. The specific steps are:

1. Compute $U_X/\bar{U}_X$ as a function of y for various constant values of $\bar{t}_X/\delta_o$.

2. Numerically integrate the plot of U_X/U_X versus y to obtain F_t as a function of $\bar{t}_X/\delta_o$.

The results of this procedure are plotted in Figure 10.

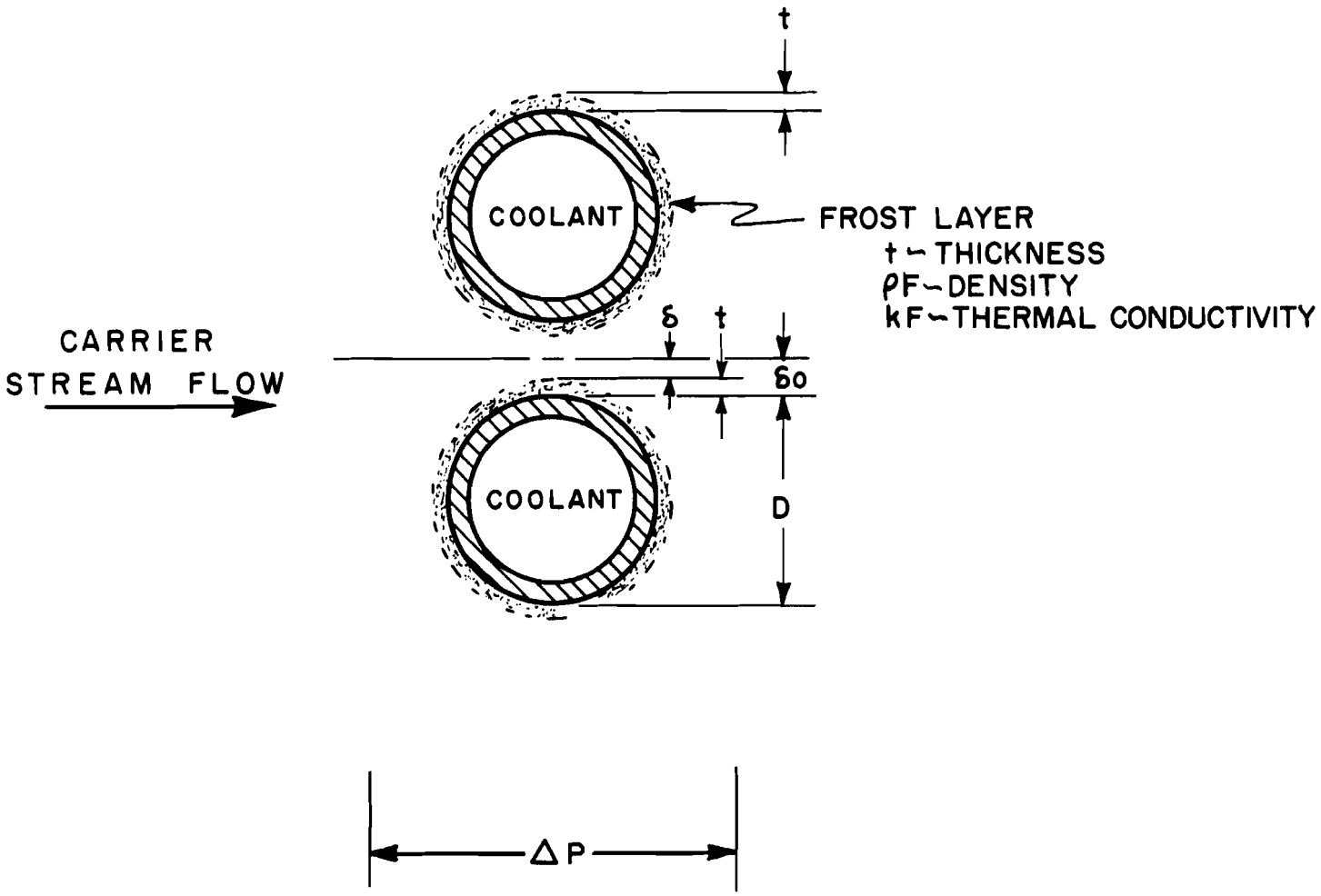

FIGURE 1 GEOMETRIC MODEL FOR SINGLE TUBE FLOW AND HEAT TRANSFER ANALYSIS

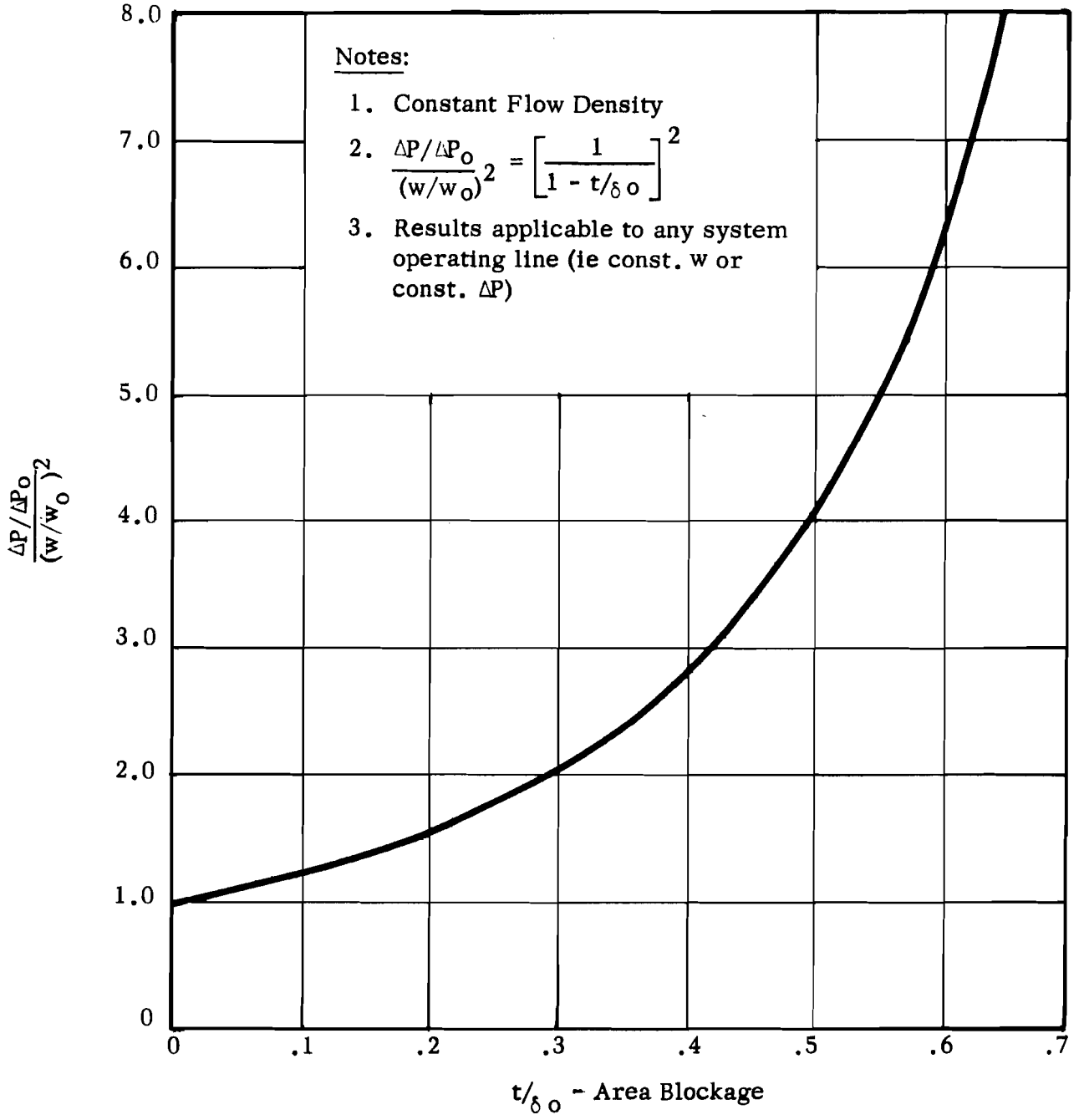

FIGURE 2 EFFECT OF AREA BLOCKAGE ON FLOW CAPACITY-SINGLE TUBE ROW ANALYSIS

Notes:

1. Close Packed Tubes ($\delta_o/D_o \ll 1$)
2. For Const ΔP

$$u_o/u = \frac{1}{1+(h_o\delta_o)(t/\delta_o)}$$

3. For Const w ----- $\frac{}{kf}$

$$u_o/u = (1-t/\delta_o) + .6\,(h_o\delta_o)(t/\delta_o)\,\frac{}{kf}$$

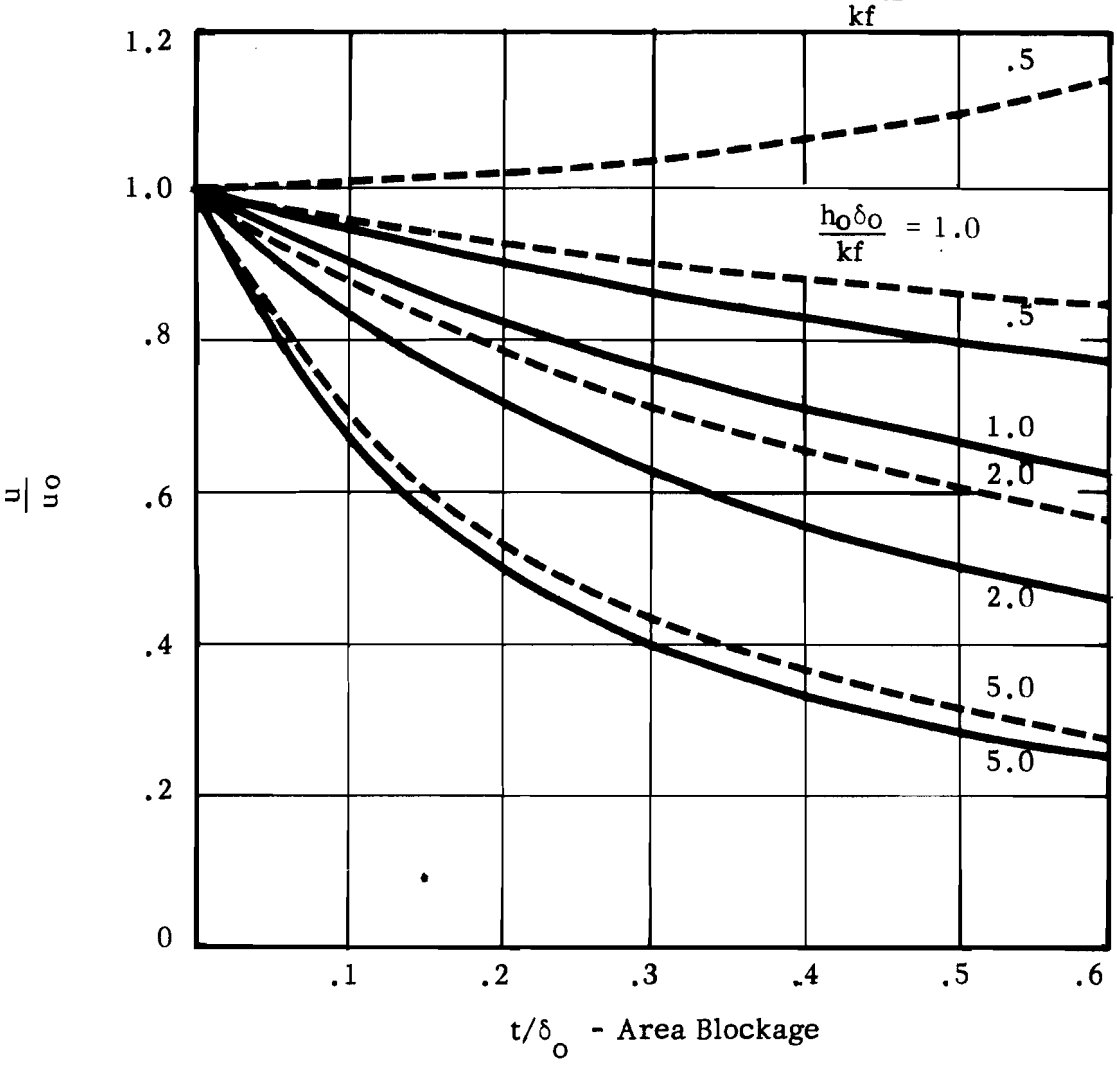

FIGURE 3 EFFECT OF FROST LAYER ON HEAT TRANSFER SINGLE TUBE ROW ANALYSIS

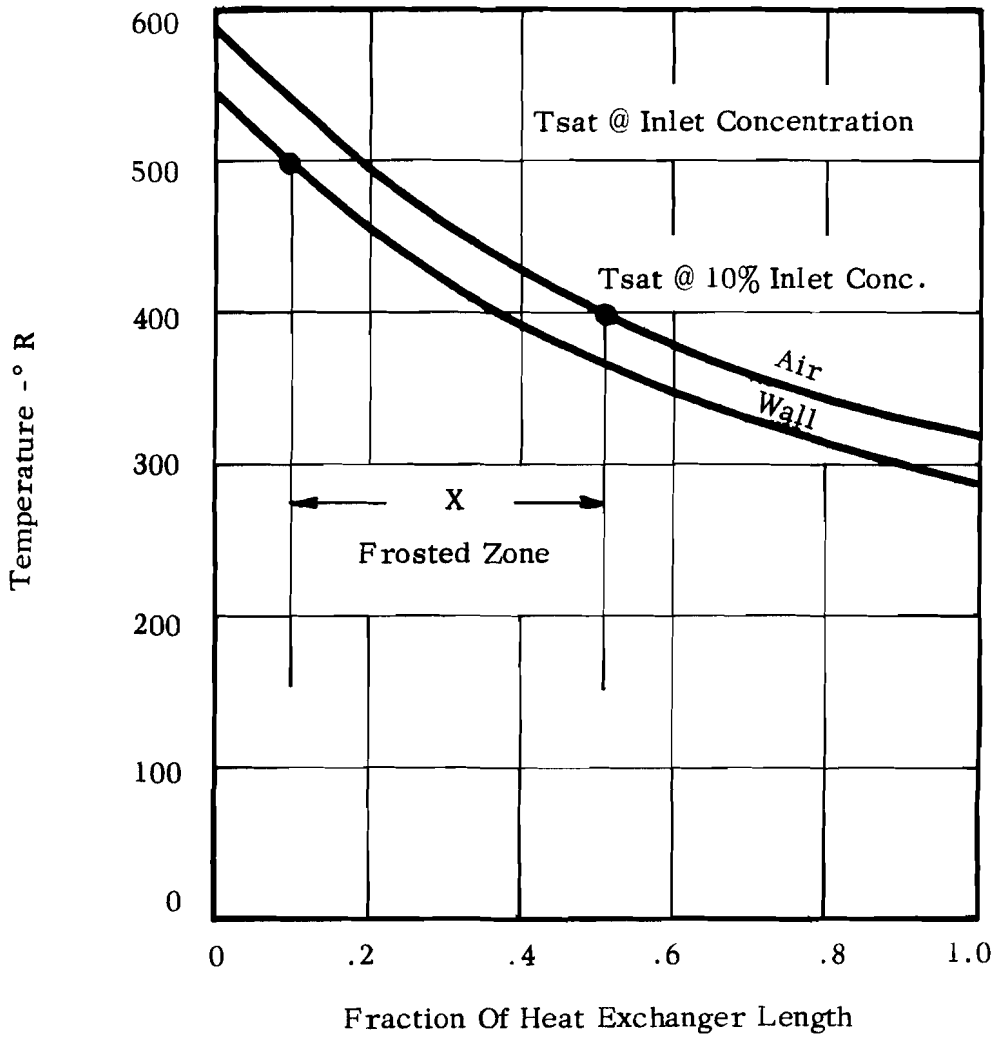

FIGURE 4 ESTIMATION OF EFFECTIVE FROSTED ZONE IN HEAT EXCHANGER

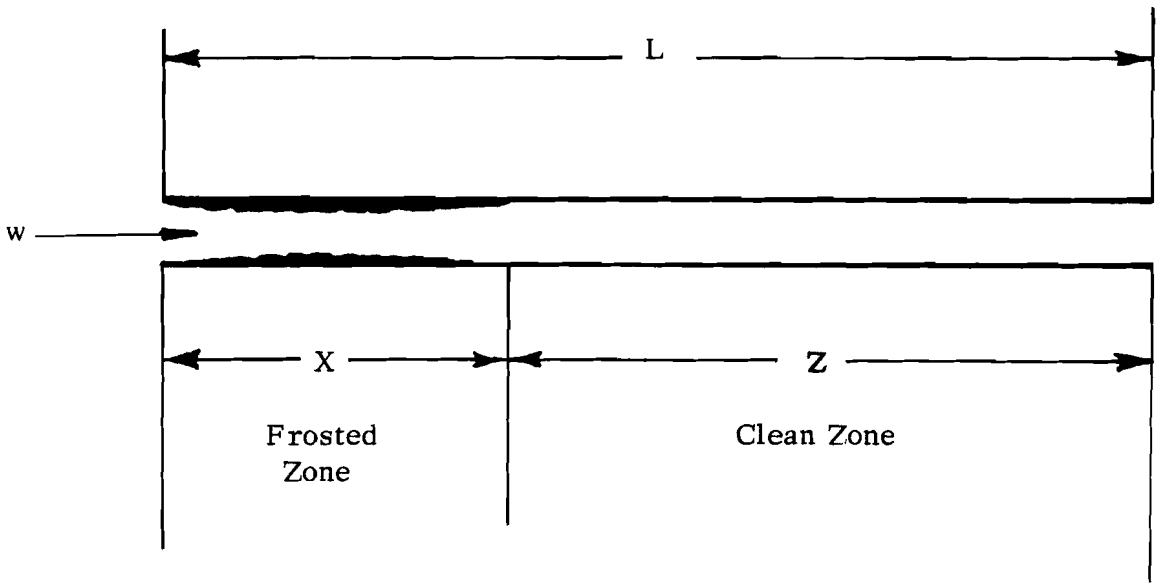

FIGURE 5 ANALYTICAL MODEL FOR FINITE HEAT EXCHANGER FLOW AND HEAT TRANSFER ANALYSIS

Legend For Analytical Curves

Case	Frost Distribution	Flow Density
1	Uniform	Constant
2	Triangle	Constant
3	Uniform	Pressure Dependent

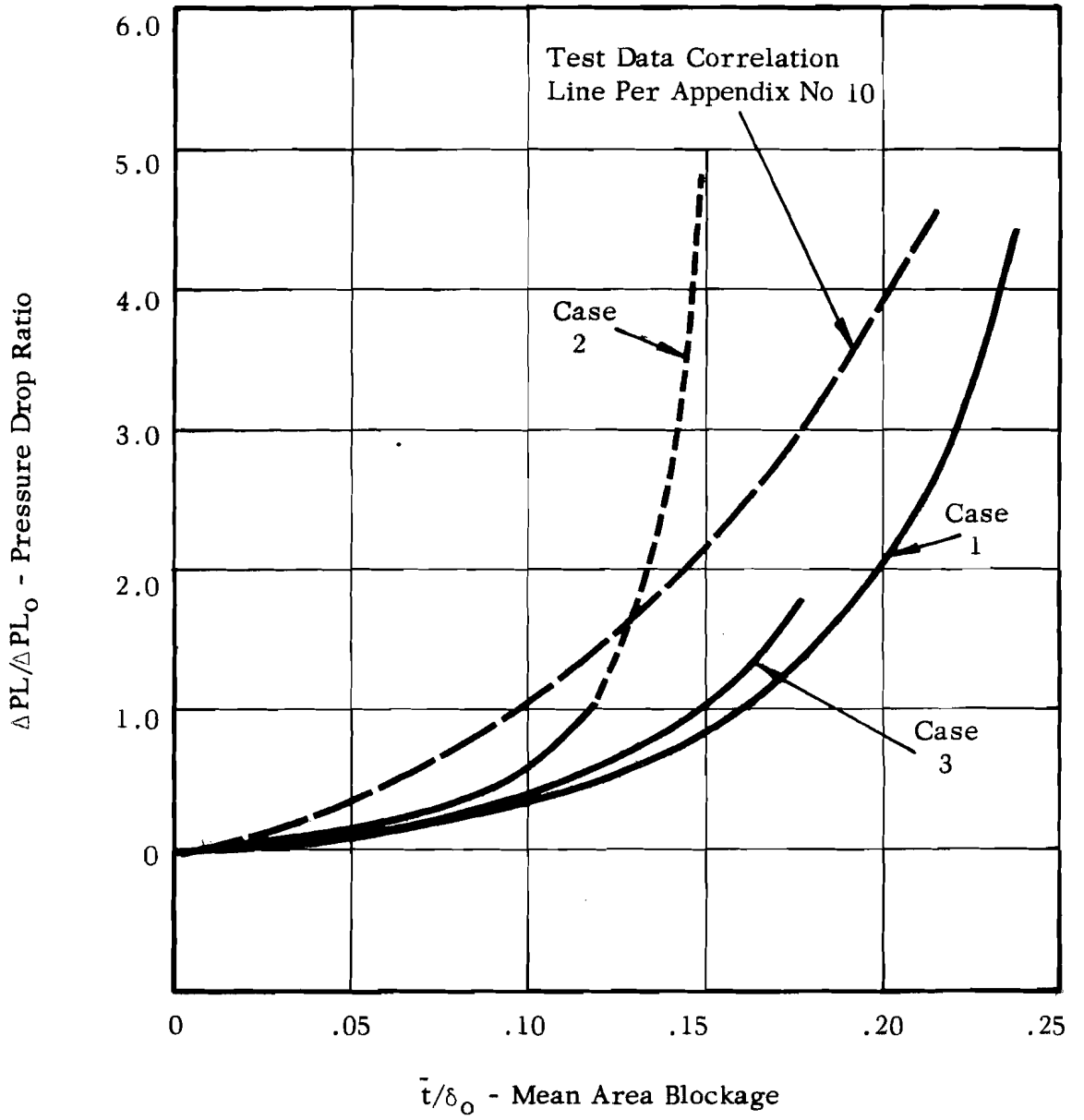

FIGURE 6 OVER-ALL WATER FROST PRESSURE DROP COMPARISON OF ANALYSIS AND TEST DATA

Notes:

1. Test Data Per Tests F-2, F-3, F-4, F-5, Numbers in Squares Denote Test No.
2. Analytical Result For Uniform Frost Thickness - Using Literature Data For "Clean" Heat Transfer Coefficients

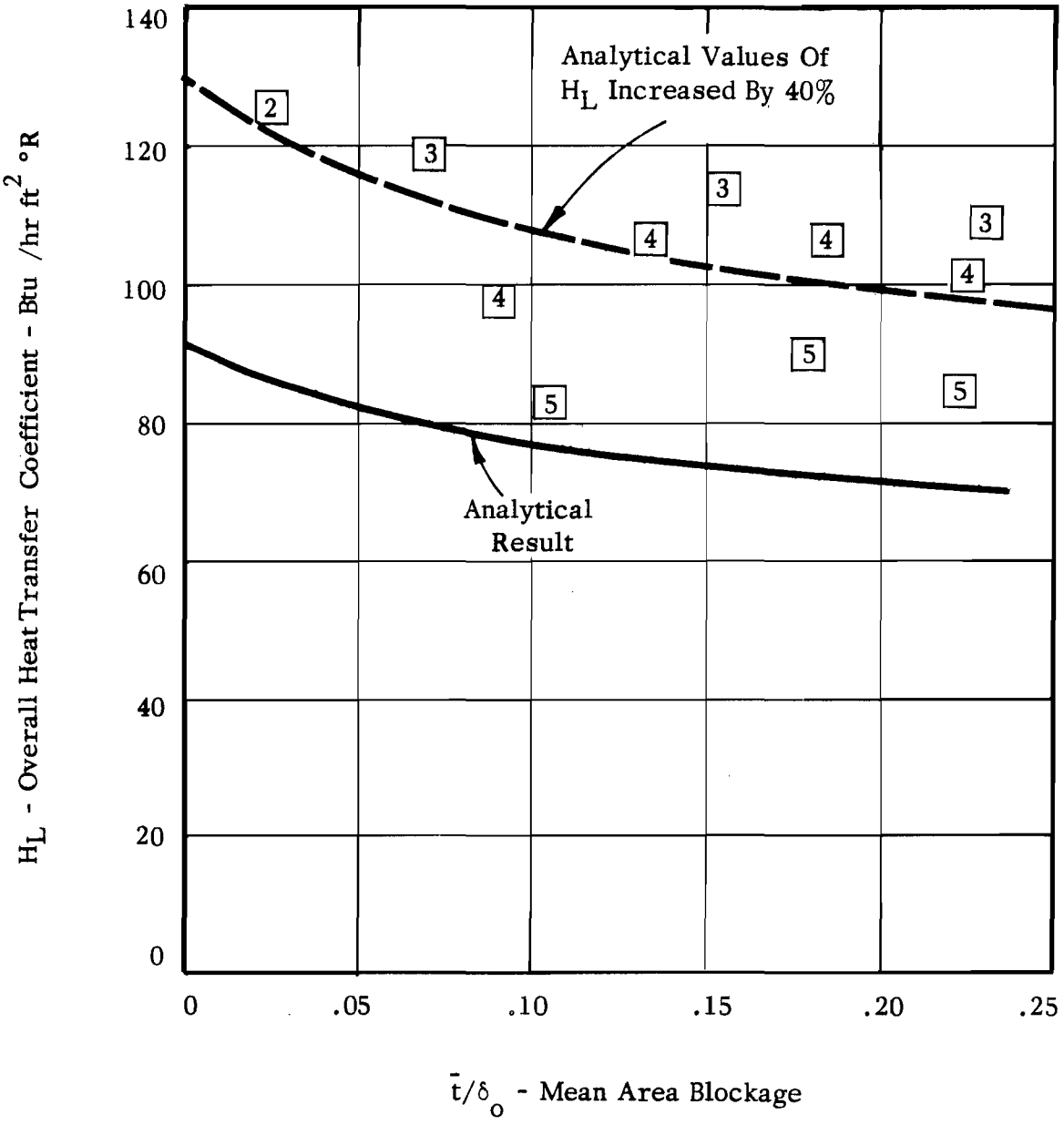

FIGURE 7 OVER-ALL WATER FROST HEAT TRANSFER COMPARISON OF ANALYSIS AND TEST DATA

Notes:

1. Analysis Based On Uniform Frost Thickness, Constant Flow Density, And Test V-7 Air And Contaminant Flows. ρ_F = 65 #/ft^3
2. ● V-7 Test Data

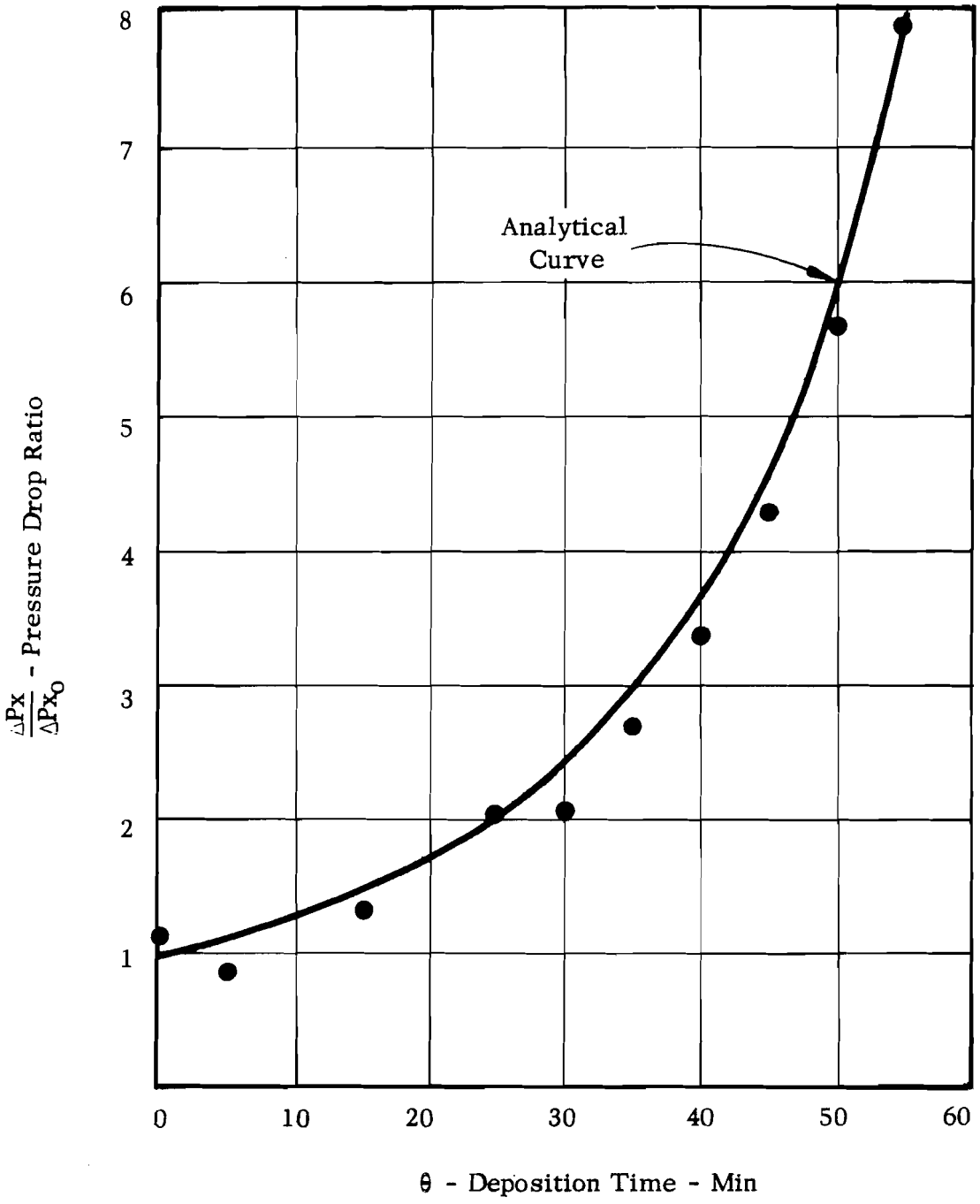

FIGURE 8 CARBON DIOXIDE PRESSURE DROP-COMPARISON OF ANALYSIS AND TEST DATA

Notes:

1. $t_x/\bar{t}_x = 2\,(1-y)$

2. AS $\bar{t}_x/\delta_o \rightarrow .5$, $(t_x/\delta_o)_{max} \rightarrow 1.0$
   $\therefore F_p \rightarrow \infty$

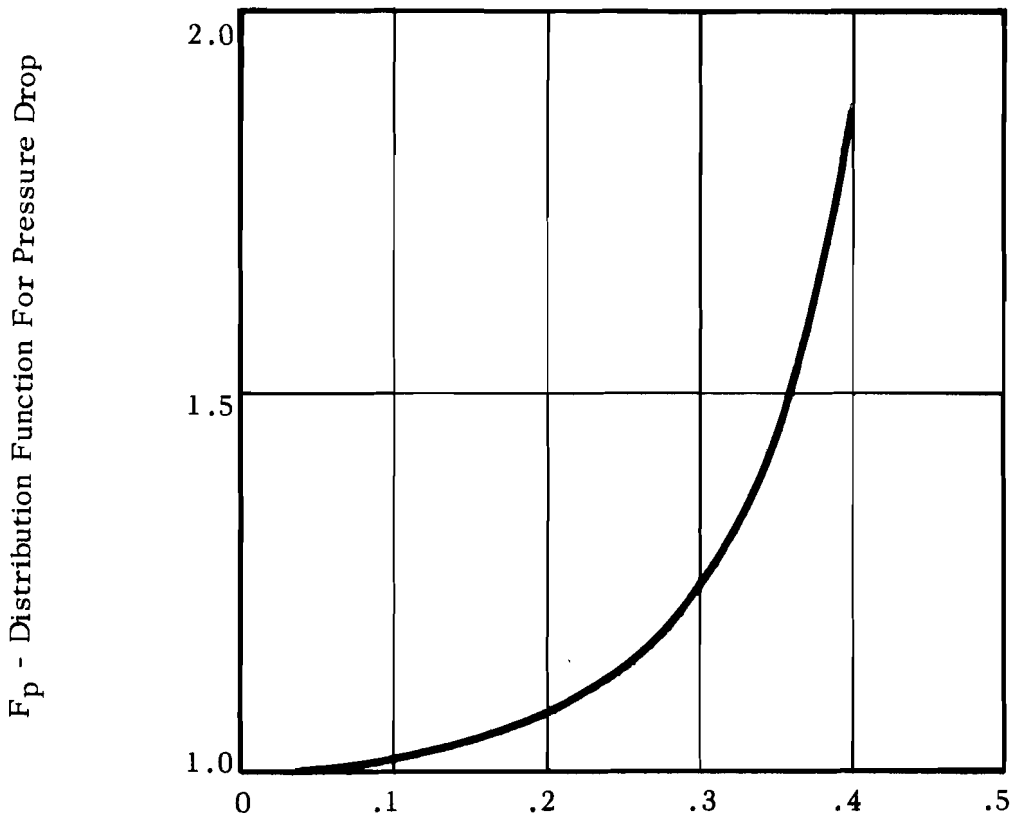

FIGURE 9 DISTRIBUTION FUNCTION FOR PRESSURE DROP

Notes:

1. Triangular Frost Distribution $t_x/\bar{t}_x = 2\ (1-y)$

2. Constant w, $h_o\delta_o/kF = 5.0$

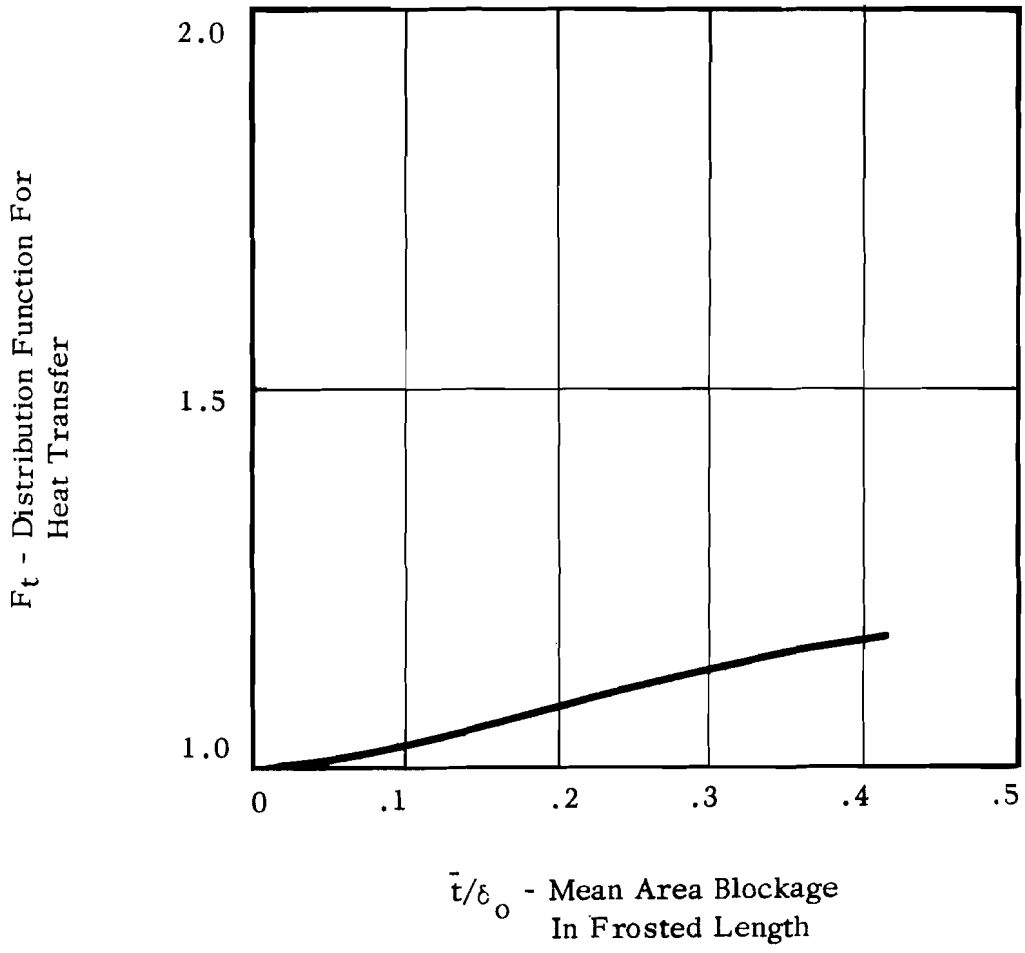

FIGURE 10 DISTRIBUTION FUNCTION FOR HEAT TRANSFER

APPENDIX 12

SIMPLIFIED COMPUTER STUDY - THE CONSTANT HEAT TRANSFER MODEL

TABLE OF CONTENTS

SUMMARY

The equations describing the heat and mass transfer behavior of a frosting countercurrent exchanger are derived. The equations do not cover the transient cooldown of an exchanger but are written to describe the transient behavior of the cold exchanger after the contaminants have been "turned on." For all cases considered quasi static assumptions are justified.

A simplified model was derived from these equations to test the utility of a computer solution for the frosting exchanger. This model assumes that heat transfer rates are constant with time and position within the exchanger. With this assumption heat transfer rates were calculated for the clean exchanger and then assumed constant with time. Experimental air and coolant temperatures were used for this calculation. Mass transfer and pressure drop were then computed as functions of time.

The results of these computer calculations and comparison with the test data showed

1. Frost deposition starts when the wall temperature reaches the dew point of the inlet gas in agreement with the test data

2. Experimental water frost thickness profiles are well predicted by this analysis

3. Experimental CO_2 frost thickness profiles have a shape different from that predicted by the model

4. Model pressure drop and plugging time are in reasonable agreement with test data

5. Frost density has a strong effect on computed thicknesses and pressure drop

6. Frost thermal conductivity has a small effect on pressure drop and thickness for this model. This is due, in part, to the assumption of constant heat transfer.

SIMULATION OF A FROSTING HEAT EXCHANGER

I. General equations

An overall counter flow exchanger is considered as shown schematically below:

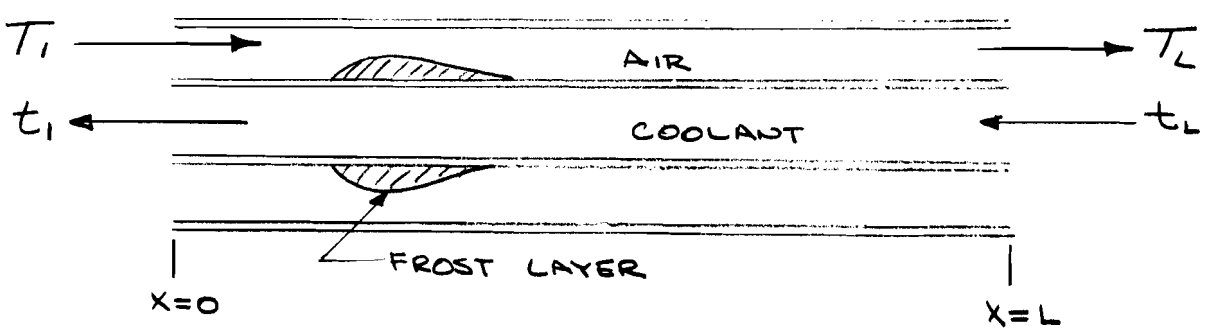

The air stream may contain any number of condensible vapors which may deposit on the walls as a frost layer. The coolant is dry and the exchanger is assumed adiabatic (no heat leak from outside).

Enthalpy, Material and Momentum balances were made on a differential section of the exchanger.

The following assumptions were made

1. Adiabatic exchanger

2. Air and coolant are ideal gases (i.e., no effect of pressure on enthalpy)

3. No nucleation in the gas phase (i.e., no fog or snow formed)

Under these conditions we may write the following

a) Material Balances

   1) air (1 for each component of stream)
   2) coolant
   3) frost layer

b) Enthalpy Balances

   1) air
   2) coolant
   3) frost layer
   4) tube wall

c) Momentum Balances

   1) air
   2) coolant

We consider that we know the temperature, pressure, humidity of the inlet air stream and the inlet temperature and pressure of the coolant. These quantities are known although they may be functions of time.

In writing the general equations we assume that all heat fluxes can be written as

$$Q = hA\Delta T \tag{1}$$

and all mass transfer fluxes as

$$M = k'A\Delta H \tag{2}$$

where H is the humidity in lb vapor/lb dry air.

The coefficients in (1) and (2) are assumed to be known functions of the fluid properties, flow rates, etc. (See Reference 1, Chapter 9, for example.)

The driving force ΔT is the temperature of the gas stream minus the temperature of the surface the gas "sees". Similar remarks apply to ΔH.

The following equations and boundary conditions can then be formulated:

a) Coolant Material Balance

$$-\frac{\partial w}{\partial x} = -\frac{\partial}{\partial \theta}(\rho V_i) \tag{3}$$*

B/C

$$\text{at } X = L \qquad w = w_L \tag{3a}$$

$$\text{at } \theta = 0 \qquad \rho = \rho(x) \tag{3b}$$

b) Air Stream Material Balance

$$-W\frac{\partial H_j}{\partial x} - k'_j A_x (H_j - H_j^s) = \rho_G V_x \frac{\partial H_j}{\partial \theta} \tag{4}$$

B/C

$$\text{at } x = 0 \qquad H_j = H_{j_1} \tag{4a}$$

$$\text{at } \theta = 0 \qquad H_j = 0 \quad \text{all } x \tag{4b}$$

One equation like (4) can be written for every component of the air stream. For the air itself:

$$-\frac{\partial W}{\partial x} = \frac{\partial}{\partial \theta}(\rho_G V_x) \tag{5}$$

B/C

$$\text{at } x = 0 \qquad W = W_1 \tag{5a}$$

$$\text{at } \theta = 0 \qquad \partial W/\partial x = 0 \tag{5b}$$

c) Frost Layer Material Balance

$$A_x \sum_j^+ k'_j (H_j - H_j^s) = \frac{\partial}{\partial \theta}(\rho_f V_f) \tag{6}$$

B/C

$$\text{at } \theta = 0 \qquad V_f = 0 \tag{6a}$$

The summation in (5) is over all components with $(H_j - H_j^s) > 0$.

*Nomenclature at end of appendix.

d) Coolant Enthalpy Balance

$$- wc \frac{\partial t}{\partial x} + A_i h_i \ (t - T_W{}^i) = \rho V_i c \frac{\partial t}{\partial \theta} \tag{7}$$

B/C

$$\text{at } X = L \qquad t = t_L \tag{7a}$$

$$\text{at } \theta = 0 \qquad t = t(x) \tag{7b}$$

e) Air Enthalpy Balance

$$- W \left[c_A + \sum_j H_j c_j \right] \frac{T}{x} - A_x h_o \ (T - T_s) = \rho_G V_x \left[c_A + \sum H_j c_j \right] \frac{T}{\theta} \tag{8}$$

B/C

$$\text{at } x = 0 \qquad T = T_1 \tag{8a}$$

$$\text{at } \theta = 0 \qquad T = T(X) \tag{8b}$$

In equation (7) the summation is over <u>all</u> j components in the air stream.

f) Tube Wall Enthalpy Balance

$$k_f A_x \frac{T_s - T_w}{\Delta} + A_i h_i \ (T - T_w{}^i) = M_t C_t \frac{\partial T_{TUBE}}{\partial \theta} \tag{9}$$

B/C

$$\text{at } \theta = 0 \qquad T_{TUBE} = T_{TUBE}\ (X) \tag{9a}$$

g) Frost Layer Enthalpy Balance

$$A_x h_o \ (T - T_s) - A_x k_f \frac{T_s - T_w}{\Delta} + A_x \sum_j^{+} k'_j \ (H_j - H_j{}^s)(\lambda_{j_s} + \int_{T_s}^{T} c_j dT - \int_{T_s}^{T} c_j{}^s dT)$$

$$= \rho_f V_f \ (\sum_j f_j c_j{}^s) \ \frac{\partial T_f}{\partial \theta} \tag{10}$$

B/C

$$\text{at } \theta = 0 \qquad T_f = T_{TUBE} \tag{10a}$$

h) Saturation Relationship at Frost Surface

$$H_j{}^s = f(T_s) \tag{11}$$

Equation (11) relates the surface humidity to the surface temperature.

i) Pressure Drop (Momentum Balance) - Coolant

$$-\frac{\partial P_c}{\partial x} = \frac{G_i^2}{2gc}\frac{\partial}{\partial x}\left(\frac{1}{\rho}\right) + \frac{2f_i G_i^2}{gcD_i \rho} \tag{12}$$

B/C

$$\text{at } x = L \qquad P = P_L \tag{12a}$$

j) Pressure Drop (Momentum Balance) - Air Stream

$$-\frac{\partial P}{\partial X} = \frac{G^2_{MAX}}{2gc}\frac{\partial}{\partial x} + \frac{4f'' G^2_{MAX}}{2gc\,\rho_G}\wedge \tag{13}$$

B/C

$$\text{at } x = 0 \qquad P = P_1 \tag{13a}$$

Equations (3) - (13) describe the frosting process. They are a set of simultaneous non-linear differential equations.

k) Analyzing the orders of magnitude of the terms in the above equations shows that neglecting the time derivative terms in (3), (4), (7), (8), (9) and (10) results in less than 5% error. This is equivalent to a quasi-static approximation to the problem. We thus conclude

1. W,w are constant with length
2. The tube temperature at any x is a single value T_w
3. Holdup of vapor is negligible compared to total vapor thruput.
4. For low humidities $\sum H_j c_j$ can be neglected compared to C_A

l) Additional Assumptions

Due to the uncertanity in frost data we will assume

1) frost density constant

2) frost thermal conductivity constant

m) Simplified General Equations

$$w = w_2 \tag{14}$$

$$W = W_1 \tag{15}$$

$$- W \frac{\partial H_j}{\partial x} = A_x k'_j (H_j - H_j^s) \tag{16}$$

B/C at $x = 0$ $H_j = H_{j_1}$ (16a)

$$- WC_A \frac{\partial T}{\partial X} = A_x h_o (T - T_s) \tag{17}$$

B/C at $x = 0$ $T = T_1$ (17a)

$$- wc \frac{\partial t}{\partial x} = A_i h_i (T_W - t) \tag{18}$$

B/C at $x = L$ $t = t_L$ (18a)

$$A_x \sum_j^+ k'_j (H_j - H_j^s) = \rho_f \frac{\partial V_f}{\partial \theta} \tag{19}$$

B/C at $\theta = 0$ $V_f = 0$ (19a)

$$h_o A_x (T - T_s) + A_x \sum_j^+ k'_j (H_j - H_j^s) \lambda_j = k_f A_x \frac{T_s - T_w}{\Delta} \tag{20}$$

$$A_i h_i (T_w - t) = k_f A_x \frac{T_s - T_W}{\Delta} \tag{21}$$

$$H_j^s = f(T_s) \tag{11}$$

we also have the volumetric relationship

$$V_x = V_x^o - V_f \tag{22}$$

and

$$A_x = f(\Delta, V_x) \tag{23}$$

We have therefore:

11 Unknowns - w, W, H_j, H_j^s, T, T_s, t, T_W, V_f, Δ, A_x

II Equations- (14), (15), (16), (17), (18), (19), (20), (21), (22), (23), (11).

assuming the coefficients and properties are given.

The pressure drop equations can then be solved from the solution to the 11 equations above.

Note that the system of equations derived here can be used for either the case of constant W, or constant Δ P. In the latter case W becomes an unknown, but ΔP is given so we still have the same number of equations as unknowns.

II. Constant Heat Transfer Model

a) Basic Assumptions

Because of the complexity of the system of equations a simpler approach was tried. In our tests with in-line tubes and constant flow of air and coolant, it was noted that air temperatures did not vary appreciably during any single run. This experimental fact implies that

1) all coolant and air temperature are constant at their unfrosted values

2) tube wall temperatures are constant

3) at every point the heat load is a constant, i.e., the right hand side of equation (17) is constant and equal to its value in the clean exchanger.

A simple model was based on 1, 2 and 3. If they are assumed to be true, the heat transfer calculation need be made only once, at the start of the frosting process (i.e., for the clean, but cooled down exchanger). The wall, air and coolant temperatures thus calculated are taken as constants for the remainder of the calculation. The frost surface temperature, T_s, is calculated from equation (21). Since the thickness of frost increases with time (Δ increases), the surface temperature increases since the left hand side of (21) remains constant (because of the assumption of constant heat load).

This model is based on experimental results for constant mass flow rate of coolant and air, constant inlet pressure, constant air and coolant inlet temperatures and constant inlet humidities. Its validity has not been tested for other modes of operation.

b) Method of Calculation

For testing the model proposed here, actual air temperatures and inlet coolant temperature were used. The values were taken from those experimental runs which will be used to check the predictions of the model.

Since only temperature, geometry and flow conditions were taken from experimental data, comparison of the predicted frost thicknesses and pressure drop with the experimental data will provide a good check on the model.

The calculation proceeds as follows

1) Given T as function of x

2) Given W, w, c_A, c, t_L

3) Calculate t as function of x from a simple enthalpy balance:

$$Wc_A (T - T_L) = wc (t - t_L) \qquad (24)$$

4) Calculate h_o, h_i from flow rates, temperatures and fluid properties

5) Calculate T_W by combining (20) and (21) for a dry exchanger (no humidity)

$$A_i h_i (T_W - t) = A_x h_o (T - T_W)$$

6) From T calculate heat load as function of x

$$\text{heat load} = h_o A_x (T - T_s) - Wc_A \frac{T}{X} \qquad (25)$$

7) Use humidity equation (16) to calculate the humidity profile a zero time

8) Use equation (19) with (22) and (23) to calculate a new frost thickness

9) With this new thickness and the heat load use (21) to calculate a new T_s

10) Repeat cycle - using the new T_s and the saturation relationship (11) go back to step 7.)

11) From the frost thickness and original geometry the pressure drop can be calculated from (13).

c) Details of the Computational Procedure

1) The exchanger is split into a number of segments and each point is numbered consecutively from 1 at the hot fluid (air) inlet to N at the other end

2) For the calculation of cold fluid temperatures

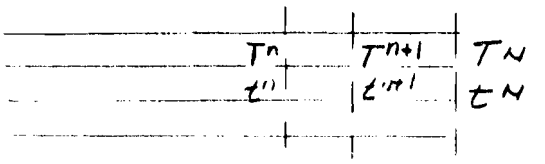

$$t^n = t^N + \frac{Wc_A}{wc} \quad (T^n - T^N) \tag{26}$$

3) Calculation of coefficients

$$St_o = \frac{h_o}{C_A G_{MAX}} = B_1 \quad \left(\frac{DG_{MAX}}{\mu_G} \right)^{B_2} \tag{27}$$

(see Reference 1, pg 273)

$$St_i = 0.026 \left(\frac{D_i \, G_i}{\mu_c} \right)^{-0.2} \tag{28}$$

(see Reference 1, pg 240)

$$\frac{h_o}{k'_j C_A} = \frac{0.294}{C_A} \left(\frac{\mu_A}{\rho_A D_j} \right)^{0.56} = \alpha_j \tag{29}$$

(see Reference 2, pg 100)

4) Calculation of T_W - from (20)

$$T_W{}^n = \frac{T^n + r^n \Gamma^n \eta^n t^n}{1 + r^n \Gamma^n \eta^n} \tag{30}$$

$$r^n = \left(\frac{St_i}{St_o} \right)^n \quad \text{(at } n^{\underline{th}} \text{ distance point, } \underline{\text{not}} \text{ exponent)}$$

$$\Gamma^n = (CG_i / C_A G_{MAX})^n$$

$$\eta^n = (A_i / A_x)^n$$

5) Calculation of Heat Load

$$(\text{Heat Load})^n = \frac{WC_A}{2} \left(T^{n-1} - T^{n+1}\right) \tag{31}$$

6) Humidity Profile of Air Stream

Approximate the derivative as follows

$$\frac{\partial H}{\partial X} = \frac{H^{n+1} - H^N}{\Delta X} \tag{32}$$

with (32) and (16) we can obtain (33)

$$H^{n+1} = \left(\frac{1-Z^{n+1/2}}{1+Z^{n+1/2}}\right) H^n + \frac{Z^{n+1/2}}{1+Z^{n+1/2}} \left(H^{s,n+1} + H^{s,n}\right)$$

where

H^s is calculated from the saturation equation

$$Z^{n+1/2} = \frac{\Delta z}{2} \left[\frac{1}{2}\left(\frac{\gamma_o St_o}{\alpha}\right)^n + \frac{1}{2}\left(\frac{\gamma_o St_o}{\alpha}\right)^{n+1}\right]$$

$z = X/L \qquad \gamma_o = A_x L / a_o$

7) Calculation of mass flux to surface

$$\sum F_j^n = G_{MAX}^n \; St_o^n \left[\sum_j^+ \frac{H_j^n - H_j^{s,n}}{\alpha_j}\right] \tag{34}$$

8) Calculation of new thickness

from (19): $A_x \sum F_j^n = \rho_f \left(\frac{\partial V_f}{\partial \theta}\right)^n$ (35)

but for frost layers outside of tubes

$$V_f = \pi R^2 \left[1 - \left(\frac{R_o}{R}\right)^2\right] \tag{36}$$

$$\frac{\partial V_f}{\partial \theta} = 2\pi R \frac{\partial R}{\partial \theta} \tag{37}$$

but, for frost formation outside of tubes

$$A_x = 2\pi R \tag{38}$$

and also $$R = R_o + \delta \tag{39}$$

Combining (35), (37), (38) and (39) with the time derivative approximated as in (32), we get

$$\delta_{i+1}^{n} = \delta_{i}^{n} \frac{\sum F_j^{n} \Delta\theta}{\rho_f} \tag{40}$$

where $\theta = i\Delta\theta$

9) Calculation of new T_s - equation (21) written for every point n gives

$$T_s^{n} = T_W^{n} + \frac{(\text{Heat Load})^{n}}{k_f A_x^{n}} \delta^{n} \tag{41}$$

keeping in mind that the heat load is constant at its initial value

With the value of T_s just calculated we use the saturation equation and then go to step 3.) to recalculate the coefficients which will have changed slightly since the frost layer has blocked off some of the flow area. We then go stepwise through to 9.)

10) Pressure Drop

Equation (13) is rewritten in difference equation form using the same approximation for the first derivative as used in (32).

$$P^{n+1} = P^{n} - Y^{n+1/2} \left(\frac{1}{\rho_G^{n+1}} - \frac{1}{\rho_G^{n}} \right) - X^{n+1/2} \left(\frac{8}{\rho_G^{n} + \rho_G^{n+1}} \right) \tag{42}$$

TABLE 1

CASE	FROST DENS LB/FT^3	FROST COND BTU/HR FT$^\circ$F	TEMPERATURE AIR IN $^\circ$R	TEMPERATURE COOLANT IN $^\circ$R	INLET WATER PPM(VOL)	INLET CO_2 WT%	AIR FLOW LB/SEC	AIR HEAT CAPACITY BTU/LB$^\circ$F	CAPACITY RATIO (NOTE 1)	TUBE O.D. INCHES	COMPARABLE EXPERIMENTAL RUN
I		TO DEBUG PROGRAM									
II-VII		TO DETERMINE CONVERGENCES AND STABILITY - SAME INPUT DATA AS CASE VIII									
VIII	15.5	0.125	557	330	1110	0	.031	0.248	1.0	3/16	V-2
IX	15.5	0.0125	557	330	1110	0	.031	0.248	1.0	3/16	V-2
X	30.0	0.125	557	330	1110	0	.031	0.248	1.0	3/16	V-2
XI	15.5	0.125	568	393	255	0	.031	0.248	1.0	3/16	V-5) NOTE 2
XII	15.5	0.0125	568	393	255	0	.031	0.248	1.0	3/16	V-5)
XIII	18.1	0.067	568	393	255	0	.031	0.248	1.0	3/16	V-5)
XIV	60	0.222	323	169	0	.044	.032	0.248	1.01	3/16	V-7
XV	60	0.222	323	169	0	.044	.032	0.248	1.01	3/16	V-7

NOTES: (1) CAPACITY RATIO = AIR FLOW X AIR HEAT CAPACITY/COOLANT FLOW X COOLANT HEAT CAPACITY.
(2) INLET WATER CONCENTRATION FOR TEST V-5 WAS 430 PPM(VOL)--65% GREATER THAN CASES XI, XII and XIII.
(3) FOR ALL RUNS: ORIGINAL TUBE PITCH = 1.33; INLET AIR PRESSURE = 90 PSIA.
(4) RUNS XIV & XV: DENSITY AND CONDUCTIVITY ARE FOR CO_2 FROST. SUPERCRITICAL N_2 WAS USED AS COOLANT. CALCULATIONS WERE MADE ONLY OVER LAST 36% OF HEAT EXCHANGER.
(5) RUN XV: ALTERNATE FRICTION FACTOR EXPRESSION USED.

where

$$Y^{n+1/2} = \frac{1}{4gc}\left[\left(G_{MAX}^{n+1}\right)^2 + \left(G_{MAX}^{n}\right)^2\right] \tag{42a}$$

$$X^{n+1/2} = Y^{n+1/2}\left(\frac{f''^{n} + f''^{n+1}}{2}\right)\Lambda(\Delta x) \tag{42b}$$

where f'' is the fiction factor for the particular exchange geometry

Unfortunately, the unknown pressure P^{n+1} occurs on the right hand side of (42) in the density terms. The calculation has been made as follows

a) use equation (42) with ρ^{n+1} evaluated at P^{n}, T^{n+1} to calculate a first approximation to P^{n+1}

b) use this first approximation to P^{n+1} to evaluate ρ^{n+1} for the calculation for P^{n+1} from (42).

III. Results of Constant Heat Transfer Model

The model was applied to exchanger operation with

1) constant coolant and air mass flow rates
2) constant inlet air and coolant temperatures
3) constant inlet contaminant concentration
4) constant inlet air pressure

Table 1 summarizes the cases run on the IBM 7090 digital computer. The important program input data are given along with the number of the experimental test from which the flow rates, inlet contaminant concentrations and air and coolant temperatures were taken. A detailed analysis of the results follows.

a) Convergence and Stability: Cases II-VII

The size of distance and time increments was varied to determine the largest values of these parameters that could be used to obtain accurate, stable results. The time and distance increments for each run are summarized below.

TABLE 2

CASE	ΔX INCHES	$\Delta\theta$ MIN
II	0.49	0.001
III	0.49	0.1
IV	0.49	1.0
V	1.02	0.1
VI	1.02	1.0
VII	0.49	0.01

These runs showed that distance increments of 0.49 inches and time increments of 0.1 minutes gave results that agreed well with those of Case II. The agreement between Cases II and V was satisfactory. However, distance increments of 0.49 inches were used for all other cases because they plotted a smoother thickness–length curve than the larger increments.

The values of ΔX and $\Delta \theta$ from Case III were used for the remaining runs. No stability problems were encountered in any of the Cases in Table 2.

b) Friction Factor Expressions

For Cases II through XIV the friction factor equation for in-line tubes presented as equation (6-13a) in Reference 1 was used:

$$f'' = \left[0.044 + \frac{0.08 X_L}{(X_T - 1)^a} \right] \left(\frac{DG_{MAX}}{\mu_G} \right)^{-0.15} \qquad (43)$$

where $a = 0.43 + (1.13/X_L)$

This equation fits in-line tube data fairly well ($\pm$ 20%) for all values of X_T and X_L greater than 1.4. However, for square in-line arrays ($X_T = X_L$) as used in our experiments the friction factor data (see Reference 3 for data) are more accurately approximated by

$$f'' = 0.254 \, (X_T - 1)^{-0.475} \left(\frac{DG_{MAX}}{\mu_G} \right)^{-0.15} \qquad (44)$$

This expression was used instead of (43) in Case XV.

The pressure drop computed in Cases XIV and XV is shown in Figure 1 in comparison with the experimental data from test V-7. The very steep rise in the computed pressure drop as plugging is approached is probably due to two phenomena which are not included in the model.

1) This model makes no allowance for any variation of thickness around the individual tubes. The rate of frost accumulation will be a minimum at the sides of the tube (see Reference 1 pg 257), and it is the transverse clearance between tubes which determines G_{MAX} and thus pressure drop. The model overestimates the frost thickness at the sides of the tube.

2) As plug-up approaches and the clearance between tubes decreases, there may be some reduction in frost thickness at the point of maximum air velocity due to the increased shear forces on the frost layer.

c) Effect of Frost Properties: Cases VIII-XIII

1) Frost density

Figure 2 shows computed pressure drop from Cases VIII and X along with the data from test V-2. Since frost thickness is inversly proportional to density, the plug-up time is almost directly proportional to the frost density. In order to predict the increase in pressure drop, it is very important to have an accurate value for frost density.

2) Frost thermal conductivity

Figure 2 shows computed pressure drop from cases VIII and IX along with the data from V-2. Figure 3 is a similar plot for cases XI, XII and XIII. These plots show the frost conductivity has a small effect on pressure drop. This effect is larger for smaller inlet humidities as can be seen by comparing Figures 2 and 3. The inlet humidity for the runs in Figure 2 is about 5 times higher than in Figure 3.

The frost thermal conductivity has a negligible effect on these results since the surface temperature is low enough (beyond the point of maximum thickness) so that the surface humidity is negligible compared to the gas stream humidity.

However, frost conductivity will be an important variable if we are to solve the general equations (i.e., remove the restriction of constant heat transfer) since it has a strong effect on T_s and therefore on the air side ΔT.

In Figure 3 the experimental points are from test V-5 which is the run whose conditions are closest to those of Cases XI thru XIII. However, in V-5 the inlet humidity is about 1.65 times that for Cases XI, XII and XIII.

d) Computed Thickness Profiles

Figure 4 shows the computed frost thickness profiles and the thickness profiles measured from photographs for Run V-2 as explained in Appendix 9 to this report. The dashed curve for 11 minutes was obtained from the curves for 4 and 7 minutes by projecting the growth rates. This was required because the computer run was stopped after 8 minutes. The linear projection is justified by the almost linear increase of thickness with time up to 8 minutes.

The profile shape and starting point are well predicted by the model. This is not surprising since experimental air temperatures were used. However, the agreement is good verification for the fact that frost first forms when the tube wall temperature reaches the dew point of the inlet gas.

Figure 5 shows a similar plot for run V-7 in which CO_2 frost formed near the outlet of the exchanger. The computed start of frosting again agrees with the experimental value, but the shapes of the curves are not similar. The experimental thicknesses peak near the exchanger outlet while the computed results peak near the start of the frosted length. The "late" peak in the experimental data could be due, in part,

to the fact that the CO_2 is "on" while the exchanger is cooling down. Thus CO_2 frost would form first at the exchanger outlet and as cooldown proceeded would form farther upstream. Also, it might be possible that the assumption of constant heat transfer had a more pronounced effect on the CO_2 frost profile than was the case for water frost.

NUMERICAL VALUES OF TRANSFER COEFFICIENTS

For these calculations the following form of equation was used

$$St_o = B1 \left(\frac{DG_{MAX}}{\mu} \right)^{B2}$$

where

$B1 = 0.31^*$
$B2 = 0.39$

for an exchanger with transverse and longitudinal pitch of 1.33. For the coolant

$$St_i = 0.026 \ (Re_i)^{-0.2}$$

Fluid property variation:

density $\alpha \ T^{-1}$

viscosity $\alpha \ T^{0.7}$

*Additional data indicates that B1 should be about 30% higher.

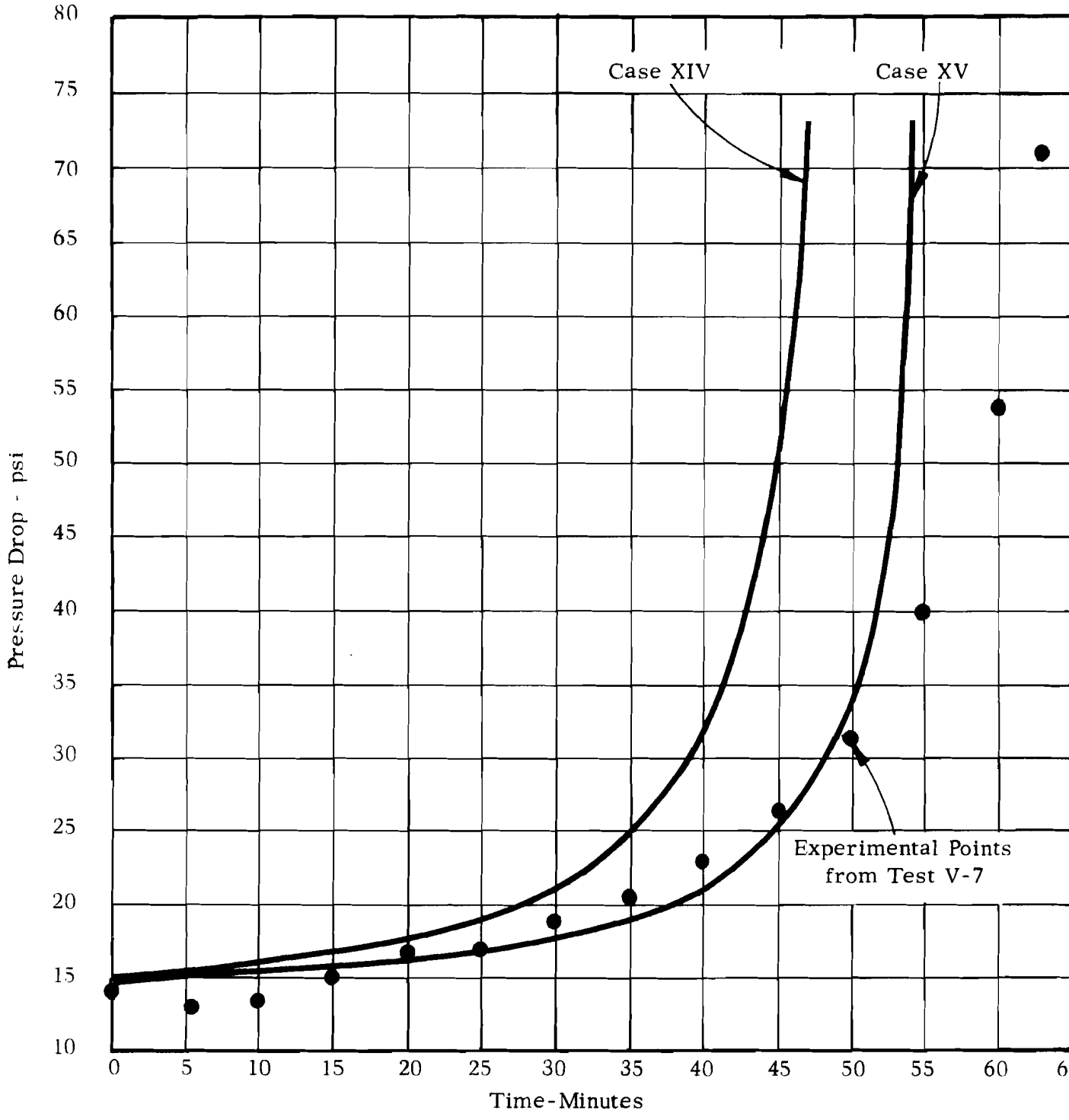

FIGURE 1 PRESSURE DROP VS TIME - EFFECT OF FRICTION FACTOR

	Frost Density (lb/ft^3)	Properties Conductivity (Btu/hr ft °R)
Case VIII	15.5	0.125
IX	15.5	0.0125
X	30.0	0.125

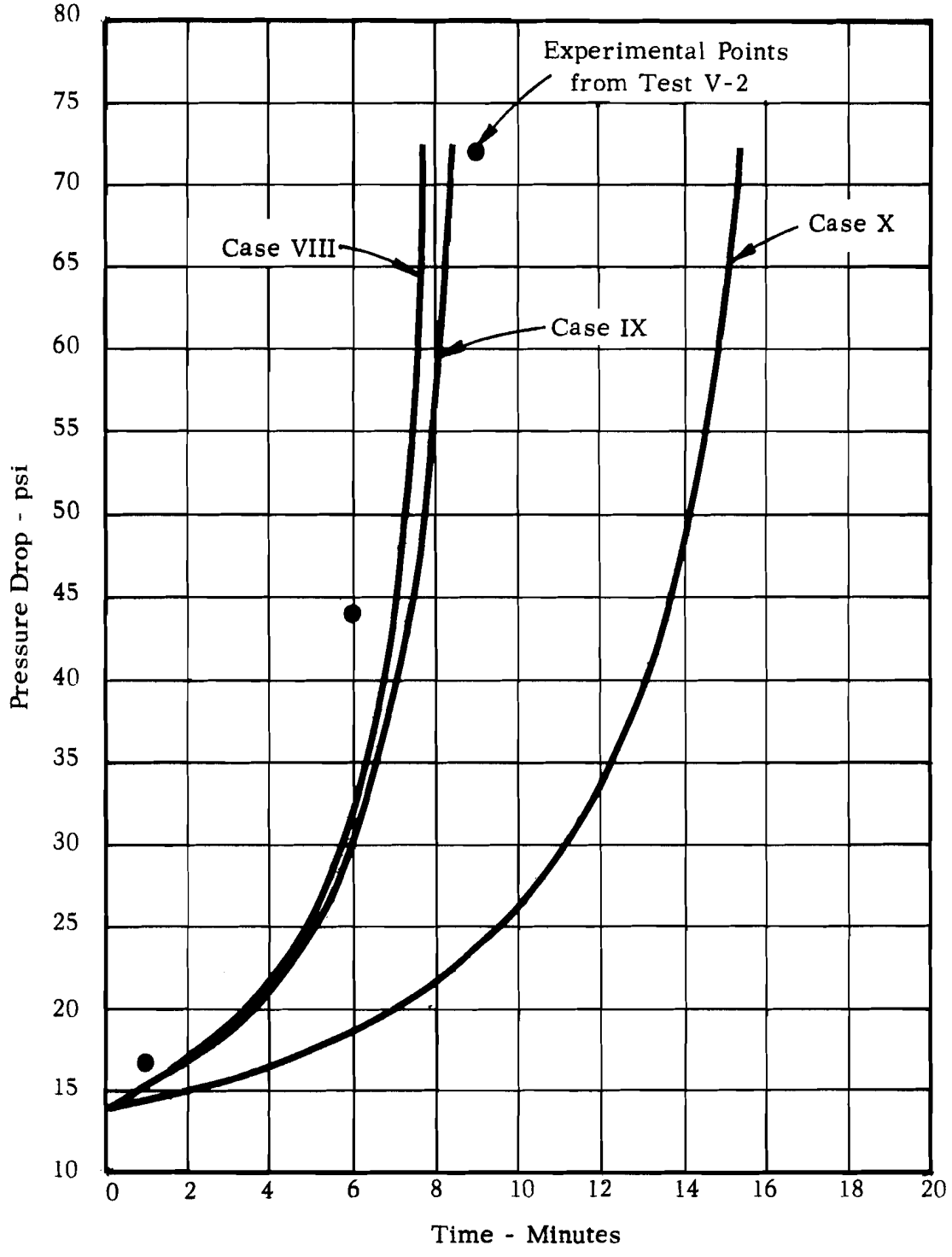

FIGURE 2 PRESSURE DROP VS TIME--EFFECT OF DENSITY AND CONDUCTIVITY

	Frost Density (lb/ft^3)	Properties Conductivity (Btu/hr ft °R)
Case XI	15.5	0.125
XII	15.5	0.0125
XIII	18.1	0.067

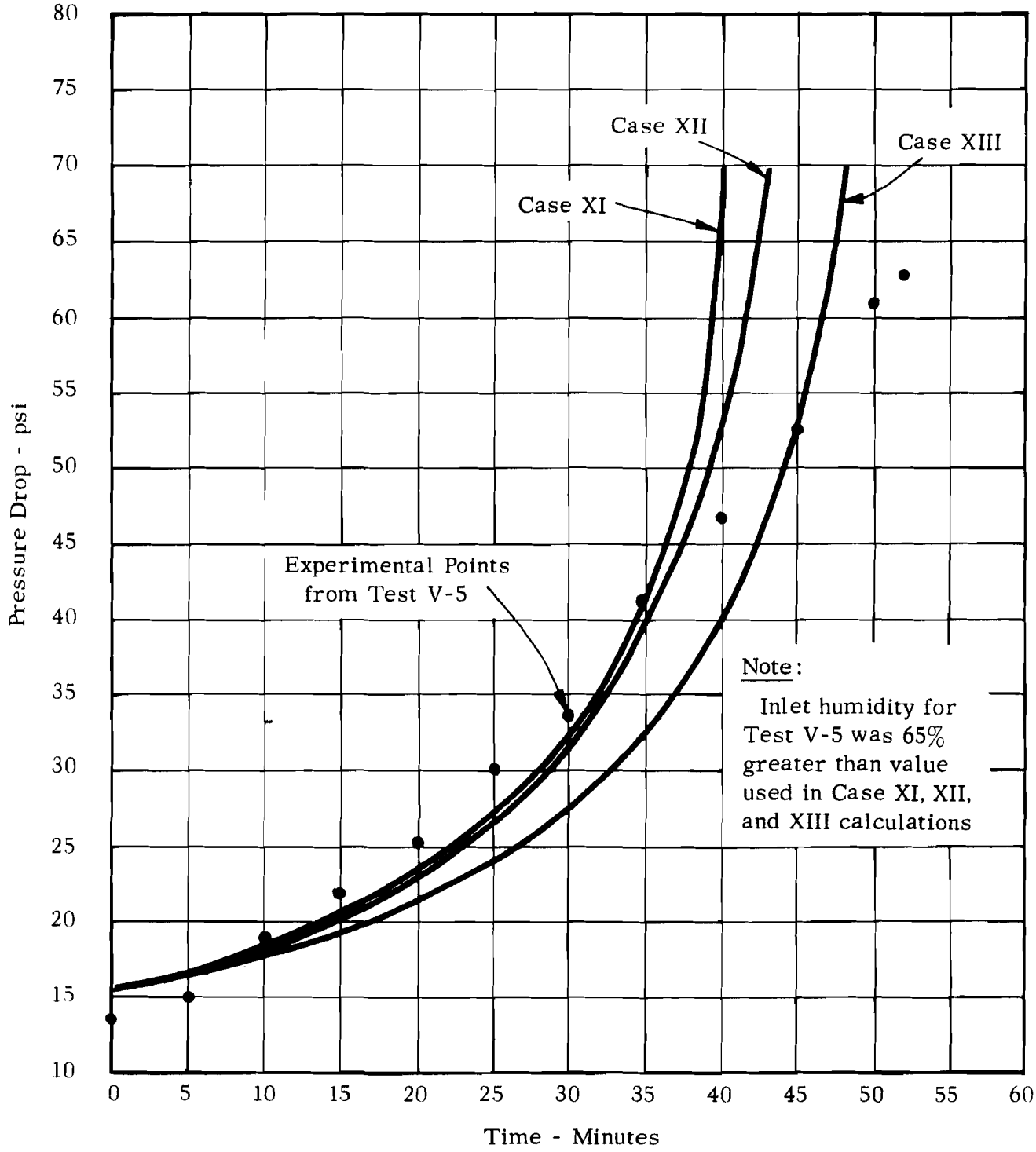

FIGURE 3 PRESSURE DROP VS TIME--EFFECT OF FROST CONDUCTIVITY

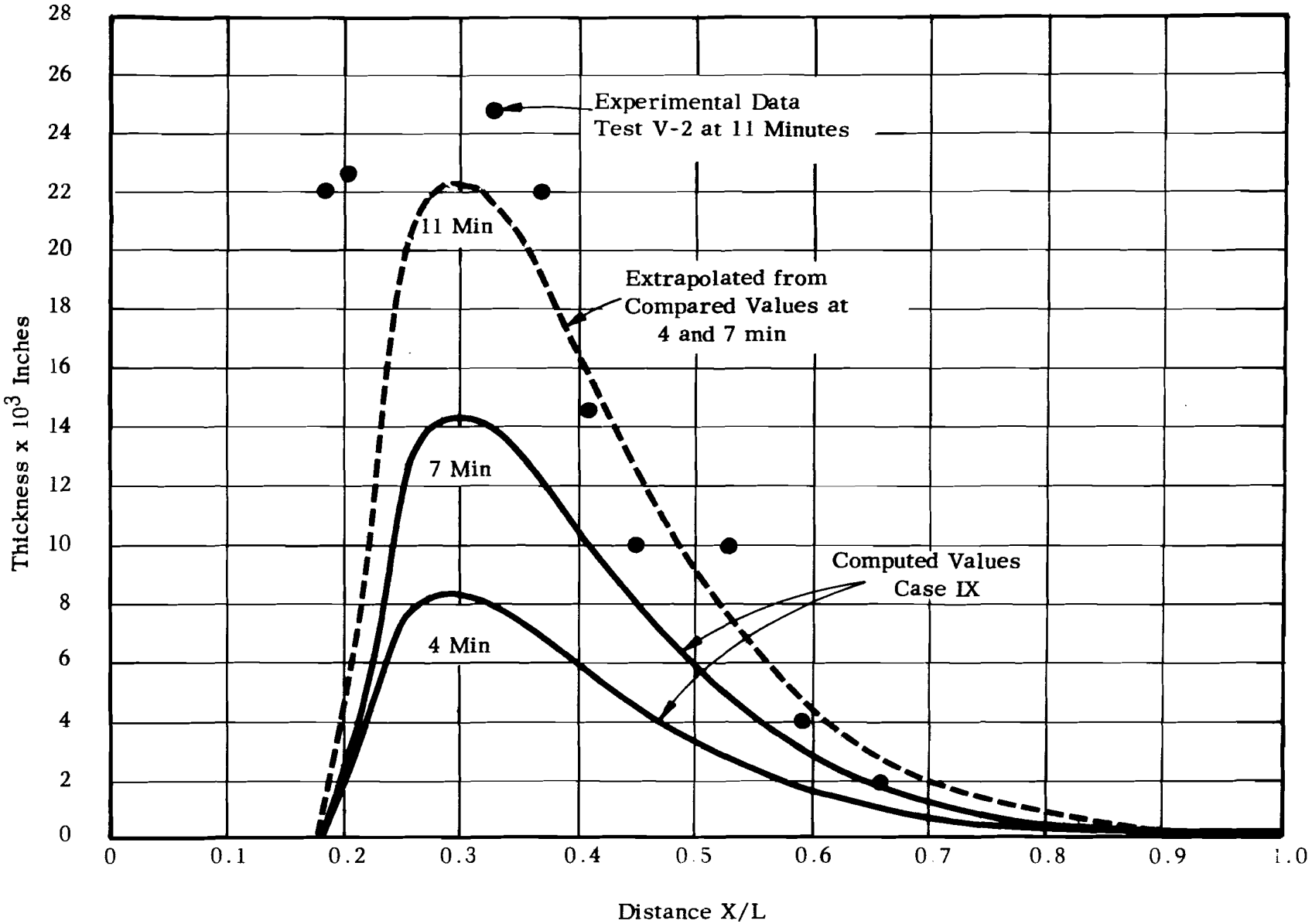

FIGURE 4 WATER FROST THICKNESS PROFILE

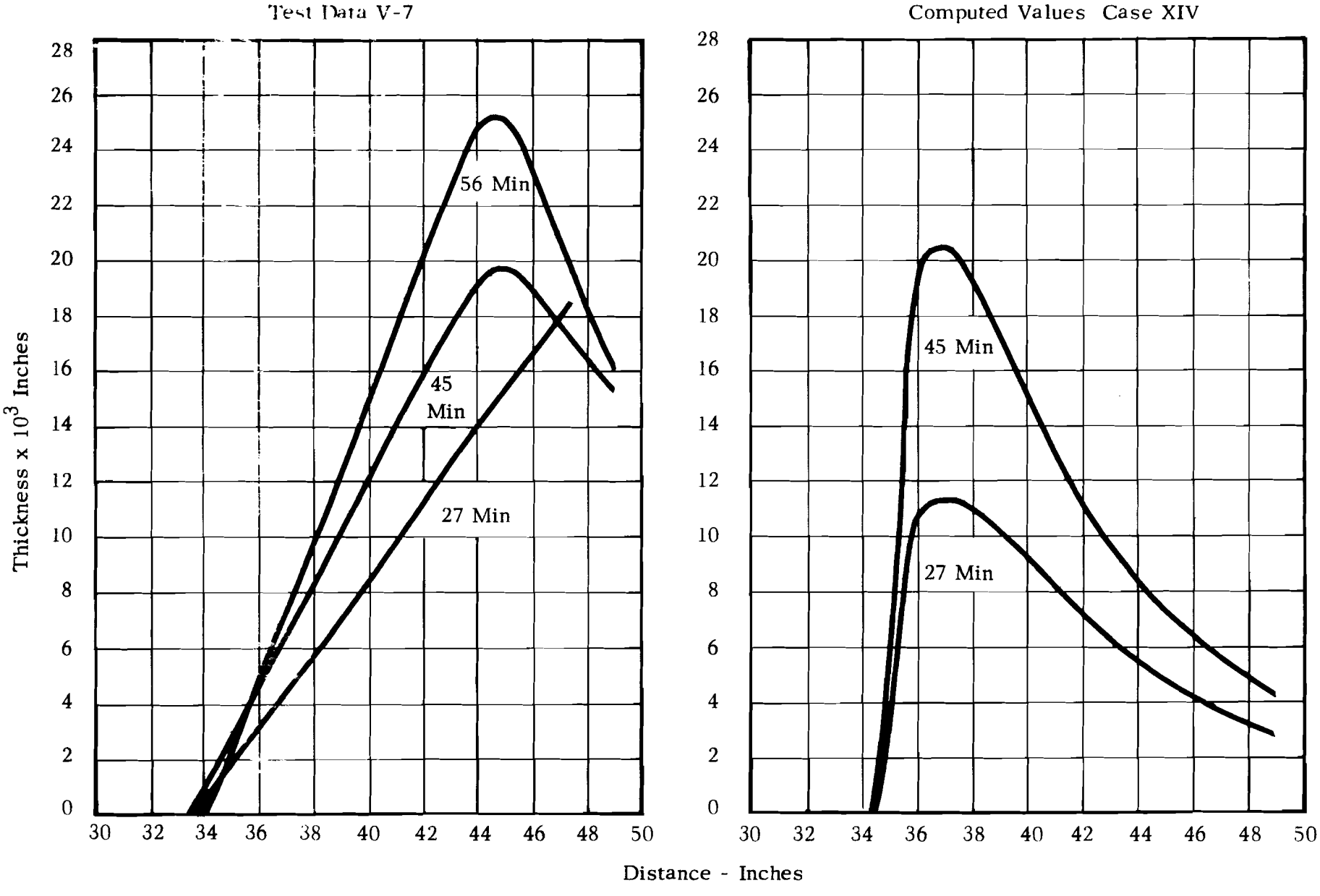

FIGURE 5 CO_2 FROST THICKNESS PROFILES

REFERENCES

1. McAdams, W. H., "Heat Transmission", 3rd Edition, McGraw-Hill, 1954

2. Sherwood, T. K., and Pigford,"Adsorption and Extraction", McGraw-Hill, 1950

3. Boucher, D. F, and Lapple, C. E., Chem Eng Progr. 44, 117-34 (1948).

NOMENCLATURE

X	distance measured from hot end	ft
L	total length of exchanger	ft
T	air (hot fluid) temperature	^{o}R
t	coolant temperature	^{o}R
w	mass flow rate of coolant	lb/hr
ρ	density of coolant	lb/ft^3
V_i	volume per unit length on coolant side	ft^3/ft
θ	time	hr
W	mass flow rate air	lb/hr
H_j	humidity of vapor j	lb j/lb air
k'_j	mass transfer coefficient of vapor j	lb j/hr ft^2
A_x	surface area of frost per unit length	ft^2/ft
H_j^s	humidity of vapor j at frost surface	lb j/lb air
ρ_G	density of air stream (includes vapors)	lb/ft^3
V_x	free volume per unit length on air side	ft^3/ft
$\sum_j^+$	summation over positive terms only	
$\sum_j$	summation over all j	
ρ_f	frost density	lb/ft^3
V_f	volume frost per unit length	ft^3/ft
C	heat capacity coolant	BTU/lb ^{o}R
C_A	heat capacity air	BTU/lb ^{o}R
T_W	wall temperature	^{o}R

T_W^i	wall temperature on inside of wall (coolant side)	^oR
h_i	heat transfer coefficient on coolant side	BTU/hr ft^2 ^oR
A_i	heat transfer area per unit length on coolant side	ft^2/ft
c_j	heat capacity of vapor j	BTU/lb ^oR
k_f	thermal conductivity of frost layer	BTU/hr ^oR ft
m_t	mass of metal in tube per unit length	lb/ft
C_t	heat capacity of tube	BTU/lb ^oR
T_{TUBE}	average tube wall temperature	^oR
h_o	heat transfer coefficient air to frost surface	BTU/hr ft^2 ^oR
T_s	frost surface temperature	^oR
λ_{js}	latent heat of sublimation of vapor j at T_s	BTU/lb
C_j^s	heat capacity of solid "j"	BTU/lb ^oR
fj	fraction of frost by weight that is from vapor "j"	--
P	coolant pressure	lb/ft^2
G_i	mass velocity coolant	lb/hr ft^2
f_i	friction factor coolant	--
D_i	internal diameter coolant tube	ft
gc	conversion factor = $32.2 \frac{\text{lb matter x ft}}{\text{lb force x (sec)}^2}$	
P	air pressure	lb_f/ft^2
G_{MAX}	maximum mass velocity = W/a_o	lb/hr ft^2
a_o	minimum cross sectional area available for flow on air side	ft^2
f"	friction factor - air side	--
$\wedge$	number of tubes per unit length	1/ft

V_x^o	original free volume per unit length on air side	ft^3/ft
B_1, B_2	constants in equation (27)	--
z	= X/L dimensionless length	--
St_o	Stanton number on air side ($St_o = \frac{h_o}{C_A G_{MAX}}$)	--
δ	frost thickness	ft
R_o	original outside radius of tubes	ft
R	radius of frosted tube	ft
D	diameter of frosted tube = 2R	ft
a	exponent in equation (43) ($a = 0.43 + 1.13/X_L$)	
X_L	longitudinal pitch - center to center distance between adjacent tubes in flow direction divided by D	--
X_T	transverse pitch-center to center distance between adjacent tubes to flow divided by D	--
μ_G	viscosity of air + vapors	lb/hr ft
μ_C	viscosity of coolant	lb/hr ft
Δ	thickness parameter	ft

Δ = frost thickness for flat surfaces

$\Delta = R \ln \frac{R_o}{R}$ for frost on tubes

Subscripts

1	hot end of exchanger (x=0)
L	cold end of exchanger (x=L)
i	inside tubes (coolant side)

APPENDIX 13

A DIGITAL COMPUTER PROGRAM

TO PREDICT THE PERFORMANCE OF FREEZE-OUT HEAT EXCHANGERS

TABLE OF CONTENTS

A DIGITAL COMPUTER PROGRAM
TO PREDICT THE PERFORMANCE OF FREEZE-OUT HEAT EXCHANGERS

I INTRODUCTION

The successful completion of this study of freeze-out heat exchangers requires a theoretical understanding of the physical process. This process may be described mathematically with some confidence in the physical assumptions. (See Appendix 12 for a complete derivation.) The purpose of this section of the final report is to describe the numerical solution of this mathematical model. The numerical integration of the nonlinear partial differential equations has been accomplished by a digital computer program utilizing the IBM 7090 Data Processing System. The coding of the program is in FORTRAN II, an automatic machine coding system for the 709 series.

II A BRIEF REVIEW OF THE THEORETICAL ANALYSIS

A. Basic Analysis

In Appendix 12 to Volume II of the Final Report, the following equations were derived for the mass transfer, heat transfer, thermal equilibrium and pressure variation along the length, x, of the exchanger and with time, θ, of operation.

In this derivation, the following assumptions are made:

a) Air and coolant flow is countercurrent.
b) Ideal gas (i.e., no effect of pressure on enthalpy).
c) The exchanger is adiabatic.
d) No nucleation occurs in the gas.
e) Frost density is independent of time.
f) The exchanger operates in quasi-steady state (i.e., the change in mass and internal energy of the coolant, air and exchanger is negligible with respect to time).

1. Mass transfer of frost to tube wall*

$$W = W_{inlet} \quad \text{(air flow rate)} \tag{1}$$

$$\omega = \omega_{inlet} \quad \text{(coolant flow rate)} \tag{2}$$

---

* NOTATION given in Section III of this appendix.

$$- W \frac{dH_j}{dX} = k'_j A_X (H_j - H_j^s) \quad (3)$$

$$\text{at } X = 0; \quad H_j = H_{jo} \quad (3a)$$

where the subscripted integer, j, refers to the condensible components. There is one restraint on equation 3. That is, evaporation of the frost component in the frost layer may occur only if the component is present in the frost. For example, a bare tube may well have a wall temperature (and thus a saturation humidity) greater than the actual humidity in the air flow. Equation 3 does not hold for this case, and dH_j/dX must be set equal to zero. (A bare tube cannot evaporate a frost component.)

2. Frost accumulation

The mass transfer of frost varies not only along the surface of the exchanger but also is time dependent. The accumulation of frost results in fouling of the exchanger and occurs as freeze-out progresses. This changes the free area, frost thickness, etc. All these quantities may be stated as a change in tube geometry with time:

$$\frac{dV_f}{d\theta} = A_X \sum \frac{K'_j}{\rho_{fj}} (H_j - H_j^s) \quad (4)$$

And again, the restriction on evaporation is implied.

3. Heat transfer - air side

$$- WC_A \frac{dT}{dX} = h_o A_X (T - T_s) \quad (5)$$

$$\text{at } X = 0; \quad T = T_{inlet} \quad (5a)$$

4. Heat transfer - coolant side

$$\omega C \frac{dt}{dX} = h_i A_i (T_W - t) \quad (6)$$

$$\text{at } X = L; \quad t = t_{inlet} \quad (6a)$$

5. Thermal equilibrium

$$h_o A_X (T - T_s) + A_X \sum k_j' (H_j - H_j^s) \lambda_j = k_F A_X \frac{T_s - T_W}{\Delta} \quad (7)$$

$$A_i h_i (T_W - t) = k_F A_X \frac{T_s - T_W}{\Delta} \quad (8)$$

$$H_j^s = f(T_s) \quad (9)$$

$$V_F = f(\Delta, A_X) \quad (10)$$

$$A_X = f(\Delta) \quad (11)$$

6. Pressure drop

$$-\frac{dP}{dX} = f(W, V_F, \text{geometry}) \quad (12)$$

We have 12 equations for the dependent variables:

$$P, W, \omega, T, T_s, T_W, t, H_j, H_j^s, \Delta, A_X, V_F$$

as functions of the independent variables, X and θ.

B. The Cross-Flow Counterflow Exchanger

This type of heat exchanger is cross-flow with respect to flow geometry. The air stream flows normal to tubes containing the coolant stream. However, it is counterflow with respect to air and coolant temperature profiles. At any time the air and coolant temperatures can be adequately described as single-valued functions of axial length in accordance with equations 5 and 6 above. In practice this stipulation implies a large number of cross-flow passes to minimize the temperature change for each individual pass.

For the cross-flow heat exchanger flow geometry, the following relationships exist:

a) The exchanger is made up of tubes in cross-flow, air outside and coolant inside.

b) The frost resistance to heat flow is uniform around the tube.

c) Uneven frost distribution affects only the pressure drop.

Looking at a single tube in cross section:

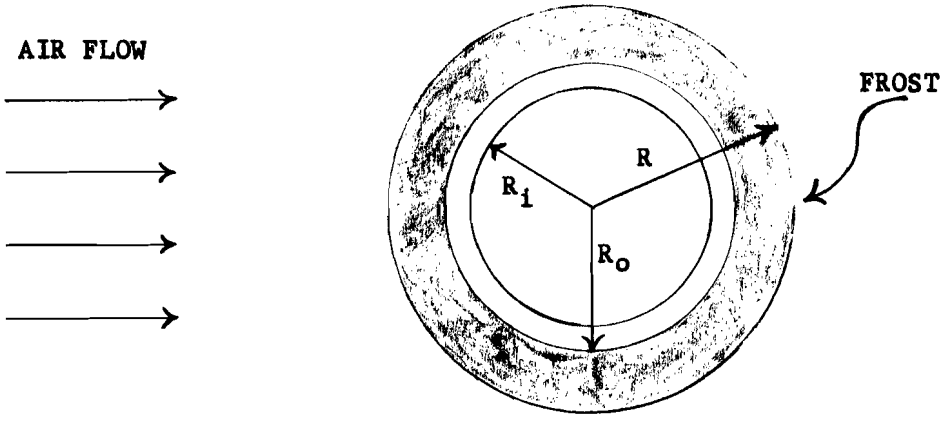

Therefore:

$$A_X = 2\pi R \tag{13}$$

$$V_F = \pi (R^2 - R_o^2) \tag{14}$$

and for the cylindrical geometry:

$$\Delta = R \ln \frac{R}{R_o} \tag{15}$$

and for tubes in cross-flow:

$$-\frac{dP}{dX} = \frac{G^{*2}_{max}}{2g_c} \frac{d}{dX} \left(\frac{1}{\rho_G}\right) + \frac{4 f'' G^{*2}_{max} \Lambda}{2g_c \rho_G} \tag{16}$$

$$\text{at } X = 0; \quad P = P_{inlet} \tag{16a}$$

d) The saturated humidity at the frost surface temperature may be stated as:

$$H_{js} = \frac{C_{6j}}{P} \exp \left(C_{7j} - \frac{C_{8j}}{T}\right) \tag{17}$$

C. Simplification of the Equations

The above geometric and vapor properties may be combined and simplified by the use of the following non-constant coefficients.

$$St_o = h_o/C_A\, G_{max} \tag{18}$$

$$St_i = h_i/C\, G_i \tag{19}$$

$$\alpha_j = h_o/C_A\, k_j \tag{20}$$

$$z = X/L \tag{21}$$

$$\gamma_o = A_X\, L/a_o \tag{22}$$

$$\beta_o = k_F/\Delta h_o \tag{23}$$

$$\gamma_i = A_i\, L/a_i \tag{24}$$

$$\Gamma = C\, G_i/C_A\, G_{max} \tag{25}$$

$$q = \gamma_i/\gamma_o \tag{26}$$

$$r = St_i/St_o \tag{27}$$

$$\eta = A_i/A_X \tag{28}$$

$$C_1 = \gamma_o\, St_o \tag{29}$$

$$C_2 = \gamma_i\, St_i/ \left(1 + \frac{r\Gamma\eta}{\beta_o}\right) \tag{30}$$

$$C_{3j} = C_1/\alpha_j \tag{31}$$

$$C_4 = 1/C_A \tag{32}$$

$$C_5 = G_{max}\,(St_o) \tag{33}$$

$$C_9 = r\Gamma\eta \,/\, (1 + \frac{r\Gamma\eta}{\beta_o}) \tag{34}$$

$$C_{10} = 2g_c\, K/G^{*2}_{max} \tag{35}$$

$$C_{11} = 4\, f''\, N \tag{36}$$

where

N = total number of tube rows in the exchanger

K = ρ_G T/P

and all other symbols are the same as Appendix 12. (See the following Section for a list of symbols.)

With these definitions, we can solve (8) for T_W:

$$T_W = \frac{T_s + \frac{r\Gamma\eta}{\beta_o}\, t}{1 + \frac{r\Gamma\eta}{\beta_o}} \tag{37}$$

and use this to eliminate T_W from the other equations. In addition, substitution of the above coefficients gives the following set of equations:

$$-\frac{\partial T}{\partial z} = C_1\,(T - T_s) \tag{38}$$

$$-\frac{\partial t}{\partial z} = C_2\,(T_s - t) \tag{39}$$

$$-\frac{\partial H_j}{\partial z} = C_{3j}\,(H_j - H_{js}) \tag{40}$$

$$T - T_s + C_4 \sum \left(\frac{\lambda_j}{\alpha_j}\right)(H_j - H_j^s) = C_9 (T_s - t) \tag{41}$$

$$C_5 \sum \frac{1}{\rho_{Fj}\ \alpha_j} (H_j - H_j^s) = \frac{\partial R}{\partial \theta} \tag{42}$$

$$-\frac{\partial P}{\partial z} = \frac{P}{C_{10}\frac{P^2}{T} - 1}\left(C_{11} + \frac{1}{T}\ \frac{\partial T}{\partial z}\right) \tag{43}$$

$$H_{js} = \frac{C_{6j}}{P} \exp\ \left(C_{7j} - \frac{C_{8j}}{T_s}\right) \tag{44}$$

We have seven equations (38)-(44) and seven unknowns:

$$T,\ t,\ H_j,\ H_{js},\ T_s,\ R,\ P.$$

This is the form that has been used in the digital computer program.

D. Expressions for Heat and Mass Transfer Coefficients and Friction Factors

1. Outside coefficient: air to frost surface

$$\frac{h_o}{C_A\ G_{max}} = B_1 \left(\frac{2RG_{max}}{\mu_{air}}\right)^{B_2} \tag{45}$$

where

μ_{air} = air viscosity.

(Data for B_1 and B_2 for various geometries are contained in McAdams, "Heat Transmission" 3rd Edition, McGraw-Hill, 1954, p. 273.)

2. Inside coefficient: coolant to tube wall

$$\frac{h_i}{C\ G_i} = 0.21 \left(\frac{2\ R_i\ G_i}{\mu_{cool}}\right)^{-0.2} (Pr_c)^{-2/3} \tag{46}$$

where

μ_{cool} = coolant viscosity

Pr_c = coolant Prandtl number.

3. Mass transfer coefficients:

$$\alpha_j \equiv \frac{h_o}{C_A k'_j} = \frac{0.294}{C_A} \left(\frac{\mu_{air}}{D_j \rho_G} \right)^{0.56} \tag{47}$$

where

D_j = diffusivity of component j in air.

4. Friction factor:

General expressions are available for staggered and in-line tubes (see McAdams, p. 163). However, data for a particular array (e.g., square in-line array as used in some of our tests), an equation which fits the data better than the more general equations, can easily be derived. (See Boucher & Lapple, Chem. Eng. Prog. 44, 117 (1948) for an extensive summary of data.)

For a square in-line array, we found that:

$$f'' = 0.254 \, (X_T - 1)^{-0.475} \left(\frac{2RG_{max}}{\mu_{air}} \right)^{-0.15} \tag{48}$$

fit the data much more closely than McAdams equation (6-13a) especially as X_T approached 1.0 (i.e., thick frost layers).

In cases in which the air side is baffled, the baffle loss can be incorporated in the expression for the friction factor.

III THE COMPUTER PROGRAM

A. The Numerical Analysis

As shown in the previous section, a series of first order, nonlinear, differential equations must be integrated to predict exchanger performance. The precise number of equations is dependent on the number of freeze-out components in the air stream. For the present, two components will be considered (H_2O and CO_2).

The numerical solution of these equations that was chosen is based on two physical assumptions:

a) that there is no heat flow along the wall of the exchanger (i.e., each differential element along the exchanger is independent of the adjacent elements).

b) at any instant of time, the entire exchanger may be considered to exhibit steady state performance (i.e., the process is quasi-steady).

These assumptions are realistic as the actual performance of the exchanger is well behaved, and no abrupt changes in the heat transfer, pressure drop, or frost buildup were noticed.

The general logic and numerical solution to the set of equations can be assumed independent of time at each time step. Thus the differentials $\partial T/\partial z$ (Eq. 38), $\partial t/\partial z$ (Eq. 39), $\partial H_1/\partial z$, $\partial H_2/\partial z$ (Eq. 40) and $\partial P/\partial z$ (Eq. 43) may be evaluated at the initial boundary of the exchanger if the boundary values, T, t, T_s, H_1, H_2 and P, are known. T_s may be determined from Equation 41. However, this boundary value of t, the coolant temperature, is in actuality the exit temperature. The known inlet coolant temperature is at the final boundary in a cross or counterflow heat exchanger. Thus, an initial value of t must be assumed.

By use of the elementary difference equation,

$$f(z)_j = \Delta z \frac{d}{dz} (f(z))_{j-1} + f(z)_{j-1}$$

a step by step integration of Equations 38, 39, 40 and 43 may be accomplished along the length of the exchanger. At each step, T_s may be calculated from Equation 41. When the final boundary conditions are calculated, the actual coolant inlet temperature may be compared to the calculated value. If the two differ, a new initial value of t must be assumed and the entire process repeated until convergence is attained.

For a constant flow process, gas and frost temperatures throughout the exchanger would now be complete. However, if the air side pressure drop were specified, the air flow must be altered to approach the required pressure drop. This air flow variation will change the heat transfer rates within the exchanger and upset the calculated value of coolant inlet temperature. Thus, an iteration process must be followed until the correct coolant inlet temperature and pressure drop are calculated.

When this is complete, the increase in frost thickness may be calculated for a short time interval by use of Equation 42 in difference equation form.

This procedure, alternating a step by step solution of Equations 38, 39, 40 and 43 along the length of the exchanger with the solution of Equation 42, is continued until a time limit or flow stoppage occurs.

A complete flow chart for this logical process is shown in the following sections along with the notation which was used in the computer analysis.

An overall check on energy transfer is made at the completion of each finite difference integration. The coolant heat gain is compared to the air heat loss and freeze-out load. The integrating mesh is set to maintain an energy difference to one thousands of one percent.

B. Computer Notation

The algebraic notation of Appendix 12 has been changed to a form which is compatible with FORTRAN II. The equations which are to be integrated are rewritten as:

```
DTA  = -C1*(TA - TS)                                              (38)

DTC  = -C2*(TS - TC)                                              (39)

DH1  = -C31*(H1 - H1S)                                            (40)

DH2  = -C32*(H2 - H2S)                                            (40)

TA - TS + A1*(H1 - H1S) + A2*(H2 - H2S) = C9*(TS - TC)            (41)

DRT  = C5*((H1-H1S)/(RHØ1*ALP1) + (H2-H2S)/(RHØ2*ALP2))           (42)

DP   = -(P/(C10*P**2/T - 1)*(C11 + DTA/TA)                        (43)

H1S  = (C61/P)*EXPF(C71 - C81/TS)                                 (44)

H2S  = (C62/P)*EXPF(C72 - C82/TS)                                 (44)
```

COMPUTER NOTATION

FORTRAN	ALGEBRAIC	DESCRIPTION	UNITS
	X	Distance measured from hot end	ft
EL	L	Total length of exchanger	ft
TA	T	Air (hot fluid) temperature	^{o}R

TC	t	Coolant temperature	^{o}R
CØØL	ω	Mass flow rate of coolant	lb/hr
T	θ	Time	hr
FLØW	W	Mass flow rate air	lb/hr
H1, H2	H_j	Humidity of vapor j	lb j/lb air
	k'_j	Mass transfer coefficient of vapor j	lb j/hr ft^2
	A_X	Surface area of frost per unit length	ft^2/ft
H1S, H2S	H_j^s	Humidity of vapor j at frost surface	lb j/lb air
	ρ_G	Density of air stream (includes vapors)	lb/ft^3
	$\sum_j^+$	Summation over positive terms only	
	$\sum_j$	Summation over all j	
RHØ1, RHØ2	ρ_f	Frost density	lb/ft^3
	V_f	Volume frost per unit length	ft^3/ft
CC	C	Heat capacity coolant	Btu/lb-^{o}R
CG	C_A	Heat capacity air	Btu/lb-^{o}R
	T_W	Wall temperature	^{o}R
	h_i	Heat transfer coefficient on coolant side	Btu/hr-ft^2-^{o}R
	A_i	Heat transfer area per unit length on coolant side	ft^2/ft
	C_j	Heat capacity of vapor j	Btu/lb-^{o}R
FK1, FK2	k_f	Thermal conductivity of frost layer	Btu/hr-^{o}R-ft

	h_o	Heat transfer coefficient air to frost surface	Btu/hr-ft^2-^oR
TS	T_s	Frost surface temperature	^oR
GAM1, GAM2	λ_{js}	Latent heat of sublimation of vapor j at T_s	Btu/lb
	C_j^s	Heat capacity of solid "j"	Btu/lb-^oR
	f_j	Fraction of frost by weight that is from vapor "j"	
P	P	Coolant pressure	lb_f/ft^2
	G	Mass velocity coolant	lb/hr-ft^2
RI	R_i	Internal radius coolant tube	ft
	g_c	Conversion factor = 32.2 (lb matter x ft)(lb force x (sec)^2)	
P	P	Air pressure	lb_f/ft^2
	G^*_{max}	Mass velocity = W/a^*_o	lb/hr-ft^2
	G_{max}	Mass velocity = W/a_o	lb/hr-ft^2
AØ	a_o	Uniform cross-sectional area available for flow on air side	ft^2
	a^*_o	Minimum cross-sectional area (uneven frost considered)	ft^2
FPRIME	f"	Friction factor - air side	
	Λ	Number of tubes per unit length	1/ft
TNT	N	Number of tubes	
B1	B_1	Constants in equation (27)	
B2	B_2		
Z	z	= X/L, dimensionless length	
STØ	St_o	Stanton number on air side = hC_A/G_{max}	

STI	St_i	Stanton number on coolant side	
	δ	Frost thickness	ft
RØ	R_o	Original outside radius of tubes	ft
R	R	Radius of frosted tube based on uniform frost distribution	ft
XL	X_L	Longitudinal pitch--center to center distance between adjacent tubes in flow direction divided by D	
XT	X_T	Transverse pitch--center to center distance between adjacent tubes transverse to flow divided by D	
	μ_G	Viscosity of air + vapors	lb/hr-ft
	μ_C	Viscosity of coolant	lb/hr-ft
	Δ	Thickness parameter Δ = frost thickness for flat surface Δ = R lw (R_o/R) for frost on tubes	ft
	K	Gas constant for air	ft/^oR
ALP1, ALP2	α_j	Equation 20 and 47	
CCØ	C_o		
PRØ	P_{ro}		
CGØ	C_{go}		
GAMØ	α_o		
W	q		
ARE	r		
BETA	β_o		
DTA	$\partial T/\partial z$		^oR

DTC	$\partial t/\partial z$	^{o}R
DH1	$\partial H_1/\partial z$	lb H_2O/lb air
DH2	$\partial H_2/\partial z$	lb CO_2/lb air
DP	$\partial P/\partial z$	lb/ft^2
DRT	$\partial R/\partial \theta$	ft/hr
C1	C_1	
C2	C_2	
C31, C32	C_{3j}	
C4	C_4	
C5	C_5	
C61, C62	C_{6j}	
C71, C72	C_{7j}	
C81, C82	C_{8j}	
C9	C_9	
C10	C_{10}	
C11	C_{11}	

C. Computer Program Logic

The logical process which governs the exact method of computation is the FORTRAN II listing. This listing is attached to this section of the report. As an aid to interpret the logical process, a flow chart is also attached for the use of the programmer. Specific operating instructions follow in the next section.

FLOW CHART FOR
ASD FREEZE-OUT HEAT EXCHANGER

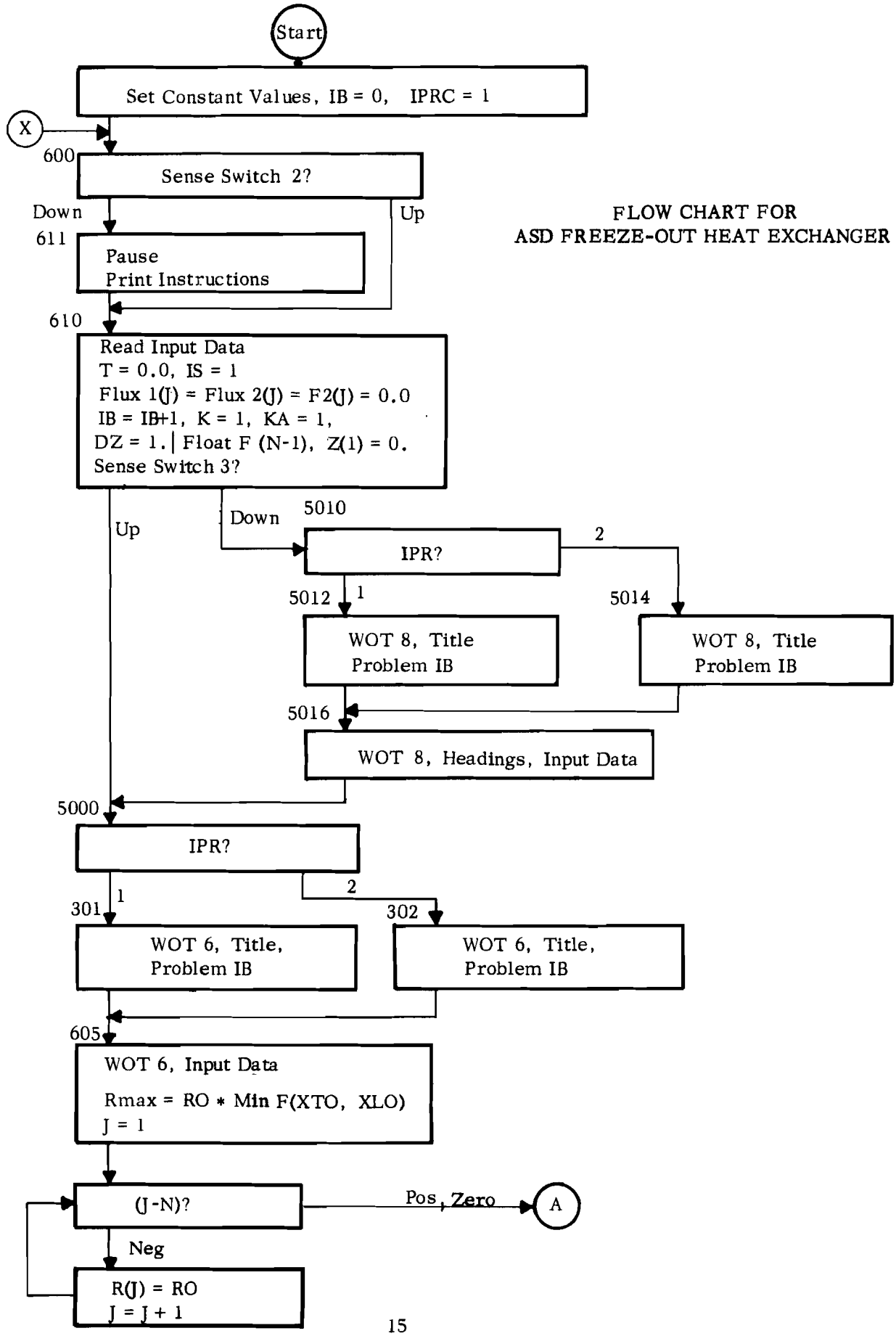

INITIAL BOUNDARY CONDITIONS

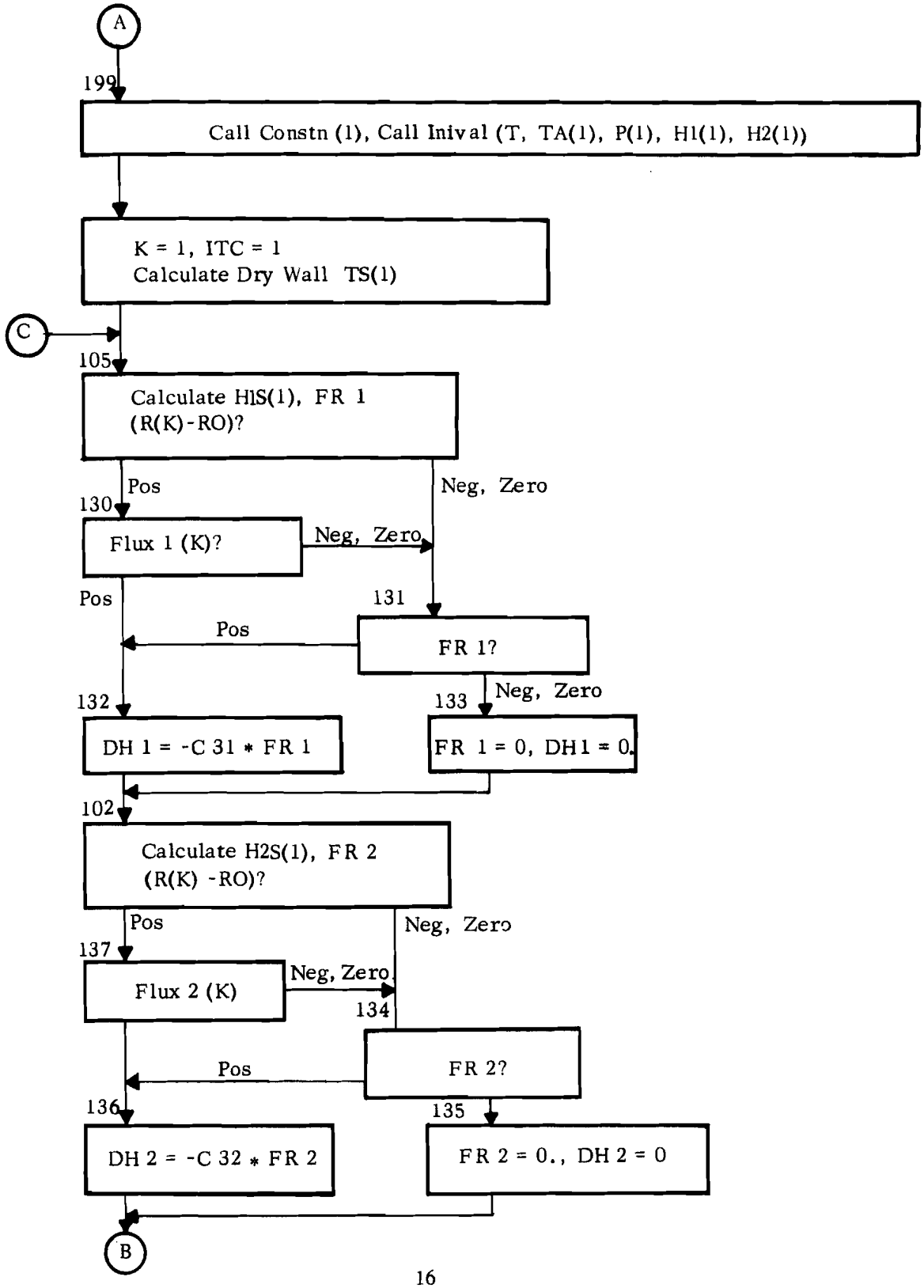

INITIAL BOUNDARY CONDITIONS
(Continued)

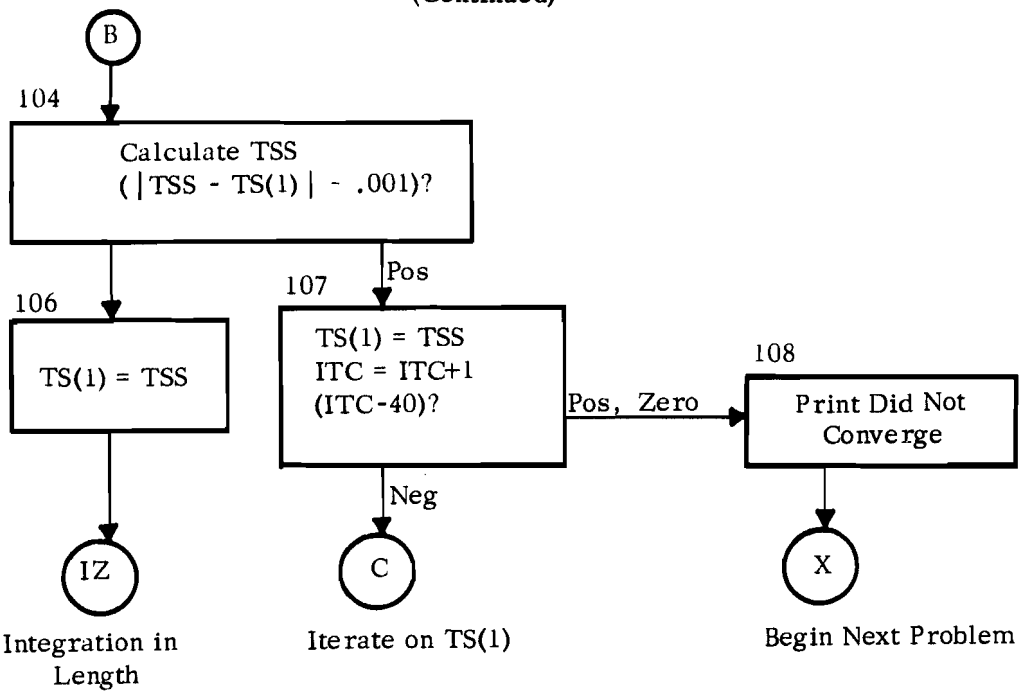

Integration in Length

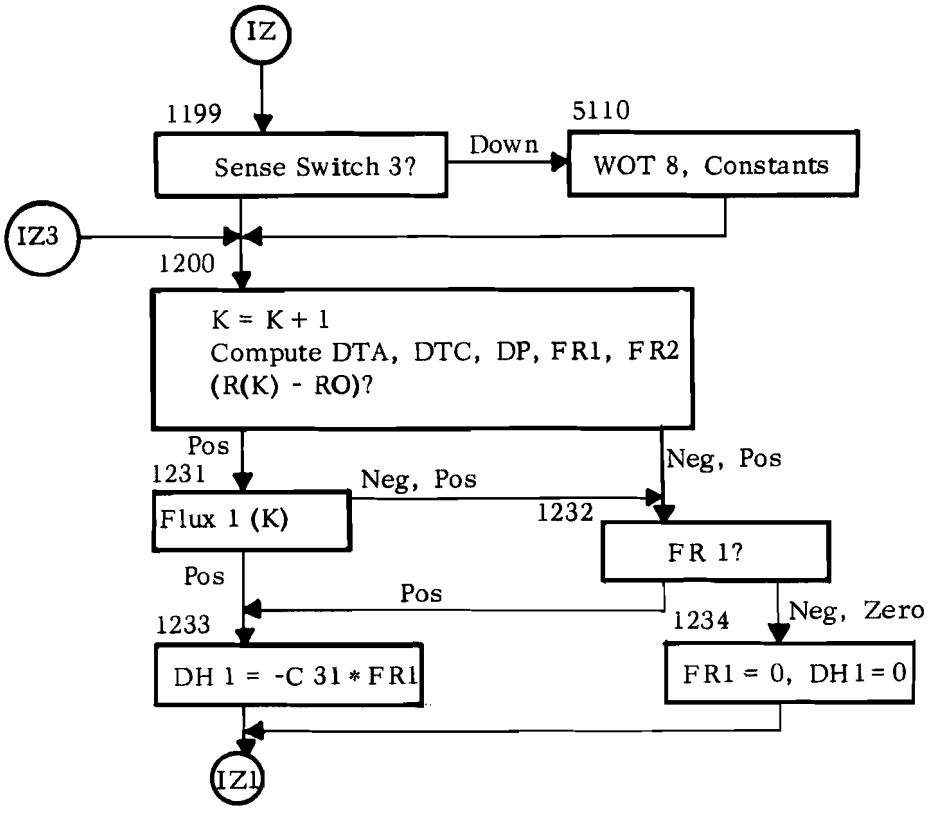

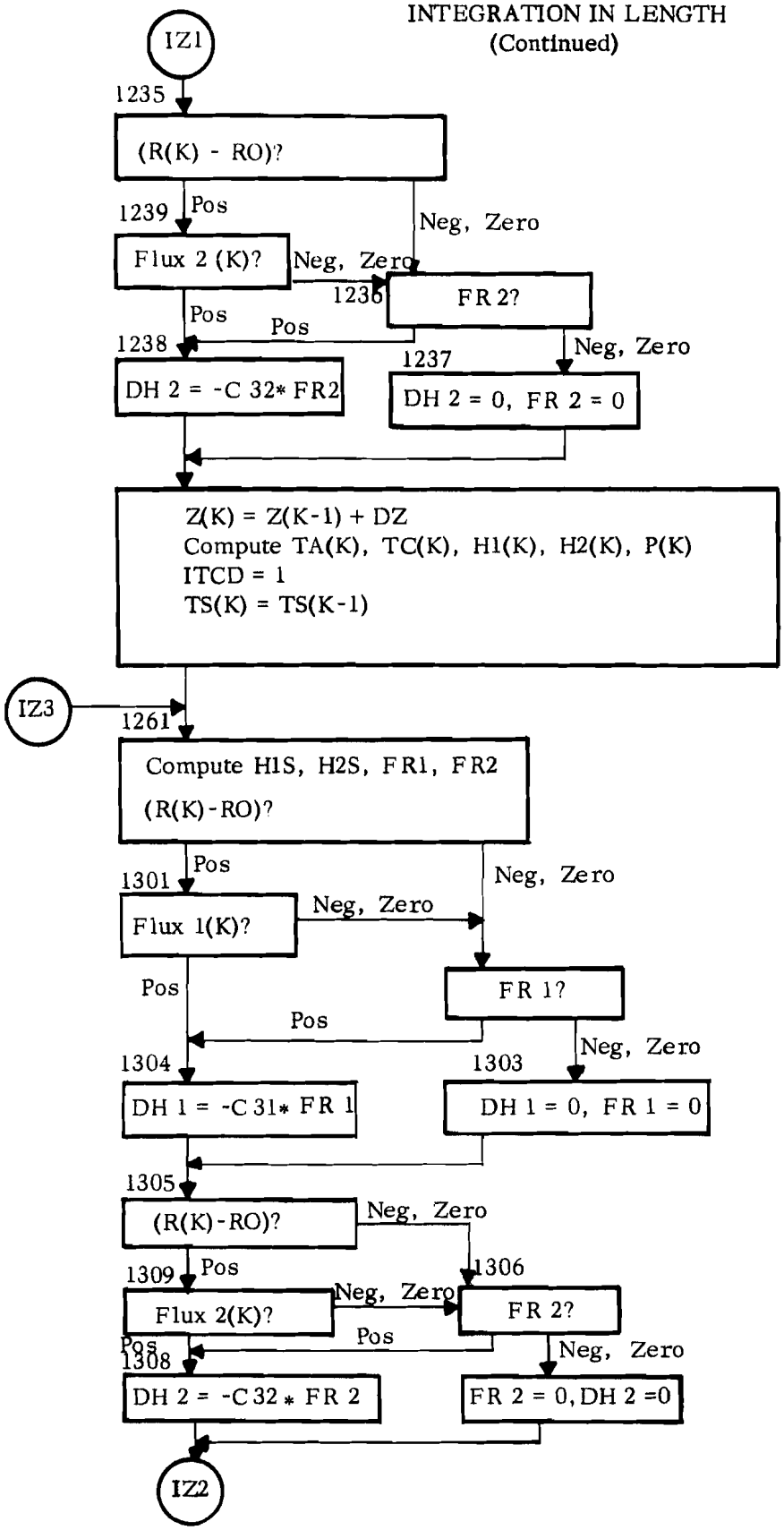
IZ1
1235
(R(K) - RO)?
1239
Pos
Neg, Zero
Flux 2 (K)?
Neg, Zero
1236
FR 2?
Pos
Pos
1238
DH 2 = -C 32* FR2
1237
Neg, Zero
DH 2 = 0, FR 2 = 0
Z(K) = Z(K-1) + DZ
Compute TA(K), TC(K), H1(K), H2(K), P(K)
ITCD = 1
TS(K) = TS(K-1)
IZ3
1261
Compute H1S, H2S, FR1, FR2
(R(K)-RO)?
Pos
1301
Neg, Zero
Flux 1(K)?
Pos
FR 1?
Pos
Neg, Zero
1304
1303
DH 1 = -C 31* FR 1
DH 1 = 0, FR 1 = 0
1305
(R(K)-RO)?
Neg, Zero
1309
Pos
1306
Flux 2(K)?
Neg, Zero
FR 2?
Pos
Pos
Neg, Zero
1308
DH 2 = -C 32 * FR 2
FR 2 = 0, DH 2 =0
IZ2

INTEGRATION IN LENGTH
(Continued)

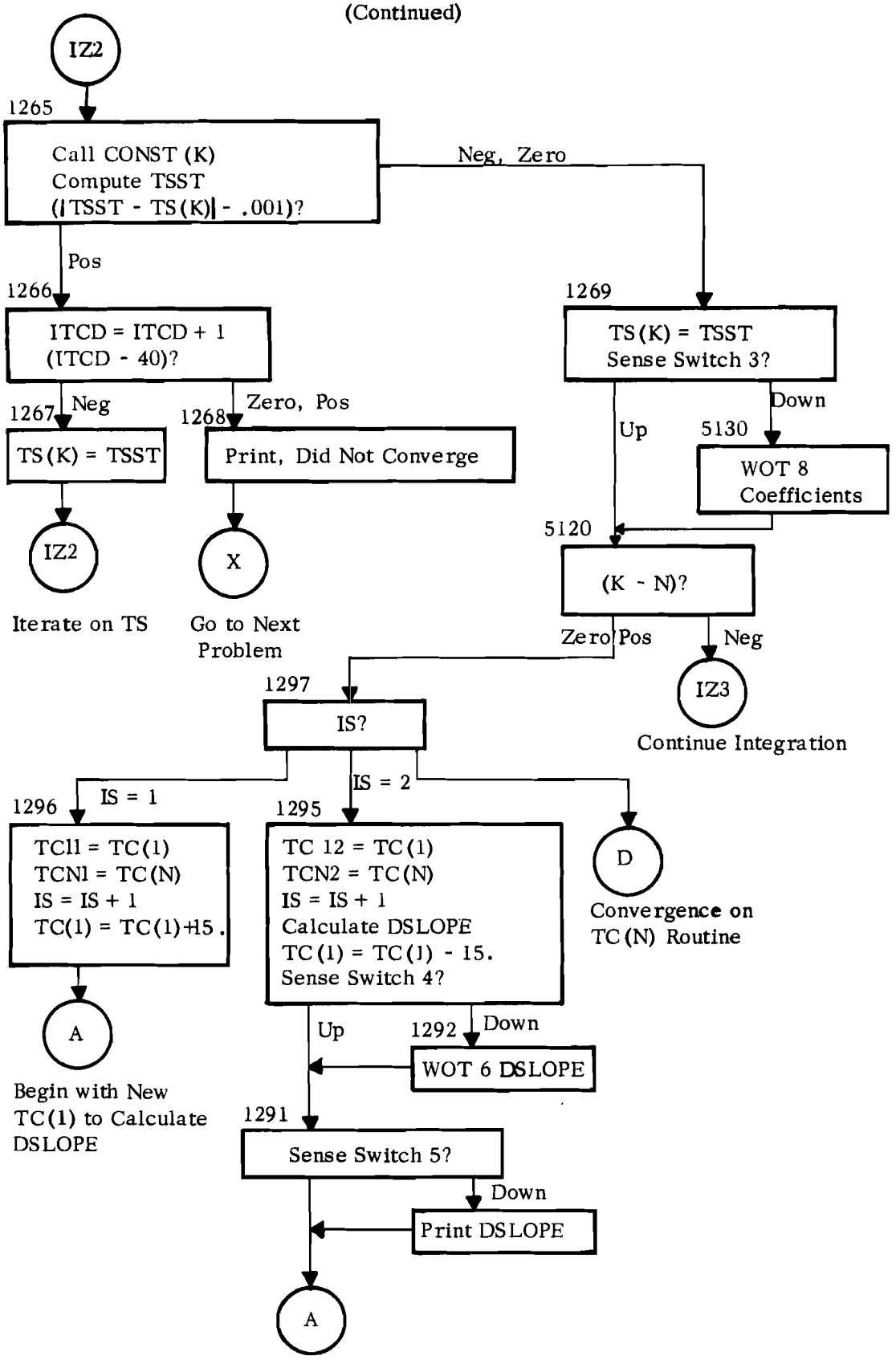

CONVERGENCE ON TC(N) ROUTINE

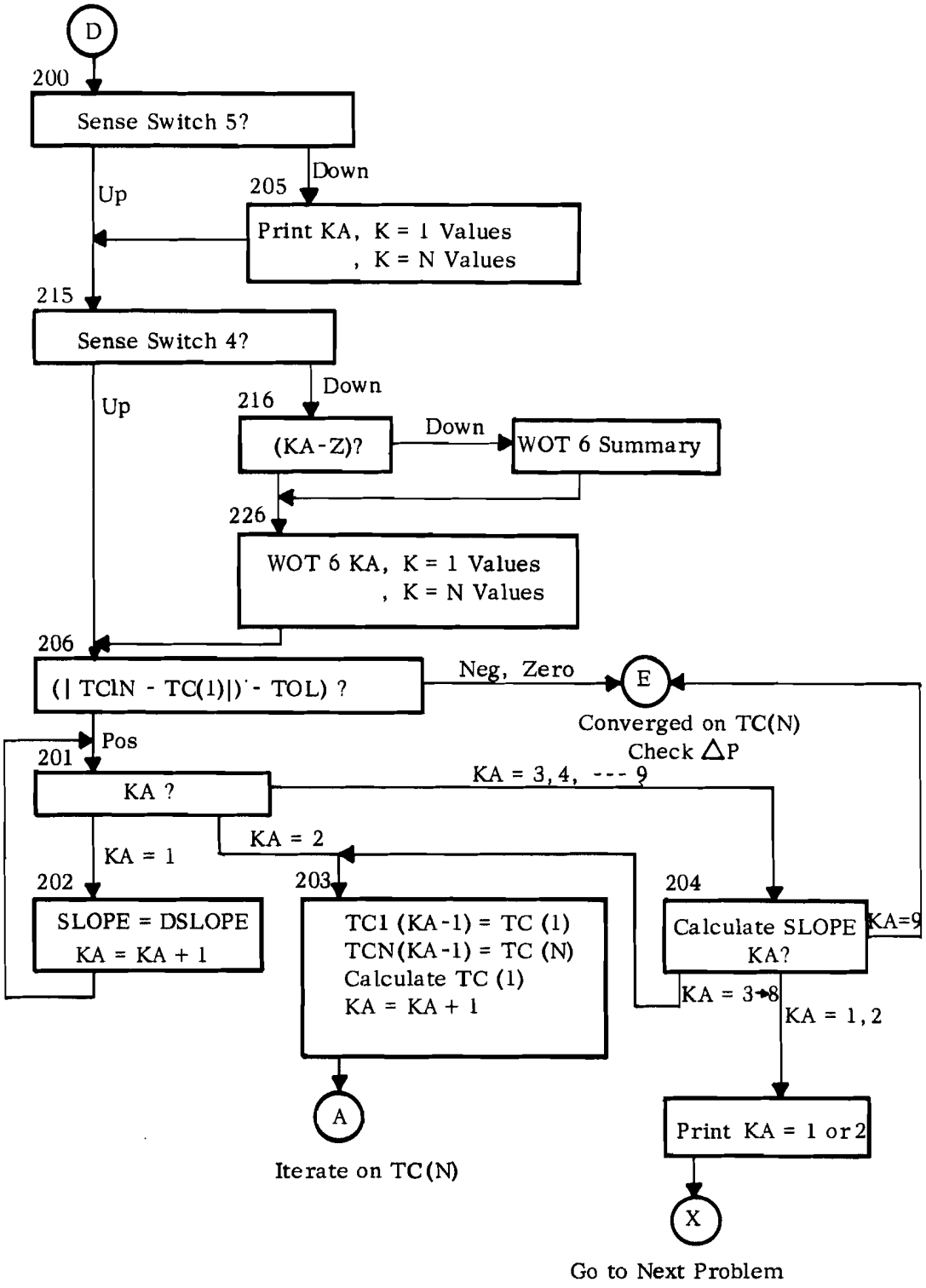

CONSTANT PRESSURE ITERATION ROUTINE

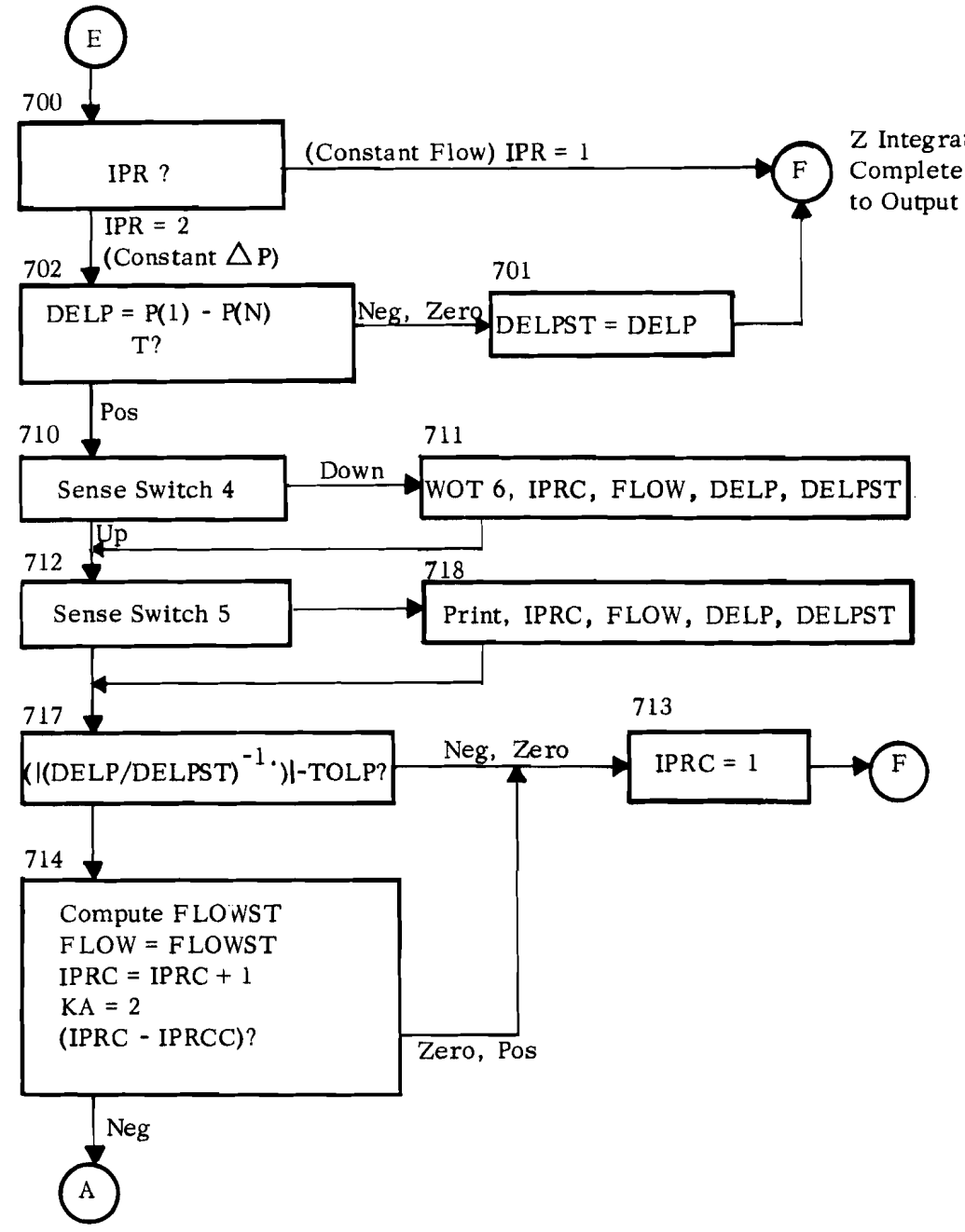

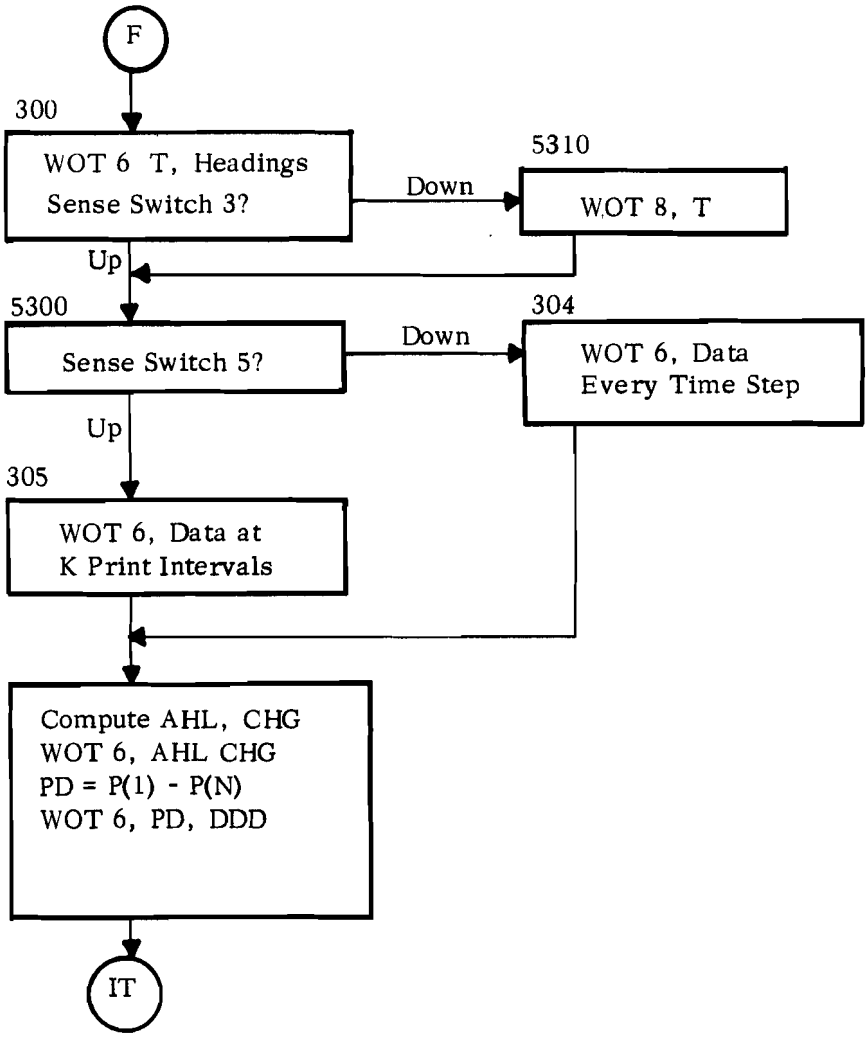

Integrate in Time

INTEGRATION IN TIME

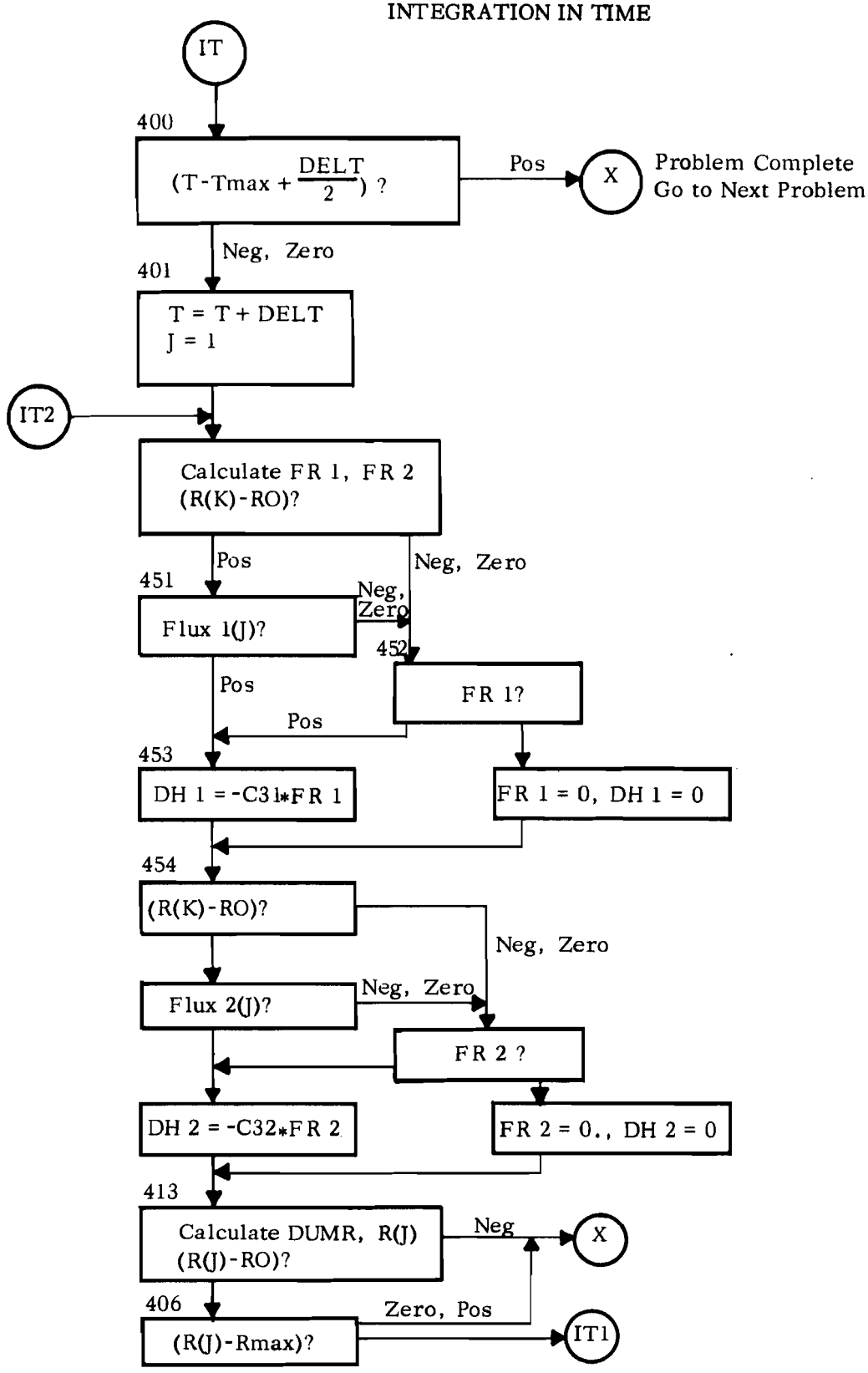

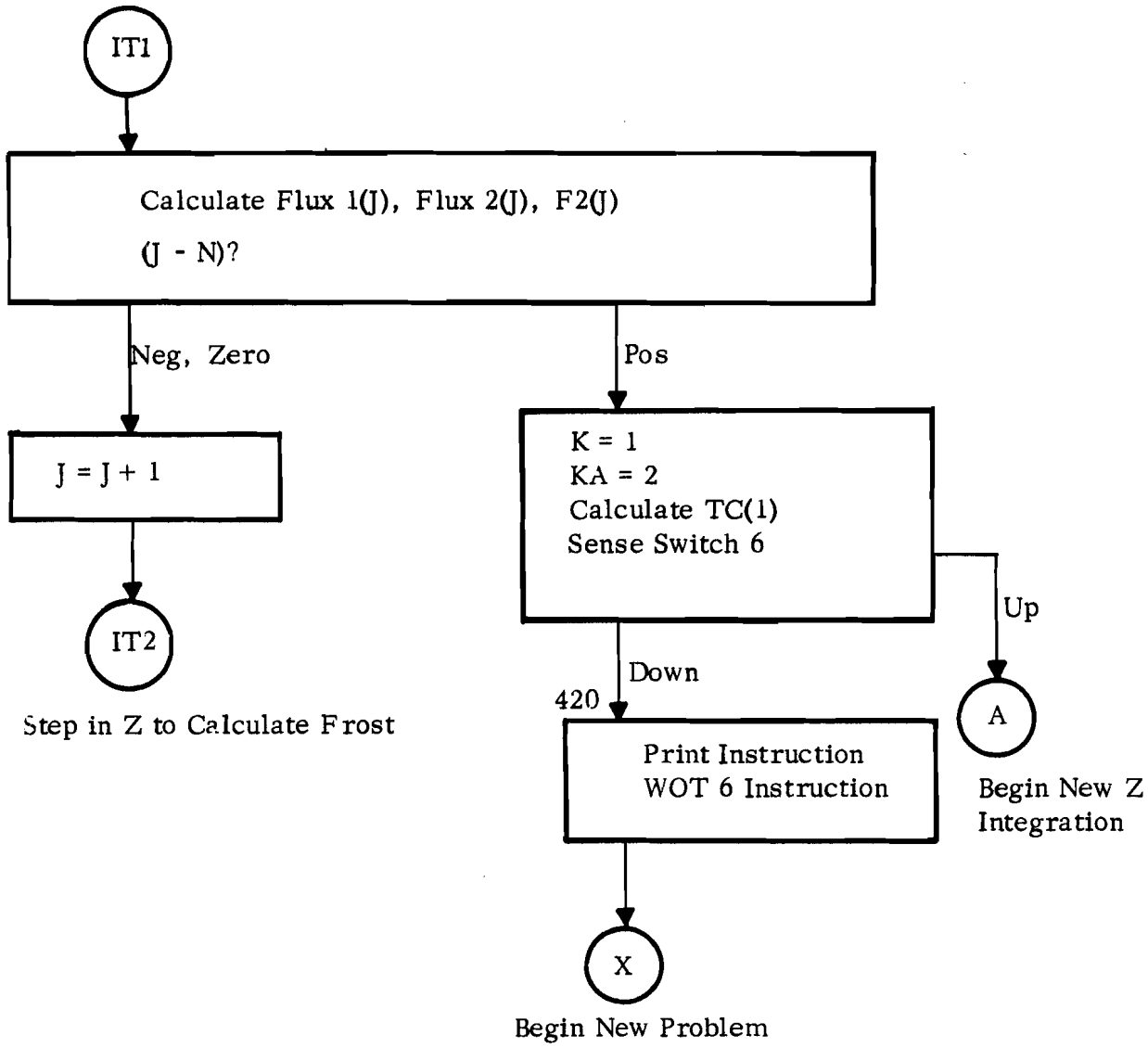
IT1
Calculate Flux 1(J), Flux 2(J), F2(J)
(J - N)?
Neg, Zero
Pos
J = J + 1
IT2
Step in Z to Calculate Frost
K = 1
KA = 2
Calculate TC(1)
Sense Switch 6
Up
Down
420
A
Begin New Z Integration
Print Instruction
WOT 6 Instruction
X
Begin New Problem

```
F H E       HEAT EXCHANGER PROGRAM

C       FREEZE OUT HEAT EXCHANGER
C       SENSE SWITCH 1 DOWN PRINTS EVERY LINE
C       SENSE SWITCH 2 DOWN PAUSES BETWEEN PROBLEMS
C       SENSE SWITCH 3 DOWN TO WRITE ALL CONSTANTS COMPUTED ON TAPE 8 (B1)
C       SENSE SWITCH 4 DOWN PRINTS TC(N) SUMMARY OFF LINE
C       SENSE SWITCH 5 DOWN TO PRINT TC(N) ON LINE
C       SENSE SWITCH 6 DOWN SKIPS TO NEXT PROBLEM
        COMMON H1,H2,H1S,H2S,TA,TC,TS,P,Z,T,R,H1F,H2F,F2,DELT
        COMMON B3,B4,CGC,CCO,B5,PRO
        COMMON XTC,XLO,RO,EL,CSAO,B1,B2,RI,TNT,APLO
        COMMON RHO1,RHO2,FK1,FK2,BF
        COMMON C1,C2,C31,C32,C4,C5,C61,C62,C71,C72,C81,C82,C9,C10,C11
        COMMON GAM1,GAM2,ALP1,ALP2,A1,A2,FLOW,COOL
        DIMENSION H1(1005),H2(1005),H1S(1005),H2S(1005),TA(1005),TC(1005)
        DIMENSION TS(1005),P(1005),R(1005),C5(1005),F2(1005)
        DIMENSION Z(1005),TC1(5),TCN(5)
        DIMENSION FLUX1(1005),FLUX2(1005)
        DIMENSION  RELH1(1005),RELH2(1005)
      2 FORMAT(1HO,9HPROBLEM  ,I3)
      4 FORMAT(1HO,2X,1HZ,6X,2HTA,7X,2HTS,7X,2HTC,8X,2HH1,10X,2HH2,10X,
       11HP,
       19X,1HR,10X,3HH1S,8X,3HH2S,6X,5HRELH1,2X,5HRELH2)
      5 FORMAT(1HO,6HTIME= ,E14.5,6H HOURS)
     10 FORMAT(15HOAIR HEAT LOSS=,E15.7,20H COOLANT HEAT GAIN= ,E15.7)
     12 FORMAT(1H1,51HCALCULATION FOR TS(1) DID NOT CONVERGE IN 40 CYCLES)
     13 FORMAT(6E10.4)
     14 FORMAT(2E10.4)
     15 FORMAT(4I5)
     16 FORMAT(1HC,2I5,E12.4)
     17 FORMAT(1HO,5HDELT=,E10.4,2X,5HTMAX=,E10.4)
     18 FORMAT(6E12.4)
     19 FORMAT(F7.3,3F9.3,1P2E12.4,0PF9.1,1PE12.4,1P2E11.3,0P2F7.3)
     20 FORMAT(1HO,3X,4HKA =,I3,3X,15HVALUES AT K=1,N,3X,25H(FOR CAPTIONS
       1SEE BELOW) )
     21 FORMAT(6F10.6)
     22 FORMAT(49H KA=1 OR 2 INSTEAD OF 3 OR 4, GO TO NEXT PROBLEM )
     23 FORMAT(55H THIS PROBLEM HAS BEEN COMPLETED, HIT START TO CONTINUE)
     24 FORMAT(1HO,5HTC1N=,E10.4,2X,6HTC(1)=,E10.4)
     25 FORMAT(1HO,2HN=,I5,2X,7HKPRINT=,I5,2X,4HIPR=,I5,2X,6HIPRCC=,I5)
     26 FORMAT(49H YOU HAVE STARTED THE NEXT PROBLEM BY USING SS 6 )
     27 FORMAT(2E10.4)
     28 FORMAT(15HOPRESSURE DROP=,E14.5,4H PSF,2H= ,E14.5,4H PSI)
     29 FORMAT(1HO,5HIPRC=,I5,2X,5HFLOW=,E12.5,5HLB/HR,2X,5HDELP=,E12.5,3H
       1PSF,2X,7HDELPST=,E12.5,3HPSF)
     30 FORMAT(5F10.6)
     31 FORMAT(1HO,4HTOL=,E10.4,2X,5HTOLP=,E10.4)
     32 FORMAT(1HO,4HCGC=,F10.6,2X,3HB3=,F10.6,2X,4HCCO=,F10.6,2X,3HB4=,F1
       10.6,2X,4HPRO=,F10.6,2X,3HB5=,F10.6)
     33 FORMAT(1HO,10HINPUT DATA)
     34 FORMAT(1HO,3HRI=,F10.6,2X,3HRO=,F10.6,2X,4HXTO=,F10.6,2X,4HXLO=,F1
       10.6,2X,4HTNT=,F10.6)
     35 FORMAT(1HO,3HEL=,F10.6,2X,5HAPLO=,F10.6,2X,5HCSAO=,F10.6,2X,3HB1=,
       1F10.6,2X,3HB2=,F10.6)
     36 FORMAT(1HO,5HRHO1=,F10.6,2X,4HFK1=,F10.6,2X,5HRHO2=,F10.6,2X,4HFK2
       1=,F10.6,2X,3HBF=,F10.6)
```

```
F H E       HEAT EXCHANGER PROGRAM

   37 FORMAT(1HO,5HFLOW=,E10.4,2X,5HCOOL=,E10.4)
   38 FORMAT(1H1,26HSUMMARY OF TC(N) ITERATION)
   39 FORMAT(1HO,17H INITIAL SLOPE = ,E10.5)
   40 FORMAT(1H1,40HCONSTANT FLOW FREEZE OUT HEAT EXCHANGER )
   41 FORMAT(1H1,48HCONSTANT PRESSURE DROP FREEZE OUT HEAT EXCHANGER)
   42 FORMAT(1HO,39HTHE VALUE OF TA(1) FOR THIS TIME STEP =,E10.4)
   46 FORMAT(1HO,70HCOMPRESSIBLE FLOW EFFECTS OCCURING ON AIRSIDE,
     1PROBLEM TERMINATED      )
 5020 FORMAT( 1H1,2X,1HK,6X,2HC1,12X,2HC2,12X,3HC31,11X,3HC32,11X,2HC4,
 50201 12X,2HC5,12X,2HC9,12X,3HC10,11X,3HC11 )
 5030 FORMAT(1H ,I5,9E14.5)
      C61=2.129E-05
      C62=5.655E-05
      C71=35.9
      C72=34.5
      C81=11320.
      C82=5800.
      GAM1=1258.
      GAM2= 264.
      ALP1=  .89
      ALP2= 1.16
      IB=0
      IPRC=1
  600 IF(SENSE SWITCH 2)611,610
  611 PRINT 23
      PAUSE
C           ----- INITIAL VALUES , T=0. -----
  610 READ INPUT TAPE 5,13,TC1N,TC(1)
      READ INPUT TAPE 5,14,DELT,TMAX
      READ INPUT TAPE 5,15,N,KPRINT,IPR,IPRCC
      READ INPUT TAPE 5,14,TOL,TOLP
      READ INPUT TAPE 5,21,CGO,B3,CCO,B4,PRC,B5
      READ INPUT TAPE 5,30,RI,RC,XTC,XLC,TNT
      READ INPUT TAPE 5,30,EL,APLO,CSAO,B1,B2
      READ INPUT TAPE 5,30,RHO1,FK1,RHO2,FK2,BF
      READ INPUT TAPE 5,27,FLOW,COOL
      ICCN=1
      IS=1
      T=0.0
      DO 5400 J=1,N
      FLUX1(J)=0.0
      FLUX2(J)=0.0
 5400 F2(J)=0.0
      IB=IB+1
      K=1
      KA=1
      DZ=1.0/FLOATF(N-1)
      Z(1)=0.
      IF(SENSE SWITCH 3)5010,5000
 5010 GO TO(5012,5014),IPR
 5012 WRITE OUTPUT TAPE 8,40
      WRITE OUTPUT TAPE 8,2,IB
      WRITE OUTPUT TAPE 8,5020
      GO TO 5016
 5014 WRITE OUTPUT TAPE 8,41
      WRITE OUTPUT TAPE 8,2,IB
```

```
F H E      HEAT EXCHANGER PROGRAM

      WRITE OUTPUT TAPE 8,5020
 5016 WRITE OUTPUT TAPE 8,33
      WRITE OUTPUT TAPE 8,24,TC1N,TC(1)
      WRITE OUTPUT TAPE 8,17,DELT,TMAX
      WRITE OUTPUT TAPE 8,25,N,KPRINT,IPR,IPRCC
      WRITE OUTPUT TAPE 8,31,TOL,TOLP
      WRITE OUTPUT TAPE 8,32,CGC,B3,CCO,B4,PRO,B5
      WRITE OUTPUT TAPE 8,34,RI,RO,XTO,XLO,TNT
      WRITE OUTPUT TAPE 8,35,EL,APLC,CSAO,B1,B2
      WRITE OUTPUT TAPE 8,36,RHC1,FK1,RHO2,FK2,BF
      WRITE OUTPUT TAPE 8,37,FLCW,CCOL
 5000 GO TO (301,302),IPR
  301 WRITE OUTPUT TAPE 6,40
      WRITE OUTPUT TAPE 6,2,IB
      GO TO 605
  302 WRITE OUTPUT TAPE 6,41
      WRITE OUTPUT TAPE 6,2,IB
  605 WRITE OUTPUT TAPE 6,33
      WRITE OUTPUT TAPE 6,24,TC1N,TC(1)
      WRITE OUTPUT TAPE 6,17,DELT,TMAX
      WRITE OUTPUT TAPE 6,25,N,KPRINT,IPR,IPRCC
      WRITE OUTPUT TAPE 6,31,TOL,TOLP
      WRITE OUTPUT TAPE 6,32,CGC,B3,CCO,B4,PRO,B5
      WRITE OUTPUT TAPE 6,34,RI,RO,XTO,XLO,TNT
      WRITE OUTPUT TAPE 6,35,EL,APLC,CSAO,B1,B2
      WRITE OUTPUT TAPE 6,36,RHC1,FK1,RHO2,FK2,BF
      WRITE OUTPUT TAPE 6,37,FLCW,CCOL
      RMAX=RO*(MIN1F(XTO,XLO))
      DO 120 J=1,N
      R(J)=RO
  120 CONTINUE
C           ----- INITIAL BOUNDARY CONDITIONS , Z=0. -----
  199 CALL CONSTN(1)
      CALL INIVAL(T,TA1,P1,H11,H21)
      TA(1)=TA1
      P(1)=P1
      H1(1)=H11
      H2(1)=H21
      K=1
      ITC=1
      TS(1)=(TA(1)+C9*TC(1))/(1.+C9)
  105 H1S(1)=C61*EXPF(C71-C81/TS(1))/P(1)
      FR1=H1(1)-H1S(1)
      H1SAT=C61*EXPF(C71-C81/TA(K))/P(K)
      H2SAT=C62*EXPF(C72-C82/TA(K))/P(K)
      RELH1(K)=H1(K)/H1SAT
      RELH2(K)=H2(K)/H2SAT
      IF(R(K)-RO)131,131,130
  130 IF(FLUX1(K))131,131,132
  131 IF(FR1)133,133,132
  132 DH1=-C31*(FR1)
      GO TO 102
  133 FR1=0.
      DH1=0.
  102 H2S(1)=C62*EXPF(C72-C82/TS(1))/P(1)
      FR2=H2(1)-H2S(1)
```

```
F H E       HEAT EXCHANGER PROGRAM

      IF(R(K)-RC)134,134,138
  138 IF(FLUX2(K))134,134,136
  134 IF(FR2)135,135,136
  135 FR2=0.
      DH2=0.
      GO TO 104
  136 DH2=-C32*(FR2)
  104 TSS=(TA(1)+C9*TC(1)+A1*FR1+A2*FR2)/(1.+C9)
      IF(ABSF(TSS-TS(1))-.001)106,106,107
  106 TS(1)=TSS
  110 GO TO 1199
  107 TS(1)=TSS
      ITC=ITC+1
      IF(ITC-40)105,108,108
  108 PRINT 12
      WRITE OUTPUT TAPE6,12
      GO TO 600
 1199 IF(SENSE SWITCH 3)5110,1200
 5110 WRITE OUTPUT TAPE 8,5030,K,C1,C2,C31,C32,C4,C5(K),C9,C10,C11
C           ----- Z INTEGRATION -----
 1200 K=K+1
      DTA=-C1*(TA(K-1)-TS(K-1))
      DTC=-C2*(TS(K-1)-TC(K-1))
      PCOM=C10*P(K-1)**2./TA(K-1)
      IF(PCOM-2.)1201,1201,1202
 1201 ICOM=2
      PCOM=2.
 1202 DP=(C11+DTA/TA(K-1))*P(K-1)/(1.-PCOM)
      FR1=H1(K-1)-H1S(K-1)
      FR2=H2(K-1)-H2S(K-1)
 1230 IF(R(K)-RO)1232,1232,1231
 1231 IF(FLUX1(K))1232,1232,1233
 1232 IF(FR1)1234,1234,1233
 1233 DH1=-C31*(FR1)
      GO TO 1235
 1234 FR1=0.
      DH1=0.
 1235 IF(R(K)-RC)1236,1236,1239
 1239 IF(FLUX2(K))1236,1236,1238
 1236 IF(FR2)1237,1237,1238
 1237 FR2=0.                                          1
      DH2=0.
      GO TO 1250
 1238 DH2=-C32*(FR2)
 1250 Z(K)=Z(K-1)+DZ
 1270 TA(K)=DTA*DZ+TA(K-1)
      TC(K)=DTC*DZ+TC(K-1)
      H1(K)=DH1*DZ+H1(K-1)
      H2(K)=DH2*DZ+H2(K-1)
      P(K)=DP*DZ+P(K-1)
      ITCO=1
 1260 TS(K)=TS(K-1)
 1261 H1S(K)=C61*EXPF(C71-C81/TS(K))/P(K)
      H2S(K)=C62*EXPF(C72-C82/TS(K))/P(K)
      FR1=H1(K)-H1S(K)
      FR2=H2(K)-H2S(K)
```

```
F H E        HEAT EXCHANGER PROGRAM

      H1SAT=C61*EXPF(C71-C81/TA(K))/P(K)
      H2SAT=C62*EXPF(C72-C82/TA(K))/P(K)
      RELH1(K)=H1(K)/H1SAT
      RELH2(K)=H2(K)/H2SAT
 1300 IF(P(K)-RC)1302,1302,1301
 1301 IF(FLUX1(K))1302,1302,1304
 1302 IF(FR1)1303,1303,1304
 1303 FR1=0.
      DH1=0.
      GO TO 1305
 1304 DH1=-C31*(FR1)
 1305 IF(R(K)-RC)1306,1306,1309
 1309 IF(FLUX2(K))1306,1306,1308
 1306 IF(FR2)1307,1307,1308
 1307 FR2=0.
      DH2=0.
      GO TO 1265
 1308 DH2=-C32*(FR2)
 1265 CALL CONSTN(K)
      TSST=(1./(1.+C9))*(TA(K)+C9*TC(K)+A1*FR1+A2*FR2)
      IF(ABSF(TSST-TS(K))-.001)1269,1269,1266
 1269 TS(K)=TSST
      IF(SENSE SWITCH3)5130,5120
 5130 WRITE OUTPUT TAPE 8,5030,K,C1,C2,C31,C32,C4,C5(K),C9,C10,C11
 5120 IF(K-N)1200,1297,1297
 1297 GO TO(1296,1295,200),IS
 1296 TC11=TC(1)
      TCN1=TC(N)
      IS=IS+1
 1294 TC(1)=TC(1)+15.
      GO TO 199
 1295 TC12=TC(1)
      TCN2=TC(N)
      IS=IS+1
 1293 DSLOPE=(TC12-TC11)/(TCN2-TCN1)
      TC(1)=TC(1)-15.
      IF(SENSE SWITCH 4)1292,1291
 1292 WRITE OUTPUT TAPE 6,39,DSLOPE
 1291 IF(SENSE SWITCH 5)1290,199
 1290 PRINT 39,DSLOPE
      GO TO 199
 1266 ITCO=ITCO+1
      IF(ITCO-40)1267,1268,1268
 1268 PRINT 12
      WRITE OUTPUT TAPE 6,12
      GO TO 600
 1267 TS(K)=TSST
      GO TO 1261
C          ----- CONVERGENCE ON COOLANT INLET TEMPERATURE -----
  200 IF(SENSE SWITCH 5)205,215
  205 PRINT 20,KA
      PRINT 19,Z(1),TA(1),TS(1),TC(1),H1(1),H2(1),P(1),R(1),H1S(1),
     1H2S(1),RELH1(1),RELH2(1)
      PRINT 19,Z(N),TA(N),TS(N),TC(N),H1(N),H2(N),P(N),R(N),H1S(N),
     1H2S(N),RELH1(N),RELH2(N)
  215 IF(SENSE SWITCH 4)216,206
```

```
F H E       HEAT EXCHANGER PROGRAM

  216 IF(KA-2)225,225,226
  225 WRITE OUTPUT TAPE 6,38
  226 WRITE OUTPUT TAPE 6,20,KA
      WRITE OUTPUT TAPE 6,19,Z(1),TA(1),TS(1),TC(1),H1(1),H2(1),P(1),
     1R(1),H1S(1),H2S(1),RELH1(1),RELH2(1)
      WRITE OUTPUT TAPE 6,19,Z(N),TA(N),TS(N),TC(N),H1(N),H2(N),P(N),
     1R(N),H1S(N),H2S(N),RELH1(N),RELH2(N)
  206 IF(ABSF(TC1N-TC(N))-TOL)700,700,201
  201 GO TO(202,203,204,204,204,204,204,204,204),KA
  202 SLOPE=DSLOPE
      KA=KA+1
      GO TO 201
  203 TC1(KA-1)=TC(1)
      TCN(KA-1)=TC(N)
      TC(1)=SLOPE*(TC1N-TC(N))+TC(1)
      KA=KA+1
      GO TO 199
  204 SLOPE=(TC(1)-TC1(KA-2))/(TC(N)-TCN(KA-2))
      GO TO(207,207,203,203,203,203,203,203,700),KA
C           ----- CONSTANT PRESSURE DROP ROUTINE -----
  700 GO TO(300,702),IPR
  702 DELP=P(1)-P(N)
      IF(1)701,701,710
  701 DELPST=DELP
      GO TO 300
  710 IF(SENSE SWITCH 4)711,712
  711 WRITE OUTPUT TAPE6,29,IPRC,FLOW,DELP,DELPST
  712 IF(SENSE SWITCH 5)718,717
  718 PRINT 29,IPRC,FLOW,DELP,DELPST
  717 IF(ABSF((DELP/DELPST)-1.0)-TOLP)713,713,714
  713 IPRC=1
      GO TO 300
  714 FLOWST=FLOW*(SQRTF(DELPST/DELP))
      FLOW=FLOWST
      IPRC=IPRC+1
      KA=2
  715 IF(IPRC-IPRCC)199,716,716
  716 IPRC=1
      GO TO 300
  207 PRINT22
      WRITE OUTPUT TAPE 6,22
      GO TO 600
C           ----- OUTPUT -----
  300 WRITE OUTPUT TAPE 6,5,T
      WRITE OUTPUT TAPE 6,4
      IF(SENSE SWITCH 3)5310,5300
 5310 WRITE OUTPUT TAPE 8,5,T
 5300 IF(SENSE SWITCH 1)304,305
  304 DO 306 J=1,N
      WRITE OUTPUT TAPE 6,19,Z(J),TA(J),TS(J),TC(J),H1(J),H2(J),P(J),
     1R(J),H1S(J),H2S(J),RELH1(J),RELH2(J)
  306 CONTINUE
      AHL=(0.248*(TA(1)-TA(N))+GAM1*(H1(1)-H1(N))+GAM2*(H2(1)-H2(N)))*FL
     1OW
      CHG=(0.248*(TC(1)-TC(N)))*COOL
      WRITE OUTPUT TAPE 6,10,AHL,CHG
```

```
F H E       HEAT EXCHANGER PROGRAM

      PD=P(1)-P(N)
      PDD=PD/144.
      WRITE OUTPUT TAPE 6,28,PD,PDD
      GO TO 400
  305 DO 307 J=1,N,KPRINT
      WRITE OUTPUT TAPE 6,19,Z(J),TA(J),TS(J),TC(J),H1(J),H2(J),P(J),
     1R(J),H1S(J),H2S(J),RELH1(J),RELH2(J)
  307 CONTINUE
      CGM=.5*(TA(1)+TA(N))*B3+CCO
      CCM=.5*(TC(1)+TC(N))*B4+CCO
      AHL=(  CGM*(TA(1)-TA(N))+GAM1*(H1(1)-H1(N))+GAM2*(H2(1)-H2(N)))*FL
     1CM
      CHG=(  CCM*(TC(1)-TC(N)))*CCOL
      WRITE OUTPUT TAPE 6,10,AHL,CHG
      PD=P(1)-P(N)
      PDD=PD/144.
      WRITE OUTPUT TAPE 6,28,PD,PDD
C           ----- T INTEGRATION -----
  400 IF(T-TMAX+DELT/2.)401,401,600
  401 GOTO(402,403),ICOM
  403 WRITE OUTPUT TAPE 6,46
      GO TO 600
  402 T=T+ DELT
      DO 404 J=1,N
      FR1=H1(J)-H1S(J)
      FR2=H2(J)-H2S(J)
  450 IF(R(J)-RO)452,452,451
  451 IF(FLUX1(J))452,452,453
  452 IF(FR1)455,455,453
  455 FR1=0.
      DH1=0.
      GO TO 454
  453 DH1=-C31*(FR1)
  454 IF(R(J)-RO)456,456,459
  459 IF(FLUX2(J))456,456,457
  456 IF(FR2)458,458,457
  458 FR2=0.
      DH2=0.
      GO TO 413
  457 DH2=-C32*(FR2)
  413 DUMR=(1./(ALP1*RHO1))*(FR1)+(1./(ALP2*RHO2))*(FR2)
      R(J)=R(J)+DUMR*C5(J)*DELT
  405 IF(R(J)-RO)600,406,406
  406 IF(R(J)-RMAX)407,600,600
  407 FLUX1(J)=FLUX1(J)+ALPO*DELT*C5(J)*(H1(J)-H1S(J))*R(J)/(RO*ALP1)
      FLUX2(J)=FLUX2(J)+ALPO*DELT*C5(J)*(H2(J)-H2S(J))*R(J)/(RO*ALP2)
      F2(J)=FLUX2(J)/(FLUX2(J)+FLUX1(J))
  404 CONTINUE
      K=1
      KA=
      TC(1)=SLOPE*(TCIN-TC(N))+TC(1)
      IF(SENSE SWITCH 6)420,421
  421 GO TO 199
  420 PRINT 26
      WRITE OUTPUT TAPE 6,26
      GO TO 600
      END (1,1,0,0,0,0,1,1,0,0,0,0,0,0,0)
```

```
SUBROUTINE INIVAL(T,TA1,P1,H11,H21)
```

```
SUBROUTINE INIVAL(T,TA1,P1,H11,H21)
TA1=568.
P1=12960.
H11=0.000248
 H21=0.
RETURN
END(1,0,0,0,0,0,0,0,0,0,0,0,0,0,0)
```

CONSTANT CALCULATIONS FOR HEAT EXCHANGER PROGRAM

```
      SUBROUTINE CONSTN(J)
      COMMON H1,H2,H1S,H2S,TA,TC,TS,P,Z,T,R,H1F,H2F,F2,DELT
      COMMON B3,B4,CGO,CCO,B5,PRO
      COMMON XTO,XLO,RO,EL,CSAO,B1,B2,RI,TNT,APLO
      COMMON RHO1,RHO2,FK1,FK2,BF
      COMMON C1,C2,C31,C32,C4,C5,C61,C62,C71,C72,C81,C82,C9,C10,C11
      COMMON GAM1,GAM2,ALP1,ALP2,A1,A2,FLOW,COOL
      DIMENSION H1(1005),H2(1005),H1S(1005),H2S(1005),TA(1005),TC(1005)
      DIMENSION TS(1005),P(1005),R(1005),C5(1005),F2(1005)
      DIMENSION Z(1005)
      K=J
      IF(R(K))100,100,10
   10 IF( FLOW ) 100,100,20
   20 RRO=R(K)/RO
      IF(RRO-XTO)30,100,100
   30 IF(RRO-XLO)40,100,100
   40 XT=XTO/RRO
      XL=XLO/RRO
      AO=CSAO*(XTO-RRO)/(XTO-1.0)
      UMI=0.0365*((TC(K)/492.0)**0.85)
      CC=CCO+B4*TC(K)
      PR=PRO+B5*TC(K)
      FK=(FK2-FK1)*F2(K)+FK1
      AOSTR=AO*(XTO-BF*RRO)/(XTO-RRO)
      UM=0.0365*((TA(K)/492.0)**0.85  )
      SFUM=2.0*R(K)*FLOW  / (AO*UM)
      FPRIME=0.254*((XL-1.)**(-.475))*(SFUM**(-.15))
      GAMO=APLO*EL*RRO/AO
      STO=B1*(SFUM**B2)
   41 STI=0.021*((2.0*COOL  / (3.1415927 *RI*UMI))**(-0.2))*(PR**
  411(-0.666666667))
      ARE=STI/STO
      W=AO/(3.14159   *RI*R(K))
      C1=GAMO*STO
      C4=1.0/(CGO+B3*TA(K))
      GAMNU=C4*COOL  * AO*CC/(FLOW  * 3.1415927 *RI*R(K))
      IF(RRO-1.0)100,50,55
   50 C2=C1*W*ARE
      GO TO 60
   55 BETA=C4*FK*AO/(FLOW  * STO*LOGF(RRO)*R(K))
      C2=C1*W*ARE/(1.0+GAMNU*ARE/BETA)
   60 C31=C1/ALP1
      C32=C1/ALP2
      C9=C2*GAMNU/(C1*W)
      C10=1.513E+7/((FLOW/AOSTR)**2)
      C11=4.0*TNT*FPRIME
      C5(K)=STO*FLOW/AO
      A1=C4*GAM1/ALP1
      A2=C4*GAM2/ALP2
      RETURN
  100 PRINT 101
  101 FORMAT(49HOERROR IN PROGRAM OR MACHINE OR DATA - OFF YOU GO )
      WRITE OUTPUT TAPE 6,101
      PRINT 102
  102 FORMAT(20HOMEMORY DUMP FOLLOWS )
```

```
CONSTANT CALCULATIONS FOR HEAT EXCHANGER PROGRAM

      WRITE OUTPUT TAPE 6,102
      CALL DUMP
      END(1,1,0,0,0,0,1,1,0,0,0,0,0,0,0)
```

IV PROGRAM OPERATING INSTRUCTIONS

A. Input--Programs

The program has been designed to operate with the FORTRAN Monitor System (FMS) adapted to the IBM 7090 Data Processing System. The proper use of FMS is included in the 7090 FORTRAN Reference Manual.

The MAIN FORTRAN program has been designed for a cross flow-counter flow exchanger with H_2O and CO_2 vapor in an air stream. Once the MAIN program is compiled and a binary card version produced, there is no need to change the binary version unless the fluids or freeze-out components are changed.

Two SUBROUTINES are required by the MAIN program:

1. The coefficient subprogram

```
SUBRØUTINE CØNSTN (J)
```

The subprogram calculates the non-constant coefficients required by the differential equations. The content of the program is fixed and need not be changed unless the mathematical analysis is changed.

2. The initial value subprogram

```
SUBRØUTINE INIVAL (T, TA1, P1, H11, H21)
```

This routine enables the programmer to vary the air inlet temperature, TA1; air inlet pressure, P1; the H_2O inlet humidity, H11; and the CO_2 inlet humidity as functions of time, T (in hours). The coolant inlet temperature is fixed and independent of time.

The variables, TA1, etc., must be used in the above form to specify the variables. Attached to the MAIN FORTRAN listing is a sample set of SUBROUTINES.

B. Input-Data Cards

Attached to the MAIN and SUBROUTINE decks are 9 data cards which describe the exchanger, properties of fluids and other data.

This data is systematically arranged on nine data cards located at the back of the program deck. The format and content of these cards are as follows:

CARD 1 - Coolant Temperature Data

FORMAT (2E10.4)

LIST TC1N, TC(1)

where: TC1N = coolant inlet temperature, ^{o}R
TC(1) = best estimate of coolant outlet temperature, ^{o}R

CARD 2 - Time Data

FORMAT (2E10.4)

LIST DELT, TMAX

where: DELT = time interval used in calculations and printout, HRS
TMAX = length of test, HRS

We recommend DELT equal TMAX divided by 21. This value may be adjusted, of course, depending on the nature of the experiment.

CARD 3 - Printing Instructions, Iteration Limits, Miscellaneous

FORMAT (4I5)

LIST N, KPRINT, IPR, IPRCC

where: N = number of mesh points desired along distance z in solution of problem. Should be one more than the number of mesh intervals; i.e., for 200 mesh intervals, use 201 points. (N = 201, is recommended.)

KPRINT = output printing frequency. This allows the operator to print out any number of mesh points which he desires:

Example: KPRINT = 2, N = 201

Under these conditions only every second point will be printed making a total of 100 printed points. However, all 201 points will still be used in the solution of the problem.

IPR = an indicator to designate the problem as constant flow rate or constant pressure drop.

IPR = 1 = constant flow rate

IPR = 2 = constant pressure drop

IPR must be either 1 or 2.

IPRCC = establishes maximum number of iterations on pressure allowed in solution of constant pressure drop problems. (Recommend IPRCC equal 5).

CARD 4 - Tolerances

FORMAT (2E10.4)

LIST TØL, TØLP

where: TØL = accuracy required in iteration to set TC(N), ^{o}R
TØLP = accuracy required in pressure iteration of constant pressure drop problems where .01 = 1% accuracy.

CARD 5 - Fluid Properties

FORMAT (6F10.6)

LIST CGØ, B3, CCØ, B4, PRØ, B5

where: CGØ = air heat capacity constant, Btu/lb(^{o}F)
B3 = air heat capacity temperature coefficient, Btu/lb(^{o}F)^2
CCØ = coolant heat capacity constant, Btu/lb(^{o}F)
B4 = coolant heat capacity temperature coefficient, Btu/lb(^{o}F)^2
PRØ = coolant Prandtl number constant
B5 = coolant Prandtl number temperature coefficient

CARD 6 - Exchanger Geometry

FORMAT (5F10.6)

LIST RI, RØ, XTØ, XLØ, TNT

where: RI = inside tube radius, ft
RØ = radius of unfrosted tube, ft
XTØ = transverse pitch (clean exchanger)
XLØ = longitudinal pitch (clean exchanger)
TNT = total number of tubes in exchanger

CARD 7 - Exchanger Geometry

FORMAT (5F10.6)

LIST EL, APLØ, CSAØ, B1, B2

where: EL = length of exchanger, ft
APLØ = area per unit length (clean exchanger), ft^2/ft
CSAØ = minimum cross-sectional area (clean exchanger), ft^2
B1 = constant for Stanton number equation
B2 = constant for Stanton number equation

CARD 8 - Frost Data

FORMAT (5F10.6)

LIST RHØ1, FK1, RHØ2, FK2, BF

where: RHØ1 = density of H_2O frost, lb/ft^3
FK1 = thermal conductivity of H_2O frost, $Btu/ft^2\text{-}hr\text{-}^oF/ft$
RHØ2 = density of CO_2 frost, lb/ft^3
FK2 = thermal conductivity of CO_2 frost, $Btu/ft^2\text{-}hr\text{-}^oF/ft$
BF = radial distribution factor

CARD 9 - Flow Data

FORMAT (2E10.4)

LIST FLØW, CØØL

where: FLØW = air flow rate, lb/hr
CØØL = coolant flow rate, lb/hr

It is possible to run several problems consecutively by placing the data card sets of each separate problem at the end of the program in the order in which the problems are to be executed. For example, if two problems were to be run, the data cards would be so arranged that the first nine cards were cards 1-9 of problem 1. These would then be followed by cards 1-9 of problem 2. It is extremely important that the cards be properly arranged with a data set.

C. Program Operation

As this program is to be operated together with the FORTRAN MONITOR SYSTEM, a minimum effort will be required in the solution of a problem. The following recommendations, if properly employed, will result in an extremely efficient and flexible program capable of providing a detailed analysis of the heat exchanger's performance.

1. Program Deck

Both the main and subprograms should be complete and capable of handling any situations which may arise thus enabling the operator to use binary program decks throughout. However, in the event changes are indicated, it is possible to recompile either the main or subprogram prior to problem execution. The following ordering of the program deck should be used, with all control cards prepared according to 7090 FMS requirements:

a) FMS control cards
b) MAIN program
c) Two SUBROUTINE programs
d) DATA control card
e) Data cards (9 cards per problem).

2. Tape requirements

The following tapes are required by the program:

a) Logical Tape 5 - Input tape (FMS A2)
b) Logical Tape 6 - Output tape for main program (FMS A3)
c) Logical Tape 8 - Output tape for listing of variable coefficients used in problem solution--optional, under control of Sense Switch 3 (FMS B1)
d) Logical Tape 7 - Used in off-line punching of any binary decks which have been compiled (FMS B4).

3. Sense switches

Considerable flexibility has been built into the program through the use of sense switches which allow several modifications to be made to the input or output formats either before or during problem execution. All sense switches are normally up. Down sense switches are not required unless special operation of the program is required.

SENSE SWITCH 1

When in the down position, this switch causes every line of output to be written on Tape 6 for off-line printing. If in the up position, only a fraction of the total output will be printed, this fraction depending on the value of KPRINT supplied as input data on input data card 3.

Example: N = 201, KPRINT = 2.

SS1 DOWN - every mesh point will be printed for a total of 201 points.
SS1 UP - only every second mesh point will be printed for a total of 100 points.

SENSE SWITCH 2

By placing Sense Switch 2 down, the computer will be instructed to pause prior to the execution of each problem. This will allow the operator time to examine any on-line printout which has occurred during the execution of the preceding problem. This pause will give the operator time to make any further sense switch adjustments required in the solution of the forthcoming problem. At the same time, the pause will serve to indicate that one problem has been finished and another is about to be initiated. If a pause does occur through the use of this sense switch, the computer will so indicate via an on-line printout which will state that SS2 has been used to temporarily halt the program and that the next problem may be begun by hitting START. Any pauses occurring during execution which are not accompanied by this on-line printout should not be attributed to SS2 even though it may be in the on position at the time.

If SS2 is in the off position, the program will execute succeeding problems without pausing between them.

SENSE SWITCH 3

The use of SS3 in the down position enables the operator to obtain a detailed printout of all variable coefficients employed in problem solution, on FMS Tape B1 (Logical Tape 8). Should the operator choose not to print out the variable coefficients, he would leave SS3 up.

SENSE SWITCH 4

Through SS4, the operator can obtain a summary of the TC(N) iteration on FMS Tape A3 (Logical Tape 6) for off-line printing. This summary gives values of TC(N), H1(1) and any other pertinent quantities at the first and last mesh points for each step of the TC(N) iteration. Such a summary shows at a glance the conditions existing at the beginning and end of the heat exchanger and enables the operator to study the effectiveness of the TC(N) iteration procedure. Should SS4 be off, the problem will still be solved in the same manner, but the TC(N) summary will not be included as part of the output. SS4 in the down position also causes the computer to write on FMS Tape A3 the flow rates occurring in problems of constant pressure drop. If SS4 is up in a problem of this nature, the flow rates will still be computed but will not be written on tape.

SENSE SWITCH 5

Sense Switch 5 performs exactly the same function as SS4 except that it causes the TC(N) summary to be printed directly on-line as the problem is being executed rather than on Tape FMS A3 for off-line printing. This can be an extremely valuable tool to the operator when he is running a series of problems for the first time as it presents him with a clear, concise picture of exactly how the solution is progressing and provides him with sufficient information to decide whether or not the problem is executing properly. Should the on-line printout indicate that an error is present, the operator will be able to halt the execution and/or take any steps necessary to eliminate the trouble. This should help to eliminate the chance of using large amounts of computer time.

SS5 has also been found helpful when one is running a long problem as it allows the operator to check the results periodically throughout the problem execution and may possibly enable him to terminate the execution sooner than he had originally anticipated.

SENSE SWITCH 6

This sense switch allows the operator to skip to the next problem, if it is placed in the down position. Should the on-line printout indicate that the execution is not proceeding properly or if for any other reason it is felt that the remainder of the execution should be deleted, the next problem can be begun by means of SS6. It is advisable to use SS2 in conjunction

with SS6 because otherwise one would run the risk of skipping the new problem as well, if the initial calculations of the new problem were performed before SS6 could be returned to the off position. Thus the proper procedure to skip the remainder of a problem would be to place SS2 down and then SS6 down. This would cause a pause in execution and the on-line printout would indicate that the rest of the solution had been dispensed with. To restart the next problem, SS6 would then be returned to the off position following which the START button should be depressed causing the execution to be resumed.

D. Program Output

The output can vary considerably in both content and appearance depending upon both the input data and the use of sense switches. Nevertheless there are certain features of the output that remain unchanged from problem to problem. The first output sheet of each problem contains the following:

a) heading describing the type of problem.
b) listing of input data supplied to program by means of data cards 1-9.
c) initial slope of TC(N) versus TC(1) line as calculated (Refer to Section III).

The second page may or may not contain a summary of the TC(N) iteration depending upon the setting of Sense Switch 4. Following this data is the calculation of the various parameters as function of z. (See attached computer output.)

In addition, output may be determined on Logical Tape 8 for the evaluation of the coefficients. This output is monitored by Sense Switch 3. It is recommended that this output not be included in regular operation because of excessive tape writing time.

```
CONSTANT FLOW FREEZE OUT HEAT EXCHANGER
PROBLEM    1
INPUT DATA
TC1N=0.3930E 03  TC(1)=0.5350E 03
DELT=0.4000E-01  TMAX=0.1200E-00
N=  201  KPRINT=    5  IPR=    1  IPRCC=    6
TOL=0.5000E 00  TOLP=1.0000E-02
CGO=  0.248000  B3= -0.        CCO=  0.248000  B4= -0.        PRO=  0.720000  B5= -0.
RI=  0.005300  RO=  0.007810  XTO=  1.333300  XLO=  1.333330  TNT=176.000000
EL=  4.080000  APLO=  0.432000  CSAO=  0.001020  B1=  0.430000  B2= -0.390000
RHO1= 15.500000  FK1=  0.150000  RHO2= 60.000000  FK2=  0.160000  BF=  1.000000
FLOW=0.1092E 03  COOL=0.1121E 03
 INITIAL SLOPE = .12911E-00
```

SUMMARY OF TC(N) ITERATION

KA = 1 VALUES AT K=1,N (FOR CAPTIONS SEE BELOW)

0.	568.000	544.714	535.000	2.4800E-04	0.	12960.0	7.8100E-03	6.046E-03	9.970E 01	0.017	0.
1.000	330.926	310.632	302.834	2.2059E-07	0.	11320.7	7.8100E-03	1.094E-09	3.739E-02	21.581	0.

KA = 3 VALUES AT K=1,N (FOR CAPTIONS SEE BELOW)

0.	568.000	552.912	546.641	2.4800E-04	0.	12960.0	7.8100E-03	8.227E-03	1.168E 02	0.017	0.
1.000	411.089	397.860	392.618	1.0751E-05	0.	11121.8	7.8100E-03	3.285E-06	2.282E 00	1.310	0.

TIME= 0. HOURS

Z	TA	TS	TC	H1	H2	P	R	H1S	H2S	RELH1	REL
0.	568.000	552.912	546.641	2.4800E-04	0.	12960.0	7.8100E-03	8.227E-03	1.168E 02	0.017	0.
0.025	563.542	548.531	542.299	2.4800E-04	0.	12909.3	7.8100E-03	7.013E-03	1.078E 02	0.020	0.
0.050	559.118	544.182	537.989	2.4800E-04	0.	12858.9	7.8100E-03	5.970E-03	9.945E 01	0.024	0.
0.075	554.728	539.867	533.713	2.4800E-04	0.	12808.7	7.8100E-03	5.076E-03	9.168E 01	0.028	0.
0.100	550.371	535.584	529.469	2.4800E-04	0.	12758.7	7.8100E-03	4.309E-03	8.447E 01	0.033	0.
0.125	546.047	531.334	525.257	2.4800E-04	0.	12709.0	7.8100E-03	3.653E-03	7.776E 01	0.038	0.
0.150	541.756	527.116	521.077	2.4800E-04	0.	12659.6	7.8100E-03	3.092E-03	7.153E 01	0.045	0.
0.175	537.498	522.930	516.928	2.4800E-04	0.	12610.4	7.8100E-03	2.614E-03	6.576E 01	0.053	0.
0.200	533.272	518.776	512.811	2.4800E-04	0.	12561.4	7.8100E-03	2.207E-03	6.040E 01	0.062	0.
0.225	529.077	514.653	508.726	2.4800E-04	0.	12512.7	7.8100E-03	1.860E-03	5.544E 01	0.073	0.
0.250	524.914	510.562	504.670	2.4800E-04	0.	12464.3	7.8100E-03	1.565E-03	5.085E 01	0.086	0.
0.275	520.783	506.501	500.646	2.4800E-04	0.	12416.1	7.8100E-03	1.316E-03	4.661E 01	0.102	0.
0.300	516.682	502.470	496.651	2.4800E-04	0.	12368.1	7.8100E-03	1.104E-03	4.268E 01	0.121	0.
0.325	512.613	498.470	492.687	2.4800E-04	0.	12320.3	7.8100E-03	9.250E-04	3.906E 01	0.143	0.
0.350	508.574	494.500	488.752	2.4800E-04	0.	12272.8	7.8100E-03	7.738E-04	3.571E 01	0.170	0.
0.375	504.565	490.560	484.847	2.4800E-04	0.	12225.6	7.8100E-03	6.463E-04	3.263E 01	0.202	0.
0.400	500.586	486.649	480.971	2.4800E-04	0.	12178.6	7.8100E-03	5.390E-04	2.978E 01	0.241	0.
0.425	496.636	482.767	477.124	2.4800E-04	0.	12131.8	7.8100E-03	4.488E-04	2.717E 01	0.287	0.
0.450	492.716	478.914	473.306	2.4800E-04	0.	12085.3	7.8100E-03	3.730E-04	2.476E 01	0.343	0.
0.475	488.826	475.090	469.516	2.4800E-04	0.	12039.0	7.8100E-03	3.096E-04	2.254E 01	0.410	0.
0.500	484.964	471.294	465.754	2.4800E-04	0.	11992.9	7.8100E-03	2.565E-04	2.051E 01	0.491	0.
0.525	481.135	467.571	462.007	2.4458E-04	0.	11947.1	7.8100E-03	2.127E-04	1.867E 01	0.581	0.
0.550	477.342	463.835	458.246	2.3121E-04	0.	11901.5	7.8100E-03	1.757E-04	1.696E 01	0.660	0.
0.575	473.570	460.079	454.476	2.1202E-04	0.	11856.1	7.8100E-03	1.445E-04	1.537E 01	0.728	0.
0.600	469.809	456.313	450.705	1.9018E-04	0.	11811.0	7.8100E-03	1.184E-04	1.391E 01	0.788	0.
0.625	466.055	452.544	446.938	1.6775E-04	0.	11766.1	7.8100E-03	9.665E-05	1.256E 01	0.840	0.
0.650	462.307	448.777	443.179	1.4601E-04	0.	11721.4	7.8100E-03	7.865E-05	1.132E 01	0.887	0.
0.675	458.564	445.017	439.432	1.2572E-04	0.	11677.0	7.8100E-03	6.379E-05	1.019E 01	0.930	0.
0.700	454.827	441.269	435.701	1.0729E-04	0.	11632.8	7.8100E-03	5.159E-05	9.153E 00	0.968	0.
0.725	451.097	437.535	431.987	9.0876E-05	0.	11588.9	7.8100E-03	4.161E-05	8.213E 00	1.003	0.
0.750	447.378	433.818	428.292	7.6471E-05	0.	11545.2	7.8100E-03	3.366E-05	7.359E 00	1.036	0.
0.775	443.670	430.120	424.618	6.3984E-05	0.	11501.8	7.8100E-03	2.684E-05	6.585E 00	1.067	0.
0.800	439.975	426.442	420.967	5.3267E-05	0.	11458.6	7.8100E-03	2.147E-05	5.884E 00	1.097	0.
0.825	436.297	422.786	417.338	4.4147E-05	0.	11415.6	7.8100E-03	1.719E-05	5.251E 00	1.125	0.
0.850	432.635	419.153	413.733	3.6439E-05	0.	11372.9	7.8100E-03	1.363E-05	4.680E 00	1.152	0.
0.875	428.992	415.543	410.152	2.9965E-05	0.	11330.4	7.8100E-03	1.082E-05	4.165E 00	1.179	0.
0.900	425.368	411.958	406.596	2.4557E-05	0.	11288.2	7.8100E-03	8.569E-06	3.702E 00	1.205	0.
0.925	421.765	408.396	403.064	2.0061E-05	0.	11246.3	7.8100E-03	6.768E-06	3.287E 00	1.231	0.
0.950	418.184	404.859	399.557	1.6340E-05	0.	11204.5	7.8100E-03	5.332E-06	2.914E 00	1.257	0.
0.975	414.625	401.347	396.075	1.3271E-05	0.	11163.1	7.8100E-03	4.191E-06	2.580E 00	1.283	0.
1.000	411.089	397.860	392.618	1.0751E-05	0.	11121.8	7.8100E-03	3.285E-06	2.282E 00	1.310	0.

AIR HEAT LOSS= 0.4281991E 04 COOLANT HEAT GAIN= 0.4281983E 04

PRESSURE DROP= 0.18382E 04 PSF= 0.12765E 02 PSI

SUMMARY OF TC(N) ITERATION

KA = 2 VALUES AT K=1,N (FOR CAPTIONS SEE BELOW)

0.	568.000	552.947	546.691	2.4800E-04	0.	12960.0	7.8100E-03	8.238E-03	1.168E 02	0.017	0.
1.000	414.456	401.379	395.958	1.3010E-05	0.	11045.3	7.8243E-03	4.245E-06	2.611E 00	1.259	0.

KA = 3 VALUES AT K=1,N (FOR CAPTIONS SEE BELOW)

0.	568.000	552.678	546.309	2.4800E-04	0.	12960.0	7.8100E-03	8.156E-03	1.162E 02	0.017	0.
1.000	411.743	398.434	392.924	1.1147E-05	0.	11052.4	7.8243E-03	3.444E-06	2.345E 00	1.292	0.

TIME= 0.40000E-01 HOURS

Z	TA	TS	TC	H1	H2	P	R	H1S	H2S	RELH1	RELH2
0.	568.000	552.678	546.309	2.4800E-04	0.	12960.0	7.8100E-03	8.156E-03	1.162E 02	0.017	0.
0.025	563.473	548.228	541.899	2.4800E-04	0.	12909.3	7.8100E-03	6.934E-03	1.072E 02	0.020	0.
0.050	558.980	543.812	537.523	2.4800E-04	0.	12858.9	7.8100E-03	5.887E-03	9.879E 01	0.024	0.
0.075	554.522	539.430	533.180	2.4800E-04	0.	12808.7	7.8100E-03	4.990E-03	9.089E 01	0.028	0.
0.100	550.098	535.081	528.870	2.4800E-04	0.	12758.8	7.8100E-03	4.224E-03	8.361E 01	0.033	0.
0.125	545.708	530.766	524.594	2.4800E-04	0.	12709.1	7.8100E-03	3.571E-03	7.686E 01	0.039	0.
0.150	541.351	526.483	520.349	2.4800E-04	0.	12659.7	7.8100E-03	3.014E-03	7.059E 01	0.046	0.
0.175	537.027	522.233	516.138	2.4800E-04	0.	12610.6	7.8100E-03	2.540E-03	6.479E 01	0.054	0.
0.200	532.737	518.015	511.958	2.4800E-04	0.	12561.7	7.8100E-03	2.137E-03	5.942E 01	0.063	0.
0.225	528.478	513.829	507.810	2.4800E-04	0.	12513.1	7.8100E-03	1.796E-03	5.445E 01	0.075	0.
0.250	524.252	509.675	503.693	2.4800E-04	0.	12464.7	7.8100E-03	1.506E-03	4.986E 01	0.089	0.
0.275	520.058	505.553	499.607	2.4800E-04	0.	12416.5	7.8100E-03	1.262E-03	4.562E 01	0.105	0.
0.300	515.895	501.461	495.552	2.4800E-04	0.	12368.6	7.8100E-03	1.055E-03	4.170E 01	0.125	0.
0.325	511.764	497.401	491.528	2.4800E-04	0.	12321.0	7.8100E-03	8.808E-04	3.809E 01	0.149	0.
0.350	507.664	493.371	487.534	2.4800E-04	0.	12273.6	7.8100E-03	7.342E-04	3.476E 01	0.177	0.
0.375	503.595	489.371	483.570	2.4800E-04	0.	12226.4	7.8100E-03	6.110E-04	3.170E 01	0.211	0.
0.400	499.556	485.401	479.636	2.4800E-04	0.	12179.5	7.8100E-03	5.077E-04	2.888E 01	0.252	0.
0.425	495.548	481.461	475.731	2.4800E-04	0.	12132.9	7.8100E-03	4.211E-04	2.629E 01	0.302	0.
0.450	491.570	477.551	471.856	2.4800E-04	0.	12086.5	7.8100E-03	3.487E-04	2.391E 01	0.362	0.
0.475	487.621	473.670	468.009	2.4800E-04	0.	12040.3	7.8100E-03	2.882E-04	2.173E 01	0.434	0.
0.500	483.702	469.834	464.192	2.4795E-04	0.	11994.4	7.8100E-03	2.380E-04	1.974E 01	0.522	0.
0.525	479.870	466.869	460.424	2.4096E-04	0.	11947.7	7.8743E-03	2.051E-04	1.832E 01	0.609	0.
0.550	476.206	463.785	456.787	2.2710E-04	0.	11898.4	7.9217E-03	1.753E-04	1.694E 01	0.686	0.
0.575	472.637	460.488	453.219	2.0883E-04	0.	11847.4	7.9454E-03	1.478E-04	1.556E 01	0.751	0.
0.600	469.111	457.045	449.683	1.8823E-04	0.	11795.9	7.9536E-03	1.233E-04	1.421E 01	0.807	0.
0.625	465.599	453.497	446.157	1.6694E-04	0.	11744.3	7.9518E-03	1.021E-04	1.292E 01	0.855	0.
0.650	462.082	449.876	442.628	1.4610E-04	0.	11693.2	7.9440E-03	8.385E-05	1.171E 01	0.896	0.
0.675	458.550	446.204	439.090	1.2647E-04	0.	11642.7	7.9329E-03	6.846E-05	1.058E 01	0.933	0.
0.700	454.998	442.498	435.540	1.0845E-04	0.	11593.1	7.9202E-03	5.559E-05	9.526E 00	0.966	0.
0.725	451.425	438.772	431.981	9.2263E-05	0.	11544.3	7.9072E-03	4.493E-05	8.559E 00	0.996	0.
0.750	447.835	435.038	428.412	7.7945E-05	0.	11496.4	7.8946E-03	3.615E-05	7.673E 00	1.025	0.
0.775	444.229	431.303	424.838	6.5446E-05	0.	11449.2	7.8829E-03	2.898E-05	6.864E 00	1.052	0.
0.800	440.612	427.576	421.261	5.4652E-05	0.	11402.8	7.8722E-03	2.315E-05	6.130E 00	1.079	0.
0.825	436.988	423.861	417.685	4.5413E-05	0.	11357.1	7.8627E-03	1.843E-05	5.465E 00	1.105	0.
0.850	433.361	420.162	414.114	3.7568E-05	0.	11312.0	7.8544E-03	1.462E-05	4.864E 00	1.131	0.
0.875	429.736	416.483	410.549	3.0950E-05	0.	11267.5	7.8471E-03	1.157E-05	4.322E 00	1.157	0.
0.900	426.116	412.825	406.995	2.5401E-05	0.	11223.6	7.8409E-03	9.130E-06	3.835E 00	1.183	0.
0.925	422.504	409.190	403.454	2.0773E-05	0.	11180.1	7.8356E-03	7.184E-06	3.399E 00	1.209	0.
0.950	418.903	405.580	399.927	1.6932E-05	0.	11137.1	7.8312E-03	5.638E-06	3.007E 00	1.236	0.
0.975	415.315	401.994	396.417	1.3759E-05	0.	11094.5	7.8274E-03	4.412E-06	2.657E 00	1.264	0.
1.000	411.743	398.434	392.924	1.1147E-05	0.	11052.4	7.8243E-03	3.444E-06	2.345E 00	1.292	0.

AIR HEAT LOSS= 0.4264214E 04 COOLANT HEAT GAIN= 0.4264207E 04

PRESSURE DROP= 0.19076E 04 PSF= 0.13248E 02 PSI

V A CORRELATION OF PREDICTED AND EXPERIMENTAL HEAT EXCHANGER PERFORMANCE

This section is devoted to a comparison of the predicted performance of the freeze-out exchanger with the experimental results. The predicted performance has been calculated by hand calculations in Appendix 11, a constant heat transfer analysis of Appendix 12, and the general heat transfer analysis presented in this appendix.

Test V-5 figured heavily in these comparisons since frost thickness profile data was available at three time points during the progress of the test. However, in addition, pressure drop and flow comparisons were also applied to tests F-3, E-2 and V-7, and heat transfer comparisons were made with tests F-3 and E-2.

A. Effect of Water Frost Thermal Conductivity on Computer Results

The results of Appendix 6 indicate that for the temperature and frost density conditions of Test V-5, we should expect a water frost thermal conductivity of the order of .067 Btu/hr-ft-^{o}R. The analysis of Appendix 6 is, however, somewhat qualitative and much of the experimental data on frost thermal conductivities tends to fall higher than that predicted by the analysis. Therefore, we have chosen values of water frost thermal conductivity of .067, .15, and .30 Btu/hr-ft-^{o}R as inputs to the computer program. By comparing the computer results with test data, we are able to determine the importance of thermal conductivity and establish an optimum value for subsequent calculations. It should be noted here that a water frost density of 15.5 pounds per cubic foot, which is in agreement with the correlation of Appendix 6, has been used in all the computer calculations discussed in this Appendix.

The results shown in Figures 1 and 2 indicate that increasing the thermal conductivity of the frost increases the peak frost thickness and accelerates the rate of pressure rise predicted by the computer solution. The frost thickness profiles of Figure 2 indicate that a choice of water frost thermal conductivity of .15 Btu/hr-ft-^{o}R seems to agree with the experimental data better than the purely analytical estimate of .067. Comparisons made at other test times have agreed with this trend. The pressure drop data is somewhat less clear cut, even though water frost thermal conductivity has an appreciable effect on the predicted pressure drop. However, the effect of thermal conductivities is to cause the high values of thermal conductivity to be in slightly better agreement with the experimental result near the beginning of the test, whereas the lower values of thermal conductivity tend to be in much better agreement near "plug-up." Here, a value of .15 would seem to be a reasonable "middle-of-the-road" choice.

It was not possible to get a valid comparison between experimental and analytical heat transfer results for Test V-5 in that the relatively small change in the experimental heat transfer was obscured by an oscillation in the coolant inlet temperature in this test. However, many of our preliminary computer checks applied to other test runs had indicated that a thermal

conductivity of .15 Btu/hr-ft-^{o}R resulted in somewhat better agreement with experimental heat transfer than did a thermal conductivity of .067.

On the basis of these results, we have concluded that a value of .15 Btu/hr-ft-^{o}R would be the best input value for water frost thermal conductivity for our computer studies.

B. Comparison of Analytical Methods for Predicting Pressure Drop and Frost Distribution

Figure 3 presents a comparison of frost thickness profiles computed by three analytical techniques. These three methods are:

a) the variable heat transfer computer program, which is the subject of this Appendix;
b) the constant heat transfer simplified computer program, which is discussed in Appendix 12;
c) the hand-calculation method, which was discussed in Appendix 11.

The results indicate that the variable heat transfer computer program results in a more representative distribution of frost than does the constant heat transfer program. The difference is most apparent at the upstream end of the frost layer. Here, the constant heat transfer program predicts a very steep increase in frost, much deeper, in fact, than is the case experimentally. The variable heat transfer program, however, which includes a more realistic evaluation of the changes in surface temperature due to the thermal resistance of the frost, results in an increase which is very similar to the experimental data. The variable heat transfer program also predicts the peak frost thicknesses more accurately than the constant heat transfer program. It may be noted that all analytical techniques predict the start of frosting somewhat in advance of the experimental data. The significance of this is not completely clear, nor is it felt to be especially significant. It may, in fact, be due to the coolant inlet temperature input to the computer solutions being slightly lower than the true experimental value.

Figure 3 also presents the uniform frost thickness profile to be used for the hand-calculation method. Here, it is assumed that all the frost is distributed uniformly in a hypothetical frosted length. The beginning of this frosted length is taken to be the point at which the wall reaches saturation. The end of the effective frosted length is taken to be the point at which the air stream saturation humidity drops to 10% of the initial humidity.

Figure 4 presents a comparison of the pressure drops predicted by these three techniques with the experimental data. The constant heat transfer program which results in the greater peak frost thickness also results in the more accelerated rate of pressure rise. The variable heat transfer program and the hand-calculation method are in surprisingly close agreement. It is felt that, in general, these two methods would not produce

such similar results considering the wide differences in calculation techniques.

C. Additional Pressure Drop and Flow Comparisons

Figure 5 presents comparisons between the variable heat transfer computer solution and experimental data for tests F-3, V-5, V-7 and E-2. Tests F-3 and V-5 are constant flow tests, in which water frost is the only contaminant. Test V-7 is a constant flow test, in which carbon dioxide frost is the major contaminant. Test E-2 is a constant pressure drop test, having initial conditions very similar to those of Test F-3. It should be noted that the results for tests F-3, V-5 and E-2 refer to over-all heat exchanger performance. The results for V-7 apply to the last quarter of the test heat exchanger.

The results show excellent agreement between analysis and experimental data for test F-3.

As discussed previously, in test V-5 the analytical result tends to underpredict the pressure drop at the beginning of the test and overpredict the pressure drop near plug-up. This effect seems to be somewhat characteristic of the comparison between experiment and analysis, although especially pronounced in test V-5. The heat exchanger air flow results for test E-2, constant pressure test, appear to be in reasonably good agreement. Here, too, we note that the analysis tends to underestimate the effects of deposit formation near the beginning of the test. This discrepancy might arise from a number of causes. Our experimental measurements of frost density have indicated that frost density may increase with time, whereas the computer solution assumes a constant frost density. Effects due to surface roughness and non-uniform circumferential distribution of frost on the heat exchanger tubes may also play a part. It should also be noted that the state of the art on friction factor data for tube banks of extremely small pitch to diameter ratio, as is the case in a frosted heat exchanger, are really not too well defined. In view of all these possible complications, it is felt that the agreement between analysis and experiment is certainly as good as could reasonably be expected.

For test V-7, the agreement between analysis and experiment seems to be quite good throughout the majority of the test. However, as the heat exchanger approaches plug-up, the analytical pressure drop appears to lag behind the experimental value. The shape of the curves is very similar, and it may be noted that the discrepancy shown could easily result from an error in frost density of about 10-15%.

D. Heat Transfer Results

It has been generally difficult to obtain valid comparisons between experimental and analytical heat transfer effects; since in most of our tests, the reduction in heat transfer due to deposit formation has been extremely small and almost within the range of experimental error.

Figure 6 presents comparisons of predicted and experimental coolant temperature rise for tests F-3 and E-2. The coolant temperature rise is, of course, directly proportional to the heat transfer in the test heat exchanger. The computer solution when applied to test F-3 indicates that the coolant temperature rise should drop about four degrees during the progress of the test. The experimental data is roughly in accordance with the computer predictions, particularly if the initial two points, which may be influenced by the initial heat exchanger cool-down, are disregarded. The agreement between experiment and analysis for test E-2 appears to be quite good. In this test, we note that the over-all heat transfer changes quite substantially during the course of the test since test E-2 is a constant pressure drop test, in which the air flow decreases as deposits accumulate. A major portion of the loss in heat transfer is directly related to the reduction in air flow.

E. Estimated Accuracy of Computer Solution

In quoting estimated accuracies for the computer program, a tolerance band should be applied to the time scale as well as the normal dependent variables such as pressure drop or heat transfer. This dual tolerance stems from the method of calculation which is essentially divided into two areas: (1) the calculation of frost volume ingested, and (2) the determination of the effects of a given frost volume on heat exchanger flow and heat transfer characteristics. The calculation of frost volume ingested depends on the use of frost density values, which are subject to prediction error, as well as known inputs of time, air-flow and contaminate concentration. Errors due to frost density can be reasonably thought to be equivalent to errors in establishing the true deposition time. In going from frost volume to changes in pressure drop or heat transfer, the calculation procedures utilize many factors which are subject to some error, such as the model for frost distribution, data on frost friction factor, data on frost thermal conductivity and the assumption that the frost is uniformly distributed around the heat exchanger tubes in a circumferential direction. Errors associated with any of these factors should logically be applied against the dependent variables such as heat transfer, flow or pressure drop.

We would expect this density information to have a tolerance of approximately $\pm$ 20%. This estimate is reasonably well substantiated for water frost where a fair amount of data is available. However, for CO_2 frost where very little data is available, the tolerance has not been well established. However, our best judgment is that a tolerance of $\pm$ 20% should be applied to the time scale for all calculation methods to account for errors in frost density.

The errors intendent in computing pressure drop and heat transfer with the computer solution should be somewhat greater than the tolerances associated with the heat transfer and friction factor data available for the configurations under consideration. This additional tolerance results from factors such as the frost distribution and the surface roughness effects of the frost layer. In general, we would expect the over-all error to be in the neighborhood of $\pm$ 20%.

It must be pointed out that the above estimates of calculation accuracy are in themselves very approximate. Our comparisons with experimental data, while very encouraging and generally within the tolerances mentioned above, have not been sufficient to establish errors in a statistical fashion. We would expect the tolerances associated with the analytical solution to be somewhat a function of the circumstances to which the solution is being applied.

In particular, we might expect the error to be increased in the case when the inlet humidity is high enough to cause the water to deposit as liquid. The computer model assumes all contaminant deposits as a porous solid. The distribution of this frost is established by mass transfer theory, and frost density is estimated from an empirical correlation. In the actual case when the water content is high enough to cause the water to deposit as liquid, the liquid flows downstream and eventually freezes as water ice after it passes into a region below its freezing point. The net result is that both the distribution of frost and the density of the frost are influenced by transition through the liquid phase. We have not applied the computer program extensively to this case, although preliminary comparisons with test V-2, in which some transition through the liquid phase occurred, showed normal agreement between experiment and analysis. We might also note that the high water content pressure drop results (see Figures 2 and 3 of Appendix 9) are not markedly different than the low water content tests when compared on the basis of equal area blockage (or equal water mass addition). For these reasons we feel that the computer program is capable of handling water contents up to about 1% without drastic increases in the calculation tolerances applicable to the low water content situation.

F. Summary

The variable heat transfer computer program appears to be reasonably adequate for predicting the distribution of frost in the test heat exchanger and the effect of frost deposition on heat exchanger performance. The agreement between the computer results and experimental data has been reasonably good for both constant flow and constant pressure drop operation. Also, the comparison appears to be valid for both water frost and carbon dioxide frost.

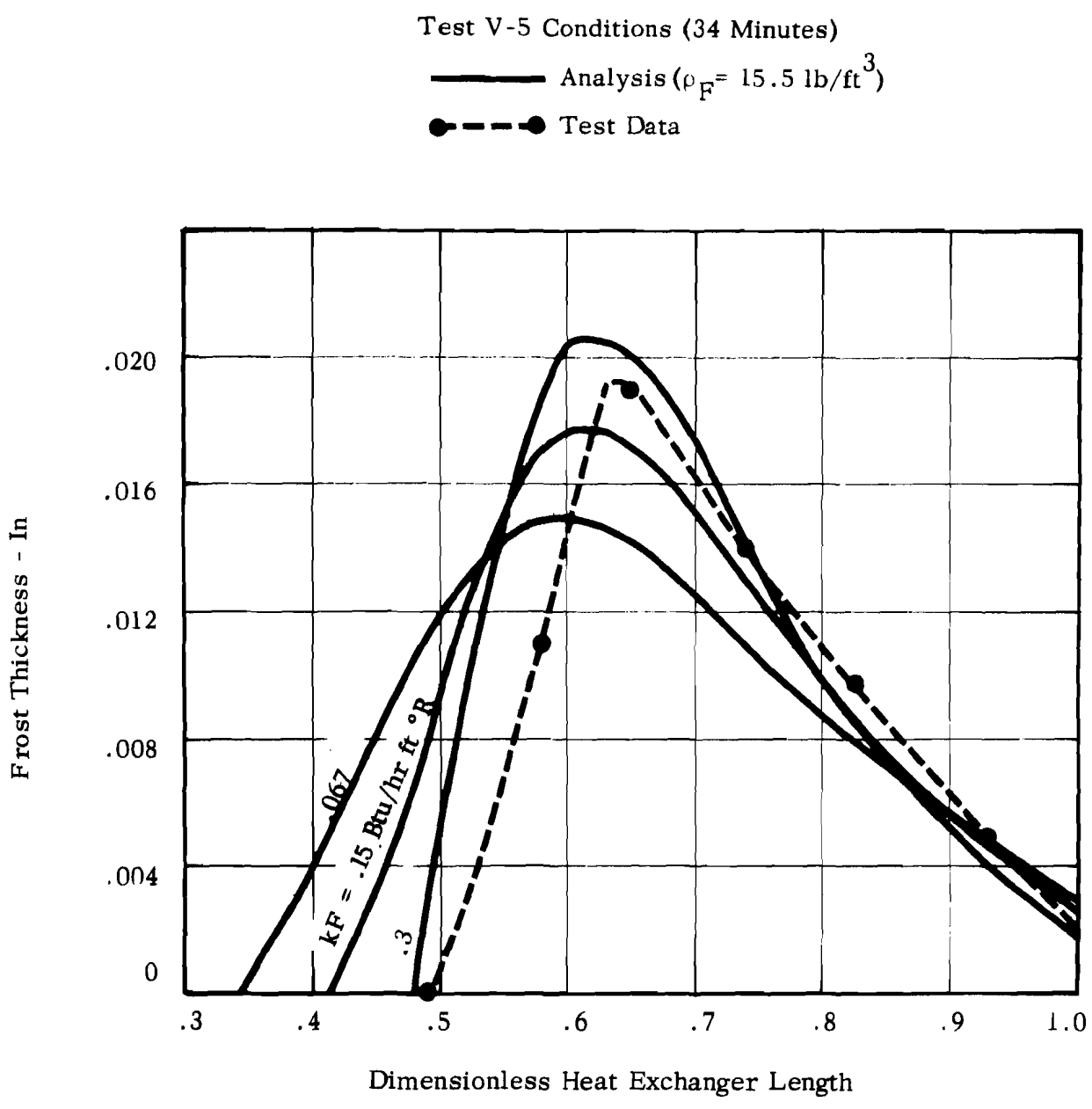

FIGURE 1 FROST THICKNESS PROFILES-EFFECT OF THERMAL CONDUCTIVITY

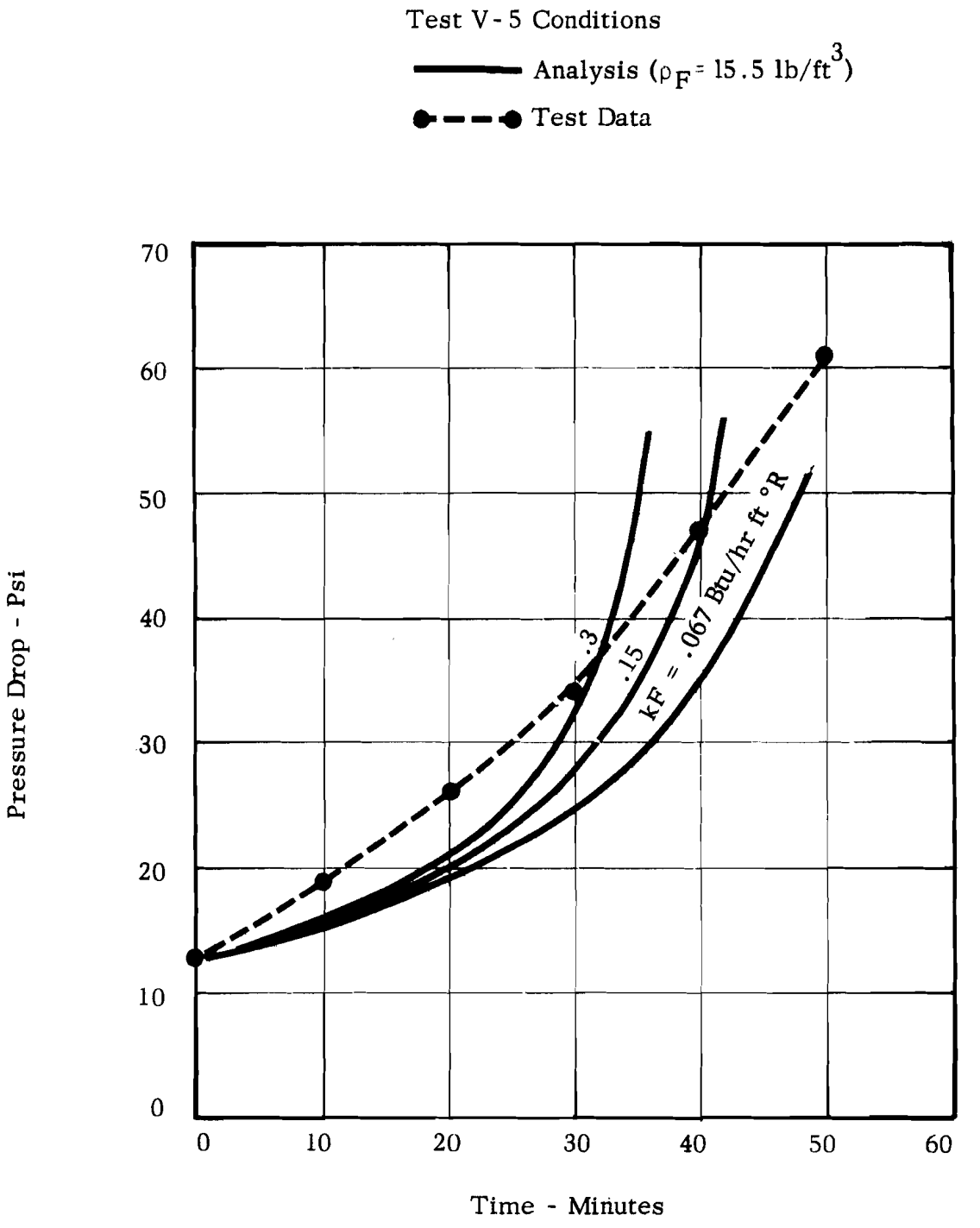

FIGURE 2 HEAT EXCHANGER PRESSURE DROP-EFFECT OF FROST THERMAL CONDUCTIVITY

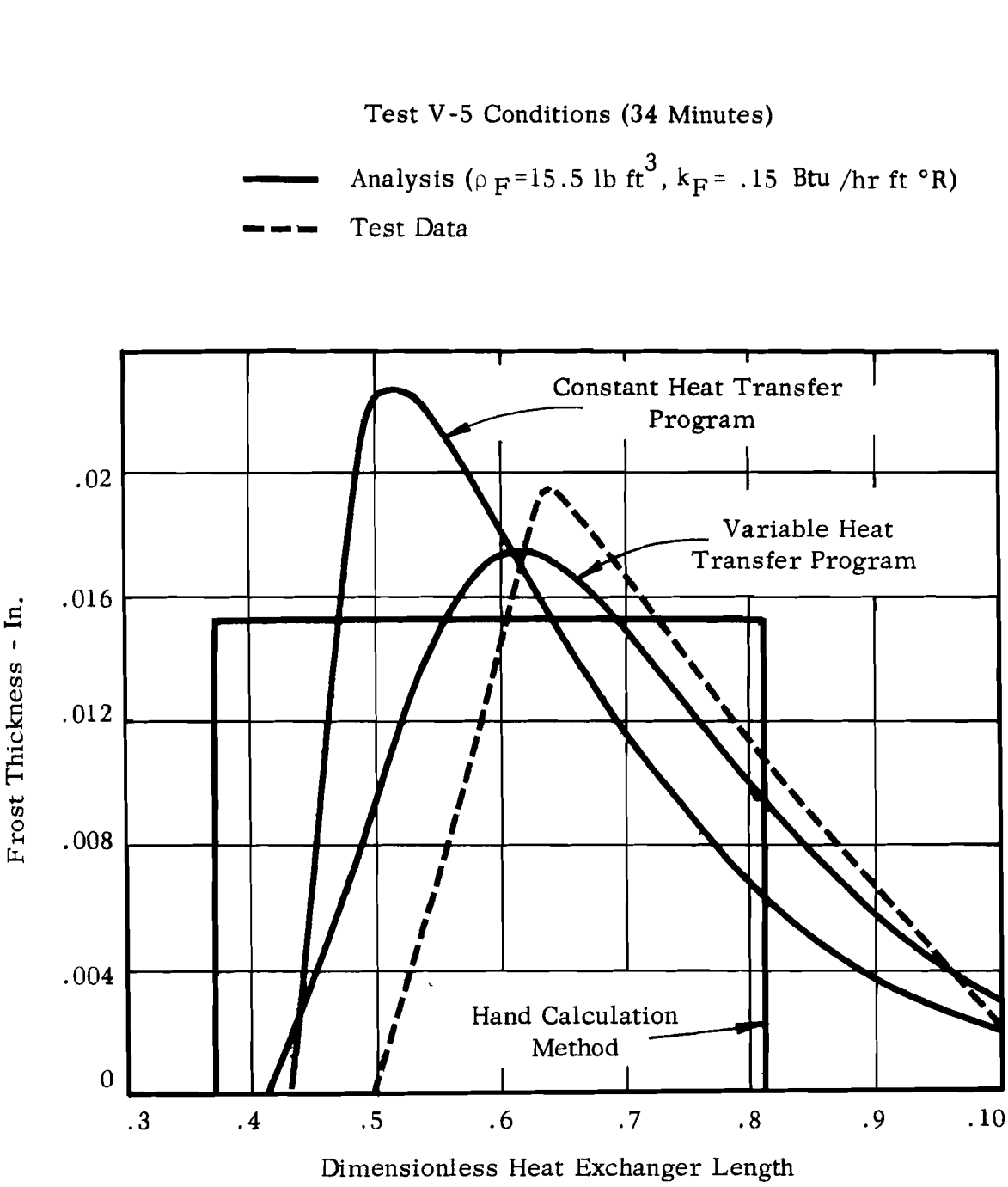

FIGURE 3 FROST THICKNESS PROFILES-COMPARISON OF ANALYTICAL METHODS

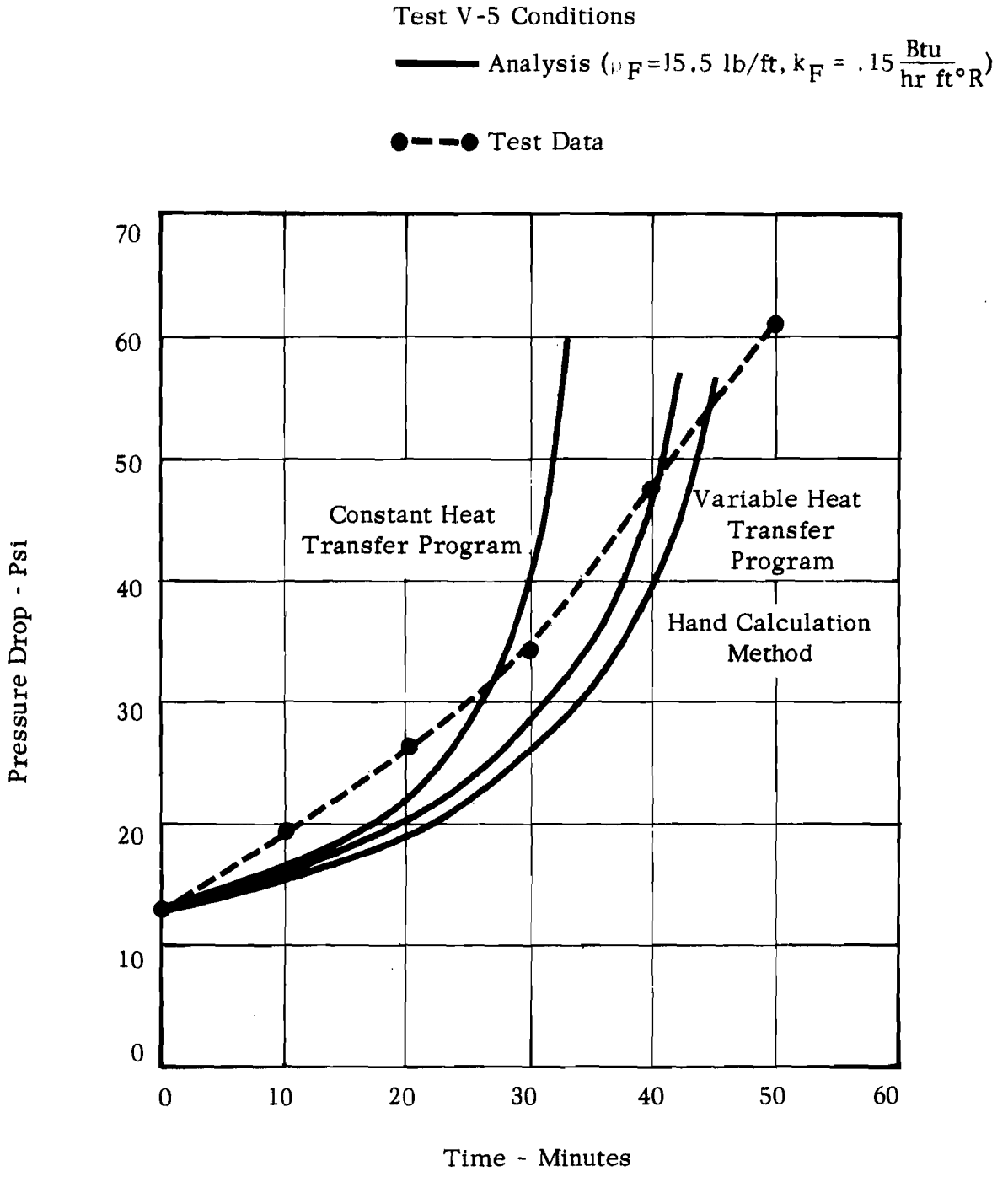

FIGURE 4 HEAT EXCHANGER PRESSURE DROP-COMPARISON OF ANALYTICAL METHODS

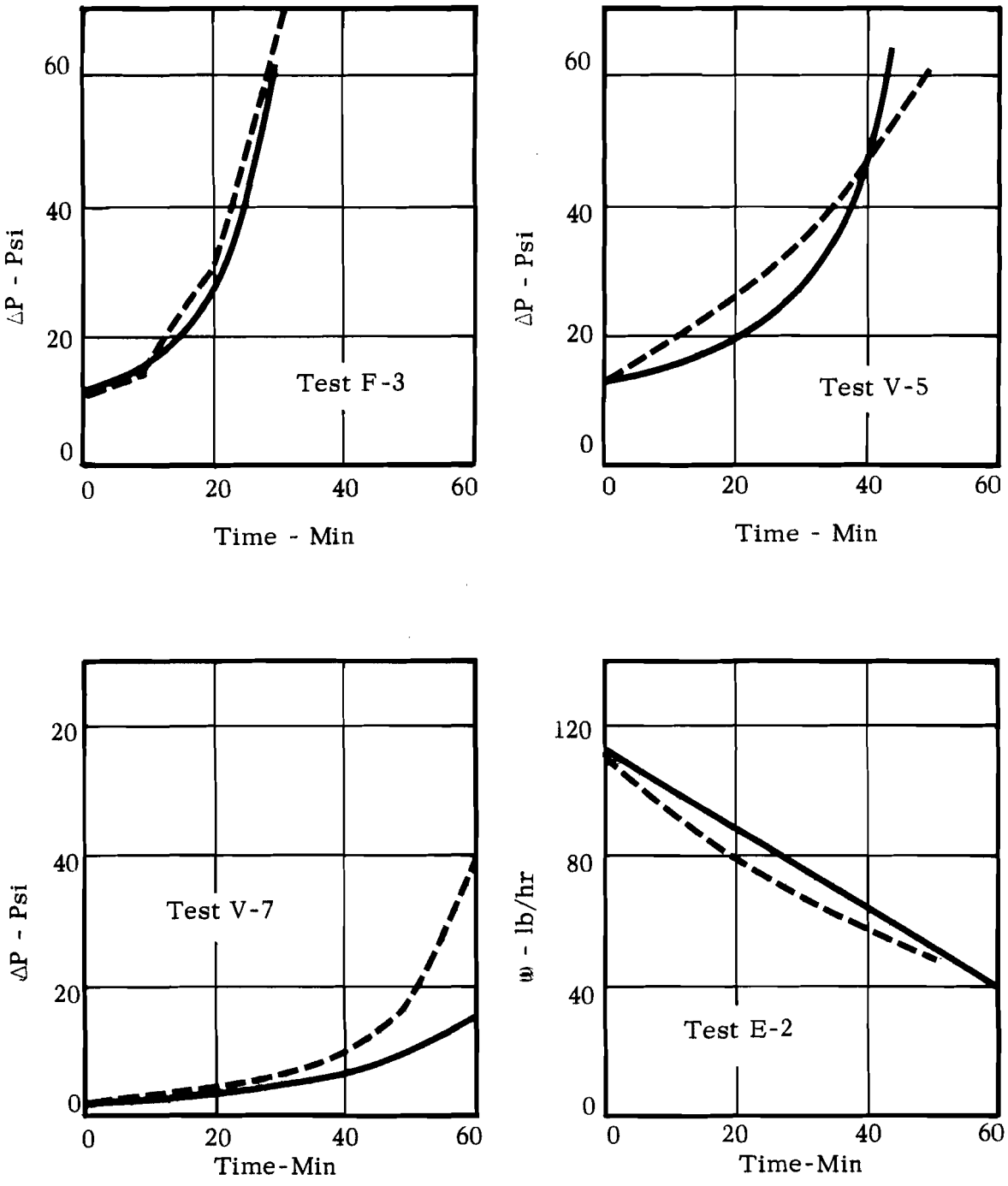

Notes:

- Test Data
- Analysis

1. Tests F-3 and V-5 - Const. Flow - Water Frost
2. Test F-2 - Const. ΔP - Water Frost
3. Test V-7 - Const. Flow - Co_2 Frost
   (V-7 Results Apply To Last 1/4 of H.E.)

FIGURE 5 PRESSURE DROP AND FLOW COMPARISONS

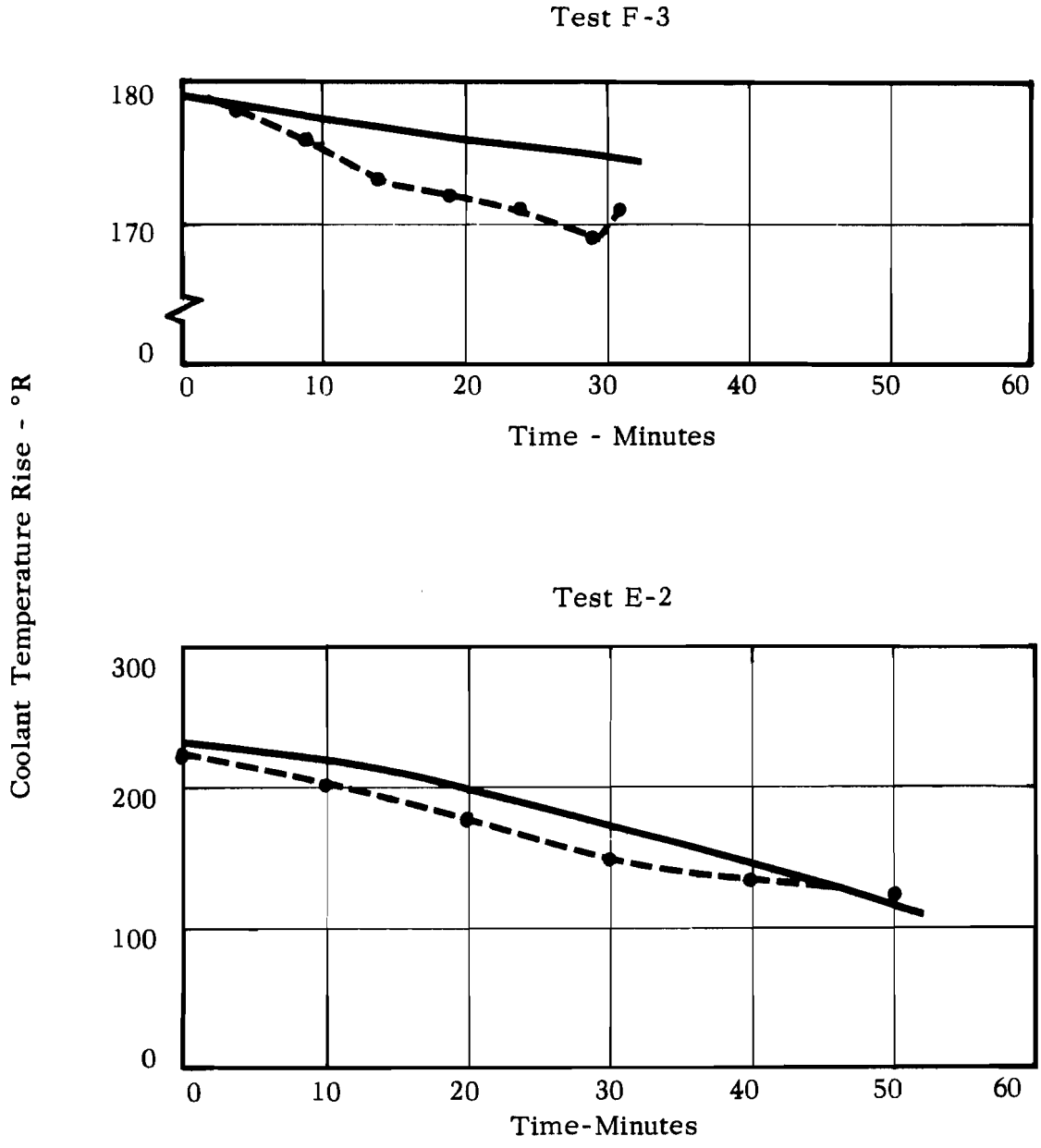

FIGURE 6 HEAT TRANSFER COMPARISONS